Annual reports on
NMR Spectroscopy

Volume 58

ANNUAL REPORTS ON

NMR SPECTROSCOPY

This page is left intentionally blank

ANNUAL REPORTS ON

NMR SPECTROSCOPY

Edited by

G. A. WEBB

Royal Society of Chemistry, Burlington House, London, England

VOLUME 58

Amsterdam • Boston • Heidelberg • London • New York
Oxford • Paris • San Diego • San Francisco • Singapore
Sydney • Tokyo
Academic Press is an Imprint of Elsevier

Academic Press is an imprint of Elsevier
84 Theobald's Road, London WC1X 8RR, UK
Radarweg 29, PO Box 211, 1000 AE Amsterdam, The Netherlands
The Boulevard, Langford Lane, Kidlington, Oxford OX5 1GB, UK
30 Corporate Drive, Suite 400, Burlington, MA 01803, USA
525 B Street, Suite 1900, San Diego, CA 92101-4495, USA

First edition 2006

ISBN-13: 978-0-12-505458-4
ISBN-10: 0-12-505458-0

ISSN: 0066-4103

For information on all Academic Press publications visit our website at books.elsevier.com

Printed and bound in the United Kingdom.

06 07 08 09 10 9 8 7 6 5 4 3 2 1

List of Contributors

I. Ando, *Department of Chemistry and Materials Science, Tokyo Institute of Technology, 2-12-1 Ookayama, Meguro-ku, Tokyo, Japan*

T. Fujiwara, *Institute for Protein Research, Osaka University, 3-2 Yamadaoka, Suita 565-0871, Japan*

B.P. Hills, *Institute of Food Research, Norwich Research Park, Colney, Norwich NR4 7UA, UK*

W. Hu, *Immunology Division, BRI, City of Hope, Duarte Rd. 1500, Duarte, CA 91010, USA*

K. Kamiguchi, *Department of Chemistry and Materials Science, Tokyo Institute of Technology, 2-12-1 Ookayama, Meguro-ku, Tokyo, Japan*

S. Kanesaka, *Department of Chemistry and Materials Science, Tokyo Institute of Technology, 2-12-1 Ookayama, Meguro-ku, Tokyo, Japan*

S. Kim, *Department of Chemistry and Materials Science, Tokyo Institute of Technology, 2-12-1 Ookayama, Meguro-ku, Tokyo, Japan*

S. Kuroki, *Department of Chemistry and Materials Science, Tokyo Institute of Technology, 2-12-1 Ookayama, Meguro-ku, Tokyo, Japan*

M. Matsui, *Department of Chemistry and Materials Science, Tokyo Institute of Technology, 2-12-1 Ookayama, Meguro-ku, Tokyo, Japan*

A. Ramamoorthy, *Biophysics Research Division and Department of Chemistry, University of Michigan, Ann Arbor, MI 48109-1055, USA*

L. Wang, *Computer Science Department, Dartmouth College, Hanover, NH 03755, USA*

A.G. Webb, *Department of Bioengineering, Pennsylvania State University, 315 Hallowell Building, University Park, PA 16802, USA*

Y. Yamane, *Department of Chemistry and Materials Science, Tokyo Institute of Technology, 2-12-1 Ookayama, Meguro-ku, Tokyo, Japan*

This page is left intentionally blank

Preface

It is a pleasure for me to introduce Volume 58 of Annual Reports on NMR, which consists of exciting contributions from five areas of NMR. The volume opens with a report on Advances in Probe Design for Protein NMR by A.G. Webb; following this is an account on Diffusion in Soft Polymer Systems as Approached by Field Gradient NMR by Y. Yamane, S. Kanesaksa, S. Kim, K. Kamiguchi, M. Matsui, S. Kuorki and I. Ando; the question How Far Can the Sensitivity of NMR be Increased? is addressed by T. Fujiwara and A. Ramamoorthy; B.P. Hills covers Applications of Low-Field NMR to Food Science; the final contribution is by W. Hu and L. Wang who report on Residual Dipolar Couplings: Measurements and Applications to Biomolecular Studies.

My sincere thanks go to all of these authors for their timely and interesting accounts.

Royal Society of Chemistry
Burlington House
Piccadilly
London, UK

G. A. WEBB
October 2005

This page is left intentionally blank

Contents

Applications of Low-Field NMR to Food Science
B.P. HILLS

Residual Dipolar Couplings: Measurements and Applications to Biomolecular Studies
WEIDONG HU AND LINCONG WANG

Advances in Probe Design for Protein NMR

A.G. WEBB

Department of Bioengineering, Pennsylvania State University, 315 Hallowell Building, University Park, PA 16802. USA

Advances in pulse sequences and increases in static magnetic fields have played major, and well-documented, roles in extending the experimental boundaries of NMR spectroscopy. An equally important component has been the improvement in NMR-probe technology, particularly in terms of sensitivity: this article summarizes some of these recent improvements. The most important breakthrough has been in cryogenic-probe technology, which has resulted in signal-to-noise improvements of up to a factor-of-four in biological samples. There has also been significant progress in NMR probes which can be used for mass-limited samples, and also for reducing sample heating in samples of high ionic concentration.

ANNUAL REPORTS ON NMR SPECTROSCOPY
VOLUME 58 ISSN 0066 4103
DOI 10.1016/S0066-4103(05)58001-3

1. INTRODUCTION

On the basis of the recent sequencing of a large number of genomes, several ambitious projects have been established, ranging in scope from determination of the three-dimensional (3D) structures of every protein from a single given organism, to the elucidation of the chemical structures of all major pharmaceutical targets in the human body. The success of a number of such genomic sequencing projects presents protein investigators with a substantial challenge in characterizing the large number of gene products that have already been identified, and this number is expected to increase considerably in the future.

X-ray crystallography and nuclear magnetic resonance (NMR) spectroscopy are two of the main experimental techniques used to obtain protein structure information at the atomic level. These methods are particularly powerful since they can be used to determine the 3D shape of the protein, which is known to encode protein function.[1] Major efforts are underway to identify, express and purify, as rapidly and efficiently as possible, proteins that are amenable to NMR spectroscopy, X-ray crystallography and other biophysical techniques.[2,3] The process of structure determination by X-ray crystallography is already relatively streamlined, incorporating robotics for optimizing crystallization conditions, parallel data acquisition from synchrotons, and semi-automated analysis software.[4,5] Although structure determination by NMR spectroscopy is, in comparison, relatively time-consuming and requires ^{15}N, ^{13}C and, for larger proteins ^{2}H, isotopic enrichment, NMR spectroscopy is one of the very few experimental methods that provides detailed insights into both the structure and dynamics of unfolded and partially folded states of proteins.[6–8] High-throughput analyses of protein NMR spectra are an area of intense interest, as described in detail in a recent review.[9]

NMR studies of proteins can be performed in the solution-state (in which the protein is dissolved in an aqueous buffer), solid-state (with the protein sample in powder or micro-/nanocrystalline form), or as samples which are partially aligned (either mechanically aligned by placement between glass plates or *via* preparation in some form of gel). Solution-state NMR spectroscopy has become a standard method for the characterization of the 3D structure and dynamics of proteins that undergo fast molecular reorientations in solution.[10–17] The advantages of solution-state NMR include being able to investigate protein structure in a state closely resembling physiological conditions, to monitor binding processes, to extract dynamic properties from relaxation and chemical exchange data, and to provide important information for crystallization-resistant targets. Although many methodological advances have been made for NMR studies of large proteins and protein complexes using deuterium labeling,[18] transverse relaxation optimized spectroscopy (TROSY)-based pulse sequences,[19] and very high magnetic field strengths,[20] NMR methods are applied mostly to proteins under ~20 kDa molecular weight to avoid problems associated with spectral overlap and broad spectral linewidths. Approaches to higher-molecular-weight proteins include the cloning, expression, and purification of individual constituent domains of the full protein.

Membrane proteins are also increasingly being studied using solution-state NMR, although presenting considerable challenges.[21–27] It should also be noted that solution-state NMR is widely used for the investigation of complex-binding interactions within proteins, as well as for large-scale screening by the pharmaceutical industry of molecular libraries *via* their interaction with proteins.[28–31]

Solid-state NMR spectroscopy is used in cases where proteins do not form crystals for X-ray studies, or are not amenable to solution-state NMR techniques. Examples include many membrane proteins, protein aggregates, and other fibrous proteins such as amyloids.[32] Either magic angle spinning (MAS) experiments[33,34] or static solid-state NMR techniques can be used in such studies. MAS and strong proton decoupling are both necessary to achieve linewidths <1 part-per-million (ppm). Homonuclear couplings can also be removed by selective isotopic labeling.[35–37] Certain membrane proteins have also been studied using techniques involving various methods of fully or partially orienting the sample with respect to magnetic field.[38–42] For example, lipid bilayers can be aligned on glass plates,[38–40] and are prepared either by fusion of unilamellar-reconstituted lipid vesicles with the glass plates, or *via* deposition from organic solvents followed by evaporation and lipid hydration. The membranes form planar bilayers whose normal axis is parallel to the glass plate.[39,40,43–49] Because of the alignment of the membranes and the magnetic field direction, measurements of anisotropic NMR chemical shifts and dipolar couplings can provide information about the peptide orientation relative to the membrane.[50–52]

Although there are many review articles on various aspects of protein NMR, including pulse sequences, data processing, and sample preparation,[53] discussions of the developments in NMR-probe technology, which have contributed significantly to the expansion of the field, are relatively rare. A number of excellent general reviews on NMR-probe design have been published.[54–58] This review article aims to provide information specifically relevant to the design and construction of, as well as to recent developments in, probes for NMR spectroscopy of proteins. Section 2 reviews typical pulse sequences used for solution- and solid-state NMR protein studies, and outlines the requirements imposed by these sequences on the design of the NMR probe. Section 3 describes the basics of radio frequency (RF) coil design in terms of optimizing the B_1 and B_0 homogeneity over the sample, and electrical circuit optimization for multiple-frequency operation. Sections 4–6 concentrate on important recent developments in probe design for protein NMR: Section 4 describes the development and applications of cooled-NMR probes, often referred to as ''cryoprobes'', Section 5 on new designs for coils designed to reduced sample heating during high-power decoupling by minimizing the electric field present in the sample, and Section 6 on small-coil NMR for mass-limited proteins.

2. PROTEIN NMR EXPERIMENTS

In order to design NMR probes for protein studies, it is necessary to consider the requirements of specific pulse sequences in terms of, for example, the required B_1

homogeneity over the sample, decoupling field strength and power-handling requirements, and efficient multiple-frequency channel operation. The following sections review briefly typical pulse sequences used in solution and solid-state protein NMR studies.

2.1. Solution-state pulse sequences

For NMR experiments a protein is typically either single labeled with ^{15}N or double-labeled with ^{13}C and ^{15}N, and can in addition be partially or fully deuterated if the protein is particularly large. The protein is normally dissolved in 95% H_2O/5% D_2O, with the appropriate amount of NaCl (10–200 mM) and a buffer, usually phosphate-based, added to bring the solution to the desired pH value.

A typical set of experiments to obtain structural information on a protein might include an initial two-dimensional (2D) HSQC, followed by 3D HNCO,[59,60] HNCA,[59,60] and/or HN(CO)CA[60,61] sequences to assign backbone resonances, and then assignment of aliphatic side-chain resonances using HCCH–COSY[62–64] and HCCH-TOCSY[65,66] or aromatic side-chain resonances using TOCSY–HCH–COSY. Finally, assignment of nuclear overhauser effect (NOE) cross-peaks and measurement of residual dipolar couplings may be performed in order to improve the local geometry calculations.[67–71] More specialized sequences such as HCA(CO)N or CBCANH may also be used to determine specific structural characteristics. For NMR-based screening of small molecule binding to proteins, experiments are usually based on detecting changes in chemical shifts from rapidly acquired HSQC spectra,[28,72–80] although proton only[31,81–89] and ^{19}F-based variations[90–92] also exist.

In terms of NMR-probe design, experiments such as ^{1}H–^{15}N HSQC require short, simultaneous RF pulses on both proton and nitrogen channels, with nitrogen decoupling applied during data acquisition on the proton channel. Variants such as constant-time ^{13}C HSQC incorporate additional nitrogen-decoupling during the evolution period. Three-dimensional sequences such as HSQC–NOESYand HMQC–NOESY–HMQC are identical in probe requirements to ^{1}H–{^{15}N} HSQC. Sequences such as HSQC–TOCSY require proton spin-locking pulses, whereas HNCA, HNCO, and HN(CO)CA require simultaneous pulsing on ^{1}H, ^{13}C, and ^{15}N channels, with ^{15}N decoupling during data acquisition. Constant-time H(CA)NH requires simultaneous pulsing on ^{1}H, ^{15}N, and ^{13}C channels, with carbon decoupling and proton spin-locking during the sequence, and nitrogen decoupling during acquisition of the proton signal. HCA(CO)N requires simultaneous pulsing on ^{1}H, ^{15}N, and ^{13}C channels with carbon decoupling during acquisition on the proton channel. Sequences such as CBCA(CO)NH[93] and CBCANH[93] require pulsing on ^{1}H, ^{15}N, and ^{13}C channels, with simultaneous nitrogen and proton decoupling during the sequence and nitrogen decoupling during signal acquisition, as shown in Fig. 1(a). Some of the most challenging sequences for probe design are those such as four-dimensional TROSY triple resonance spectroscopy,[94,95] which requires pulsing on ^{1}H, ^{15}N, ^{13}C, and ^{2}H with ^{2}H decoupling during the carbon pulses, as shown in Fig. 1(b).

From the brief description above, it is clear that the NMR probes must operate simultaneously at a number of different frequencies with excellent electrical

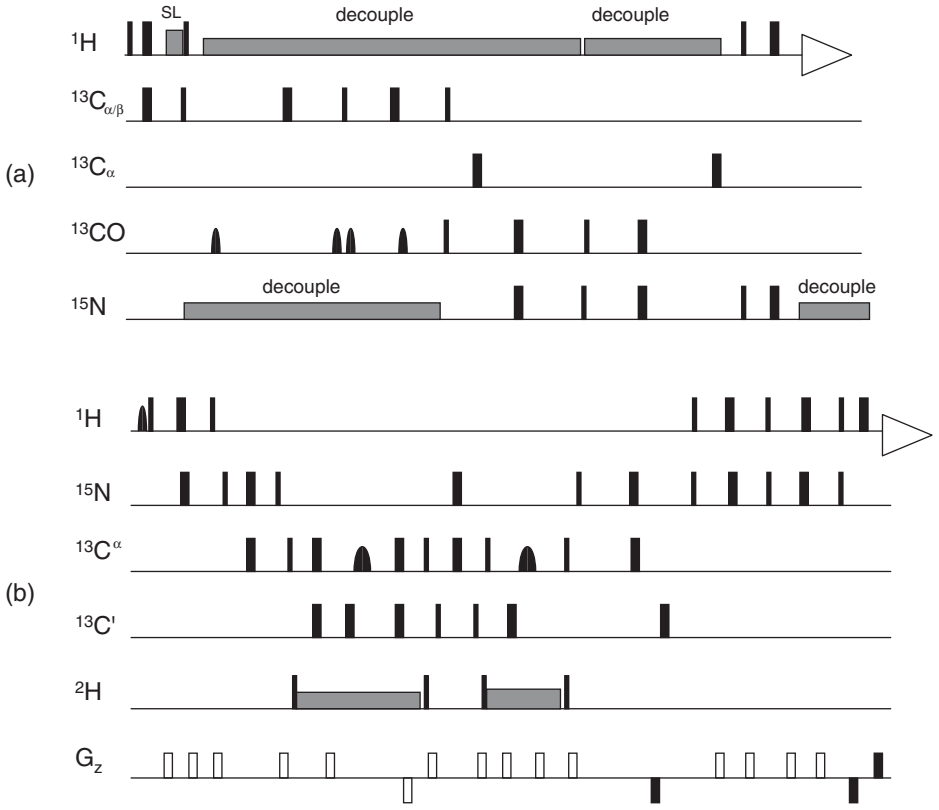

Fig. 1. Two pulse sequences for solution-state NMR that represent significant challenges to probe design: (a) 3D CBCA(CO)NH sequence and (b) four-dimensional HNCACO TROSY sequence. Thin-rectangular lines represent 90° pulses, thick-rectangular lines 180° pulses, and thin/thick hemispherical shapes frequency-selective 90° and 180° pulses, respectively. For simplicity incremental delays t_1, t_3, and t_4 are not shown.

isolation between individual channels. For example, if electrical isolation is not very high, there will be significant noise added to the detected proton signal from simultaneous nitrogen decoupling in the CBCA(CO)NH sequence.

For solution-state NMR experiments, commercial vendors offer a number of different types of probes. For standard heteronuclear experiments triple resonance, commonly called TXI (triple resonance/X-nucleus/inverse detection), probes enable pulsing on proton, deuterium, carbon, and nitrogen channels. The usual configuration, described in more detail later, is to have two RF coils, one inside the other, with the inner coil operating at the ^{1}H and ^{2}H frequencies, and the outer one at the ^{13}C and ^{15}N frequencies. The inner coil, having a higher filling factor, has a higher sensitivity than the outer coil. The term inverse detection refers to the fact that the signal is acquired on the proton channel, and thus in this configuration the proton channel is the inner coil, which also provides deuterium decoupling and detects the lock signal. For nucleic acid

applications, the outer coil is usually tuned to ^{13}C and ^{31}P. Some vendors offer a "combined probe" in which the inner coil is triple-tuned to ^{1}H, ^{2}H, and ^{31}P, with the outer coil tuned to ^{13}C and ^{15}N frequencies to allow both protein and nucleic acid studies. If triple-resonance experiments are not required, as in for example protein screening using ^{1}H–^{15}N HSQC sequences, then a simple indirect detection probe can be used, in which the inner coil is now tunable to either ^{1}H or ^{19}F frequencies, as well as ^{2}H, and the outer coil is resonant at only one frequency, but this resonance can be single-tuned over a range of frequencies, typically covering ^{15}N, ^{13}C, and ^{31}P.

One other factor, as shown in Figs. 1(a) and 1(b), is the requirement for pulsed magnetic field gradients in the NMR probe. These are used primarily for coherence selection within the sequences, and have largely replaced phase cycling as a way to minimize artifacts in NMR spectroscopy.[96,97] Although not discussed in detail here, the gradients must be rapidly switchable, and can be designed as magic angle,[98–101] single- or triple-axis configurations. Many vendors have also introduced "automatic tuning" into their probe design, such that long-term drifts in probe tuning can be minimized and probes can also be retuned rapidly and automatically retuned if the dielectric and conductivity properties of successive samples vary significantly. Although information on exact probe configurations is proprietary, a good discussion of the issues involved in automatic tuning is covered in the paper by Hwang and Hoult.[102]

2.2. Solid-state pulse sequences

As outlined previously, solid-state NMR is used in cases where proteins do not form crystals easily, are too disordered for X-ray crystallography, or are not amenable to solution-state techniques owing to limited solubility. For solid-state NMR the protein is usually selectively or fully isotopically labeled with either ^{13}C, ^{15}N, or a combination of the two: labeling strategies and sample preparation have been reviewed by Straus.[103] The NMR spectrum of randomly oriented solid-phase molecules is extensively broadened by anisotropic interactions, with the linewidth (LW) generally being dominated by homonuclear scalar and dipolar ^{13}C coupling in uniformly labeled samples.[104,105] Rapid spinning at the magic angle, high-power proton decoupling during acquisition, and high magnetic fields can improve the spectral resolution considerably. Alternatively, homonuclear couplings can be minimized by selective isotopic labeling.[35–37] If the protein is uniformly ^{13}C and ^{15}N labeled typical experiments involve multi-dimensional ^{13}C–^{13}C and ^{13}C–^{15}N correlation sequences.[106,107] Low γ-nuclei have smaller dipolar couplings and larger chemical shift dispersions than protons, and so spectral resolution is greater for these nuclei. The primary structure of the protein can be determined starting with intra-residue resonance assignment *via* homonuclear ^{13}C–^{13}C correlation experiments.[108] Pulse sequences using selective polarization transfer from backbone ^{15}N to $^{13}C_{\alpha}$ atoms, followed by ^{13}C–^{13}C correlation can be used to determine ^{15}N–^{13}C connectivities. More recently, high sensitivity indirect detection experiments such as ^{13}C–^{1}H or ^{15}N–^{1}H HSQC spectroscopy, have been reported,[109] in which the authors obtained high-quality $^{15}N/^{1}H$ HSQC spectra with 500 nmol of perdeuterated

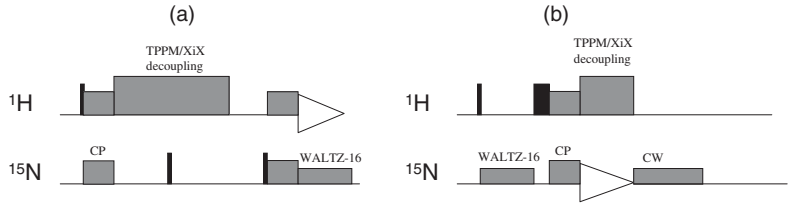

Fig. 2. (a) Inverse detection sequence for solid-state HSQC spectroscopy. Either TPPM or XiX high-power decoupling may be used on the proton channel. (b) Conventional sequence for ^{15}N-detected solid-state HSQC.

nanocrystalline ubiquitin in <15 min at 800 MHz. Average LWs of 0.22 ppm FWHM were achieved using a spinning rate of 20 kHz, and ^{15}N decoupling was applied during data acquisition.

Fig. 2 shows both a conventional heteronuclear-detected and a relatively recently developed inverse-detection sequence[109] for solid-state HSQC spectroscopy. High power proton decoupling and proton/nitrogen irradiation for cross-polarization are required in both sequences.

The major issue for solid-state probe design, in addition to the mechanics of rapid spinning, which are not considered here but dealt with in great detail by Doty,[56,110] is the requirement for very high decoupling fields, and the associated problems of sample heating. Typically, solenoidal coils oriented at the magic angle and tuned to multiple frequencies are used for most solid-state studies. New developments in this area are covered in Section 5.2.

2.3. Pulse sequences for aligned samples

Specialized NMR probes are needed for studies of membrane proteins in mechanically aligned bilayers. The glass plates used to align the samples are typically wrapped in a thin plastic film in order to maintain sample hydration. The proteins are normally either selectively or fully labeled with ^{15}N. Typical experiments are polarization inversion spin exchange at the magic angle (PISEMA)[46,111] or SAMMY.[112] These sequences are designed to remove H–^{1}H couplings during ^{1}H–^{15}N dipolar evolution using, in the former case, Lee–Goldburg decoupling and in the latter case by refocusing unwanted coupling using a magic sandwich.[113] As in the case for MAS probes, the major concerns in probe design are minimizing sample heating that results from high-power irradiation, particularly on the ^{1}H channel (Fig. 3).

3. PROBE DESIGN

NMR coils are designed to maximize the near-field magnetic energy stored in the sample. The desirable properties of such a coil include: (a) a homogeneous B_1 distribution within the sample, (b) minimum electric fields within the sample since these lead to signal-to-noise losses and also to sample heating in conductive

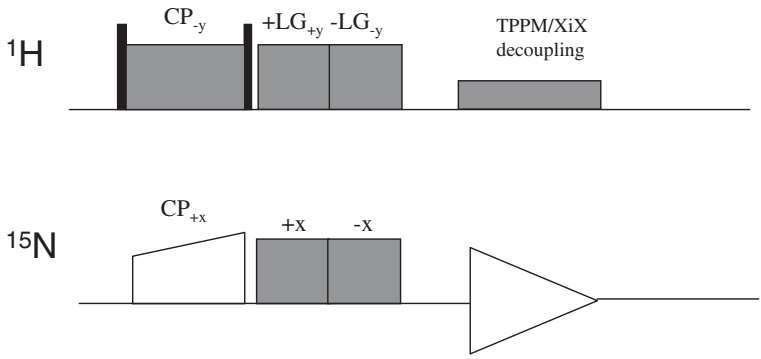

Fig. 3. PISEMA pulse sequence used for oriented solid-state protein samples. LG refers to Lee–Goldburg decoupling.

Table 1. Larmor frequencies at field strengths between 11.7 and 21.1 T

	21.1 T	18.8 T	17.6 T	14.1 T	11.7 T
^{1}H	900	800	750	600	500
^{19}F	846.7	752.6	705.6	564.7	470.4
^{31}P	364.3	323.8	303.6	242.9	202.4
^{13}C	226.3	201.2	188.6	150.9	125.7
^{2}H	138.2	122.8	115.1	92.1	76.8
^{15}N	91.2	81.1	76.0	60.8	50.7

samples, (c) maximum B_1 intensity per unit driving current, which enables shorter pulses to be used for higher bandwidth excitation and decoupling, as well as increasing the S/N *via* the principle of reciprocity,[114,115] (d) minimum resistive losses in the RF coil, and (e) maximum tuning range for samples of different dielectric constant and conductivity.

Table 1 lists Larmor frequencies for commonly used nuclei at commercially available magnetic fields. In designing NMR probes at high frequency, one must consider the conductor skin-depth and non-uniform current distribution within the conductor, as well as the frequency-dependent sample and coil losses.

3.1. B_1 field homogeneity

A uniform B_1 field within the sample is particularly important for maximum S/N in multiple-pulse sequences, the efficient creation and manipulation of multiple quantum coherences, as well as effective water suppression. The geometric shape of the RF coil for solution-state NMR is usually cylindrical as this allows easy and rapid sample positioning and sample changing using cylindrical NMR tubes. Elementary electromagnetic analysis can be used to derive the condition necessary to produce a perfectly uniform B_1 field in a direction perpendicular to that of the B_0 field, namely

an infinitely long cylinder carrying a surface current, J_s, given by

$$J_s = \hat{z} J_0 \sin \phi \tag{1}$$

where ϕ is the azimuthal angle subtended at the center of the cylinder, as shown in Fig. 4. The field, $B(\rho,\phi)$, inside the cylinder is given by

$$\begin{aligned} B(\rho,\phi) = & -\hat{\rho} \sum_{m=1}^{\infty} m\rho^{m-1}(A_m \cos m\phi + B_m \sin m\phi) \\ & + \hat{\phi} \sum_{m=1}^{\infty} m\rho^{m-1}(A_m \sin m\phi - B_m \cos m\phi) \end{aligned} \tag{2}$$

By applying boundary conditions at the cylinder surface (considering the B_1 field created outside the cylinder), all the B_m coefficients must be zero, and the only non-zero A_m coefficent is given by $A_1 = -\mu_0 J_0/2$. Therefore,

$$B(\rho,\phi) = \frac{\mu_0 J_0}{2}\left(\hat{\rho} \cos \phi - \hat{\phi} \sin \phi\right) = \hat{x}\frac{\mu_0 J_0}{2} \tag{3}$$

This shows that a perfectly uniform B_1 field, directed along the x-direction, is produced by a sinusoidal current along the surface of a cylinder of infinite length. Of course, this configuration cannot be realized in practice, but the basic tenet of

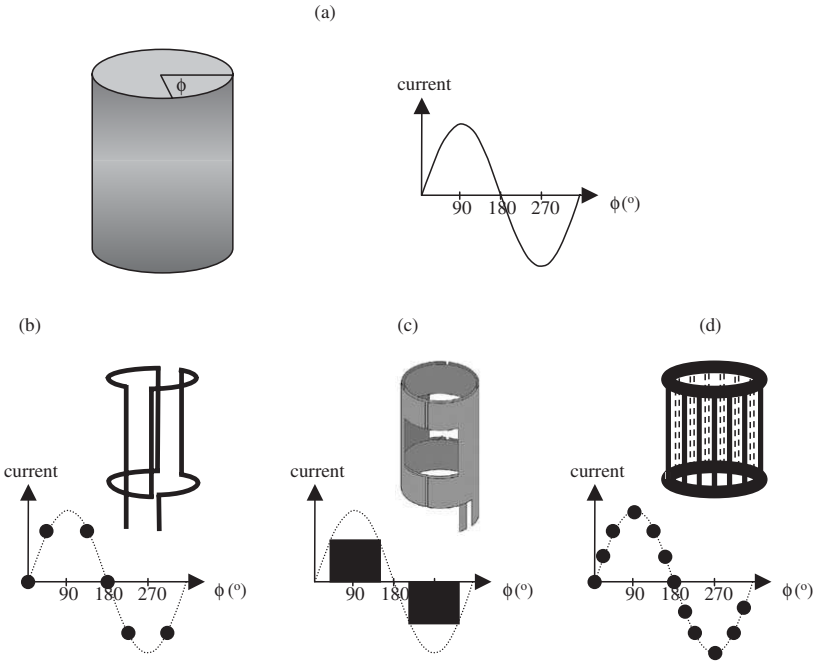

Fig. 4. (a) Theoretical surface current density required to produce a perfectly uniform axial magnetic field. (b)–(d) Practical approximations to the ideal current density: (b) saddle-coil, (c) Alderman–Grant coil, and (d) birdcage coil.

coil design is to approximate the sinusoidal surface current. The most common realization in high resolution NMR is the "saddle" or "Helmholz" coil, shown in Fig. 4(b), which can be thought of as a "six-point" approximation of the continuous sinusoidal current distribution.[116]

Fig. 4(c) shows an Alderman–Grant coil[117] which follows original design ideas of Kan *et al.*[118] and Schneider and Dullenkopf.[119,120] This design provides, at first sight, a fairly crude approximation to the sinusoidal current distribution: however, it has many advantageous features. Primarily, it is a very low inductance design, and therefore is a low-voltage, high-current structure. This feature intrinsically reduces the electric fields, present within the sample, thus minimizing sample heating since the power, P_s, dissipated in the sample is given by[121,122]

$$P_s = \frac{1}{2}\int \sigma E^2 \, \mathrm{d}V \tag{4}$$

Distributing the capacitance around the coil, as shown in Fig. 4, also reduces the electric fields, and two guard rings placed inside the coil reduce them yet further. As covered later in this section, the NMR probe must operate at a number of frequencies, typically four for protein NMR. Although it is possible to design circuitry such that a single coil is used for all four frequencies, it is usually more efficient to use two RF coils, arranged one inside the other. The outer, low-frequency coil is usually a multiple-turn, foil or wire saddle design. The inner coil is required for high-power proton decoupling, and is normally a version of the Alderman–Grant coil.

Increasing the number of conductor elements of the coil increases the B_1 uniformity. In magnetic resonance imaging the "birdcage resonator",[123–125] Fig. 4(d), is widely used, and consists of a series of equidistantly spaced "rungs" and two "end rings". The birdcage coil has multiple resonant modes, with one set of doubly degenerate modes producing homogeneous transverse B_1 fields in quadrature. The coil, therefore, can produce a circularly polarized B_1 field, reducing the power required for RF transmission by a factor of two, and increases the S/N by a factor of $\sqrt{2}$ over a coil driven in linear mode. The price to pay for the increased B_1 uniformity of the birdcage coil is, especially at small size scales, a structure of far greater physical and electrical complexity than the saddle coil. Another practical issue is that of B_0 homogeneity: the requirement for a large number of capacitors close to the sample in the birdcage design makes it very challenging to maintain the necessary narrow lineshape necessary for high-resolution NMR. For this reason, at present no commercial high-resolution probes use the birdcage coil geometry.

An alternative approach to producing a homogenous B_1 field is to use a horizontally oriented sample with a solenoidal coil. Although the solenoid has an intrinsically higher S/N per unit volume than the saddle/Alderman–Grant/birdcage coil designs,[115] the difficulty of rapid sample changing means that relatively few solution-state NMR probes employ a solenoidal geometry. One notable exception is the commercial and academic[126–133] uses of solenoids for very small volume NMR, which has also been used extensively to couple NMR detection with hyphenated chemical microseparations.[134–141] Commercial development has also resulted in

small solenoidal probes in which successive samples flow through the coil.[142] The use of small solenoids with mass-limited protein samples is discussed further in Section 6.

Solid-state MAS probes incorporate a solenoidal coil, with the coil and sample aligned at the magic angle with respect to B_0. Extensive details on various aspects of probe and stator design and construction can be found elsewhere.[56] Since one of the most important design criteria is to produce a very strong proton-decoupling field, a single coil is typically double- or triple-tuned, rather than using the double-coil approach in solution-state NMR. The electrical circuit is then designed to maximize efficiency on the proton channel. It should be noted, however, that recent work by Doty *et al.*,[143] covered in more detail in Section 5.2, has suggested that a cross-coil approach has some important advantages in terms of reducing sample heating. Transmission line elements, rather than lumped elements, have traditionally been used for high-power, high-frequency solid-state NMR circuits, and are covered further in Section 3.3.2. NMR studies of mechanically oriented samples typically use rectangular solenoids, as shown in Fig. 5. Sample heating under high-power decoupling is a major issue, causing sample degradation and/or dehydration. In recent work, Saha *et al.*[144] have shown that the electric field in the sample can be reduced substantially by placing two Faraday shields at the top and bottom of the sample, as shown in Fig. 5.

In order to predict accurately the magnetic and electric fields produced within the sample by a given coil geometry, one has to calculate the exact current distribution within the conductor. At high frequencies, the current does not distribute uniformly within the conductor, but rather concentrates toward the edges, to a degree determined by the value of the skin depth. The skin depth (δ) is defined as the distance

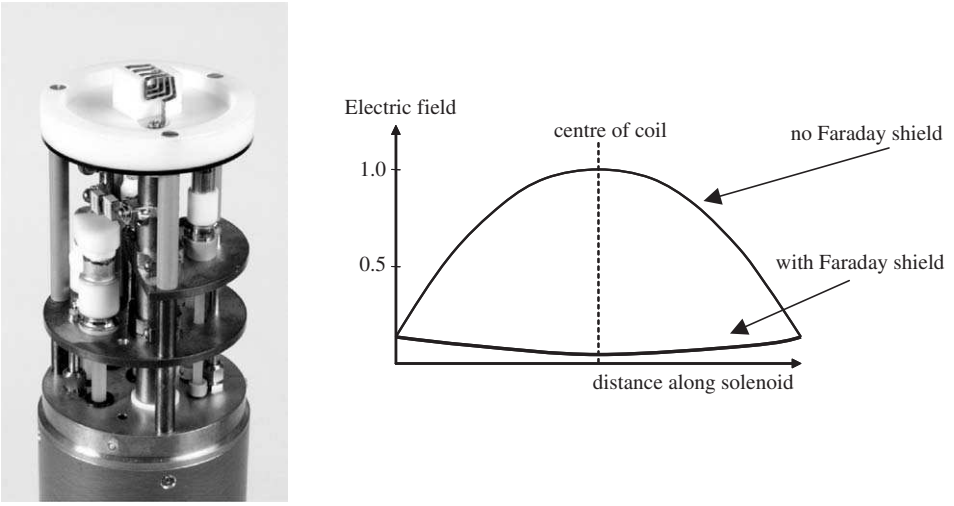

Fig. 5. (left) Photograph of a rectangular solenoidal coil used for aligned membrane studies. (right) Electric field profile along the center of the coil with and without a Faraday shield.[118]

into the conductor at which the value of the current density decreases to $1/e$ of its value at the surface, and is given by

$$\delta = \frac{1}{\sqrt{\mu \pi f \sigma}} \tag{5}$$

where σ is the conductivity, f the frequency and μ the permeability of the conductor. As outlined in the articles by Doty *et al.*,[55,56] the thickness of the conductor in a saddle or Alderman–Grant coil, which uses planar conductor elements, should be at least five to eight times the skin depth for the highest quality factor, but in practice should be considerably thicker for the requirements for high power decoupling and for stabilizing the coil temperature during decoupling. Carlson[145] has analyzed the current distribution within a saddle-coil made from foil elements, showing that current concentrates at the edges of the conductor, and the highest current density is found at the corners of any conductor. A full comparison between measured and theoretical profiles was presented by Boyer *et al.*,[146] with illustrative results shown in Fig. 6.

Assuming that the wavelength in the conductor is much larger than the conductor length in the coil, one can use a quasi-static calculation of the B_1 field. The phase of the current is assumed not to vary significantly along the length of the conductor and the magnetic field can be calculated directly from the Biot–Savart law.

$$\mathrm{d}B = \frac{\mu_0 I \mathrm{d}L \times r}{r^3} \tag{6}$$

Where $\mathrm{d}B$ is the magnetic field at position r produced by a length ($\mathrm{d}L$) of conductor carrying current I and μ_0 the permittivity of free space. In cases where the conductor length is a substantial fraction of a wavelength, solution of Maxwell's equations is necessary. Typically, this is accomplished using finite-element,

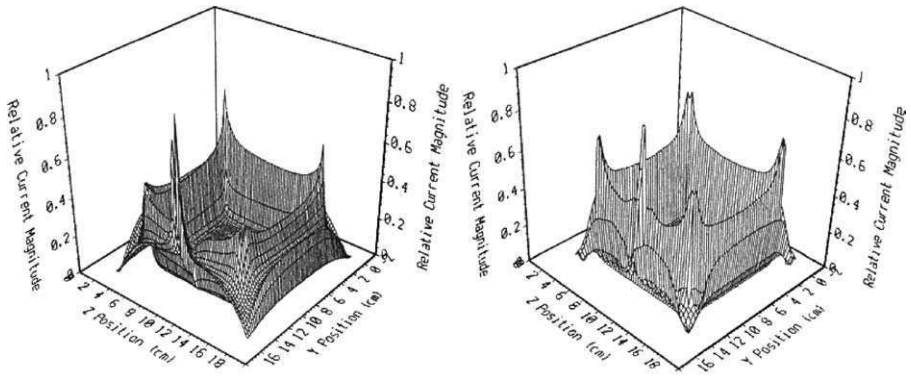

Fig. 6. Measured (left) and calculated (right) current distributions for a 15-cm outer diameter square coil at 41 MHz. The current flows primarily on the inside edge of the conductor and peaks at the inside corner of each, and at the feed point (center of front leg). Figure reproduced from ref. 146, copyright 1998, with permission from Wiley.

finite-difference-time-domain, or method-of-moments numerical techniques. Several commercial software packages are available for such analysis including CST Microwave Studio, Opera, HFSS, and XFDTD.

3.2. B_0 homogeneity and susceptibility matching

The requirements for B_0 homogeneity within the sample are extremely high for solution-state NMR experiments. LWs and lineshapes are quoted at the 50, 0.55 and 0.11% of full height of the peak: typical values for non-spinning liquid probes are ~0.5/5/15 Hz, corresponding to considerably less than 1 part-per-billion (ppb) variation in the local magnetic field within the sample. Narrow spectral LWs are desirable for a number of reasons including high sensitivity, minimal spectral overlap and, particularly important in most protein experiments, efficient water suppression.

Before considering the effects of the RF coil on the B_0 homogeneity, a brief description is given of the magnetic field produced by superconducting magnets, and corrections that can be performed using shim coils. The spatial variation in the static magnetic field within the bore of the magnet satisfies Laplace's equation and can be described by an expansion in orthogonal spherical harmonic functions:

$$B_0(r,\theta,\phi) = \sum_{n=0}^{\infty}\sum_{m=0}^{n} c_{nm}\left(\frac{r}{a}\right)^n P_{nm}(\cos\theta)\cos\left(m\left(\phi-\phi_{nm}\right)\right) \tag{7}$$

in which a is the radius of the magnet bore, c_{nm} and ϕ_{nm} are constants and $P_{nm}(\cos\theta)$ are the associated Legendre polynomials. If the field were perfectly homogeneous then the only non-zero value of c_{nm} would be c_{00}. Ideally then, having measured the inhomogeneity in the magnetic field, and expressed this in spherical harmonics, one would have a method for correcting for these terms. Shim coils can be constructed to correct for both zonal and azimuthal harmonics of the magnetic field, but perfect cancellation is not possible. An excellent review article on shimming, which covers this topic in much finer detail, has been written by Chmurny and Hoult.[147] The net result is that the NMR LW is governed both by the T_2 value of the sample and the spatial inhomogeneity of the magnetic field (ΔB_0) over the sample.

$$LW = \frac{1}{\pi T_2^*} = \frac{1}{\pi T_2} + \frac{\gamma \Delta B_0}{2\pi} \tag{8}$$

If the shim corrections are effective, then the dominant term in the LW is the T_2 value of the sample, and this condition can be achieved using almost all NMR magnets. However, significant and highly nonlinear distortions of the magnetic field within the sample can be introduced by the RF coil if sufficient care is not taken in its design. Magnetization is induced in the conductors of the RF coil when it is placed in the magnetic field, magnetization which then generates a secondary field, which adds to the primary field. Analytical solutions to Maxwell's equations exist for the additional magnetic field, ΔB_z, generated for simple geometries.[148]

Of relevance to a vertically oriented NMR probe, is a cylinder with its long axis parallel to B_0. Assuming that $|\chi| \ll 1$, the additional magnetic field inside and outside the cylinder is given by

$$\Delta B_z(\text{inside}) = \Delta\chi B_0 \quad \Delta B_z(\text{outside}) = 0 \tag{9}$$

Relevant to solenoidal coils is the case of a cylinder, radius a, with its axis perpendicular to B_0, in which case the additional magnetic fields inside and outside the cylinder are given by

$$\Delta B_z(\text{inside}) = \frac{\Delta\chi B_0}{2} \quad \Delta B_z(\text{outside}) = \frac{\Delta\chi B_0 a^2\left(z^2 - a^2\right)}{2\left(x^2 + z^2\right)^2} \tag{10}$$

Clearly, neither the sample nor the RF coil is infinite in length. If one considers the practical case of a cylindrical shell, with radius b and thickness t (with $t \ll b$), aligned along the z-axis and extending from z_0 to z_1, then the deviation in the z-component of the magnetic field, ΔB_z, is given by[149]

$$\Delta B_z = \frac{\kappa B_z t b}{2}\left\{\frac{(z - z_0)}{\left[(z - z_0)^2 + b^2\right]^{1.5}} - \frac{(z - z_1)}{\left[(z - z_1)^2 + b^2\right]^{1.5}}\right\} \tag{11}$$

where κ is the volume susceptibility of the conductor. This function is plotted in Fig. 7 for a copper cylinder at a magnetic field of 11.7 T, i.e., a proton resonance frequency 500 MHz.

For more complex geometries, i.e., actual NMR coils, numerical methods have to be used to solve for the perturbations of the magnetic field within the sample.[150–153] A number of authors have considered the effects of magnetism specifically on high-resolution NMR probe design.[149,154,155] For example, Fuks[149] performed numerical simulations of suceptibility-induced magnetic fields, derived using an analog of Columb's law applied to equivalent magnetic surface charges induced by the applied static magnetic field. One can approximate lineshape distortions to be caused by only the component of the perturbing field parallel to B_0. The effects of shimming were simulated by subtracting the components formed from up to 20 spherical harmonic functions from the inhomogeneous field. The overall lineshape was given by integrating over a large number of voxels in which the overall field was calculated. Fuks *et al.*[149] also considered both the effects of the glass or quartz cylinder which forms the mount for the NMR coils, and a coil of saddle/Alderman–Grant geometry. The effects of the cylindrical tube, which is much longer than the active volume of the sample, could be shimmed out using simple second-order terms. Fig. 8 shows the geometry of the saddle coil used, and the resulting simulations which show the lineshape distortions introduced by the coil. Interestingly, the results are very similar to those obtained from a solid conductor cylinder, indicating that the "missing windows" of the coil have very little effect on the lineshape.

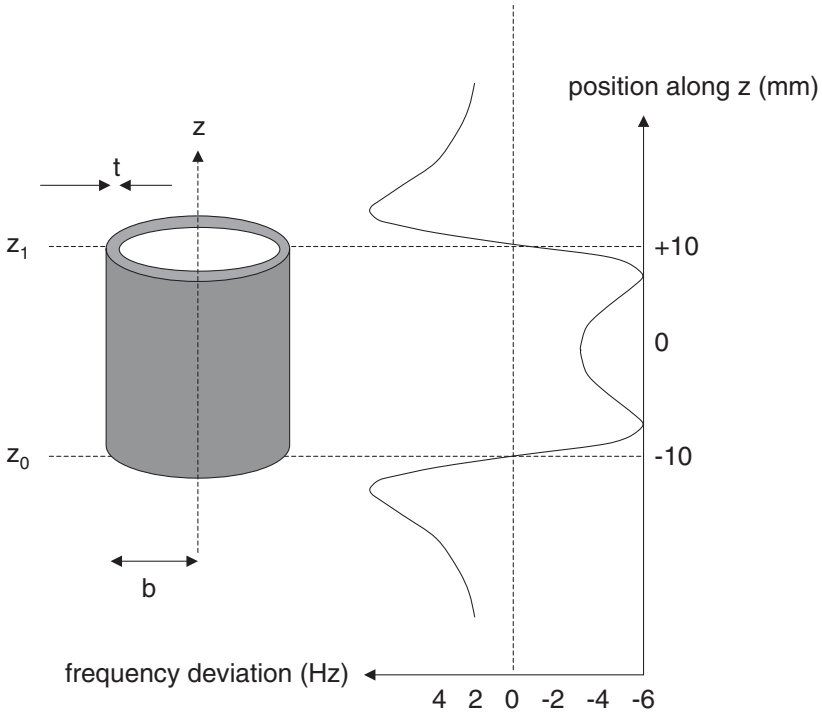

Fig. 7. Simulated perturbation field at a 500 MHz operating frequency for a copper cylinder with volume susceptibility -9.64×10^{-6}, $b = 4$, $t = 0.025$, $z_0 = -10$, and $z_1 = +10$ mm. Figure adapted from ref. 149, copyright (1992), with permission from Elsevier.

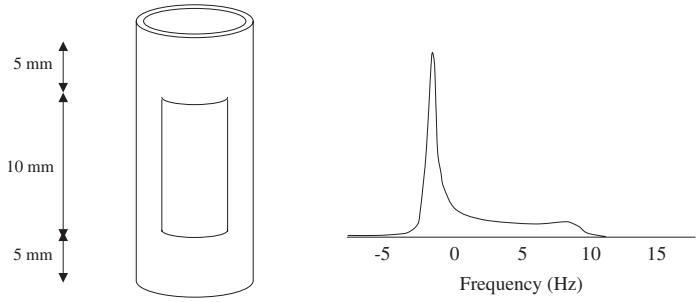

Fig. 8. (left) Schematic of a saddle coil, with windows subtending 120°. The thickness of the conductor is 0.025 mm and the outer diameter is 8 mm. (right) Simulated lineshape obtained from a sample placed in the saddle coil. Figure adapted from ref. 149. Copyright (1992), with permission from Elsevier.

Clearly, the magnitude of the magnetic-field distortions introduced by the coil depends on the magnetic susceptibility of the conductor. Table 2 lists the conductivities and magnetic susceptibilities of some metals commonly used in NMR probes. Noting from Table 2 that metals can be either paramagnetic or diamagnetic suggests that a

Table 2. Magnetic susceptibilities and conductivities of commonly used metals at 7 T and 300 K

Metal	Conductivity M(Ωm)−1	Magnetic susceptibility 10^{-6}
Aluminum	36.6	+20.9
Copper	58.0	−9.6
Gold	44.0	−34
Silver	61.4	−24
Palladium	9.3	+840
Rhodium	20.9	+168

method of improving lineshape is to use susceptibility-compensated materials. Soffe *et al.*[155] described in detail the construction of a high-resolution NMR probe for liquids applications at 750 MHz. They used electroplated rhodium on copper for the RF shield around the coil. The main coil was constructed from wire drawn from a billet of pure copper with an aluminum core. This was designed to give a volume fraction of copper of 68.2%. Since aluminum was preferentially extruded, the resulting wire was electroplated with a very thin layer (<1 μm) of rhodium to compensate and give zero net-magnetic susceptibility. A 1 μm layer is much less than the skin depth (3.9 μm) of rhodium at 750 MHz, and therefore the Q value of the coil was not degraded significantly despite rhodium having a much poorer conductivity than copper. Solder joints were formed from a special formulation of pure tin and lead in an appropriate volume ratio to give zero susceptibility. The LWs obtained were 0.38, 5.2, and 11.3 Hz at 50/0.55/0.11% of maximum height. A similar approach has been used by Zelaya *et al.*[156] for imaging applications. Alternatives to rhodium plating include metals such as palladium, the properties of which are also listed in Table 2.

In terms of the materials used for the cylindrical former on which the RF coils are fixed, the major criteria in their choice for solution-state NMR probes is to minimize both the dielectric loss of the material and any background NMR signal. Properties of coil adhesives and other materials used in NMR probes are covered in detail in the review article by Doty *et al.*[154]

An alternative method for magnetic susceptibility matching was devised by Olson *et al.*[126] for very small solenoidal coils. The solenoid, typically with diameter $\ll 1$ mm, is surrounded by a perfluorinated compound which has a magnetic susceptibility very similar to copper. This effectively produces an infinite cylinder of uniform magnetic susceptibility perpendicular to the main magnetic field, which as shown in Eq. (10) results in a homogeneous magnetic field within the sample. Using this scheme sub-Hz LWs can be achieved even when the copper conductor is only a few tens of microns away from the sample. Fig. 9 shows the effect on the NMR spectral lineshape of adding the susceptibility-matching fluid. Typical lineshape specifications offered by the commercial manufacturer of high-resolution solenoidal NMR probes (Protasis/MRM) are 0.5/5/15 Hz for the 50/0.55/0.11% LWs.

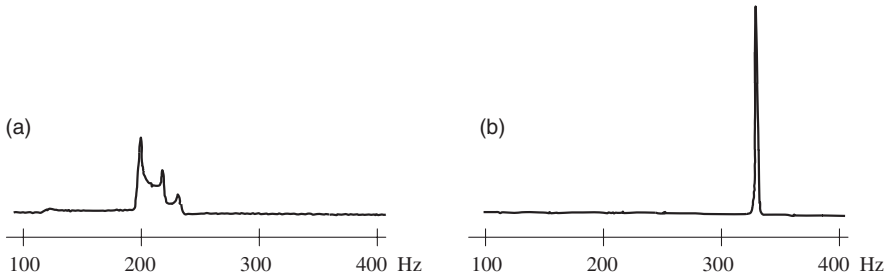

Fig. 9. Spectra of water without (a) and with (b) addition of a perfluorinated magnetic susceptibility-matching fluid with a solenoidal coil of dimensions 350 μm o.d. and 250 μm i.d. wrapped around a fused silica capillary. Figure adapted from ref. 126, copyright (1997), with permission from Elsevier.

3.3. Electrical circuit design

As an introduction to electrical circuit design for NMR probes, a very brief review is given here of the properties and characteristics of lumped elements and transmission lines, both of which are used in probe design.

3.3.1. *High frequency models of lumped elements*

Although most lumped element circuit designs for RF probes are depicted as simple representations of the specific elements, i.e., inductors or capacitors, the properties of these elements are in fact frequency dependent. For example, a capacitor may actually behave as an inductor, i.e., have a purely inductive reactance, at very high frequency! A realistic model of a capacitor must include its equivalent series resistance (ESR) and also equivalent series inductance (ESL), shown in Fig. 10(a), the latter quantity being dominated by the capacitor leads. The value of the ESR is given by

$$\mathrm{ESR} \approx R_s + \frac{\tan\delta}{\omega C} \tag{12}$$

where R_s is the loss component of the conductor in the capacitor and $\tan\delta$ the loss tangent of the dielectric in the capacitor. At low frequencies, the value of R_s is negligible and the ESR is correspondingly very small. At high frequencies, the value of R_s increases owing to the skin-depth of the conductor and the ESR can become considerable, leading to losses in S/N. Also, at high frequencies, the capacitor values needed for impedance matching can become very small, and stray capacitance in the circuit may make the overall design unstable. If the physical size of the capacitor is made smaller to achieve a smaller capacitance value, then the power handling capability of the circuit is reduced, and the ESR also increases owing to a smaller physical surface area of the capacitor. As noted previously, at frequencies above the series resonance frequency (at which point the capacitor acts as a pure resistor), the capacitor actually acts as an inductor.

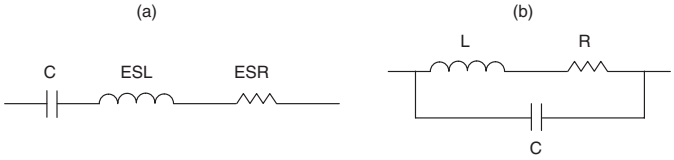

Fig. 10. Realistic circuit models of (a) capacitors and (b) inductors at high frequency.

Similarly, the behavior of an inductor is frequency dependent. A realistic model, as shown in Fig. 10(b), includes the resistance of the conductor, and also the inter-turn capacitance. At low frequencies, the lumped element acts as an inductor, at parallel resonance as an infinite impedance, and at frequencies above parallel resonance as a capacitor.

3.3.2. *Characteristics of transmission lines*

In its simplest form, a transmission line consists of an inner conductor and an outer conductor separated by a material with relative dielectric constant ε_r. At high frequencies, the value of Z_0 is given by

$$Z_0 \approx 60 \ln\left(\frac{b}{a}\right)\sqrt{\frac{1}{\varepsilon_r}} \tag{13}$$

where a is the outer diameter of the inner conductor and b the inner diameter of the outer conductor. The input impedance, Z_s, of a transmission line of length l and characteristic impedance Z_0 is given by

$$Z_s = Z_0 \frac{Z_T + Z_0 \tanh(\gamma l)}{Z_0 + Z_T \tanh(\gamma l)} \tag{14}$$

The value of γ is given by $\alpha + j\beta$, where α is the attenuation per unit length and $\beta = 2\pi/l$ represents the phase shift per unit length. The value of α is given by

$$\alpha = 0.5\left(\frac{R_l}{Z_0} + G_l Z_0\right) \tag{15}$$

where R_l is the ac resistance per unit length and G_l the conductance of the dielectric between the inner and outer conductors. The values of R_l and G_l are given by

$$R_l = \left(\frac{1}{a} + \frac{1}{b}\right)\sqrt{\frac{\rho\omega\mu}{8\pi^2}},\ G_l = C_l \omega \tan\delta_\varepsilon \tag{16}$$

where the value of C_l, the capacitance per unit length of transmission line, is given by

$$C_l = \frac{2\pi\varepsilon}{\ln(b/a)} \tag{17}$$

Transmission lines of various lengths, inner/outer dimensions, and different terminations "mimic" the effects of lumped elements. For example, a transmission line which is an open-circuit at one end has a purely capacitive impedance given by $(j\omega C_l l)^{-1}$, and a line which is short-circuited has a purely inductive reactance $j\omega L_l l$,

where L_l is the inductance per unit length. As pointed out by Martin *et al.*[157] the main advantages of transmission lines over lumped elements occurs when very small capacitances are required to impedance match the probe at high frequencies, and also when high power is required. As outlined earlier, small capacitances/capacitors result in a high-ESR value owing to the small physical size of the capacitor. For transmission lines, the equivalent structure has a much larger physical size and thus a lower ESR. The larger physical structure also results in improved thermal handling and heat dissipation, and also higher power handling abilities.

3.3.3. *Balanced electrical circuits*

At high frequencies, the total length of conductor in an NMR coil may be a substantial fraction of a wavelength. In this case, there are considerable differences in the performances, in terms particularly of B_1 homogeneity, produced by balanced and unbalanced electrical circuits. In an unbalanced series resonant circuit, such as the one shown in Fig. 11(a), the voltages across the capacitor and inductor are equal in magnitude, $QV(t)$, and opposite in phase. However, the voltage drop across the coil is asymmetric, and if the conductor length is a substantial fraction of a wavelength then the B_1 homogeneity may be poor. If the capacitance is split into a balanced configuration, as shown in Fig. 11(b), then the voltages across each capacitor are halved to $(Q/2)V(t)$. An equal voltage at each end of the coil forces the current distribution through the coil to be more symmetric than for the unequal voltages in the unbalanced case, and this leads in turn to a more uniform B_1 field within the coil. Other advantages of electrical balancing are that it enables a greater number of turns to be used in a multi-turn coil before approaching the self-resonant frequency, and the reduced voltage across each capacitor reduces the electric field losses in the sample, and also reduces potential breakdown problems.

The effects of circuit balancing can be seen in Fig. 12. This shows measurements of the B_1 homogeneity along the axis of a solenoidal coil in an MAS probe at 800 MHz.[158] Fig. 12(a) shows results from a circuit which is unbalanced at the high frequency (the circuit was tuned to both ^{1}H and ^{13}C), showing considerable asymmetry in the field profile. Fig. 12(b) shows considerable improvements in homogeneity achieved by balancing the circuit.

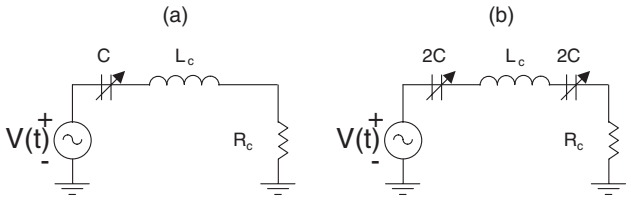

Fig. 11. (a) Schematic of an unbalanced series resonant circuit. (b) Schematic of the same basic circuit, except this time balanced.

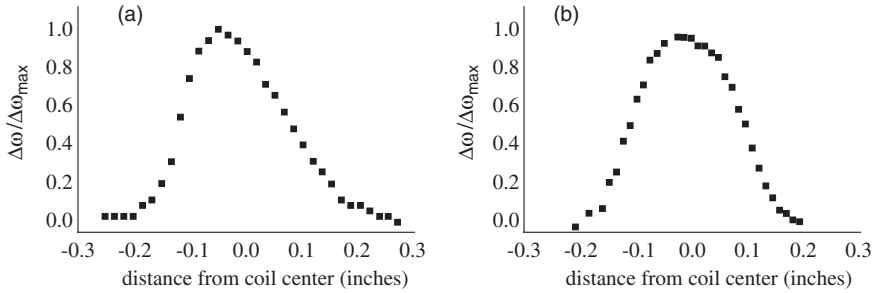

Fig. 12. Measurement of proton B_1 axial profile along a solenoidal coil at 800 MHz for a double-resonant circuit, measured *via* the frequency shift as a function of position of a small perturbing copper disk. (a) Unbalanced circuit, (b) balanced circuit. Figure adapted from ref. 158, copyright (2004), with permission from Elsevier.

In the same paper, the authors were primarily interested in maximizing the efficiency of cross-polarization experiments, and had noted asymmetric patterns in plots of the CP signal vs. RF field mismatch for an unbalanced circuit. Fig. 13 compares results from balanced and unbalanced circuits. The matching conditions for the balanced probe were found to be significantly narrower and more intense than that for the unbalanced probe, resulting in an S/N improvement of roughly a factor-of-two for the optimal matching condition in each configuration.

It should also be noted that balanced matching circuits are very important in reducing samples losses in *in vivo* magnetic resonance imaging and spectroscopy.[159]

3.3.4. *Double-resonant circuits*

As described previously, NMR probes for protein studies must typically operate at four different frequencies. Most commonly, the NMR probe contains two coils, each of which is tuned to two different frequencies. It is not possible to maintain maximum sensitivity for each of the two frequencies in a single coil, but the circuit can be designed to maximize the efficiency of either the higher or lower frequency channel. In the TXI configuration, the inner coil is tuned to ^{1}H and ^{2}H: the ^{1}H channel is designed to have optimal sensitivity, almost equivalent to that of a single-tuned ^{1}H circuit. The outer coil operates at ^{13}C and ^{15}N frequencies, with higher efficiency on the ^{13}C channel owing to the much higher chemical shift range of ^{13}C compared to ^{15}N.

There are a large number of circuit designs used by both academic and commercial groups, although these tend to have only minor differences. For example, Fig. 14(a) shows a circuit proposed by Paulson *et al.*,[158] which is electrically balanced on the high-frequency channel. Looking in from the high-frequency channel, the $\lambda/4$ line on the left acts as an open circuit, the parallel combination of C_B and L_B is identical to the value of $2C_{TH}$, and the open λ /4 line acts as a ground path, isolating the low-frequency port. Looking in from the low frequency (X) channel, the open $\lambda/4$ acts as a small capacitance in parallel with C_{TL}, the parallel L_BC_B circuit looks like a small inductor in series with the coil inductance, and the $\lambda/4$ line

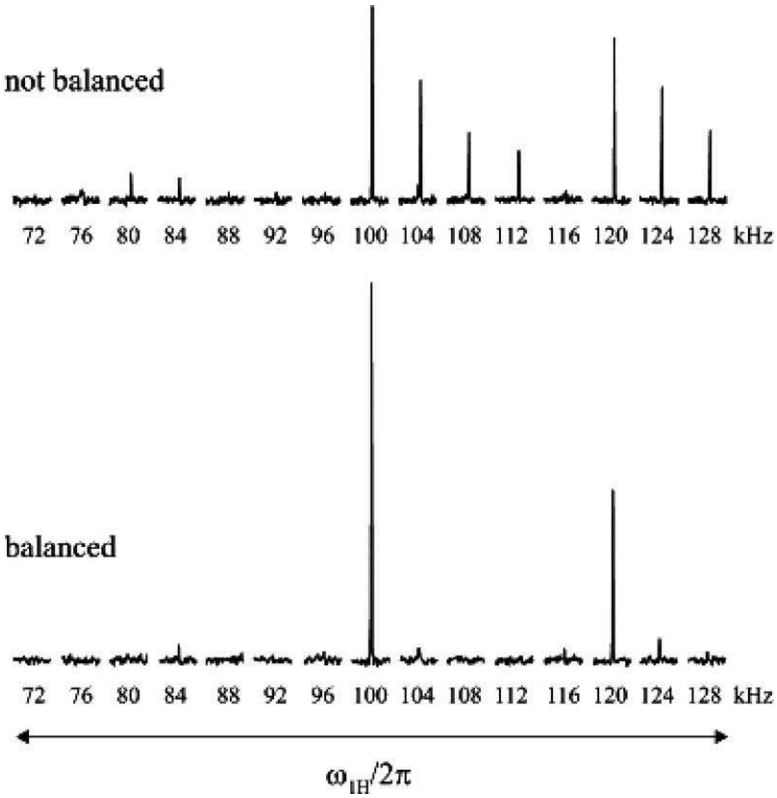

Fig. 13. Comparison of CP matching in an unbalanced and balanced solenoid coil using ^{13}C MAS spectra of the methylene resonance in adamantane at 20 kHz MAS as a function of the ^{1}H CP RF-field amplitude. Upper: for a probe not balanced in the hf channel. Lower: for the same probe with a balanced hf channel. The larger volume of sample that can be cross-polarized in the balanced probe at a single power setting translates into a much higher signal-to-noise. A 1 ms CP time was used to acquire these data and ω_{1C} was fixed at 80 kHz. Figure reproduced from ref. 158, copyright (2004), with permission from Elsevier.

on the left appears as a very low impedance pathway providing isolation from the high-frequency channel. For optimum probe efficiency, the value of L_B should be made as small as possible. Fig. 14(b) shows a variation on this general design, proposed by Gorkov *et al.*,[160] which also incorporates electrical balancing into the high-frequency channel, and which has been used in NMR studies of mechanically oriented membrane proteins.

3.3.5. *Triple-resonant circuits*

Since CPMAS probes need to produce much stronger ^{1}H decoupling fields than are used in solution-state NMR, triple-resonance probes often use a single coil, which is tuned to all three frequencies, rather than using a two-coil arrangement. As for

double-tuned networks, several variations exist. One recent example is shown in Fig. 15,[157] with both lumped element and transmission line representations.

An alternative three-frequency circuit was put forward by Li *et al.*[161] for solution-state NMR using a small solenoidal coil. The RF circuit is shown in Fig. 16. The L1–C1 trap presents a short circuit at low frequencies and an open circuit at high frequencies. A high quality (Q) factor L2–C6–C7 tank results in a high impedance at the proton frequency and a short-circuit path at the ^{15}N frequency. Thus, balanced matching is achieved for the proton channel. The proton channel has the shortest electrical path to the sample coil in order to minimize signal loss. In terms of efficiency, the least important channel is the lock channel, for which inductive matching

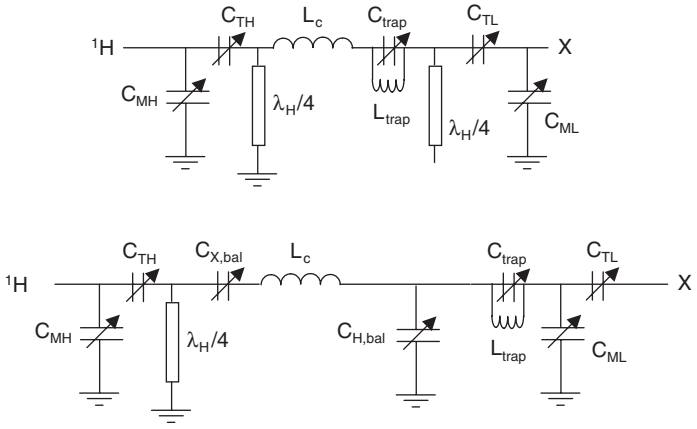

Fig. 14. (top) Double resonance probe circuit balanced on the proton channel by using a balancing trap. Adapted with permission from ref. 157, American Institute of Physics, 2003. (bottom) Related circuit incorporating balancing capacitors and an isolation trap circuit.

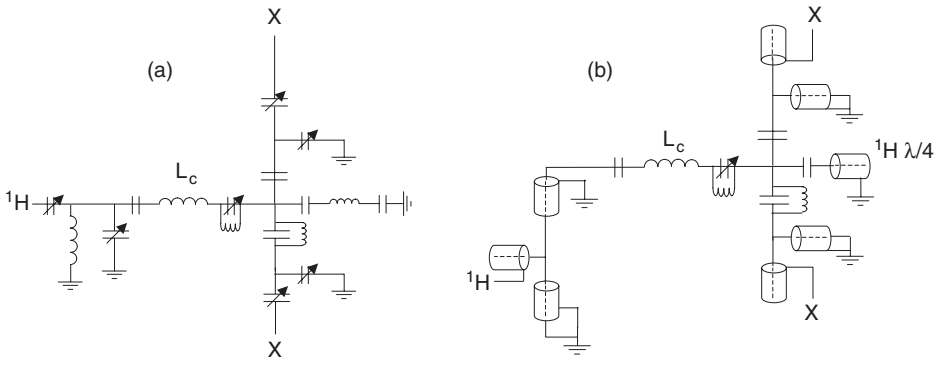

Fig. 15. (a) A triple resonance probe circuit using lumped elements. (b) The same circuit using tuning tube elements. Adapted with permission from ref. 157, American Institute of Physics, 2003.

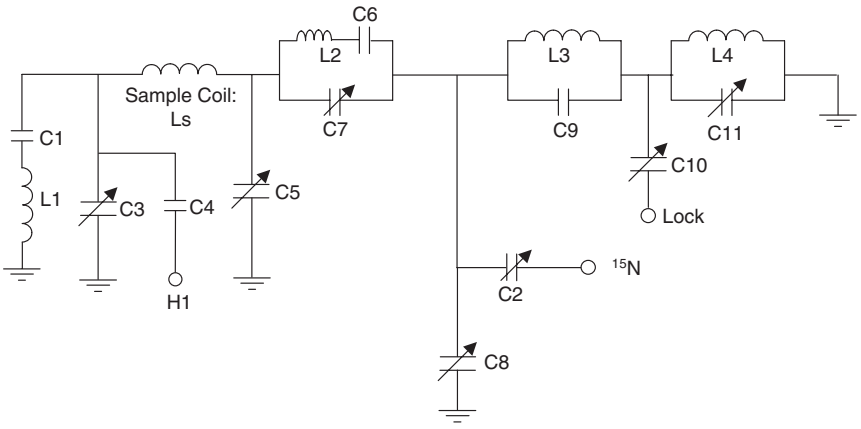

Fig. 16. RF circuit for a three-channel probe based on a single solenoid. Variable capacitors are either single 0.5–8 pF units, or are in parallel with a fixed capacitor. Component values: C1 = 200, C2 = 8.7–16.2, C3 = 0.5–8, C4 = 0.5, C5 = 0.5–8, C6 = 188, C7 = 0.5–8, C8 = 50.5–58, C9 = 82, C10 = 7.3–14.8, and C11 = 12.5–20 pF and L1 = 34, L2 = 36, L3 = 84, and L4 = 66 nH. Figure reproduced from ref. 161, copyright (2003), with permission from Elsevier.

was necessary since the lock frequency is higher than the ^{15}N frequency. A parallel LC (L3–C9) trap, resonant at the ^{15}N frequency, is used between the ^{15}N channel and lock channel.

4. CRYOGENIC PROBES

In recent years, the use of cooled RF coils, usually termed "cryoprobes", has become widespread in high-resolution NMR spectroscopy, particularly in studies of protein structure and dynamics. The coils are either constructed from high-temperature superconductors (HTS), or copper or aluminum, and cooled to temperatures between 10 and 77 K.[162–169] Substantial increases in signal-to-noise, up to a factor-of-four, have been achieved in protein NMR studies, and commercial probes are available in most of the standard configurations, e.g., triple-resonance inverse-detection, at operating frequencies up to and including 900 MHz. An extensive review of cryoprobe applications was published in 2005.[170]

4.1. Theory

In a given NMR experiment the signal voltage, V_s, is given by

$$V_s \propto \frac{B_1}{I\sqrt{R_{coil} + R_{sample}}} \tag{18}$$

where the respective resistance values are given by

$$R_{\text{coil}} = \frac{\omega_0 L_{\text{coil}}}{Q_{\text{unloaded}}}, R_{\text{sample}} = \omega_0 L_{\text{coil}} \left(\frac{1}{Q_{\text{loaded}}} - \frac{1}{Q_{\text{unloaded}}} \right) \tag{19}$$

and the coil sensitivity, B_1/I, is inversely proportional to the coil diameter, which for a given sample diameter, corresponds to an inverse relationship with the filling factor.

The noise voltage, V_{noise}, is given by

$$V_{\text{noise}} \propto \sqrt{4k\Delta f \left(T_{N,\text{probe}} + T_{N,\text{preamplifier}} \right)} \tag{20}$$

where $T_{N,\text{probe}}$ and $T_{N,\text{preamplifier}}$ are the noise temperatures (as opposed to the physical temperatures) of the devices. These noise temperatures are defined as

$$T_{N,\text{probe}} = \frac{T_{\text{coil}} R_{\text{coil}} + T_{\text{sample}} R_{\text{sample}}}{R_{\text{coil}} + R_{\text{sample}}} \tag{21}$$

$$T_{N,\text{preamplifier}} = 290 \left(10^{\frac{\text{NF}}{10}} - 1 \right) \tag{22}$$

where NF is the noise figure of the preamplifier. A narrow-band GaAsFET- or HEMT-based preamplifier can readily be constructed with a noise figure of ~0.3 dB. Careful choice of the components used for impedance matching the input of the preamplifier to 50 Ω is a key component to achieving the minimum noise figure. A 0.3 dB noise figure corresponds to an equivalent noise temperature of ~20 K. Cooling the preamplifier to liquid nitrogen temperatures and below can reduce the preamplifier noise figure to ~0.1 dB, an equivalent noise temperature of ~10 K. Preamplifier cooling is therefore advantageous for coils which are cooled to temperatures well below liquid nitrogen.

Eqs. (18)–(20) show that the effectiveness of the cryogenic approach depends upon the relative values of the sample and coil resistances. An increase in the absolute signal (Eq. (18)) and a decrease in the noise level (Eq. (20)) combine to give an increased S/N. Sample loading reduces the gain, up to the point at which the sample noise dominates that of the coil. S/N gains for non-lossy samples are around a factor-of-four, while for protein studies in aqueous solutions with a high concentration of salt, typically a factor-of-two increase results. As an example of the S/N increases using a cryoprobe, Fig. 17 shows a comparison of two HSQC spectra, one acquired with an inverse Cryoprobe and the other from a room temperature inverse probe.[171] The measured S/N improvement was a factor of 2.4, corresponding to a time reduction of almost a factor of 6 for a given S/N.

It should also be noted that a number of magnetic resonance imaging studies have also been performed using HTS or cooled copper coils.[164,172–184] These studies usually involve biological samples, which are inherently lossy. The largest S/N advantages occur at low magnetic fields or for small coils, both cases in which coil losses tend to dominate.

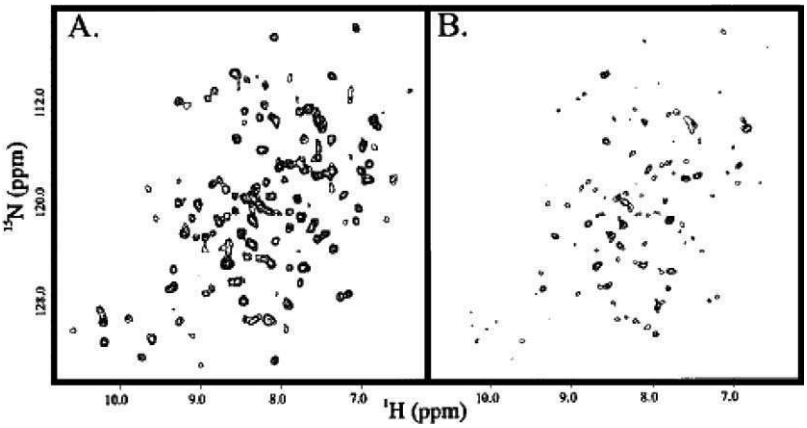

Fig. 17. Sensitivity-enhanced $^{1}H/^{15}N$ HSQC spectra acquired in 10 min on a 50 μM sample of the catalytic domain of stromelysin using (A) a dual ($^{15}N/^{1}H$) inverse Cryoprobe (Bruker) equipped with a lock and a *z*-gradient and (B) a conventional triple-resonance ($^{13}C/^{15}N/^{1}H$) inverse probe (Nalorac). On the basis of peak volumes, an average gain in signal-to-noise of 2.4 was realized with the Cryoprobe as compared to the conventional TXI probe. Reproduced with permission from ref. 171, copyright 1999 American Chemical Society.

4.2. Practical implementation

Most superconducting probes are constructed from yttrium–barium–copper compounds, $Yba_2Cu_3O_{7-\delta}$ (YBCO). Very high-quality films are required to carry the currents necessary for short RF pulses. Fig. 18 shows a schematic of the conductor layout for one-half of a typical HTS coil, with the complete arrangement comprising two such coils, which act as an inductively coupled system. Each coil is a self-resonant circuit consisting of an inductive loop and interdigitated capacitance, and is etched from an epitaxial film of HTS between 300 and 650 nm in thickness, deposited on a planar substrate of lanthanum aluminate or sapphire. Adjustment of the resonant frequency is achieved by laser trimming of the capacitive fingers. *Q* values of between 10,000 and 20,000 have been reported. For particular experiments, fine tuning of the probe uses a conductive "paddle", and impedance matching *via* a moveable coupling loop, as shown in Fig. 18. It is important to place the preamplifier as close to the inductive coupling loop as possible: otherwise, a long length of transmission line will introduce a considerable noise voltage, as analyzed by Kim *et al.*[185]

The probe and connections are shown schematically in Fig. 19.[186] The coil substrate is thermally anchored to a cold head, which is cooled to ~25 K by flowing helium gas from a closed-cycle refrigerator. The temperature must be controlled extremely tightly, and uses a thermometer, heater, and feedback control loop. The major challenge in cryoprobe design is clearly the requirement for an extremely high thermal gradient between the coil conductor and the sample, which must be at room temperature. A high vacuum provides a good thermal insulating layer around the sample, and various forms of air or nitrogen heating can also be used to establish

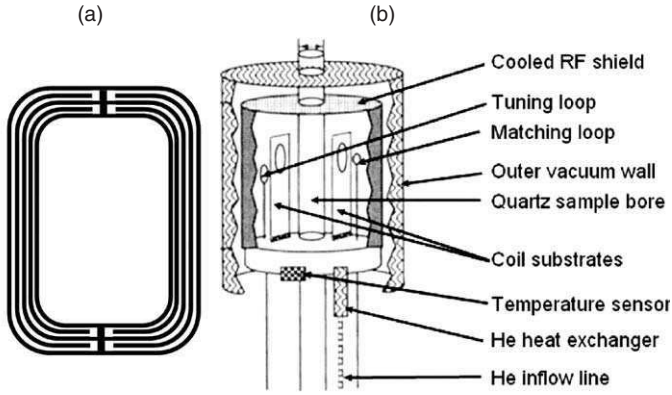

Fig. 18. (a) Schematic of a typical layout of a thin YBCO film on a substrate. (b) Schematic of an HTS probe, reproduced from ref. 172, copyright (1999), with permission from Wiley.

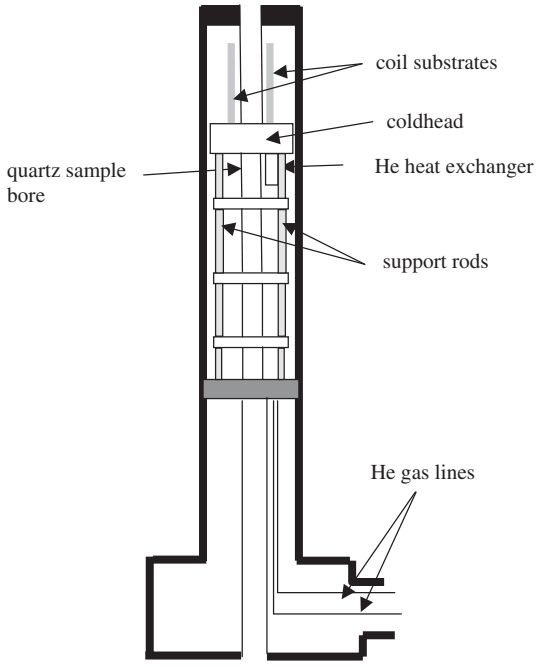

Fig. 19. Schematic of the internal structure of a superconducting cryoprobe. Figure reproduced from ref. 186, copyright (1997), with permission from IEEE.

such a thermal gradient. The probe body is evacuated so that only a single non-conductive wall separates the sample space from the coil. The filling factor of cryogenic probes is somewhat less than their room temperature counterparts: a typical reduction being 30–50%.

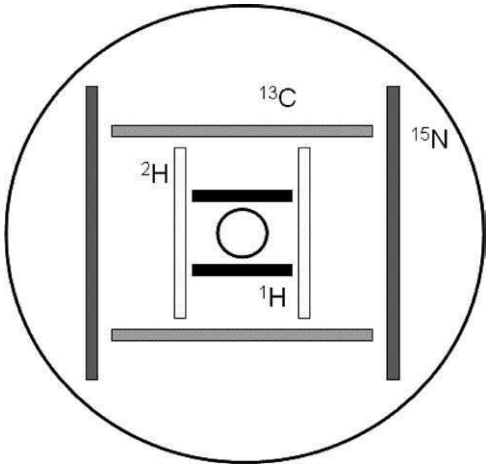

Fig. 20. Top-down view of the coil arrangement for a triple-resonance cryoprobe. All HTS coil pairs are cooled by liquid He gas by a commercial Bruker cryoplatform. The center sample region can accommodate a 1 mm NMR tube, is at ambient room temperature, and can be temperature regulated.

4.3. Multiple frequency operation

Unlike conventional probes, it is not possible to tune individual YBCO coils to multiple frequencies, since each coil is a self-resonant structure. Therefore, multiple coils have to be nested within one another, as shown in Fig. 20.[187]

As with conventional coils, the NMR sensitivity is inversely proportional to the coil diameter, and so higher mass sensitivities can be achieved by making smaller cryoprobes. The smallest diameter cryoprobe which is commercially available is currently about 3 mm in diameter. However, Saha *et al.*[187] have recently shown results from a 1 mm triple-resonance high-temperature superconducting probe.

4.4. Effect of buffer properties on cryogenic probe performance

As outlined previously, the vast majority of protein samples for solution-state NMR spectroscopy must be prepared in buffered solutions to maintain a given pH with the protein in a defined protonation state. Often, additional salts must be added to increase the protein solubility and prevent aggregation. The buffered solution produces loss in the sample, and therefore degrades the loaded Q of the probe and the S/N of the NMR experiment, as shown in Fig. 21.

As mentioned previously, the S/N from cryoprobes depends upon the relative loss from the coil and sample. As demonstrated by Kelly *et al.*[188] the sample resistance is proportional to the conductivity of the sample, which is a function of both the ion

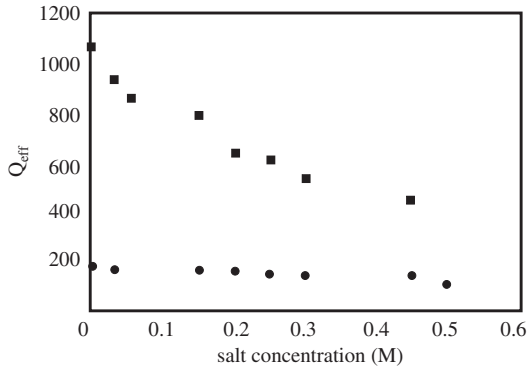

Fig. 21. Effective probe quality factor as a function of salt concentration at 400 MHz using a room temperature probe (circles) and a cryogenic probe (squares). Adapted with permission from ref. 192, copyright 2000 American Chemical Society.

concentration and ion mobility, and can be expressed as

$$\sigma = \sum_i c_i q_i \lambda_i \tag{23}$$

where c is the ionic concentration, q the charge, and λ the ionic mobility of each species i. Therefore, if the buffer has a low-ionic mobility, even if the concentration of salt is high, then the sample resistance is also low. The ratio of sample resistance to coil resistance was estimated for a number of buffers by measuring the loaded and unloaded Q values:

$$\frac{R_{\text{sample}}}{R_{\text{coil}}} = \frac{Q_{\text{unloaded}} - Q_{\text{loaded}}}{Q_{\text{loaded}}} \tag{24}$$

Using the formula for the sensitivity factor, L, introduced in Kelly's paper:

$$L = \frac{(S/N)_{\text{loaded}}}{(S/N)_{\text{unloaded}}} = \sqrt{\frac{R_c(T_c + T_a)}{R_c T_c + R_s T_s + T_a(R_c + R_s)}} \tag{25}$$

and parameters $T_a = 15$, $T_s = 298$, and $T_c = 27$ K, one can simplify this equation to

$$L = \frac{(S/N)_{\text{loaded}}}{(S/N)_{\text{unloaded}}} = \frac{1}{\sqrt{\left(1 + 7.45\frac{R_s}{R_c}\right)}} \tag{26}$$

Fig. 22 shows spectra from 1 mM lysozyme dissolved in two of the best buffers investigated, namely 50 mM MOPS/BIS-TRIS propane and 50 mM HEPES/NaOH, at pH 7.0. As a comparison, a spectrum is also shown using the most commonly used NMR buffer, sodium phosphate, at identical concentration and pH. The S/N was approximately 50% higher using the former two buffers. Also

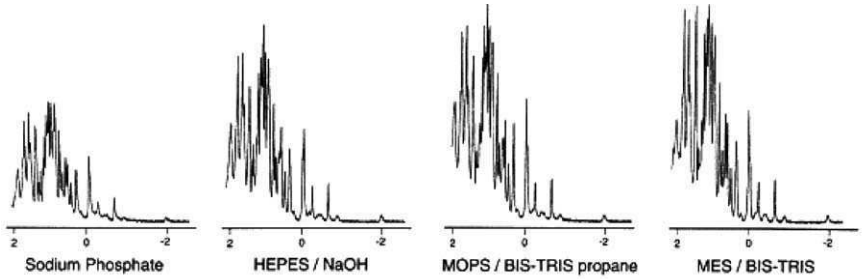

Fig. 22. One-dimensional spectra of a 1 mM lysozyme sample measured in 50 mM sodium phosphate, 50 mM HEPES/NaOH, 50 mM MOPS/BIS-TRIS propane buffer, all pH 7, and in 50 mM MES/BIS-TRIS pH 6.0. Only the most high-field-shifted regions of the spectra are shown. Reproduced with permission from ref. 188,. copyright 2002 American Chemical Society.

shown in Fig. 22 is a spectrum from a buffer, MES/BIS-TRIS, at a slightly acidic pH of 6.0, which shows essentially identical S/N to the MOPS/BIS-TRIS propane.

Kelly *et al.*[188] concluded that, as an aid in identifying potential buffers that would maximize the S/N, one should focus on singly charged ions with low diffusion coefficients, since by Einstein's equation (Eq. (27)) relating ionic mobility and molecular diffusion coefficient, D, these buffers should have a low value of λ:

$$\frac{\lambda}{D} = \frac{q}{kT} \tag{27}$$

Horiuchi *et al.*[189] have extended the work of Kelly and presented an in-depth analysis of the effects of the dielectric properties of different solvents on the Q value, and therefore S/N, of cryogenic probes. They targetted their investigation to a proton Larmor frequency of 930 MHz, but presented data at both much higher and lower frequencies. The effective sample resistance contains two contributions, one from the ionic conductivity σ_{ion} as already considered, and the other from the dielectric conductivity $\omega\varepsilon''\varepsilon_0$, where ε'' is the imaginary component of the relative dielectric permittivity and ε_0 the dielectric permittivity of vacuum. The effective conductivity is given by the sum of the two components:

$$\sigma_{\text{eff}} = \sigma_{\text{ion}} + \omega\varepsilon''\varepsilon_0 \tag{28}$$

Table 3 shows data for a number of different buffers relevant to protein NMR, together with the sensitivity factor, L, as defined in Kelly. The real component of the relative dielectric permittivity is denoted by ε', and affects the magnitude of the transverse electric field in the sample, and as discussed previously, the sample loss.

The authors found that the effective conductivity of pure water at 930 MHz is essentially determined by the value of the dielectric conductivity ($\omega\varepsilon''\varepsilon_0$) and has a value of 0.2 S/m. This is equivalent to the ionic conductivity (σ_{ion}) of 20 mM NaCl.

Table 3. Complex dielectric, conductivity and Q values of different buffers, and the effect on the loaded Q and sensitivity factors

Sample	ε'	$\sigma_{ion} + \omega\varepsilon''\varepsilon_0$	Q_L	Q_s	Sensitivity factor
Unloaded	1	0	1480		1
Water	79	0.2	1080	3996	0.34
100 mM NaCl	78	1.26	460	667	0.15
50 mM Mes	79	0.24	1015	3231	0.31
50 mM Hepes	80	0.32	940	2576	0.28
50 mM K_2PO_4 (pH 7.0)	79	1.03	540	850	0.17
50 mM Na_2PO_4 (pH 4.1)	78	1.41	442	630	0.14

For 100 mM NaCl solution, the effective conductivity was measured to be 1.26 S/m at 930 MHz. This value was dominated by the ionic conductivity of NaCl, but at higher frequencies the dielectric conductivity of water also becomes an important term. For "good" buffers such as HEPES and MES the value of σ_{eff} is dominated by the $\omega\varepsilon''\varepsilon_0$ term of both the water and the buffer solute at low frequencies, and by the $\omega\varepsilon''\varepsilon_0$ term of water at high frequencies (>2 GHz). This work showed that the analysis of Kelly is valid at low frequencies, but the dielectric conductivity, $\omega\varepsilon''\varepsilon_0$, which was not considered, plays an increasingly important role at very high frequencies.

Horiuchi also showed that the value of ε' affects the sample quality factor, Q_s, and therefore the loaded Q value of the coil and the overall S/N. The value of Q_s increases as a function of ε' until its saturation point, $Q_{s,sat}$, with the value of $Q_{s,sat}$ being inversely proportional to the effective conductivity. The dielectric sample loss can be modeled as a simple electrical circuit,[190] in which C_g denotes the tuning capacitance of the coil, and the sample loss is modeled as a parallel combination of a capacitor $\varepsilon' C_s$ and resistor $(\omega\varepsilon'' C_s)^{-1}$ in series with C_g. Following the analysis of Minard[190] the value of Q_s is given by

$$Q_s = \left(\frac{C_g + \varepsilon' C_s}{C_g}\right)^2 \left(\frac{1}{\omega L}\right)\left(\frac{1}{\omega\varepsilon'' C_s}\right) \tag{29}$$

which demonstrates the dependence of Q_s on frequency, ε' and ε''.

Lane and Arumugam[191] showed that the use of dipolar ions might be an attractive alternative to salts for maintaining protein solubility. Zwitterions at a pH near their isoelectric point do not contribute to solution conductivity, and dipolar ions also solubilize and stabilize proteins, although at relatively high-ionic concentrations. The dipolar ions must therefore be deuterated to avoid a substantial background signal. The authors used d_5-glycine since it has high solubility in water, high-dielectric increment, excellent biological compatibility, low molecular weight and ready availability in perdeuterated form. Fig. 23 compares spectra of lysozyme in 90% H_2O/10% D_2O solution with 0.5 M d_5-glycine added, and with 0.2 NaCl added, respectively. The S/N of the spectrum with d_5-glycine shows very little loss

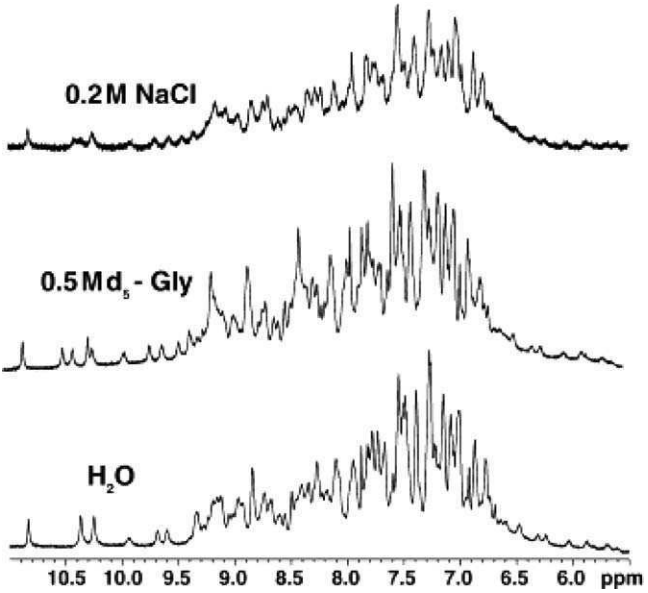

Fig. 23. 1D spectra of lysozyme at 14.1 T using an HCN cold probe. Spectra were recorded using WATERGATE suppression. Thirty-two steady states were used and the spectra acquired from a single transient. The spectra were zero-filled once. Figure reproduced from ref. 191, copyright (2005), with permission from Elsevier.

compared to simple 90% H_2O/10% D_2O, and is significantly higher than that with the added NaCl.

A final, intriguing approach to optimizing sample properties for cryogenic probe performance is to use proteins that have been encapsulated in the water cavity formed by reverse micelles in low-viscosity fluids.[192] This approach was developed originally to reduce the tumbling correlation time of large proteins *via* such encapsulation.[193–199] The authors used ubiquitin encapsulated within reverse-micelles prepared in *n*-pentane. ^{13}C- and ^{15}N-enriched protein was solvated by aqueous buffer containing 50 mM sodium acetate and 250 mM NaCl, at a pH of 5.0, and then encapsulated in reverse micelles to a concentration of 0.3 mM. The authors found that the sample did not reduce significantly the Q of the cryogenic probe used, allowing the full S/N enhancement of cryogenic probes to be achieved. This approach has also been validated by the work of Horiuchi *et al.*[189]

4.5. Effect of sample geometry on cryogenic probe performance

Despite much work on buffer optimization for cryogenic coils, the simple question of optimum sample geometry has attracted far less attention: the sample is simply assumed to be a cylindrical tube with diameter generally in the 3–5 mm range. De Swiet[200] recently considered the question of what geometric form of the electric

field produced by an NMR coil would minimize the value of the power dissipated in the sample (Eq. 4) given a uniform B_1 field over the entire sample. For a cylindrical sample of length L, with circular cross-section radius r_0, and a linearly polarized B_1 field applied along the x-axis, the minimum dissipated power is given by

$$P_s = \frac{1}{8}\sigma B_1^2 \omega_0^2 \pi r_0^4 L \left(1 - \frac{16 r_0}{L} \sum_{n=1,2\ldots} \frac{\tanh\left(j'_{1,n} L/2r_0\right)}{j'^3_{1,n}(j'^2_{1,n} - 1)}\right) \tag{30}$$

where $j'_{1,n}$ is the nth zero of the derivative of a cylindrical Bessel function J_1. For a 5 mm NMR tube at 600 MHz, with $L = 18$ mm, $r_0 = 2.1$ mm, a sample of 100 mM NaCl in water, and using a 5 μs 90° pulse, the minimum possible dissipated power was calculated from Eq. (31) to be 10.2 W. Using a cryoprobe a value of 11.6 W was measured experimentally. De Swiet then showed that a rectangular shaped sample could reduce the minimum dissipated power considerably. For a sample of length L, with a rectangular width b in the x-direction and a in the y-direction, the minimum value of P_s was calculated to be

$$P_s = \frac{1}{24}\sigma B_1^2 \omega_0^2 a^3 b L \left(1 - \frac{192 a}{L\pi^5} \sum_{n=1,3,5\ldots} \frac{\tanh(n\pi/2a)}{n^5}\right) \tag{31}$$

This equation suggests that the value of P_s can be made arbitrarily small by making the value of b large relative to the value of a. Thus, rectangular sample tubes should offer considerable increases in S/N over cylindrical ones in the case where the power dissipated in the sample dominates that dissipated in the coil.

5. PROBE DESIGNS FOR MINIMIZING SAMPLE HEATING

As discussed many times thus far, a limiting factor in probe performance, and indeed the types of NMR experiments that can currently be performed, is sample heating. Practical limits on proton decoupling power are dictated by temperature rises within the sample that can denature or dehydrate the sample. For example, proton-decoupling powers of 100 W applied for several hundred milliseconds can cause temperature increases of 50°C or more in samples with high conductivity. This effect is particularly important at high field since the dielectric heating experienced by the sample is proportional to the cube of the frequency. Much recent work has concentrated on how to design practical NMR probes, which minimize sample heating, but maintain a strong and homogeneous B_1 field. The key to all of the approaches outlined in this section is reducing the electric field in the sample produced by the RF coil.

5.1. Scroll coils for solid-state MAS

As pointed out by Stringer *et al.*[201] sample heating currently limits the potential of a number of solid-state experiments. Dipolar LWs decrease with ^{1}H-decoupling power at fields well beyond 100 kHz,[202] but most studies use decoupling powers of only

~70 kHz[203] to limit sample heating. Polarization transfer experiments, which currently use dipolar recoupling pulse sequences, could potentially be performed using more efficient windowless RF pulse trains[204–208] but these have not been widely used owing to heating problems from the high-power heteronuclear pulses and ^{1}H-decoupling power.

Stringer *et al*. approached the design of high-frequency MAS probes which minimize sample heating by using the principle that dielectric loading of a sample resonator can be minimized by decreasing the coil inductance, e.g., by reducing the number of turns in a solenoid. If one reduces the number of turns to one, one ends up with a loop gap resonator (LGR).[209] Although more commonly used in electron-paramagnetic resonance (EPR), the LGR has also been used for solid-state MAS NMR.[210] The great advantage of the LGR is that the electric field is contained almost exclusively in the gap between the conductors, and not within the sample. Fig. 24 shows measurements of the magnetic and electric field components from a LGR with a single gap.[211] The major problem with the LGR for small samples is that the inductance of the coil is so low that a large parallel capacitance is required to resonate such a coil. Given the small space available inside the probe, this means that small capacitors with high ESR and relatively low breakdown voltage have to be used. The inductance of the LGR can be increased by increasing the number of turns into a "scroll coil",[201,212] constructed from a single "ribbon" of a conductor/insulator sandwich. In the solenoid, the driving voltage is applied along the axis of the coil, with the result that the maximum electric field is at the center of the coil

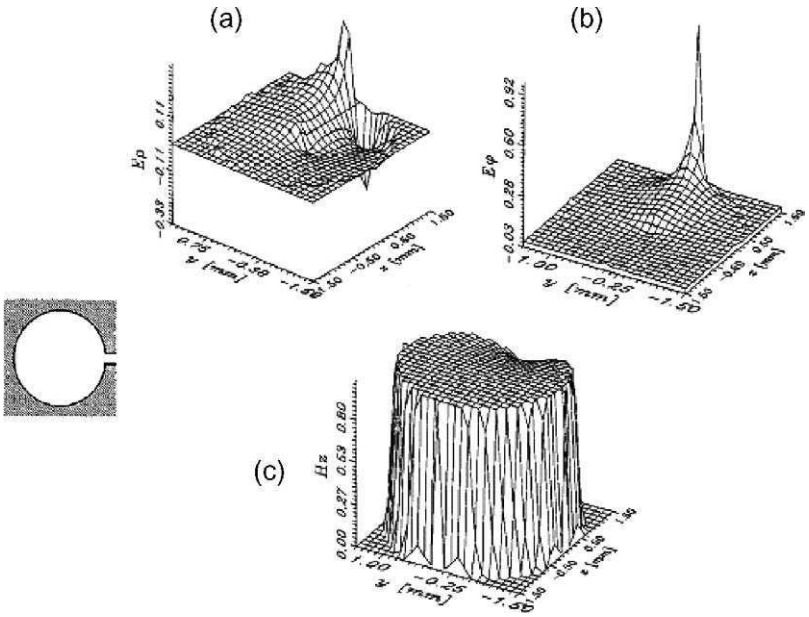

Fig. 24. Distribution of (a) E_ρ, (b) E_ϕ, and (c) H_z through the center of a LGR coil. Reproduced with permission from ref. 211, copyright (1993), Institute of Physics.

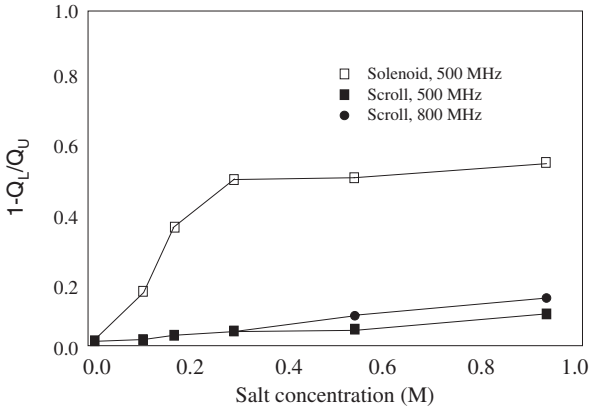

Fig. 25. Effect of dielectric loading on the quality factor of scroll and solenoid coils. The parameter 1-($Q_{loaded}/Q_{unloaded}$) is plotted as a function of salt concentration. Data at 500 MHz are presented for both the scroll and solenoid, and at 800 MHz for the scroll only. Figure reproduced from ref. 201, copyright (2005), with permission from Elsevier.

and penetrates the sample: in contrast, in the scroll the driving voltage is applied from the inner to outer turn, so very little electric field penetrates the sample.

The authors compared similarly sized scroll and solenoidal coils in terms of the Q value under different sample loads. As shown in Fig. 25, as the salt concentration was increased from 0.1 to 0.94 M, the loaded Q of the solenoid decreased by ~50%, whereas the loaded Q of the scroll coil decreased by $<10\%$. These measurements were confirmed by much smaller shifts in the resonance frequency and smaller increases in the 90° pulse widths for the scroll coil.

Tests were then performed to test differences in sample heating. The solenoid was found to give a temperature rise of 1.0°C/kHz^2 (the square of the B_1 field) for 0.94 M salt and 0.45°C/kHz^2 for 0.16 M salt. The values for the scroll coil were 0.07°C/kHz^2 and 0.028°C/kHz^2, respectively. The temperature gradient within the sample was also found to be much higher with the solenoidal coil. Finally, a direct comparison of the respective heating effects was performed on a sample of microcrystalline human ubiquitin. Fig. 26 shows spectra obtained every hour for 16 h. No significant changes in sample integrity were found for the scroll coil, but severe degradation is evident in the sample placed in the solenoidal coil, despite the fact that the salt concentration was only 8 mM.

It should be noted that the only disadvantage of the scroll coil mentioned by the authors is that the intrinsic sensitivity is lower than that of a solenoid for low frequencies, an important consideration for ^{13}C and ^{15}N direct detection experiments.

5.2. Low electric field cross-coil probes for MAS

An alternative approach to reducing RF heating in MAS probes has been presented by Doty *et al.*[143] They proposed a two-coil arrangement, rather than a multiple-tuned

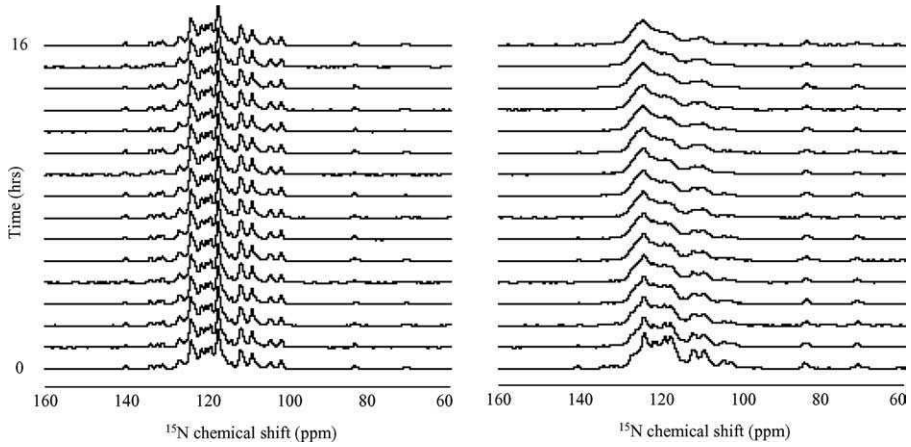

Fig. 26. Time-dependent 1D ^{15}N spectra of microcrystalline ubiquitin in the scroll (left) and solenoid (right) probes at a spinning rate of 13.3 kHz. 1D ^{15}N CP-MAS acquisition parameters were: 2 ms ^{1}H–^{15}N CP (at 43 kHz ^{1}H, 30 kHz ^{15}N with a tangent ramp), 75 kHz decoupling for 120 ms, 1.5 s pulse delay. Each spectrum was acquired at 1 h intervals. Figure reproduced from ref. 201, copyright (2005), with permission from Elsevier.

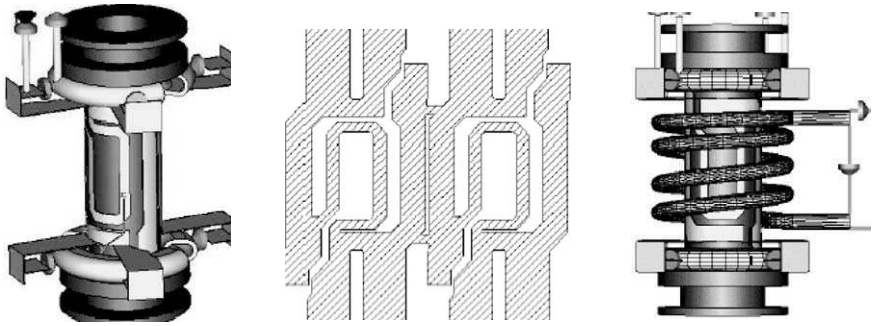

Fig. 27. (a) 3D schematic and (b) plane-view of a segmented half-turn split Alderman–Grant coil, used as the inner coil for reduced heating in solid-state MAS probes.[143] (c) Full schematic of the probe with the outer solenoidal coil.

solenoid, in which the inner coil is a variation of the previously discussed Alderman–Grant design: in order to improve the RF transparency and B_1 homogeneity the coil was segmented and an inner loop added, as shown in Fig. 27. A similar philosophy has been described in detail in the development of Litz coils by the same group.[213] This segmented coil is tuned to the proton frequency and is used for high power decoupling. A solenoidal coil is wrapped around the outside and is used for the low frequency pulses and decoupling. The ratio of the electric field to magnetic field

produced within the sample by the inner coil is reduced to roughly one-fifth that of an equivalently sized solenoid, corresponding to a reduction in sample heating of well over an order of magnitude. The authors also showed that thermal gradients within the sample were reduced substantially using this arrangement, which is referred to as an "XC" or cross-coil geometry.

5.3. Low electric field probes for aligned samples

The typical geometry of RF coils used for studying membrane proteins, mechanically oriented as bilayers between thin glass plates, is a rectangular solenoid, tuned to ^{1}H and ^{15}N frequencies. Since such samples often have high conductivity, sample heating is again an important issue, particularly since this leads to the loss of sample hydration and can cause problems with sample stability over the typically long data acquisition times. Gorkov *et al.*[214] recently presented a new design for a low-electric-field probe, consisting of a 5-turn $7.5 \times 5.5 \times 12$ mm rectangular solenoid for the low-frequency ^{15}N channel, wound inside a rectangular, electrically orthogonal, low-inductance ^{1}H resonator, as shown in Fig. 28.[214] The outer ^{1}H resonator is slit to cancel low-frequency eddy currents, which would otherwise be induced by the inner coil. The authors found that the RF homogeneity of the outer resonator was considerably higher than that of a double-tuned solenoid. Operation of the proton resonator in single resonance mode compensates for the lower-filling factor compared to a double-tuned solenoid, resulting in a ^{1}H channel efficiency similar to that of a double-tuned solenoid. Since the ^{1}H and

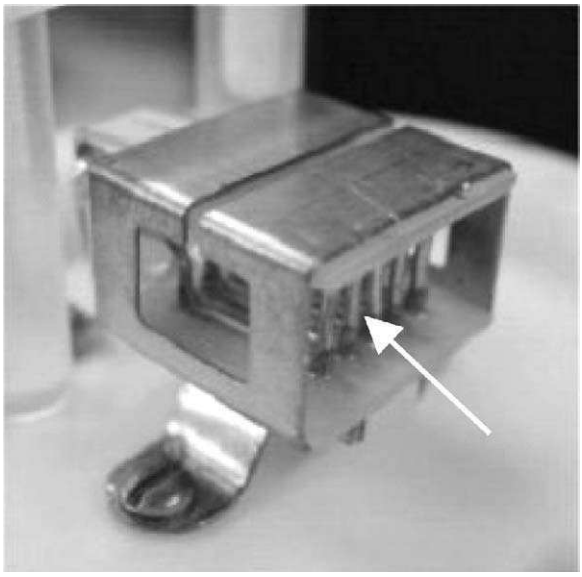

Fig. 28. Photograph of a low electric-field probe used for studies of mechanically aligned membrane proteins on glass slides. The outer coil is tuned to the proton frequency and the inner solenoid (arrow) to nitrogen.

^{15}N coils are separate in the double-coil probe, more turns could also be used in the low-frequency ^{15}N solenoid in order to increase the efficiency of the observe channel.

An experimental performance comparison between the low-inductance probe and a conventional $^{15}N/^{1}H$ static probe using a double-tuned four-turn solenoid coil of similar dimensions was performed. The extent of sample RF heating was measured on a hydrated bilayer sample by observing the increase in the length of the 90° pulse on the ^{1}H channel at 600 MHz. For non-lossy samples, the ^{1}H 90° pulse lengths were similar for the two different configurations, but the 90° pulse length for the low electric field double-coil probe was roughly one-half that of the solenoid using a lossy biological sample. The authors estimated that 13% of the applied RF power resulted in sample heating for the low-inductance coil, whereas the value was 72% for the multiple-tuned solenoid.

6. SOLENOIDAL COILS FOR LIQUID STATE NMR

Although NMR probes containing small solenoidal coils were developed originally for mass-limited samples of small molecules, they have also been used recently in a number of protein studies. The mass sensitivity of such coils (diameter ~1–1.5 mm) is similar to 5 mm cryoprobes, without the requirement of dedicating an entire system to cryoprobe operation. Small solenoidal coils allow considerably reduced amounts of protein to be used: this facet is likely to be particularly important in the case of proteins produced in eukarotic cells rather than bacteria, where isotopic enrichment is considerably more difficult and expensive.

6.1. Single coil probes

The first study discussed here used a 2.5-mm diameter, solenoid TXI probe, which was tuned to four different frequencies using the circuit shown in Fig. 29.[161] The L1–C1 trap presents a very low impedance at low frequency and high impedance at high frequency. The L2–C6–C7 tank circuit appears as a high impedance at the proton frequency, but as a very low impedance path at the ^{15}N frequency. The proton channel has the shortest electrical path to the sample coil in order to minimize signal loss. LC trap circuits at both ^{15}N and ^{13}C frequencies are used between the ^{15}N and ^{13}C channels, and the lock channel is attached to the ^{13}C channel with a trap circuit at the ^{13}C frequency. The 90° pulse widths for all channels were compared with those from a commercial 5 mm TXI probe: the values were 4.0 vs. 12 μs (^{1}H, 50 W amplifier, 6 dB attenuation), 3.8 vs. 43 μs (^{15}N, 300 W amplifier, full power), and 1.8 vs. 14 μs (^{13}C, 300 W amplifier, full power). The much shorter ^{13}C pulses are particularly important for experiments at high B_0 fields since they enable a much higher-excitation bandwidth to be achieved. Fig. 29 shows specific 2D ^{1}H, ^{15}N planes extracted at different $^{13}C = O$ frequencies from a 3D HNCO spectrum

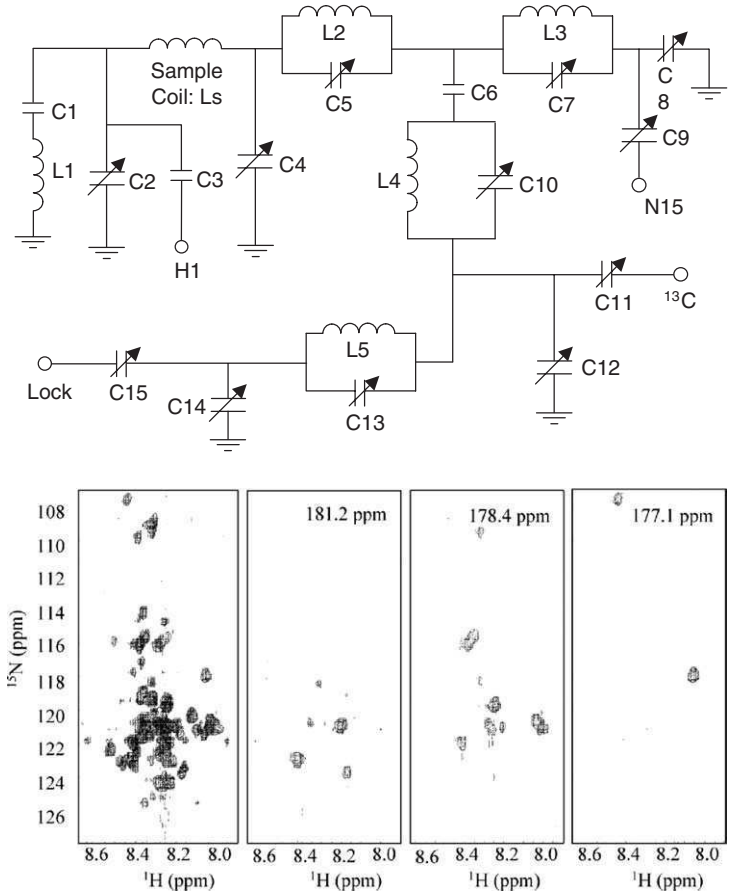

Fig. 29. (top) Circuit diagram for a solenoidal probe, diameter 2.5 mm, used to acquire the 3D HNCO data (bottom) of double-labeled 1 mM $^{15}N/^{13}C$ IA-3. Experimental parameters: sw 6614 Hz, sw1 (^{15}N) 1302 Hz, sw2 (^{13}C) 3001 Hz, 32 signal averages, 64 real data points in the $^{13}C = O$ dimension, 60 real data points in the ^{15}N dimension, 4096 complex acquisition data points, total data acquisition time 59 h. Solvent suppression used presaturation. The 2D projection of all the $^{13}C = O$ frequencies is shown in the leftmost panel, and the plots of selected single $^{13}C = O$ slices are shown in the other three panels. Figure reproduced from ref. 161, copyright (2003), with permission from Elsevier.

collected on a 1 mM, double-labeled $^{15}N/^{13}C$ IA-3 sample, an intrinsically unstructured 68 amino acid protein inhibitor of yeast proteinase A.[215]

A second protein study[216] used a commercial microcoil probe from Protasis/MRM. The volume of the TXI HCN *z*-gradient microcoil NMR probe was 5 μL with an active volume of 1.5 μL. Most of the experiments were performed using proteins from the Thermotoga maritima proteome, in particular, the conserved hypothetical protein, TM0979.[216] Fig. 30 compares 2D [^{1}H,^{15}N] HSQC spectra

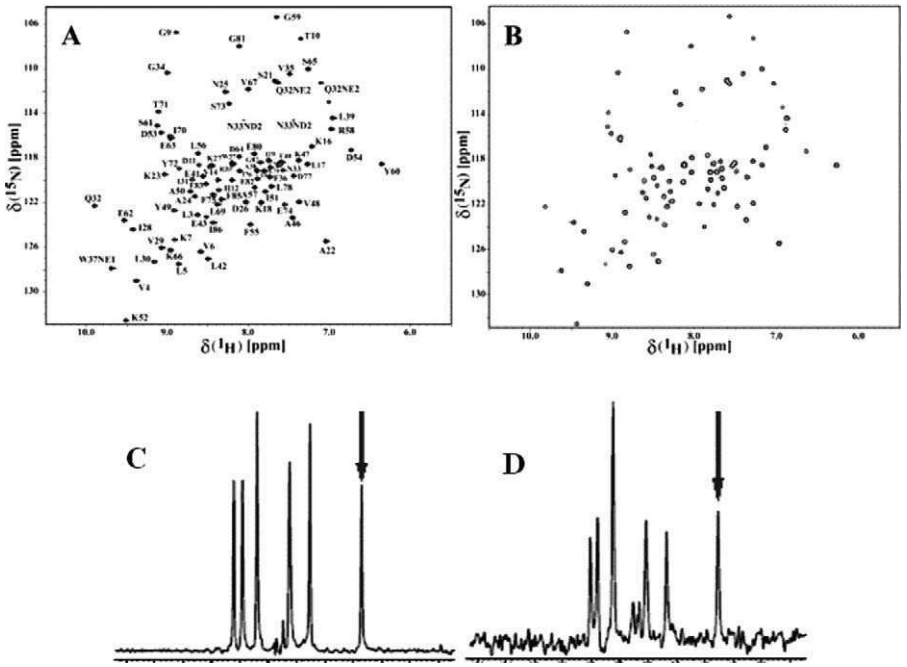

Fig. 30. 2D [^{1}H,^{15}N] HSQC spectra using (A) 5 mm TXI HCN *z*-gradient probe (Bruker, Billerica, USA) with a 2 mM sample of TM0979: 8 scans, 1 k × 128 complex points, experiment time: 30 min, (B) TXI HCN *z*-gradient CapNMR® (MRM Corporation, Savoy, USA) micro-coil probe using 5 μL of the same 2 mM sample: 16 scans, 1 k × 128 complex points, experiment time: 60 min; for both spectra the measurement temperature was set to 313 K. (C) and (D) Traces taken from 2D [^{1}H,^{15}N] HSQC spectra. The arrow marks the HN cross-peak of Tyr 60. This was one of the peaks used to measure the *S*/*N* ratio of the spectra (noise was measured over 1 ppm). Reproduced with permission from ref. 216. Copyright 2004 American Chemical Society.

obtained using a commercial 5 mm TXI HCN *z*-gradient probe with a TXI HCN *z*-gradient CapNMR® micro-coil probe.

HNCA/HNCOCA spectra were acquired using the microprobe to test the ability to perform the sequential backbone assignment of TM0979. In the HNCA spectrum, all inter- and intraresidue peaks were detectable, nearly all C_α and C_β peaks were observed in the CBCACONH spectrum, and all CO correlation peaks could be identified from the HNCO spectrum, allowing complete backbone assignment of TM0979. A subsection of the panels used for sequential analysis is shown in Fig. 31.

As outlined previously, the very short ^{13}C pulse widths are particularly important in a number of pulse sequences: in this particular study it was possible to record a single HCCH TOCSY spectrum across the full aliphatic and aromatic side-chain carbon range. This experiment allows complete side-chain assignment of all amino acids in a protein within a single spectrum. Correlation between the

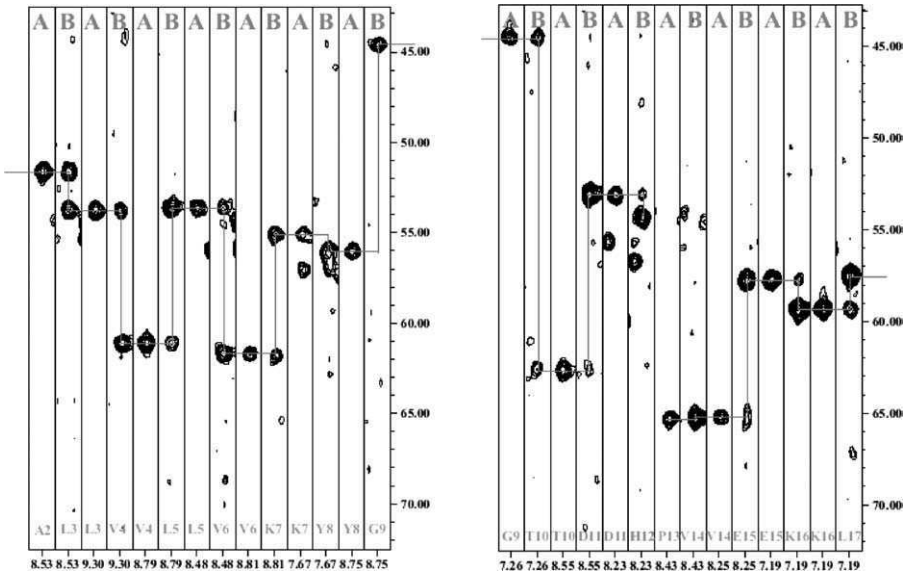

Fig. 31. Two panels showing the "sequential walk", indicated by a line connecting the C_α chemical shifts in the different spectra. Strips marked with A show the HNCOCA spectrum and strips marked with *B* the HNCA spectrum. Reproduced with permission from ref. 216. Copyright 2004 American Chemical Society.

aliphatic and aromatic carbons is hindered owing to the large carbon chemical shift ranges (aliphatic carbons, 0–75 ppm; aromatic carbons, 115–140 ppm), which corresponds to a bandwidth of roughly 20 kHz at 14.1 T. Standard 5 mm NMR probes or cryoprobes are not rated for the high power levels required to produce Hartman–Hahn mixing over this broad chemical shift range. An HCCH–TOCSY spectrum with a *z*-filter FLOPSY-16 mixing sequence using a 20 kHz spin lock field was used to acquire the spectra shown in Fig. 32. This type of spectrum can be used for the assignment of connectivities between the aliphatic C_α and C_β atoms and the rest of the aromatic side-chain, and also within the aromatic ring itself, in one measurement, thus accelerating greatly aromatic side-chain assignment.

A final example shows results obtained using a 1-mm diameter solenoidal coil wrapped using rectangular wire. Triple resonance NMR data were collected on PF1061, a 8.7 kDa protein at 750 MHz.[217] The active sample volume was 1.2 µl, and the concentration of the ($^{15}N + {}^{13}C$)-labeled protein was 4 mM. Thus, these experiments contained only about 4.7 nmol (~41 µg) of protein in the active volume of the probe. Fig. 33 shows a 1D ^1H spectrum collected with eight scans using WATERGATE solvent suppression.[218] To test for standard protein NMR experiments, 2D ^{15}N-HSQC and 3D HNCO triple resonance datasets were acquired. Both multi-dimensional protein datasets have good S/N, showing that useful data can be obtained on very small amounts of sample using optimized RF coils.

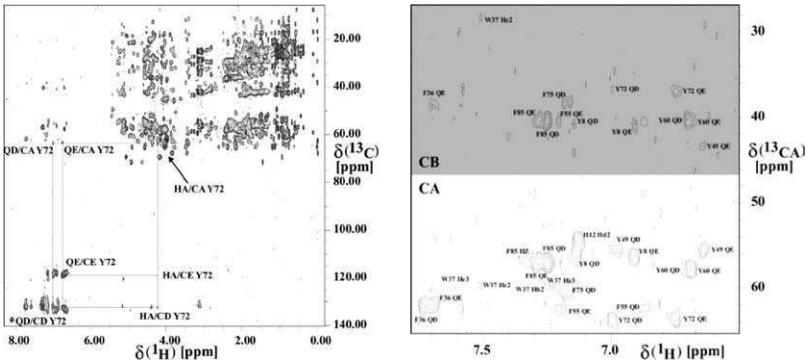

Fig. 32. (left) 2D [^{1}H, ^{13}C] aliphatic-aromatic HCCH-TOCSY FLOSPY-16 spectrum recorded with a mixing time of $\tau_m = 11.77$ ms. The assignment of Tyr 72 based on the C_α chemical shift is indicated in the spectrum (10 mM ^{13}C/^{15}N TM0979, 313 K, measurement time 30 h). (right) Enlargement of the C_α/C_β carbon chemical shift-proton aromatic chemical shift region. All cross-peaks are annotated, and the complete aromatic chemical shift assignment can be achieved. The C_β cross-peak area is highlighted with a gray box. Reproduced with permission from ref. 216, copyright 2004 American Chemical Society.

6.2. Multiple-coil probes

Typical biomolecular NMR studies involve a series of heteronuclear multi-dimensional experiments that are run in a purely serial fashion, and the total data acquisition time for a protein may be several weeks to months. In contrast to NMR, X-ray crystallography is highly parallel in its use of synchrotron facilities for structural biology data collection. Since the solenoidal coils described previously are physically small compared to the extent of homogeneous B_0 field within the magnet bore, this potentially allows multiple coils to be incorporated into a single probehead, and multiple-NMR experiments to be performed on multiple samples simultaneously. The technical challenges in producing a practical multi-coil probe include maintaining high B_0 homogeneity for each sample, maintaining maximum sensitivity for each sample, and ensuring that there is no cross-talk between the signals from each sample. Demonstrated applications of multiple coil technology include increasing NMR throughput, removing line-broadening effects in NMR-detected electrophoretic separations, monitoring rapid chemical reactions, speeding up data acquisition in multi-dimensional sequences, and performing solvent suppression.[219–233]

In terms of using multiple-coil probes for samples such as proteins, multi-frequency coils must be designed with high isolation between all the operating frequencies of the complete set of coils. One such probe, capable of acquiring two simultaneous ^{1}H–^{15}N HSQC spectra, has been designed for operation at 500 MHz, with two 3.5-mm-long coils wrapped on a 2.6 mm o.d. polyimide sheath: a glass tube of 2.5 mm o.d., 2.2 i.d. containing the protein sample can be slid into each polyimide sheath.[234] Each of the two coils was double-tuned to ^{1}H and ^{15}N frequencies, and an external lock coil was incorporated: this lock coil consisted of a

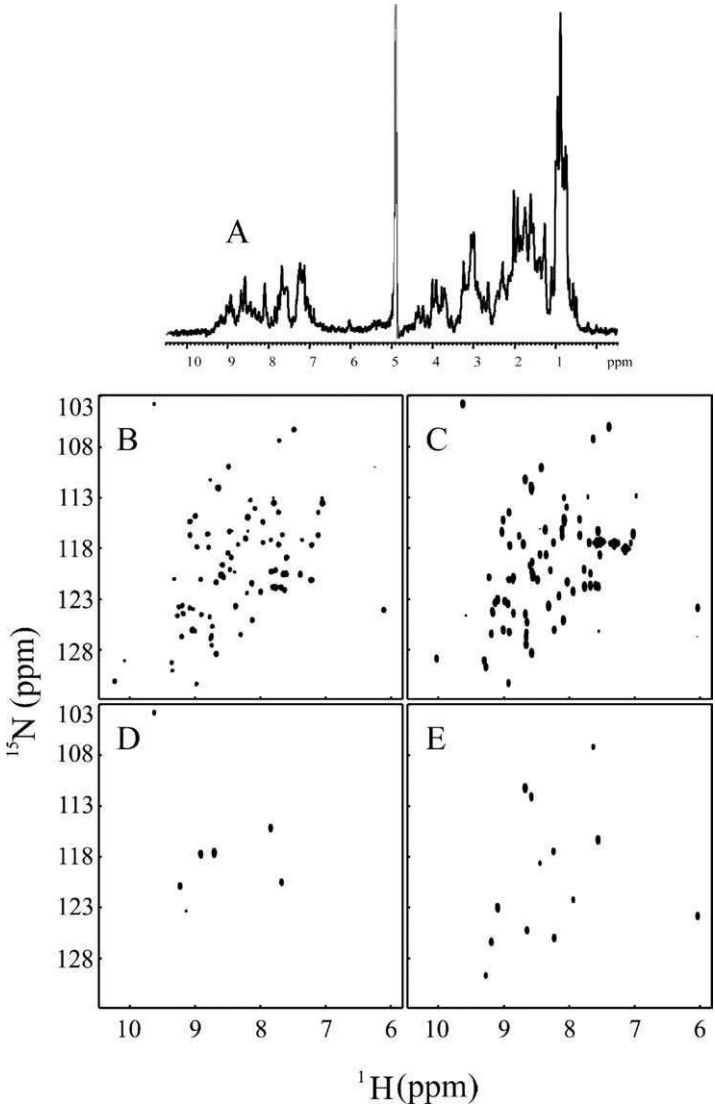

Fig. 33. NMR data on 4 mM PF1061 protein in a 1.2 μL active volume of a 1-mm diameter solenoidal coil wound with rectangular wire. (A) 1D NMR spectrum collected with eight scans and WATERGATE water suppression. The 2D ^{15}N-HSQC spectrum (B) is compared to the projection of the ^{13}C′ dimension of a 3D HNCO spectrum (C). Slices of the HNCO spectrum at 176.3 ppm (D) and 175.8 ppm (E) are shown below.

three turn solenoid with outer diameter 1 mm, contained a capillary of D_2O, and was placed approximately 5 mm from the two detection solenoidal coils. The two sample coils were situated 6 mm apart, separated by a thin copper shield for increased electrical isolation. The electrical circuits were balanced for optimum B_1

homogeneity at the ^{1}H frequency. Electrical measurements showed that there was greater than 40 dB isolation between sample coils at all frequencies. A perfluorinated liquid was used for magnetic susceptibility matching in order to improve sample shimming. Two low-loss single-pole-five-throw switches were used to multiplex the signal into a single receiver.

In order to demonstrate that heteronuclear NMR spectra acquired from one sample were not contaminated by signals from the second sample, two proteins with widely different chemical shifts were used. One protein was unfolded (characterized by poorly dispersed chemical shifts) and the other folded (usually characterized by a

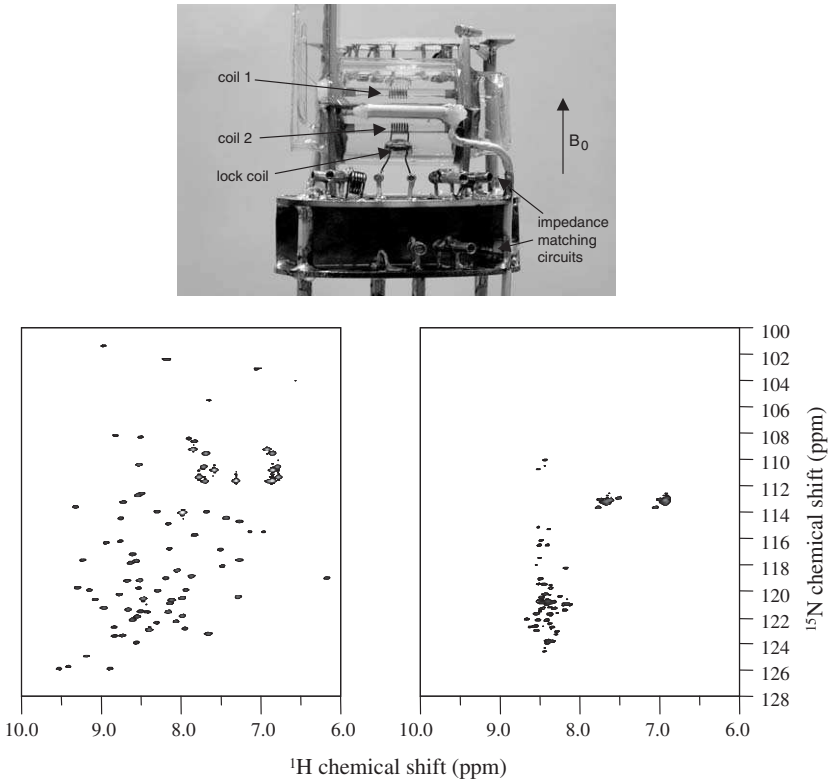

Fig. 34. (top) A photograph of the two-coil probe assembly, together with the lock coil and impedance matching circuits. The samples are slid horizontally into the thin clear tubes around which the coils are formed. (left) A ^{1}H–^{15}N HSQC spectrum of 1.25 mM ^{15}N-labeled ubiquitin in 90% H_2O/10% D_2O, 50 mM phosphate buffer, pH 5.5. Data acquisition parameters: sw = 4000 Hz, sw1 = 1600 Hz, 1024 complex data points, 192 t_1 increments acquired in States mode, 1 s water presaturation, 32 signal averages. Total data acquisition time 3.5 h. (right) A ^{1}H-^{15}N HSQC spectrum of 1 mM ^{15}N-labeled IA-3 in 90% H_2O/10% D_2O, 50 mM phosphate buffer, pH 5.5. Identical data acquisition parameters were used. Data were acquired in interleaved fashion with pulse transmission and data reception routed through an RF switch controlled from the console. Figure reproduced from ref. 234, copyright (2005), with permission from Elsevier.

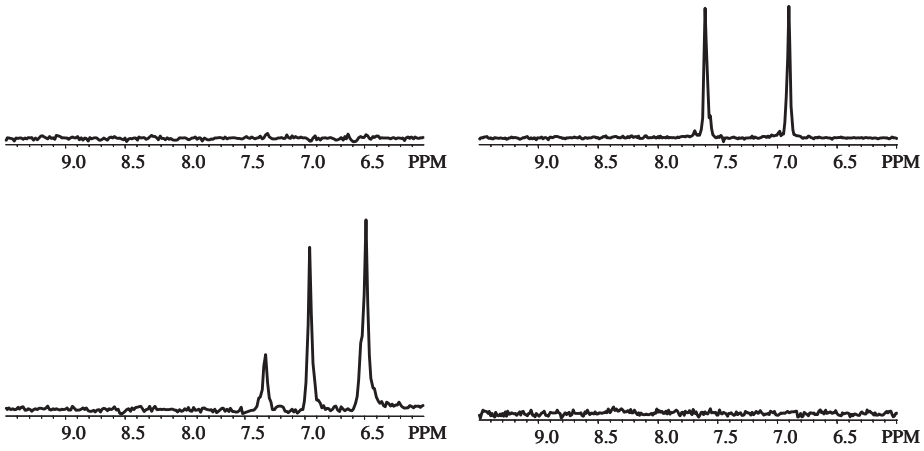

Fig. 35. Two one-dimensional slices through the ^{15}N dimensions of the 2D spectra shown in Fig. 3. The left plots correspond to ubiquitin, and those on the right to IA-3. (Top) Slice corresponding to a ^{15}N chemical shift of 113 ppm, (bottom) Slice corresponding to a ^{15}N chemical shift of 116 ppm. There is no evidence of inter-sample signal contamination.

large chemical shift dispersion). The first coil was loaded with 1.25 mM ^{15}N-labeled ubiquitin (VLI, Malvern, PA) in 90% H_2O/10% D_2O, 50 mM phosphate buffer at a pH of 5.5 and the second coil was loaded with 1 mM ^{15}N-labeled IA-3 in 90% H_2O/10% D_2O, 50 mM phosphate buffer, also at a pH of 5.5.

Fig. 34 shows two 500 MHz ^1H–^{15}N HSQC spectra of the two proteins collected at the same time. Fig. 35 shows selected one-dimensional slices through the two data sets shown in Fig. 34 in order to demonstrate the high degree of isolation between the signals detected by the two coils. In agreement with the electrical measurements, signal ''cross-talk'' was well below the noise level of the experiment.

7. CONCLUSIONS

The role of NMR in studying protein structure, dynamics, and binding continues to expand rapidly. Significant advances in pulse sequence design and sample preparation have enabled investigations of high molecular weight proteins, investigations that could not have been envisioned even a decade ago. From the hardware point-of-view, the static magnetic field strength continues to increase, offering advantages in signal-to-noise and spectral dispersion, and is approaching the optimal point for TROSY-based experiments. Cryogenic probe technology has become an enabling feature in high-throughput studies of proteins, typically offering close to an order-of-magnitude saving in data acquisition time compared to the best room temperature probes. Small-NMR probes have also increased in use, with some protein studies now being carried out with coils as small as 1 mm in diameter. Higher frequencies, larger proteins, new sequences; all present considerable challenges and opportunities for the next generation of NMR probes.

REFERENCES

1. R. B. Russell, *J. Mol. Biol.*, 1998, **279**, 1211.
2. D. Christendat, A. Yee, A. Dharamsi, Y. Kluger, M. Gerstein, C. H. Arrowsmith and A. M. Edwards, *Prog. Biophys. Mol. Biol.*, 2000, **73**, 339.
3. A. M. Edwards, C. H. Arrowsmith, D. Christendat, A. Dharamsi, J. D. Friesen, J. F. Greenblatt and M. Vedadi, *Nat. Struct. Biol.*, 2000, **7(Suppl)**, 970.
4. V. S. Lamzin and A. Perrakis, *Nat. Struct. Biol.*, 2000, **7(Suppl)**, 978.
5. E. Abola, P. Kuhn, T. Earnest and R. C. Stevens, *Nat. Struct. Biol.*, 2000, **7(Suppl)**, 973.
6. H. J. Dyson and P. E. Wright, *Unfolded Proteins*, 2002, **62**, 311.
7. D. J. Brockwell, D. A. Smith and S. E. Radford, *Curr. Opin. Struct. Biol.*, 2000, **10**, 16.
8. J. Juneja and J. B. Udgaonkar, *Curr. Sci.*, 2003, **84**, 157.
9. D. Malmodin and M. Billeter, *Prog. NMR Spectrosc.*, 2005, **46**, 109.
10. K. Wuthrich, *Eur. J. Med. Chem.*, 1995, **30**, S67.
11. K. Wuthrich, *Acta Cryst. D. Biol. Cryst.*, 1995, **51**, 249.
12. L. E. Kay, *J. Magn. Reson.*, 2005, **173**, 193.
13. D. Wishart, *Curr. Pharm. Biotechnol.*, 2005, **6**, 105.
14. G. Gao, J. G. Williams and S. L. Campbell, *Methods Mol. Biol.*, 2004, **261**, 79.
15. J. G. Kempf and J. P. Loria, *Cell Biochem. Biophys.*, 2003, **37**, 187.
16. E. R. Zuiderweg, *Biochemistry*, 2002, **41**, 1.
17. G. Wider, *Biotechniques*, 2000, **29**, 1278–1292.
18. K. H. Gardner and L. E. Kay, *Ann. Rev. Biophys. Biomol. Struct.*, 1998, **27**, 357.
19. K. Pervushin, R. Riek, G. Wider and K. Wuthrich, *Proc. Natl. Acad. Sci. USA*, 1997, **94**, 12366.
20. S. Miller, *Anal. Chem.*, 2001, **73**, 253A.
21. C. Fernandez, C. Hilty, G. Wider, P. Guntert and K. Wuthrich, *J. Mol. Biol.*, 2004, **336**, 1211.
22. P. M. Hwang, W. Y. Choy, E. I. Lo, L. Chen, J. D. Forman-Kay, C. R. H. Raetz, G. G. Prive, R. E. Bishop and L. E. Kay, *PNAS, USA*, 2002, **99**, 13560.
23. R. D. Krueger-Koplin, P. L. Sorgen, S. T. Krueger-Koplin, A. O. Rivera-Torres, S. M. Cahill, D. B. Hicks, L. Grinius, T. A. Krulwich and M. E. Girvin, *J. Biomol. NMR*, 2004, **28**, 43.
24. C. R. Sanders and K. Oxenoid, *Biochim. Biophys. Acta-Biomembranes*, 2000, **1508**, 129.
25. C. R. Sanders, K. Oxenoid, F. Soennichsen and V. Olga, *Biophys. J.*, 2000, **78**, 483A.
26. A. Arora, F. Abildgaard, J. H. Bushweller and L. K. Tamm, *Nat. Struct. Biol.*, 2001, **8**, 334.
27. L. K. Tamm, F. Abildgaard, A. Arora, H. Blad and J. H. Bushweller, *FEBS Lett.*, 2003, **555**, 139.
28. S. B. Shuker, P. J. Hajduk, R. P. Meadows and S. W. Fesik, *Science*, 1996, **274**, 1531.
29. J. Fejzo, C. Lepre and X. L. Xie, *Curr. Top. Med. Chem.*, 2003, **3**, 81.
30. J. W. Peng, C. A. Lepre, J. Fejzo, N. Abdul-Manan and J. M. Moore, *NMR Biol. Mol. Pt. A*, 2001, **338**, 202.
31. C. Dalvit, M. Fasolini, M. Flocco, S. Knapp, P. Pevarello and M. Veronesi, *J. Med. Chem.*, 2002, **45**, 2610.
32. R. Tycko, *Curr. Opin. Struct. Biol.*, 2004, **14**, 96.
33. A. E. McDermott, *Curr. Opin. Struct. Biol.*, 2004, **14**, 554.
34. L. K. Thompson, *Curr. Opin. Struct. Biol.*, 2002, **12**, 661.
35. M. K. Rosen, K. H. Gardner, R. C. Willis, W. E. Parris, T. Pawson and L. E. Kay, *J. Mol. Biol.*, 1996, **263**, 627.
36. D. M. LeMaster and D. M. Kushlan, *J. Am. Chem. Soc.*, 1996, **118**, 9255.
37. D. M. LeMaster, *Prog. NMR Spectrosc.*, 1994, **26**, 371.
38. S. J. Opella and F. M. Marassi, *Chem. Rev.*, 2004, **104**, 3587.
39. S. J. Opella, C. Ma and F. M. Marassi, *NMR Biol. Mol. Pt. B*, 2001, **339**, 285.
40. S. J. Opella, A. Nevzorov, M. F. Mesleh and F. M. Marassi, *Biochem. Cell. Biol.*, 2002, **80**, 597.
41. D. H. Jones and S. J. Opella, *J. Magn. Reson.*, 2004, **171**, 258.
42. J. R. Quine and T. A. Cross, *Math. Meth. Protein Struct. Anal. Design*, 2000, **2666**, 131.
43. F. M. Marassi and K. J. Crowell, *J. Magn. Reson.*, 2003, **161**, 64.
44. F. M. Marassi, *Conc. Magn. Reson.*, 2002, **14**, 212.

45. F. M. Marassi, *Biophys. J.*, 2001, **80**, 994.
46. F. M. Marassi, A. Ramamoorthy and S. J. Opella, *PNAS, USA*, 1997, **94**, 8551.
47. F. M. Marassi, F. C. L. Almeida, A. Ramamoorthy, Y. Kim, M. Zasloff, S. L. Schendel, W. A. Cramer and S. J. Opella, *Biophys. J.*, 1996, **70**, SU397.
48. A. Ramamoorthy, F. M. Marassi, M. Zasloff and S. J. Opella, *J. Biomol. NMR*, 1995, **6**, 329.
49. J. R. Quine, T. A. Cross, M. S. Chapman and R. Bertram, *Bull. Math. Biol.*, 2004, **66**, 1705.
50. R. R. Ketchem, W. Hu and T. A. Cross, *Science*, 1993, **261**, 1457.
51. A. Mascioni, C. Karim, J. Zamoon, D. D. Thomas and G. Veglia, *J. Am. Chem. Soc.*, 2002, **124**, 9392.
52. K. A. H. Wildman, D. K. Lee and A. Ramamoorthy, *Biochemistry*, 2003, **42**, 6545.
53. T. B. Acton, K. C. Gunsalus, R. Xiao, L. C. Ma, J. Aramini, M. C. Baran, Y. W. Chiang, T. Climent, B. Cooper, N. G. Denissova, S. M. Douglas, J. K. Everett, C. K. Ho, D. Macapagal, P. K. Rajan, R. Shastry, L. Y. Shih, G. V. Swapna, M. Wilson, M. Wu, M. Gerstein, M. Inouye, J. F. Hunt and G. T. Montelione, *Meth. Enzymol.*, 2005, **394**, 210.
54. H. D. W. Hill, Probes for high resolution, in: *Encyclopedia of NMR*, D. M. Grant and R. K. Harris, eds., Wiley, New York, 1996.
55. F. D. Doty, Probe design and construction, in: *Encyclopedia of NMR*, D. M. Grant and R. K. Harris, eds., Wiley, New Yorks, 1996.
56. F. D. Doty, Solid state probe design, in: *Encyclopedia of NMR*, D. M. Grant and R. K. Harris, eds., Wiley, New York, 1996.
57. J. Link, The design of resonator probes with homogeneous radiofrequency fields, in *NMR Basic principles and progress*, 26th edition, Springer, Berlin Heidelberg, 1992.
58. R. A. McKay, Probes for special purposes, in: *Encyclopedia of NMR*, D. M. Grant and R. K. Harris, eds., Wiley, New York, 1996.
59. L. E. Kay, M. Ikura, R. Tschudin and A. Bax, *J. Magn. Reson.*, 1989, **89**, 496.
60. S. Grzesiek and A. Bax, *J. Magn. Reson.*, 1992, **96**, 432.
61. A. Bax and M. Ikura, *J. Biomol. NMR*, 1991, **1**, 99.
62. M. Ikura, L. E. Kay and A. Bax, *J. Biomol. NMR*, 1991, **1**, 299.
63. A. Bax, G. M. Clore, P. C. Driscoll, A. M. Gronenborn, M. Ikura and L. E. Kay, *J. Magn. Reson.*, 1990, **87**, 620.
64. L. E. Kay, M. Ikura and A. Bax, *J. Am. Chem. Soc.*, 1990, **112**, 888.
65. A. Bax, G. M. Clore and A. M. Gronenborn, *J. Magn. Reson.*, 1990, **88**, 425.
66. E. T. Olejniczak, R. X. Xu and S. W. Fesik, *J. Biomol. NMR*, 1992, **2**, 655.
67. C. A. Fowler, F. Tian and J. H. Prestegard, *Biophys. J.*, 2000, **78**, 480A.
68. J. H. Prestegard, K. L. Mayer, H. Valafar and G. C. Benison, *NMR Biol. Mol. Pt. C*, 2005, **394**, 175.
69. E. de Alba and N. Tjandra, *Prog. NMR Spectrosc.*, 2002, **40**, 175.
70. H. M. Al-Hashimi and D. J. Patel, *J. Biomol. NMR*, 2002, **22**, 1.
71. A. Bax, G. Kontaxis and N. Tjandra, *NMR Biol. Mol. Pt. B*, 2001, **339**, 127.
72. S. W. Fesik, S. B. Shuker, P. J. Hajduk and R. P. Meadows, *Protein Eng.*, 1997, **10**, 73.
73. C. M. Park, C. H. Sun, E. T. Olejniczak, A. E. Wilson, R. P. Meadows, S. F. Betz, S. W. Elmore and S. W. Fesik, *Bioorg. Med. Chem. Lett.*, 2005, **15**, 771.
74. P. J. Hajduk, J. R. Huth and S. W. Fesik, *J. Med. Chem.*, 2005, **48**, 2518.
75. P. J. Hajduk and D. J. Burns, *Comb. Chem. High Throughput Screening*, 2002, **5**, 613.
76. P. J. Hajduk, D. J. Augeri, J. Mack, R. Mendoza, J. G. Yang, S. F. Betz and S. W. Fesik, *J. Am. Chem. Soc.*, 2000, **122**, 7898.
77. P. J. Hajduk, R. P. Meadows and S. W. Fesik, *Quart. Rev. Biophys.*, 1999, **32**, 211.
78. G. Liu, B. G. Szczepankiewicz, Z. H. Pei, D. A. Janowick, Z. L. Xin, P. J. Hajduk, C. bad-Zapatero, H. Liang, C. W. Hutchins, S. W. Fesik, S. J. Ballaron, M. A. Stashko, T. Lubben, A. K. Mika, B. A. Zinker, J. M. Trevillyan and M. R. Jirousek, *J. Med. Chem.*, 2003, **46**, 2093.
79. A. Medek, P. J. Hajduk, J. Mack and S. W. Fesik, *J. Am. Chem. Soc.*, 2000, **122**, 1241.
80. J. R. Huth, L. P. Yu, I. Collins, J. Mack, R. Mendoza, B. Isaac, D. T. Braddock, S. W. Muchmore, K. M. Comess, S. W. Fesik, G. M. Clore, D. Levens and P. J. Hajduk, *J. Med. Chem.*, 2004, **47**, 4851.

81. C. Dalvit, G. Papeo, N. Mongelli, P. Giordano, B. Saccardo, A. Costa, M. Veronesi and S. Y. Ko, *Drug Dev. Res.*, 2005, **64**, 105.
82. C. Dalvit, E. Ardini, M. Flocco, G. P. Fogliatto, N. Mongelli and M. Veronesi, *J. Am. Chem. Soc.*, 2003, **125**, 14620.
83. C. Dalvit, D. T. A. Hadden, R. W. Sarver, A. M. Ho and B. J. Stockman, *Comb. Chem. High Throughput Screening*, 2003, **6**, 445.
84. C. Dalvit, M. Flocco, B. J. Stockman and M. Veronesi, *Comb. Chem. High Throughput Screening*, 2002, **5**, 645.
85. C. Dalvit, M. Flocco, S. Knapp, M. Mostardini, R. Perego, B. J. Stockman, M. Veronesi and M. Varasi, *J. Am. Chem. Soc.*, 2002, **124**, 7702.
86. C. Dalvit, G. Fogliatto, A. Stewart, M. Veronesi and B. Stockman, *J. Biomol. NMR*, 2001, **21**, 349.
87. C. Dalvit, P. Pevarello, M. Tato, M. Veronesi, A. Vulpetti and M. Sundstrom, *J. Biomol. NMR*, 2000, **18**, 65.
88. C. Dalvit, P. Ramage and U. Hommel, *J. Magn. Reson.*, 1998, **131**, 148.
89. B. J. Stockman and C. Dalvit, *Prog. NMR Spectrosc.*, 2002, **41**, 187.
90. C. Dalvit, E. Ardini, G. P. Fogliatto, N. Mongelli and M. Veronesi, *Drug Disc. Today*, 2004, **9**, 595.
91. C. Dalvit, P. E. Fagerness, D. T. A. Hadden, R. W. Sarver and B. J. Stockman, *J. Am. Chem. Soc.*, 2003, **125**, 7696.
92. C. Dalvit, M. Flocco, M. Veronesi and B. J. Stockman, *Comb. Chem. High Throughput Screening*, 2002, **5**, 605.
93. S. Grzesiek and A. Bax, *J. Am. Chem. Soc.*, 1992, **114**, 6291.
94. D. Yang and L. E. Kay, *J. Am. Chem. Soc.*, 1999, **121**, 2571.
95. R. Konrat, D. Yang and L. E. Kay, *J. Biomol. NMR*, 1999, **15**, 309.
96. W. S. Price, *Ann. Rep. NMR Spectrosc.*, 1996, **32**, 51.
97. T. Parella, *Magn. Reson. Chem.*, 1998, **36**, 467.
98. T. M. Barbara and C. E. Bronnimann, *J. Magn. Reson.*, 1999, **140**, 285.
99. W. E. Maas, A. Bielecki, M. Ziliox, F. H. Laukien and D. G. Cory, *J. Magn. Reson.*, 1999, **141**, 29.
100. R. Bowtell and A. Peters, *J. Magn. Reson. Ser. A*, 1994, **115**, 55.
101. D. L. Mattiello, W. S. Warren, L. Mueller and B. T. Farmer, *J. Am. Chem. Soc.*, 1996, **118**, 3253.
102. F. Hwang and D. I. Hoult, *Magn. Reson. Med.*, 1998, **39**, 214.
103. S. K. Straus, *Phil. Trans. Roy. Soc. Lond. B*, 2004, **359**, 997.
104. T. I. Igumenova and A. E. McDermott, *J. Magn. Reson*, 2003, **164**, 270.
105. S. K. Straus, T. Bremi and R. R. Ernst, *Chem. Phys. Lett.*, 1996, **262**, 709.
106. M. Baldus, *Prog. NMR Spectrosc.*, 2002, **41**, 1.
107. M. Baldus, D. G. Geurts and B. H. Meier, *Solid State NMR*, 1998, **11**, 157.
108. S. K. Straus, T. Bremi and R. R. Ernst, *J. Biomol. NMR*, 1998, **12**, 39.
109. E. K. Paulson, C. R. Morcombe, V. Gaponenko, B. Dancheck, R. A. Byrd and K. W. Zilm, *J. Am. Chem. Soc.*, 2003, **125**, 15831.
110. F. D. Doty, G. Entzminger and Y. A. Yang, *Conc. Magn. Reson.*, 1998, **10**, 239.
111. C. H. Wu, A. Ramamoorthy and S. J. Opella, *J. Magn. Reson. Ser A*, 1994, **109**, 270.
112. A. A. Nevzorov and S. J. Opella, *J. Magn. Reson.*, 2003, **164**, 182.
113. K. Takegoshi and C. McDowell, *Chem. Phys. Lett.*, 1985, **116**, 100.
114. D. I. Hoult, *Conc. Magn. Reson.*, 2000, **12**, 173.
115. D. I. Hoult and R. E. Richards, *J. Magn. Reson.*, 1976, **24**, 71.
116. D. M. Ginsberg and M. J. Melchner, *Rev. Sci. Instrum.*, 1970, **41**, 122.
117. D. W. Alderman and D. M. Grant, *J. Magn. Reson.*, 1979, **36**, 447.
118. S. Kan, P. Gonord, C. Duret, J. Salset and C. Vibet, *Rev. Sci. Instrum.*, 1973, **44**, 1725.
119. H. J. Schneider and P. Dullenkopf, *Rev. Sci. Instrum.*, 1977, **48**, 68.
120. H. J. Schneider and P. Dullenkopf, *Rev. Sci. Instrum.*, 1977, **48**, 832.
121. D. G. Gadian and F. N. H. Robinson, *J. Magn. Reson.*, 1979, **34**, 449.
122. D. I. Hoult and P. C. Lauterbur, *J. Magn. Reson.*, 1979, **34**, 425.
123. F. D. Doty, G. Entzminger, D. Cory and J. P. Staab, *J. Magn. Reson.*, 1998, **138**, 144.

124. C. E. Hayes, W. A. Edelstein, J. F. Schenck, O. M. Mueller and M. Eash, *J. Magn. Reson.*, 1985, **63**, 622.
125. J. Tropp, *J. Magn. Reson.*, 1991, **95**, 235.
126. D. L. Olson, T. L. Peck, A. G. Webb, R. L. Magin and J. V. Sweedler, *Science*, 1995, **270**, 1967.
127. A. G. Webb, *Prog. NMR Spectrosc.*, 1997, **31**, 1.
128. M. E. Lacey, R. Subramanian, D. L. Olson, A. G. Webb and J. V. Sweedler, *Chem. Rev.*, 1999, **99**, 3133-+.
129. R. Subramanian, J. V. Sweedler and A. G. Webb, *J. Am. Chem. Soc.*, 1999, **121**, 2333.
130. R. Subramanian, M. M. Lam and A. G. Webb, *J. Magn. Reson.*, 1998, **133**, 227.
131. R. Subramanian and A. G. Webb, *Anal. Chem.*, 1998, **70**, 2454.
132. A. G. Webb and S. C. Grant, *J. Magn. Reson. Ser. B*, 1996, **113**, 83.
133. N. A. Wu, T. L. Peck, A. G. Webb, R. L. Magin and J. V. Sweedler, *Anal. Chem.*, 1994, **66**, 3849.
134. R. A. Kautz, M. E. Lacey, A. M. Wolters, F. Foret, A. G. Webb, B. L. Karger and J. V. Sweedler, *J. Am. Chem. Soc.*, 2001, **123**, 3159.
135. M. E. Lacey, A. G. Webb and J. V. Sweedler, *Anal. Chem.*, 2002, **74**, 4583.
136. M. E. Lacey, Z. J. Tan, A. G. Webb and J. V. Sweedler, *J. Chromatogr. A*, 2001, **922**, 139.
137. M. E. Lacey, A. G. Webb and J. V. Sweedler, *Anal. Chem.*, 2000, **72**, 4991.
138. Y. Li, M. E. Lacey, J. V. Sweedler and A. G. Webb, *J. Magn. Reson.*, 2003, **162**, 133.
139. D. L. Olson, M. E. Lacey, A. G. Webb and J. V. Sweedler, *Anal. Chem.*, 1999, **71**, 3070.
140. A. G. Webb, *Magn. Reson. Chem.*, 2002, **43**, 688.
141. N. Wu, T. L. Peck, A. G. Webb, R. L. Magin and J. V. Sweedler, *J. Am. Chem. Soc.*, 1994, **116**, 7929.
142. M. Gronquist, J. Meinwald, T. Eisner and F. C. Schroeder, *J. Am. Chem. Soc.*, 2005, **127**, 10810.
143. F. D. Doty, J. Kulkarni, G. Entzminger, S. Shevgoor, K. P. Shevgoor, J. P. Staab, and C. Xiao, *Experimental NMR Conference*, Asilomar, 2004.
144. S. Saha, E. Y. Chekmenev, P. L. Gorkov, W. W. Brey, *Experimental NMR Conference*, Rhode Island, 431, 2005
145. J. W. Carlson, *Magn. Reson. Med.*, 1986, **3**, 778.
146. J. S. Boyer, S. M. Wright and J. R. Porter, *J. Magn. Reson. Imaging*, 1998, **8**, 740.
147. G. N. Chmurny and D. I. Hoult, *Conc. Magn. Reson.*, 1990, **2**, 131.
148. D. T. Edmonds and M. R. Wormald, *J. Magn. Reson.*, 1988, **77**, 223.
149. L. F. Fuks, F. S. C. Huang, C. M. Carter, W. A. Edelstein and P. B. Roemer, *J. Magn. Reson.*, 1992, **100**, 229.
150. R. Bhagwandien, M. A. Moerland, C. J. G. Bakker, R. Beersma and J. J. W. Lagendijk, *Magn. Reson. Imaging*, 1994, **12**, 101.
151. R. Bhagwandien, R. Vanee, R. Beersma, C. J. G. Bakker, M. A. Moerland and J. J. W. Lagendijk, *Magn. Reson. Imaging*, 1992, **10**, 299.
152. J. P. Marques and R. Bowtell, *Conc. Magn. Reson. B*, 2005, **25B**, 65.
153. S. Burkhardt, A. Schweikard and R. Burgkart, *Med. Imag. Anal.*, 2003, **7**, 221.
154. F. D. Doty, G. Entzminger and Y. A. Yang, *Conc. Magn. Reson.*, 1998, **10**, 133.
155. N. Soffe, J. Boyd and M. Leonard, *J. Magn. Reson. Ser. A*, 1995, **116**, 117.
156. F. O. Zelaya, S. Crozier, S. Dodd, R. Mckenna and D. M. Doddrell, *J. Magn. Reson. Ser. A*, 1995, **115**, 131.
157. R. W. Martin, E. K. Paulson and K. W. Zilm, *Rev. Sci. Instrum.*, 2003, **74**, 3045.
158. E. K. Paulson, R. W. Martin and K. W. Zilm, *J. Magn. Reson.*, 2004, **171**, 314.
159. J. Murphy-Boesch and A. P. Koretsky, *J. Magn. Reson.*, 1983, **54**, 526.
160. P.L. Gorkov, K.S. Shetty, S. Saha, E.Y. Chekmenev, J. Hu, R. Fu and W.W. Brey, *Experimental NMR Conference*, Asilomar, (2004).
161. Y. Li, T. M. Logan, A. S. Edison and A. Webb, *J. Magn. Reson.*, 2003, **164**, 128.
162. P. Styles, N. F. Soffe, C. A. Scott, D. A. Cragg, F. Row, D. J. White and P. C. J. White, *J. Magn. Reson.*, 1984, **60**, 397.
163. M. Jerosch-Herold and R. K. Kirschman, *J. Magn. Reson.*, 1989, **85**, 141.

164. W. H. Wong, R. S. Withers, R. Nast, V. Y. Kotsubo, M. E. Johansson, H. D. W. Hill, L. F. Fuks, K. A. Kelin, B. Cole, W. W. Brey, A. Barfknecht and W. A. Anderson, *Adv. Cryo. Eng.*, 1996, **42**, 953.
165. T. M. Logan, N. Murali, G. S. Wang and C. Jolivet, *Magn. Reson. Chem.*, 1999, **37**, 762.
166. R. C. Crouch, W. Llanos, K. G. Mehr, C. E. Hadden, D. J. Russell and G. E. Martin, *Magn. Reson. Chem.*, 2001, **39**, 555.
167. D. J. Russell, C. E. Hadden, C. E. Martin, A. A. Gibson, A. P. Zens and J. L. Carolan, *J. Nat. Prod*, 2000, **63**, 1047.
168. J. L. Griffin, H. Keun, C. Richter, D. Moskau, C. Rae and J. K. Nicholson, *Neurochem. Int.*, 2003, **42**, 93.
169. H. C. Keun, O. Beckonert, J. L. Griffin, C. Richter, D. Moskau, J. C. Lindon and J. K. Nicholson, *Anal. Chem.*, 2002, **74**, 4588.
170. H. Kovacs, D. Moskau and M. Spraul, *Prog. NMR Spectrosc.*, 2005, **46**, 131.
171. P. J. Hajduk, T. Gerfin, J. M. Boehlen, M. Haberli, D. Marek and S. W. Fesik, *J. Med. Chem.*, 1999, **42**, 2315.
172. S. E. Hurlston, W. W. Brey, S. A. Suddarth and G. A. Johnson, *Magn. Reson. Med.*, 1999, **41**, 1032.
173. A. C. Wright, H. K. Song and F. W. Wehrli, *Magn. Reson. Med.*, 2000, **43**, 163.
174. F. Odoj, E. Rommel, M. von Kienlin and A. Haase, *Rev. Sci. Instrum.*, 1998, **69**, 2708.
175. R. D. Black, P. B. Roemer, A. Mogrocampero, L. G. Turner and K. W. Rohling, *App. Phys. Lett.*, 1993, **62**, 771.
176. R. D. Black, T. A. Early, P. B. Roemer, O. M. Mueller, A. Mogrocampero, L. G. Turner and G. A. Johnson, *Science*, 1993, **259**, 793.
177. R. D. Black, T. A. Early and G. A. Johnson, *J. Magn. Reson. Ser. A*, 1995, **113**, 74.
178. A. S. Hall, N. M. Alford, T. W. Button, D. J. Gilderdale, K. A. Gehring and I. R. Young, *Magn. Reson. Med.*, 1991, **20**, 340.
179. L. Darrasse and J. C. Ginefri, *Biochimie*, 2003, **85**, 915.
180. J. R. Miller, K. Zhang, Q. Y. Ma, I. K. Mun, K. J. Jung, J. Katz, D. W. Face and D. J. Kountz, *IEEE Trans. Biomed. Eng.*, 1996, **43**, 1197.
181. J. R. Miller, K. Zhang, Q. Y. Ma and I. K. Mun, *Radiology*, 1996, **201**, 886.
182. R. S. Withers, G. C. Liang, B. F. Cole and M. Johansson, *Trans. App. Supercon.*, 1993, **3**, 2450.
183. J. G. Vanheteren, T. W. James and L. C. Bourne, *Magn. Reson. Med.*, 1994, **32**, 396.
184. J. C. Ginefri, L. Darrasse and P. Crozat, *Magn. Reson. Med.*, 2001, **45**, 376.
185. Y. M. Kim, W. L. Earl and R. E. Norberg, *J. Magn. Reson. Ser. A*, 1995, **116**, 139.
186. H. D. W. Hill, *IEEE Trans. App. Supercon.*, 1997, **77**, 3750.
187. S. Saha, W.W. Brey, R.S. Withers and A.S. Edison, *Experimental NMR Conference*, Rhode Island, (2005), 430.
188. A. E. Kelly, H. D. Ou, R. Withers and V. Dotsch, *J. Am. Chem. Soc.*, 2002, **124**, 12013.
189. T. Horiuchi, M. Takahashi, J. Kikuchi, S. Yokoyama and H. Maeda, *J. Magn. Reson.*, 2005, **174**, 34.
190. K. R. Minard and R. A. Wind, *Conc. Magn. Reson.*, 2001, **13**, 190.
191. A. N. Lane and S. Arumugam, *J. Magn. Reson.*, 2005, **173**, 339.
192. P. F. Flynn, D. L. Mattiello, H. D. W. Hill and A. J. Wand, *J. Am. Chem. Soc.*, 2000, **122**, 4823.
193. A. J. Wand, M. R. Ehrhardt and P. F. Flynn, *PNAS, USA*, 1998, **95**, 15299.
194. C. R. Babu, P. F. Flynn and A. J. Wand, *J. Biomol. NMR*, 2003, **25**, 313.
195. C. R. Babu, P. F. Flynn and A. J. Wand, *J. Am. Chem. Soc.*, 2001, **123**, 2691.
196. M. R. Ehrhardt, P. F. Flynn and A. J. Wand, *J. Biomol. NMR*, 1999, **14**, 75.
197. P. F. Flynn, A. Wendt and P. Gollnick, *Prot. Struct. Funct. Gen.*, 2002, **49**, 432.
198. P. F. Flynn, M. J. Milton, C. R. Babu and A. J. Wand, *J. Biomol. NMR*, 2002, **23**, 311.
199. P. F. Flynn and A. J. Wand, *NMR Biol. Mol. Pt. B*, 2001, **339**, 54.
200. T. M. de Swiet, *J. Magn. Reson.*, 2005, **174**, 331.
201. J. A. Stringer, C. E. Bronnimann, C. G. Mullen, D. H. H. Zhou, S. A. Stellfox, Y. Li, E. H. Williams and C. M. Rienstra, *J. Magn. Reson.*, 2005, **173**, 40.
202. A. Detken, E. H. Hardy, M. Ernst and B. H. Meier, *Chem. Phys. Lett.*, 2002, **356**, 298.

203. F. Castellani, B. van Rossum, A. Diehl, M. Schubert, K. Rehbein and H. Oschkinat, *Nature*, 2002, **420**, 98.
204. M. Hohwy, C. M. Rienstra, C. P. Jaroniec and R. G. Griffin, *J. Chem. Phys.*, 1999, **110**, 7983.
205. A. Brinkmann, M. Eden and M. H. Levitt, *J. Chem. Phys.*, 2000, **112**, 8539.
206. M. Carravetta, M. Eden, X. Zhao, A. Brinkmann and M. H. Levitt, *Chem. Phys. Lett.*, 2000, **321**, 205.
207. D. M. Gregory, D. J. Mitchell, J. A. Stringer, S. Kiihne, J. C. Shiels, J. Callahan, M. A. Mehta and G. P. Drobny, *Chem. Phys. Lett.*, 1995, **246**, 654.
208. Y. K. Lee, N. D. Kurur, M. Helmle, O. G. Johannessen, N. C. Nielsen and M. H. Levitt, *Chem. Phys. Lett.*, 1995, **242**, 304.
209. W. Froncisz and J. S. Hyde, *J. Magn. Reson.*, 1982, **47**, 515.
210. F. H. Larsen, P. Daugaard, H. J. Jakobsen and N. C. Nielsen, *J. Magn. Reson. Ser. A*, 1995, **115**, 283.
211. W. Piasecki and W. Froncisz, *Meas. Sci. Technol.*, 1993, **4**, 1363.
212. S. C. Grant, L. A. Murphy, R. L. Magin and G. Friedman, *IEEE Trans. Magn.*, 2001, **37**, 2989.
213. F. D. Doty, G. Entzminger and C. D. Hauck, *J. Magn. Reson.*, 1999, **140**, 17.
214. P. L. Gorkov, E. Y. Chekmenev and W. W. Brey, *Experimental NMR Conference*, Rhode Island, 464 (2005).
215. M. Li, L. H. Phylip, W. E. Lees, J. R. Winther, B. M. Dunn, A. Wlodaawer, J. Kay and A. Gustchina, *Nat. Struct. Biol.*, 2000, **7**, 113.
216. W. Peti, T. Herrmann, O. Zagnitko, S. K. Grzechnik and K. Wuthrich, *Proteins*, 2005, **59**, 387.
217. H. Valafar, K. L. Mayer, C. M. Bougault, P. D. LeBlond, F. E. Jenney Jr., P. S. Brereton, M. W. Adams and J. H. Prestegard, *J. Struct. Funct. Genom.*, 2004, **5**, 241.
218. M. Piotto, V. Saudek and V. Sklenar, *J. Biomol. NMR*, 1992, **2**, 661.
219. G. Fisher, C. Petucci, E. MacNamara and D. Raftery, *J. Magn. Reson.*, 1999, **138**, 160.
220. T. Hou, J. Smith, E. MacNamara, M. Macnaughtan and D. Raftery, *Anal. Chem.*, 2001, **73**, 2541.
221. T. Hou, E. MacNamara and D. Raftery, *Anal. Chim. Acta*, 1999, **400**, 297.
222. E. MacNamara, T. Hou, G. Fisher, S. Williams and D. Raftery, *Anal. Chim. Acta*, 1999, **397**, 9.
223. M. A. Macnaughtan, A. P. Smith, P. B. Goldsbrough, R. E. Santini and D. Raftery, *Anal. Bioanal. Chem.*, 2004, **378**, 1520.
224. M. A. Macnaughtan, T. Hou, J. Xu and D. Raftery, *Anal. Chem.*, 2003, **75**, 5116.
225. M. A. Macnaughtan, T. Hou, E. MacNamara, R. E. Santini and D. Raftery, *J. Magn. Reson.*, 2002, **156**, 97.
226. D. Raftery, *Anal. Bioanal. Chem.*, 2004, **378**, 1403.
227. D. Raftery, *Anal. Chim. Acta*, 2000, **397**, 1.
228. H. Wang, L. Ciobanu, A. S. Edison and A. G. Webb, *J. Magn. Reson.*, 2004, **170**, 206.
229. H. Wang, L. Ciobanu and A. Webb, *J. Magn. Reson.*, 2005, **173**, 134.
230. L. Ciobanu, D. A. Jayawickrama, X. Z. Zhang, A. G. Webb and J. V. Sweedler, *Angew. Chem. Intl.* Ed., 42 (2003) 4669.
231. Y. Li, A. M. Wolters, P. V. Malawey, J. V. Sweedler and A. G. Webb, *Anal. Chem.*, 1999, **71**, 4815.
232. A. M. Wolters, D. A. Jayawickrama, A. G. Webb and J. W. Sweedler, *Anal. Chem.*, 2002, **74**, 5550.
233. X. Zhang, J. V. Sweedler and A. G. Webb, *J. Magn. Reson.*, 2001, **153**, 254.
234. A. G. Webb, *J. Pharm. Biomed. Anal.*, 2005, **38**, 892.

Diffusion in Soft Polymer Systems as Approached by Field-Gradient NMR

Y. YAMANE, S. KANESAKA, S. KIM, K. KAMIGUCHI, M. MATSUI, S. KUROKI AND I. ANDO

Department of Chemistry and Materials Science, Tokyo Institute of Technology, 2-12-1 Ookayama, Meguro-ku, Tokyo, Japan

Recent developments in the diffusion of soft polymer systems, such as gels and liquid crystals, as studied by field-gradient NMR spectroscopy are reviewed. It is shown that field-gradient NMR spectroscopy gives us new and useful information about the diffusion process of soft polymer systems which are one of the most important fields in polymer science.

1. INTRODUCTION

Most recently, the term "soft polymers" has been commonly used in the field of polymer science and polymer materials science.[1] Polymer gels, polymer liquid

ANNUAL REPORTS ON NMR SPECTROSCOPY
VOLUME 58 ISSN 0066 4103
DOI 10.1016/S0066-4103(05)58002-5

crystals, vulcanized elastomers, etc. are contained in the category of soft polymers, in which molecular motion is much higher when compared with solid polymers. Most recently *soft* polymers have attracted attention as useful materials. Polymer gels consist of two components namely network polymer chains and solvent, a third component such as a low molecular weight compound or polymer is often contained in the gels. They have attracted considerable attention from the point-of-view of various physical and chemical properties. These properties lead to the vitality of polymer research and development of a diversity of interests in polymer gel systems. On the other hand, polymer liquid crystals with new functions have been increasingly expanded by excellent molecular design on the basis of liquid crystal science and technology. From such situations, new structures of forming polymer liquid crystals have been discovered associated with new functions. Nevertheless, in order to develop further new polymer liquid crystalline materials, polymer liquid crystal design must been carried out on the basis of advanced polymer liquid crystal science and technology. Therefore, it can be said that polymer gels and polymer liquid crystals must be developed by precise structural and dynamic characterization. The former has been successfully made by solid-state NMR methods.[2] On the other hand, the latter has been made by NMR relaxation times and solid-state NMR spectral patterns.[2,3] Most recently, a new aspect for elucidating dynamic behavior of soft polymers has appeared. It is based upon a study of diffusion that is one of the dynamic quantities of soft polymers.

It is well known that NMR spectroscopy provides very sophisticated structural and dynamic characterization, and that has contributed to polymer science and polymer technology. Such a situation has been introduced by review articles and books.[4–8] Most recently, the field-gradient NMR method has been developed by designing high field-gradient probe systems to measure extremely small diffusion coefficient D of about $10^{-11}\,cm^2\,s^{-1}$ and to handle polymer systems with small diffusion coefficients and short spin–spin relaxation times T_2.[9] It leads to an expansion of polymer gel science and polymer liquid crystal science. From such a background, we aim to introduce some aspects of the diffusion of polymer gels and liquid crystalline polymers as most recently studied by field-gradient NMR. In addition, diffusion of probe molecules in polymer systems with soft channels is employed.

2. DIFFUSIONAL BEHAVIOR OF PROBE MOLECULES IN POLYMER NETWORKS

2.1. Diffusion of solvents in polystyrene gels

It is well known that Merrifield network polymer systems, considered in this work, have been applied to a solid-phase reaction field, which is used in synthesizing peptides by reactions of amino acids. The rate of reaction in the solid-phase reaction field is closely associated with the structure and dynamics of the polymer gels used, and the intermolecular interactions between the polymer network and the

amino acids. Further, it can be said that network polymer chains in the gel are more immobile when compared with polymer chains in solution at the same polymer concentration because of the existence of chemical cross-linking points.

It has been demonstrated that NMR gives very useful information about the structure and dynamics of polymer gel systems.[2,3,5–10] The spin–lattice relaxation time (T_1) and spin–spin relaxation time (T_2) give information about the microscopic molecular motion of solvent and probe polymer in polymer gel systems. Also, ^{1}H NMR imaging can provide spatial information about the diffusion process of molecules in polymer gels.[1–20] Further, the ^{1}H pulsed field-gradient spin-echo (PFGSE) NMR method[2b,4–7,9c,21–26] has become a useful technique for studying self-diffusion in polymer gels[5,7,10,27–47] in addition to the diffusion studies on substances in polymer gels by the dynamic light scattering (DLS) method,[50–52] and also molecular lateral diffusion in membrane systems has been studied by fluorescence recovery after photobleaching.[53–57] Most recently, by using the PFGSE NMR method, the diffusional behavior of polymer and solvent in polymer gel systems has been systematically elucidated.[27–47] The diffusional behavior of the solvent in network polystyrene gels is introduced as a function of the degree of volume swelling (Q) by means of ^{1}H PFGSE NMR method.

The Merrifield polystyrene network (MPS) resin beads are cross-linked by 1% of divinylbenzene (DVB) and have been functionalized with chloromethyl groups.[48,49] Three types of resins (A, B and C) with the fraction of chloromethylation in the phenyl rings (f_{cm}) are used.[58] The average diameters of the beads (resins A, B and C) were 75–150 μm. The degree of volume swelling of network polystyrene gel (Q) is defined as the ratio of the volume of a swollen network polystyrene gel at room temperature ($V_{swollen}$) to the volume of a dried network polystyrene gel (V_{dry}) [$Q = V_{swollen}/V_{dry}$].

2.1.1. *^{1}H PFGSE NMR spectra and their assignments*

For convenience, we will describe the self-diffusion coefficient measurements by means of an NMR spectrometer with a pulse gradient generator using a standard PFGSE pulse sequence[22] (the Hahn echo sequence:[21] $\pi/2$ pulse-τ–π pulse) with field-gradient pulse in between the $\pi/2$ and π pulses, and in between the π pulse and the spin echo. In the method to measure very small diffusion coefficients, field-gradient strengths from 0 to 22 T m^{-1} are used. Also, a pulsed field-gradient stimulated-echo (PFGStE) pulse sequence[21] ($\pi/2$ pulse-τ_1–$\pi/2$ pulse-τ_2–$\pi/2$ pulse) for soft polymer systems with very short T_2 can be used instead of the PFGSE pulse sequence. This has been successfully used in our previous works on diffusional behavior in polymer systems such as gel systems,[22–47] polymer liquid crystals,[9a,c,59,60] *n*-alkanes,[61,156] etc. The relationship between the echo signal intensity and the pulse field-gradient parameters is given by

$$A(\delta \text{ or } G)/A(0) = \exp[-\gamma^2 G^2 D\delta^2(\Delta - \delta/3)] \quad (1)$$

where $A(\delta$ or $G)$ and $A(0)$ are echo signal intensities at $t = 2\tau$ with and without the magnetic field-gradient pulse, respectively. The field-gradient pulse width is δ. τ is

the pulse interval, γ the gyromagnetic ratio of the proton, G the field-gradient strength, D the self-diffusional coefficient and Δ the field-gradient pulse interval. The echo signal intensity was measured as a function of δ or G. The plot of $\ln[A(\delta$ or $G)/A(0)]$ against $\gamma^2G^2\delta^2(\Delta-\delta/3)$ gives a straight line with a slope of $-D$. As one of the examples, the τ, Δ and δ values employed in these experiments were 4, 4 and 0.001–0.4 ms, respectively. The diffusion coefficient D of water of $2.5 \times 10^{-5}\,\mathrm{cm^2\,s^{-1}}$ at 303 K was used for the calibration of the field-gradient strength. The experimental error for the D value was estimated to be within 5%.

As probe molecules in the biphasic phase have two-diffusion components in diffusion on the measurement timescale, the total echo attenuation is given by a superposition of contributions from the individual components as expressed by

$$A(\delta \text{ or } G)/A(0) = f_1 \exp[-\gamma^2G^2D_1\delta^2(\Delta - \delta/3)] + f_2 \exp[-\gamma^2G^2D_2\delta^2(\Delta - \delta/3)] \tag{2}$$

where D_i is the self-diffusion coefficient of the ith component, and f_i is the fraction of the ith component and thus $f_1+f_2 = 1$. The fraction for the fast and slow diffusion components can be determined from the intercept of the least-squares fitted straight line.

Fig. 1 shows ^{1}H PFGSE NMR spectra of DMF in gel A with $Q = 2.20$ obtained by varying the field-gradient pulse duration δ at 30 °C.[40] Two peaks can be assigned to DMF in the gel A by using reference data for neat DMF. The rate of diffusion of the corresponding DMF molecules influences the peak intensity decay. No peaks that come from gel A appear in the ^{1}H PFGSE NMR experiments. This is due to the slow motion of the network chains. Thus, the peaks of gel A decay during the echo time (2τ) because these protons have very short T_2 values. The plots of $\ln[A(\delta)/A(0)]$ against $\gamma^2G^2\delta^2(\Delta-\delta/3)$ are shown over a wide range of temperatures in Fig. 2.

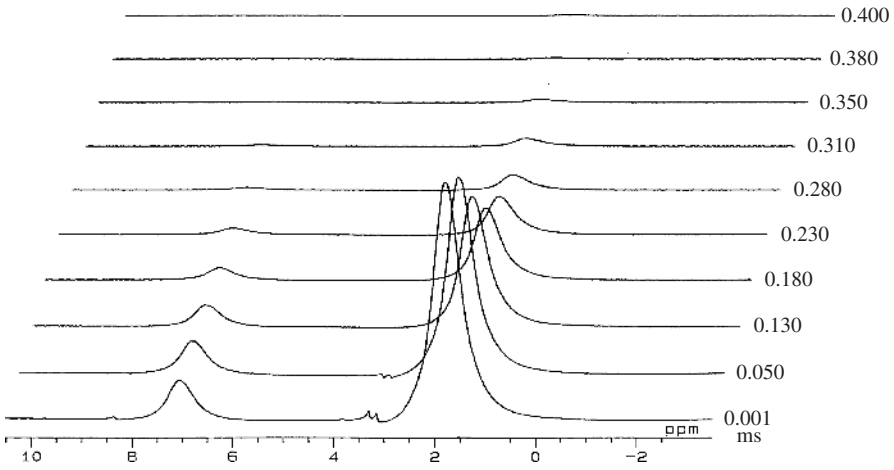

Fig. 1. ^{1}H PFGSE NMR spectra of DMF in resin A gel with $Q = 2.20$ by varying field-gradient pulse duration δ at 30 °C.

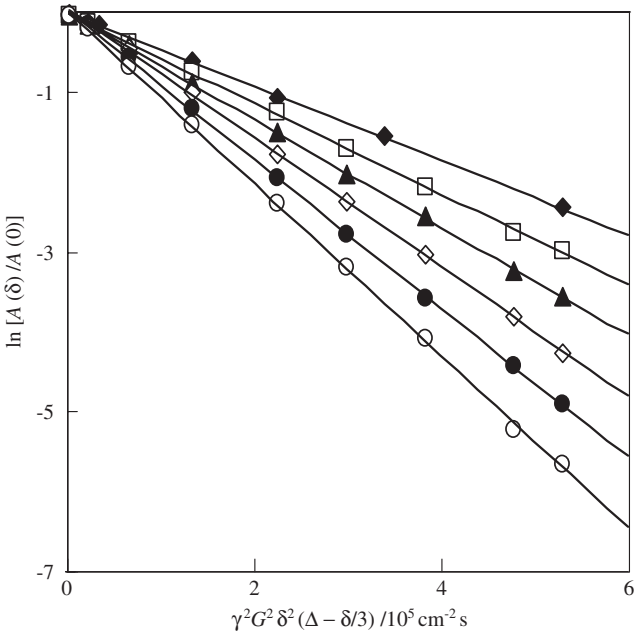

Fig. 2. Diffusional spin-echo attenuation of DMF in resin A gel with $Q = 2.20$ in the temperature range from 30 to 80 °C. 30 (♦), 40 (□), 50 (▲), 60 (◇), 70 (●) and 80 °C (○)

It is seen that the experimental data lie on a straight line. This shows that DMF in gel A is a single component, diffusion during the observation time, because the DMF decay is mono-exponential. The signal of DMF in the network polystyrene gels was observed to be showing restricted diffusion by ^{1}H PFGSE NMR measurements over the Δ range from 5 to 300 ms. It seems that at $\Delta = 10$ ms the D value determined in this work is close to the real diffusion coefficient.[23,24,62] As for DMF in the resin A gel at 30 °C, at $\Delta = 5$, 10 and 200 ms the determined D values were 9.46, 8.38 and 2.38×10^{-6} cm^2 s^{-1}, respectively. The D values were calculated from the slope of the straight line obtained from the least-mean squares plots, and the experimental error estimated by its standard derivation is less than 5%.

2.1.2. *Diffusion coefficient of DMF in network polystyrene gels*

The diffusion coefficients of DMF (D^{DMF}) in resin A and resin C gels were determined by the ^{1}H PFGSE NMR method as a function of Q over the temperature range from 30 to 80 °C.[40] The D^{DMF} values obtained were plotted against Q at 50 °C as shown in Fig. 3. As seen from this figure, the D^{DMF} value increases with an increase in Q. The D values for the DMF in network polystyrene gels increase linearly with an increase of Q in the $Q < 3.2$ range, the change of the D value for DMF in the $Q > 3.2$ range is smaller than that in the $Q < 3.2$ range. The D_0^{DMF} value in neat DMF was 2.26×10^{-5} cm^2 s^{-1} at 50 °C. Therefore, it can be said that the

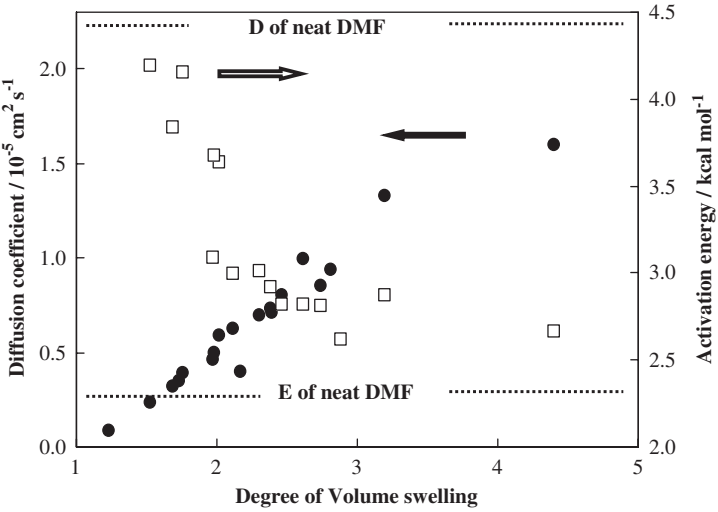

Fig. 3. Dependence of the diffusion coefficient of DMF in resin A and resin C gel (●) and activation energy for diffusion (□) on the degree of volume swelling Q at 50 °C.

intermolecular interaction between DMF and the polymer network, which depends on the size of the polymer network, restrains the translational motion of the DMF molecules.

In order to better understand the diffusional behavior of DMF in network polystyrene gels, the activation energy of self-diffusion (E) can be determined. The E value was obtained from the plots of $\ln D$ against $1/T$ (the Arrhenius plots) within the temperature range from 30 to 80 °C. The E value was calculated from the slope obtained from the least mean squares fit. As for DMF in the resin A gel with $Q = 1.5$ and 2.2, in the resin C gel with $Q = 4.4$ and in neat DMF, the determined E^{DMF} values were 4.19, 3.61, 2.66 and 2.36 kcal mol^{-1}, respectively. The E^{DMF} values obtained were plotted against Q as shown in Fig. 3. As seen from this figure, the E^{DMF} value in the $Q < 1.8$ range decreases with an increase in Q, and the change of the E^{DMF} value in the $Q > 1.8$ range is very small. Further, it is suggested that the probability of intermolecular collisions between DMF and the polymer network in network polystyrene gels are changed by an increase of Q in the $Q < 1.8$ range from the E^{DMF} values. The probability of intermolecular interactions between DMF and the polymer network become higher, i.e., intermolecular interactions become stronger.

2.1.3. *Diffusion coefficient of THF in network polystyrene gels*

The diffusion coefficients of THF in the resin A and the resin C gels were determined in the same way as for DMF.[40] The swelling of the network polystyrene by THF is much larger than DMF. The D_0^{THF} value of 2.90×10^{-5} cm^2 s^{-1} is larger than the D_0^{DMF} value of 1.75×10^{-5} cm^2 s^{-1} at 30 °C. The D^{THF} values obtained

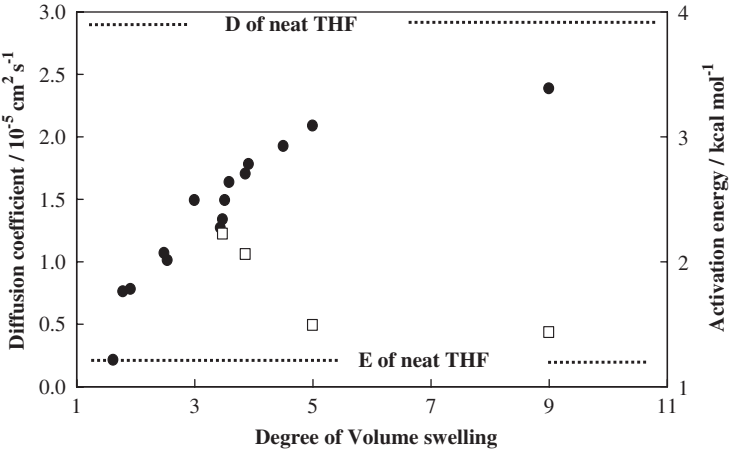

Fig. 4. Dependence of the diffusion coefficient of THF in resin A and resin C gel (●) and activation energy of self-diffusion (□) on the degree of volume swelling Q at 30 °C.

were plotted against Q at 30 °C as shown in Fig. 4. As seen from this figure, the D^{THF} value increases with an increase in Q. The change of the D^{THF} value in the small Q region is much larger than that in the large Q region, especially the change of the D^{THF} value in the $Q > 4.8$ range is small. Therefore, as for the diffusional behavior of THF in network polystyrene gels, it can be said that the intermolecular interaction between THF and the polymer network, which depends on the size of a network, restrains the translational motion of THF. Thus, the D^{THF} value is larger than the D^{DMF} value at the same Q value.

The reduced diffusion coefficient of the solvent in gels A and C divided by the diffusion coefficient of solvent in neat liquid ($D_0^{\mathrm{Solvent}} = D_Q/D_0$, where D_Q is the diffusion coefficient of solvent in gel at Q) was plotted against Q at 30 °C, in order to clarify the effect of intermolecular interactions between the solvent and the polymer network on the diffusion as shown in Fig. 5. From this figure, there is almost no difference between DMF and THF in the effect of intermolecular interactions between the solvent and the polymer network on the diffusion. It seems that the effect of the network size on diffusion are more important than the effect of intermolecular interactions between the solvents and the polymer network. Therefore, it can be said that the D^{Solvent} values in the network polystyrene gels can be estimated by the D_0^{Solvent} value and the Q value, when there is no strong intermolecular interactions between the solvent molecules and polymer network.

It is known from PFGSE NMR studies that the D^{Solvent} values in polystyrene solutions in the 0–80 wt/wt% polymer range show "universal" behavior among butyl acetate, ethyl benzene, cyclohexane and toluene. The diffusion data from the solution can be interpreted with free volume theory, and that the D^{Solvent} values in the network polystyrene gels when $Q = 2.1$, 1.8 and 1.4 are similar to those in the polystyrene solutions of the same solvent concentrations.[65–67] In this work, the D^{Solvent} value in the network polystyrene gels (called Merrifield resin) in the broad

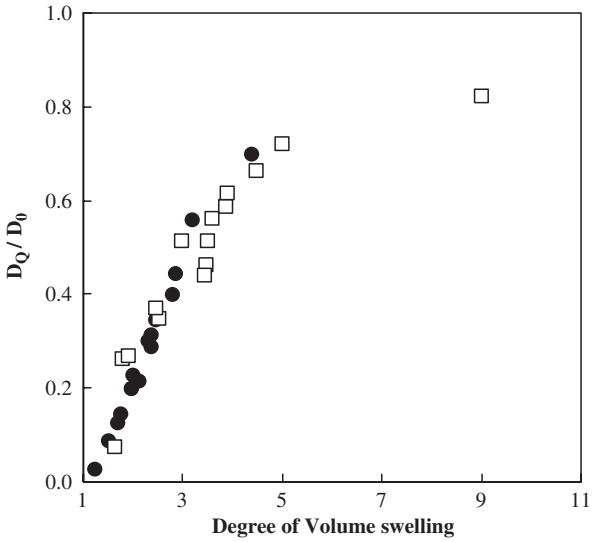

Fig. 5. The reduced diffusion coefficient of solvent in resin A and resin C gel divided by diffusion coefficient of solvent in neat liquid ($D_0^{\text{Solvent}} = D_Q/D_0$, where D_Q is the diffusion coefficient of solvent in the gel at Q) was plotted against Q at 30 °C. DMF (●) and THF (□).

Q range showed "universal" behavior between DMF and THF. The diffusional behavior of the solvent in the polymer gel systems can be analyzed by the modified free volume theory proposed by Fujita.[68,69] This theory can be applied to a solvent in polymer gel systems only when the E^{Solvent} values are nearly equal over a wide range of Q values. In this polymer gel system, the E^{Solvent} value increases with a decrease of Q in the small Q region. But the theoretical curve agrees with the experimental data. From this result and the result that the Q dependence of the D value for THF in the network polystyrene gels is very similar to that of DMF, it seems that a rapid decrease of the D^{Solvent} value with a decrease of Q can be explained by a decrease of the free volume of the solvent.

2.1.4. *Effect of the fraction of chloromethylation in the phenyl rings of network polystyrene on the diffusion coefficient of DMF in the gels*

We are concerned with the effect of the fraction of chloromethylation in the phenyl rings (f_{cm}) of network polystyrene on the diffusion coefficient of DMF in the gels.[40] The f_{cm} values of resins A and B are 1.5 and 0.3 mmol g^{-1}, respectively. The determined D^{DMF} values in resin A and resin B gels are plotted against Q at 50 °C as shown in Fig. 6. Here, the experimental error bars are shown to provide a detailed comparison of the effect of the f_{cm} on the D^{DMF} values in the network polystyrene gels.

As for DMF in the $Q<1.8$ range, the D^{DMF} values in the resin A gel are larger than those in the resin B gel. In the $Q>1.8$ range, there are no difference between

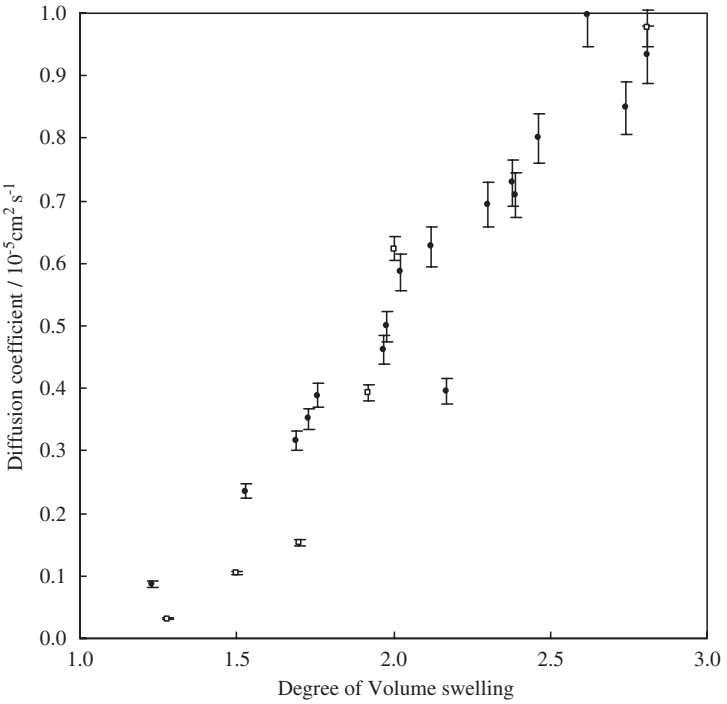

Fig. 6. Dependence of the diffusion coefficient of DMF in resin A gel [● ($fcm = 1.5\,\text{mmol g}^{-1}$)] and in resin B gel [□ ($fcm = 0.3\,\text{mmol g}^{-1}$)], on the volume swelling degree Q at 50 °C. fcm is the fraction of chloromethylation in the phenyl rings of network polystyrene.

them. In other words, the D^{DMF} values in the network polystyrene gels in the $Q < 1.8$ range increase with an increase of f_{cm}, but in the $Q > 1.8$ range these are almost not affected by f_{cm}. This phenomenon can be explained by weak intermolecular interactions between DMF and the polymer chains. It seems that there are weak electrostatic interactions between a DMF molecule and the phenyl rings of polystyrene chains, and so the chloromethyl group on the phenyl rings prevents the approach of a DMF molecule to the phenyl rings. In the small Q range, this leads to an effect of f_{cm} on the D^{DMF} value in the network polystyrene gels because most of the DMF molecules usually contact with polystyrene chains and can interact with the polystyrene chains.

2.2. Diffusion of amino acids in polystyrene gels

In this section, we attempt to understand deeply the diffusional behavior of amino acids in MPS gels, and, further, to determine the diffusion coefficient of Boc-Phe · Cs(tert-butyloxycarbonyl-L-phenylalanine cesium) salt in the solid-phase

reaction field.[41] This permits us to clarify the diffusional behavior of reagents used in the solid-phase reaction field during a chemical reaction. MPS resin beads were used with the fraction of cross-linking of 1% (MPS1) and 2% (MPS2). The average diameter of the dried beads was in the range of 75–150 μm in the dry state. The gels of beads were prepared by soaking them in a DMF-d_7 solution of amino acids for three days.

Boc-Phe · Cs(tert-butyloxycarbonyl-L-phenylalanine cesium) salt was synthesized as follows. A solution of Boc-Phe (2.5 g) dissolved in water (5 mL) and methanol (50 mL) was placed in a 100 mL flask. By adding 20 wt/wt% cesium carbonate aqueous solution, the reaction system was kept at pH 7. The crude products obtained were concentrated under reduced pressure, washed with 30 mL of DMF and then concentrated under reduced pressure again. Furthermore, this procedure was repeated twice with 20 mL of DMF. Then, it was dried over P_2O_5 under reduced pressure.

2.2.1. *^{1}H PFGSE NMR spectra and their assignments*

Fig. 7 shows the typical ^{1}H PFGSE NMR spectra of Boc-Phe in the resin MPS1 gel with $Q = 2.48$ obtained by varying the field-gradient pulse duration δ at 30 °C. The MPS1 beads were soaked in 10 wt/wt% DMF-d_7 solution of Boc-Phe. Two intense peaks can be straight forwardly assigned to the methyl groups and phenyl groups of Boc-Phe molecules in the resin MPS1 gel. The intensity decay for the peaks of Boc-Phe is affected by the rate of diffusion. The peaks that come from the resin A

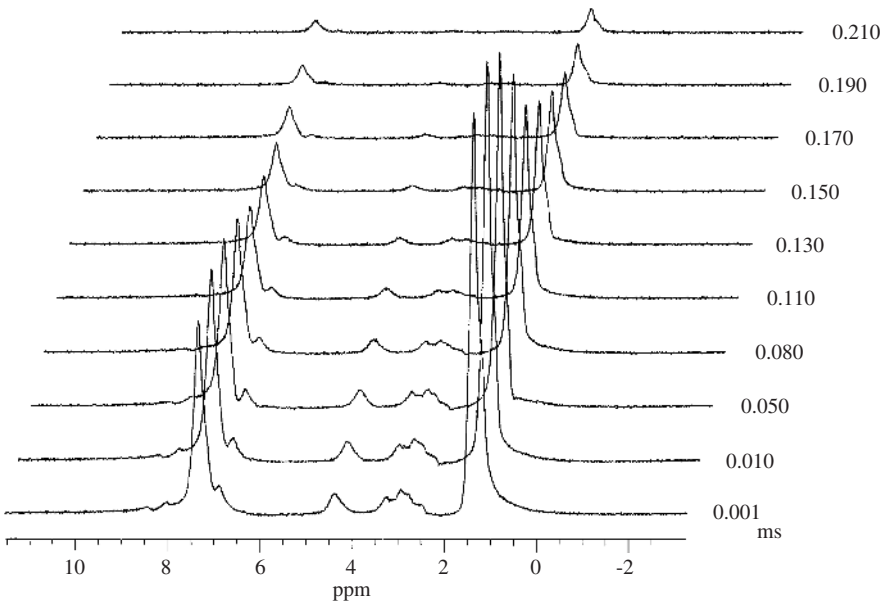

Fig. 7. ^{1}H PFGSE NMR spectra of Boc-Phe in resin A gel with $Q = 2.45$ by varying field-gradient pulse duration δ at 30 °C.

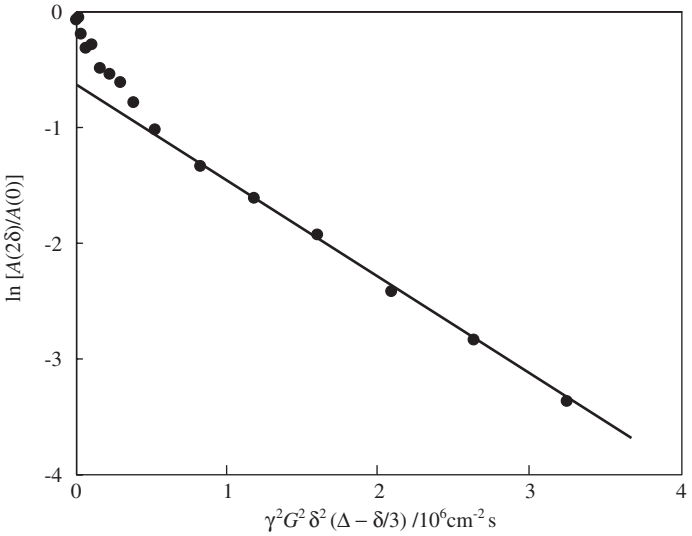

Fig. 8. Diffusional spin-echo attenuation of Boc-Phe in resin A gel with $Q = 2.45$ at 30 °C.

gel and the deuterated DMF (DMF-d_7) molecule do not appear in the ^{1}H PFGSE NMR spectrum. The non-appearance of the peaks from the resin MPS1 gel is due to the slow motion of the network polystyrene chains.

The plots of $\ln[A(\delta)/A(0)]$ against $\gamma^2G^2\delta^2(\Delta-\delta/3)$ are shown in Fig. 8. From this figure, it is seen that the experimental data do not lie on a straight line, although the experimental data for Boc-Phe in DMF in the absence of the network polystyrene chains do lie on a straight line. This means that Boc-Phe in MPS1 gels has multi-components for the diffusion during the observation time. The multi-component diffusion shows a multi-exponential decay. The solvent in the MPS1 gel has a single component for diffusion. It is assumed that the Boc-Phe molecules are transported to some sites with different environments during the observation time (diffusing time), in which case intermolecular interactions between Boc-Phe and the polymer network are largely different from each other. Here, the different environments mean a different probability of intermolecular interactions between Boc-Phe and the polymer network during the observation time. This means that by adjusting the observation time, i.e., the two field-gradient pulse interval, the Boc-Phe molecules with different diffusion coefficients in sites with different environments may be differentiated. In all of the present experiments, Boc-Phe and Boc-Gly in MPS1 gel have multi-kinds of components for the diffusion such as a slow diffusion component and the multi-fast diffusion components. It seems that Boc-Phe molecules interacting strongly with the polymer network contribute to the slow diffusion component, and Boc-Phe molecules interacting weakly with the polymer network contribute to the fast-diffusion components. These interactions depend on the intermolecular distance between the Boc-Phe molecules and the polystyrene chains. The diffusion coefficient and the fraction for the diffusion

component can be determined from the slope and the intercept of the least-squares fitted straight line ($\delta > 0.11$ ms). The slow diffusion component of the $D^{\text{Boc-Phe}}$ value in the resin MPS1 gel with $Q = 2.45$ at 30 °C is $8.50 \times 10^{-7}\,\text{cm}^2\,\text{s}^{-1}$ and the fraction for the slow diffusion component is about 0.6.

2.2.2. *Diffusion coefficient of Boc-Gly in network polystyrene gels*

We are concerned with the diffusional behavior of Boc-Gly in the MPS1 gel as studied by using the above-mentioned analytical procedure.[44] The $D^{\text{Boc-Gly}}$ values of Boc-Gly in the MPS1 gel, as obtained from the slow diffusion component, are shown in Table 1. The $D^{\text{Boc-Gly}}$ values going from $Q = 1.50$ to 3.74 increase from 1.79×10^{-7} to $1.48 \times 10^{-6}\,\text{cm}^2\,\text{s}^{-1}$ and the diffusion coefficient $D_0^{\text{Boc-Gly}}$ of Boc-Gly in DMF-d_7 in the absence of the network polystyrene is $4.83 \times 10^{-6}\,\text{cm}^2\,\text{s}^{-1}$ at 30 °C. The reduced diffusion coefficient $D_Q^{\text{Boc-Gly}}$ of the Boc-Gly molecules divided by the $D_0^{\text{Boc-Gly}}$ value was plotted against Q at 30 °C, in order to clarify the effect of intermolecular interactions between the Boc-Gly molecule and the polymer network on the diffusion as shown in Fig. 9. From this figure, the change of the $D^{\text{Boc-Gly}}$ value in the $1.0 < Q < 4.0$ range is not as large as that of the D^{Solvent} value. Therefore, it can be said that the diffusional behavior of Boc-Gly in the network polystyrene gels depends not only on the intermolecular interactions between a Boc-Gly molecule and the polymer network, but also on the electrostatic interactions between a Boc-Gly molecule and the polymer chains.

The diffusion coefficients $D^{\text{Boc-Gly}}$ for Boc-Gly in the MPS1 gel with $Q = 3.74$, 2.45 1.50 and in DMF in the absence of MPS1 determined as a function of temperature are shown in Table 1. From this table, it is seen that the $D^{\text{Boc-Gly}}$ values increase with an increase in temperature. The activation energies of diffusion ($E^{\text{Boc-Gly}}$) for Boc-Gly in the MPS1 gel with $Q = 3.74$, 2.45 and 1.50, and in DMF in the absence of MPS1 are determined from the Arrhenius plots of $\ln D$ against $1/T$. As for Boc-Gly in the MPS1 gels with $Q = 1.50$, 2.45 and 3.74 and in DMF solution in the absence of the gel, the determined $E^{\text{Boc-Gly}}$ values are 9.51, 5.36, 5.26 and 3.18 kcal mol^{-1}, respectively. The reduced $E^{\text{Boc-Gly}}$ values obtained with Q divided

Table 1. Diffusion coefficients D and activation energies E of Boc-Gly and Boc-Phe in resin A gel

Sample	Q	Diffusion coefficient D ($10^{-7}\,\text{cm}^2\,\text{s}^{-1}$)					Activation energy E (kcal mol^{-1})
		30°C	35°C	40°C	45°C	50°C	
Boc-Gly[a]		48.3	52.6	59.6	61.5	67.2	3.18
	3.74	14.8	18.1	21.9	23.0	25.8	5.26
	2.45	8.14	9.88	11.1	12.8	14.2	5.36
	1.50	1.79	2.38	3.09	3.78	4.81	9.51
Boc-Phe[a]		48.4	53.1	57.6	61.7	66.9	3.10
	2.48	8.82	9.34	10.9	13.4	14.2	5.14

[a]In DMF solution in the absence of resin A.

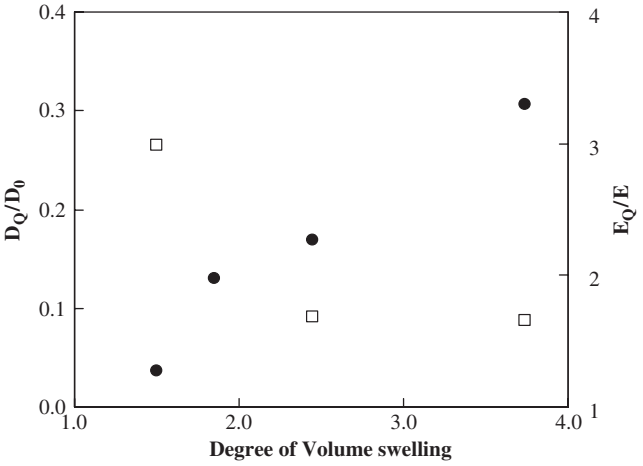

Fig. 9. The reduced diffusion coefficient of Boc-Gly 10 wt/wt% (solvent:DMF) in resin A gel divided by diffusion coefficient of Boc-Gly in the absence of resin A ($D_0^{\text{Boc-Gly}} = D_Q/D_0$ (●), where D_Q is the diffusion coefficient of Boc-Gly in gel at Q) was plotted against Q at 30 °C. $E_0^{\text{Boc-Gly}} = E_Q/E_0$ (□).

by the $E_0^{\text{Boc-Gly}}$ value is plotted against Q in Fig. 9. As seen from this figure, in the $1.5 < Q < 2.5$ range, the $E^{\text{Boc-Gly}}$ values decrease with an increase in Q. This shows that the network size decreases as Q decreases and the intermolecular interactions between Boc-Gly and the polymer network increase. In other words, the environment of Boc-Gly in the network polystyrene gels is changed by an increase of Q, especially, in the $Q < 2.5$ range. In large Q regions, the $E^{\text{Boc-Gly}}$ value with $Q = 3.74$ is 1.7 times larger than that in DMF-d_7 solution in the absence of MPS1 ($E_0^{\text{Boc-Gly}}$). It can be said that the environment of Boc-Gly in the network polystyrene gels is significantly different from that of Boc-Gly in DMF in the absence of the network polystyrene. In other words, the diffusional behavior of amino acids in a peptide solid-phase reaction field differs from that of amino acids in a liquid-phase one. It is thought that this phenomenon may be caused by strong intermolecular interactions between a Boc-Gly molecule and the polystyrene chains.

2.2.3. *Diffusion coefficient of Boc-Phe in network polystyrene gels*

We are concerned with a comparison of the diffusional behavior of Boc-Phe molecules with that of Boc-Gly. Network polystyrene beads were soaked in a 10 wt/wt% DMF-d_7 solution of Boc-Phe. The $D^{\text{Boc-Phe}}$ values of Boc-Phe in DMF in the absence of the network polystyrene and in the presence of the network polystyrene gels are determined from the Arrhenius plots of $\ln D$ against $1/T$.[41] From Table 1, it is shown that there is almost no difference between the $D^{\text{Boc-Phe}}$ value and the $D^{\text{Boc-Gly}}$ value. It is shown that the diffusional behavior of Boc-Phe in the network polystyrene gels is very similar to that of Boc-Gly when the wt/wt% concentrations

are equal to each other. When the wt% concentrations are equal, it is assumed that the volume fractions are equal. When the mole fractions are equal, it is assumed that the $D^{\text{Boc-Gly}}$ value is larger than the $D^{\text{Boc-Phe}}$ value. There is no difference in diffusional behavior between Boc-Phe and Boc-Gly in spite of the structural difference between them. Therefore, it can be said that strong intermolecular interactions between an amino acid molecule and the polystyrene chains come from intermolecular interactions between the carboxyl terminal of an amino acid molecule and the polystyrene chains.

2.2.4. *Dependence of the diffusion coefficients of Boc-Phe in network polystyrene gels on the concentration of amino acids*

We are concerned with the dependence of the diffusion coefficients of amino acids in network polystyrene gels on the concentration of the amino acids ($C_{\text{amino acid}}$). First, the plots of the $D^{\text{Boc-Phe}}$ in DMF-d_7 solution in the absence of the resin at 40 °C and the $E^{\text{Boc-Phe}}$ against the $C_{\text{amino acid}}$ are shown in Fig. 10. From this figure, it is found that the $D^{\text{Boc-Phe}}$ value decreases with an increase in $C_{\text{amino acid}}$, and further that the $E^{\text{Boc-Phe}}$ value is constant (3.10 kcal mol^{-1}) within the $C_{\text{amino acid}}$ range from 4 to 12 wt/wt%. The reduction of the $D^{\text{Boc-Phe}}$ value may be explained by a consideration that the Boc-Phe molecule interacts with itself with an increase in $C_{\text{amino acid}}$ in addition to interacting with DMF-d_7 and thus the diffusion of Boc-Phe is reduced. Further, we may explain the $C_{\text{amino acid}}$ independent activation energy of diffusion by a consideration that the strengths of the intermolecular interactions between Boc-Phe molecules, and Boc-Phe and DMF-d_7 are close to each other.

As for Boc-Phe in the MPS1 gels and in the MPS2 gels at 40 °C, in Figs. 11 and 12, the $D^{\text{Boc-Phe}}$ values obtained from the slow diffusion components and the

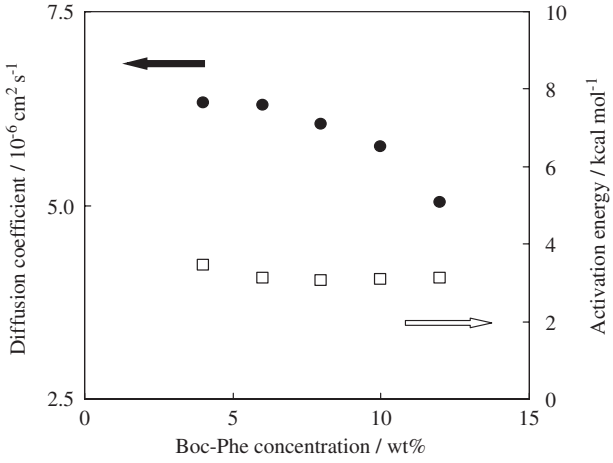

Fig. 10. The plots of the diffusion coefficient of Boc-Phe in DMF-d_7 solution (●) and activation energy of self-diffusion (□) against the concentration $C_{\text{amino acid}}$ at 40 °C.

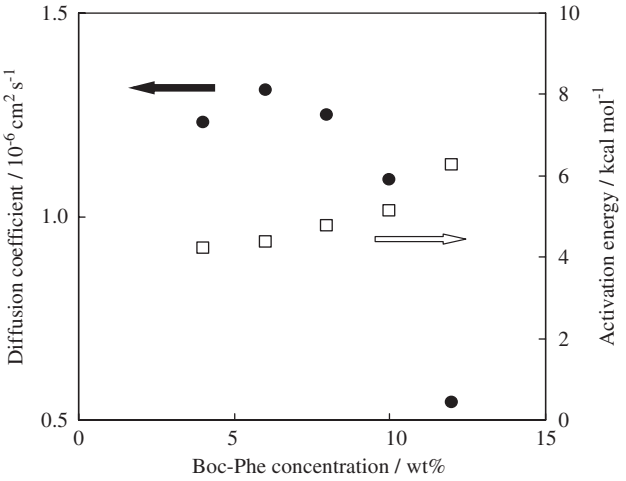

Fig. 11. The plots of the diffusion coefficient of Boc-Phe in MPS1 gels (●) with DMF-d_7 as solvent at 40 °C and activation energy of diffusion (□) against the concentration $C_{\text{amino acid}}$.

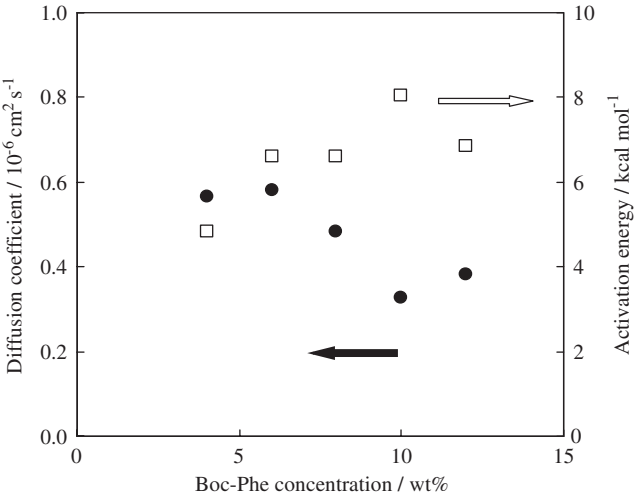

Fig. 12. The plots of the diffusion coefficient of Boc-Phe in MPS2 gels (●) with DMF-d_7 as solvent at 40 °C and the activation energy of diffusion (□) against the concentration $C_{\text{amino acid}}$.

$E^{\text{Boc-Phe}}$ values of Boc-Phe in the MPS1 gels and in the MPS2 gels at 40 °C are plotted against $C_{\text{amino acid}}$. By comparison with the experimental data as shown in Figs. 10–12, it is found that the $D^{\text{Boc-Phe}}$ value in the MPS1 gels is much smaller than that in DMF-d_7 solution in the absence of the resin. This indicates that Boc-Phe interacts strongly with the polymer network. As seen from Fig. 11, the $D^{\text{Boc-Phe}}$ value in MPS1 gels below $C_{\text{amino acid}} = 10$ wt/wt% is independent of $C_{\text{amino acid}}$, but

decreases largely at $C_{\text{amino acid}} \geqq 10\,\text{wt/wt\%}$. Such a reduction of the $D^{\text{Boc-Phe}}$ value may be explained by the consideration that the Boc-Phe molecule interacts strongly with the polymer network and interacts with itself with an increase in $C_{\text{amino acid}}$ in addition to interacting with DMF-d_7 and thus it leads to a slow diffusion of Boc-Phe. On the other hand, the activation energy of diffusion for Boc-Phe increases with an increase in $C_{\text{amino acid}}$. This is very different from the observation made in the absence of the resin. Such an increase of the activation energy of diffusion for Boc-Phe may come from an increase of intermolecular interaction with the polymer network. As mentioned in Section 2.2.2, $E^{\text{Boc-Gly}}$ values in the $1.5 < Q < 2.5$ range increase with a decrease in Q. The Q values of the resin A gels are 2.4 ± 0.1 at $4 < C_{\text{amino acid}} < 10\,\text{wt/wt\%}$, but 2.1 at $C_{\text{amino acid}} = 12\,\text{wt/wt\%}$. The $E^{\text{Boc-Phe}}$ value in the MPS1 gels at $C_{\text{amino acid}} = 12\,\text{wt/wt\%}$ is larger than that of Boc-Phe at $4 < C_{\text{amino acid}} < 10\,\text{wt/wt\%}$. The Q value of MPS2 gels is 1.7 at $C_{\text{amino acid}} = 4\,\text{wt/wt\%}$, but is 1.5 at $C_{\text{amino acid}} = 12\,\text{wt/wt\%}$. Thus, the $E^{\text{Boc-Phe}}$ value in MPS2 gels increases with an increase in $C_{\text{amino acid}}$.

Further, it is found from Figs. 11 and 12 that the $D^{\text{Boc-Phe}}$ value for the slow diffusion component in MPS1 gels at $C_{\text{amino acid}} = 12\,\text{wt/wt\%}$ ($5.43 \times 10^{-7}\,\text{cm}^2\,\text{s}^{-1}$) is close to the $D^{\text{Boc-Phe}}$ values in the MPS2 gels at $C_{\text{amino acid}} = 4$ ($6.21 \times 10^{-7}\,\text{cm}^2\,\text{s}^{-1}$) and 6 wt% ($5.82 \times 10^{-7}\,\text{cm}^2\,\text{s}^{-1}$), and the fraction of the slow diffusion component in the MPS1 gels at $C_{\text{amino acid}} = 12\,\text{wt/wt\%}$ is about 0.6, while the $D_{\text{Boc-Phe}}$ value for the slow diffusion component in the MPS2 gels at $C_{\text{amino acid}} = 6\,\text{wt/wt\%}$ is $5.82 \times 10^{-7}\,\text{cm}^2\,\text{s}^{-1}$ and the fraction is about 0.8. Therefore, it can be said that there is a difference in the diffusional behavior of Boc-Phe between the MPS1 gels at $C_{\text{amino acid}} = 12\,\text{wt/wt\%}$ and the MPS2 gels at $C_{\text{amino acid}} = 6\,\text{wt/wt\%}$, but the rate of diffusion for Boc-Phe in the region close to the polystyrene chains is nearly equal. From these experimental results, it can be said that the factors controlling the diffusion of Boc-Phe in the MPS1 and MPS2 gels are $C_{\text{amino acid}}$ and Q.

2.3. Diffusion of regents in polymer supports in for solid-phase synthesis

Solid-phase peptide synthesis has been widely applied to produce combinatorial libraries for peptides, oligosaccharides, functional polymers, liquid crystals and catalysts in addition to the successful development of new medical drugs. Polystyrene network gels have been used as the most popular polymer supports in solid-phase synthesis,[48,49] column chromatography,[70–72] ion-exchange resins, polymer supports for catalysts,[73–75] etc. These functionalities are closely associated with the diffusional behavior of solvents and probe molecules, intermolecular interactions between networked polymer chains and probe molecules, and also the structure and dynamics of polymer supports. A number of papers on solid-phase synthesis for combinatorial libraries have been reported, and also reviews and monographs in this field have appeared.[76] However, there is little work on elucidating problems as to the design of a new series of solid-phase syntheses and how to understand the diffusional behavior of probe molecules in polymer supports. A solid-phase

reaction field consists of solvents, reagents, networked polymer chains, reactive sites and spacers. In general, it is known that the rate of a solid-phase reaction is closely associated with the diffusion rates of the reagents and reaction products.[77–83] However, it is shown that a shake of the resins by gas bubbling does not affect the rate of reaction. Therefore, it is important to clarify the diffusion process of the reaction reagents in popular polymer supports.[44]

In this section we elucidate the diffusion process of Boc-Gly (tert-butyloxycarbonyl-glycine) [molecular weight (M_w) 175], Boc-Trp (tert-butyloxycarbonyl-L-tryptophan) [M_w 304], Boc-Phe (tert-butyloxycarbonyl-L-phenylalanine) [M_w 265] and Fmoc-Phe (9-fluorenylmethoxycarbonyl-L-phenylalanine) [M_w 387] in polymer supports for solid-phase peptide synthesis with MPS resin, polyethyleneglycol-grafted polystyrene network (PEG-PS) resin and cross-linked ethoxylate acrylate (CLEAR) resin selected as popular polymer supports. Further, we will discuss the collision frequency between reactive sites and amino acids. The amino acid concentration used in this work is fixed to be 10 wt%.

2.3.1. *Diffusion coefficients of amino acids in polystyrene network gels with DMF-d_7 as solvent*

To determine the diffusion coefficient of Boc-Gly ($D^{\text{Boc-Gly}}$) in the MPS1 gels with DMF-d_7 as solvent at $Q = 1.50$ in the temperature range from 30 to 50 °C, Fig. 13 shows the temperature dependence of the $D^{\text{Boc-Gly}}$ value for the slow diffusion component in the MPS1 gels at $Q = 1.50$ and 2.45, and of the fraction of the slow diffusion component ($f_{\text{slow(Boc-Gly)}}$). It seems that the Boc-Gly molecules, which interact strongly with the polymer network to contribute to the slow diffusion component, and the Boc-Gly molecules, which interact weakly with the polymer network contribute to the fast-diffusion components. These interactions depend on the intermolecular distances between the Boc-Gly molecules and the PS network chains. The $D^{\text{Boc-Gly}}$ values for the slow diffusion component in the MPS gels at $Q = 1.50$ and 2.45 at 30 °C are 1.79×10^{-7} and $8.14 \times 10^{-7}\,\text{cm}^2\,\text{s}^{-1}$, respectively. Their differences are very large. This comes from the large difference in the network size. The $E^{\text{Boc-Gly}}$ value for the slow diffusion component in the MPS1 gels at $Q = 1.50$ and 2.45 are 9.50 and 5.34 kcal mol^{-1}, respectively. The former is much larger than the latter. This shows that as an increase in the volume fraction of the networked PS chains in the MPS1 gels leads to a reduction of the PS network size. Also a reduction of the intermolecular distance between the Boc-Gly molecules and the networked PS chains leads to an increase in intermolecular interactions between the Boc-Gly molecules and the PS network. Therefore, the diffusion process as well as the diffusion rate is sensitively influenced by Q. Next, we look at the fraction of slow diffusion component ($f_{\text{slow(Boc-Gly)}}$). It is found that the $f_{\text{slow(Boc-Gly)}}$ value for the slow diffusion component in the MPS1 gels at $Q = 1.50$ is slightly increased from 0.72 to 0.78 with an increase in temperature over the range from 30 to 50 °C. However, the $f_{\text{slow(Boc-Gly)}}$ value in the MPS gels at $Q = 2.45$ is almost independent of temperature to be about 0.6. The $f_{\text{slow(Boc-Gly)}}$ value at $Q = 1.50$ is much larger than that at $Q = 2.45$. This suggests that the Boc-Gly molecules, which are

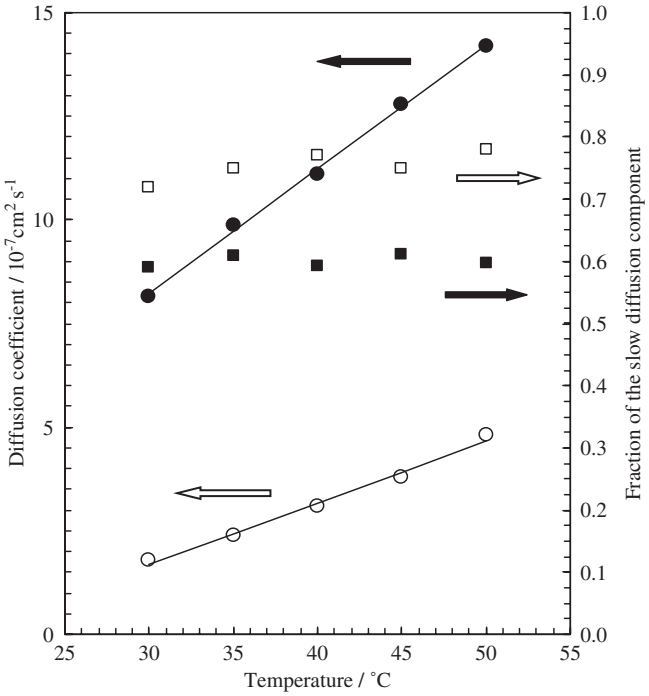

Fig. 13. Temperature dependence of the diffusion coefficient (●) and the fraction (■) for the slow diffusion component of Boc-Gly in MPS gel with DMF-d_7 at $Q = 2.45$, and those of the corresponding diffusion coefficient (○) and fraction (□) at $Q = 1.50$.

interacting strongly with the PS network predominantly contribute to the slow diffusion component and their interactions depend on the intermolecular distance between the Boc-Gly molecules and the PS chains. Thus, the network size plays an important role for the intermolecular interactions. Consequently, it can be said that the large difference in the $D^{\text{Boc-Gly}}$, $E^{\text{Boc-Gly}}$ and $f_{\text{slow(Boc-Gly)}}$ values of Boc-Gly in the MPS1 gels at $Q = 1.50$ and 2.45 comes from their different PS network sizes.

A plot of $\ln[A(\delta)/A(0)]$ against $\gamma^2G^2\delta^2(\Delta-\delta/3)$ for Boc-Gly, Boc-Trp and Fmoc-Phe in DMF-d_7 solution in the absence of resin at 30 °C shows that the experimental data lie on a straight line. This means that the amino acids have a single component in diffusion during the observation time. The $D^{\text{Boc-Gly}}$, $D^{\text{Boc-Trp}}$ and $D^{\text{Fmoc-Phe}}$ values were obtained to be 4.83×10^{-6}, 4.21×10^{-6} and 3.61×10^{-6} cm^2 s^{-1}, respectively. It is shown that the magnitude of the D values depends on the molecular weights, i.e., the molecular size. As the molecular weight increases, the D value decreases. The $D^{\text{Boc-Gly}}$, $D^{\text{Boc-Phe}}$, $D^{\text{Boc-Trp}}$ and $D^{\text{Fmoc-Phe}}$ values in the absence of resin are shown as a function of temperature in the temperature range from 30 to 50 °C in Table 2. The D values increase with an increase in temperature. The activation energy of diffusion (E) for the amino acids was obtained as shown in Table 2. It is shown that the determined E values for the four kinds of the amino acids studied are close to each other.

Table 2. Diffusion coefficients D and activation energies E of amino acids in MPS gel[a]

Amino acids		MPS gel	Diffusion coefficient D ($10^{-7}\,cm^2\,s^{-1}$)					Activation energy E ($kcal\,mol^{-1}$)
			30°C	35°C	40°C	45°C	50°C	
Boc-Gly[a]		D	48.3	52.6	59.6	61.5	67.2	3.18
	1 mol%	D_{fast}	17.7	17.3	20.8	22.1	22.0	2.65
	DVB	D_{slow}	8.14	9.88	11.1	12.8	14.2	5.34
	2 mol%	D_{fast}	6.15	6.32	6.98	7.54	8.01	2.74
	DVB	D_{slow}	2.08	2.59	3.28	3.84	4.77	5.34
Boc-Trp[a]		D	42.1	45.4	48.8	53.3	57.5	3.05
	1 mol%	D_{fast}	12.0	12.8	14.5	15.2	16.1	2.95
	DVB	D_{slow}	5.16	5.40	6.65	7.62	8.02	4.77
	2 mol%	D_{fast}	7.26	6.46	6.83	7.37	8.02	1.26
	DVB	D_{slow}	2.43	3.02	3.57	4.16	4.96	6.77
Boc-Phe[a]		D	36.1	41.2	43.9	46.9	51.6	3.29
	1 mol%	D_{fast}	11.5	12.3	13.0	15.0	15.1	2.89
	DVB	D_{slow}	4.22	4.95	5.66	5.85	7.24	4.85
	2 mol%	D_{fast}	8.42	11.4	9.95	9.96	11.4	1.84
	DVB	D_{slow}	2.40	3.11	3.95	4.13	4.80	6.52

[a]In DMF-d_7 solution in the absence of resin.

As for Boc-Gly, Boc-Trp and Fmoc-Phe in the MPS1 gels with DMF-d_7 as solvent at 30 °C, the plots of $\ln[A(\delta)/A(0)]$ against $\gamma^2G^2\delta^2(\Delta-\delta/3)$ show that the experimental data do not lie on a straight line. This shows that Boc-Trp and Fmoc-Phe in the MPS1 gels have multi-components in diffusion within the observation time, where $Q_{\text{Boc-Gly}}$, $Q_{\text{Boc-Phe}}$, $Q_{\text{Boc-Trp}}$ and $Q_{\text{Fmoc-Phe}}$ are 2.45, 2.48, 2.55 and 2.50, respectively. This can arise from significant intermolecular interactions between the amino acids and the network. The observed diffusion echo signal is approximately deconvoluted by a slow and a fast diffusion component. From such plots, the diffusion coefficients of the slow and fast diffusion components are determined as shown in Table 2. The determined $D^{\text{Boc-Gly}}$, $D^{\text{Boc-Phe}}$, $D^{\text{Boc-Trp}}$ and $D^{\text{Fmoc-Phe}}$ values for the slow diffusion component are 8.14×10^{-7}, 8.82×10^{-7}, 5.16×10^{-7} and $4.22\times10^{-7}\,cm^2\,s^{-1}$, respectively, and the $f_{\text{slow(Boc-Gly)}}$, $f_{\text{slow(Boc-Phe)}}$, $f_{\text{slow(Boc-Trp)}}$ and $f_{\text{slow(Fmoc-Phe)}}$ values are 0.6, 0.6, 0.5 and 0.5, respectively. The determined $D^{\text{Boc-Gly}}$, $D^{\text{Boc-Phe}}$, $D^{\text{Boc-Trp}}$ and $D^{\text{Fmoc-Phe}}$ values for the fast diffusion component are 1.77×10^{-6}, 2.14×10^{-6}, 1.20×10^{-6} and $1.15\times10^{-6}\,cm^2\,s^{-1}$, respectively, and the $f_{\text{fast(Boc-Gly)}}$, $f_{\text{fast(Boc-Phe)}}$, $f_{\text{fast(Boc-Trp)}}$ and $f_{\text{fast(Fmoc-Phe)}}$ values are 0.4, 0.4, 0.5 and 0.5, respectively. It is shown that the diffusion coefficient for the fast diffusion component of the amino acids is approximately twice that for the slow diffusion component, and the fractions of the two components are almost equal to each other. The $D^{\text{amino acids}}$ values in the MPS1 gels over a temperatures range from 30 to 50 °C and the determined $E^{\text{amino acids}}$ values for the slow and fast diffusion components are shown in Table 2. From these determined $D^{\text{amino acids}}$ values, it can be said that the $D^{\text{amino acids}}$ values in the MPS1 gels decrease with an increase in the molecular weight of the amino acids and that the four kinds of amino acids have very close values for $E^{\text{amino acids}}$, $f_{\text{slow(amino acids)}}$ and $f_{\text{fast(amino acids)}}$.

As for Boc-Gly, Boc-Trp and Fmoc-Phe in the MPS2 gels with DMF-d_7 as solvent at 30 °C, the plots are made $\ln[A(\delta)/A(0)]$ against $\gamma^2G^2\delta^2(\Delta-\delta/3)$. The determined D values for the slow and fast diffusion components in the MPS2 gels at temperatures over the range from 30 to 50 °C and the determined E values are shown in Table 2. The determined $D^{\text{Boc-Gly}}$, $D^{\text{Boc-Phe}}$, $D^{\text{Boc-Trp}}$ and $D^{\text{Fmoc-Phe}}$ values for the slow diffusion component are 1.79×10^{-7}, 2.08×10^{-7}, 2.43×10^{-7} and $2.40 \times 10^{-7}\,\text{cm}^2\,\text{s}^{-1}$, respectively, and the $f_{\text{slow(Boc-Gly)}}$, $f_{\text{slow(Boc-Phe)}}$, $f_{\text{slow(Boc-Trp)}}$ and $f_{\text{slow(Fmoc-Phe)}}$ values are 0.8, 0.8, 0.8 and 0.6, respectively. On the other hand, the determined $D^{\text{Boc-Gly}}$, $D^{\text{Boc-Phe}}$, $D^{\text{Boc-Trp}}$ and $D^{\text{Fmoc-Phe}}$ values for the fast diffusion component are 6.15×10^{-7}, 6.43×10^{-7}, 7.26×10^{-7} and $8.42 \times 10^{-7}\,\text{cm}^2\,\text{s}^{-1}$, respectively, and the $f_{\text{fast(Boc-Gly)}}$, $f_{\text{fast(Boc-Phe)}}$, $f_{\text{fast(Boc-Trp)}}$ and $f_{\text{fast(Fmoc-Phe)}}$ values are 0.2, 0.2, 0.2 and 0.4, respectively. As expected from the network size of the gels, the $D^{\text{amino acids}}$ values of the slow diffusion component in the MPS2 gel are much smaller than those in the MPS1 gel, where $Q_{\text{Boc-Gly}}$, $Q_{\text{Boc-Phe}}$, $Q_{\text{Boc-Trp}}$ and $Q_{\text{Fmoc-Phe}}$ are 1.50, 1.59, 1.68 and 1.65, respectively. Further, it is shown that the $D^{\text{Boc-Gly}}$ and $D^{\text{Boc-Phe}}$ values are smaller than the $D^{\text{Boc-Trp}}$ and $D^{\text{Fmoc-Phe}}$ values in spite of the fact that the molecular weights of Boc-Gly and Boc-Phe are smaller than those of Boc-Trp and Fmoc-Phe.

Next, we are concerned with the activation energy of diffusion for these amino acids as obtained from the temperature dependence of D. The $E^{\text{Boc-Gly}}$ and the $E^{\text{Boc-Phe}}$ values for the slow diffusion components are larger than the $E^{\text{Boc-Trp}}$ and $E^{\text{Fmoc-Phe}}$ values, although the $E^{\text{amino acids}}$ values determined for the four kinds of amino acids studied in the MPS1 gels are very close to each other. Such an experimental finding may be explained by taking into account the $Q_{\text{amino acid}}$ behavior. In the MPS1 gels and the MPS2 gels, the $Q_{\text{Boc-Gly}}$ and the $Q_{\text{Boc-Phe}}$ values are smaller than the $Q_{\text{Boc-Trp}}$ and $Q_{\text{Fmoc-Phe}}$ values because the $Q_{\text{amino acid}}$ values depends on the cross-linking density and intermolecular interactions between the networked PS chains and amino acid/solvent.

Further, we are concerned with the activation energy of diffusion for the fast diffusion component of the amino acids as shown in Table 2. The E values in the gels are 2.5–3.0 kcal mol^{-1} and are very close to those of about 3 kcal mol^{-1} found in solution. This shows that there are very weak intermolecular interactions between the amino acids and the PS network chains.

2.3.2. *Diffusion coefficients of amino acids in polyethylene-glycol-grafted polystyrene network gels and cross-linked ethoxylate acrylate gels with DMF-d_7 as solvent*

In the ^{1}H PFGSE NMR experiments on PEG-PS gels and CLEAR gels in addition to MPS gels, the Δ value was fixed to be 10 ms.[44] The plots of $\ln[A(\delta)/A(0)]$ for Boc-Phe, Boc-Trp and Fmoc-Phe in the gels against $\gamma^2G^2\delta^2(\Delta-\delta/3)$ do not lie on a straight line. Thus, it is shown that these amino acids have multi-components in diffusion within the observation time. The diffusion echo signal was approximately deconvoluted by a slow and a fast diffusion component. In the PEG-PS gels, the determined $f_{\text{slow(Boc-Phe)}}$, $f_{\text{slow(Boc-Trp)}}$ and $f_{\text{slow(Fmoc-Phe)}}$ values for the slow diffusion component at 30 °C are 0.7, 0.6 and 0.6, respectively. In the CLEAR gels,

Table 3. Diffusion coefficients D of amino acids in MPS, PEG-PS and CLEAR gel

Amino acid (M_w)	State	Diffusion coefficient D ($10^{-7}\,cm^2\,s^{-1}$)				
			2 mol% DVB	1 mol% DVB	PEG-PS resin	CLEAR resin
Boc-Phe (265.30)	Solution	D		48.4		
	in gel	D_{fast}	6.43(1.59)[a]	21.4(2.48)[a]	14.2(2.87)	17.3(2.64)[a]
		D_{slow}	2.08	8.82	9.17	12.5
Boc-Trp (304.34)	Solution	D		42.1		
	in gel	D_{fast}	7.26(1.68)[a]	12.0(2.55)[a]	12.3(3.09)[a]	17.1(2.91)[a]
		D_{slow}	2.43	5.16	7.04	10.8
Boc-Phe (387.43)	Solution			36.1		
	in gel	D_{fast}	8.42(1.65)[a]	11.5(2.50)[a]	11.4(2.90)[a]	14.0(2.64)[a]
		D_{slow}	2.40	4.22	5.61	8.46

[a]Swelling ratio Q.

the determined $f_{slow(Boc\text{-}Phe)}$, $f_{slow(Boc\text{-}Trp)}$ and $f_{slow(Fmoc\text{-}Phe)}$ values for the slow diffusion component at 30 °C are 0.7, 0.6 and 0.6, respectively. These $D^{amino\ acids}$ values for the slow diffusion component in the MPS1, the MPS2, the PEG-PS and the CLEAR gels at 30 °C, and corresponding $Q_{amino\ acids}$ values are shown in Table 3. In DMF-d_7 solution, the order of the $D^{amino\ acids}$ values is Boc-Phe > Boc-Trp > Fmoc-Phe. As expected, amino acids with lower molecular weight diffuse more fastly. Also, in the MPS1 gels, the PEG-PS gels and the CLEAR gels, the order of the $D^{amino\ acids}$ values is Boc-Phe > Boc-Trp > Fmoc-Phe. Therefore, it can be said that the $D^{amino\ acids}$ value is sensitively dependent on molecular weight, i.e., the molecular size, of the corresponding amino acids except for the MPS2 gels in the range of $Q < 2.0$. As for the diffusion process of the amino acids in the four kinds of polymer gels, it is found that the order in the $D^{amino\ acids\ values}$ of Boc-Phe, Boc-Trp and Fmoc-Phe in the gels is CLEAR gels > PEG-PS gels > MPS1 gels > MPS2 gels, although the magnitude of the $Q_{amino\ acids}$ value in the gels is PEG-PS gels > CLEAR gels > MPS1 gel > MPS2 gels. These experimental results are different from those as reported previously[40,41] that the $D^{amino\ acids}$ value in the MPS gel increase with an increase in $Q_{amino\ acids}$. In the MPS gels and the PEG-PS gels with a PS backbone, such a trend agrees with the previous experimental results as shown in Table 3. On the other hand, the $D^{amino\ acids}$ values in the CLEAR gels with a polyethylene glycol backbone are much larger in spite of the small Q values as compared with the PEG-PS gels with a PS backbone. It seems that in the PEG-PS gels the amino acid molecules strongly interact with the phenyl groups of the PEG-PS network, and then their diffusion is more strongly restrained as compared with the case of the CLEAR gels. Further, this may be explained as follows. MPS gels and PEG-PS gels have bulky phenyl groups with six π-electrons. In the case that the corresponding gels have the same Q value, the cavity size in the gels with a PS

backbone is predicted to become much smaller than that in the CLEAR gels with a polyethylene glycol backbone because of the existence of the bulky phenyl rings.

Next, the D_{fast} values of Boc-Gly, Boc-Phe, Boc-Trp and Fmoc-Phe are shown in Table 3. The D_{fast} values in the polymer gels are two–three times larger than the D_{slow} values. The PEG-PS gels and the CLEAR gels as well as the MPS gels have a broad distribution in the diffusion rate, and, consequently, the D_{fast} values in these gels are different from each other. However, some amino acid molecules have similar diffusion rates to each other in the different gels. This is a remarkable point.

2.3.3. *Diffusion coefficients of Boc-Phe in polystyrene network gels with THF-d_8 as solvent*

It has been reported that the D^{THF} value of THF in the MPS gel is much larger than the D^{DMF} value of DMF in the MPS gel with the same Q value and the volume swelling of the PS network resins with THF is much larger than that with DMF.[40] Therefore, it can be assumed that the $D^{amino\ acid}$ value of amino acids in the MPS gels with THF as solvent is larger than that in the MPS gels with DMF as solvent. The diffusion coefficients of Boc-Phe in THF-d_8 as solvent and in DMF-d_7 as solvent were determined. As for Boc-Phe in THF-d_8 solution in the absence of the resin, Boc-Phe in the MPS1 gels with THF-d_8 as solvent and Boc-Phe MPS2 gels with THF-d_8 as solvent at 30 °C, a plot of $\ln[A(\delta)/A(0)]$ against $\gamma^2G^2\delta^2(\Delta-\delta/3)$ show that the points lie on a straight line, when the Boc-Phe concentration is 10 wt/wt%, and $Q_{DVB\ 1\,mol\%\text{-}THF}$ and $Q_{DVB\ 2\,mol\%\text{-}THF}$ are 3.71 and 2.98, respectively. In the PFGSE NMR experiments, the Δ value was fixed to be 10 ms. It can be said that Boc-Phe in the MPS gels with THF-d_8 as solvent as well as Boc-Phe in THF-d_8 solution has a single component of diffusion within the observation time. The $D^{solution\text{-}THF}$, $D^{MPS1\text{-}THF}$ and $D^{MPS2\text{-}THF}$ values are 8.51×10^{-6}, 2.57×10^{-6} and $2.29 \times 10^{-6}\,cm^2\,s^{-1}$, respectively, at 30 °C and, on the other hand, the $D^{solution\text{-}DMF}$, $D^{MPS1\text{-}DMF}$ and $D^{MPS2\text{-}DMF}$ values are 4.84×10^{-6}, 8.82×10^{-7} and $2.08 \times 10^{-7}\,cm^2\,s^{-1}$, respectively, at 30 °C. It is shown that the diffusion rate of the amino acid in the MPS/THF gel system in a solid-phase peptide reaction field is much faster than that in the MPS/DMF system.

In Fig. 14, the determined $D^{MPS1\text{-}THF}$, $D^{MPS2\text{-}THF}$ and $D^{MPS1\text{-}DMF}$ values at 30 °C are plotted against the gradient pulse interval Δ, i.e., the observation timescale. In a previous work, we have reported that the $D^{Boc\text{-}Gly}$ value in MPS1 gels with DMF-d_7 as solvent depends on Δ, the $f_{slow(Boc\text{-}Gly)}$ value depends on the Δ which is related to the diffusion distance, and the multi-components in diffusion are averaged over the observation time within $\Delta = 50$ ms.[41] However, Boc-Phe in the MPS gels with THF-d_8 as solvent as well as Boc-Phe in THF-d_8 solution has a single component in diffusion within the observation time in the Δ range of 5–100 ms, and the effect of heterogeneity of the gels on diffusion could not be observed. Further, the Δ dependence of the $D^{MPS1\text{-}THF}$ is different from that of the $D^{MPS1\text{-}DMF}$.

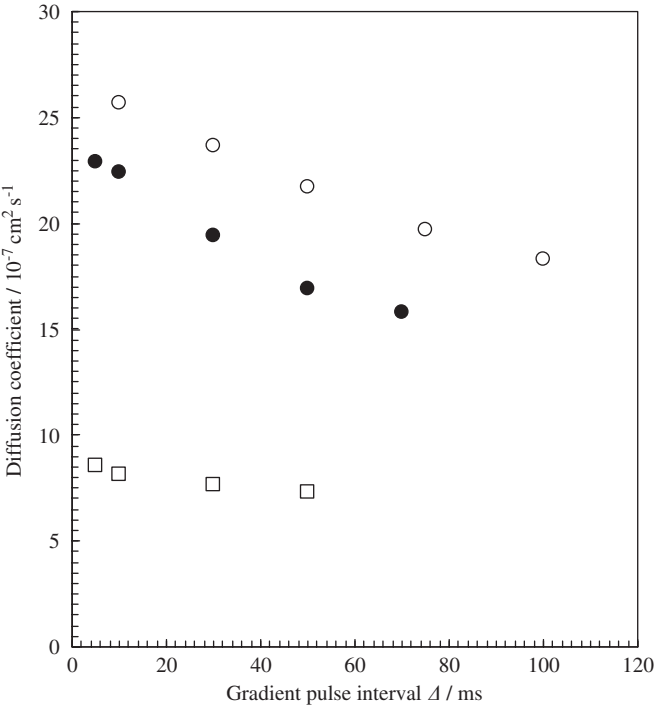

Fig. 14. Dependence of the diffusion coefficient of Boc-Phe in MPS gel with THF-d_8 at $Q = 3.71$ (○) and $Q = 2.98$ (●), and in MPS gel with DMF-d_7 at $Q = 2.48$ (□) for the gradient pulse interval Δ and at 30 °C.

2.3.4. *Diffusion coefficients of Boc-Phe · Cs in network polystyrene gels as a solid-phase reaction field*

We are concerned with the diffusional behavior of Boc-Phe · Cs in network polystyrene gels which act as a solid-phase reaction field for the Boc-Phe group. The $D^{\text{Boc-Phe} \cdot \text{Cs}}$ value is determined in the MPS1 gels undergoing a chemical reaction at 50 °C at $\Delta = 10$ ms. The $D^{\text{Boc-Phe} \cdot \text{Cs}}$ measurement starts after the resin A and Boc-Phe · Cs 10 wt/wt% DMF-d_7 solutions are mixed and then left for 3 h. Fig. 15 shows the diffusional spin-echo attenuation of the Boc-Phe in the network polystyrene gels and Boc-Phe · Cs in the solid-phase reaction field obtained by varying the field-gradient pulse duration δ at 50 °C.

The D values are determined from the slopes of the plots. From this figure it is found that Boc-Phe · Cs in the solid-phase reaction field, as well as Boc-Phe in the network polystyrene gels, has multi-components for diffusion such as the slow and the multi-fast-diffusion components. The slow $D^{\text{Boc-Phe} \cdot \text{Cs}}$ value and the slow $D^{\text{Boc-Phe}}$ value are determined as 1.06×10^{-6} and 1.42×10^{-6} cm^2 s^{-1}, respectively, and the f_{slow} s of the corresponding diffusions are about 0.6. In a previous paper,[15] it

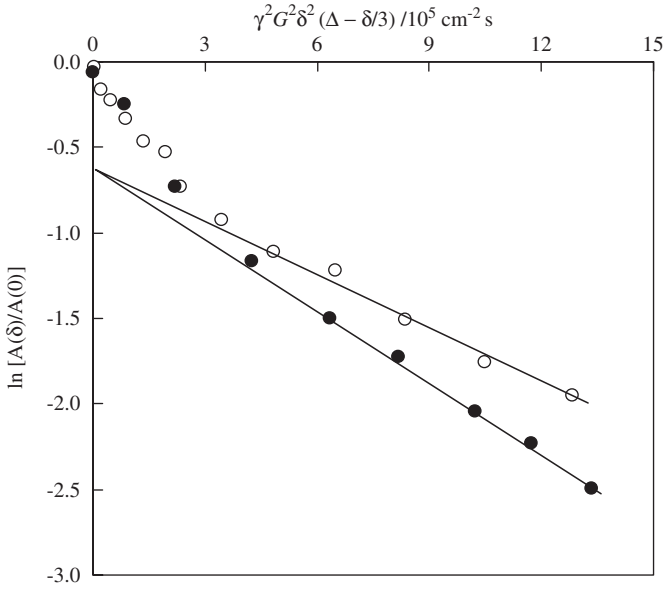

Fig. 15. Diffusional spin-echo attenuation of 10 wt/wt% Boc-Phe in MPS1 gels (●) with DMF-d_7 as solvent and 10 wt/wt% Boc-Phe.Cs in solid-phase reaction field (○) by the varying field-gradient pulse duration at 50 °C.

was shown that the diffusion coefficient of Boc-Phe in the network polystyrene gels is very similar to that of Boc-Gly at the same concentration in spite of the different molecular weight. Further, in the above section, we have described that the $D^{\text{Boc-Phe}}$ value decrease with an increase in $C_{\text{Boc-Phe}}$. When this measurement was performed, the $C_{\text{Boc-Phe.Cs}}$ value is smaller than 10 wt/wt% because the solid-phase reaction proceeds, but the $D^{\text{Boc-Phe}\cdot\text{Cs}}$ value is 0.75 times larger than the $D^{\text{Boc-Phe}}$ value. It can be said that there is a strong intermolecular interaction between the Cs group of Boc-Phe · Cs and the chloromethyl group on the phenyl rings of the network polystyrene gels in the solid-phase reaction field under the chemical reaction. Further, from the experimental results that both of the f_{slow} values are almost equal, it can be said that except for diffusional behavior in the neighboring region of the polystyrene chains, the diffusional behavior of Boc-Phe · Cs in the solid-phase reaction field is similar to that of Boc-Phe in the network polystyrene gels.

2.4. Application of diffusion analysis to solid-phase systems

We are concerned with the reaction rate of solid-phase synthesis as reported previously.[84–87] It is shown that the reaction rate of 9-fluorenylmethoxycarbonyl (Fmoc) deprotection by using 25 μm sized TentaGel particles becomes above three times faster than that with 90 μm sized TentaGel particles.[11,46] This indicates that

reduction of the particle size of the polymer support leads to a dramatic increase in the reaction rate. Thus, it can be said that the rate of reaction depends on the diffusion rate. Further, it is shown that the reaction rate in the MPS1 gels becomes much faster than that in the MPS2 gels. From these experimental findings, it can be said that the reaction rate depends on the diffusion rate associated with the collision frequency between the amino acids and the reactive sites.

2.4.1. *"Required time" (T_r) that solvents and amino acids in polymer supports for a solid-phase peptide synthesis diffuse between average diameters of swollen beads*

In a series of solid-phase peptide syntheses, the solvent plays an important role for carrying amino acids to the reactive sites in a polymer matrix, and to remove the reaction products, unreacted starting materials and impurities from the gels. For these reasons, it seems that the diffusion rate of a solvent in polymer gels is closely related to the "required time" (T_r) in a series of syntheses. Here, T_r is defined as the required time that solvents diffuse in a polymer gel with $d_{swollen}$, which is the averaged diameter of the polymer gel beads.[44] In this work, MPS gels with an averaged diameter of 150 μm in dried state are employed. Then, $d_{swollen}$ in the gel at $Q = 2.0$ is 189 μm and $d_{swollen}$ in the gel at $Q = 3.0$ is 216 μm. When the Q value is large, the solvent molecules must move a long distance. In that case, the diffusion rate becomes fast. Thus, T_r depends on D and Q. The T_r value was estimated as follows. On the measurement timescale of Δ, the self-diffusion coefficient D corresponds to a Gaussian distribution of a squared standard deviation as expressed by

$$\langle z^2 \rangle = 2D\Delta \tag{3}$$

where $\langle z^2 \rangle$ is the mean square displacement in the z direction from its starting point after the diffusion time Δ. The $\langle z^2 \rangle$ value gives us information on the diffusion distance $\langle z \rangle$ that reflects the experimental results as expressed by the following equation.

$$\langle z \rangle = \sqrt{2D\Delta} \tag{4}$$

Thus, T_r becomes Δ if $\langle z \rangle = d_{sowllen}$ in Eq. (4). Here, the D values obtained in the previous work[40] are employed. In order to determine exactly T_r, the D value must be determined on the timescale of Δ if $\langle z \rangle = d_{sowllen}$ because of restricted diffusion, and thus the D value obtained at $\Delta = 10$ ms is employed. In practice, it is very difficult to measure the D value of the probe molecules in swollen beads at a minute timescale as studied by the NMR method. As for DMF-d_7 in MPS gels at 30 and 50 °C and THF-d_8 in the MPS gels at 30 °C, the $T_{req.time}$ dependence of Q is shown in Fig. 16. At 30 °C, the $T_{r\ (DMF)}$ value decreases with an increase in Q and, especially, in the range of $Q < 2.0$, change of the $T_{r\ (DMF)}$ value is very large. In the range of $Q > 3.0$, the $T_{r\ (DMF)}$ value is independent of Q. At 50 °C, the Q dependence of the $T_{r\ (DMF)}$ value is similar to that of the $T_{r\ (DMF)}$ value at 30 °C. As shown in Fig. 16, the $T_{r\ (THF)}$ value is somewhat smaller than the $T_{r\ (DMF)}$ value at the same Q value. Further, the $T_{r\ (THF)}$ value is independent of Q in the range of $Q > 2.0$. From these results, it is found that the "required time" (T_r) of a series of solid-phase

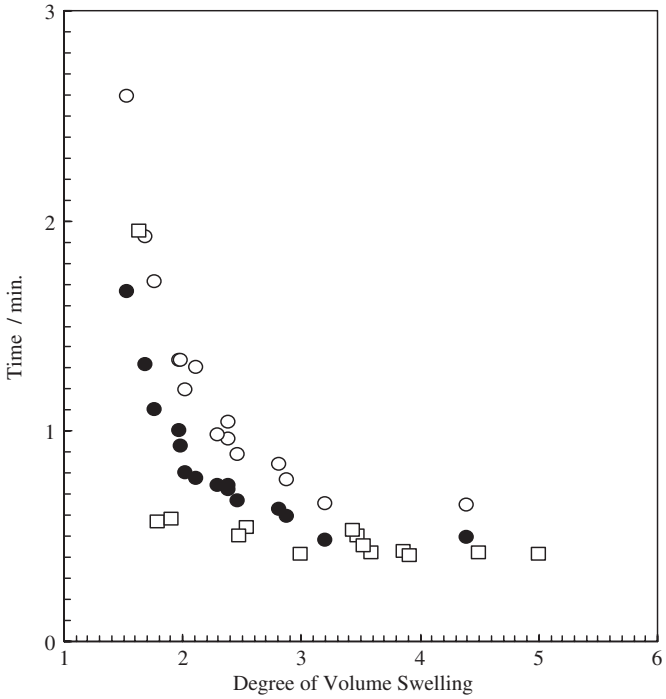

Fig. 16. Dependence of the "required time" T_r for solvents in MPS gel between $d_{swollen}$ on Q. DMF-d_7 at 30 °C (○) and 50 °C (●), and THF-d_8 at 30 °C (□).

synthesis could not be simply reduced by using gels at large Q, but it seems that the required time of a series of solid-phase synthesis increases with a decrease in Q in the range of $Q < 2.0$.

The reaction rate depends on the collision frequency and the collision energy. It is not easy to determine the collision frequency. Nevertheless, a parameter being related with the collision frequency is discussed. We consider the "required time" within which amino acids transfer from one reactive site to another site. As dried beads, the distance between the two reactive sites is assumed to be a. When a dried bead with d_{dry} is swollen by solvent at equilibrium, the diameter of a bead gel becomes $d_{swollen}$. In the swollen bead gel, the distance between the two reactive sites is assumed to be l. Thus, l is expressed by the following equation:

$$l = a \times \frac{d_{swollen}}{d_{dry}} \tag{5}$$

and can be expressed by using Q

$$l = a \times \sqrt[3]{Q} \tag{6}$$

In order to relate this equation with the collision frequency, we may use the required time ($T_{t\ (amino\ acids)}$) that amino acids in polymer gels diffuse within $d_{swollen}$,

instead of the required time that amino acids transfer from one reactive site to another site. Thus, $T_{t\ (\text{amino acids})}$ is expressed by the following equation:

$$T_{t\ (\text{amino acids})} = \frac{(d_{\text{swollen}})^2}{2D} \tag{7}$$

and d_{swollen} can be expressed by Eqs. (5) and (6).

$$d_{\text{swollen}} = d_{\text{dry}} \times \sqrt[3]{Q} \tag{8}$$

Fig. 17 shows the temperature dependence of $T_{t(\text{Boc}-\text{Phe})}$ in the MPS1 and the MPS2 gels in the temperature range from 30 to 50 °C. The $d_{\text{swollen-DVB1 mol\%}}$ value of the MPS1 gels is 202 μm and the $d_{\text{swollen-DVB2 mol\%}}$ value of the MPS2 gels is 172 μm. The smaller is the $T_{t(\text{Boc-Phe})}$ value, the greater is the collision frequency between the amino acids and the reactive sites. As seen from Fig. 17, the collision frequency in the MPS1 gels is greater than that in the MPS2 gels. Further, it was found that the collision frequency in the MPS2 gels could be greatly increased by temperature.

As for Boc-Phe, Boc-Trp and Fmoc-Phe in the MPS, the PEG-PS and the CLEAR gels, the $T_{t(\text{amino acids})}$ values are estimated in the same way as for Boc-Phe in the MPS gels. Fig. 18 shows $T_{t(\text{amino acids})}$ values at 30 °C. As for Boc-Phe, the magnitude

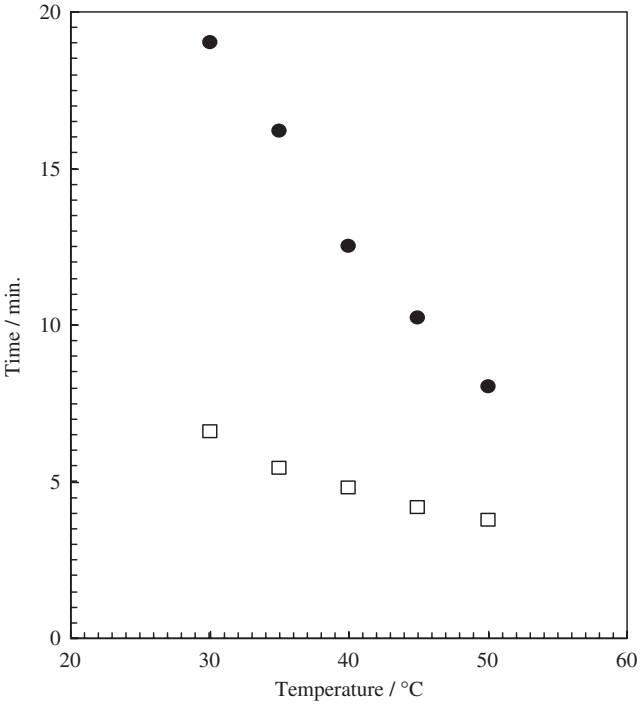

Fig. 17. Temperature dependence of the $T_{t\ (\text{Boc}-\text{Phe})}$ for Boc-Phe in 1% cross-linked MPS gels (□) with DMF-d_7 and 2% cross-linked MPS gels (●) in the temperature range from 30 to 50 °C.

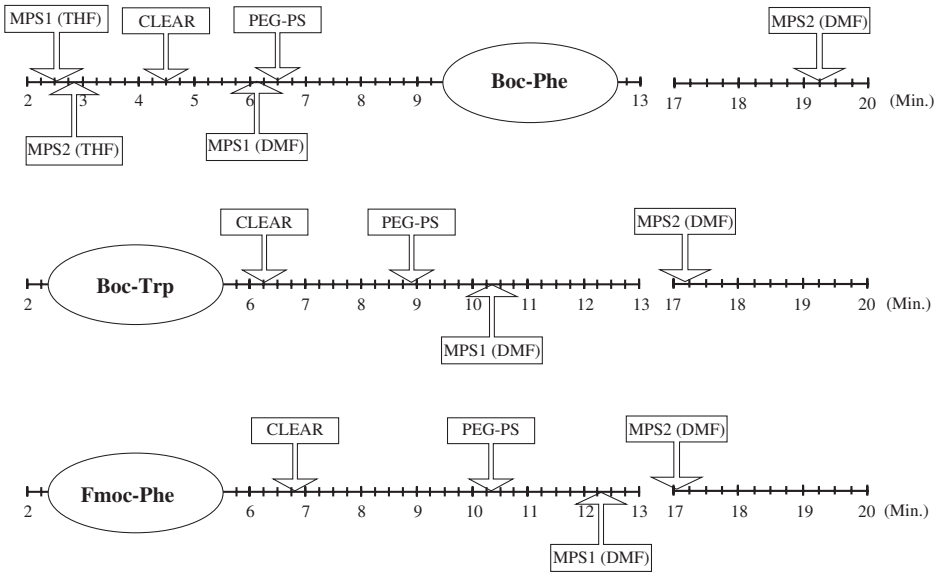

Fig. 18. $T_{t\ (\text{amino acids})}$, within which the amino acids in the polymer gel diffuse in d_{swollen} at 30 °C. MPS1 is 1% cross-linked by DVB and MPS2 is 2% cross-linked by DVB.

of the $T_{t(\text{Boc-Phe})}$ values in gels becomes of the order of the MPS1 gel with THF solution < in MPS2 gel with THF solution < in CLEAR gel with DMF solution < in MPS1 gel with DMF solution < in PEG-PS gel with DMF solution < in MPS2 gel with DMF solution. It is interesting that the collision frequency for the MPS2 gel is very low. As for Boc-Trp and Fmoc-Phe, a similar tendency is obtained. As seen from this figure, it can be said that the collision frequency between the amino acids and the reactive sites is in CLEAR gel > in PEG-PS gel > in MPS1 gel > in MPS2 gel.

As mentioned above, the collision frequency for the MPS, PEG-PS and CLEAR solid-phase peptide reaction fields could be roughly estimated by diffusion coefficients. In general, it can be said that the reaction rate of the solid-phase synthesis depends on the rate of diffusion for the amino acid. In practice, it seems that the solid-phase reaction rate depends on the dynamics of the reactive sites in addition to the diffusional behavior of solvents and reagents. The reactive sites of the MPS resin are in the neighboring region of the main chain, but that of the PEG-PS resin is at a distance from the main chain owing to the existence of the spacer of polyethylene-glycol groups. Therefore, the mobility of the reactive sites in the PEG-PS gel is better than that of the reactive sites in the MPS gel.

2.5. Diffusion analysis and inhomogeneity of the network size in polymer gels by time-dependent diffusion NMR

The polystyrene gels considered here have been used as the most popular polymer supports in solid-phase peptide synthesis and supports for catalysts, column

chromatography, ion-exchange resins and so on. These functionalities are closely associated with the diffusional behavior of the probe molecules and solvents, structure and dynamics of polymer gel systems, network size, distribution of network size and particle size. Especially, the diffusion process of the probe molecules must be deeply understood.[9b,46] Further, it can be said that polymer gels have a general inhomogeneity of network size, and the properties of the polymer gels depend on their spatial inhomogeneity. The existence of spatial inhomogeneity has been studied by light scattering as speckles.[88–90] One of the clearest manifestations of the inhomogeneity is the appearance of a speckle pattern. As for chemically cross-linked polymer gels, the relationship between speckles and spatial inhomogeneity has been elucidated.[91–95] Nevertheless, some problems on intermolecular interactions between the network and probe molecules associated with inhomogeneity of the network size in polymer gels remain.

In this section, inhomogeneity of the network size in chemically cross-linked polymer gels is characterized through observation of the diffusion coefficients of probe molecules, amino acids, in the gels by means of ^{1}H PFGSE NMR. This is achieved by varying the time interval between two field-gradient pulses (Δ) in the PFGSE pulse sequence corresponding to the diffusing time. It is thus possible to elucidate intermolecular interactions between the network and probe molecules associated with the inhomogeneity of the network size. The gel systems Boc-Phe and PEO (poly(ethylene oxide)) ($M_w = 1{,}500$) in the MPS1, the MPS2 and the CLEAR gels have been employed.

The diffusion coefficients of Boc-Phe in the polymer gels are measured as a function of diffusing time Δ (i.e., field-gradient pulse-interval time) by the ^{1}H PFGSE NMR method. As for Boc-Phe in the MPS1 gels, the plots of $\ln[A(\delta)/A(0)]$ against $\gamma^2G^2\delta^2(\Delta-\delta/3)$ at $\Delta = 10$, 30, 40 and 100 ms at 30 °C are shown in Fig. 19. As for the plots at $\Delta = 40$ and 100 ms, it is seen that the experimental data lie on a straight line. This shows that Boc-Phe has a single diffusion component in the observation time Δ range from 40 to 100 ms corresponding to the diffusing time. On the other hand, in the plots at $\Delta = 10$ and 30 ms, it is seen that the experimental data do not lie on a straight line. This shows that Boc-Phe in the MPS1 gels has two diffusion components such as, for example, a slow and a fast diffusion component during the observation time Δ. As for echo attenuation curvature at short diffusion times, any diffusant polydispersity, trace solvents, T_2-weighting and host inhomogeneity of the gel could produce curvature at short diffusion times but give a single apparent D at longer times. Probe molecules used in this work have monodispersity and single component T_2. It is reported that probe molecules in solution have a single diffusion component.[28,41,44] Therefore, it is thought that the echo attenuation curvature is not due to diffusant polydispersity, trace solvents, T_2-weighting and artifacts, but is due to host inhomogeneity. The slow diffusion components are more sensitive to interactions between the gel network and probe molecules than is the fast-diffusion component. This arises because the slow diffusion component comes from strong intermolecular interactions between the probe molecule and a smaller network in the gels. The slow diffusion component increases with an increase in Δ, i.e., the averaged D approaches to the slow D. It cannot be said that the

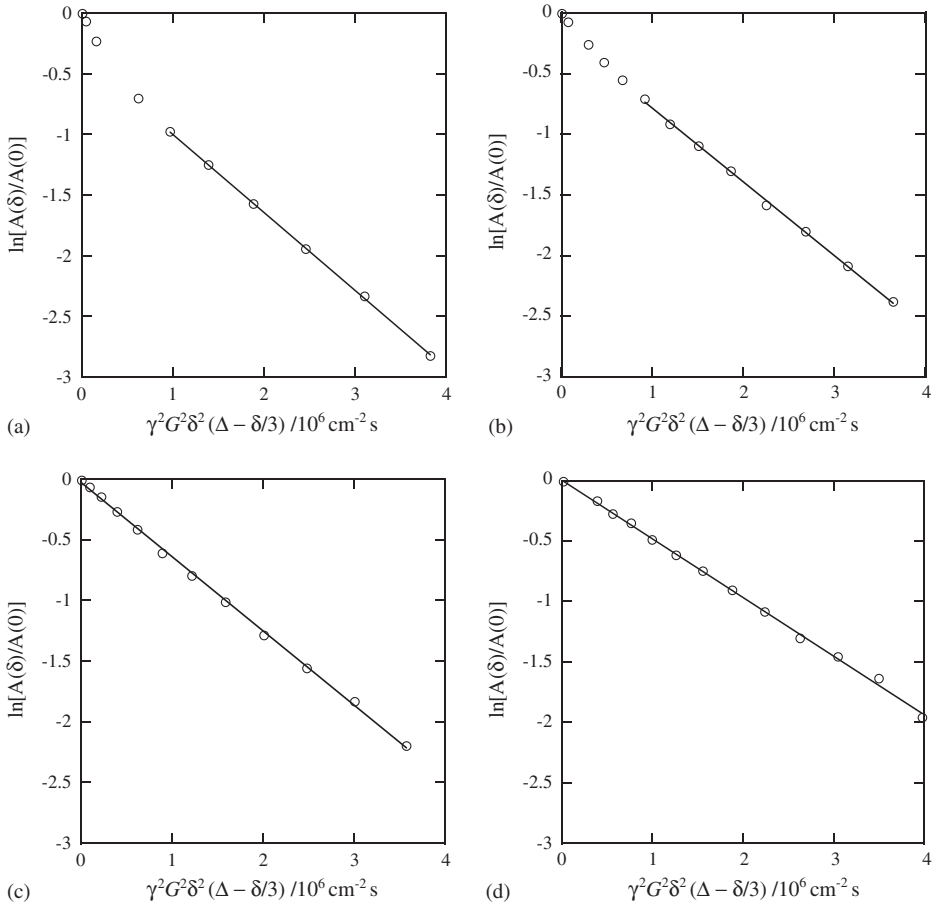

Fig. 19. Diffusional spin-echo attenuation of Boc-Phe in the MPS1 gels with DMF-d_7 as solvent on Δ at 30 °C by varying the field-gradient pulse duration δ, where the Boc-Phe concentration is 10 wt%. (a) Δ = 10 ms, (b) Δ = 30 ms, (c) Δ = 40 ms and (d) Δ = 100 ms.

fast diffusion component is exactly one component or multi-components, but the observed diffusion echo signal is approximately deconvoluted by a slow and a fast diffusion component. From such plots (Fig. 19), the fractions of the slow and fast diffusion components can be straightforwardly determined. The fractions of the slow and fast diffusion components (f_{slow} and f_{fast}, respectively) may depend on Δ. This shows that when Boc-Phe molecules are transported in some network cells with different network size during Δ, they have the two diffusion components. This implies that by varying the diffusing time Δ the diffusion of Boc-Phe molecules with different diffusion coefficients in different network cells is observed. If probe molecules diffuse over a long Δ time, the observed diffusion coefficient may become an averaged value owing to diffusion through the network cells with different network sizes. Therefore, a series of these experiments give useful information about the

diffusion process of Boc-Phe and the inhomogeneities of network size. In other words, the slow diffusion component gives useful information about the inhomogeneity of network size for gels through strong intermolecular interactions between the probe molecules and the network of the gels.[9b,46,190]

Fig. 20 shows the dependence of the f_{slow} value for Boc-Phe in the MPS1 gels using DMF-d_7 as solvent on Δ at 30 °C, where the Boc-Phe concentration is 10 wt/wt%. The slow and fast D values are shown in Table 4. As seen from this figure, the f_{slow} value increases with an increase in Δ. The f_{slow} value at $\Delta = 5$ ms is about 0.5. On this timescale, the diffusion distance for most of the Boc-Phe molecules in the MPS1 gels is different from each other. The f_{slow} value at $\Delta > 40$ ms is 1.0. On these timescales, the diffusion distance for all of the Boc-Phe molecules in the MPS1 gels is almost equal to each other. Therefore, when the Boc-Phe molecules in the MPS1 gels are diffusing during $\Delta > 40$ ms, the diffusion coefficients are observed to be single. Here, we focus on the Δ value in order to understand why the observed diffusion changes from having two components to a single component. Let us name this specified Δ value the "specific" diffusion time (S_{time}).

The experimental results obtained at $\Delta = 5$, 10, 40 and 100 ms lead to the diffusion distances $d = 0.6$, 0.9, 1.7 and 2.5 μm, respectively. The d values in these experiments are much larger than the network size (12–24 nm) considered here, but much smaller than the particle size of swollen gel beads (140–304 μm). The network size in the equilibrium-swollen state is estimated by using the fraction of DVB

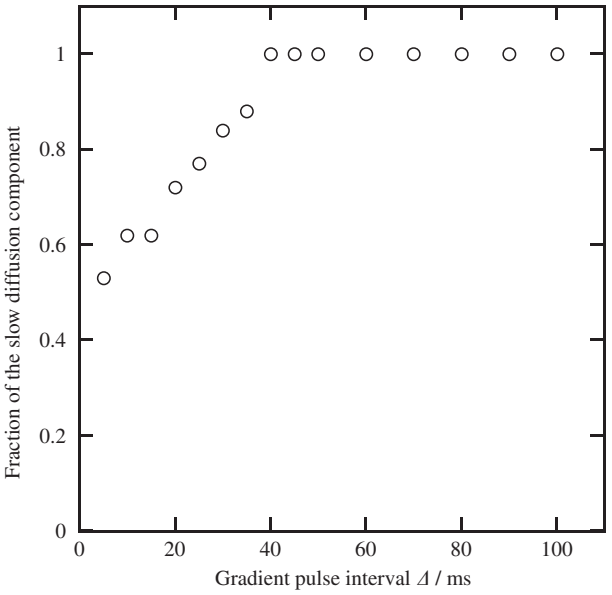

Fig. 20. Dependence of the fraction of the slow diffusion component of Boc-Phe (○) in the MPS1 gels with DMF-d_7 as solvent at 30 °C on the gradient pulse interval Δ, where the Boc-Phe concentration is 10 wt/wt%.

Table 4. Diffusion coefficients D of probe molecules in MPS and CLEAR gels

Diffusing time (Δ/ms)		Diffusion coefficient D (10^{-7} cm^2 s^{-1})				
		MPS1 resin (1 mol% DVB)	MPS2 resin (2 mol% DVB)	CLEAR resin	CLEAR resin	CLEAR resin
		Boc-Phe (10 wt/wt%)	Boc-Phe (10 wt/wt%)	Boc-Phe (10 wt/wt%)	Boc-Phe (10 wt/wt%)	PEO (10 wt/wt%)
5	D_{fast}	36.4	30.7	33.3	50.6	50.3
	D_{slow}	3.50	2.76	9.46	13.9	7.02
10	D_{fast}	42.7	14.3	45.6	48.3	45.1
	D_{slow}	3.68	2.65	12.3	14.6	4.00
15	D_{fast}	35.8	7.11	44.2	45.2	
	D_{slow}	3.99	2.43	11.7	15.7	
20	D_{fast}	36.8	2.78[a]	27.7	16.3[a]	51.5
	D_{slow}	3.75		12.4		3.73
25	D_{fast}	23.1		23.1	16.5[a]	
	D_{slow}	3.68		12.0		
30	D_{fast}	31.5	2.42[a]	12.0[a]	15.4[a]	50.3
	D_{slow}	3.66				3.63
35	D_{fast}	29.6		11.1[a]	14.4[a]	
	D_{slow}	3.74				
40	D_{fast}	3.42[a]	2.24[a]	11.3[a]	14.3[a]	26.2
	D_{slow}					3.46
45	D_{fast}	3.30[a]		11.2[a]	13.6[a]	
	D_{slow}					
50	D_{fast}	3.24[a]	2.16[a]	10.8[a]	12.5[a]	23.1
	D_{slow}					3.31
60	D_{fast}	3.13[a]		10.6[a]		3.52[a]
	D_{slow}					
70	D_{fast}	2.96[a]		10.4[a]		3.30[a]
	D_{slow}					
80	D_{fast}	2.97[a]		14.2[a]		3.18[a]
	D_{slow}					
90	D_{fast}	2.89[a]		10.6[a]		3.51[a]
	D_{slow}					
100	D_{fast}	2.98[a]		10.4[a]		2.99[a]
	D_{slow}					

[a] D_{fast} is equal to D_{slow}.

cross-linking. This is based on the assumption that polystyrene chains between cross-linking points stretch much longer in the equilibrium-swollen state. Therefore, as seen from the obtained S values, it can be said that Boc-Phe molecules go through some network cells during the diffusing time Δ.

As for Boc-Phe in the MPS1 gels with DMF-d_7 as solvent at 30 °C, the f_{slow} value increases with an increase in d and changes from the two diffusion components to the single diffusion component at $d = 1.7\,\mu m$. Here, this specified d value is named as the "specific" diffusion distance ($S_{distance}$). In the short Δ range, in which $d < 1.7\,\mu m$, Boc-Phe molecules cannot diffuse to a large distance through many network cells, and so the diffusion distance is not enough to obtain the single diffusion component, but the two diffusion components are observed. In the long Δ range, in which $d > 1.7\,mm$, the Boc-Phe molecules can diffuse through many network cells and so the single diffusion component is observed. Therefore, it can be said that a series of time-dependent diffusion experiments give useful information about the network structure of polymer gels. If gel systems are formed with a larger network size as compared with the $S_{distance}$, the observed diffusion coefficients of Boc-Phe in individual gel beads become the same value. However, if gel systems are formed with a smaller network size as compared with the $S_{distance}$, the diffusion coefficients of Boc-Phe in the individual gel beads are observed. In other words, all of the gel beads with a larger size than the $S_{distance}$ have the same function as molecular separation materials, but gel beads with a smaller size than the $S_{distance}$ have different functions. Therefore, it is said that $S_{distance}$ is a measure for the diffusional inhomogeneity of probe molecules, the spatial inhomogeneity of the network and the functionalities of the network.

Next, let us estimate the $S_{distance}$ for Boc-Phe in the CLEAR gels with DMF-d_7 as a function of temperature, where the Boc-Phe concentration is 10 wt/wt%. This type of gel has no volume-transition in the temperature range from 30 to 50 °C. Therefore, we can predict that the $S_{distance}$ is independent of temperature, if intermolecular interactions between Boc-Phe and the polystyrene network in this gel system are very negligibly weak in a series of time-dependent experiments, i.e., if the diffusional behavior of Boc-Phe is independent of temperature. As a result, it is found that the $S_{distance}$ is independent of temperature in the temperature range from 30 to 50 °C. This bears out the foregoing prediction, and indicates that the dependence of the f_{slow} value on the Δ value is significantly indicates the distribution of network size in this gel system. As for Boc-Phe in the CLEAR gels with DMF-d_7 as solvent, the $S_{distance}$ values at 30, 35, 40, 45 and 50 °C are 2.7, 2.7, 2.8, 2.9 and 2.8 μm, respectively.

Fig. 21 shows the dependence of the f_{slow} value for Boc-Phe in the MPS2, the MPS1 and the CLEAR gels with DMF-d_7 as solvent at 30 °C on the gradient pulse interval Δ, where the Boc-Phe concentration is 10 wt%. The slow and fast D values are shown in Table 4. As seen from this figure, the f_{slow} value increases with an increase in Δ and changes from having two components to a single component at larger Δ values. The S_{time} value as estimated from these plots for Boc-Phe in the MPS2, the MPS1 and the CLEAR gels are 20, 40 and 30 ms, respectively. It is found that S_{time} depends on the kind of gel.

As for $S_{distance}$, it is found that the f_{slow} values for Boc-Phe molecules in the three types of gel increase with an increase in d and become 1.0 at large d but the dependence differs from each other. As for Boc-Phe in the MPS2, the MPS1 and the CLEAR gels at 30 °C, the $S_{distance}$ values are 1.1, 1.7, and 2.7 μm, respectively,

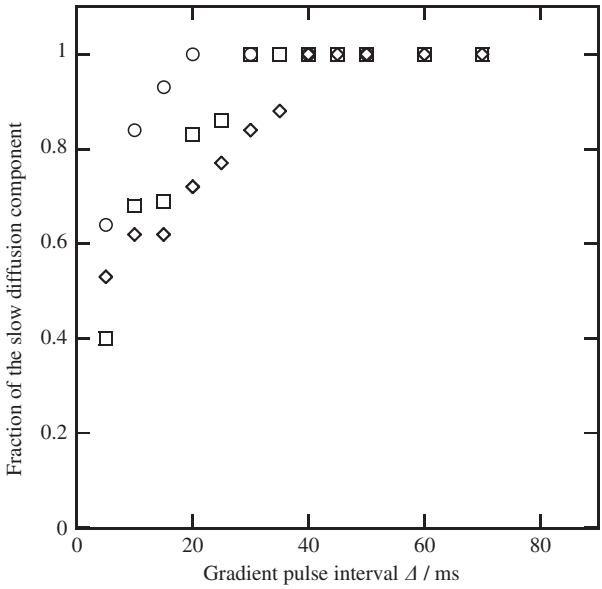

Fig. 21. Dependence of the fraction of the slow diffusion component of Boc-Phe in the MPS2 gels (○), in the MPS1 gels (◇) and CLEAR gels (□) with DMF-d_7 as solvent at 30 °C on the gradient pulse interval Δ, where the Boc-Phe concentration is 10 wt/wt%.

where the Boc-Phe concentration is 10 wt/wt%. The MPS2 gels are cross-linked by 2 wt/wt% DVB, while the MPS1 gels are cross-linked by 1 wt/wt% DVB. It can be said that gels with high density cross-linking have much shorter $S_{distance}$ values than gels with low density cross-linking, and the $S_{distance}$ value depends on the kind of gel. Gels with low density cross-linking have more cross-linker of which one side does not react with the PS chains as compared with high density cross-linking. As a result, when the density of the cross-linking is low, the distribution of the network size in the gels becomes broad. Further, it can be thought that the distribution of the network size depends on the volume, length and reactivity of the cross-linker. It is found that the $S_{distance}$ value of Boc-Phe in the CLEAR gels is much larger than that of Boc-Phe in the MPS gels. The cross-linker of the MPS gels is DVB, and the cross-linker of the CLEAR gels is acrylate. The degree of volume swelling for the MPS2, MPS1 and CLEAR gels is 1.59, 2.48 and 2.64, respectively.

Fig. 22 shows the dependence of the fraction of the slow diffusion component of Boc-Phe in the CLEAR gels with DMF-d_7 as solvent at 4 and 10 wt/wt% concentrations at 30 °C on the gradient pulse interval Δ. The slow and fast D values are shown in Table 4. At the given concentrations, the S_{time} values are 20 and 30 ms, respectively. The S_{time} at 10 wt/wt% is 1.5 times longer than that at 4 wt/wt%.

At the given concentrations, the $S_{distance}$ values are 2.6 and 2.7 μm, respectively. From this result, as for Boc-Phe in the CLEAR gels, it is found that the value of $S_{distance}$ is independent of the Boc-Phe concentration between 4 and 10 wt/wt%. This result indicates that intermolecular interactions between Boc-Phe and the

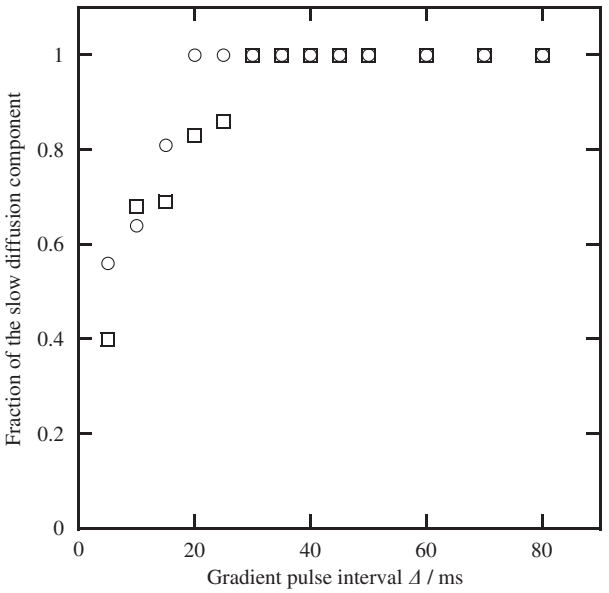

Fig. 22. Dependence of the fraction of the slow diffusion component of Boc-Phe (○) and Boc-Phe (□) in the CLEAR gels with DMF-d_7 as solvent at 4 and 10 wt/wt% concentrations at 30 °C on the diffusion distance S for the slow diffusion components in the gradient pulse interval Δ.

polyethoxylate network in this gel are very negligibly weak at the $S_{distance}$, and that the diffusional behavior of Boc-Phe in the CLEAR gels is independent of the Boc-Phe concentration although their averaged diffusion rates are different.

Fig. 23 shows the dependence of the fraction of the slow diffusion component for Boc-Phe and PEO ($M_w = 1{,}500$) in the CLEAR gels with DMF-d_7 as solvent at 30 °C on the gradient pulse interval Δ, where the Boc-Phe and PEO concentrations are 4 wt/wt% The slow and fast D values are shown in Table 4. The S_{time} values of PEO are longer than those of Boc-Phe, and the S_{time} values are 60 and 20 ms, respectively.

Next, the $S_{distance}$ of PEO is shorter than that of Boc-Phe, and the $S_{distance}$ values are 2.1 and 2.6 μm, respectively. As for the same kind of gel, the $S_{distance}$ contribution to the inhomogeneity of the network size for gels must be the same for different kinds of probe molecules, if the diffusional behaviors of the probe molecules are the same. This result can be explained as follows. There is a difference between the diffusional behavior of PEO and that of Boc-Phe. Boc-Phe molecules can diffuse through all network cells in the size range from the smallest to the largest, but PEO molecules cannot diffuse through smaller network cells of gels. For this reason, it can be said that the diffusional behavior of PEO is not influenced by all of the network cells, therefore the $S_{distance}$ values of PEO are smaller than that of Boc-Phe. It is found that the $S_{distance}$ depends on the diffusional behavior of probe molecules as well as the network structure of gels.

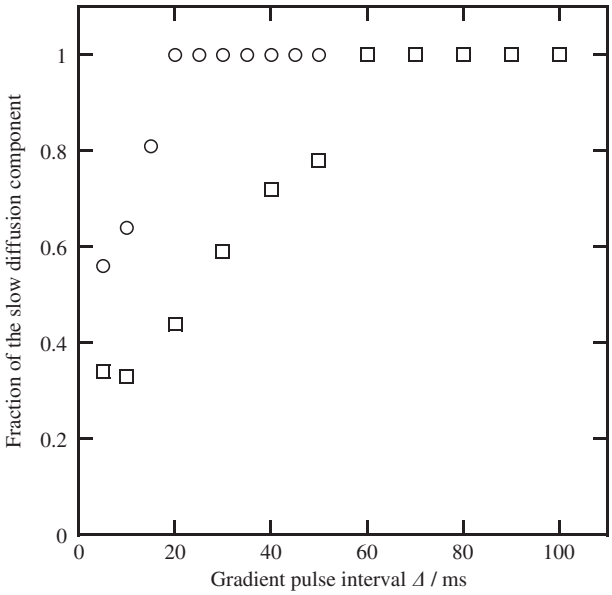

Fig. 23. Dependence of the fraction of the slow diffusion component of Boc-Phe (solvent: DMF-d_7) (○) and PEO ($M_w = 1{,}500$) (□) in the CLEAR gels with DMF-d_7 as solvent at 30 °C on the gradient pulse interval Δ, where the Boc-Phe and PEO concentrations are 4 wt/wt%.

Most recently, the inhomogeneity in poly(acrylic acid) (PAA) gels differing in their degree of cross-linking as prepared at 70 °C by simultaneous polymerization and cross-linking of a mixture of acrylic acid (AA), sodium carbonate, cross-linker (1,4-butanediol diacrylate), and the redox couple sodium persulfate/sodium isoascorbate as the initiator, was detected as a function of Q in the Q range of 2.8–10.[46] Two types of networks were prepared by using the same monomer concentration (30 wt/wt%) and the same amount of sodium carbonate but different amounts of the cross-linker, 1.1 (gel 1) and 0.5 wt/wt% (gel 2), respectively, in the monomer mixture. Detection of heterogeneities was based on measuring the diffusion coefficients of the probe poly(ethylene glycol) as a function of Q and the diffusing time Δ by the PFGSE method. The inhomogeneities emerged as the Q value of the gels was reduced. For the highly swollen gels ($Q = 10.0$ and 5.2 for gel 1 and $Q = 10.0$, 5.1 and 4.5 for gel 2) only one diffusion coefficient was detected, independent of the diffusing time Δ in the range 30–500 ms. For less swollen gels ($Q =$ 2.9–4.5 for gel 1 and 2.8–3.9 for gel 2) two diffusion coefficients were detected, D_{fast} and D_{slow}, with values that depended on Δ; for these swollen gels the f_{fast} and f_{slow} values were calculated. A specific degree of swelling Q_s above which the diffusion of the probe in the two gel systems changed from one to two components is defined. A larger value of Q_s in gel 1 was taken as an indicator of a more inhomogeneous gel. Analysis of the effect of Δ on the diffusion coefficients, diffusion distances and fractions of slow and fast diffusion components indicate that

the gels form a highly cross-linked region in a narrow Q range. In this Q range, the polymer chains interact and form a highly restricted diffusion region. The extent and distribution of the cross-links form different restricted diffusion regions in the gel 1 and gel 2 systems.

2.6. Diffusion of solvent in highly oriented PBLG gel with long channel cavities with micrometer-scale diameters

It is well known that poly(γ-benzyl L-glutamate) (PBLG) forms the lyotropic liquid crystalline phase in dichloromethane, 1,4-dioxane, chloroform, and so on,[96–98] and then forms the nematic liquid crystalline phase from the lyotropic liquid crystalline phase in a magnetic field because the PBLG chains in the lyotropic liquid crystalline phase are highly oriented in the magnetic field.[99–104] Kishi *et al.*[105,106] have prepared PBLG gels in cholesteric and nematic liquid crystalline phases and the properties of the obtained gels have been elucidated. Zhao *et al.*[107–109] have reported a study by using the diffusion process of probe molecules in polypeptide gels. It has been reported that highly oriented PBLG gels having channel cavities with micrometer-scale diameters have been prepared by cross-linking PBLG chains with ethylenediamine as cross-linker in 1,4-dioxane in the presence of a strong magnetic field from an NMR magnet with a strength of 10.5 T due to the phase separation in the cross-linking reaction process and have been made structural characterization of the polypeptide gels by ^{1}H NMR imaging.[107] In order to develop this PBLG network as smart membranes with multi-functions, a more precise and detailed three-dimensional (3D) structural characterization of the channel cavities is needed. In this section, the diffusional behavior of 1,4-dioxane in highly oriented PBLG gels having channel cavities with micrometer-scale diameters is studied by PFGSE ^{1}H NMR. The results show that solvent molecules can be isolated in the channel cavities.[110]

The PBLG ($M_w = 277{,}000$) solution (0.2 g) in a Teflon tube with a diameter of 5 mm was placed in a strong NMR magnetic field (10.5 T) for 24 h at room temperature to orient the α-helical PBLG chains in the magnetic field direction, and the orientation degree was ca. 0.81.[35] After the Teflon tube with highly oriented PBLG chains was removed from the NMR magnet, ethylenediamine as a cross-linker was added by changing the concentration (concentrations: (A) 5 μL and (B) 10 μL) in the tube. The sample tube was placed for three days in an NMR magnet at room temperature again leading to a cross-linking of the PBLG chains in the lyotropic liquid crystalline phase by the ester-amide exchange reaction. The obtained highly oriented PBLG samples A and B were washed by 1,4-dioxane to remove unreacted cross-linker. The dried samples were opaque cylindrical rods with an average diameter of 3.2 mm and a length of 15 mm.

If solvent molecules in a micrometer-scale channel cavity of highly oriented PBLG gel are assumed to be isolated, their diffusion is restricted. Therefore, if the diffusion time Δ is changed to observe the field-gradient spin-echo signal, it shows the characteristic behavior of restricted diffusion. For example, according to the partially

absorbing wall model on diffusion in the sphere with the radius R, the plots of the PFG spin-echo attenuation $E(q, \Delta)$ for diffusion of the solvent molecules against the "tunable" parameter $q(=(2\pi)^{-1}\gamma\delta G)$ are expressed by the following equation, where $E(q, t)$ is the spin-echo signal normalized by dividing the echo signal obtained in the absence of field gradients as $E(q, t) = A(q, t)/A(q = 0, t)$.[26]

$$E(q, \infty) = \frac{2[1 - \cos(4\pi qR)]}{(4\pi qR)^2} \tag{9}$$

This equation shows that from the plots of the PFG spin-echo attenuation $E(q, \Delta)$ for the diffusion of the solvent molecules against the "tunable" parameter q, the diameter $2R$ of the sphere, i.e., the diameter $(2R)$ of a channel cavity in the PBLG gel may be approximately estimated as well as in the case of the 3D NMR imaging method.

Three-dimensional NMR imaging patterns of a cylindrical highly oriented PBLG gel (sample B) with channel cavities were observed, in order to clarify whether the long channels are formed in the direction parallel to the cylindrical axis through the whole sample or not. The PBLG gel sample B swollen with 1,4-dioxane was placed in an NMR tube with a diameter of 5 mm. The observed 3D ^{1}H spin-density NMR image patterns of this sample were obtained by 3D NMR imaging, where 32 pieces of the XY-plane-sliced images were measured with the thickness of an 84 μm per image in the Z direction and one piece of them was shown in Fig. 24. In this image, there are many white circular regions in the background. This shows that the signal intensity of the solvent in the channel cavities is very intense, but that of the solvent in the PBLG network matrix is very weak because the density of the solvent in a channel cavity is much higher than that in the network. Therefore, it can be said that the white circular regions come from 1,4-dioxane as solvent in long channel cavities with a micrometer-scale diameter in the PBLG sample, and the black region indicates the PBLG network matrix with solvent.

If we look at the white circular regions carefully, it can be seen that the diameter of the white circular regions is not homogeneous. Therefore, the distribution of the diameter size in the gel sample was analyzed using a two-dimensional (2D) slice image taken from the 3D NMR image data sets.[107] The plots of the number of the white circular regions against the diameter size are shown in Fig. 25. It is shown that most of the diameter sizes are in the range from 50 to 150 μm, and that the mode diameter is ca. 70 μm. The statistical distribution of the circular channel size may be approximately represented by a χ^2 distribution.

Let us reconstruct the 3D image pattern of a cylindrical highly oriented PBLG gel sample B with channel cavities from the XY-plane-sliced images. The 3D image pattern can be looked at from various directions by using a 3D image analysis system. Here, the 3D images observed from the four directions are shown in Fig. 26. As seen from the 3D image pattern, there are no long channel cavities with micrometer-scale diameters until about 500 μm in the inside direction from the outside surface of the gel rod.

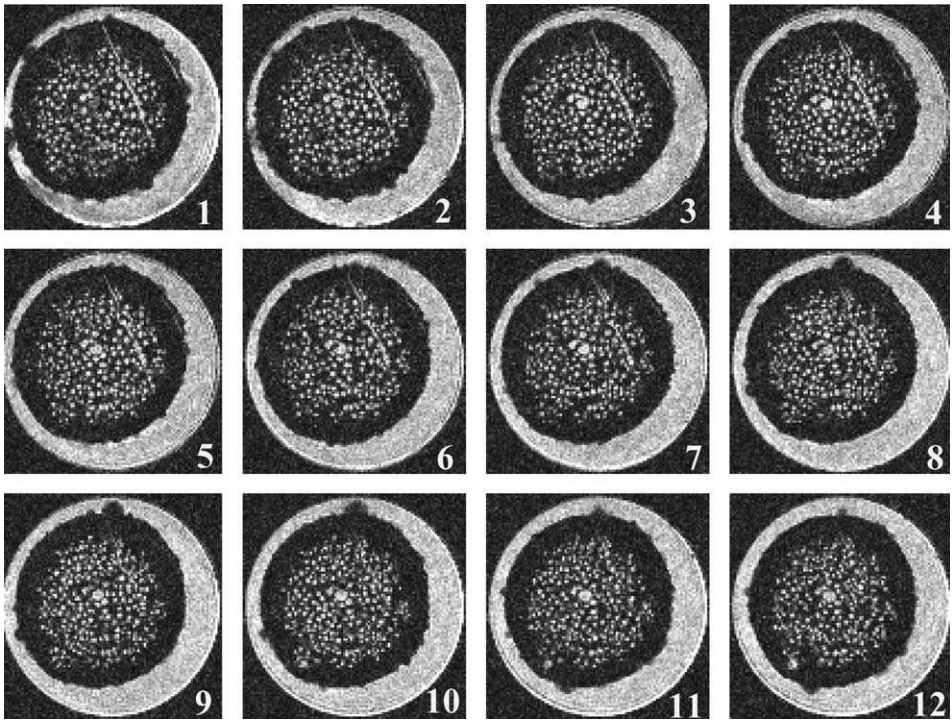

Fig. 24. A typical 2D ^{1}H spin-density NMR image pattern of a highly oriented PBLG gel sample B with 1,4-dioxane as solvent. Thirty-two pieces of the XY-plane-sliced images are observed, where each of images has a thickness of 84 μm in the Z direction. The 2D image slices are taken from the 3D NMR image data sets of PBLG gel sample B.

Further, we can look at the inside of a channel cavity in the gel sample B by the 3D NMR imaging system by using stacked 2D NMR image data. The view position is gradually moving toward the more deep inside of a circular channel cavity with a micrometer-scale diameter from the cross-section of the gel rod. Therefore, we can make an animation video of the adventure in the gel sample. The animation video clip for a channel cavity with micrometer-scale diameters in the PBLG gel is shown in Fig. 27. From the above results, it can be seen that the long channel cavity is formed in the direction parallel to the cylindrical axis through the whole sample as circular channels, and such situations for some channel cavities chosen at random can be recognized. Further, it can be said that there are no long channel cavities with micrometer-scale diameters until about 500 μm from the outside surface of the gel rod. Further, it can be estimated that the volume fraction of the channels in the PBLG gels is about 0.3, and the average of the distance between the two nearest neighboring channels is ca. 257 μm (the distances between the two nearest neighboring centers of the channels) as shown in Fig. 28.

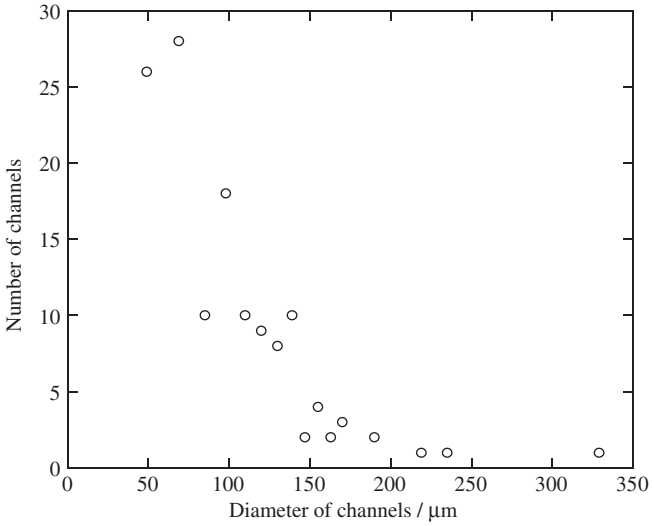

Fig. 25. Plots of the number of the white and circular regions of highly oriented PBLG gel sample B with 1,4-dioxane in a 2D slice image taken from 3D NMR image data sets against the diameter size.

The PBLG network is swollen by 1,4-dioxane as solvent. In previous work,[35] it has been reported that in the highly oriented gel system, with the degree of orientation of 0.81, the diffusion coefficient of the 1,4-dioxane molecule in the direction parallel to the α-helical PBLG axis ($D_{||}$) is $5.4 \times 10^{-6}\,cm^2\,s^{-1}$, which is significantly larger than that perpendicular to the α-helical PBLG axis ($D_{\perp}$), which is $4.5 \times 10^{-6}\,cm^2\,s^{-1}$ and the $D_{||}/D_{\perp}$ value is 1.20.[37] This means that the diffusion is anisotropic. Thus the $D_{||}/D_{\perp}$ value becomes a measure of the orientation of the α-helical chains in the highly oriented PBLG gel together with the amide carbonyl ^{13}C NMR chemical shift components.[35] In the present diffusion NMR experiments the same PFGSE ^1H NMR method was used as previously to determine the diffusion coefficients of the 1,4-dioxane molecule parallel to the α-helical PBLG axis ($D_{||}$) and in the direction perpendicular to the α-helical PBLG axis ($D_{\perp}$).

As for 1,4-dioxane in the PBLG gel sample A, from the plot of the $\ln[A(\delta)/A(0)]$ against $\gamma^2G^2\delta^2(\Delta-\delta/3)$, it is found that the experimental data lie on a straight line. This shows that the solvent molecules in the PBLG gel have a single diffusion component during the observation time $\Delta = 10$ ms at 20 °C. As mentioned above, the PBLG gel sample B has two regions consisting of a long channel cavity (with micrometer-scale diameters) region and the remaining gel matrix region without a long channel cavity. In the diffusion experiments, spin-echo signals coming from the solvent molecules in the corresponding two regions were observed by the PFGSE ^1H NMR method. The $D_{||}$ and $D_{\perp}$ values of 1,4-dioxane in the PBLG gel samples A and B are shown in Table 5. The $D_{||}$ and $D_{\perp}$ values of 1,4-dioxane in the PBLG gel sample A are 6.4×10^{-6} and $5.3 \times 10^{-6}\,cm^2\,s^{-1}$, respectively. The $D_{||}/D_{\perp}$ value is 1.21. This value is very close to that mentioned above.[35] This means that the values

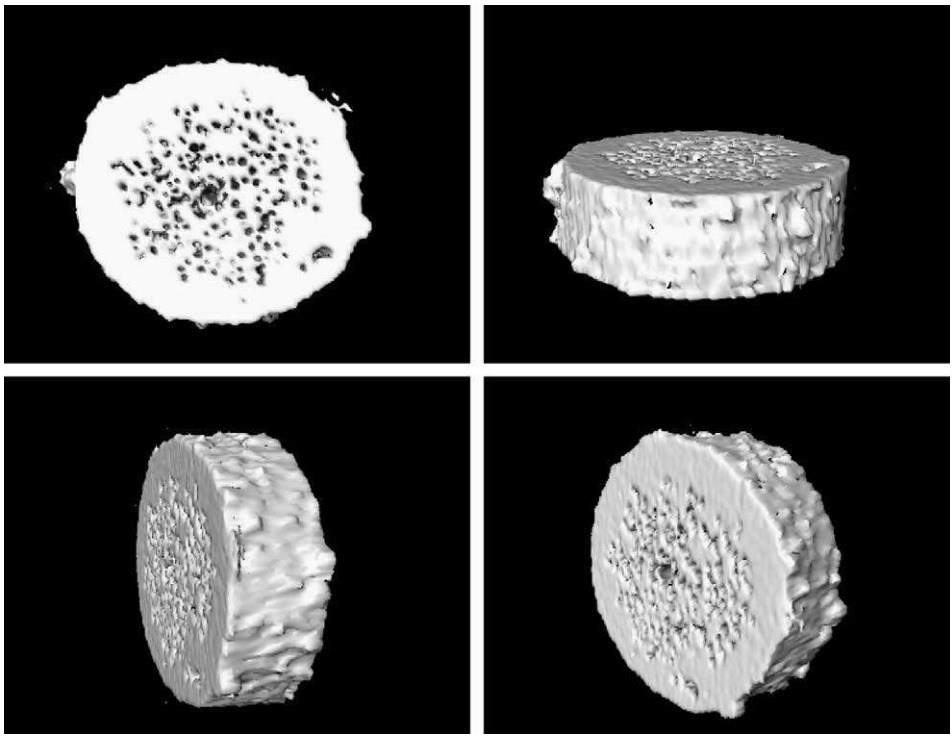

Fig. 26. Three-dimensional images of highly oriented PBLG gel sample B with 1,4-dioxane taken from the 3D NMR image data sets. The 3D image is observed from four directions.

of the orientation degree for these gels are close to each other. In the PBLG gel matrix region, the $D_{||}$ value of 1,4-dioxane in the PBLG gel sample B is $6.2 \times 10^{-6}\,cm^2\,s^{-1}$ and the $D_{\perp}$ value is $4.8 \times 10^{-6}\,cm^2\,s^{-1}$, thus the $D_{||}/D_{\perp}$ value is 1.29. It is found that the $D_{||}$ value in the direction parallel to the α-helical PBLG axis is significantly larger than that perpendicular to the α-helical PBLG axis. This shows that the diffusion is anisotropic. It can be said that the PBLG gel matrix region has an anisotropic channel cavity on a nanometer-scale. This shows that the nanometer-scale structure of the PBLG gel matrix region in the PBLG gel sample B is similar to nanometer-scale structure of the PBLG gel sample A.

Next, we focus on the diffusional behavior of 1,4-dioxane molecules in the micrometer-scale channel cavities of the PBLG gel sample B. The 1,4-dioxane molecules may be trapped in the channel cavities or may permeate partially and slowly from the channel cavity region to the gel matrix region and the reverse through the network of the wall of the channel cavity. This arises because the network density near the wall of the channel cavity as formed by a cross-linking reaction with phase separation may be higher than that in the PBLG gel matrix region. Thus, the partially absorbing wall model on diffusion in a sphere with a radius R as above-mentioned may be approximately used to analyze the diffusion behavior of

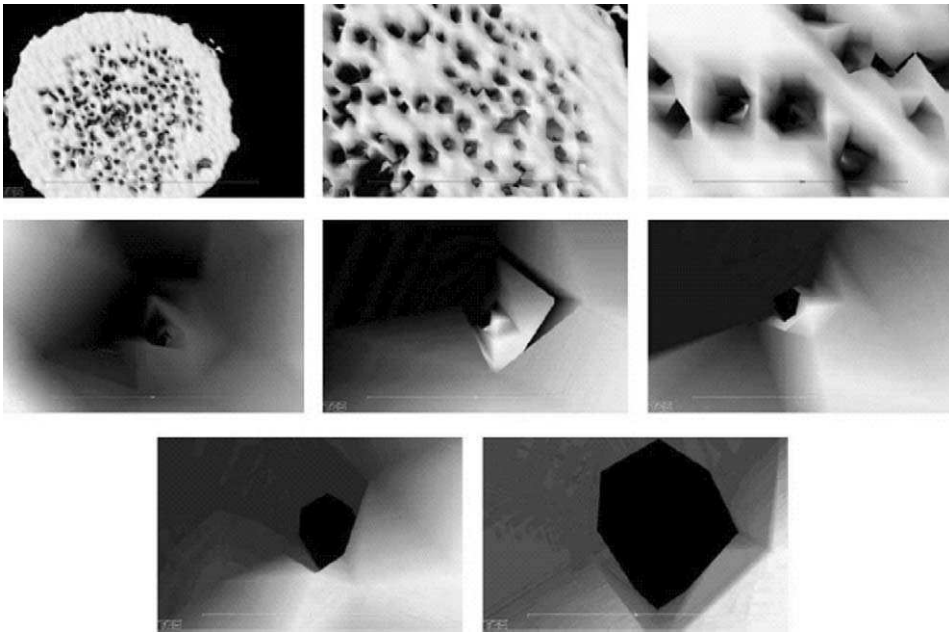

Fig. 27. The animation video clip as for the inside of channel cavities in PBLG gel sample B.

1,4-dioxane in the channel cavity of the PBLG gel sample B. Fig. 29 shows the plots of the PFG spin-echo attenuation $E(q, \Delta)$ for the diffusion of 1,4-dioxane in the PBLG gels with channel cavities against the "tunable" parameter q. As seen from this figure, there are two diffraction minima. When the probe molecules are trapped in the restricted space as mentioned, diffraction minima corresponding to the size scale of the restricted space are often observed as seen from Eq. (2). The simulated PFG spin-echo attenuation $E(q, \Delta)$ for q, by assuming $2R = 50$ and 60 μm as the channel cavity diameters, are shown together with the experimental data in Fig. 29. The tendencies for the simulated curves and the experimental plots are very similar to each other. The slight difference between the experimental and simulated curves may come from the fact that solvent molecules may permeate partially and slowly from the channel cavity region to the gel matrix region and the reverse through the network of the wall of the channel cavity. From this, it can be said that the simulated results do not conflict with the experimental results and thus the mode diameter of the long channel cavities may be estimated to be about 50–60 μm. This is very close to the result obtained by 3D NMR imaging (about 70 μm). Further, it can be said that most of the 1,4-dioxane molecules are reflected at the surface of the wall of channel cavities.

From an accurate diffusional characterization of the gels with long channels, it may be expected to be of interest as one of future material. Most recently, Parker *et al.*[63] have studied the sea mouse with spines that normally appear deep red in color, where the sea mouse, humble marine worm, is living in the Australian sea. The

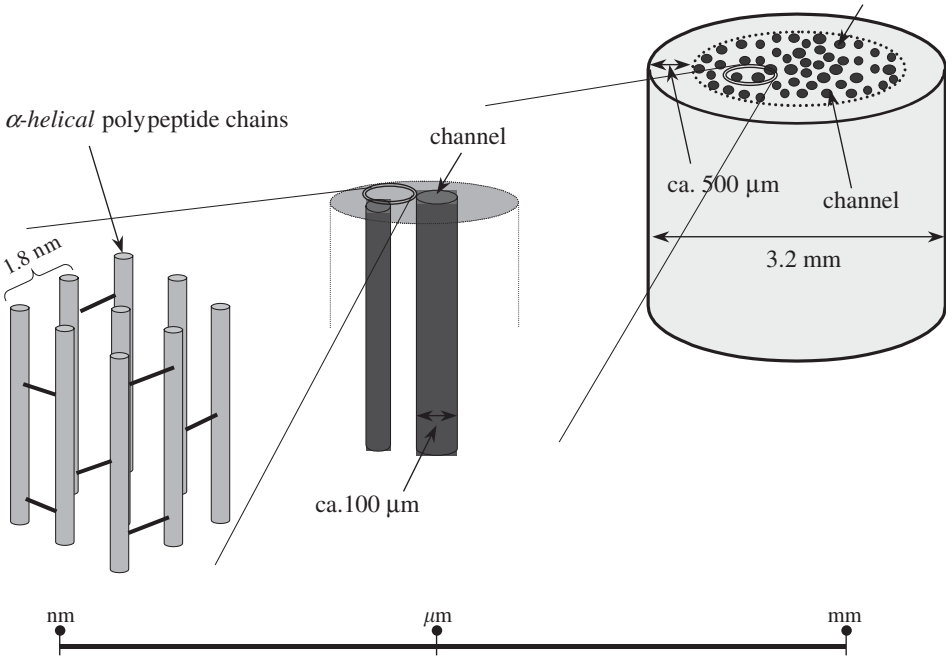

Fig. 28. A schematic diagram of a rod-like highly oriented PBLG gel sample B with long channel cavities in some distance scales.

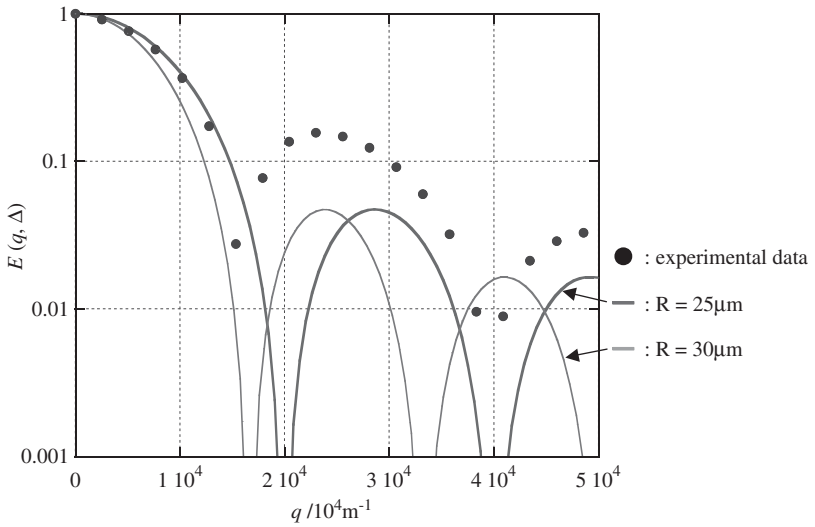

Fig. 29. Plots of $E(q, \Delta)$ versus q for the PFGSE ^{1}H experiment of 1,4-dioxane diffusing in PBLG gel sample B with channel cavities at $\Delta = 5$ ms. (●), experimental data; (____), $2R = 50\,\mu$m; (____), $2R = 60\,\mu$m.

Table 5. Swelling property and diffusion coefficient of highly oriented PBLG

	Dwelling ratio in x, y and z directions		Volume swelling ratio[a]	Diffusion coefficients D in x, y and z directions[b]	
PBLG gel	x, y	2.5	2.8	$D_{\perp}$	5.3
	z	1.1		$D_{\parallel}$	6.4
PBLG gel	x, y	2.6	2.6	$D_{\perp}$	4.8
	z	1.0		$D_{\parallel}$	6.2

[a]Relative to the dried state. The z direction and the x and y directions are in parallel and perpendicular to a cylindrical PBLG gel.
[b]Diffusion coefficient of 1,4-dioxan in PBLG gel at 20°C.

iridescence of spines caused by a highly regular, sub-micrometer-scale structure resembling that being developed for photonic crystals. From such a background, by developing our previous work on highly oriented PBLG gels having channel cavities with learning of the sea mouse, we have prepared highly oriented PBLG gels having channel cavities with sub-micrometer-scale diameters by cross-linking PBLG chains with an increase in ethylenediamine concentration as cross-linker in 1,4-dioxane in the presence of a strong NMR magnetic field. Then, we have successfully obtained the iridescent PBLG gels.[64]

3. DIFFUSIONAL BEHAVIOR OF ROD-LIKE POLYMERS IN THE ANISOTROPIC PHASE

3.1. Diffusion of poly(γ-*n*-dodecyl L-glutamate) in the thermotropic liquid crystalline phase

It has been reported that poly(γ-*n*-octadecyl L-glutamate) (POLG)[111] with long *n*-alkyl [–$(CH_2)_{17}CH_3$] side chains and poly(γ-oleyl L-glutamate) (POLLG)[112] with long oleyl [–$(CH_2)_8CH = CH(CH_2)_7CH_3$] side chains form a thermotropic liquid crystalline state by melting of the side chains. From solid-state high-resolution ^{13}C NMR experiments on POLG over a wide range of temperatures from 27 to 100 °C,[113–117] it has been clarified that the main chain of POLG assumes a right-handed α-helical conformation and the paraffin-like *n*-alkyl ($n = 18$) side chains take an all-*trans* zigzag conformation in the side-chain crystallites at room temperature. It undergoes *trans–gauche* exchange above the melting temperature at 60 °C, while the main chain is undergoing fast molecular motion at a frequency of ca. 60 kHz. Further, from pulse ^1H NMR experiments on POLG and POLLG, details of their dynamics are elucidated.[117] From solid-state high-resolution ^{13}C NMR and DSC experiments on POLLG over a range of temperatures from −40 to 80 °C, it is found that POLLG can maintain a liquid crystalline state because the side chains become too flexible to form a liquid crystalline state even on cooling

to −40 °C.[112] Due to the existence of an unsaturated double bond in the side chain, POLLG is in the liquid crystalline state over a wider range of temperatures compared with the case of POLG.

In order to elucidate the dynamics of the polypeptides in the thermotropic liquid crystalline state, it is very significant to have knowledge of the magnitude of the diffusion coefficient and the anisotropy of the diffusion for the directions parallel and perpendicular to the α-helical chain axis. For the diffusion coefficient measurements, it has been stated that PFGSE ^{1}H NMR can provide very useful information for helping in the elucidation of the diffusion process of solvents for polypeptides in the liquid crystalline state, in addition to the polymer gel systems.

The isotropic and anisotropic diffusion coefficients of the POLG chain in an highly oriented sample, prepared in the magnetic field produced by NMR equipment, and the isotropic diffusion coefficients of the POLLG chain in the thermotropic liquid crystalline state obtained over a wide range of temperatures have been studied, in order to elucidate the diffusion process of the polypeptides.[9a]

POLG and POLLG are synthesized by ester-exchange reactions between poly (γ-methyl L-glutamate) (PMLG) (average molecular weight: $M_w = 100{,}000$ and the number of amino acid residues: ca. 780) and the corresponding *n*-octadecyl alcohol and oleyl alcohol, respectively.

A highly oriented POLG sample is prepared by the following procedure. At first, POLG is dissolved in 1,2-dichloroethane in an NMR glass tube to form the lyotropic liquid crystalline state. Then, it is placed into the magnetic field of a 500 MHz NMR magnet for 60 h until the POLG chains in an NMR glass tube with a diameter of 5 mm were aligned in parallel to the direction of the magnetic field.[35,37,44,47] The direction of the magnetic field is along the long axis of the NMR tube. After the complete orientation of the polypeptide chains, the solvent was vaporized from the NMR tube and then a highly oriented film was obtained on the wall of the NMR tube. The complete orientation of the POLG chains in the film is confirmed by cross-polarized microscopy.

The self-diffusion coefficient measurements on both the POLG and POLLG compounds in the liquid crystalline state in a wide range of temperatures were carried out by means of a 270 NMR MHz spectrometer operating for ^{1}H with a pulse field-gradient generator with a field-gradient strength of about 5.9 T m^{-1} (590 G/cm). The highly oriented POLG film was placed in an NMR tube in the directions parallel and perpendicular to the magnetic field.

3.1.1. *Diffusional behavior and dynamics of POLG and POLLG*

Fig. 30 shows typical spin-echo ^{1}H NMR spectra of POLG and POLLG in the liquid crystalline state at 80 °C as a function of field-gradient pulse length (δ) by using PFGSE ^{1}H NMR.[9a] In the spin-echo ^{1}H NMR spectra of POLG, an asymmetric sharp signal appears, of which the chemical shift position of the signal peak is 0.9 ppm. This peak can be straightforwardly assigned to the methyl protons in the side chains. The upper shoulder peaks may be assigned to the methylene protons in

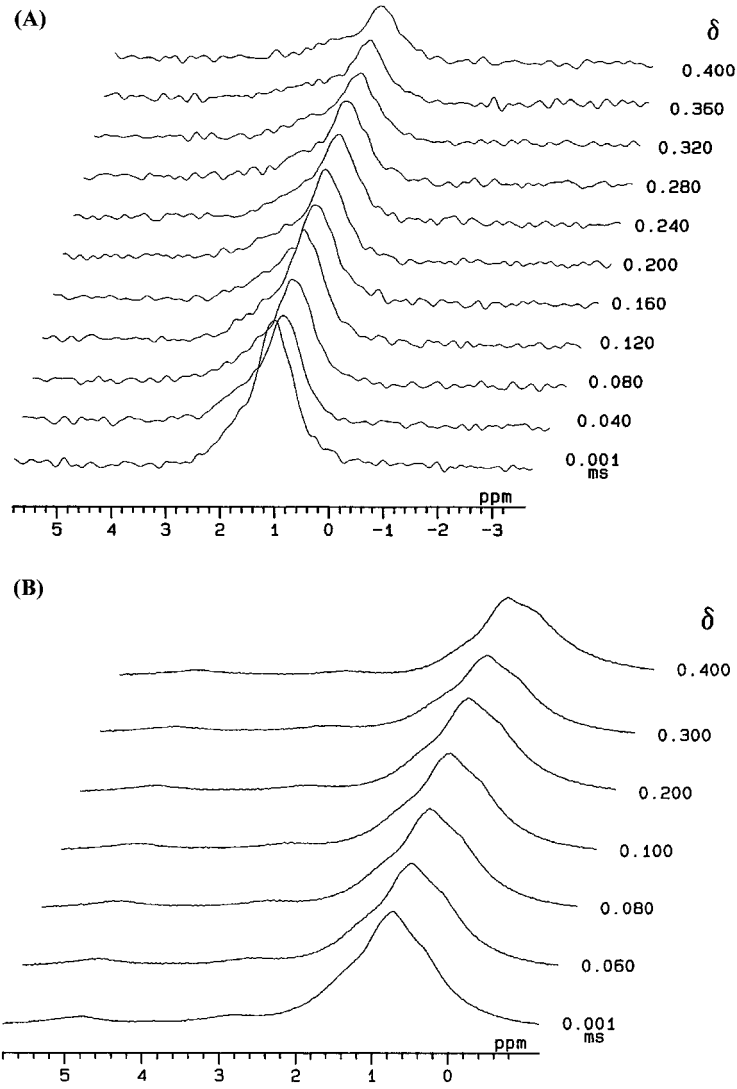

Fig. 30. Typical spin-echo ^{1}H NMR spectra of POLLG (A) and POLG (B) in the thermotropic liquid crystalline state at 80 °C, respectively, as a function of field-gradient pulse length (δ) by using PFGSE ^{1}H NMR.

the side chains. The peaks that come from the main-chain protons such as the α-CH proton and the amide proton do not appear within the measurement temperature range. This is due to the signal broadening because of the extremely slow molecular motion on the ^{1}H NMR timescale. The obtained spin-echo ^{1}H NMR spectra of POLLG are similar to those of POLG. Thus, the peak assignment can be made in a similar way.

Table 6. Determined diffusion coefficients D of POLG and POLLG in the liquid crystalline state as a function of temperature by ^{1}H PFGSE NMR method

	Temperature (°C)	Diffusion coefficient D ($10^{-7}\,cm^2\,s^{-1}$)		
		$D_\perp$	$D_{||}$	D_{iso}
POLG	60	1.41	5.48	3.53
	65	3.12	6.56	5.56
	70	5.56	8.01	6.29
	75	6.34	9.29	8.11
	80	8.87	11.1	10.2
POLLG	30	–	–	4.94
	40	–	–	5.20
	50	–	–	7.96
	60	–	–	9.97
	70	–	–	12.6
	80	–	–	14.0

The plots of $\ln[A(\delta)/A(0)]$ against $\gamma^2G^2\delta^2$ $(\Delta-\delta/3)$ for the above-mentioned peak (at ca. 0.9 ppm) in the PFGSE ^{1}H NMR spectra of POLG and POLLG provide a straight line. This shows that the diffusion of POLG and POLLG is a single component during the observation time. Then, the diffusion coefficients for POLG and POLLG considered here are determined from the slope of the straight line as seen from Eq. (1) and the values are listed in Table 6.

The diffusion coefficients of POLG in the liquid crystalline state were plotted against temperature as shown in Fig. 31. The diffusion coefficients of the rod-like polypeptide chains for the directions parallel ($D_{||}$) and perpendicular ($D_\perp$) to the α-helical chain axis were determined, and the isotropic diffusion coefficient (D_{iso}) was estimated by an average of the determined $D_{||}$ and $D_\perp$ values as $(D_{||}+2D_\perp)/3$. As the temperature is increased from 60 to 80 °C, the determined $D_{||}$ values of POLG in the liquid crystal state are monotonously increased from 5.48×10^{-7} to $1.11\times10^{-6}\,cm^2\,s^{-1}$ and the determined $D_\perp$ values monotonously increase from 1.41×10^{-7} to $8.87\times10^{-7}\,cm^2\,s^{-1}$. The determined $D_{||}$ and $D_\perp$ values at 60 °C are 5.48×10^{-7} and $1.41\times10^{-7}\,cm^2\,s^{-1}$, respectively, and those at 80 °C are 1.11×10^{-6} and $8.87\times10^{-7}\,cm^2\,s^{-1}$, respectively. It is found that the diffusion of POLG in the thermotropic liquid crystalline state is anisotropic. The diffusion of the polypeptide along the long α-helical chain axis at 60 °C is much faster, by roughly four times, than that perpendicular to the long α-helical chain axis. At 80 °C, their diffusion coefficients are close to each other. As reported previously, the determined $D_{||}$ and $D_\perp$ values of *n*-alkane, *n*-$C_{24}H_{50}$, in the rotator phase like the liquid crystalline state, which takes all-*trans* zigzag conformation, are 1.64×10^{-6} and $2.70\times10^{-6}\,cm^2\,s^{-1}$, respectively.[61] The diffusion of the *n*-alkane in the rotator phase along the long chain axis is much slower by roughly two times than that perpendicular to the long chain axis. This is opposite to the results obtained for

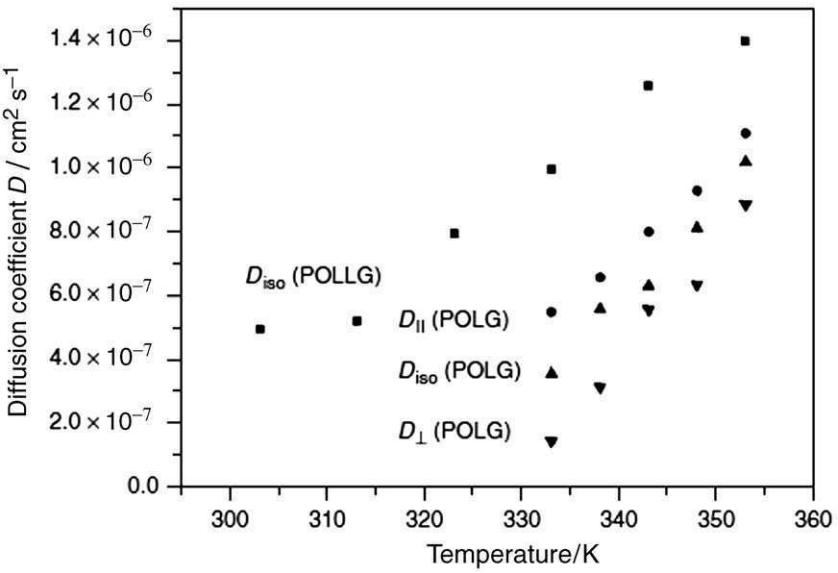

Fig. 31. Temperature dependence of self-diffusion coefficients (D) of POLLG and POLG in the thermotropic liquid crystal state. (●), D_{iso} for POLLG; (▲), $D_{||}$ for POLG; (▼), $D_{||}$ for POLG; and (■), D_{iso} ($= D_{||} + 2D_{||}$) for POLG.

POLG. From the number of amino acid residues of POLG (ca. 780) considered here, the α-helical chain length is roughly estimated to be ca. 1,170 Å by using the pitch of an α-helix chain per one amino acid residue to be 1.5 Å. On the other hand, the chain length of *n*-$C_{24}H_{50}$ with the all-*trans* zigzag conformation is roughly estimated to be ca. 18 Å. From these simple estimations, it is seen that the corresponding rod-like POLG is much longer than *n*-$C_{24}H_{50}$. Therefore, such a situation leads to the experimental finding that the diffusion of the POLG along the long α-helical chain axis is much faster than that perpendicular to the long α-helical chain axis.

As for POLLG, only the isotropic diffusion coefficients were determined at an interval of 10 °C in the temperature range from 30 to 80 °C and are listed in Table 6. The diffusion coefficients of POLLG in the liquid crystalline state are plotted against temperature as shown in Fig. 35. It is shown that with an increase in temperature from 30 to 80 °C, the D value increases gradually from 4.9×10^{-7} to $1.4 \times 10^{-6}\,cm^2\,s^{-1}$. Let us compare these D_{iso} values with those of POLG calculated from the determined $D_{||}$ and $D_{\perp}$ values as shown in Table 6. As the temperature is increased from 60 to 80 °C, the D_{iso} values of POLG increase gradually from 3.53×10^{-7} to $1.02 \times 10^{-6}\,cm^2\,s^{-1}$ and those of POLLG increase from 9.9×10^{-7} to $1.40 \times 10^{-6}\,cm^2\,s^{-1}$. At 60 °C, POLLG in the thermotropic liquid crystalline state diffuses faster by ca. 2.8 times than POLG irrespective of the same α-helical chain length and at 80 °C they are close to each other. At 60 °C such a large difference in D_{iso} between POLG and POLLG may come from a large difference in

their side-chain conformation and molecular motion (as will be seen from the T_2 experiments below). The melting temperature of the side chain crystallites in POLG is ca. 60 °C and that of POLLG is below −40 °C as shown by DSC measurements.[112,117] This means that at 60 °C the side chains of POLLG are undergoing much faster *trans–gauche* exchange around the C–C bond compared with those of POLG, and then the expansion of the side chains from the main chain in the former is much smaller than that of the latter. At higher temperature (80 °C) their mobility is close to each other. Such a situation leads to the difference in the D_{iso} values between POLG and POLLG.

In order to understand the diffusion process of polypeptides in the thermotropic liquid crystalline state, the activation energy E for the diffusion process can be determined by using the following equation:

$$D = (a_0^2/\tau_0)\exp(-E/kT) \tag{10}$$

where a_0 is the interval of the diffusant, τ_0 the time of diffusing, k the Boltzmann constant and E the activation energy for the diffusion process. The activation energy E can be obtained from plots of $\ln D$ against $1/T$ within the temperature range from 60 to 80 °C as shown in Fig. 32. As for POLG, the determined E values are 8.0, 18.5 and 11.9 kcal mol^{-1} for $D_{||}$, $D_{\perp}$ and D_{iso}, respectively. The determined activation energy for D_{iso} of POLLG is 4.9 kcal mol^{-1}. From these experimental results, it can be said that the activation energy for the diffusion process

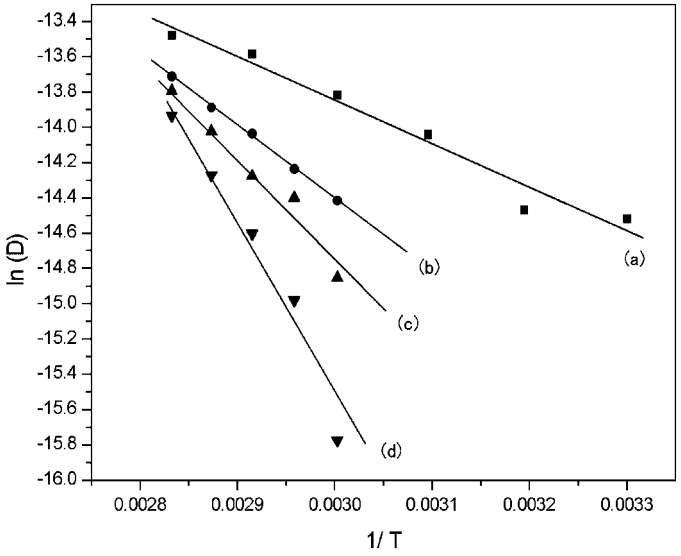

Fig. 32. The Arrhenius plots of $\ln D$ against 1/T for the diffusion ($D_{||}$) of POLLG (a) and POLG (b) chains in the direction parallel to the magnetic field, the isotropic diffusion ($D_{iso} = (D_{||} + 2D_{\perp})/3$) of POLG (c) chains, and the diffusion ($D_{||}$) (d) of POLG chains in the direction parallel to the magnetic field within the temperature range from 30 to 80 °C.

for POLLG in the thermotropic liquid crystalline state is much lower than that of POLG. In the case of POLG, the activation energy for diffusion along the α-helical chain axis is much lower than that in the direction perpendicular to the α-helical chain axis.

3.1.2. *Diffusion of rod-like polypeptides with different main-chain lengths in the thermotropic liquid crystalline state as studied by field-gradient ^1H NMR method*

The diffusion process of the highly oriented poly(γ-*n*-dodecyl L-glutamate) (PDLG) in the thermotropic liquid crystalline state has been studied as a function of the main-chain length by measuring the isotropic and anisotropic diffusion coefficients of the polypeptides as a function of temperature within the temperature range from 50 to 80 °C by means of the PFGSE ^{1}H NMR method. This has clarified how the diffusion is affected by changes of the main-chain length.[59] The diffusion behavior in the thermotropic liquid crystalline state is analyzed by the translational diffusion equation on the basis of the Kirkwood theory[118] of the diffusion process for rod-like polymers derived by Doi and Edwards.[119]

A series of PDLGs synthesized by ester-exchange reactions between PBLG (average molecular weight: $M_w = 7{,}000$, 30,000 and 130,000) and *n*-dodecyl alcohol are used. The highly oriented PDLG films are prepared by casting the solutions in 1,2-dichloroethane at room temperature after being placed in an NMR magnetic field of 11 T for 60 h. The orientation of the polypeptide chains in the film was confirmed by cross-polarized microscopy. The order parameter S of the obtained film is about 0.87 as determined by the ^{13}C chemical shift value of the amide carbonyl carbon at room temperature.

The self-diffusion coefficient measurements of poly(γ-*n*-alkyl L-glutamates) over the temperature range from 50 to 80 °C were carried out by means of a 270.1 MHz NMR spectrometer operating for ^{1}H with a home-made pulse gradient generator using a standard PFGSE pulse sequence ($\pi/2$ pulse-τ – π pulse), which is the Hahn echo sequence. Two field-gradient pulses are added between the $\pi/2$ and π pulses (with a maximum field strength of about 20 T m^{-1} (2,000 G cm^{-1})) to suppress the eddy currents induced. In this experiment, a field-gradient strength of about 13.1 T m^{-1} (1,310 G cm^{-1}) was used. The $D_{||}$ and $D_{\perp}$ values were determined by rotation of the oriented polypeptide sample in an NMR probe which leads to a change of the direction of the field gradient.

Analysis of diffusional behavior of rod-like polypeptides. The main chain of poly (γ-glutamate) considered in this work takes the α-helical form like a long rod. At temperatures above the melting point of the side-chain crystallites the side chains take the liquid-like phase such as liquid *n*-alkane and are working as a solvent for the main chain. The diffusion process of the polypeptide is assumed to follow the Kirkwood theory for the diffusion process of rod-like polymers.

The derivation to obtain the translational diffusion coefficient of rod-like polymers are derived by Doi and Edwards[119] on the basis of Kirkwood theory.[118] The

isotropic diffusion coefficient D_{iso} of a rod-like polymer chain given followed by the following equation:

$$D_{iso} = (D_{\parallel} + 2D_{\perp})/3 = [\ln(L/b)/L]kT/3\pi\eta_s \quad (11)$$

in which

$$D_{\parallel} = [\ln(L/b)/L]kT/2\pi\eta_s \quad (12)$$

$$D_{\perp} = [\ln(L/b)/L]kT/4\pi\eta_s \quad (13)$$

where $D_{||}$ and $D_{\perp}$ are the diffusion coefficients parallel to and perpendicular to the rod-like polymer chain axis, respectively, L the rod-like polymer length, b the diameter of the rod-like polymer, η_s the viscosity of the solvent corresponding to long *n*-alkyl side chains in the thermotropic liquid crystalline state, k the Boltzmann constant and T is the absolute temperature.

By using the standard bond lengths and bond angles determined by X-ray diffraction we can straightforwardly estimate the rod-like main-chain length and the diameter of the α-helical polypeptides. Then, the main-chain lengths of α-helical poly(γ-*n*-alkyl L-glutamate)s with average molecular weights of 7,000, 30,000 and 130,000 can be estimate to be L = ca. 30, 200 and 890 Å, respectively, and the diameter of the α-helical main chain including the ester group of the side chain to be ca. 10 Å. The diffusion process of these rod-like polypeptides is expected to follow Eq. (11). This equation shows that the plots of D_{iso} against $\ln(L/b)/L$ become a straight line.

In this polypeptide system, by melting of long *n*-alkyl side chain crystallites, the side chains play the role of solvent in the liquid crystal system. Therefore, we may take into account the case that the viscosities η_s' and η_s'' of the solvent in parallel to and perpendicular to the rod-like polymer chain axis, respectively, may be, in principle, different. In this case, η_s in Eqs. (12) and (13) must be replaced by η_s' and η_s'', respectively. Then, η_s in Eq. (11) must be replaced by $(\eta_s' + \eta_s'')/2\eta_s' + \eta_s''$. When η_s' and η_s'' are equal to each other, $D_{||}/D_{\perp}$ becomes 2. When η_s' and η_s'' are different, $D_{||}/D_{\perp}$ becomes $2\eta_s'/\eta_s''$. As predicted from this polypeptide system, we have $\eta_s' \geq \eta_s''$. Thus, we may expect $D_{||}/D_{\perp} < 2$. Such a situation may be associated with the degree of the orientation of the polypeptide liquid crystal system.

Fundamental theories of diffusion for low molecular weight liquid crystals in the nematic phase have been studied by Franklin[120–122] based on the Oseen–Kirkwood hydrodynamic theory for isotropic liquids. Further theories of diffusion for low molecular weight liquid crystals have been developed. These theories explain partially the experimental data on $D_{||}$ and $D_{\perp}$. Chu and Moroi,[123] and Leadbetter *et al.*[124] have obtained the anisotropy ratio of the diffusion coefficients, $D_{||}/D_{\perp}$, for low-molecular weight liquid crystals which is expressed by $[2\gamma(1-S)+2S+1]/[\gamma(S+2)+1-S]$, where $\gamma = \pi d/4l$ in which l is the length and d the diameter of the rod-like molecules. This equation shows that if S becomes less than 1, $D_{||}/D_{\perp}$ is reduced.

Diffusional behavior of PDLGs with different main-chain lengths. Spin-echo ^{1}H NMR spectra are reported of unoriented PDLG films with molecular weights of 7,000, 30,000 and 130,000 in the thermotropic liquid crystalline state over the temperature range from 50 to 80 °C as a function of field-gradient pulse length (δ) by using PFGSE ^{1}H NMR.[59] In the spin-echo ^{1}H NMR spectra of PDLG with low-molecular weight ($M_w = 130{,}000$) as shown in Fig. 33 an asymmetric sharp signal with a shoulder peak appears at about 1 ppm. The intense peak and the shoulder peak at about 0.9 ppm on the right can be straightforwardly assigned to the inside methylene protons and the methyl protons, respectively, in the side chains. The other minor signals at about 2 ppm may be assigned to the remaining methylene protons in the side chains. The peaks from the main-chain protons such as the α-CH and amide protons do not appear due to broadening because of the extremely slow molecular motion on the ^{1}H NMR timescale within the measurement temperature range. However, in the spectra of the polypeptides with higher molecular weight only a single intense peak appears at about 1 ppm within the measurement temperature range.

As seen from Fig. 33, the intensities of the peaks are reduced with an increase in field-gradient pulse duration (δ). This is due to the translational diffusion of the polypeptide chain within the observation time, which is the time interval between two gradient pulses. This shows that the rod-like polypeptides are diffusing in the

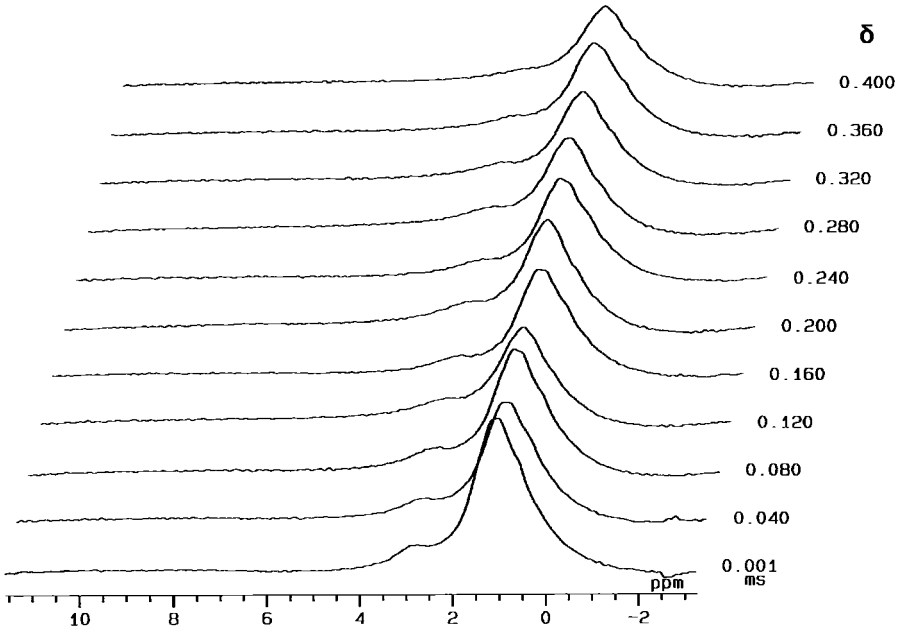

Fig. 33. Typical spin-echo ^{1}H NMR spectra of PDLG with molecular weight of 130,000 in the thermotropic liquid crystalline state at 80 °C as a function of the field-gradient pulse length δ by using PFGSE ^{1}H NMR.

Table 7. Determined diffusion coefficients D of PDLG at the range of temperature from 50 to 80°C by PFGSE ^{1}H NMR method

M_w	$D/10^{-7}$ cm^2 s^{-1}	Temperature (°C)						
		50	55	60	65	70	75	80
7,000	$D_{\|\|}$	17.6	18.3	19.1	19.7	20.4	21.2	21.8
	D_{iso}	16.7	17.3	18.1	18.9	19.9	20.6	21.3
	$D_{\perp}$	15.7	16.2	17.2	18.1	19.1	19.8	20.6
	$D_{\|\|}/D_{\perp}$	1.12	1.13	1.11	1.09	1.07	1.07	1.06
30,000	$D_{\|\|}$	10.4	11.1	11.9	12.8	13.6	14.3	15.4
	D_{iso}	9.21	9.96	10.7	11.7	12.6	13.5	14.5
	$D_{\perp}$	7.94	8.72	9.51	10.5	11.6	12.6	13.6
	$D_{\|\|}/D_{\perp}$	1.31	1.27	1.25	1.22	1.17	1.13	1.13
130,000	$D_{\|\|}$	6.33	7.33	8.44	9.31	10.6	11.4	12.1
	D_{iso}	5.67	6.44	7.56	8.43	9.63	10.6	11.2
	$D_{\perp}$	4.77	5.65	6.78	7.62	8.67	9.73	10.8
	$D_{\|\|}/D_{\perp}$	1.33	1.30	1.24	1.22	1.22	1.17	1.12

thermotropic liquid crystalline state. These results are the same as the experimental results on the diffusional behavior of POLG in the thermotropic liquid crystalline state. By using these decay signals, the diffusional coefficient D of PDLG can be determined from the slope of the plot of $\ln[A(\delta)]/A(0)]$ against $\gamma^2G^2\delta^2(\Delta-\delta/3)$ as listed in Table 7. As seen from this table, the diffusion coefficients of PDLG decrease with an increase in the main-chain length. This shows that the diffusion coefficient of the longer rod-like polypeptides becomes much smaller. Such a diffusional behavior can be analyzed by using the translational diffusion equation of rod-like polymers derived by Doi and Edwards[119] on the basis of the Kirkwood theory.[118]

The main-chain length dependence of the diffusion coefficients of the rod-like polypeptide chain in the thermotropic liquid crystalline state is expected to follow Eq. (11). This shows that the plots of D_{iso} against $\ln(L/b)/L$ become a straight line at any given temperature. Here, it is assumed that the viscosity of the solvent corresponding to long *n*-dodecyl side chains is independent of the main-chain length. The chains are undergoing rapid exchange between the *trans* and *gauche* conformations like in liquid *n*-alkanes. In Fig. 34, the plots of the isotropic diffusion coefficients of PDLG in the thermotropic liquid crystalline state against $\ln(L/b)/L$ are shown at various temperatures. Therefore, it can be said that the isotropic diffusion of rod-like PDLG chains follows approximately the translational diffusion equation of rod-like polymers derived by Doi and Edwards[119] on the basis of the Kirkwood theory.[118] Further, it seen from Fig. 34 that the slope of the plots of D_{iso} against $\ln(L/b)/L$ increase with an increase in temperature. This agrees with the theoretical prediction as seen from Eq. (11) because the slope is a function of temperature.

We are concerned with the anisotropic diffusion of PDLG in the thermotropic liquid crystalline state.[59] The diffusion coefficients of the highly oriented polypeptide

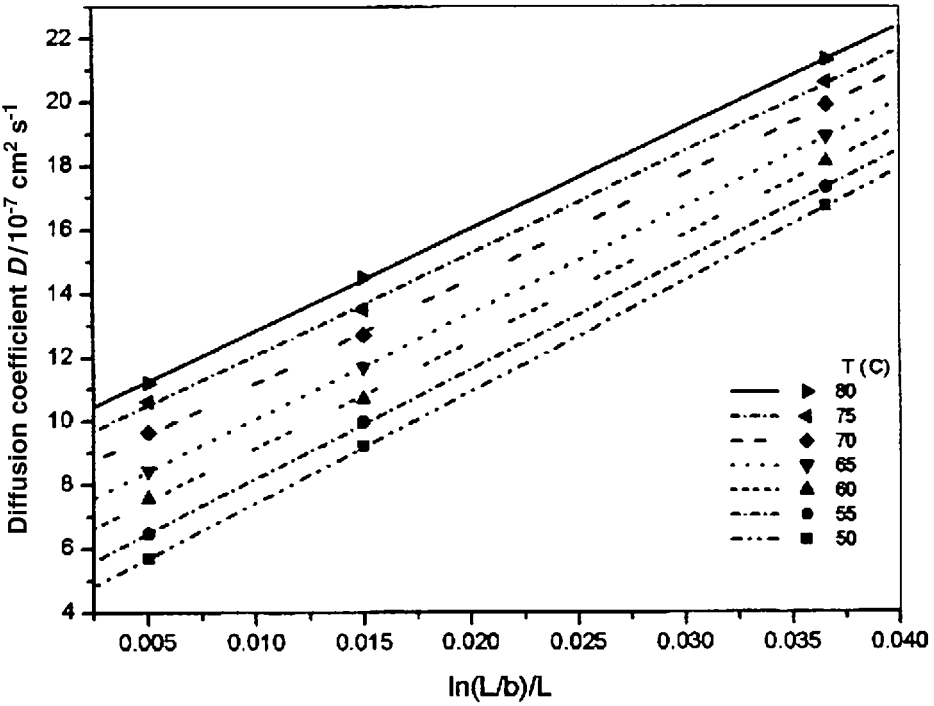

Fig. 34. The plots of the isotropic diffusion coefficients of PDLG in the thermotropic liquid crystalline state against $\ln(L/b)/L$ are shown at various temperatures.

films for directions parallel and perpendicular to the α-helical main chain are determined. In Table 7, the diffusion coefficients, $D_{||}$ and $D_{\perp}$, of the polypeptides with different main-chain lengths and the ratio of $D_{||}$ to $D_{\perp}$ are listed. It is seen that the $D_{||}$ value is larger than the $D_{\perp}$ value. The values decrease with an increase in temperature. These data agree with the previous results for POLG in the thermotropic liquid crystalline state. Further, as seen from Fig. 35, it can be said that these experimental results can be qualitatively explained by the Kirkwood theory. As above-mentioned, when η'_s and η''_s are equal to each other, $D_{||}/D_{\perp}$ becomes 2, when η'_s and η''_s are different, $D_{||}/D_{\perp}$ becomes $2\eta'_s/\eta''_s$, and as predicted from this polypeptide system, we have $\eta'_s \geq \eta''_s$ and, thus, we may expect $D_{||}/D_{\perp} < 2$. As seen from Table 7, at 50 °C the ratio of $D_{||}$ to $D_{\perp}$ is 1.33 and at 80 °C it is 1.12. This means that $\eta'_s \geq \eta''_s$. These values are close to those for low-molecular weight liquid crystals[125] such as *p*-azoxyanisole (PAA) and *p*-methoxybenzylidene-*p'*-*n*-butylaniline (DMBBA) which are 1.33 and 1.44, respectively.

In order to understand the diffusion process from the concept of the activation energy E for the diffusion of PDLG in the thermotropic liquid crystalline state, Eq. (10) was used.

The activation energy E can be obtained from the plots of $\ln D$ against $1/T$ as listed in Table 8. From this table, the E values for the diffusion coefficients D_{iso},

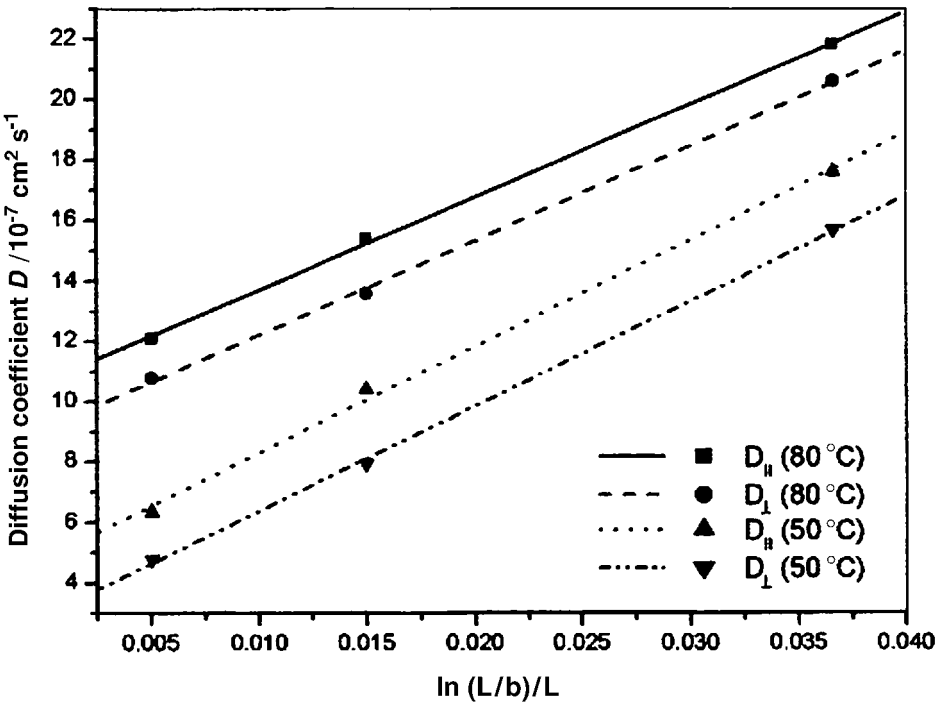

Fig. 35. The plots of the diffusion coefficients $D_{||}$ and $D_{\perp}$ of PDLG in the thermotropic liquid crystalline state against $\ln(L/b)/L$ are shown at various temperatures.

Table 8. Determined activation energy E of PDLG at the range of temperature from 50 to 80 °C by ^{1}H PFGSE NMR method

M_w	Temperature range (°C)	Activation energy E/kcal mol^{-1}		
		$E_{||}$	E_{iso}	$E_{\perp}$
7,000	50–80	1.62	1.90	2.14
30,000	50–80	2.94	3.47	4.13
130,000	50–80	4.97	5.28	6.14

$D_{||}$ and $D_{\perp}$ increase with an increase in the main-chain length. The E values for the diffusion coefficient $D_{||}$ is larger than that for the $D_{\perp}$. This agrees with the case of POLG in the thermotropic liquid crystalline state.

3.2. Diffusion of POLG/$CDCl_3$ in the lyotropic liquid crystalline phase

It is well known that poly(glutamate) systems such as PBLG, poly(γ-*n*-alkyl L-glutamate), etc. in solvents form the isotropic, biphasic and liquid crystalline

phases depending on the polypeptide concentration.[99–104] However, in these phases the diffusional behavior of the polypeptides is not clarified. In this section, the diffusional behavior of α-helical POLG and chloroform as solvent are studied in the isotropic, biphasic and liquid crystalline phases, by PFGSE ^{1}H NMR.

A POLG solution is prepared by placing POLG and deuterated chloroform ($CDCl_3$) in an NMR tube with a diameter of 5 mm the NMR tube is sealed off and kept at 50 °C. Protonated chloroform ($CHCl_3$) is used for the diffusion coefficient measurement of chloroform in the POLG solution. The POLG concentrations employed in this work are 5, 10, 15, 17.5 and 20 wt/wt%. The 5 and 10 wt/wt% POLG solutions are in the isotropic phase, 15 and 17.5 wt/wt% POLG solutions are in the biphasic phase and 20 wt/wt% POLG solution is in the cholesteric liquid crystalline phase as seen from the phase diagram.[126] When the 20 wt/wt% POLG solution is placed in a 13.5 T NMR magnet for 80 h, it forms a highly oriented nematic liquid crystalline phase. The degree of order parameter is 0.86 as determined by static ^{13}C NMR.[35]

As the probe molecules in the biphasic phase have two-diffusion components on the measurement timescale, the total echo attenuation is given by a superposition of contributions from the individual components as expressed by Eq. (2). The fraction for the fast and slow diffusion components can be determined from the intercept of the least-squares fitted straight line.

^{1}H NMR imaging measurements of the diffusion coefficient of chloroform as solvent in the POLG/$CHCl_3$ liquid crystalline solution are carried out at 300.13 MHz with a diffusion imaging system with a field gradient of 100 G cm^{-1} at 30 °C. The diffusion imaging pulse sequence is based on the spin-echo sequence including field-gradient pulses.[4] The slice selection is achieved with the field gradient in the z or x direction. In an NMR magnet, POLG chains in the liquid crystalline solution are oriented in the magnetic field direction that is the z direction. Thus, by the slice selection in the z direction, the parallel diffusion coefficient of $CHCl_3$ ($D_{||}$) in the direction parallel to the α-helical POLG chain axis in POLG lyotropic liquid crystalline solution is determined and the perpendicular diffusion coefficient ($D_{\perp}$) by the slice selection in the x direction perpendicular to the α-helical POLG chain axis is determined. The values of Δ and δ are 10 and 0.001–0.1 ms, respectively.

3.2.1. *Diffusional behavior of POLG in the isotropic, biphasic and liquid crystalline phases*

Fig. 36 shows typical PFGSE ^{1}H NMR spectra of the POLG solutions in the isotropic, biphasic and liquid crystalline phases at various POLG concentrations at 30 °C as a function of the field-gradient pulse length (δ).[60] In the PFGSE ^{1}H NMR spectra of 5 wt/wt% POLG solution in the isotropic phase, as shown in Fig. 39(a), an asymmetric sharp signal and a shoulder appear at about 1.4 and 1 ppm, respectively. The intense peak and the shoulder can be straightforwardly assigned to the internal methylene protons and the terminal methyl protons in the side chains, respectively. The peaks for the main-chain protons such as the α-CH and amide

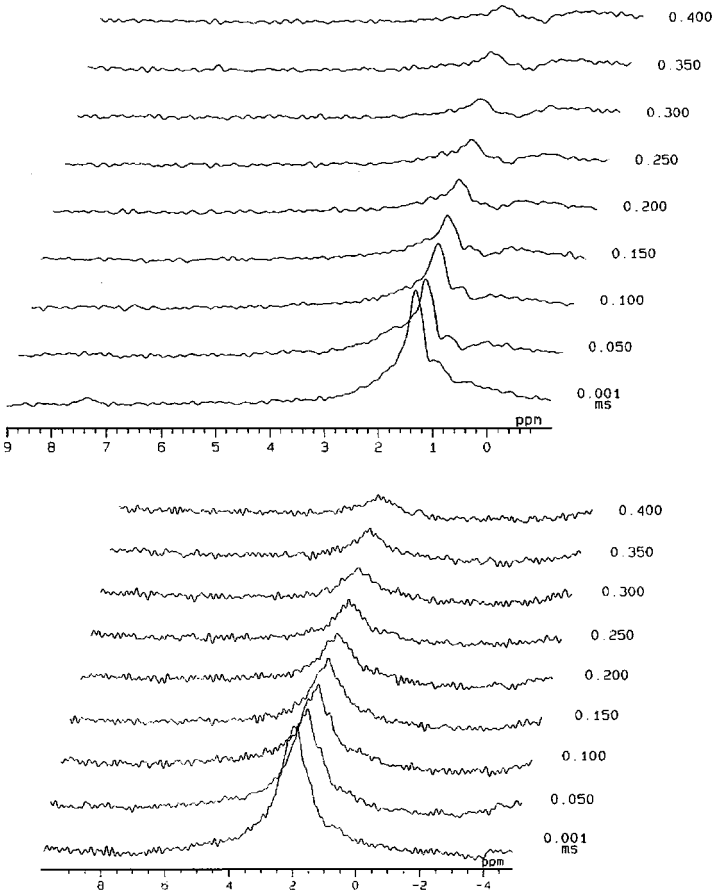

Fig. 36. Typical PFGSE ^{1}H NMR spectra of POLG in 5 (a) and 20 (b) wt/wt% POLG/deuterated chloroform solutions as a function of field-gradient pulse length δ at 30 °C.

protons do not appear due to line-broadening because of the slow molecular motion in the ^{1}H NMR timescale within the measurement temperature. Fig. 36(b) shows typical PFGSE ^{1}H spectra for the 20 wt/wt% POLG solution in the liquid crystalline phase at 30 °C. It is noted that the signal becomes much broader as compared with that in the isotropic phase. The signal intensity for the former is more slowly reduced, with an increase in field-gradient pulse duration (δ), as compared with the latter as shown in Fig. 36(a). This is due to a large reduction of the diffusion rate in the liquid crystalline phase.

By using these decay signals, the diffusion coefficient of POLG in solution can be determined from the slope of the plots of $\ln[A(\delta)/A(0)]$ against $\gamma^2G^2\delta^2(\Delta-\delta/3)$ as shown in Table 1. As shown in Fig. 37(a) and (b), the plots of $\ln[A(\delta)/A(0)]$ for 5 and 10 wt/wt% POLG solutions against $\gamma^2G^2\delta^2(\Delta-\delta/3)$ are a straight line.

This shows that the diffusion of POLG becomes a single diffusion component. The diffusion coefficients D for α-helical POLG in 5 and 10 wt/wt% POLG solutions that are in the isotropic phase are obtained as shown in this table.

In 15 and 17.5 wt/wt% POLG solutions, which are in the biphasic phase, the plots of $\ln[A(\delta)/A(0)]$ against $\gamma^2G^2\delta^2(\Delta-\delta/3)$ consist of two straight lines with different slopes as shown in Fig. 37(c) and (d). This shows that there are two kinds of diffusion components such as a slow and a fast diffusion component. The diffusion coefficients for the slow and fast diffusion components are determined from the slopes as shown in Table 9. The fast and the slow diffusion components in the biphasic phase correspond to the isotropic region and the liquid crystalline region, respectively. The D value for the fast diffusion component is very close to the D values for the 5 and 10 wt/wt% POLG solutions in the isotropic phase as shown in Table 9. The diffusion coefficient of the slow diffusion component is very close to that for the 20 wt/wt% POLG solution in the liquid crystalline phase. These results mean that the diffusion processes for the isotropic region and the liquid crystalline region in the biphasic phase are very similar to those in the isotropic phase and in the liquid crystalline phase, respectively. The fractions of the two kinds of diffusion components can be determined by analyzing the plots of $\ln[A(\delta)/A(0)]$ against $\gamma^2G^2\delta^2(\Delta-\delta/3)$ which give two straight lines as shown in Fig. 37(c) and (d). As for the 15 wt/wt% POLG solution, the fractions of the diffusion components for the isotropic and liquid crystalline regions in the biphasic phase are determined to be 62 and 38%, respectively, and as for the 17.5 wt/wt% POLG solution they are 31 and 69%, respectively. The fraction of the fast diffusion component corresponding to the isotropic region is largely decreased in spite of a small concentration increase in going from 15 wt/wt% POLG concentration to 17.5 wt/wt% POLG concentration. Fig. 37(a), (b) and (e) shows the first data point to be somewhat higher than the straight line indicates. It is thought that it does not come from a faster-moving species. It may be an artifact.

In 20 wt/wt% POLG solution which is in the liquid crystalline phase, as shown in Fig. 37(e), the plots of $\ln[A(\delta)/A(0)]$ for α-helical POLG against $\gamma^2G^2\delta^2(\Delta-\delta/3)$ give a straight line. This shows that the diffusion of POLG has a single diffusion component. The diffusion coefficient for α-helical POLG in 20 wt/wt% POLG solution is obtained and found to be very close to that for the liquid crystalline region in the biphasic phase. The determined D value is listed in Table 9. For example, the diffusion coefficient as determined from Fig. 37(a) is $2.76 \times 10^{-6}\,\mathrm{cm^2\,s^{-1}}$. This diffusion for a polypeptide chain of length 200 Å is very fast. Probably such a fast diffusion comes from the fluidity of the liquid crystal.

In Fig. 38 the determined D values are plotted against the POLG concentration in order to understand the diffusional behavior of α-helical POLG in the isotropic, biphasic and liquid crystalline phases. From this figure, it is seen that the diffusion coefficient of the α-helical POLG chain in the isotropic and biphasic phases decreases with an increase in the POLG concentration and transitionally decreases in going from the isotropic region to the liquid crystalline region. The diffusion coefficient of the α-helical POLG chain in the liquid crystalline region slightly decreases with an increase in the POLG concentration.

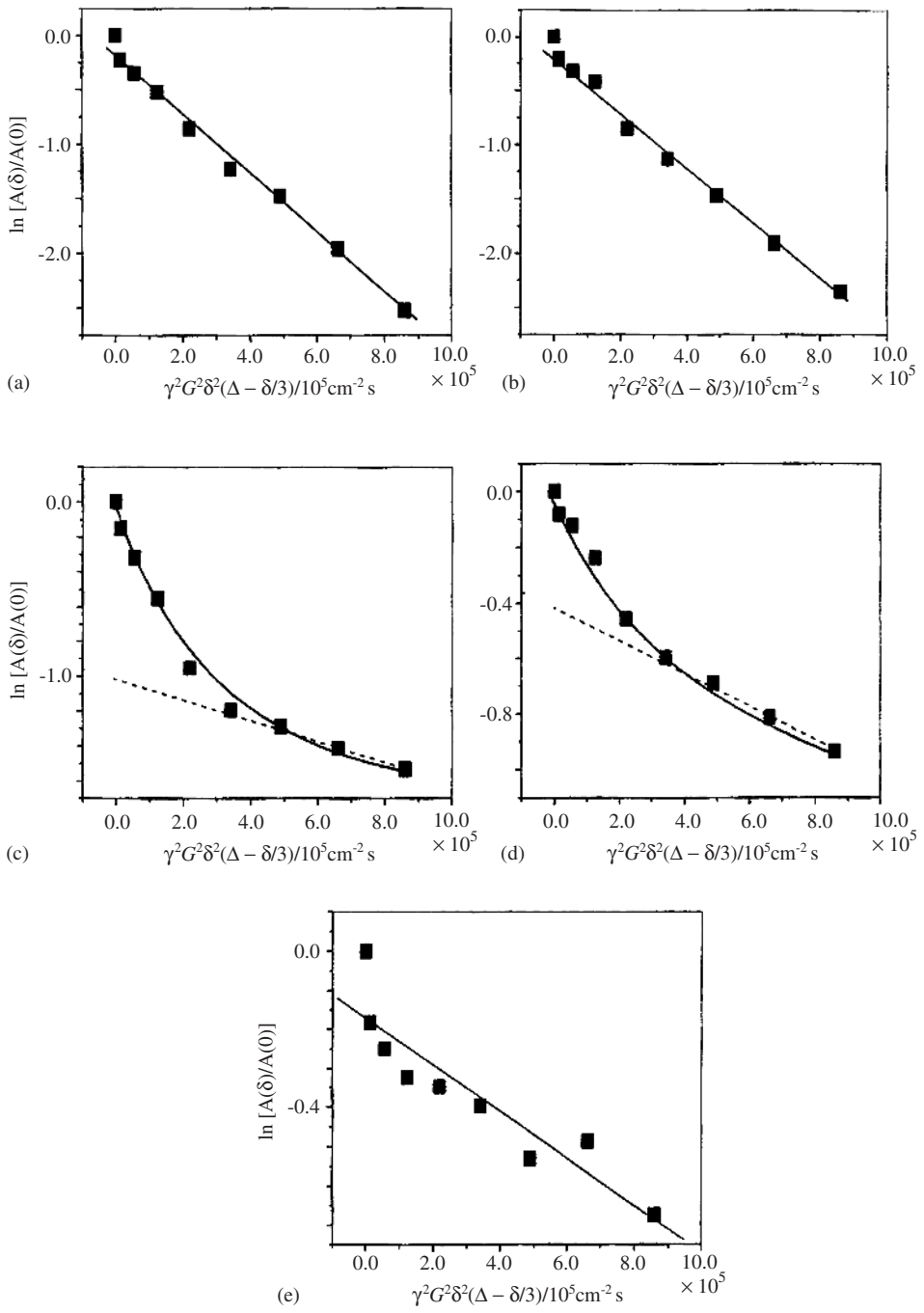

Fig. 37. The plots of $\ln[A(\delta)/A(0)]$ against $\gamma^2G^2\delta^2(\Delta-\delta/3)$ for determining the diffusion coefficients D of POLG in 5 (a), 10 (b), 15 (c), 17.5 (d) and 20 (e) wt/wt% POLG/deuterated chloroform solutions at 30 °C.

Table 9. Determined diffusion coefficients D of POLG in POLG/deuterated chloroform solutions at various POLG concentrations

State	Diffusion coefficient D ($cm^2 s^{-1}$)				
	POLG concentration (wt/wt%)				
	5	10	15	17.5	20
Liquid crystalline region	–	–	6.83	6.34	5.94
Isotropic region	27.6	26.3	23.7	21.5	–

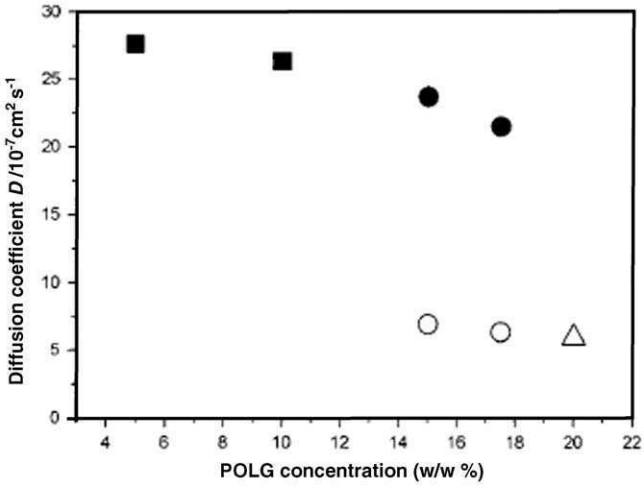

Fig. 38. The plots of diffusion coefficients D of POLG in POLG/deuterated chloroform solutions against the POLG concentration at 30 °C. (■), 5 and 10 wt/wt% POLG concentration (the isotropic phase), (●), 15 and 17.5 wt/wt% POLG concentration (isotropic region in the biphasic phase), (○), 15 and 17.5 wt/wt% POLG concentration (liquid crystalline region in the biphasic phase and (△), 20 wt/wt% POLG concentration (the liquid crystalline phase).

As described above, POLG and POLLG (poly(γ-oleyl L-glutamate)) with the same α-helical chain length as the POLG sample used in this work forms a thermotropic liquid crystalline phase above 60 °C and above 30 °C, respectively. The D_{iso} values for POLG at 60 °C and that for POLLG in the thermotropic liquid crystalline phase at 30 °C are determined to be 3.53×10^{-7} and $4.94 \times 10^{-7}\,cm^2\,s^{-1}$, respectively. The D_{iso} for POLG in the liquid crystalline phase at 30 °C is much larger than these D_{iso} values for POLG at 60 °C and for POLLG at 30 °C. This may be explained by Doi and Edwards theory[119] on the basis of the Kirkwood theory[118] as shown below.

The isotropic diffusion coefficient D_{iso} of a rod-like polymer chain is given by $D_{iso} = [\ln(L/b)/L]kT/3\pi\eta_s$ in which L is the rod-like polymer length, b the diameter of the rod-like polymer, η_s the viscosity of the solvent corresponding to long *n*-alkyl side chains in the thermotropic liquid crystalline state, k the Boltzmann constant and T is the absolute temperature. By using the standard bond lengths and bond angles determined by X-ray diffraction we can straightforwardly estimate the rod-like main-chain length and the diameter of the α-helical polypeptides. The main-chain lengths of a α-helical polypeptide with an average molecular weight of 30,000 can be estimate to be L = ca. 200 Å, and the diameter of the α-helical main chain including the ester group of side chain is b = ca. 10 Å. The diffusion process of these rod-like polypeptides is expected to follow $D_{iso} = [\ln(L/b)/L]kT/3\pi\eta_s$. This equation shows that the plots of D_{iso} against $\ln(L/b)/L$ give a straight line.

In the thermotropic liquid crystalline state, formed by the melting of long *n*-alkyl side chain crystallites, the side chains play a role as solvent in the liquid crystal system. It is suggested that difference in $D_{iso} = [\ln(L/b)/L]kT/3\pi\eta_s$ between the thermotropic liquid crystalline phase and the lyotropic liquid crystalline phase is only η_s. It is apparent that η_s for the lyotropic liquid crystalline phase is much smaller than that for the thermotropic liquid crystalline phase at 30 °C. The difference in η_s may lead to the experimental fact that the D_{iso} for POLG in the lyotropic liquid crystalline phase is much larger than the D_{iso} values for POLG and for POLLG in the thermotropic liquid crystalline phase.

3.2.2. *Diffusional behavior of chloroform solvent in highly oriented POLG liquid crystalline solution*

In order to clarify the anisotropic diffusional behavior of $CHCl_3$ as solvent in the lyotropic liquid crystalline system, a polypeptide nematic liquid crystalline solution is prepared with the α-helical POLG chain highly oriented in an NMR magnet.[60] Thus, the diffusion coefficient of the $CHCl_3$ solvent in the directions parallel ($D_{||}$) and perpendicular ($D_{\perp}$) to the α-helical POLG chain axis is reliably determined by using ^{1}H NMR imaging with a field-gradient strength of 100 G cm^{-1}. However, this field-gradient strength is not sufficient to determine the anisotropic diffusion coefficient of POLG in the liquid crystalline solution. For this reason, we are concerned with the anisotropic diffusion of the $CHCl_3$ solvent in the liquid crystalline solution. The 3D profiles for the diffusion image in the x and z directions were measured as a function of field-gradient pulse length δ. By using the image profiles, the diffusion coefficients $D_{||}$ and $D_{\perp}$ of the chloroform solvent in the POLG nematic liquid crystal solution were determined from the plots of $\ln[A(\delta)/A(0)]$ against $\gamma^2G^2\delta^2(\Delta-\delta/3)$. Moreover, the diffusion coefficients of chloroform in the neat liquid state and in 20 wt/wt% unoriented POLG/chloroform cholesteric liquid crystalline solution were determined by using the same method. The diffusion coefficient measurement on the cholesteric liquid crystalline solution is carried out immediately after the NMR sample tube is placed in an NMR magnet. At this time, the POLG chain is still unoriented to the magnetic field. The diffusion coefficient of $CHCl_3$ in the neat liquid state, the diffusion coefficient D_{iso} of $CHCl_3$ in the POLG liquid

Table 10. Determined diffusion coefficients D of chloroform in 20 wt/wt% POLG/chloroform solution

Solvent	Neat liquid	Diffusion coefficient D (10^{-5} cm s^{-1})			
		D_{iso}[a]	$D_{\|\|}$	$D_{\perp}$	$(D_{\|\|}+2D_{\perp})/3$[b]
Chloroform	2.55	1.82	1.61	1.18	1.32

[a]The diffusion coefficient measurement on the cholesteric liquid crystalline solution was carried out immediately after the POLG sample tube was placed in an NMR magnet. At that time, the POLG chain is still unoriented to the magnetic field.
[b]Averaged over anisotropic diffusion coefficients of $CHCl_3$ in POLG liquid crystalline phase highly oriented in the magnetic field.

crystalline phase unoriented in the magnetic field and the averaged diffusion coefficient $(D_{||}+2D_{\perp})/3$ of $CHCl_3$ in the POLG liquid crystalline phase highly oriented in the magnetic field as determined from the above experiments are listed in Table 10.

As shown in Table 10,[60] the determined diffusion coefficient of chloroform in the neat liquid is larger than that in the 20 wt/wt% POLG/chloroform cholesteric liquid crystalline solution at 30 °C. This means that the diffusion of chloroform in the liquid crystalline solution is restrained by intermolecular interaction with the POLG chains. After an NMR tube containing a 20 wt/wt% POLG/chloroform cholesteric liquid crystalline solution is placed in a 13.5 T field for 80 h, the POLG chains are highly oriented to the magnetic field, and the solution forms a nematic liquid crystalline solution. The diffusion coefficients $D_{||}$ and $D_{\perp}$ for the chloroform are determined to be 1.61×10^{-5} and 1.18×10^{-5} cm^2 s^{-1}, respectively, as shown in Table 10 and the diffusion rate is ca. 1.4. This shows that the diffusion of chloroform in the direction parallel to the α-helical POLG chain axis is much faster than that perpendicular to the α-helical POLG chain axis. The diffusion process of chloroform in the highly oriented POLG field is anisotropic. This result is very similar to the previous results which show that the diffusion of dioxane solvent and probe *n*-alkanes in highly oriented PBLG gel in the direction parallel to the α-helical PBLG chain axis is much faster than that in the direction perpendicular to the α-helical PBLG chain axis and thus the diffusion process is anisotropic.[108,109] Such behavior appears in the diffusion of solvents in lyotropic low-molecular weight liquid crystal systems.[127–131]

3.3. Diffusion of poly(diethylsiloxane) in the liquid crystalline and isotropic phases

It is well known that poly(diethylsiloxane) (PDES) with a high molecular weight[132,133] (M_w > 30,000) forms a liquid crystalline phase in the vicinity of 30 °C. This is due to a balance of intra- and intermolecular interactions between the main chain and side chains in spite of the absence of typical mesogenic groups. The phase diagram for PDES has been elucidated by DSC.[134] Further, the structure of

the polymer in the solid phase, the liquid crystalline phase and the isotropic phase has been characterized by static solid-state ^{29}Si NMR and ^{29}Si CP/MAS NMR.[135,136] The molecular motion of PDES has been studied by NMR.[137–139] Nevertheless, the diffusional behavior of PDES in the liquid crystalline phase has not been clarified. It can be expected that a PDES chain in the isotropic phase behaves as a random coil because of the flexible main chain and PDES chains in the liquid crystalline phase behave as rigid-rods.

It is difficult to determine the diffusion coefficient of polymers with short ^{1}H T_2 values (<2 ms) in the isotropic phase and the liquid crystalline phase by PFGSE ^{1}H NMR because the echo signal is predominantly decayed due to the short T_2 before decay by diffusion occurs. For this reason, modified pulse field-gradient NMR techniques must be used for polymer systems with short ^{1}H T_2 values. In this section, the diffusion coefficients of PDES obtained by using a PFGSE ^{13}C NMR method with ^{1}H CW decoupling and a PFGSE ^{1}H NMR method are described. Thus the diffusional behavior of PDES with $M_w = 215{,}000$ in the liquid crystalline phase and the isotropic phase are clarified as a function of temperature.

The PFGSE ^{1}H NMR measurements (Fig. 39(a)) and PFGSE ^{13}C NMR measurements under ^{1}H CW decoupling (Fig. 39(b)) are carried out with a NMR spectrometer operating at 75.47 MHz for ^{13}C and 300.11 MHz for ^{1}H, respectively. In the PFGSE ^{13}C NMR measurements under ^{1}H CW decoupling and PFGSE ^{1}H NMR measurements, the echo signal intensity is measured by changing the gradient strength G from 0 to 11.6 T m^{-1}, and the gradient pulse interval Δ is 100 and 500 ms for ^{1}H, and 750 and 1,000 ms for ^{13}C, and the gradient pulse width δ is changed from 0.5 to 8 ms. The recycle delay and the numbers of scans are 5 and 16 s for ^{1}H, and are 20 and 128 s for ^{13}C, respectively. The echo signal decay depends on T_2 and

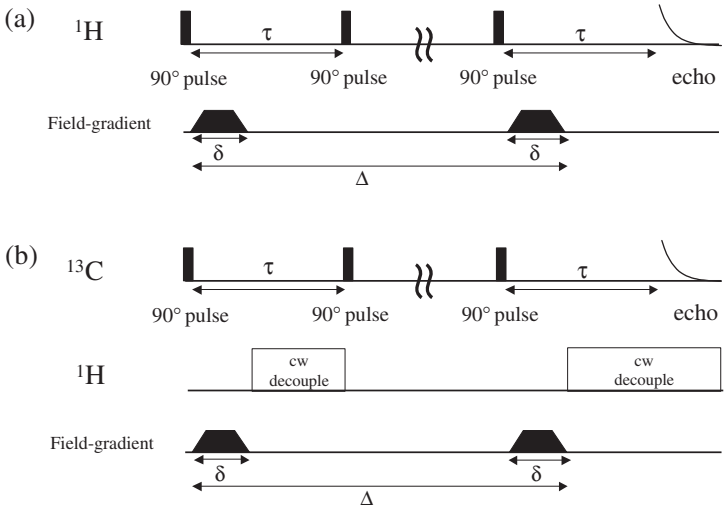

Fig. 39. A diagram of PFGSE ^{1}H NMR pulse sequence (a) and PFGSE ^{13}C NMR pulse sequence with ^{1}H CW decoupling (b).

the diffusion coefficient. The appropriate Δ value must be chosen to determine the diffusion coefficient by considering the T_2 value. For example, if Δ is too long, the echo signal decays by T_2 and disappears within the chosen Δ, if Δ is too short, the echo signal does not decay by diffusion and so it is difficult to determine the diffusion coefficient from such a small decay signal.

In ^{13}C NMR measurements under ^{1}H CW decoupling, the ^{1}H decoupling is made following the application time of the field-gradient pulse. If the CW decoupling is made during the application of the high field-gradient pulse, the ^{1}H decoupling efficiency is apparently reduced by the application of the field-gradient.[140] In PFGSE experiments, as δ or G is employed as a variable parameter to determine the diffusion coefficient, the decoupling efficiency varies with changes of δ and G. Therefore, the echo signal decay induced by the displacement of the probe molecules contains the artifact of the ^{1}H decoupling efficiency induced by changes of δ or G. However, if the ^{1}H decoupling with any specified time duration, instead of steady CW decoupling is used, it provides three significant advantages. The first is that the artifact of the ^{1}H decoupling efficiency induced by changes of δ or G can be neglected, the second is that the decoupling suppresses the spin–spin relaxation caused from strong ^{1}H–^{13}C dipolar interactions and the dipolar dephasing of the coherence is prolonged and the third is that the high field-gradient pulse strength can be applied by changing the diffusion time.

3.3.1. *Static solid-state ^{29}Si NMR and ^{1}H solid echo NMR spectral analyses*

It is known that the transition from the crystalline phase to the biphasic phase consisting of the isotropic region and liquid crystalline region occurs at 17 °C for PDES.[135] The liquid crystalline region in the biphasic phase changes to the isotropic phase over ca. 50 °C. This transition temperature depends on molecular weight.[135] Such behavior can be clarified by using static solid-state ^{29}Si NMR at temperatures from −20 to 50 °C as shown in Fig. 40, where the sample is not rotated in the NMR probe. At −20 °C, the observed static ^{29}Si NMR spectrum in the crystalline phase shows a typical powder pattern and the chemical shift anisotropy is very large.[136] The observed static ^{29}Si NMR spectra at 20, 30 and 40 °C appear as superpositions of an asymmetrical and a sharp powder pattern and a sharp peak which come from the liquid crystalline and isotropic regions in the biphasic phase, respectively.[136] The chemical shift anisotropy of the asymmetrical and sharp powder pattern becomes very small because the two chemical shift components perpendicular to the long axis are averaged out by fast rotation of the PDES chain around the long chain axis. The fractions of the liquid crystalline region at 20, 30 and 40 °C are approximately estimated to be 0.86, 0.83 and 0.55, respectively, by computer fitting. The fraction of the liquid crystalline region in the biphasic phase decreases with an increase in temperature. Then, the signal corresponding to the liquid crystalline region disappears completely at 50 °C. This shows that PDES is in the isotropic phase.

The ^{1}H T_2 values of the liquid crystalline and isotropic regions in the biphasic phase are determined together with their fractions by ^{1}H solid echo (Fig. 44) and

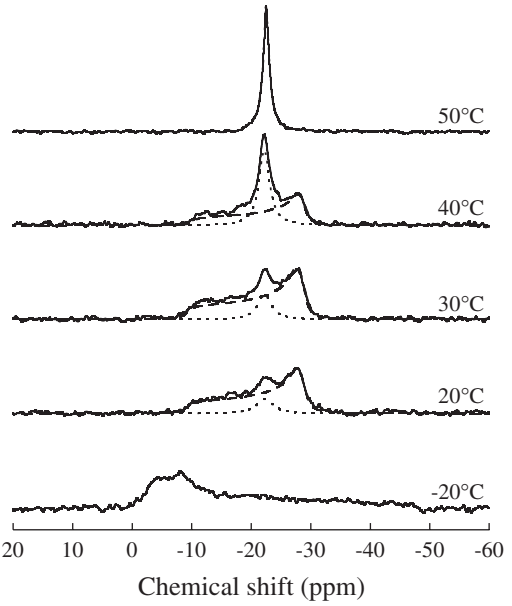

Fig. 40. Observed static solid-state ^{29}Si NMR spectra of PDES at temperatures from −20 to 50 °C by single 90° pulse with high power ^{1}H decoupling. The solid, dashed and dotted lines indicate the observed spectra, the simulated liquid crystalline component and the simulated isotropic component, respectively.

Hahn spin-echo measurements. The ^{1}H free induction decay (FID) measured by the solid echo method shows the presence of the three T_2 components (Fig. 41). The appearance of the three T_2 components can be explained as follows. In this temperature range, PDES is in the biphasic phase consisting of the liquid crystalline and isotropic region as seen from static solid-state ^{29}Si NMR spectra. The fractions of the three components corresponding to the shorter, intermediate and longer ^{1}H T_2 components at 20 °C are 0.50, 0.31 and 0.19, respectively, and those at 30 °C are 0.42, 0.27 and 0.31, respectively. In the liquid crystalline region, the polymer chains strongly interact with each other by forming the ordered structure. It is thought that the ^{1}H T_2 values of the methyl and methylene groups are different from each other due to their different dipolar–dipolar interactions. This may be supported from the experimental finding that the fraction ratio of the first ^{1}H T_2 component to the second ^{1}H T_2 component is nearly 3:2 and this corresponds to the ratio of their proton numbers. The fraction ratio of the third ^{1}H T_2 component to the sum of the first and second ^{1}H T_2 components agrees nearly with that of the liquid crystalline component to the isotropic component as estimated from static solid-state ^{29}Si NMR. Therefore, the three ^{1}H T_2 components can be reasonably explained as mentioned above. The fractions of the liquid crystalline component in the biphasic phase at 20, 30 and 40 °C are estimated to be 0.81, 0.69 and 0.32, respectively. It is shown that the fraction of the liquid crystalline region decreases with an increase in

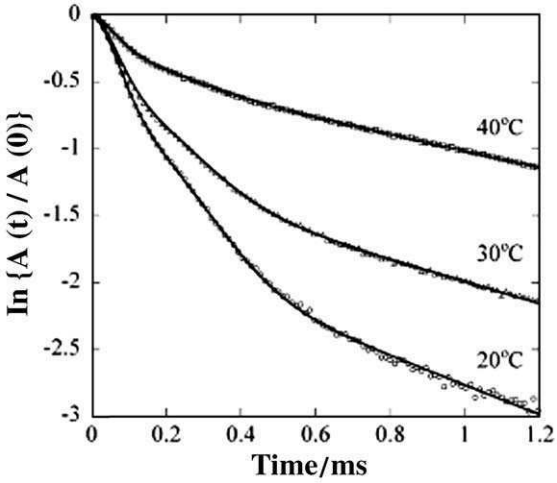

Fig. 41. Temperature dependence of the ^{1}H FID signal of PDES at 20 (○), 30 (Δ) and 40 °C (□) as measured by the solid echo method.

temperature which agrees with the static solid-state ^{29}Si NMR results. In the diffusion experiments, the decay signal of the second ^{1}H T_2 component corresponding to the liquid crystalline region is used. The ^{1}H T_2 values for the liquid crystalline region and the isotropic region are about 0.2 and 7.4 ms, respectively. The ^{1}H T_2 value of PDES in the liquid crystalline region is much shorter than that of the isotropic region. Thus, it is thought that it is very difficult to determine the diffusion coefficient of PDES in the liquid crystalline region by PFGSE ^{1}H NMR because of the extremely short ^{1}H T_2 value. However, it is possible to determine the diffusion coefficient of PDES in the isotropic region by the PFGSE ^{1}H method because it has a sufficiently long ^{1}H T_2.

3.3.2. *Diffusion of PDES in the isotropic phase and in the isotropic region of the biphasic phase*

Fig. 42(a) shows the plots of $\ln[A(G)/A(0)]$ for PDES in the isotropic phase at 50, 60, 70 and 80 °C against $\gamma^2G^2\delta^2(\Delta-\delta/3)$ obtained by changing G from 0 to 11.6 T m^{-1} at $\Delta = 500$ ms, at $\delta = 8$ ms and $\tau = 11.2$ ms using the PFGSE ^{1}H NMR method.[9c] It is seen from these plots that the experimental data lie on a straight line. This shows that the diffusion of PDES in the isotropic phase is a single diffusion component. Diffusion coefficients D of the order of 10^{-11} cm^2 s^{-1}, determined from the slope, are summarized in Table 11. This shows that such extremely small diffusion coefficients are successfully determined by using the present PFGSE ^{1}H method. From these experimental results, it is seen that the diffusion coefficient of PDES slowly increases from 6.2 to 7.4×10^{-11} cm^2 s^{-1} with an increase in temperature from 50 to 80 °C. The polymer chains are completely in the isotropic phase. We must consider the cause why the polymer chains are very slowly diffusing. As

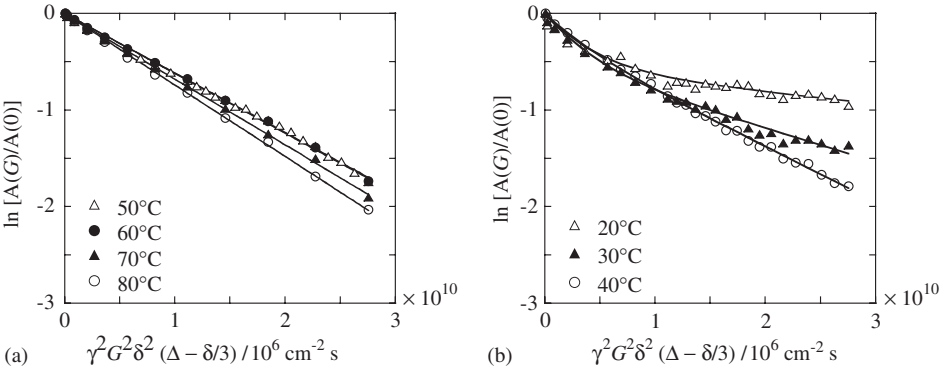

Fig. 42. The plots of $\ln[A(G)/A(0)]$ against $\gamma^2G^2\delta^2(\Delta-\delta/3)$ for determining the diffusion coefficients D of PDES by the PFGSE ^{1}H NMR method: (a) for the isotropic region in the isotropic phase at 50 (Δ), 60 (●), 70 (▲) and 80 °C (○); (b) for the isotropic region of the biphasic phase at 20 (Δ), 30 (▲) and 40 °C (○).

Table 11. Determined diffusion coefficients D of PDES in the liquid crystalline region in the biphasic region by PFGSE ^{13}C NMR method and in the isotropic region of the biphasic phase and the isotropic phase by PFGSE ^{1}H NMR method as a function of temperature

Temperature (°C)	Diffusion coefficient D/cm^2 s^{-1}					
	$D \times 10^{-9}$ (liquid crystalline component)		Isotropic component[a]			
			$D_1 \times 10^{-10}$ (fast diffusion component)	$D_2 \times 10^{-11}$ (slow diffusion component)	Fraction[b]	
					f_{D_1}	f_{D_2}
20	9.9[c]		2.6	1.3	0.43	0.57
30	75[d]	50[c]	2.8	3.5	0.39	0.61
40	–		2.8	5.7	0.21	0.79
50	–		–	6.2	0	1
60	–		–	6.2	0	1
70	–		–	6.8	0	1
80	–		–	7.4	0	1

[a]For the isotropic region of the biphasic phase at temperatures from 20 to 40 °C and for the isotropic phase at temperatures from 50 to 80 °C.
[b]D_1 and D_2 for the fast and slow diffusion components, respectively, at temperatures from 20 to 40 °C.
[c]For $\Delta = 1{,}000$ ms.
[d]For $\Delta = 750$ ms.

suggested earlier for any specified viscosity behavior for liquid polymers and highly concentrated polymer solutions,[141] it is thought that extremely slow diffusion of PDES chains in the isotropic phase may come from entanglements between the polymer chains.

Let us consider the diffusion of PDES in the isotropic region of the biphasic phase. In the biphasic phase at 20, 30 and 40 °C, the PDES chains are in the isotropic region and liquid crystalline region, thus the PDES chains in the isotropic region are surrounded by the liquid crystalline region, and vice-versa. The ^{1}H T_2 value of PDES in the liquid crystalline region is strongly influenced by strong dipolar interactions and the ^{1}H T_2 value becomes shorter by roughly one thirty-seventh of that in the isotropic region at same temperature. Therefore, the echo signal of the liquid crystalline component in this PFGSE ^{1}H NMR experiment disappears within the time interval τ of 11.2 ms between the first $\pi/2$ pulse and the second $\pi/2$ pulse, but the signal derived from PDES in the isotropic region of the biphasic phase remains in the echo finally obtained. The plots of $\ln[A(G)/A(0)]$ against $\gamma^2G^2\delta^2(\Delta-\delta/3)$ consist of two straight lines with different slopes as shown in Fig. 42(b). This shows that the diffusion has two kinds of diffusion components in the isotropic regions a slow and a fast diffusion component. The diffusion coefficients D's of PDES for the fast diffusion component in the isotropic region as determined from the large slope of the plots are of the order of $10^{-10}\,cm^2\,s^{-1}$ and those for the slow diffusion component as determined from the small slope of the plots are of the order of $10^{-11}\,cm^2\,s^{-1}$ as shown in Table 11. The magnitude of the diffusion coefficient for the slow diffusion component is close to that found in the isotropic phase at 50 °C.

Next, we consider whether in the diffusional behavior at 20, 30 and 40 °C the partial-restriction effect on diffusion which comes from the obstruction at the interface between the isotropic and liquid crystalline regions is important or not. The slow diffusion component is more sensitive to the obstruction of the interface. However, the diffusing time Δ of 500 ms, used in this experiment, is not so long that the diffusion is hindered by the interface. For example, the slow diffusion species with $D = 3.5 \times 10^{-11}\,cm^2\,s^{-1}$ at 30 °C can diffuse only 59 nm as calculated from the relation $\sqrt{2D\Delta}$ within the diffusing time of 500 ms. This is much smaller than the domain size of the isotropic region which is over several micrometer as estimated by an optical micrograph. Therefore, it is difficult to observe the partial-restriction effect on diffusion. If the observed non-Fickian behavior in the isotropic region of the biphasic phase comes from the partial-restriction effect, the slow diffusion component may be assigned to PDES in the interface region because PDES in the interface region must suffer strongly from the partial-restriction effect in diffusion. Thus, the fraction of the slow diffusion component must be small because the fraction of the interface region is very small. Nevertheless, the slow diffusion component is dominantly observed. From these experimental results, it can be said that the slow and fast diffusion components should be assigned to the inside and outside areas of the isotropic region in the biphasic phase. The determined D values and the fractions of the two diffusion components are summarized in Table 11. From this table, it is seen that the D values of the slow diffusion components of the isotropic region in the biphasic phase very largely increase with an increase in temperature, and those in the isotropic phase very slowly increase. The plots are abruptly changed at 50 °C. The activation energy E for diffusion can be obtained from the Arrhenius plots of $\ln D$ against $1/T$ to be 1.6 and 0.17 kcal mol^{-1} for the slow

diffusion component of the isotropic region in the biphasic phase and in the isotropic phase, respectively.

The fraction of the fast diffusion component of the isotropic region in the biphasic phase decreases with an increase in temperature and that of the slow diffusion component of the isotropic region in the biphasic phase increases. Therefore, it is expected that the PDES chains are diffusing from the isotropic region to the liquid crystalline region of the biphasic phase through their interface and at the same time from the liquid crystalline region to the isotropic region. The balance may be changed by a temperature change. The origin of the extremely small diffusion coefficient of the order of 10^{-10}–$10^{-11}\,cm^2\,s^{-1}$ may be due to the entanglement of the PDES chains. In order to recognize the effect of entanglements on the diffusion process, the PDES concentration dependence of the diffusion coefficient of the PDES in PDES/toluene-d_8 solution is measured at 50 °C. Fig. 43 shows the plots of the D values determined by changing G from 0 to $10\,T\,m^{-1}$ at $\Delta = 100$ ms, $\delta = 1$–4 ms and $\tau = 11.2$ ms by using the PFGSE ^{1}H NMR method. It is seen that as the polymer concentration increases, the D value of the PDES chains in the PDES/toluene-d_8 solution decreases and approaches to the D value of the PDES chains in the melt state. This shows that the entanglements effect exists in the polymer system, which leads to a reduction of the translational diffusion coefficient of the polymer chains.

In order to clarify the diffusional behavior of PDES in the liquid crystalline region, the PFGSE ^{13}C NMR experiments under ^{1}H CW decoupling are made at 20 and 30 °C by changing G from 0 to $11.5\,T\,m^{-1}$ at $\Delta = 750$ and 1,000 ms, $\delta = 0.5$ ms and $\tau = 1.7$ ms. At these temperatures, the PDES chains are in the biphasic phase consisting of the liquid crystalline region and the isotropic region as characterized

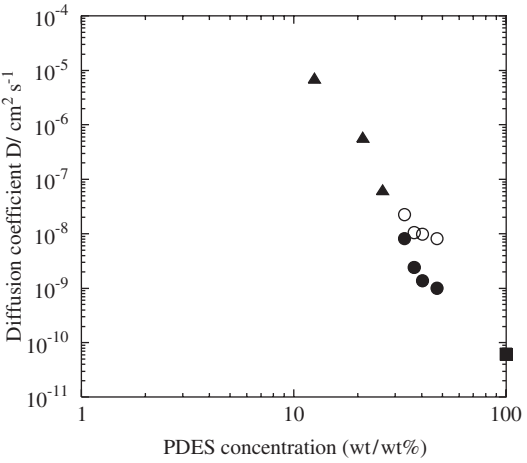

Fig. 43. The log–log plots of diffusion coefficients D of PDES in PDES/toluene-d_8 solutions against the PDES concentration at 50 °C by the PFGSE ^{1}H NMR method: (▲) 12.5, 21.1 and 26.2 wt/wt%; (●) 33.2, 36.9, 40.3 and 47.3 wt/wt% (slow diffusion component); (○) 33.2, 36.9, 40.3 and 47.3 wt/wt% (fast diffusion component); (■) 100 wt/wt%.

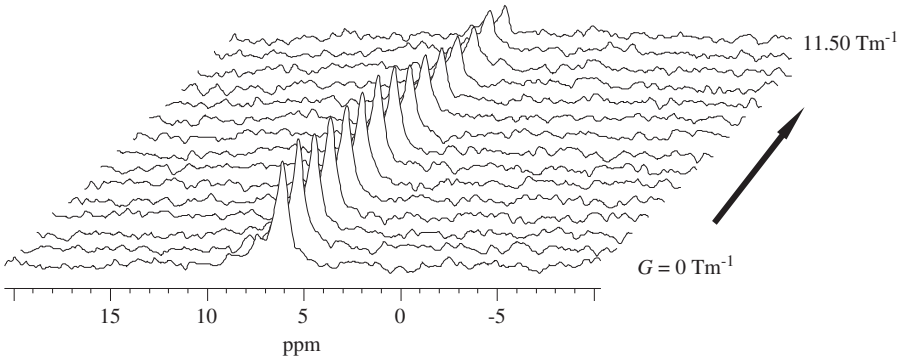

Fig. 44. Observed PFGSE ^{13}C NMR spectra of PDES in the biphasic phase as a function of field-gradient strength G at 30 °C.

by static solid-state ^{29}Si NMR. The fraction of the liquid crystalline region is 0.81 at 20 °C, and is 0.69 at 30 °C as determined by the ^{1}H solid echo method. The typical observed PFGSE ^{13}C NMR spectra of PDES in the liquid crystalline region at 30 °C and at $\Delta = 1{,}000$ ms are shown in Fig. 44. An asymmetric signal appears at about 6.3 ppm. This peak can be straightforwardly assigned to the methyl carbons in the side chains of PDES.[142] In PFGSE experiments, the magnetization is attenuated by T_2 during τ. The ^{13}C T_2 value for the methyl carbons in the side chains of PDES in the liquid crystalline region is roughly 16 times longer than ^{1}H T_2 as estimated by using the magnetogyric ratios of $^{13}C(\gamma_{^{13}C})$ and $^{1}H(\gamma_{^{1}H})$ nuclei and the BPP theory (^{13}C $T_2/^{1}H$ $T_2 \approx (\gamma_{^{1}H}/\gamma_{^{13}C})^2 \approx 4^2 = 16$).[143] Therefore, it is better to use the ^{13}C nucleus in determining the diffusion coefficient as compared with the ^{1}H nucleus by the PFGSE NMR method. The echo signal comes from the PDES chains in the liquid crystalline region and does not disappear at the echo time interval during τ. Seventy-four percent of the initial magnetization decays by ^{13}C T_2 during τ and ^{13}C T_1 between the second and third $\pi/2$ pulses at $\Delta = 1{,}000$ ms and $\tau = 1.7$ ms. Then, the remaining magnetization is reduced by diffusion.

The plots of $\ln[A(G)/A(0)]$ for PDES as obtained from the PFGSE ^{13}C NMR spectra against $\gamma^2G^2\delta^2(\Delta-\delta/3)$ at 20 and 30 °C and at $\Delta = 1{,}000$ ms give a straight line as shown in Fig. 45. This shows that the diffusion is a single diffusion component with $D \approx 10^{-8}\,cm^2\,s^{-1}$. The reduction of the diffusion coefficient of PDES in the liquid crystalline region with an increase in Δ from 750 to 1,000 ms shows that there clearly exists a partial-restriction effect for the diffusion.

The diffusion of poly(*n*-octadecyl L-glutamate) (POLG)/chloroform-d solution in the lyotropic liquid crystalline phase and the isotropic phase has been reported.[60] The diffusion coefficient of POLG in the liquid crystalline phase ($\approx 10^{-7}\,cm^2\,s^{-1}$) is much smaller than that for POLG in the isotropic phase ($\approx 10^{-6}\,cm^2\,s^{-1}$). This is opposite to the results of PDES in the liquid crystalline region and the isotropic region. In the case of POLG, the polymer takes the α-helix form in both the liquid crystalline and isotropic phases, and then diffuses as a rigid-rod. As predicted, POLG chains in the liquid crystalline phase may more strongly interact with each

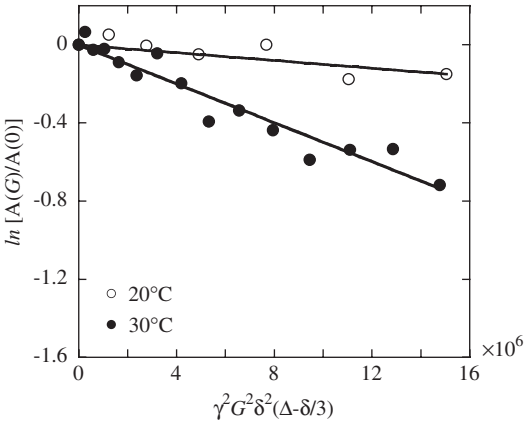

Fig. 45. The plots of $\ln[A(G)/A(0)]$ against $\gamma^2G^2\delta^2(\Delta-\delta/3)$ for determining diffusion coefficients D of PDES at 20 (○) and 30 °C (●) by PFGSE ^{13}C NMR method.

other as compared with those in the isotropic phase. The PDES chain takes the extended form in the liquid crystalline region, but takes the random-coil form in the isotropic region. For this reason, the random-coiled PDES chains have entanglements in the melt state and thus diffuse more slowly compared with those in the liquid crystalline region.

3.4. Diffusion of *n*-alkanes in the rotator phase

It was discovered by Müller from X-ray experiments that some *n*-alkanes from *n*-$C_{18}H_{38}$ to *n*-$C_{49}H_{90}$ have an intermediate phase between the crystalline and the liquid phases.[144] In the phase, named "rotator phase" like a liquid crystal, the *n*-alkanes are in a state of rotation around their long axis. This rotator phase has been studied by various techniques such as, X-ray diffraction,[145,146] NMR,[147–150] IR,[151] Raman,[152] neutron scattering[153] and computer science.[154,155] From these results, it has been mainly clarified that in the rotator phase the *n*-alkane chains become effectively cylindrical as a results of rotating about their long axis and some rotator phases are identified.

The structure of some *n*-alkanes, *n*-$C_{19}H_{40}$, *n*-$C_{24}H_{50}$ and *n*-$C_{32}H_{66}$ in the rotator phase have been studied by using high-resolution ^{13}C NMR.[149,150] From these results, it has been shown that the ^{13}C chemical shift values of the internal CH_2 carbons of these *n*-alkanes in the rotator phase are ca. 33 ppm. This is very close to those for the *trans* zigzag conformation in the crystalline state, which are independent of the chain length and so *n*-alkanes in the rotator phase take the *trans* zigzag conformation.[66] This is irrespective of the extremely fast exchange between the *trans* and *gauche* conformations on the NMR timescale. In addition the ^{13}C T_1 values of the CH_2 carbons for *n*-$C_{32}H_{66}$ in the rotator phase are almost the same

Table 12. The crystalline phase/rotator phases transition temperatures (T_{c-r}) and the rotator phase/liquid phase transition temperatures (T_{r-l}) of *n*-alkanes as determined by the DSC method[a]

n-Alkanes	T_{c-r} (°C)	T_{r-l} (°C)
n-$C_{21}H_{44}$	31.1	40.1
n-$C_{23}H_{48}$	37.9	46.8
n-$C_{24}H_{50}$	41.4	50.2
n-$C_{28}H_{58}$	54.0	60.6
n-$C_{32}H_{66}$	63.6	68.7
n-$C_{34}H_{70}$	68.5	72.3

[a]Measured by cooling process with the cooling rate of 0.5 °C min^{-1}.

and, thus, the main chain with the *trans* zigzag conformation is undergoing fast rotation around the long chain axis.[150]

Most recently, the self-diffusion coefficients of *n*-$C_{21}H_{44}$, *n*-$C_{23}H_{48}$, *n*-$C_{24}H_{50}$, *n*-$C_{28}H_{58}$, *n*-$C_{32}H_{66}$ and *n*-$C_{34}H_{70}$ in the rotator phase and the liquid phase over a wide range of temperatures have been measured by using the PFGSE ^{1}H NMR method, and the diffusion process of the *n*-alkanes in the rotator phase elucidated.[61,156] The diffusion coefficients of an *n*-$C_{24}H_{50}$ single crystal in the rotator phase in the directions parallel and perpendicular to the long chain axis have been determined and it is elucidated whether the diffusion process in the rotator phase is anisotropic.

The self-diffusion coefficient measurements of all *n*-alkanes in the liquid phase and the rotator phase are carried out over a wide range of temperatures by means of a 270 MHz NMR spectrometer for ^{1}H. The PFGSE measurements were performed on *n*-alkanes by a cooling process used in DSC measurements. The change of the state of the *n*-alkane samples by a temperature change is referred to the DSC data. (The crystalline phase/rotator phase transition temperatures (T_{c-r}) and the rotator phase/liquid phase transition temperatures (T_{r-l}) of the *n*-alkanes as determined by the DSC method are shown in Table 12.) The temperature control in the *D* measurements was $\pm$0.1 °C. The field-gradient strength, *G*, is 13.36 T m^{-1}. The measurements of the diffusion coefficient were performed after keeping for 1.5 h in an NMR probe at the measurement temperature. (The diffusion coefficients were measured every 20 min for 8 h and were a constant value independent of time. For this reason, the time of 1.5 h was chosen.)

3.4.1. *Diffusional behavior of n-alkanes in the rotator phase like the liquid crystalline phase*

Fig. 46 shows some typical spin-echo ^{1}H NMR spectra of *n*-$C_{32}H_{66}$ at 80 °C in the liquid phase and 71 °C in the rotator phase as a function of field-gradient pulse length (δ) obtained by using ^{1}H PFGSE NMR.[61] In the liquid phase, the peak at about 1.8 ppm can be assigned to the methylene protons and a low frequency

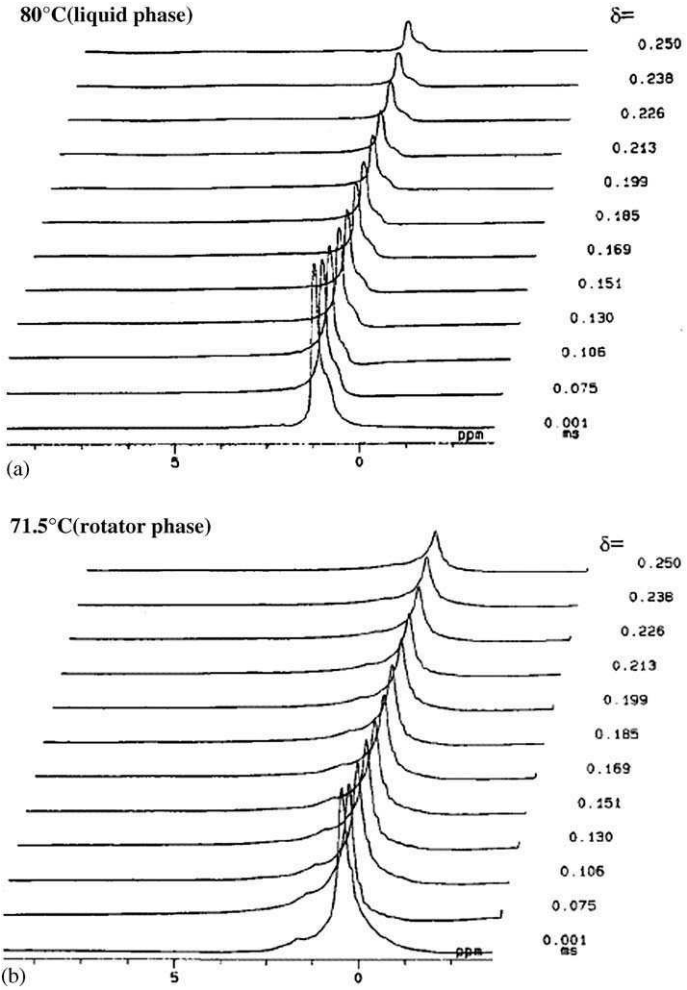

Fig. 46. Typical pulse field-gradient spin-echo ^{1}H NMR spectra of n-$C_{34}H_{70}$ at 80 °C in the liquid phase and 71 °C in the rotator phase as a function of pulse field interval δ.

shoulder at about 1 ppm can be assigned to the methyl protons by using the reference spectra of the *n*-alkane in both of the phases in solution. In the rotator phase, the spectrum becomes broadened due to a decrease in molecular motion. It is seen that the intensities of the peaks decay with an increase in field-gradient pulse duration $\tilde{\delta}$. This comes from the diffusion of the *n*-alkane molecule within the observation time, i.e., the time interval between the two gradient pulses. By using these decay signals we can determine the diffusion coefficient. The plots of $\ln[A(\delta)/A(0)]$ against $\gamma^2G^2\delta^2(\Delta-\delta/3)$ are shown over a wide range of temperatures in going from the liquid phase to the rotator phase in Fig. 47. It is seen that the experimental data lie on a straight line. This means that the *n*-alkane has a single component diffusion

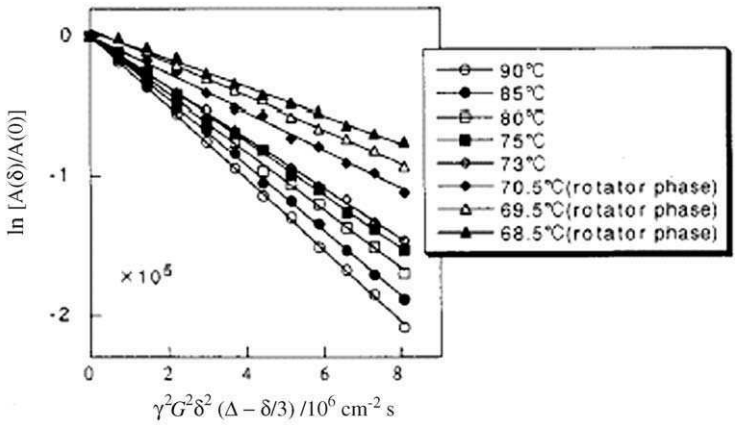

Fig. 47. The plots of $\ln[A(\delta)/A(0)]$ of n-$C_{34}H_{70}$ against $\gamma^2G^2\delta^2(\Delta-\delta/3)$ over a wide range of temperatures in going from the liquid phase to the rotator phase.

in the liquid phase and the rotator phase during the observation time. Further, it is seen that the slope of the straight line increases with an increase in temperature, and the slopes in the straight line between the rotator and the liquid phase are different, where the slope is $-D$. The other n-alkanes have similar results to n-$C_{32}H_{66}$.

By using such procedures, the D values of n-$C_{21}H_{44}$, n-$C_{23}H_{48}$, n-$C_{24}H_{50}$, n-$C_{28}H_{58}$, n-$C_{32}H_{66}$ and n-$C_{34}H_{70}$ in the rotator phase and the liquid phase over a wide range of temperatures were determined under a cooling process with a cooling rate of $0.5\,^{\circ}C\,min^{-1}$ as shown in Table 13, where the D data of n-$C_{24}H_{50}$ reported previously[13] are reproduced. The D data determined under a heating process are placed on the plots of the D data determined under a cooling process. Fig. 48 shows the plots of the diffusion coefficients D of the n-alkanes in the liquid and the rotator phase against temperature. It is shown that in the liquid phase D decreases with a decrease in temperature and, in going from the liquid phase to the rotator phase, is abruptly changed at the rotator/liquid phase transition temperature ($T_{r\text{-}l}$). The slope of the temperature dependence in the rotator phase is much larger than that in the liquid phase. The D values for the n-alkanes at the $T_{r\text{-}l}$ ($D_{r\text{-}l}$) linearly decreases with an increase in their carbon number (N) as indicated by the dashed line, and are expressed by?

$$D_{r-l} = a - bN \tag{14}$$

where $a = 5.04$ ($cm^2\,s^{-1}$) and $b = 0.047$ ($cm^2\,s^{-1}$). By using this equation, we can determined the diffusion coefficient of n-alkane with the carbon number N at the rotator /liquid phase transition temperature.

We are concerned with the temperature dependence of the diffusion coefficient of the n-alkanes in the rotator phase in going from the liquid phase. As mentioned above, the D values of n-$C_{24}H_{50}$, n-$C_{32}H_{66}$ and n-$C_{34}H_{70}$ change abruptly at the rotator/liquid phase transition temperature in going from the liquid phase to the

Table 13. Determined diffusion coefficients D of *n*-alkanes in the rotator phase and the liquid phase as a function of temperature by ^{1}H PFGSE NMR method[a]

n-Alkanes	Temperature (°C)	Phase	Diffusion coefficient[b] (D/cm^2 s^{-1} × 10^6)
n-$C_{21}H_{44}$	60	Liquid	4.74
	55	Liquid	4.11
	50	Liquid	3.69
	45	Liquid	3.30
	41	Liquid	3.07
	39	Rotator	2.94
	38	Rotator	3.05
	37.5	Rotator	2.78
	37	Rotator	2.58
n-$C_{23}H_{48}$	65	Liquid	4.12
	60	Liquid	3.83
	55	Liquid	3.42
	48	Liquid	2.90
	46	Rotator	2.84
	45	Rotator	3.13
	43	Rotator	2.89
n-$C_{24}H_{50}$[c]	65	Liquid	3.52
	60	Liquid	3.15
	55	Liquid	2.83
	51	Liquid	2.59
	50	Rotator	2.52
	49	Rotator	2.19
	47	Rotator	1.86
	45	Rotator	1.52
n-$C_{24}H_{50}$ single crystal[d]	49	Rotator	1.64 ($D_{\|}$)
			2.70 ($D_{\perp}$)
n-$C_{32}H_{66}$	85	Liquid	3.09
	80	Liquid	2.87
	75	Liquid	2.55
	71	Liquid	2.36
	68	Rotator	1.57
	67	Rotator	1.37
	66	Rotator	1.17
	65	Rotator	1.01
n-$C_{34}H_{70}$	90	Liquid	2.56
	85	Liquid	2.33
	80	Liquid	2.07
	75	Liquid	1.91
	73	Liquid	1.80
	70.5	Rotator	1.36
	69.5	Rotator	1.19
	68.5	Rotator	1.00

[a]Measured by cooling process with the cooling rate of 0.5 °C min^{-1}.
[b]Experimental error: ca. 5%.
[c]Ref. 156.
[d]See in the text.

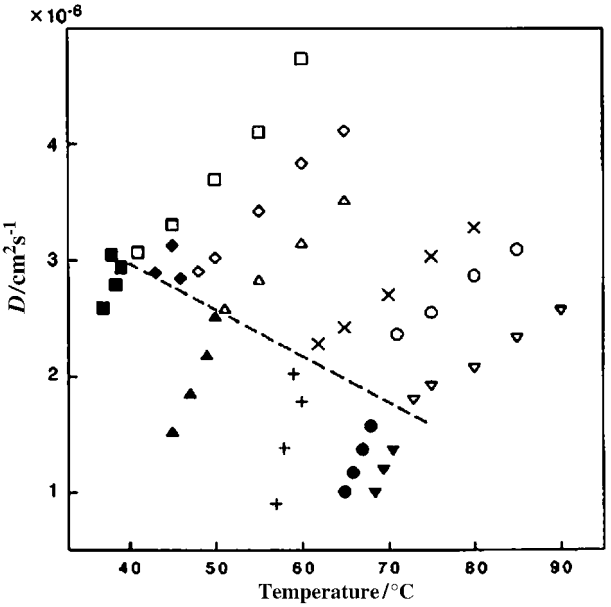

Fig. 48. Diffusion constants D of n-$C_{21}H_{44}$ (in the liquid phase (□) and in the rotator phase (■)), n-$C_{23}H_{48}$ (in the liquid phase (◇) and in the rotator phase (◆)), n-$C_{24}H_{50}$ (in the liquid phase (△) and in the rotator phase (▲)), n-$C_{28}H_{58}$ (in the liquid phase (×) and in the rotator phase (+)), n-$C_{32}H_{66}$ (in the liquid phase (○) and in the rotator phase (●)) and n-$C_{34}H_{70}$ (in the liquid phase (▽) and in the rotator phase (▼)) as a function of temperature, as determined by PFGSE ^{1}H NMR method.

rotator phase. However, the temperature dependence of n-$C_{21}H_{44}$, n-$C_{23}H_{48}$ and n-$C_{28}H_{58}$ in the rotator phase is somewhat different from that of n-$C_{24}H_{50}$, n-$C_{32}H_{66}$ and n-$C_{34}H_{70}$. The D values of these n-alkanes largely decrease in going from the liquid phase to the rotator phase, and then increase in the rotator phase. As the temperature is further increased, the D values decrease again. At present a conclusive reason for this observation cannot be clarified. A sufficient number of the D data for n-$C_{23}H_{48}$ in the rotator phase could not be obtained because of the narrow temperature range. For this reason, it is seen that the D behavior is apparently different from those of other n-alkanes in the rotator phase. Nevertheless, the trend for the obtained three D values is similar to that for n-$C_{21}H_{44}$ and n-$C_{28}H_{58}$. It is suggested that these come from the existence of some phases in the rotator phase as recognized by X-ray diffraction.[144,145]

In Fig. 49 the D values are plotted against time. It is seen that the D values are almost independent of time from 100 to 500 min. This means that the effect of supercooling on the state of the n-alkane when going from the liquid phase to the rotator phase can be neglected during the measurement time.

In order to understand the diffusion process, we obtain the activation energy (E) for diffusion by using Eq. (10). The activation energy was obtained from the plots

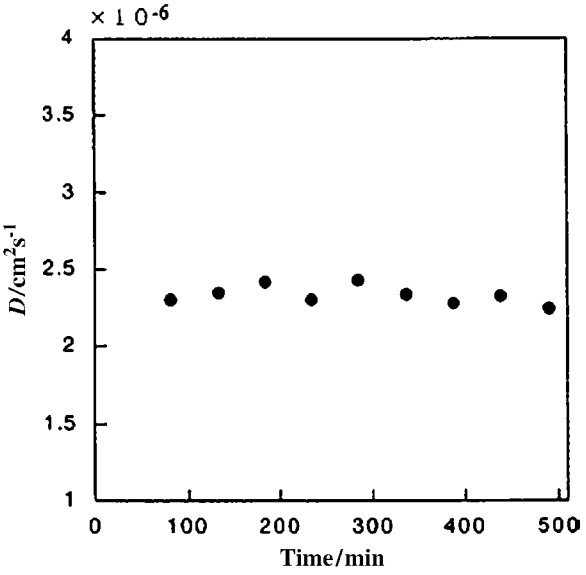

Fig. 49. Diffusion coefficients D of n-$C_{24}H_{50}$ at 49 °C in the rotator phase as a function of elapsed time after going from the liquid phase to the rotator phase.

of $\ln D$ against $1/T$ (the Arrhenius plots) as shown in Fig. 50. The slope becomes $-E$. The determined E values for diffusion of the *n*-alkanes in the liquid phase and the rotator phase are shown in Table 14. From these results, it is seen that the E values for the *n*-alkanes in the liquid phase are 4.6–5.1 kcal mol^{-1}, that is almost a constant, but those in the rotator phase are 20–36 kcal mol^{-1}. In the rotator phase the E value is much larger than that in the liquid phase and increases with an increase in the carbon number of the *n*-alkanes. This may be understood from the experimental finding that in the liquid phase the *n*-alkanes are in the random coil state and the diffusional mode is isotropic. In the rotator phase the *n*-alkanes take the *all-trans* zigzag conformation and the diffusion for the *n*-alkanes in the rotator phase is limited to being along and perpendicular to the lamellar plane.

3.4.2. *Diffusion of n-alkane in a single crystal at a temperature in the rotator phase*

The diffusion coefficients of n-$C_{24}H_{50}$ in a lamellar single crystal have been measured, at a temperature in the rotator phase, in the directions parallel and perpendicular to the long chain axis. It takes the *all-trans* zigzag conformation, where the lamellar single crystal of n-$C_{24}H_{50}$ with a size of ca. 2–4 × 4 mm with ca. 0.2–0.8 mm in thickness is prepared by slow evaporation from benzene solution.[61] The *all-trans* zigzag chains of the *n*-alkane align to the direction perpendicular to the lamellar plane. In this experiment, eight pieces of the lamellar single crystals are placed to overlap with each other in an NMR tube in directions parallel and perpendicular to the static magnetic field. The field-gradient pulse is along the static magnetic field

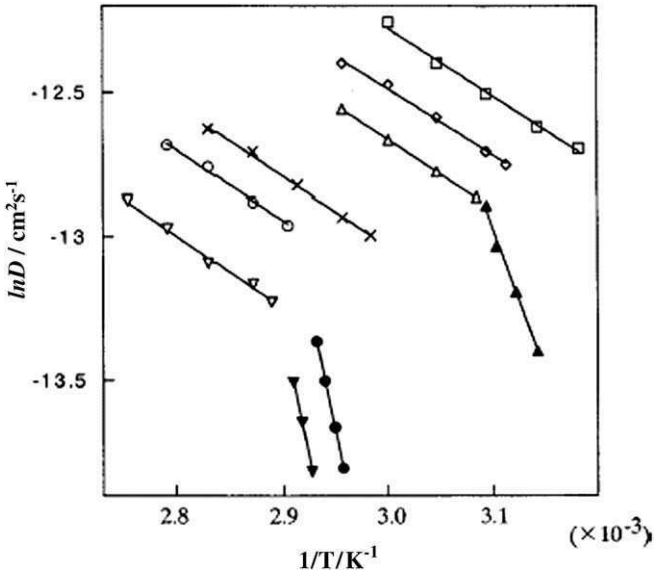

Fig. 50. The Arrhenius plots of $\ln D$ against $1/T$ for n-$C_{21}H_{44}$, n-$C_{23}H_{48}$, n-$C_{24}H_{50}$, n-$C_{28}H_{58}$, n-$C_{32}H_{66}$ and n-$C_{34}H_{70}$ in the liquid and rotator phases.

Table 14. Determined activation energies E for the diffusion of n-alkanes in the rotator phase and liquid phase

n-Alkanes	Activation energy[a] E/kcal mol^{-1}	
	Rotator phase	Liquid phase
n-$C_{21}H_{44}$	_[b]	4.7
n-$C_{23}H_{48}$	_[b]	4.6
n-$C_{24}H_{50}$	19.9	4.8
n-$C_{28}H_{58}$	_[b]	4.9
n-$C_{32}H_{66}$	33.9	4.8
n-$C_{34}H_{70}$	35.9	5.1

[a]Experimental error: 5%.
[b]Not determined with high reliability.

direction (z axis). We have determined the diffusion coefficients of the n-alkane parallel ($D_{||}$) and perpendicular ($D_{\perp}$) to the long chain axis at 49.8 °C in the rotator phase as listed in Table 13. The diffusion of the n-alkane along the long chain axis is much slower by roughly two times than that perpendicular to the long chain axis. In earlier work, the diffusion coefficients, $D_{||}$ and $D_{\perp}$, of tritium-labeled n-$C_{20}H_{42}$ in a single crystal were determined by a radioactive tracer method to be 0.56×10^{-10} and 1.06×10^{-10} cm^2 s^{-1}, respectively.[157]. From these experimental results, the diffusion of the n-alkanes in the crystalline state along the long chain axis is much

slower by roughly two times than that perpendicular to the long chain axis. Our experimental result in the rotator phase does not conflict qualitatively with this result in the crystalline state namely that $D_{||}$ is much smaller than $D_{\perp}$. By using the determined $D_{||}$ and $D_{\perp}$ values in the rotator phase to be 1.64×10^{-6} and $2.70 \times 10^{-6}\,cm^2\,s^{-1}$, respectively, we can calculate the isotropic diffusion coefficient, D_{iso}, corresponding to a state in the polycrystalline sample to be $D_{iso} = (D_{||} + 2D_{\perp})/3 = 2.35 \times 10^{-6}\,cm^2\,s^{-1}$. This is very close to the experimental value of $2.19 \times 10^{-6}\,cm^2\,s^{-1}$ in the rotator phase at the same temperature. From the above experimental results, it can be said that the diffusion of the *n*-alkane in the rotator phase is anisotropic.

3.5. Diffusion of *n*-alkanes in the channels of urea adduct

Recently, the structure and dynamics of *n*-alkanes in 1D channels of urea-d_4 have been studied by various kinds of methods such as X-ray diffraction,[158] ^2H NMR,[159–161] incoherent quasi-elastic neutron scattering,[162,163] Raman scattering[164,165] and computer science.[166,167] It is well known that urea forms urea adducts with long channels in which linear chain molecules such as *n*-alkanes, fatty acids and alkanones are embedded. From many research works on the structure of urea in the urea adducts, it has been revealed that urea inclusion compounds consist of urea molecules forming long honeycomb-like(hexagonal) channels with diameters of 5.5–5.8 Å by hydrogen bonds and molecules embedded in the channels at room temperature.[158,168,169] If the temperature is decreased from room temperature (e.g., ca. −123 °C for urea/*n*-hexadecane adduct), the urea-adduct crystals occur in a solid–solid phase transition associated with a change of the host urea network structure from the hexagonal form to the orthorhombic form. The phase transition temperature is chain-length dependent and for a given *n*-alkane in the urea adduct it is substantially lower than the rotator phase transition temperature for the crystalline phase of the *n*-alkane.[170]

Further, it is shown that *n*-alkane chains in the long channels of the urea adduct at the low temperature range take the all-*trans* zigzag conformation and its molecular motion is frozen, but in the high temperature range the *n*-alkane chains are undergoing rotational motions around the chain axis.[159,162,171–175] Most recently, molecular motion of *n*-alkane chains in long channels of urea adducts has been elucidated by solid-state NMR.[159,160,176,177] From these studies, the conformation and rotational motion of *n*-alkane chains in the long channel of urea-d_4 adduct have been clarified. Nevertheless, some problems related to the dynamics of the *n*-alkane chains in the urea adduct channel remain. For example (1) are *n*-alkane chains diffusing in channel cavities of the urea adduct? (2) what, if they are diffusing, is the diffusion coefficient? (3) what is the diffusion process? and (4) how is the diffusional behavior of *n*-alkane chains affected by varying the chain length?

The diffusion coefficients of *n*-C_8H_{18}, *n*-$C_{12}H_{26}$, *n*-$C_{21}H_{44}$, *n*-$C_{26}H_{54}$, *n*-$C_{28}H_{58}$ and *n*-$C_{32}H_{66}$ in long channels of deuterated urea-d_4 adduct at 25 °C have been observed by means of the PFGSE ^1H NMR method. Thus the chain-length

dependence of the diffusion for the guest molecules and the diffusion process of the *n*-alkanes is studied.[178,179] The diffusion coefficients of *n*-$C_{12}H_{26}$ and *n*-$C_{26}H_{54}$ in the urea-d_4 adduct channels are observed by varying the diffusing time Δ by means of PFGSE ^{1}H NMR and PFGStE NMR methods.This has clarified the diffusion process of the guest molecules in the urea adduct channels. In the NMR experiments, all the samples are hexagonal crystals with an average of 10 mm in length and a cross-section with a diameter of ca. 0.43 mm.

In the 300 MHz PFGSE ^{1}H NMR experiments, the echo signal intensity is measured by varying the field-gradient strength G from 0 to 11.60 T m^{-1}, the gradient pulse interval Δ is 5 ms, and the gradient pulse width δ is 1 ms for all of the samples. The diffusion coefficients of *n*-$C_{12}H_{26}$ and *n*-$C_{26}H_{54}$ in the urea-d_4 adduct have been measured at various diffusing times, in order to explain in detail the diffusional behavior of *n*-alkane molecules within a channel cavity.

When the probe molecules have two kinds of diffusion components on the measurement timescale, the total echo attenuation is given by a superposition of contributions from the individual components as expressed by Eq. (2).

3.5.1. *Chain-length dependence of the diffusion coefficients of n-alkanes in urea adduct*

In Fig. 51 are shown typical spin-echo ^{1}H NMR spectra of *n*-C_8H_{18} in the urea-d_4 adduct at 25 °C as a function of field-gradient pulse strength (G) as observed by using PFGSE ^{1}H NMR. The broad peak at about 5 ppm can be straightforwardly assigned to the methylene protons of *n*-C_8H_{18}. The minor methyl peak overlaps with the major methylene peak as a small shoulder on the low frequency side of the methylene peak. The origin of such a shift by about 3 ppm, as compared with the ^{1}H chemical shift for the methylene protons of *n*-alkanes in the solid and liquid states (δ = about 2 ppm), may be understood by the following. *n*-Alkane chains are in the long hexagonal channel cavities of the urea-d_4 adduct with a diameter of about 5.5 Å as formed by hydrogen bonds between the carbonyl $>C=O$ groups and the NH groups of the urea molecules. Thus the methylene and methyl protons are largely affected by the magnetic anisotropy effect of the carbonyl groups in the long channel as predicted theoretically by the magnetic anisotropy effect/chemical shift map. The intermolecular distance between the methylene protons or methyl protons of *n*-C_8H_{18} and the $>C=O$ group of urea-d_4 is roughly calculated to be about 1.3 Å, when the *n*-alkane molecules are placed at the center of a hexagonal channel cavity. Hence the calculated deshielding is about 2–3 ppm for the protons by the magnetic anisotropy effect/chemical shift map.[180] Thus, the ^{1}H chemical shift of the methylene protons may be approximately calculated to be about 5 ppm.

Fig. 52 shows the plots of $\ln[A(G)/A(0)]$ against $\gamma^2G^2\delta^2(\Delta-\delta/3)$ for the methylene and methyl protons of *n*-C_8H_{18}. The intensity of the corresponding peak decreases with an increase in G. This means that the *n*-C_8H_{18} molecules diffuse in the long channel cavity of the urea-d_4 adduct with a diameter of about 5.5 Å. It is seen that the experimental data do not lie on a straight line but lie on the curve formed by the

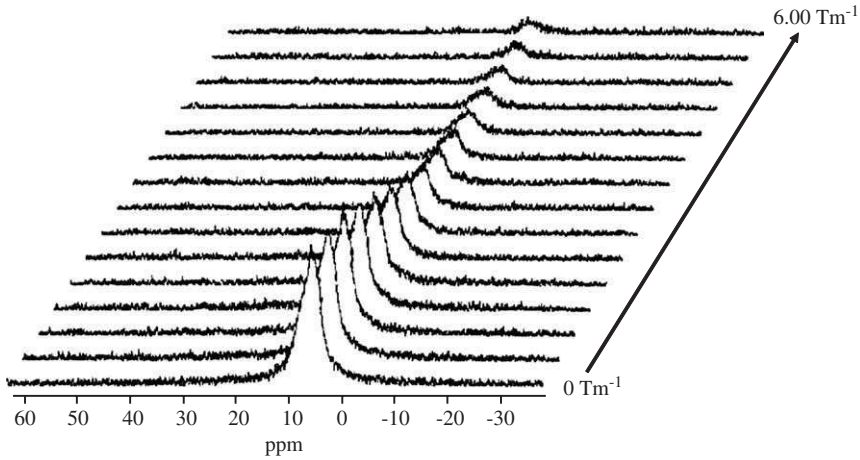

Fig. 51. Typical spin-echo ^{1}H NMR spectra of n-C_8H_{18} in urea-d_4 adduct at 25 °C as function of field-gradient pulse strength (G) as observed by using PFGSE ^{1}H NMR.

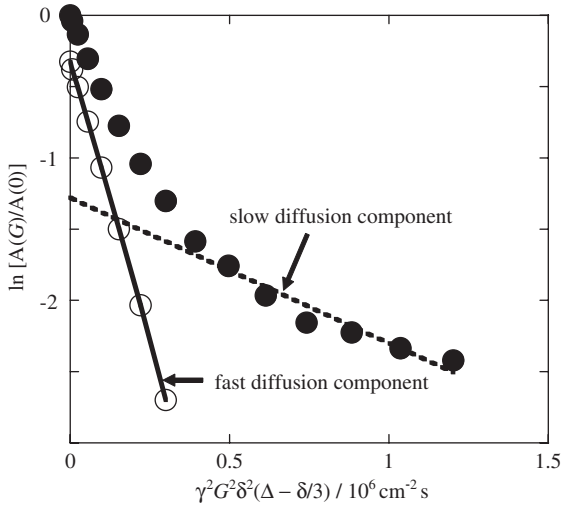

Fig. 52. The plots of $\ln[A(G)/A(0)]$ against $\gamma^2G^2\delta^2(\Delta-\delta/3)$ for the methylene and methyl protons of n-C_8H_{18} in urea-d_4/n-C_8H_{18} at 25 °C.

superposition of two straight lines as seen in Fig. 52. This means that the n-C_8H_{18} molecules in the long channels of the urea adduct have two kinds of diffusion such as a slow and a fast diffusion component during the observation time of 5 ms.

The diffusion coefficient can be determined from the slope of $-D$ for the individual straight lines by using Eq. (2). The determined D values are listed in Table 15 together with the fraction of the corresponding two diffusion coefficient components.

Table 15. Determined diffusion coefficients D^a of *n*-alkanes in urea adduct at 25°C

Urea adducts	Diffusion coefficient $D/cm^2 s^{-1}$		Fraction	
	D_{fast} ($\times 10^6$)	D_{slow} ($\times 10^6$)	f_{fast}	f_{slow}
Urea-d_4/*n*-C_8H_{18}	7.9	10.2	0.72	0.28
Urea-d_4/*n*-$C_{12}H_{26}$	7.1	5.60	0.79	0.21
Urea-d_4/*n*-$C_{21}H_{44}$	3.0	0.70	0.67	0.33
Urea-d_4/*n*-$C_{26}H_{54}$	2.8	0.94	0.64	0.36
Urea-d_4/*n*-$C_{28}H_{58}$	2.7	1.0	0.57	0.43
Urea-d_4/*n*-$C_{32}H_{66}$	3.0	0.8	0.18	0.82

[a]The experimental errors for the diffusion coefficient measurements are ca. 10%.

We are concerned with the origin of the two diffusion components of *n*-alkane molecules with largely different diffusion coefficients in long channels of the urea adduct on the basis of the above experimental results. As for the diffusional behavior of *n*-C_8H_{18} molecules in this urea adduct system, there are the following considerations to explain the origin of the existence of the fast and the slow diffusion components.

There may be two kinds of regions in long channels including *n*-C_8H_{18} molecules in the urea adduct. Namely, there are *n*-C_8H_{18} molecules in the two external regions near the ends of the urea channel, and *n*-C_8H_{18} molecules in the central inner region of the urea channel. It is thought that these contribute to the fast and the slow diffusion components, respectively. The shape of the *n*-alkane with the extended *trans* form in the urea adduct channels are roughly approximated to be a rod with an average diameter of about 0.4 nm, the urea adduct channel size is 0.55 nm. The *n*-alkane molecules do not experience tight space in the channels and are able to diffuse. From the experimental fact that the *n*-C_8H_{18} molecules in the urea channels are diffusing, it can be said that the diffusion must be cooperative (like the single-file diffusion model). In the diffusion, individual molecules cannot pass each other.[181,182] One *n*-alkane molecule can move to the space produced by movement of other *n*-alkane molecules, and then it can repeat the diffusion and collision in the inner part and the external part of the urea channels during the NMR timescale. These displacements occur in succession. In addition, as reported by Aslangul,[183] the single-file diffusion model shows that at the initial time *n*-alkane molecules are launched at a 1D space and each of them undergoes ordinary diffusional motion, but has a contact repulsive interaction with the neighbors. As a consequence, the *n*-alkane molecules located at the edges of the channel can move freely on one side and are subjected to a fluctuating boundary condition on the other, whereas the *n*-alkane molecules inside of the channel are subjected to such boundary conditions on either side. *n*-Alkane molecules in the inner part of a urea channel have a higher possibility of collision than those in the external parts near the ends of the channel. Thus, the diffusion coefficient (D_{inside}) of the *n*-alkane molecules in the inner part is much smaller than that of the *n*-alkane molecules in the outside ones ($D_{outside}$). In the limit of large N (the number of *n*-alkanes), and within a Gaussian approximation,

the diffusion constant is found to behave as N^{-1} for the central *n*-alkane molecules and as $(\ln N)^{-1}$ for the outer ones as suggested by the single-file diffusion model.[183] Absolute correlations between the edge particles increase as $(\ln N)^2$.

In the same manner, the D values of *n*-$C_{12}H_{26}$, *n*-$C_{21}H_{44}$, *n*-$C_{26}H_{54}$, *n*-$C_{28}H_{58}$ and *n*-$C_{32}H_{66}$ in the urea-d_4 adduct at 25 °C are determined. Fig. 53 shows the plots of $\ln[A(G)/A(0)]$ of these *n*-alkanes against $\gamma^2G^2\delta^2(\Delta-\delta/3)$ and the calculated curves of superposition of the echo signal intensities from the two diffusion components. The two diffusion coefficients are determined by superposition of the two straight lines. The order of the diffusion coefficients of the fast (D_{fast}) and the slow diffusion components (D_{slow}) are 10^{-6} and $10^{-7}\,cm^2\,s^{-1}$, respectively. The two diffusion components are attributed to *n*-alkane molecules in the two external regions near the ends of the urea channel, and *n*-alkane molecules in the central inner region of the urea channel.[178] The determined D values of all the *n*-alkanes in the urea-d_4 adduct are listed in Table 15.

For convenience, the diffusion coefficients of all the *n*-alkanes for both of the two diffusion components are plotted against the carbon number in Fig. 54. The diffusion coefficients decrease as the carbon number is increased from 8 to 28, and very slowly decreases as the carbon number is increased from 28 to 32. These results are similar to those of pure *n*-alkanes in the rotator phase where the diffusion coefficient becomes smaller as the chain length of the *n*-alkane molecule increases.[61]

Pure *n*-alkanes with a large number of carbons take the extended all-*trans* zigzag form in the rotator phase.[144] Such a conformational and dynamic behavior may be similar to those of *n*-alkanes in urea adducts. In the previous work on the diffusional behavior of long *n*-alkanes with the all-*trans* zigzag conformation in the rotator phase, the diffusion coefficient of the *n*-alkanes is estimated to be of the

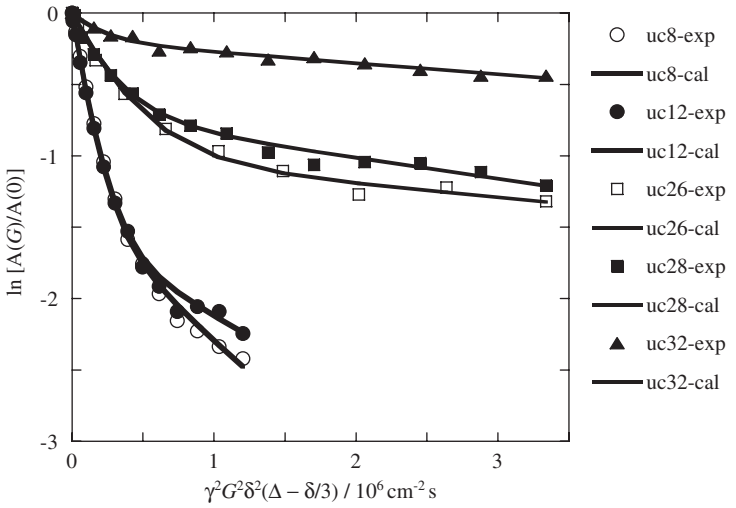

Fig. 53. The plots of $\ln[A(G)/A(0)]$ against $\gamma^2G^2\delta^2(\Delta-\delta/3)$ for the methylene and methyl protons of *n*-alkanes with the carbon number from 8 to 32 in urea-d_4 adduct at 25 °C.

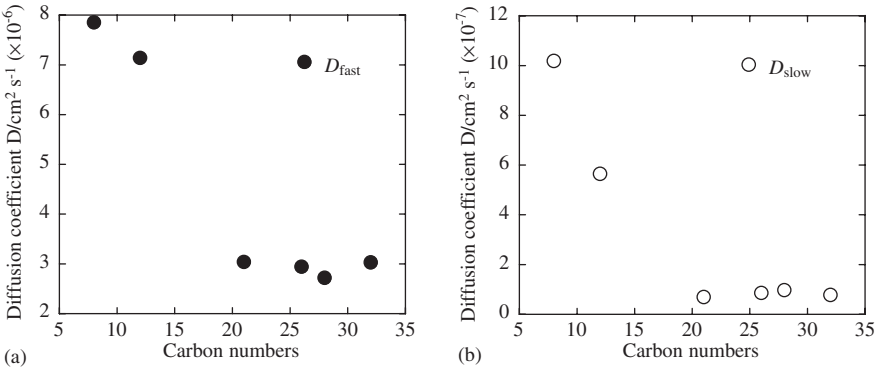

Fig. 54. Diffusion coefficients of the fast diffusion component (a) and the slow diffusion component (b) for *n*-alkanes with the carbon number from 8 to 32 in urea-d_4 adduct channels at 25 °C.

order of $10^{-6}\,cm^2\,s^{-1}$. For example, the diffusion coefficient of pure *n*-$C_{21}H_{44}$ was determined to be $D = 2.58 \times 10^{-6}\,cm^2\,s^{-1}$ in the rotator phase at 37 °C. In the rotator phase, the all-*trans* zigzag *n*-alkane chains considered here are hexagonally surrounded by six neighboring *n*-alkanes with the all-*trans* zigzag form. This is roughly similar to that for the *n*-alkane chain in a long hexagonal channel of the urea adduct. Thus, the *D* value of *n*-$C_{21}H_{44}$ for the fast diffusion component along a channel of the urea adduct is somewhat larger than that of pure *n*-$C_{21}H_{44}$ in the rotator phase.

Fig. 55 shows the plots of the fraction of the two diffusion components against the carbon number, as determined from Eq. (2). As seen in Fig. 55, as the carbon number increases from 8 to 28, the fraction of the slow diffusion component becomes larger gradually, and at the carbon number of 32 the fraction of the slow diffusion component is about 80%.

In order to understand the diffusion process, we can calculate the activation energy *E* for diffusion by using Eq. (10). The activation energy obtained from the plots of ln *D* against $1/T$ (the Arrhenius plots) for *n*-$C_{21}H_{44}$ in urea/*n*-$C_{21}H_{44}$ adduct channels and pure *n*-$C_{21}H_{44}$ in the rotator phase are shown in Fig. 56. The slope becomes $-E/k$. The determined *E* values for the *n*-$C_{21}H_{44}$ in the urea/*n*-$C_{21}H_{44}$ adduct channels and pure *n*-$C_{21}H_{44}$ in the rotator phase are 0.6 and 4.7 kcal mol^{-1}, respectively. The *E* value of pure *n*-$C_{21}H_{44}$ in the rotator phase is much larger than that of *n*-$C_{21}H_{44}$ in the urea/*n*-$C_{21}H_{44}$ adduct channels. This indicates that *n*-$C_{21}H_{44}$ chains in urea adduct channels easily diffuse as compared with pure *n*-$C_{21}H_{44}$ chains in the rotator phase. This is because the intermolecular interactions between pure *n*-$C_{21}H_{44}$ chains in the rotator phase are removed by the urea channel walls.

3.5.2. *Diffusing-time dependence of the diffusion coefficients*

The diffusion of *n*-alkanes is strongly influenced by intermolecular interactions and by interactions between *n*-alkane molecules and the wall of the channel in the urea

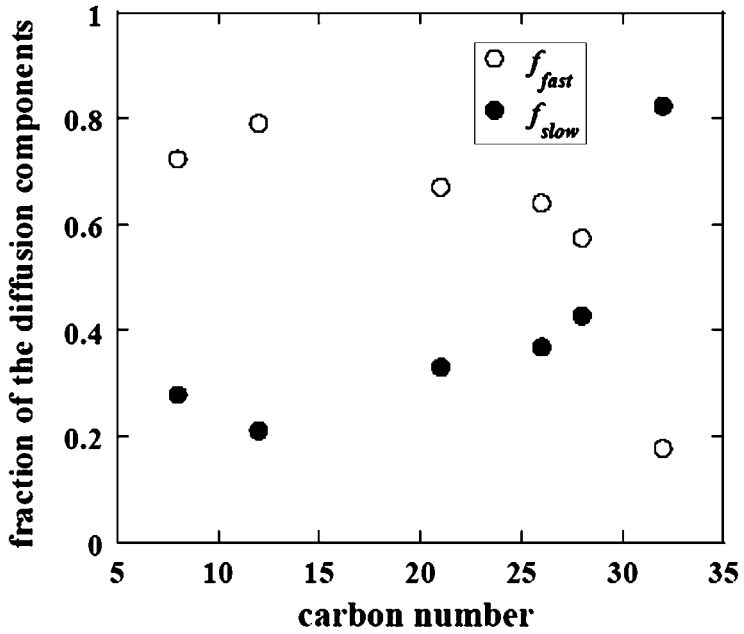

Fig. 55. Dependence of the fractions of the fast (○) and slow (♦) diffusion components on carbon number from 8 to 32 in urea-d_4 adduct at 25 °C.

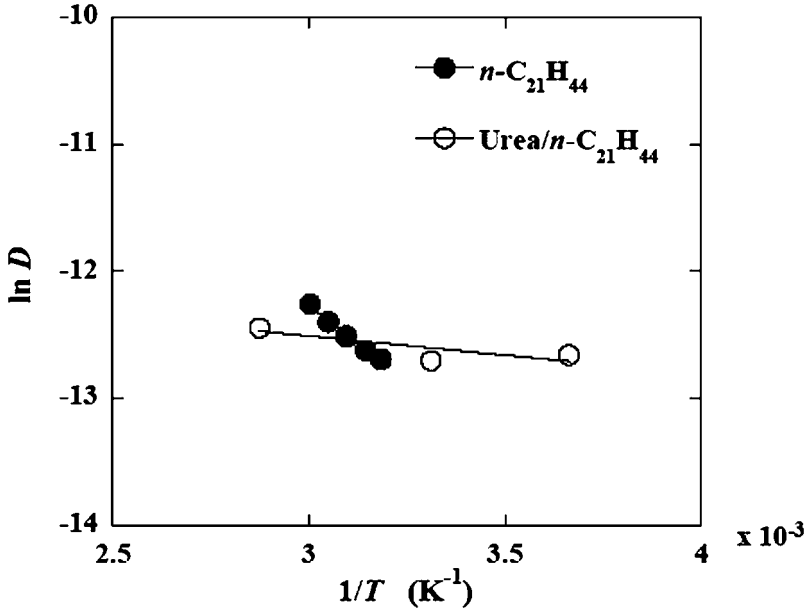

Fig. 56. The Arrhenius plots of ln D against $1/T$ of n-$C_{21}H_{44}$ in the urea/n-$C_{21}H_{44}$ adduct channels and pure n-$C_{21}H_{44}$ in the rotator phase.

molecules. It means that the diffusion coefficient of the *n*-alkane molecules may be sensitively dependent on the diffusing time Δ. Therefore, the diffusing time Δ dependence of the diffusion coefficients of *n*-$C_{12}H_{26}$ and *n*-$C_{26}H_{54}$ in the urea-d_4 adduct channels has been studied in order to understand the diffusional behavior of the *n*-alkanes molecules confined in the urea adduct channels.

Fig. 57 shows the plots of $\ln[A(G)/A(0)]$ against $\gamma^2G^2\delta^2(\Delta-\delta/3)$ in the Δ range of 5–200 ms. It is seen that *n*-$C_{12}H_{26}$ molecules in the urea-d_4 adduct have two diffusion components at 5–200 ms. The determined *D* values and the fractions of the corresponding two diffusion components of *n*-$C_{12}H_{26}$ in the urea-d_4 adduct are summarized in Table 16. For convenience, the two diffusion coefficients of *n*-$C_{12}H_{26}$ in the urea-d_4 adduct are plotted against the diffusing time Δ in Fig. 58. As the diffusing time increases, both of the *D* values for the fast and slow diffusion components of *n*-$C_{12}H_{26}$ in urea-d_4 adduct decrease. These results can be explained as follows. *n*-Alkane molecules are diffusing in a channel and colliding with neighboring molecules during the diffusing time. As the diffusing time increases, the collisions between *n*-alkane molecules increase and the apparent diffusion coefficients decrease. The *D* values for the two diffusion components are not averaged out in the Δ range from 5 to 200 ms and decrease continuously with an increase in *D*. If *n*-alkane molecules diffuse for a sufficiently long diffusing time Δ, the observed diffusion coefficient may become an averaged value.

In the same manner, *n*-$C_{26}H_{54}$ in the urea-d_4 adduct has been measured as a function of the diffusing time Δ (i.e., the field-gradient pulse interval time) by the PFGSE ^{1}H NMR method. The diffusion coefficient measurements of *n*-$C_{26}H_{54}$ in the urea-d_4 adduct have been performed at Δ = 5–40 ms. Fig. 59 shows the plots of $\ln[A(G)/A(0)]$ against $\gamma^2G^2\delta^2(\Delta-\delta/3)$ in the Δ range of 5–40 ms. It is seen that

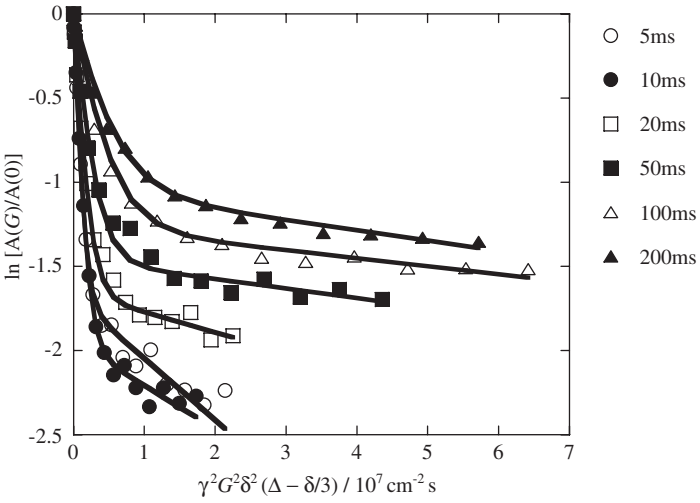

Fig. 57. The plots of $\ln[A(G)/A(0)]$ of urea/*n*-$C_{12}H_{26}$ against $\gamma^2G^2\delta^2(\Delta-\delta/3)$ at 25 °C on the gradient pulse interval Δ.

Table 16. Determined diffusion coefficients D^a of n-$C_{12}H_{26}$ in urea-d_4/n-$C_{12}H_{26}$ adduct channels as a function of the diffusing time Δ at 25°C

Δ (ms)	Diffusion coefficient D/cm^{2}s^{-1}		Fraction	
	D_{fast} ($\times 10^{-6}$)	D_{slow} ($\times 10^{-7}$)	f_{fast}	f_{slow}
5	12.3	3.1	0.83	0.17
10	9.8	1.5	0.87	0.13
20	8.5	1.2	0.81	0.19
50	7.1	1.0	0.72	0.28
100	3.6	0.8	0.70	0.30
200	2.8	0.6	0.64	0.36

[a]The experimental errors for the diffusion coefficient measurements are ca. 10%.

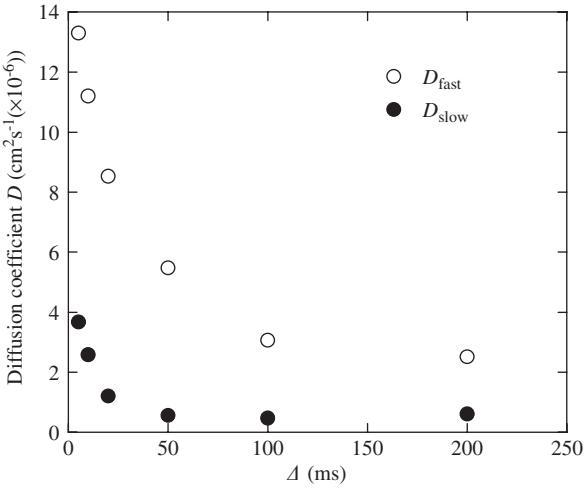

Fig. 58. Diffusing-time Δ dependence of diffusion coefficients of the fast and slow diffusion components of n-$C_{12}H_{26}$ in urea-d_4 adduct.

n-$C_{26}H_{54}$ molecules in the urea-d_4 adduct have two diffusion components at $\Delta = 5$, 10, 20 and 30 ms, but have a single diffusion component at $\Delta = 40$ ms. The determined D values and the fractions of the corresponding two diffusion components of n-$C_{26}H_{54}$ in the urea-d_4 adduct are summarized in Table 17.

Fig. 60 shows the diffusing-time dependence of the D values for the fast and the slow diffusion components of n-$C_{26}H_{54}$ in the urea-d_4 adduct, where the right hand side is an expansion of the left hand diagram. As the diffusing time increases, both of the D values for the fast and the slow diffusion components of n-$C_{26}H_{54}$ in urea-d_4 adduct decreases. This can be explained by the following fact that n-alkane molecules diffusing in a channel are colliding with neighboring molecules.

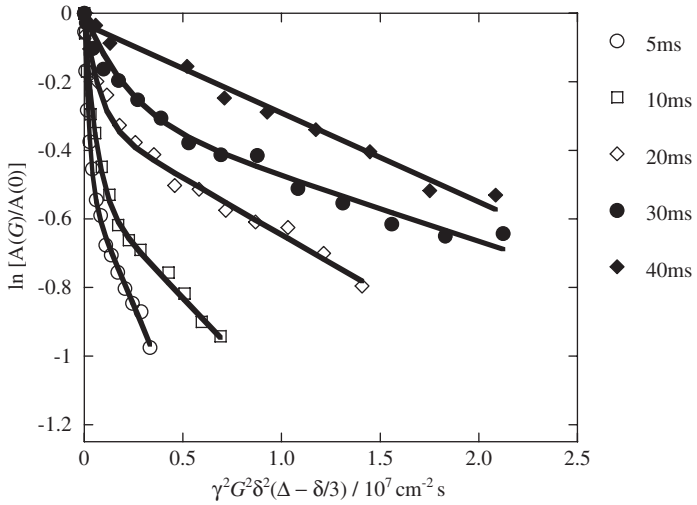

Fig. 59. The plots of $\ln[A(G)/A(0)]$ of urea-d_4/*n*-$C_{26}H_{54}$ against $\gamma^2G^2\delta^2(\Delta-\delta/3)$ at 25 °C on diffusing time Δ.

Table 17. Determined diffusion coefficients D^a of *n*-$C_{12}H_{26}$ in urea-d_4/*n*-$C_{12}H_{26}$ adduct channels as a function of the diffusing time Δ at 25°C

Δ (ms)	Diffusion coefficient D/cm^{2}s^{-1}		Fraction	
	D_{fast} ($\times 10^{-6}$)	D_{slow} ($\times 10^{-7}$)	f_{fast}	f_{slow}
5	9.9	1.26	0.31	0.69
10	4.4	0.61	0.30	0.70
20	1.8	0.26	0.24	0.76
30	0.5	0.22	0.14	0.86
40	–	0.31	–	1.00

[a]The experimental errors for the diffusion coefficient measurements are ca. 10%.

The diffusion coefficients for the two diffusion components of *n*-$C_{26}H_{54}$ in the urea-d_4 adduct become constant at $\Delta = 40$ ms the diffusion has a single diffusion component, i.e., the two diffusion coefficients for the fast and the slow diffusion components are averaged out.

The above results show the most likely evidence of restricted diffusion because the *n*-alkane molecules are confined in the urea channel. In the appropriately short diffusing time Δ, the diffusions of *n*-alkane molecules in the end parts and in the inner part of a channel are observed to be different. In the case of a long diffusing time Δ, the diffusions of the *n*-alkane molecules in the end parts and in the inner part of a channel are observed to be averaged out.

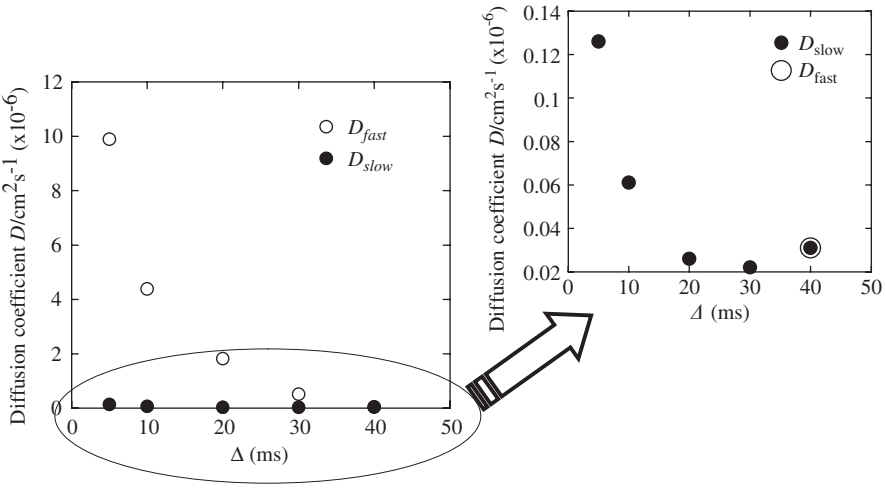

Fig. 60. Diffusing-time Δ dependence of diffusion coefficients of the fast and the slow diffusion components of n-$C_{26}H_{54}$ in urea-d_4 adduct.

3.6. Diffusion of small *n*-alkanes in the channels of polyester fiber

It has been shown that probe methane and ethane molecules diffuse in the cylindrical channel cavities formed in the hexagonal columnar phase of oriented poly(*p*-biphenylene terephthalate) (PBpT-O12) (Fig. 61) with *n*-dodecyl side chains.[184,185] This forms a thermotropic liquid crystalline phase by interactions between the rigid rod-like main chains and the flexible side chains above a specified temperature.[186,187] The polyester forms the columnar phase, the nematic phase and the isotropic phase with temperature elevation. In the columnar phase, a honeycombed network is formed which has long cylindrical channel cavities with a diameter of about 3 nm as viewed from the top (Fig. 62). The polyesters having such cavities may be expected to be smart membrane materials. Probe molecules diffusing in long channel cavities are strongly affected by interactions with the channel cavities. Therefore, we need to elucidate the structure and dynamics of PBpT-O12 forming long channel cavities and the diffusion process of probe molecules with different sizes in the long channel cavities.

The structural change of PBpT-O12 at the phase transition has been clarified by solid-state ^{13}C NMR.[188] It has been shown that *n*-dodecyl chains in the channel cavities of oriented PBpT-O12 in the hexagonal columnar phase take two types of regions at room temperature; one is the crystalline region with the all-*trans* zigzag form and the another is the mobile region where fast exchange between the *trans* and *gauche* conformations exists.

It has been shown by the PFGSE ^1H NMR method that methane and ethane molecules with small size in the channel cavities are diffusing in the direction parallel and perpendicular to the channel cavity axis. The diffusion of methane

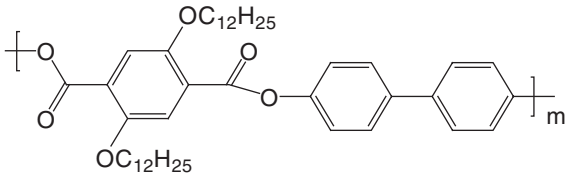

Fig. 61. Structure of poly(*p*-biphenylene terephthalate) with long *n*-alkyl side chain attached to the terephthalate moiety.

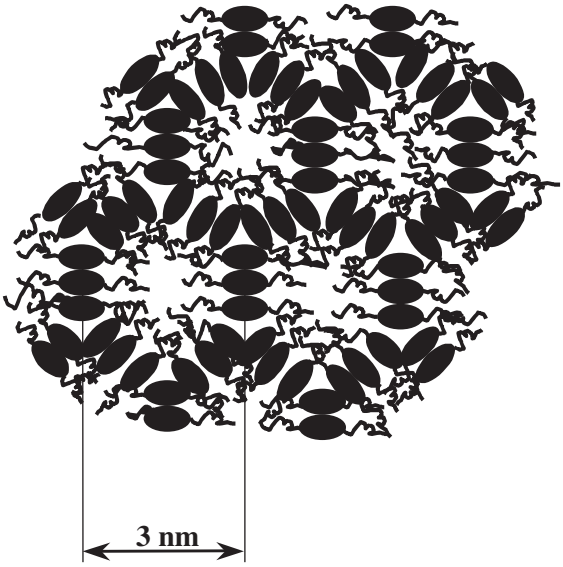

Fig. 62. Schematic diagram for the space in the long channel cavity in the columnar phase of PBpT-O12 viewed from the top. Closed ellipsoids: the main chain, and curved strings linked with the closed ellipsoid: *n*-alkyl side chains.

molecules in the direction perpendicular to the channel cavity axis comes from the existence of defects in the wall of the channels.[184,185] In addition, it is very important to clarify the size of the defects by using gaseous probe molecules with a large size, in order to characterize the nature of the channels in the polyester.

PBpT-O12 in the nematic liquid crystalline phase at 160 °C has been mechanically stretched to obtain highly oriented fibers and then cooled to room temperature. The average diameter of the PBpT-O12 fibers is about 0.6 mm. Furthermore, the channel cavity axis is oriented in the direction parallel to the oriented PBpT-O12 fiber axis. The PBpT-O12 fibers were cut into pieces with a length of about 4 mm, and then ca. 40 pieces of them were placed in an NMR tube, with an the outside diameter of 5 mm, in the direction parallel or perpendicular to the NMR tube. The schematic diagram for an NMR tube with the PBpT-O12 fibers is shown in Fig. 63. After degassing in a vacuum for 12 h, methane or ethane gas was charged into the NMR tube at ca. 1 atm, and the NMR tube was sealed off.

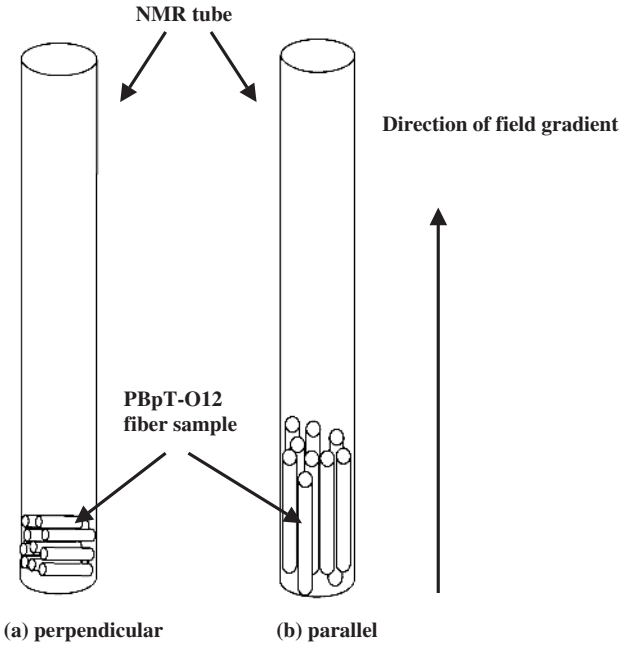

Fig. 63. The schematic diagram for an NMR tube with 50 PBpT-O12 fibers.

3.6.1. *Diffusion of methane in the channels*

The field-gradient pulses were applied to the direction in parallel to the channel cavity axis and thus the diffusion coefficient of methane molecules diffusing in the direction parallel to the channel cavity axis was determined. Fig. 64 shows typical PFGSE ^{1}H NMR spectra of methane molecules charged into the channel cavities in the direction parallel to the channel cavity axis by varying G at $\Delta = 4\,\text{ms}$. The signals for the main chain and *n*-alkyl side chains of the polyester do not appear in the spectra because their spin–spin relaxation times T_2 are very short due to low mobility and the corresponding signals become very broad. Three signals at about 0.5, 2.5 and 5 ppm appear in the spectrum at $G = 0\,\text{T m}^{-1}$. The intense signal at 2.5 ppm is rapidly decayed by application of a field-gradient and disappears completely at $G = 0.714\,\text{T m}^{-1}$. This means that the diffusion coefficient is very large ($0.22\,\text{cm}^2\,\text{s}^{-1}$). This agrees with the ^{1}H chemical shift value (2.5 ppm) and the diffusion coefficient ($0.22\,\text{cm}^2\,\text{s}^{-1}$) of pure methane gas in an NMR tube. The intense signal at 2.5 ppm can be assigned to methane gas in spaces among the PBpT-O12 fibers in an NMR tube. The weak signal at 5 ppm is very close to the chemical shift position (~4.8 ppm) of water molecules in polymer gels reported previously.[28,30] Therefore, the weak high frequency signal at 5 ppm may be assigned to water in the PBpT-O12 fibers. The signal at 0.5 ppm slowly decayes with an increase in the field-gradient strength. Therefore, this signal can be assigned to the methane molecules in the channel cavities, which are very slowly diffusing.

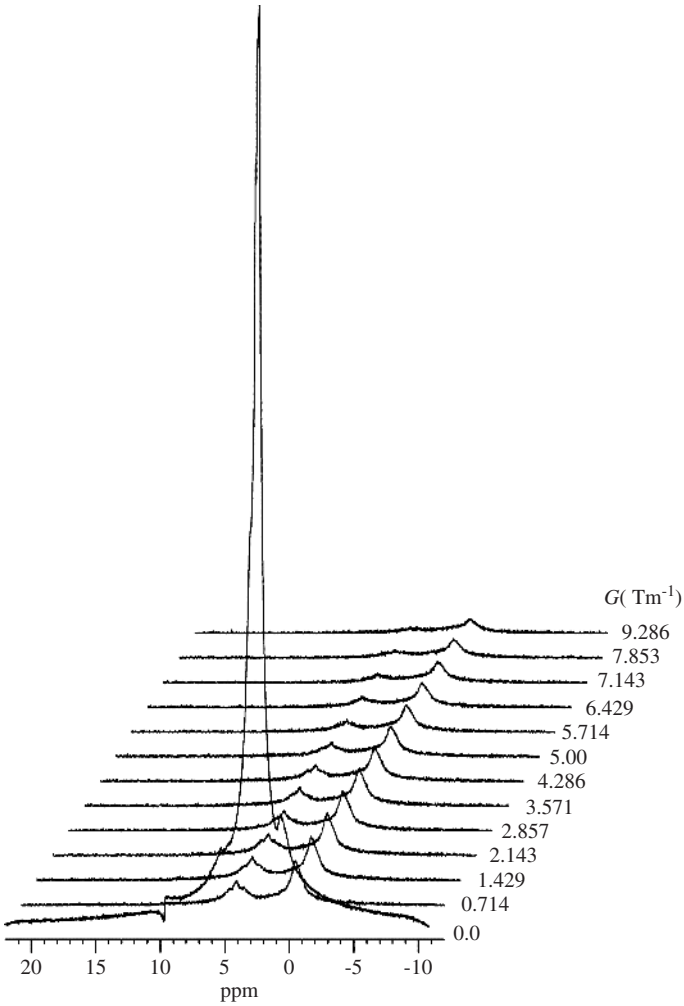

Fig. 64. PFGSE ^{1}H NMR spectra of methane molecules in the direction parallel to the cylindrical channel cavity axis at $\Delta = 4$ ms by varying field-gradient strength (G) at 25 °C.

The plot of $\ln[A(G)/A(0)]$ against $\gamma^2 G^2 \delta^2(\Delta - \delta/3)$ for the methane molecules in the cylindrical channel cavities was made. It is found that the experimental data lie on a straight line. This shows that methane molecules in the channel cavities have a single diffusion component for the diffusing time Δ used here. Hence, the diffusion coefficient ($D_{||}$) for methane molecules in the channel cavities in the direction parallel to the channel cavity axis at $\Delta = 4$ ms was determined from the slope of the straight line by using Eq. (1) to be $D_{||} = 4.1 \times 10^{-7}\,\mathrm{cm^2\,s^{-1}}$. This value is much smaller than diffusion coefficient of pure methane gas as above-mentioned. This means that the diffusion of the methane molecules is strongly restricted by

intermolecular interactions between the methane molecules and, especially, the long *n*-dodecyl side chains of the polyester.

In order to obtain useful information about the nature of the inside of the channel cavities, the diffusion coefficients of methane molecules in the channel cavities in the direction parallel to the channel cavity axis were measured as a function of the diffusing time Δ. Fig. 65 shows the Δ dependence of the diffusion coefficients for methane molecules obtained by varying $\Delta = 4$, 6, 8, 10 and 12 ms. From the plots of $\ln[A(G)/A(0)]$ against $\gamma^2G^2\delta^2(\Delta-\delta/3)$, methane molecules in the channel cavities are shown to have a single diffusion component for these diffusing times. The diffusion coefficients are not almost dependent on Δ within the experimental error.

It is known that the diffusion distance d contains useful information on the inhomogeneity of the network size of chemically cross-linked polymer gels. Here, we are concerned with the channel cavity from the aspect of the diffusion distance of methane molecules in the cavity. The diffusion distance d of methane molecules in the channel cavities can be expressed by using Eq. (4). The d values obtained from the experimental results at $\Delta = 4$, 6, 8, 10 and 12 ms are estimated to be 573, 710, 885, 894 and 1,073 nm, respectively, as shown in Fig. 66. In the unrestricted diffusion process, the plots of the diffusion distance is linearly proportional to $\Delta^{1/2}$. As seen from Fig. 66, the diffusion distance of the methane molecules proportionally increases with an increase in the value of $\Delta^{1/2}$. This result shows that the diffusion process in this experimental diffusion time range below $\Delta = 12$ ms is in the unrestricted diffusion region.

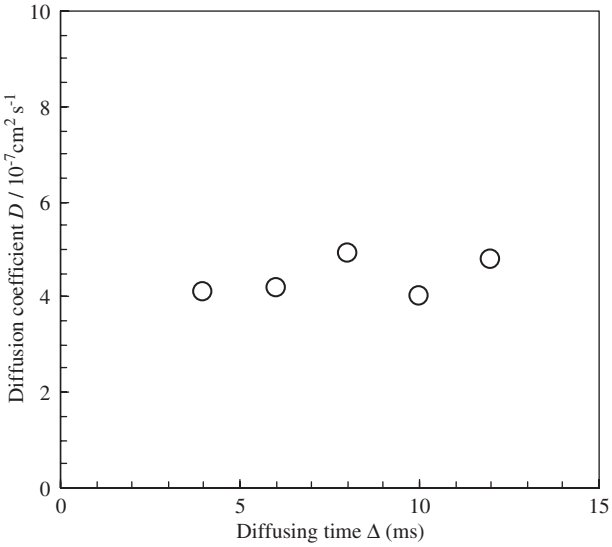

Fig. 65. Dependence of diffusion coefficients ($D_{||}$) of methane molecules in the direction parallel to the cylindrical channel cavity axis on the diffusing time Δ.

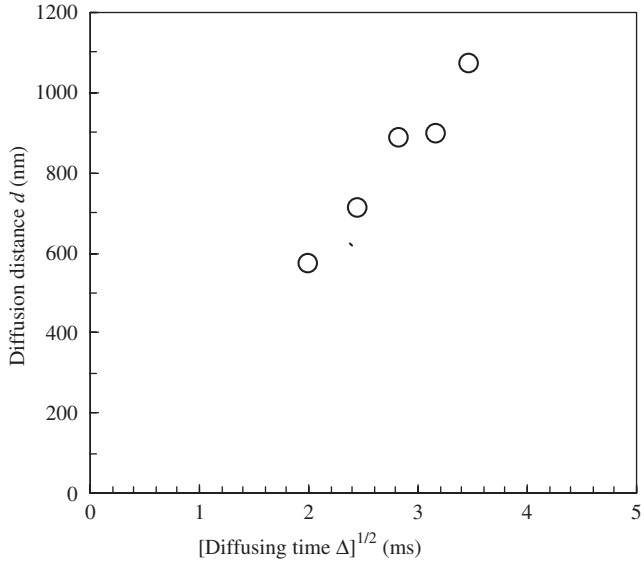

Fig. 66. Dependence of diffusion distance d of methane molecules in the direction parallel to the cylindrical channel cavity axis on a square root of the diffusing time $\Delta^{1/2}$.

If methane molecules are trapped and diffusing in a cylindrical channel cavity with a diameter of ca. 3 nm,[187] the diffusion coefficient ($D_{\perp}$) of the methane molecules in the cavity in the direction perpendicular to the channel cavity axis are largely decreased and then approach zero at long diffusing times, Δ, beyond 4 ms used in this experiment as seen from Eq. (2). Further, the diffusion distance d is independent of the diffusion time Δ and may become ca. 3 nm. However, if the methane molecules are not trapped and diffusing, the methane molecules may diffuse through the wall of the channel cavity to the neighboring channel cavities and the diffusion distance d is increases with an increase in the diffusing time Δ.

In order to measure the diffusion coefficient ($D_{\perp}$) of methane molecules in the direction perpendicular to the channel cavity axis, ca. 40 pieces of the oriented PBpT-O12 fibers were placed in an NMR tube in the direction perpendicular to the tube axis and the field-gradient pulses were applied in the direction parallel to the NMR tube. From such PFGSE ^{1}H NMR experiments, the $D_{\perp}$ values of the methane molecules are determined. Fig. 67 shows the PFGSE ^{1}H NMR spectra of methane molecules in the channel cavities in the direction perpendicular to the channel cavity axis by varying G at $\Delta = 6$ ms. In the spectrum at $G = 0\,\mathrm{T\,m^{-1}}$, an intense signal appears at about 2.5 ppm and a weak shoulder on the low frequency side of the intense signal. The intense peak at 2.5 ppm can be assigned to methane gas in spaces among the PBpT-O12 fiber pieces in the NMR tube, this is drastically decayed at $G = 0.733\,\mathrm{T\,m^{-1}}$. Another shoulder signal can be assigned to methane molecules in the channel cavities and this slowly decays with an increase in field-gradient strength. The weak broad signal at 5 ppm appears in the spectra under G (corresponding to water in the polyester).

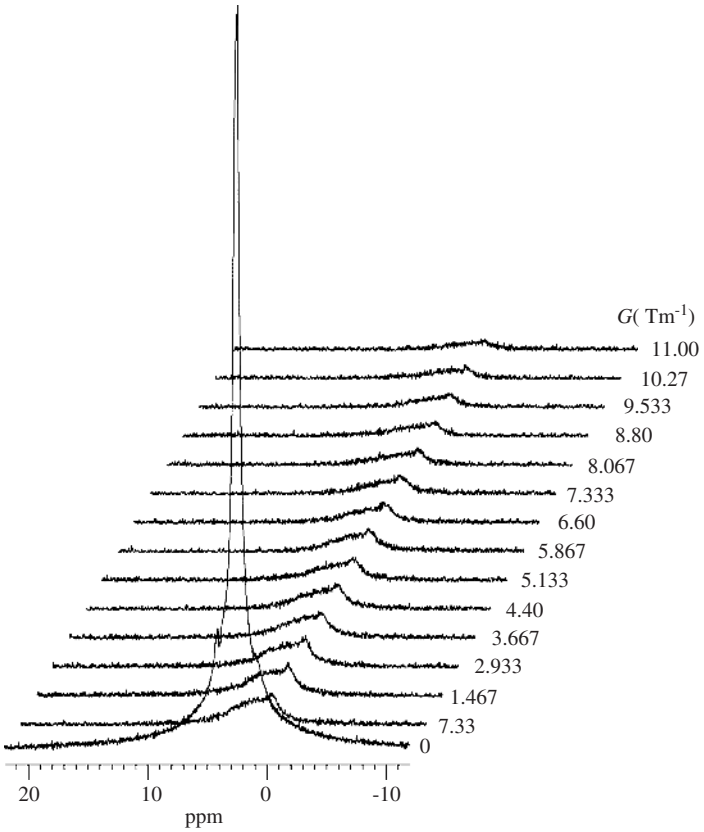

Fig. 67. PFGSE ^{1}H NMR spectra of methane molecules in the direction perpendicular to the cylindrical channel cavity axis on $\Delta = 6$ ms by varying field-gradient strength (G) at 25 °C.

The plot of $\ln[A(G)/A(0)]$ against $\gamma^2G^2\delta^2(\Delta-\delta/3)$ for the above-mentioned signal of the methane molecules in the direction perpendicular to the channel cavity axis are plotted, the experimental data lie on a straight line. This shows that methane molecules in the channel cavities have a single diffusion component in the direction perpendicular to the channel cavity axis for the diffusion time used here. From the slope of the straight line, the diffusion coefficient ($D_\perp$) for methane molecules in the direction perpendicular to the channel cavity axis at $\Delta = 6$ ms is determined to be $6.5 \times 10^{-8}\,\mathrm{cm^2\,s^{-1}}$. This value is much smaller than the diffusion coefficient ($D_{||} = 4.2 \times 10^{-7}\,\mathrm{cm^2\,s^{-1}}$) of the methane molecules in the direction parallel to the channel cavity axis. The $D_{||}/D_\perp$ ratio at $\Delta = 6$ ms becomes 6.5. This means that the diffusion of methane molecules in the direction perpendicular to the channel cavity axis is disturbed by the long *n*-alkyl side chains that are undergoing fast exchange between *trans* and *gauche* conformations. Here, we must check whether methane molecules diffusing in the channel cavities can move through the wall of the channel cavity to the neighboring channel cavities. This may be clarified by determination of

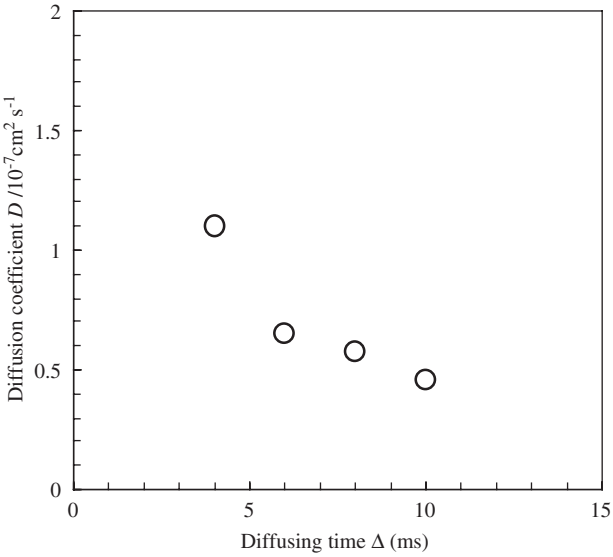

Fig. 68. Dependence of diffusion coefficients ($D_\perp$) of methane molecules in the direction perpendicular to the cylindrical channel cavity axis on the diffusing time Δ.

the $D_\perp$ values with a changing diffusing time Δ. The determined diffusion coefficients ($D_\perp$) of the methane molecules are plotted against the diffusing time Δ in Fig. 68. From these plots, the $D_\perp$ values decrease with an increase in Δ within the Δ measurement range. The diffusing distance d estimated from the diffusion coefficient determined at $\Delta = 6$ ms by using Eq. (4) becomes 279 nm. As shown in Fig. 69, the diffusion distance d slightly increase with an increase in Δ. This diffusion distance is much larger than the cavity diameter (~3 nm) in the hexagonal columnar phase of the PBpT-O12 polyester. Therefore, it can be said that the wall of the channel cavities has some defects and the methane molecules can pass through these defects. The methane molecules in the channel cavities are clearly moving through the wall of the channel cavity to neighboring channel cavities in the direction perpendicular to the channel cavity axis in a rod of oriented PBpT-O12 polyester with a diameter of 0.59 mm ($= 5.9 \times 10^5$ nm).

3.6.2. *Diffusion of ethane in the channels*

The diffusion coefficient of ethane molecules diffusing in the direction parallel to the channel ($D_{||}$) is determined by using an NMR tube with ca. 40 pieces of PBpT-O12 fibers placed in the direction parallel to the tube axis. Also for ethane molecules diffusing through defects of the wall of the channel cavity in the direction perpendicular to the channel cavities ($D_\perp$). The D values were determined by using the relationship between signal intensity and field-gradient parameters at 25 °C. The appropriate δ, Δ and G values for measuring precise diffusion coefficients of pure ethane gas and ethane molecules in the channel cavities of PBpT-O12 fibers must be

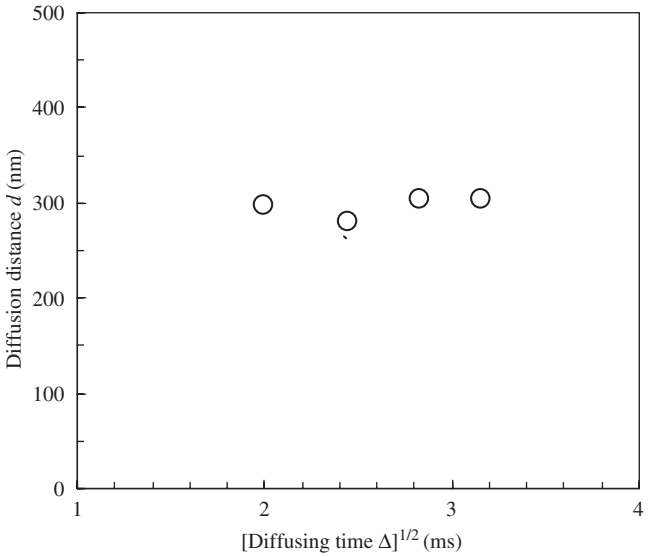

Fig. 69. Dependence of diffusion distance d of methane molecules in the direction perpendicular to the cylindrical channel cavity axis on a square root of the diffusing time $\Delta^{1/2}$.

chosen because their diffusion coefficients are considerably different from each other. For example, for absolutely large D measurements, absolutely small δ and G values must be used. The δ, Δ and G values for pure ethane gas are 0.16, 6 ms and 0 to 0.30 T m^{-1}, respectively, and those for ethane molecules in the channel cavities are 1 and 3, 6 ms and 0 to 11.00 T m^{-1}, respectively. The plots of $\ln[A(G)/A(0)]$ against $\gamma^2G^2\delta^2(\Delta-\delta/3)$ give a straight line with a slope of $-D$. The experimental errors are below 10%.

If the probe ethane molecules diffuse over a long time Δ, the self-diffusion coefficient may become an averaged value owing to the diffusion through the places with different environments in the long cavities. On the timescale of t the diffusion coefficient corresponds to a Gaussian distribution of a squared deviation as expressed by $\langle z^2\rangle = 2Dt$ according to the Einstein equation, where $\langle z^2\rangle$ is the mean square displacement in the z direction from the starting point after the diffusing time Δ. In this measurement, t is Δ. The $\langle z^2\rangle^{1/2}$ value gives us a diffusion distance (length) d. Therefore, the diffusion distance d of ethane molecules in the channel cavities can be expressed by using Eq. (4).

Fig. 70 shows typical PFGSE ^{1}H NMR spectra of ethane gas charged in an NMR tube at ca. 1 atm by varying G from 0 to 0.30 T m^{-1} at $\Delta = 0.16$ ms at 25 °C. The peak of pure ethane gas appears at 3.1 ppm. The intensity of the corresponding peak is largely reduced with an increase in G. As seen from Eq. (2), this means that ethane molecules are diffusing. The plots of $\ln[A(G)/A(0)]$ against $\gamma^2G^2\delta^2(\Delta-\delta/3)$ for ethane gas become approximately a straight line within experimental errors. The diffusion coefficient of pure ethane gas was determined from the slope ofthe straight line by using Eq. (1) to be $D = 0.07\,\mathrm{cm^2\,s^{-1}}$. It is shown that the

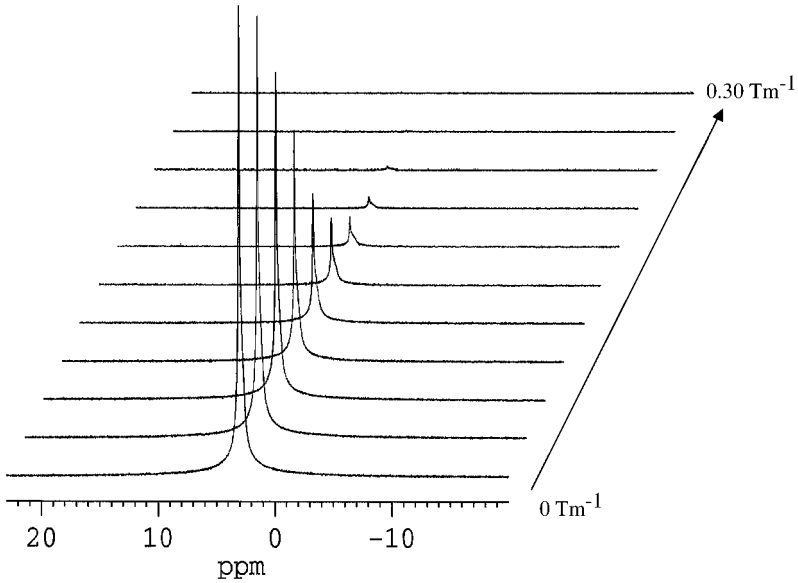

Fig. 70. PFGSE ^{1}H NMR spectra of ethane gas by varying field-gradient strength G from 0 to 30 T m^{-1} at $\Delta = 0.16$ ms and at 25 °C.

self-diffusion of pure ethane gas is very fast. There appears to be no report on the self-diffusion coefficient of pure ethane gas at a pressure of 1 atm. However, it is reported that the mutual diffusion coefficient of a mixture of ethane and nitrogen gases is 0.153 cm^2 s^{-1} at 1 atm and at 25 °C as extrapolated from the experimental data over a wide range of temperatures by a chromatographic method.[189] This value is near the diffusion coefficient determined in our measurement.

Fig. 71(a) shows typical PFGSE ^{1}H NMR spectra of ethane molecules in the cylindrical channel cavities in the direction perpendicular to the channel cavity axis obtained by varying G from 1.22 to 11.00 T m^{-1} at $\Delta = 6$ ms and $\delta = 3$ ms, respectively. The peak of the ethane molecules in the channel cavities appears at about 1 ppm, and is at a lower frequency than that of free ethane gas due to specific interactions between ethane molecules and channel cavities. The protons of the main chain and the *n*-alkyl side chains of the polyester have short spin–spin relaxation times T_2 due to low mobility. Thus their signals disappear completely in the spectra under the present measurement conditions. An intense peak of the ethane gas associated with the outside part of the fibers disappears completely at $G = 1.22$ T m^{-1}. This means that the diffusion coefficient is very large. The broad ^{1}H signal at about 1 ppm appears in the spectrum at $G = 1.22$ T m^{-1}, and its intensity is decreases with an increase in G. This means that ethane molecules are very slowly diffusing. The plots of $\ln[A(G)/A(0)]$ against $\gamma^2G^2\delta^2(\Delta-\delta/3)$ for ethane molecules in the direction perpendicular to the channel cavity axis approximately lie on a straight line within experimental errors. Ethane molecules in the channel cavities have a single diffusion component during the diffusing time Δ used here. The

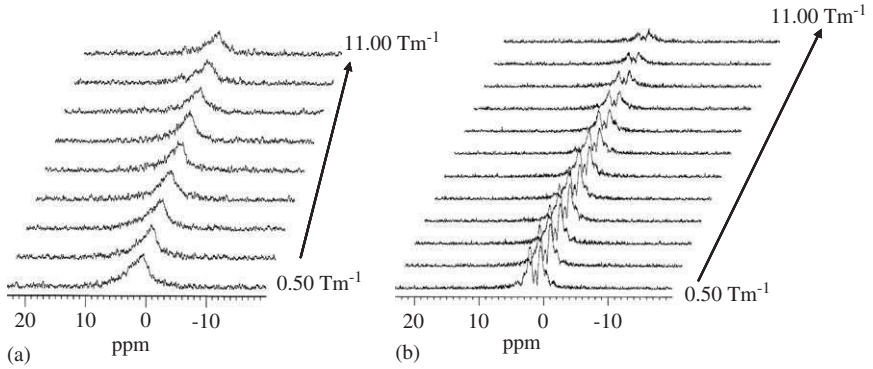

Fig. 71. PFGSE ^{1}H NMR spectra of ethane molecules in the direction perpendicular (a) to the cylindrical channel cavity axis at 25 °C. G varies from 1.22 to 11.00 T m^{-1} at $\Delta = 6$ ms and in the direction parallel (b) to the cylindrical channel cavity axis at 25 °C. G varies from 0.50 to 11.00 T m^{-1} at $\Delta = 6$ ms.

diffusion coefficient ($D_\perp$) for ethane molecules in the channel cavities in the direction perpendicular to the channel cavity axis at $\Delta = 6$ ms was determined from the slope of the straight line, by using Eq. (1), to be $D_\perp = 9.5 \times 10^{-9}$ cm^2 s^{-1}. The D value is much smaller than that of pure ethane gas as above-mentioned. Nevertheless, this means that the ethane molecules are not trapped, but diffuse through the wall of the channel cavity to the neighboring channel cavities. By using $D_\perp = 9.5 \times 10^{-9}$ cm^2 s^{-1}, $\Delta = 6$ ms and Eq. (4), we can estimate the diffusion distance d to be 107 nm. Therefore, it can be said that the wall of the channel cavity has some defects and the ethane molecules can pass through these defects. Furthermore ethane molecules in the channel cavities are clearly moving through the wall of the channel cavities to neighboring channel cavities in the direction perpendicular to the channel cavity axis in a rod of oriented PBpT-O12 polyester with a diameter of 0.6 mm ($= 6.0 \times 10^5$ nm). It is assumed that the defects come from the terminals of the polyester chains which form the long channels.

Fig. 71(b) shows typical PFGSE ^{1}H NMR spectra of ethane molecules charged into the channel cavities in the direction perpendicular to the channel cavity axis by varying G from 0.50 to 11.00 T m^{-1} at $\Delta = 6$ ms and $\delta = 3$ ms. The ethane signal splits into two intense peaks due to the inhomogeneous distribution of the bulk magnetic susceptibility for the sample in the NMR tube. The plots of $\ln[A(G)/A(0)]$ against $\gamma^2 G^2 \delta^2 (\Delta - \delta/3)$ for ethane molecules in the direction parallel to the channel cavity axis lie on a straight line within experimental errors. Ethane molecules in the channel cavities have a single diffusion component for the diffusing time Δ used here. The diffusion coefficient ($D_{||}$) for ethane molecules in the channel cavities in the direction parallel to the channel cavity axis at $\Delta = 6$ ms was determined from the slope of the straight line by using Eq. (1) to be $D_{||} = 2.9 \times 10^{-7}$ cm^2 s^{-1}. This D value is much smaller than that of ethane gas as above-mentioned. This means that the diffusion of the ethane molecules is strongly restricted by intermolecular

interactions between the ethane molecules and the long *n*-dodecyl side chains of the polyester. Further, it can be said that the $D_{||}$ value is much larger than the $D_{\perp}$ value. The ratio of $D_{||}/\ D_{\perp}$ is 31. By using $D_{||} = 2.9 \times 10^{-7}\,\mathrm{cm^2\,s^{-1}}$, $\Delta = 6\,\mathrm{ms}$ and Eq. (2), we can estimate the diffusion distance d to be 590 nm. Therefore, it can be said that the inside of the channel cavity is an anisotropic field for the diffusion process.

As compared with the previous results for the diffusion of methane in the channel cavities of PBpT-O12, the diffusion coefficients $D_{||}$ and $D_{\perp}$ of the ethane molecules are much smaller than those of methane ($D_{||} = 4.2 \times 10^{-7}\,\mathrm{cm^2\,s^{-1}}$ and $D_{\perp} = 6.5 \times 10^{-8}\,\mathrm{cm^2\,s^{-1}}$), and the ratio of $D_{||}/D_{\perp}$ for ethane is much larger than that for methane ($D_{||}/D_{\perp} = 6.5$). This means that the cannel cavities of PBpT-O12 have a high anisotropy in diffusion and the ability to recognize molecular size.

4. CONCLUSIONS

We have described in this review how high field-gradient NMR spectroscopy can give us new and useful information about the diffusion process of soft polymer systems, such as liquid crystals and gels, which are one of most important fields of polymer science. This approach is expected to the applied in various fields with new dimensions.

REFERENCES

1. (a) Y. Osada and K. Kajiwara, *Polymer Gels Handbook*, Academic Press, New York, 2000; (b) D. DeRossi, K. K Kajiwara, Y. Osada and A. Yamauchi, *Polymer Gels-Fundamentals and Biochemical Applications*, Plenum Press, New York, 1991; (c) P. J. Collings and M. Hird, *Introduction to Liquid Crystals*, Taylor and Francis, London, 1998; (d) V. P. Shibaeb and L. Lan, *Liquid Crystalline and Mesomorphic Polymers*, Springer-Verlag, Berlin, 1993.
2. (a) I. Ando and T. Asakura, eds., *Solid State NMR of Polymers*, Elsevier Science, Amsterdam, 1998; (b) I. Ando, M. Kobayashi, M. Kanekiyo, S. Kuroki, S. Ando, S. Matsukawa, H. Kurosu, H. Yasunaga and S. Amiya, *Experimental Methods in Polymer Science*, Wiley, New York, 1999 Chapter 4; (c) D. M. Grant and R. K. Harris (Eds.), *Encyclopedia of NMR*, Vol. 9, Interscience, New York, (B. C. Gerstein (ed.), Advance in NMR), 2002.
3. M. Mori and J. L. Koenig, *Ann. Rep. NMR Spectrosc.*, 1997, **34**, 231.
4. (a) P. T. Callaghan, *Principles of Nuclear Magnetic Resonance Microscopy*, Claredon, Oxford, 1991; (b) R. Kimmich, *NMR: Tomography, Diffusometry, Relaxometry*, Springer, Berlin, 1997.
5. H. Yasunaga, M. Kobayashi, S. Matsukawa, H. Kurosu and I. Ando, *Ann. Rep. NMR Spectrosc.*, 1997, **34**, 39.
6. A. K. Whittaker, *Ann. Rep. NMR Spectrosc.*, 1997, **34**, 105.
7. S. Matsukawa, H. Yasunaga, C. Zhao, S. Kuroki, H. Kurosu and I. Ando, *Prog. Polym. Sci.*, 1999, **44**, 995.
8. I. Ando, Y. Yin, C. Zhao, S. Kanesaka and S. Kuroki, *Macromol. Symp.*, 2005, **220**, 61.
9. (a) Y. Yin, C. Zhao, S. Kuroki and I. Ando, *J. Chem. Phys.*, 2000, **113**, 7635; (b) Y. Yamane, M. Matsui, H. Kimura, S. Kuroki and I. Ando, *Macromolecules*, 2003, **36**, 5655; (c) S. Kanesaka, H. Kimura, S. Kuroki, I. Ando and S. Fujishige, *Macromolecules*, 2004, **37**, 453.
10. I. Ando, H. Kurosu, S. Matsukawa, A. Yamazaki, Y. Hotta and N. Tanaka, *The Wiley Polymer Networks Review Series*, Vol. 1, In: K. te Nijenhuis and W. J. Mijs eds., Wiley, New York, 1998, 331.
11. H. Yasunaga, H. Kurosu and I. Ando, *Macromolecules.*, 1992, **25**, 6505.
12. M. Ilg, B. Pfleiderer, K. Albert, W. Rapp and E. Bayer, *Macromolecules.*, 1994, **27**, 2778.

13. T. Shibuya, H. Yasunaga, H. Kurosu and I. Ando, *Macromolecules.*, 1995, **28**, 4377.
14. H. Kurosu, T. Shibuya, H. Yasunaga and I. Ando, *Polym. J.*, 1996, **28**, 80.
15. A. Yamazaki, Y. Hotta, H. Kurosu and I. Ando, *Polymer*, 1998, **39**, 1511.
16. S. Yokota, A. Sasaki, Y. Hotta, Y. Yamane, H. Kimura, S. Kuroki and I. Ando, *Macromol. Symp.*, 2004, **207**, 105.
17. Y. Hotta, T. Shibuya, H. Yasunaga, H. Kurosu and I. Ando, *Polym. Gels Netw.*, 1998, **6**, 1.
18. A. Yamazaki, Y. Hotta, H. Kurosu and I. Ando, *J. Mol. Struct.*, 2000, **554**, 47.
19. Y. Hotta and I. Ando, *J. Mol. Struct.*, 2002, **602/603**, 165.
20. I. Ando, Y. Yamane, S. Koizumi, M. Matsui and S. Kuroki, *J. Ion Exc.*, 2003, **14**, 87.
21. E. L. Hahn, *Phys. Rev.*, 1950, **80**, 580.
22. E. O. Stejskal and J. E. Tanner, *J. Chem. Phys.*, 1965, **42**, 288.
23. J. E. Tanner and E. O. Stejskal, *J. Chem. Phys.*, 1968, **49**, 1768.
24. J. E. Tanner, *J. Chem. Phys.*, 1978, **69**, 1748.
25. T. Nose, *Ann. Rep. NMR Spectrosc.*, 1993, **27**, 217.
26. W. S. Price, *Ann. Rep. NMR Spectrosc.*, 1996, **32**, 51.
27. H. Yasunaga and I. Ando, *Polym. Gels Netw.*, 1993, **1**, 267.
28. S. Matsukawa and I. Ando, *Macromolecules*, 1996, **29**, 7136.
29. A. Ohtuka and T. Watanabe, *Carbohyd. Polym.*, 1996, **30**, 135.
30. S. Matsukawa and I. Ando, *Macromolecules*, 1997, **30**, 8310.
31. L. Masaro, X. X. Zhu and P. M. Macdonald, *Macromolecules*, 1998, **31**, 3880.
32. C. Zhao, S. Matsukawa and I. Ando, *J. Mol. Struct.*, 1998, **442**, 235.
33. S. Matsukawa and I. Ando, *Macromolecules*, 1998, **31**, 1865.
34. C. Zhao, S. Matsukawa, H. Kurosu and I. Ando, *Macromolecules*, 1998, **31**, 3139.
35. C. Zhao, H. Zhang, T. Yamanobe, S. Kuroki and I. Ando, *Macromolecules*, 1999, **32**, 3389.
36. Z. Gao, S. Schlick, S. Matsukawa, I. Ando and G. Rossi, *Macromolecules*, 1999, **32**, 1865.
37. C. Zhao, S. Kuroki and I. Ando, *Macromolecules*, 2000, **33**, 4486.
38. K. Nagashima, V. Strashko, P. M. Macdonald, R. D. Jenkins and D. R. Bassett, *Macromolecules*, 2000, **33**, 9329.
39. M. A. Winnik, S. M. Bystryak, C. Chassenieux, V. Strashko, P. M. Macdonald and J. Siddiqui, *Langmuir*, 2000, **16**, 4496.
40. Y. Yamane, M. Kobayashi, S. Kuroki and I. Ando, *Macromolecules*, 2001, **34**, 5961.
41. Y. Yamane, M. Kobayashi, H. Kimura, S. Kuroki and I. Ando, *Polymer*, 2002, **43**, 1767.
42. P. Y. Ghi, D. J. Hill and A. K. Whittaker, *Biomacromolecules*, 2002, **3**, 554.
43. G. Lin, J. Zhang, H. Cao and A. A. Jones, *J. Phys. Chem. B.*, 2003, **107**, 6179.
44. Y. Yamane, M. Matsui, H. Kimura, S. Kuroki and I. Ando, *J. Appl. Polym. Sci.*, 2003, **89**, 413.
45. E. Wentrup-Byrne, D. J. Hill and A. K. Whittaker, *Biomacromolecules*, 2004, **5**, 1194.
46. Y. Yamane, I. Ando, F. L. Buchholz, A. R. Reinhardt and S. Schlick, *Macromolecules*, 2004, **37**, 9841.
47. Y. Yamane, S. Koizumi, S. Kuroki and I. Ando, *J. Mol. Struct.*, 2005, **739**, 131.
48. R. B. Merrifield, *J. Am. Chem. Soc.*, 1963, **85**, 2149.
49. E. Bayer, *Angew. Chem. Int. Ed. Engl.*, 1991, **30**, 113.
50. M. R. Aven and C. Cohen, *Polymer*, 1990, **31**, 778.
51. N. A. Rotstein and T. P. Lodge, *Macromolecules*, 1992, **25**, 1316.
52. S. Pajevic, R. Bansil and C. Konak, *Macromolecules*, 1993, **26**, 305.
53. F. Debeaufort, A. Voilley and P. Meares, *J. Membr. Sci.*, 1994, **20**, 125.
54. S. Ladha, A. R. Mackie and D. C. Clark, *J. Membr. Biol.*, 1994, **142**, 223.
55. Z. I. Lalchev, R. K. Todorov, Y. T. Christova, P. J. Wilde, A. R. Mackie and D. C. Clark, *Biophys. J.*, 1996, **71**, 2591.
56. Z. I. Lalchev and A. R. Mackie, *Colloids Surf. B: Biointerfaces*, 1999, **15**, 147.
57. A. R. Mackie, P. S. James, S. Ladha and R. Jones, *Bio. Reprod.*, 2001, **64**, 113.
58. H. T. Toy and D. K. Janda, *Tetrahedron Lett.*, 1999, **40**, 6329.
59. Y. Yin, C. Zhao, S. Kuroki and I. Ando, *Macromolecules*, 2002, **35**, 2335.
60. Y. Yin, C. Zhao, S. Kuroki and I. Ando, *Macromolecules*, 2002, **35**, 5910.

61. H. Yamakawa, S. Matsukawa, S. Kuroki, H. Kurosu and I. Ando, *J. Chem. Phys.*, 1999, **111**, 5129.
62. E. von Meerwall and R. D. Ferguson, *J. Chem. Phys.*, 1981, **74**, 6956.
63. A. R. Parker, R. C. McPhedran, D. R. McKenzie, L. C. Botten and N. A. Nicorovici, *Nature.*, 2001, **409**, 36.
64. I. Ando, Y. Yamane, A. Ohashi, S. Kuroki and J. Watanabe, Invited lecture at *2nd International Symposium on Nano-Materials Science-Nano Technology in Organic and Polymeric Materials*, Tokyo Institute of Technology, December 9, 2004 (Abstract: p. IA1).
65. F. D. Blum and S. Pickup, *J. Coating Technol.*, 1987, **59**, 753.
66. F. D. Blum, S. Pickup and R. J. Foster, *Colloid Interface Sci.*, 1986, **113**, 336.
67. S. Pickup, F. D. Blum, T. W. Ford and M. Periyasamy, *J. Am. Chem. Soc.*, 1986, **108**, 3987.
68. H. Fujita, *Adv. Polym. Sci.*, 1961, **3**, 1.
69. E. D. von Meerwall, E. J. Amis and J. D. Ferry, *Macromolecules*, 1985, **18**, 260.
70. L. M. Gayo and M. J. Suto, *Tetrahedron Lett.*, 1997, **38**, 513.
71. M. G. Siegel, P. J. Hahn, B. A. Dressman, J. E. Fritz, J. R. Grunwell and S. W. Kaldor, *Tetrahedron Lett.*, 1997, **38**, 3357.
72. J. R. Benson and D. J. Woo, *J. Chromatogr. Sci.*, 1984, **22**, 286.
73. P. F. Marconi and W. T. Ford, *J. Catal.*, 1983, **83**, 160.
74. T. Balakrishnan and W. T. Ford, *J. Appl. Polym. Sci.*, 1981, **27**, 133.
75. M. Tomoi and W. T. Ford, *J. Am. Chem. Soc.*, 1981, **103**, 3821.
76. For example, see the *Annual Report on Combinatorial Chemistry: Ann. Rep. Combinatorial Chemistry and Molecular Diversity*, 1997–present.
77. I. Sucholeiki, *Ann. Rep. Comb. Chem. Mol. Diversity*, 1971, **1**, 41.
78. I. Sucholeiki, *Ann. Rep. Comb. Chem. Mol. Diversity*, 1999, **4**, 25.
79. E. Bayer, K. Albert, H. Willisch, W. Rapp and B. Hemmasi, *Macromolecules*, 1990, **23**, 1937.
80. R. Epton, P. Goddard and K. Irvin, *Polymer*, 1980, **21**, 1367.
81. S. L. Regen, *J. Am. Chem. Soc.*, 1974, **96**, 5275.
82. S. L. Regen, *Macromolecues*, 1975, **8**, 689.
83. F. Müller-Plathe, *Macromolecules*, 1996, **29**, 4782.
84. J. M. Ostresh, J. H. Winkle, V. T. Hamashin and R. A. Houghten, *Biopolymers*, 1994, **34**, 1681.
85. W.-Y. Chen and G. L. Foutch, *Chem. Eng. Sci.*, 1989, **44**, 2760.
86. S. Wang and G. L. Foutch, *Chem. Eng. Sci.*, 1991, **46**, 2373.
87. W. E. Rapp, *Combinatorial Chemistry – Synthesis and Application*, Wiley, New York, NY, 1997. p. 35.
88. J. C. Dainy, *Laser Speckle and Related Phenomena*, Springer, Berlin, 1975.
89. P. N. Pusey and W. van Megen, *Physica, A*, 1989, **157**, 705.
90. F. Ikkai and M. Shibayama, *Phys. Rev. E.*, 1997, **56**, R51.
91. M. Shibayama, *Macromol. Chem. Phys.*, 1998, **199**, 1.
92. M. Shibayama, M. Tsujimoto and F. Ikkai, *Macromolecules*, 2000, **33**, 7868.
93. S. Mallam, F. Horkay, A. M. Hecht and E. Geissler, *Macromolecules*, 1989, **22**, 3356.
94. F. Schosseler, R. Skouri, J. P. Munch and S. J. Candau, *J. Phys. II*, 1994, **4**, 1221.
95. Y. Cohen, O. Ramon, I. J. Kopelman, S. Mizrahi and J. Polym.Sci., *Polym. Phys. Ed.*, 1992, **30**, 1055.
96. C. Robinson, *Trans. Faraday Soc.*, 1956, **52**, 571.
97. C. Robinson and C. J. Ward, *Nature*, 1957, **180**, 1183.
98. C. Robinson, *Tetrahedron*, 1961, **13**, 219.
99. S. Sobajima, *J. Phys. Soc. Jpn.*, 1967, **23**, 1070.
100. M. Panar and D. W. Phillips, *J. Am. Chem. Soc.*, 1968, **90**, 3880.
101. R. D. Orwell and R. L. Vold, *J. Am. Chem. Soc.*, 1971, **93**, 5335.
102. T. E. Samulski and V. A. Tobolsky, *Mol. Cryst. Liq. Cryst.*, 1969, **7**, 433.
103. B. M. Fung, M. J. Gerace and L. S. Gerace, *J. Phys. Chem.*, 1970, **74**, 83.
104. I. Ando, T. Hirai, Y. Fujii, A. Nishioka and A. Shoji, *Macromol. Chem.*, 1983, **184**, 2592.
105. R. Kishi, M. Sisido and S. Tazuke, *Macromolecules*, 1990, **23**, 3779.
106. R. Kishi, M. Sisido and S. Tazuke, *Macromolecules*, 1990, **23**, 3868.

107. Y. Yamane, M. Kanekiyo, S. Koizumi, C. Zhao, S. Kuroki and I. Ando, *J. Appl. Polym. Sci.*, 2004, **92**, 1053.
108. C. Zhao, H. Zhang, T. Yamanobe, S. Kuroki and I. Ando, *Macromolecules*, 1999, **32**, 3389.
109. C. Zhao, S. Kuroki and I. Ando, *Macromolecules*, 2000, **33**, 4486.
110. Y. Yamane, S. Koizumi, S. Kuroki and I. Ando, *J. Mol. Struct.*, 2005, **739**, 137.
111. J. Watanabe, H. Ono, I. Uematsu and A. Abe, *Macromolecules*, 1985, **18**, 2141.
112. T. Yamanobe, M. Tsukahara, T. Komoto, J. Watanabe, I. Ando, I. Uematsu, K. Deguchi, T. Fujito and M. Imanari, *Macromolecules*, 1988, **21**, 48.
113. B. Mohanty, T. Komoto, J. Watanabe, I. Ando and T. Shiibashi, *Macromolecules*, 1989, **22**, 4451.
114. M. Tsukahara, T. Yamanobe, T. Komoto, J. Watanabe and I. Ando, *J. Mol. Struct.*, 1987, **159**, 345.
115. T. Yamanobe, H. Tsukamoto, Y. Uematsu, I. Ando and I. Uematsu, *J. Mol. Struct.*, 1993, **295**, 25.
116. E. Katoh, H. Kurosu and I. Ando, *J. Mol. Struct.*, 1994, **318**, 123.
117. B. Mohanty, J. Watanabe, I. Ando and K. Sato, *Macromolecules*, 1990, **23**, 4908.
118. J. G. Kirkwood, *J. Polym. Sci.*, 1954, **12**, 1.
119. M. Doi and S. F. Edwards, *The Theory of Polymer Dynamics*, Clarendon Press, Oxford, 1986 (Chapter 8).
120. W. Franklin, *Mol. Cryst. Liq. Cryst.*, 1971, **14**, 227.
121. W. Franklin, *Phys. Lett.*, 1974, **48A**, 247.
122. W. Franklin, *Phys. Rev.*, 1975, **A11**, 2156.
123. K.-S. Chu and D. S. Moroi, *J. Phys. Colloq.*, 1975, **36**, C1.
124. A. J. Leadbetter, F. P. Temme, A. Heidemann and W. S. Howells, *Chem. Phys. Lett.*, 1975, **34**, 363.
125. G. J. Krüger, *Phys. Rep.*, 1982, **82**, 229.
126. W. G. Miller and E. L. Wee, *J. Phys. Chem.*, 1971, **75**, 1446.
127. B. Halle, P. Quist and I. Furó, *Liq. Cryst.*, 1993, **14**, 227.
128. G. Lindblom and G. Oraedd, *Prog. NMR Spectrosc.*, 1994, **26**, 483.
129. R. Y. Dong, *Nuclear Magnetic Resonance of Liquid Crystals*, Springer, New York, 1994.
130. I. Furó and S. V. Dvinskikh, *Magn. Reson. Chem.*, 2002, **40**, S3.
131. E. E. Burnell and C. A. de Lange, eds., *NMR of Ordered Liquids*, Kluwer, Dordrecht, 2003.
132. A. Molenberg, M. Möller and E. Sautter, *Prog. Polym. Sci.*, 1997, **22**, 1133.
133. D. C. Sun and J. H. Magill, *Polymer*, 1987, **28**, 1243.
134. G. Kögler, K. Loufakis and M. Möller, *Polymer*, 1990, **31**, 1538.
135. A. Molenberg and M. Möller, *Macromolecules*, 1997, **30**, 8332.
136. V. M. Litvinov, A. K. Whittaker, A. Hagemeryer and H. W. Spiess, *Colloid. Polym. Sci.*, 1989, **267**, 681.
137. H. Menge, S. Hotopf, S. Pönitzsch, S. Richter, K. Arndt, H. Schneider and U. Heuert, *Polymer*, 1999, **40**, 5303.
138. V. Litvinov, V. Macho and H. W. Spiess, *Acta Polym*, 1997, **48**, 471.
139. F. Grinberg, R. Kimmich, M. Möller and A. Molenberg, *J. Chem. Phys.*, 1996, **105**, 9657.
140. S. V. Dvinskikh, R. Sitnikov and I. Furó, *I. J. Magn. Reson.*, 2000, **142**, 102.
141. F. Bueche, *Physical Properties of Polymers*, Interscience Publishers, New York, 1962.
142. G. Kögler, A. Hasenhindl and M. Möller, *Macromolecules*, 1989, **22**, 4190.
143. N. Bloembergen, E. M. Purcell and R. V. Pound, *Phys. Rev*, 1948, **73**, 679.
144. A. Müller, *Proc. R. Soc. London, Ser. A*, 1932, **138**, 514.
145. G. Ungar, *J. Phys. Chem.*, 1983, **87**, 689.
146. E. B. Sirota, H. E. King Jr, D. M. Singer and H. H. Shao, *J. Chem. Phys.*, 1993, **98**, 5809.
147. M. Stohrer and F. Noack, *J. Chem. Phys.*, 1977, **67**, 3729.
148. M. G. Taylor, E. C. Kelusky, I. C. P. Smith, H. L. Casal and D. G. Cameron, *J. Chem. Phys.*, 1983, **78**, 5108.
149. S. Ishikawa, H. Kurosu and I. Ando, *J. Mol. Struct.*, 1991, **248**, 361.
150. S. Ishikawa and I. Ando, *J. Mol. Struct.*, 1991, **273**, 227.
151. J. R. Nielsen and C. E. Hathaway, *J. Mol. Spectrosc.*, 1963, **10**, 366.
152. S. Mizushima and T. Shimanouti, *J. Am. Chem. Soc.*, 1949, **71**, 1320.

153. J. D. Barnes, *J. Chem. Phys.*, 1937, **58**, 5193.
154. J. P. Ryckaert and M. L. Klein, *J. Chem. Phys.*, 1986, **85**, 1613.
155. T. Yamamoto, *J. Chem. Phys.*, 1988, **89**, 2356.
156. H. Yamakawa, S. Matsukawa, H. Kurosu, S. Kuroki and I. Ando, *Chem. Phys. Lett.*, 1998, **283**, 333.
157. R. S. Narang and J. N. Sherwood, *Mol. Cryst. Liq. Cryst.*, 1980, **59**, 167.
158. A. E. Smith, *Acta Crystallogr*, 1952, **5**, 224.
159. H. L. Casal, D. G. Cameron and E. C. Kelusky, *J. Chem. Phys.*, 1984, **80**, 1407.
160. J. Schmider and K. Mueller, *Mol. Cryst. Liq. Cryst.*, 1998, **313**, 277.
161. M. S. Greenfield, R. L. Vold and R. R. Vold, *J. Chem. Phys.*, 1985, **83**, 1440.
162. F. Guilaume, C. Sourisseau and A. J. Dianoux, *J. Phys. (Paris)*, 1991, **88**, 1721.
163. S. P. Smart, F. Guillaume, K. D. M. Harris and A. J. Dianoux, *J. Phys. Condens. Matter.*, 1994, **6**, 2169.
164. A. El Baghdadi and F. Guillaume, *J. Raman Spectrosc.*, 1995, **26**, 155.
165. A. El Baghdadi, PhD Thesis, University of Bordeaux I, 1993.
166. R. L. Vold, R. R. Vold and N. Heaton, *Adv. Magn. Reson.*, 1989, **13**, 17.
167. K.-J. Lee, W. L. Mattice and R. G. Snyder, *J. Chem. Phys.*, 1992, **96**, 9138.
168. M. D. Hollingsworth and K. D. M. Harris, *Compr. Supramol. Chem.*, 1996, **6**, 177.
169. K. D. M. Harris and J. M. Thomas, *J. Chem. Soc., Faraday Trans.*, 1990, **86**, 2985.
170. N. G. Parsonage and L. A. K. Staveley, *Disorder in Crystals*, Clarendon, Oxford, 1978.
171. J. D. Bell and R. E. Richards, *Trans. Faraday Soc.*, 1969, **65**, 2529.
172. F. Guilaume, C. Sourisseau and A. J. Dianoux, *J. Chem. Phys.*, 1990, **93**, 3536.
173. Y. Cho, M. Kobayashi and H. Tadokoro, *J. Chem. Phys.*, 1986, **84**, 4636.
174. M. Kobayashi, H. Koisumi and Y. Cho, *J. Chem. Phys.*, 1990, **93**, 4659.
175. K. A. Wood, R. G. Snyder and H. L. Strauss, *J. Chem. Phys.*, 1989, **91**, 5255.
176. F. Imashiro, D. Kuwahara, T. Nakai and T. Terao, *J. Chem. Phys.*, 1989, **90**, 3356.
177. T. Nakaoki, H. Nagano and T. Yanagida, *J. Mol. Struct.*, 2004, **699**, 1.
178. S. Kim, H. Kimura, S. Kuroki and I. Ando, *Chem. Phys. Lett.*, 2003, **367**, 581.
179. S. Kim, S. Kuroki and I. Ando, *Chem. Phys.,* in press, 2006.
180. I. Ando and H. S. Gutowsky, *J. Magn. Reson.*, 1978, **31**, 387.
181. J. Kärger and D. M. Ruthven, *Diffusion in Zeolites and Other Microporous Solids*, Wiley, New York, 1992.
182. N. Y. Chen, T. F. Degnan and C. M. Smith, *Molecular Transport and Reaction in Zeolites*, VCH, New York, 1994.
183. C. Aslangul, *Europhys. Lett.*, 1998, **44**, 284.
184. M. Matsui, Y. Yamane, S. Kuroki, I. Ando, K. Fu and J. Watanabe, *J. Mol. Struct.*, 2005, **739**, 131.
185. M. Matsui, Y. Yamane, S. Kuroki, I. Ando, K. Fu and and J. Watanabe, *Ind. Eng. Chem. Res.*, 2005, **44**, 8694.
186. J. Watanabe, N. Sekine, T. Nematsu and M. Sone, *Macromolecules*, 1996, **29**, 4816.
187. K. Fu, N. Sekine, M. Sone, M. Tokita and J. Watanabe, *Polym. J.*, 2002, **34**, 291.
188. M. Matsui, Y. Yamane, H. Kimura, S. Kuroki, I. Ando, K. Fu and J. Watanabe, *J. Mol. Struct.*, 2003, **650**, 175.
189. W. A. Wakeham and D. H. Slater, *J. Phys. B: Atom. Mol. Phys.*, 1973, **6**, 886.
190. K. Kamiguchi, S. Kuroki, M. Satoh and I. Ando, *Polymer*, 2005, **46**, 11470.

How Far Can the Sensitivity of NMR Be Increased?

TOSHIMICHI FUJIWARA[1] AND AYYALUSAMY RAMAMOORTHY[2]

[1]*Institute for Protein Research, Osaka University, 3-2 Yamadaoka, Suita, 565-0871, Japan*
[2]*Biophysics Research Division and Department of Chemistry, University of Michigan, Ann Arbor, MI 48109-1055, USA*

Sensitivity enhancement enables the full utilization of NMR for the structural analysis of macromolecular systems. This review covers the methods for the sensitivity enhancement of NMR mainly on biological solid-state systems. Modern solid-state NMR spectroscopy is based on high-sensitivity methods, e.g. high-field superconducting magnets, cross polarization to generate large magnetization of low γ nuclei, proton detection and homo- and heteronuclear decoupling by rf fields and magic-angle spinning. Low temperature reduces the noise in the sample coil and increases the thermal equilibrium polarization. The development of the following methods will further increase the sensitivity, although it may not be straightforward to apply them to high-resolution NMR spectroscopy. Dynamic nuclear polarization, optical pumping,

ANNUAL REPORTS ON NMR SPECTROSCOPY
VOLUME 58 ISSN 0066 4103
DOI 10.1016/S0066-4103(05)58003-7

microwave induced optical nuclear polarization, photo-CIDNP, provide highly polarized nuclear magnetization using electron spins. Detection of NMR is another important factor for higher sensitivity. Use of small rf coils improves the sensitivity per sample volume. NMR can be measured by methods other than the generally used Faraday induction. SQUID is employed for NMR at low magnetic fields. NMR of a small number of spins can be detected by optical and electrical methods and also by atomic beams. The high sensitivity of magnetic resonance force detection has been demonstrated by microscopy.

1. INTRODUCTION

Solid-state NMR spectra contain a wealth of information about molecules, but the spectral lines are broad owing to their dependence on molecular properties. Thus, the sensitivity and resolution of solid-state NMR spectra are low. A number of techniques have been reported to improve the sensitivity and resolution, and are used to obtain structural information that is not available from other experimental methods.

Techniques for improving the sensitivity provide the basis for the high-resolution NMR of solids. The gyromagnetic ration γ and applied magnetic field B_0 increase the NMR sensitivity in proportion to $\gamma^{5/2}B_0^{3/21}$. Thus, cross polarization (CP) for the magnetization transfer from ^{1}H to a low γ nucleus and indirect detection with ^{1}H give stronger NMR signals.[2,3] The rapid signal accumulation using pulsed Fourier-transform NMR and short ^{1}H T_1 values also increases the S/N ratio. In addition, magic-angle spinning (MAS) and heteronuclear decoupling by rf pulses increase the signal intensities by suppressing the line broadening due to dipolar couplings and chemical shift anisotropies. Sample alignment can contribute to higher spectral sensitivity and resolution.[4] Multidimensional correlation NMR increases the resolution of NMR by separating the signals in other frequency axes. Further improvement in the sensitivity and resolution provided by uniform or selective isotope labeling makes biological solid-state NMR practical and useful.

These are commonly used methods. Solid-state NMR experiments contributes to solving problems in biology such as the structure determination of small proteins in crystalline states,[5] fibril forms,[6] and phospholipid bilayers.[4] However, further applications of these techniques are limited by poor sensitivity. This sensitivity of NMR signals primarily determines the upper size limit of biomolecular systems to which NMR is applicable.

The sensitivity of NMR is dictated by the polarization owing to the nuclear Zeeman interaction (γB_0), which is much smaller than the thermal energy (kT). Therefore, NMR experiments at low sample temperatures increase the nuclear polarization. We can also enhance the nuclear magnetization by using the polarization associated with higher energies. Electron spins, spin 1/2 particles with the largest gyromagnetic ratio, play key roles in dynamic nuclear polarization (DNP) and optical pumping.[7,8] The energy difference for parahydrogen is utilized in preparing parahydrogen-induced magnetization.[9] Hyperpolarized nuclear spins have mainly been applied to imaging[10] and nuclear physics.[11] These methods can provide a large

Table 1. Maximum sensitivity gain achieved in solid-state NMR experiments

Method	Maximum gain
Experiments at higher magnetic field[a]	3
Low temperature (~5 K)[b]	60
Para-hydrogen[c]	10^4
Cross polarization from γ_H to γ_C and detection of γ_C[d]	4
^{1}H detected 2D ^{1}H–^{15}N HSQC under MAS[e]	10
NOE[f]	3
DNP[g]	10^3
Optical pumping[c]	10^4
CP + QCPMG compared to a quadrupole echo sequence[h]	30
Micro rf coils[i]	5
Force detection[j]	10^7

[a]The enhancement factor for the 2-fold increase in B_0, and the sensitivity is proportional to $B_0^{3/2}$.
[b]Compared with room temperature in the polarization.
[c]The enhancements are relative to the equilibrium magnetization at room temperature and a static magnetic field of about 10 T.
[d]The enhancement factor is γ_H/γ_C for the ^{13}C spin in ^{1}H and ^{13}C spin systems.
[e]The enhancement for a partially deuterated solid-state protein.[12]
[f]The enhancement factor is $1+\gamma_H/2\gamma_C$ for the ^{13}C spin in ^{1}H and ^{13}C spin systems.
[g]The enhancement of the thermal equilibrium ^{13}C polarization by DNP.
[h]From ref. 13.
[i]The enhancement per unit volume with a five-times smaller radio frequency coil.
[j]From ref. 14. In comparison with magnetic-resonance microscopy.

nuclear magnetization under favorable conditions as shown in Table 1. The theoretical maximum enhancement is dictated by the Boltzmann factor, $e^{-\gamma B_0/kT}$. The maximum is 2×10^4 for 700 MHz ^{1}H-NMR at temperature of 300 K.

Improvement in the detection is the other road to sensitivity enhancement. Use of small rf coils,[15] detection by a superconducting quantum interference device (SQUID),[16] magnetic force detection,[14] and detection through electron spin and optical transitions improve the sensitivity.[17–19] The suppression of nuclear magnetic interactions increases the signal intensity by reducing the linewidths as mentioned above. Examples are also found in pulsed spin-lock detection,[13] partial deuteration and fast MAS.[12,20]

Studies have shown that a huge sensitivity gain is possible using a combination of these methods (Table 1). In this review, the methods mentioned above are covered and possible applications are discussed. We deal with high-sensitivity methods for solid-state NMR in greater detail, and mention the methods for solution NMR and imaging as well.

2. HIGH MAGNETIC FIELDS

Superconducting magnets with magnetic fields up to 21.9 T, 950 MHz in ^{1}H resonance frequency, are commercially available now and efforts are being made toward a GHz

magnet. The static magnetic field used for biological solid-state NMR has increased nearly twice in the last decade. This increase in the static field is beneficial to the sensitivity enhancement as the sensitivity is theoretically proportional to B_0.[1.5]

Signal linewidths of organic molecules in solid states are dependent on the magnetic susceptibility and the heterogeneity of molecular structure. Therefore, the increase in the linewidth with the applied magnetic field does not lead to the enhancement of spectral resolution for natural abundance carbon as expected for a solution sample.[21] Increase in the chemical-shift anisotropy (CSA) reduces the intensity of the isotropic signal in the spinning sidebands under MAS at high fields. Efficiency for generating rf fields also decreases at higher fields, while higher rf field amplitudes are required to compensate for the off-resonance effects. However, smaller sample rotors can partially alleviate these difficulties because it allows higher-spinning rate and rf amplitude.

Higher static fields enhance the spectral resolution of ^{1}H spin systems and uniformly ^{13}C-labeled systems in solids for which line broadening due to dipolar and scalar couplings is significant. This is because the chemical shift dispersion increases with B_0 whereas dipolar and J couplings do not. Increased chemical shift differences at high fields also reduce the line broadening due to homonuclear couplings.[22]

Higher fields suppress the second-order quadrupole interaction and reduce the broadening of the center transition of quadrupolar nuclear spins under MAS.[23] Thus, experiments at higher fields contribute to the analysis of ^{17}O spectra of solids at a higher sensitivity. Higher fields may also increase the sensitivity by suppressing the relaxation of nuclear spins. In favorable cases, increased CSA at high fields reduces the relaxation through the cross-correlation between CSA and dipolar couplings as in TROSY.[24,25] Particularly, the large CSA spans of amide-^{15}N[26] and carbonyl carbon[27] could play an important role in the cross-correlation effects in proteins.

3. LOW TEMPERATURE FOR STRONGER NUCLEAR SPIN POLARIZATION

3.1. NMR at low temperature

Since lowering the sample temperature increases the population difference for the energy levels determined by the Boltzmann factor, $e^{-\gamma Bo/kT}$, it enhances the sensitivity of NMR.[28,29] There are several studies that have benefited from low-temperature experiments. One recent study enabled the direct detection of zinc metal of Zn^{2+} metalloprotein.[30] The detection of zinc historically has not been possible and therefore a surrogate probe strategy (replacement of Zn with Cd for ^{113}Cd NMR experiments) was used to study metalloproteins.[31,32] In a solid-state NMR experiment, [67]the Zn spectrum of the minimal DNA-binding domain of human nucleotide excision repair protein xeroderma pigmentosum A (XPA-MBD) was obtained at 25 K (Fig. 1). In addition to the sensitivity gain attained by the low temperature, a 2-fold sensitivity gain was achieved using a cryogenic preamplifier at 77 K with a minimal noise figure of 0.2 dB. A 30-fold sensitivity gain was also acquired with a

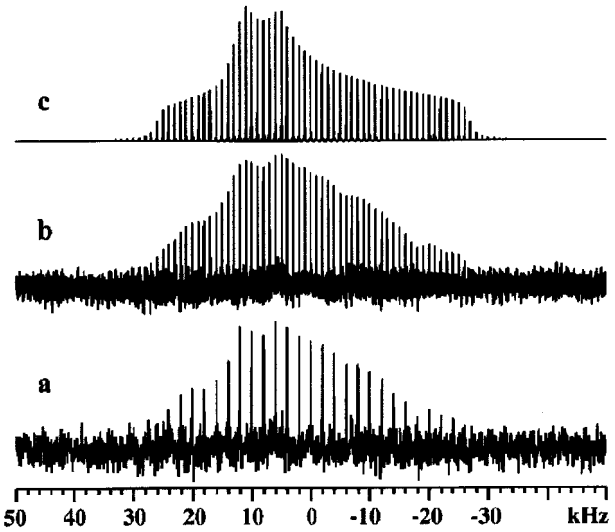

Fig. 1. (a) Experimental ^{67}Zn NMR spectrum of XPA–MBD at 9.4 T and 25 K, with 25 Hz line broadening (LB), (b) data from a part apodized with 5 Hz LB and 1 kHz matched LB and zero filled to double the echo spacing, and (c) simulation with 25 Hz LB and 1.5 kHz matched LB. A 30 ms contact time, a 60 s recycle delay with a proton flip back pulse, a 500 μs interecho separation (spikes are separated by 2 kHz) and 1090 scans were used. Spectra are reproduced with permission from the Journal of the American Chemical Society, ref. 30. Copyright 2001, American Chemical Society.

combination of CP and spikelet echo (or QCPMG) pulse sequences.[13] A further increase in sensitivity has been demonstrated by performing these ^{67}Zn NMR experiments on a 30 kDa human carbonic anhydrase at a higher magnetic field.[33] These experiments can also be applied to the characterization of Ca^{2+} and Mg^{2+}-dependent proteins. Low-temperature experiments have also been used to characterize unstable chemicals, to follow low-temperature reactions, and to study conformational or molecular exchanges.

Cryoprobes or cold probes have come into use in solution NMR studies and provide a ~4-fold increase in the sensitivity.[34,35] In a cryoprobe, high sensitivity is achieved by cooling the rf coils to about 15 K that lowers the thermal noise and increases the Q factor due to a lower rf coil resistance. Although MAS experiments of solids at cryogenic temperatures were reported,[36,37] the sensitivity improvement by the low temperature is not directly addressed. Development of low-temperature probes for solid-state NMR experiments is also beneficial to achieving the higher sensitivity.

There are additional advantages in cooling a sample. In solid-state NMR, freezing molecular motions improves the efficacy of pulse sequences by reducing the relaxation due to the interference between the motion and the magnetic interactions modulated by rf pulses and MAS. In addition, low-temperature experiments avoid the sample heating due to fast sample spinning[38] and high-power rf fields[39,40]

especially for biological samples causing dielectric loss. Low-temperature experiments prevent denaturation of samples. Thus, most MAS experiments on lipid bilayers containing a membrane-associated peptide or protein are routinely carried out at temperatures lower than $-20^{\circ}C$.

However, low temperatures may cause damages to biological samples. When the temperature of the protein water solution is reduced below the freezing point, crystallized water molecules generally disrupt the protein structures. These conformational changes of proteins and ligands broaden the linewidths of the NMR signals and deteriorate the spectral resolution and sensitivity. This line broadening can be alleviated by making the water solvent into a glass state at low temperatures. The glass state has been shown to be formed by rapid freezing or the addition of cryoprotectants such as trehalose and glycerol to the solutions.[41,42] Solid-state NMR experiments of oriented molecules face a similar problem. The loss of molecular alignment at low temperatures broadens the resonance lines. Nevertheless, the use of cryoprotectants like cholesterol preserves the mechanical alignment of lipid bilayers even at lower temperatures near about $-40^{\circ}C$.[43] Fig. 2 shows that sharp spectral lines were obtained below the liquid crystalline to gel phase-transition point $-4^{\circ}C$ of oriented phospholipid bilayers by the presence of a cryoprotectant. Another problem at low temperatures is that the slow longitudinal

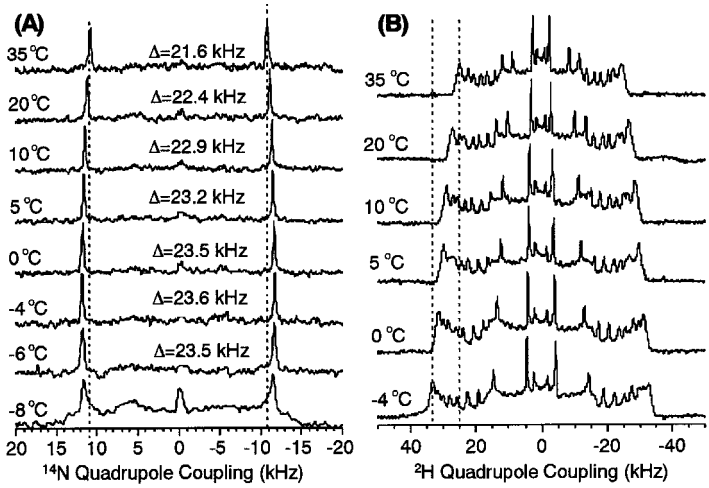

Fig. 2. Temperature dependent ^{14}N and ^{2}H NMR spectra of mechanically aligned d_{31}-POPC (1-palmitoyl 2-oleoyl phosphatidyl choline) bilayers at a magnetic field of 9.4 T. (A) The ^{14}N quadrupole coupling of the choline group in POPC head group slightly increases with decreasing temperature. (B) The ^{2}H quadrupole splitting of methylenes in the acyl chain increases with the decreasing temperature. The increases in the ^{14}N and ^{2}H splittings would indicate the reduction in the mobility of the head group and of the acyl chains, respectively. These bilayers were prepared using the naphthalene procedure.[44] Bilayer samples that were not fully hydrated did not provide good resolution at low temperatures.

relaxation lengthens the experimental time. In favorable systems, the relaxation time can be shortened by utilizing paramagnetic dopants (Fig. 2).

3.2. Parahydrogen-induced polarization

Hyperpolarized nuclear spin states can be prepared using parahydrogen (pH_2). Parahydrogen is enriched at cryogenic temperatures by virtue of the energy difference, equivalent to 190 K, between the lowest energy levels for the *para*- and *ortho*-hydorgen rovibrational states.[45] Because of the slow relaxation of the pH_2 state, room temperature pH_2 is also available.

Parahydrogen gives strong NMR signals upon breaking the symmetry of the H_2 molecule by hydrogenation.[9] The pH_2-induced polarization technique is employed for imaging using bolus tracking with hyperpolarized ^{13}C and for studying short-lived reaction intermediates.[46,47] This technique may be applied to the study of a material surface as demonstrated by using the hyperpolarized Xe gas.

4. ENHANCEMENT OF LOW γ NUCLEI BY PROTON MAGNETIZATION TRANSFER

4.1. Advantages in using magnetization transfer under rf fields

The sensitivities of nuclei with low gyromagnetic ratios γ_L, such as ^{13}C and ^{15}N, are increased by transferring magnetization from a nucleus with a larger gyromagnetic ratio γ_H, ^1H. CP transfers the magnetization by heteronuclear dipolar couplings in the rotating frame under the Hartmann–Hahn condition, and provides the enhancement of γ_H/γ_L.[48,49] An additional benefit of CP is due to the rapid relaxation of ^1H spins, which allows the acquisition of more transients in a given time. Polarization transfer efficiencies for homo- and heteronuclear spin systems have been extensively studied for solid-state NMR. Adiabatic frequency/amplitude sweep[50] and γ-encoded recoupling[51–54] have been shown to provide efficient CP. These enhancements just need modulation of the rf pulse sequences and are applicable to most biological solids. However, the enhancement of magnetization by these methods is generally much smaller than that achieved by the methods for the hyperpolarization described in Sections 5 and 6.

These heteronuclear mixing schemes allow one to make 2D NMR with ^1H detection, known as inverse detection. The gain by the proton detection is approximately expressed as $(\gamma_H/\gamma_L)^{3/2}$, and is about 8 and 30 for solution ^{13}C–^1H and ^{15}N–^1H 2D correlation spectroscopies, respectively.[1,55] However the gain by the inverse detection of solid-state NMR is much smaller due to line-broadening of the ^1H signals. It was reported that the gain by the inverse detection of ^{15}N–^1H systems in solid states was about 10 for a deuterated sample[12] and about 3 for nondeuterated peptides.[20,56] Details of the developments, advantages in using inverse detection techniques to study biological solids are discussed in a recent review by Saalwachter and Ramamoorthy.[57]

4.2. Magnetization transfer by NOE

Heteronuclear Nuclear Overhauser Effect (NOE) gives a maximum enhancement factor of $1+\gamma_H/2\gamma_L$ at the extreme narrowing limit of the nuclear magnetic relaxation. This factor is three for ^1H–^{13}C spin systems. The advantage of NOE over CP was found in uniformly ^{13}C-labeled solids with greater mobility. The CP method provides a maximum gain of about 2.4 for the ^{13}C labeled proteins mainly because of the low ^1H:^{13}C ratio of 1.6. Fast $T_{1\rho}$ relaxation due to molecular motions also reduces the gain by CP.

In a method named nuclear Overhauser polarization (NOP) for uniformly ^{13}C labeled solids, protons are irradiated with an rf field strength, ν_{rf}, sufficient to satisfy the rotary-resonance condition $\nu_{rf} = n\nu_R$ ($n = 1$ or 2) at a spinning frequency of ν_R to recover the $^1H-^{13}C$ dipolar coupling. When the $^1H-^{13}C$ dipolar coupling pattern of one of the ^{13}C spins overlaps with a spinning side band of the other ^{13}C spin, exchange of magnetization occurs by $^{13}C-^{13}C$ dipolar coupling. This recovery of the $^{13}C-^{13}C$ dipolar coupling under MAS is due to the $^1H-^{13}C$ dipolar-assisted rotational resonance (DARR).[58] This rf irradiation to protons in DARR also provides NOE for ^{13}C spins in mobile methyl groups. The transfer of the ^{13}C magnetization from the methyl groups to other ^{13}C spins leads to enhancement by NOE.[59] Since $^{13}C-^{13}C$ exchange is faster than the ^{13}C relaxation time in general, it provides a uniform transfer of magnetization to all of the ^{13}C nuclei in the labeled molecules. Thus, this method is useful also to quantify the number of carbons from the signal intensities. Recently, experiments on uniformly ^{13}C, ^{15}N-labeled proteins showed a sensitivity enhancement factor twice as large as that of CP at a high temperature[60] (Fig. 3). Since this method suppresses signals from natural abundance molecules, it can provide ^{13}C spectra of ^{13}C-labeled membrane proteins in lipid bilayers with the reduced lipid signals.

It should be noted, however, that the sensitivity for NOP is not better than that for CP for ^{13}C-labeled rigid solid-state systems in general, because a larger number of scans can be accumulated by CP within a given time owing to the difference in T_1 between the ^{13}C and ^1H spins. An additional 10–20% enhancement of the ^{13}C signal is possible for ^{13}C-uniformly labeled system by simultaneous application of ^{13}C and ^1H 90° pulses at the beginning of CP: these pulses prepare the initial ^{13}C magnetization not only from the ^1H but also from the ^{13}C longitudinal magnetization.[61]

5. DYNAMIC NUCLEAR POLARIZATION: ENHANCEMENT BY ELECTRON SPINS

Dynamic nuclear polarization (DNP) is the transfer of polarization from electron spins to nuclear spins by saturating the resonance for electron-spin energy levels.[7,62,63] This polarization transfer due to hyperfine couplings is performed by applying a microwave field near the electron-spin transition frequencies. Since the electron-spin polarization is much larger than that of the nuclear spins, DNP enhances the ^1H magnetization more than 100 times under favorable conditions.

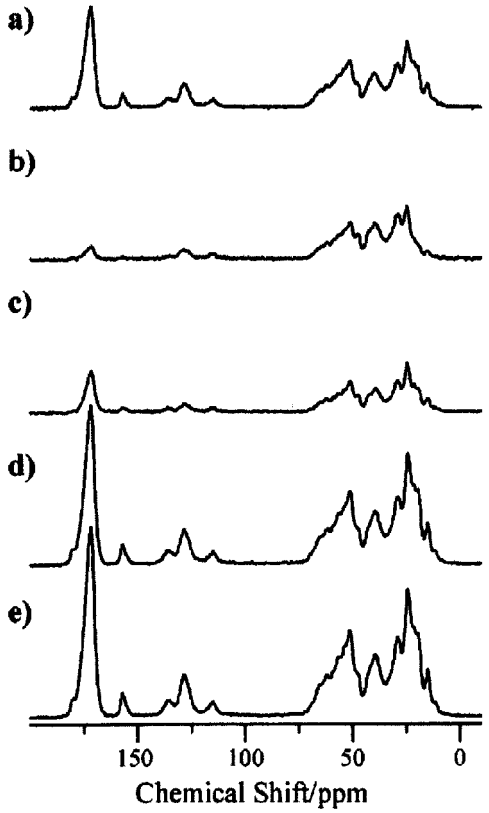

Fig. 3. Carbon-13 chemical shift spectra of lyophilized [U-^{13}C, ^{15}N]-Yhh obtained on a 400 MHz NMR spectrometer using a 20 kHz spinning frequency and a 20 kHz ^{1}H rf field irradiation. (a) Obtained by a ^{13}C 90° pulse without NOP and with a recycle delay of 50 s while the T_1 is 1.26 s. Spectra obtained using CP with a contact time of 1 ms (b) and 4 ms (c) with a recycle delay of 4 s. Spectra obtained using NOP with τ_{NOP} of 4 s (d) and 8 s (e). Spectra are reproduced with permission from the Journal of the American Chemical Society, ref. 60. Copyright 2004, American Chemical Society.

The maximum enhancement factor is about 660 for protons. This factor is determined by (ν_e/ν_n), the ratio of the resonance frequency of the electron (ν_e) relative to that of the proton (ν_n); ^{1}H and electron-spin resonance frequencies are 700 MHz and 460 GHz, respectively, at a 16.1 T external magnetic field. The maximum polarization obtained by DNP also depends on the temperature of the sample according to the Boltzmann factor. The enhancement is influenced by the relaxation of the electron and nuclear spins as well as the polarization transfer rate between the nuclear and electron spins.

DNP has been used for studying the interactions between unpaired electron and nuclear spins and for enhancing the sensitivity of NMR signals. The enhancement of

the nuclear magnetic polarization with the electron polarization was first predicted by Overhauser.[64] DNP by the Overhauser effect is due to the random fluctuation of nuclear–electron spin interactions for free electrons in metals and paramagnetic electrons in solution states. Under low magnetic field conditions, the enhancement by the forbidden transitions at $\nu_e + \nu_n$ and $\nu_e - \nu_n$, known as the solid-state effect, is the dominant mechanism for DNP in solid states, since the nuclear–electron magnetic interaction is large enough to mix pure spin states determined by nuclear Zeeman interactions. Electron–electron interactions play significant roles in DNP under high electron spin concentrations. This DNP mechanism, thermal mixing and cross effects, would be important for efficient polarization transfer at higher static magnetic fields. Adiabatic field or frequency sweep over the Hartman–Hahn condition also enables the polarization transfer from electron to nuclear spins, which is named as the integrated solid effect.[65]

The large electron-spin polarization is initially transferred to proton spins by hyperfine couplings in DNP experiments. The NMR spectral lines of these protons and nearby nuclei are broadened by the hyperfine couplings. The proton polarization in the vicinity of the unpaired electrons propagates via ^1H–^1H dipolar couplings. This spin diffusion between protons enhances the nuclear polarization throughout the sample if the diffusion is faster than the proton longitudinal relaxation time.[66] In biological solids, molecules containing nuclear spins that are far away from the electron spins, hence under negligible electron–nuclear spin interactions, can give high-resolution NMR spectra without line broadening. ^{15}N spectra of uniformly ^{15}N-labeled Y21 M fd bacteriophage and ^{31}P spectra of purple membrane were enhanced via DNP as shown in Fig. 4.

Low-field DNP has been used for the imaging of paramagnetic species through NMR, proton–electron double-resonance imaging (PEDRI).[67] Hyperpolarized nuclear spins obtained under a low-field and cryogenic condition was observed at a high field and room temperature. This experiment gave a 10^4-fold enhancement in the S/N of solution ^{13}C NMR signals.[68] DNP would be beneficial for enhancing the sensitivity of high-resolution solid-state NMR spectra obtained at high magnetic fields. However, performing DNP at high fields has several experimental difficulties[69] as explained below. (1) DNP probes for MAS experiments are bound to have a low Q factor in a submillimeter wave region where electron spins resonate. Thus, the microwave light source has to generate the stable submillimeter wave with more than 1 W. Light sources used at lower fields, such as crystron, cannot be used at high fields. For this purpose, a light source such as a gyrotron (cyclotron resonance maser)[70] must be newly developed for high-field DNP experiments. (2) Mechanism of polarization transfer under high fields is not well understood, which makes it difficult to optimize the polarization efficiency.[71] (3) DNP experiments also need a sample spinning facility at a lower temperature such as 80 K to enhance the transfer efficiency by suppressing the electron-spin relaxation.[37] This would require a large amount of low-temperature gas to carry out multidimensional solid-state NMR experiments. In spite of these problems, high-field DNP is one of the most practical methods for enhancing the high-resolution NMR spectra of biological solids by more than 100 times.

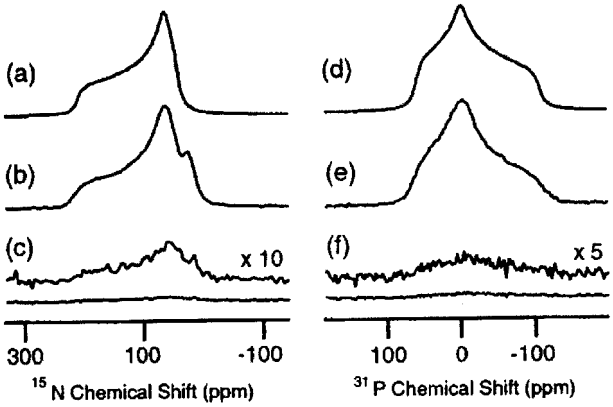

Fig. 4. DNP experiments on U-^{15}N-Y21 M bacteriophage at temperature of 13 K. (a) Simulation of amide powder pattern due to chemical shift anisotropy (CAS). (b–c) ^{15}N CP with (b) and without (c) DNP, both with 8 scans and 20 s recycle delay. (d) Simulation of phosphodiester powder pattern due to CSA. (e–f) ^{31}P CP with (e) and without (f) DNP, both with 192 scans. The signal enhancement is ca. 26 for both experiments. The sample consisted of 60 μL of H_2O/glycerol (50/50) containing Y21 M fd bacteriophage (40 mg/mL) and 30 mM 4-amino TEMPO. Spectra are reproduced with permission from the Journal of the American Chemical Society, ref. 66. Copyright 2001, American Chemical Society.

6. NUCLEAR POLARIZATION ENHANCEMENT BY OPTICAL EXCITATION

6.1. Optical pumping

The nuclear polarization can be prepared by optical pumping which is associated with exciting the electronic transition by electromagnetic waves in the optical region such as lasers.[8,72] In this method, circularly polarized light generates polarized electron spins in an alkali metal by depleting one of the atomic states. Hyperpolarized electron spin polarization of an alkali metal (for example, Rb) is transferred to Xe nuclear spins by the Fermi contact hyperfine interaction upon forming a van der Waals complex. On the other hand, helium-3 is polarized with a laser by the metastability exchange without using an alkali metal.

Optical pumping experiments using polarized ^{129}Xe and ^{3}He have been applied to the imaging of the void space in organisms and materials.[10,73] Since noble gases have fluidity, spins that are hyperpolarized at a lower field can move to other samples. The hyperpolarization in Xe nuclear spins can be transferred to various nuclei such as ^{1}H, ^{29}Si and ^{13}C through the nuclear Overhauser effect and cross polarization.[74] These polarized nuclear spins provide information on the structure and dynamics of molecules at the surface and in the bulk solution. NOE between hyperpolarized ^{129}Xe and ^{1}H in a protein has been observed as shown in Fig. 5.[75] High-resolution solid-state spectra for these nuclear spins were obtained under MAS conditions.[76]

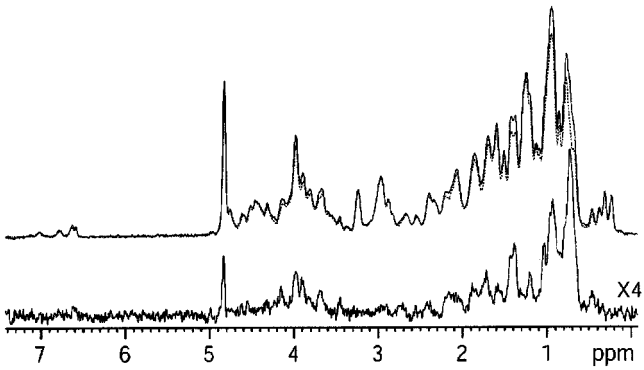

Fig. 5. NOE spectra between ^{1}H and polarized ^{129}Xe acquired on a tobacco lipid transfer protein, LTP1•1, in D_2O. The upper display corresponds to the proton spectra acquired in the presence of positively polarized xenon (solid line) and negatively polarized xenon (dotted line). Variations in the peak intensity can be observed in particular in the aliphatic region. The difference between these two spectra gives the bottom spectrum. Experimental conditions: 500 MHz spectrometer, 3 bar of 96% enriched xenon polarized at 30%, tobacco LTP1•1 concentration of 0.85 mM, mixing time for proton magnetization build-up of 500 ms, total acquisition time 2 min. The xenon T_1 was 150 s. Spectra are reproduced with permission from the Journal of the American Chemical Society, ref. 75. Copyright 2004, American Chemical Society.

Optical pumping NMR has also been demonstrated on semiconductors.[77,78] Nuclear-spin polarization is generated from the angular momentum of the photon via spin-polarized electron–hole pairs. Enhanced NMR polarization can be transferred to ^{1}H and ^{13}C nuclear spins for studying the structure and dynamics of organic molecules at the surface of a semiconductor. Optical pumping in indium phosphide was employed for this purpose. Although enhanced ^{31}P NMR signals were observed, these experiments still need optimization for practical applications.

6.2. Microwave-induced optical nuclear polarization

Microwave-induced optical nuclear polarization (MIONP) is a combination of DNP with the photo-excitation of the electron spins to the triplet state.[79] Microwaves are used for the polarization transfer from the electron triplet spins to the nuclear spins. Since the hyperpolarized electron spins are generated via selectivity in the intersystem crossing from the excited singlet state to the triplet sublevels, the hyper polarization can be prepared under low magnetic fields. The triplet state has a longer relaxation time compared to singlet states. Therefore, hyperpolarized nuclear spins can also be generated at room temperature by DNP. Solid effects and integrated solid effects have been used for polarization transfer from the electron spins to proton spins at lower magnetic fields. This low field and room temperature condition is an advantage over DNP experiments for generating hyperpolarized nuclear spins. Another merit is that NMR signals are not perturbed by the unpaired

electron spins because the triplet state decays to the diamagnetic state in a lifetime shorter than the relaxation time of the longitudinal nuclear magnetization.

Organic dye molecules have mainly been used for MIONP. Proton-spin hyperpolarization of 0.7 by MIONP in pentacene-doped naphthalene was reported.[80] MIONP experiments on proteins may also be performed without using additional molecules for generating a triplet state, since amino acid residues such as tryptophan can be excited to the triplet state at a low temperature. Although MIONP experiments under high fields have not been performed, it would be possible to make such experiments similarly to the DNP experiments at high fields.

6.3. Photo-CIDNP

A class of photochemical reactions also enhances nuclear polarization. These phenomena are known as photo-chemically induced dynamic nuclear polarization (CIDNP). The mechanism for the enhancement of the nuclear polarization in CIDNP is quite different from that of DNP. CIDNP is initiated by a photoexcitation of the electronic state followed by a chemical reaction that proceeds selectively to give a nuclear spin state under the hyperfine couplings. CIDNP was reported for solution NMR and applied to detecting the surface of a protein accessible to the photo-excited dye molecules.[81] Photo-CIDNP has been observed for a bacterial photosynthetic reaction center and photosystem I in solid states, although the mechanisms of CIDNP in solids are different from those in solutions.[82,83] This would be useful for elucidating the photo reaction schemes and for selectively observing the site relevant to a photochemical reaction. ^{13}C MAS spectra of photosystem I enhanced by photo-CIDNP are shown in Fig. 6.

7. DETECTION SCHEMES TO INCREASE THE SENSITIVITY OF NMR

7.1. Suppression of spin interactions by rf fields and MAS

Suppression of magnetic spin interactions by rf field irradiation and sample spinning improves the signal intensity by reducing the line broadening, although this suppression does not increase the integral signal intensity. The MAS frequency is generally smaller than the maximum rf field amplitude that can be generated for solid-state NMR experiments. Thus, rf fields are employed to decouple large dipolar interactions, while MAS suppresses the CSA and small dipolar couplings such as $^{14}N-^{13}C$ couplings by modulating the geometrical part of the Hamiltonians. MAS at very high spinning rates has also been shown to be very useful for suppressing ^{1}H homonuclear dipolar couplings and paramagnetic broadening to obtain high-resolution spectra.[84,85]

Rf fields affect the spin operators in the Hamiltonians and have been used for decoupling. Two-Pulse Phase-Modulation (TPPM) and related heteronuclear dipolar-decoupling schemes improve the signal intensities of high-resolution

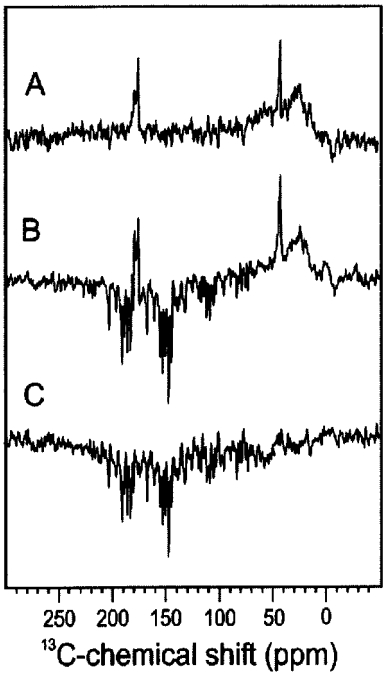

Fig. 6. ^{13}C MAS NMR spectra of photosystem I-110 particles at 223 K and a MAS frequency of 3.6 kHz. Spectra are obtained A: in the dark, B: under continuous illumination with white light, C: by subtraction B–A. Spectra are reproduced with permission from the Journal of the American Chemical Society, ref. 83. Copyright 2004, American Chemical Society.

^{13}C and ^{15}N NMR spectra under a MAS-spinning frequency of less than ca. 20 kHz.[86,87] However, under a spinning rate more than the CH dipolar coupling, ca. 30 kHz, a simpler pulse sequence such as XiX gives a better decoupling performance than TPPM.[88] Under such higher sample-spinning rates, primarily MAS decouples the CH dipolar couplings, and the rf field suppresses the residual coupling at a frequency less than that of the spinning rate. Thus, the optimal decoupling sequence depends on the sample-spinning rate, avoiding the interference between the modulations by the rf field and the sample spinning.

Applications of rf decoupling pulses to the nuclear spin species observed also improve the signal intensities. In these homo-decoupling experiments, time-domain signals were acquired in the sample windows of rf pulse sequences. Proton NMR experiments with combined magic-angle rotation and multiple-pulses (CRAMPS) increase T_2 and enhance signal intensities by suppressing ^{1}H–^{1}H dipolar couplings and chemical shift anisotropies.[89,90] These experiments provide high-resolution ^{1}H spectra with scaled isotropic chemical shifts. Several spin locking and echo pulse sequences have been employed to improve the sensitivities by decoupling solid-state nuclear magnetic interactions for biological applications.[13,56,91]

7.2. Small rf coils

The sensitivity of NMR can be enhanced by improving the detection hardware. The S/N per sample volume is proportional to the inverse of the rf coil dimension.[15,92] Therefore, when the amount of a sample is limited, we can maximize the sensitivity by using the smallest rf coil that can accommodate the sample amount.

Small rf coils have several advantages. They are efficient in generating rf fields; e.g. a coil with a diameter of 0.4 mm generated a ^{1}H rf field of 4.7 MHz.[93] The small rotors that are optimized for the small rf coils allow faster sample spinning; e.g. a rotor with a diameter of 1.8 mm spun at a MAS frequency of 50 kHz.[94] These strong rf fields and fast MAS frequencies attained with the small coil and rotor systems also increase the NMR sensitivity by decoupling as mentioned in Section 7.1.

The small coil and rotor systems permit reducing the size of the NMR probes that contain the system. The small rotor systems also decrease the gas flow for the sample rotation and temperature control, which again serves to reduce the probe size. Such small probes can be used with narrow-bore magnets. Thus, the small coil systems would generally make NMR systems inexpensive. The main disadvantage in using small coil systems is the low sensitivity due to the small sample volume. However, this low sensitivity can be compensated for by using the method for the sensitivity enhancement mentioned previously in this review.

7.3. SQUID detection

Methods other than conventional Faraday induction can be employed for detecting NMR. Under low magnetic fields $B_0 < 0.5$ T, SQUID that detect magnetic flux can give a higher S/N over the induction method.[16] Solid-state NMR at low fields has several attractive features. The Zeeman interaction can be manipulated at low fields by modulating the DC magnetic field in time-domain experiments. Line broadening due to chemical shifts and magnetic susceptibilities is much reduced at low fields. Dipolar splittings do not have an orientation dependence at the zero-field. This would allow precise distance measurements from the dipolar interactions. Low-field solid-state NMR experiments have been limited by the poor signal sensitivity. SQUID diminishes this technical difficulty. SQUID was initially applied to low-field NMR and NQR studies on solids at low temperatures. A combination of high-T_c SQUID detection with Xe hyperpolarization has been shown to enhance the ^{1}H-NMR under microtesla fields by a factor of 10^6.[95] These methods could be applied to biological solid-state NMR as well as imaging.[96,97]

7.4. Detection by optical and electrical methods and by atomic beams

It is also possible to detect NMR through the effect of nuclear spins on other spectroscopic phenomena and physical properties. Nuclear spins affect the ESR and fluorescence spectra through hyperfine interactions, such as electron nucleus double resonance (ENDOR)[17,98] and optically detected magnetic resonance (ODMR).[18,19]

Such experiments in microwave and optical regions give information on nuclear spins at higher sensitivity, because the photon energies are larger in those regions. Though the nuclear spins must interact with electron spins by hyperfine couplings, ODMR has a very high sensitivity. Observation of a single molecule by ODMR has been reported.[18,19] It is also possible to detect NMR optically by optical pumping for the selective excitation of an atomic state. In this experiment, application of an rf field at a NMR frequency affects the emission and absorption of polarized light for an atom such as ^{201}Hg.[99] Laser magnetic resonance (LMR) in the far infrared region also provides energy level splittings for nuclear spins under magnetic fields at a higher sensitivity.[100]

NMR observation by the electrical resistance of the nanoscale gallium arsenide structure has been applied to detecting about 1 f mol atoms.[101,102] In these experiments, the large nuclear polarization in GaAs was prepared by DNP at low temperatures and excited by rf fields. Such a small NMR device can be applied to quantum computing.

Molecular-beam technology combined with magnetic resonance was shown to be used for detecting the resonance frequency of the nuclear spins.[103,104] This method would have the sensitivity for detecting a single particle. A similar technique was applied to a neutron echo spectrometer for neutron diffraction, where the rf field is applied to a beam of spin-1/2 neutrons under a static magnetic field.[105] It is also interesting to note that the neutron diffraction can provide information on nuclear spin states in the sample from the dipolar interaction between the neutron and nuclear spins.

7.5. Magnetic resonance force detection

In magnetic-resonance force microscopy (MRFM), electron and nuclear spin magnetic resonances are detected by the magnetic force on the cantilever.[106] This principle for MRFM is shown in Fig. 7. This method has one of the highest sensitivities for the detection of spins in the subsurface area up to a depth of 200 nm. Recently, a single electron spin was detected by this method.[14] It is also possible to detect 10^{12} nuclear spins. This method was shown to give microscopic images of spins a resolution of 25 nm. This sensitivity can be further improved by hyperpolarizing the nuclear magnetization. High-sensitivity MRFM experiments are generally performed at very low temperatures in vacuum to reduce thermal noise, but it is possible to detect signals at room temperature and normal pressure.[107] This method can also be used for manipulating the local spin states.

The high-sensitivity methods mentioned here may not provide high-resolution NMR spectra for chemical shifts, but can be used for imaging and detecting the state of nuclear spins in the sample.

8. FUTURE SCOPE

The sensitivity and resolution of biological solid-state NMR has continuously been improved by higher static fields and refined experimental methods. Rf and digital

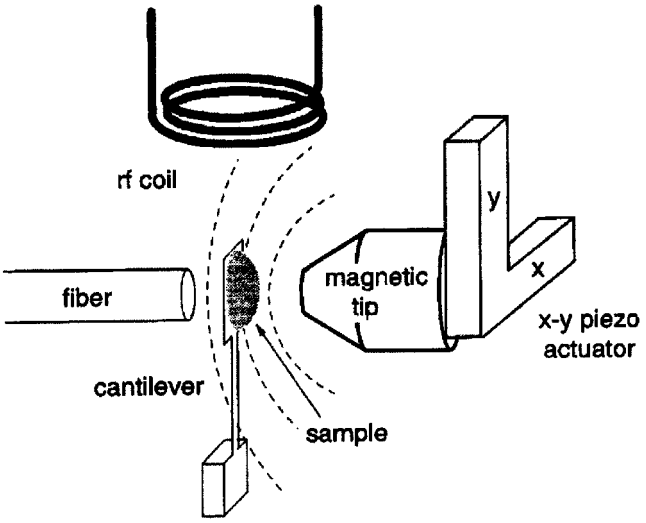

Fig. 7. Schematic setup of the NMR force microscopy. The dashed lines represent contour of constant magnetic field. The coil generates rf field at a frequency of 100 MHz. The sample is mounted on a silicon nitride cantilever that serves as a mechanical force sensor. The motion of the cantilever is monitored with a fiber-optic interferometer. The spatial resolution was about 3 μm in the axial direction and about 15 μm in the lateral direction. Reprinted with permission from O. Züger, Journal of Applied Physics, 79, 1881 (1996). Copyright 1996, American Institute of Physics.

technologies allow multidimensional NMR experiments with rotor synchronized multipulse sequences. These advanced hardware and NMR pulse sequences combined with biotechnology for the sample preparation have permitted the detailed structural and functional studies of biological molecules in solids. These lines of improvements in conventional NMR will enhance the sensitivity by up to a factor of about 10.

The improvement in the signal sensitivity is crucial for the NMR spectroscopy of biological systems. Developments in biological science require the structural analysis of more complicated molecular systems such as membrane molecular complexes. Similarly to X-ray and solution NMR, solid-state NMR techniques can target larger biological systems. The upper limit of the biomolecular mass whose molecular structure can be studied is primarily determined by the sensitivity, and is currently about 300 kDa.[108] Solid-state NMR needs about 100 nmol of a sample for detecting a single spin.[109] Much higher sensitivity is needed to measure long interatomic distances for structural analysis, because small changes in the signal intensities due to weak dipolar couplings must be observed.

The hyperpolarization of nuclear spins is a key technology to meet such demands. Higher sensitivity allows one to make experiments with smaller sample amounts. This enables the study of biological systems, such as membrane-associated proteins, that are difficult to prepare in a large quantity. Methods for increasing the sensitivity will also enable the applications of higher dimensional solid-state NMR

experiments for pursuing higher spectral resolution, because the high sensitivity compensates for the reduction in the magnetization due to the inclusion of additional mixing periods in the pulse sequence. If sensitivity permits, we can make multidimensional experiment faster by using elaborated experimental schemes like multidimensional NMR with GFT (combined G-matrix and Fourier transformation) and faster 2D experiments with field gradients.[110,111]

One class of methods for increasing the sensitivity by more than 10 times is to make use of the electron spin polarization which is much larger than the nuclear spin polarization, DNP or optical pumping. The cryogenic temperature is also significant, because it increases the polarization and reduces the noise of samples and detectors. The detection principles other than conventional NMR, such as SQUID and MRFM, also improve the sensitivity greatly for low-field NMR and microscopic imaging, respectively. Advances in instrumentation and technology have been innovative in NMR methodology. For example, the computation speed of minicomputers in 1970s enabled the application of real-time Fourier transformation in NMR spectroscopy. Super conducting magnet technology provided high-field NMR. High-power light sources in the submillimeter wave region enabled high-field DNP. Such new fundamental technologies continue to provide the opportunities to improve the sensitivity of magnetic resonance. Thus, the NMR sensitivity increases in parallel with such development in the technology. The high sensitivity gained will expand the frontier of the NMR applications to the study of more important biological systems in the near future.

REFERENCES

1. R. Freeman, *A Handbook of Nuclear Magnetic Resonance*, 2nd edition, Addison Wesley Longman, Harlow, 1997, 248.
2. R. R. Ernst, G. Bodenhausen and A. Wokaun, *Principles of Nuclear Magnetic Resonance in One and Two Dimensions*, Clarendon Press, Oxford, 1987.
3. K. Schmidt-Rohr and H. W. Spiess, *Multidimensional Solid-State NMR and Polymers*, Academic Press, London, 1994.
4. S. J. Opella and F. M. Marassi, *Chem. Rev.*, 2004, **104**, 3587.
5. (a) F. Castellani, B.-J. van Rossum, A. Diehl, K. Rehbein and H. Oschkinat, *Biochemistry*, 2003, **42**, 11476; (b) S. G. Zech, A. J. Wand and A. E. McDermott, *J. Am. Chem. Soc.*, 2005, **127**, 8618.
6. R. Tycko, *Curr. Opin. Struct. Biol.*, 2004, **14**, 96.
7. A. Abragam, M. Goldman, Nuclear Magnetism: Order and Disorder, Clarendon Press, Oxford, 1982, 339
8. B. M. Goodson, *J. Magn. Reson.*, 2002, **155**, 157.
9. J. Natterer and J. Bargon, *Prog. Nucl. Magn. Reson. Spectrosc.*, 1997, **31**, 293.
10. M. S. Albert, G. D. Gates, B. Driehuys, W. Happer, B. Saam, C. S. Springer Jr. and A. Wishnia, *Nature*, 1994, **370**, 199.
11. P. G. Sona, *Energia Nucl.*, 1967, **14**, 295.
12. (a) V. Chevelkov, B. J. van Rossum, F. Castellani, K. Rehbein, A. Diehl, M. Hohwy, S. Steuernagel, F. Engelke, H. Oschkinat and B. Reif, *J. Am. Chem. Soc.*, 2003, **125**; (b) E. K. Paulson, C. R. Morcombe, V. Gaponenko, B. Dancheck, R. A. Byrd and K. W. Zilm, *J. Am. Chem. Soc.*, 2003, **1125**, 5831.
13. F. H. Larsen, H. J. Jakobsen, P. D. Ellis and N. C. Nielsen, *J. Phys. Chem. A*, 1997, **101**, 8597.

14. D. Rugar, R. Budakian, H. J. Mamin and B. W. Chui, *Nature*, 2004, **430**, 329.
15. A. G. Web, *Prog. Nucl. Magn. Reson. Spectrosc.*, 1997, **31**, 1.
16. Y. S. Greenberg, *Rev. Mod. Phys.*, 1998, **70**, 175.
17. G. Feher, *Phys. Rev.*, 1956, **103**, 834.
18. J. Kohler, J. A. J. M. Disselhorst, M. C. J. M. Donckers, E. J. J. Groenen, J. Schmidt and W. E. Moerner, *Nature*, 1993, **363**, 242.
19. J. Wrachtrup, C. von Borczyskowski, J. Bernard, M. Orritt and R. Brown, *Nature*, 1993, **363**, 244.
20. Y. Ishii and R. Tycko, *J. Magn. Reson.*, 2000, **142**, 199.
21. D. L. Vander Hart, W. L. Earl and A. N. Garroway, *J. Magn. Reson*, 1981, **44**, 361.
22. B.-J. van Rossum, G. J. Boender and H. J. M. de Groot, *J. Magn. Reson. A*, 1996, **120**, 274.
23. U. Haeberlen, Solid-state NMR in high and very high magnetic fields, *NMR, Basic Principles and Progress*, R. Freeman and J. B. Robert, eds., vol. 25, Springer, Berlin, 1991, p. 143.
24. T. Meersmann, M. Shwager, V. Varma and G. Bodenhausen, *J. Magn. Reson. A*, 1996, **119**, 275.
25. K. Pervushin, R. Riek, R. Wider and K. Wüthrich, *Proc. Natl. Acad. Soc.*, 1997, **94**, 12366.
26. A. Poon, J. Birn and A. Ramamoorthy, *J. Phys. Chem. B*, 2004, **108**, 16577.
27. Y. Wei, D. K. Lee and A. Ramamoorthy, *J. Am. Chem. Soc.*, 2001, **123**, 6118.
28. P. L. Kuhns, S.-H. Lee, C. Coretsopoulos, P. C. Hammel, O. Gonen and J. S. Waugh, *Rev. Sci. Instrum.*, 1991, **62**, 2159.
29. R. McNamara, C. H. Wu and S. J. Opella, *J. Magn. Reson.*, 1992, **100**, 559.
30. A. S. Lipton, G. W. Buchko, J. A. Sears, M. A. Kennedy and P. D. Ellis, *J. Am. Chem. Soc.*, 2001, **123**, 992.
31. S. Kidambi, D. K. Lee and A. Ramamoorthy, *Inorg. Chem.*, 2003, **42**, 3142.
32. S. Kidambi and A. Ramamoorthy, *Inorg. Chem.*, 2003, **42**, 2200.
33. A. S. Lipton, R. W. Heck and P. D. Ellis, *J. Am. Chem. Soc.*, 2004, **126**, 4735.
34. P. Styles and N. F. Soffe, *J. Magn. Reson.*, 1984, **60**, 397.
35. Z. Serber, C. Richter, D. Moskau, J.-M. Böhlen, T. Gerfin, D. Marek, M. Häberli, L. Baselgia, F. Laukien, A. S. Stern, J. C. Hoch and V. Dötsch, *J. Am. Chem. Soc.*, 2000, **122**, 3554.
36. P. C. Myhre, G. G. Web and C. S. Yannoni, *J. Am. Chem. Soc.*, 1990, **112**, 8991.
37. D. A. Hall, D. C. Maus, G. J. Gerfen, S. J. Inati, L. R. Becerra, F. W. Dahlquist and R. G. Griffin, *Science*, 1997, **276**, 930.
38. R. W. Martin and K. W. Zilm, *J. Magn. Reson.*, 2004, **168**, 202.
39. S. C. Shekar, D. K. Lee and A. Ramamoorthy, *J. Am. Chem. Soc.*, 2001, **123**, 7467.
40. Y. S. Balazs and L. K. Thompson, *J. Magn. Reson.*, 1999, **139**, 371.
41. D. L. Jakeman, D. J. Mitchell, A. Shuttleworth and J. N. S. Evans, *J. Biomol. NMR*, 1998, **12**, 417.
42. R. H. Havlin and R. Tycko, *Pro. Natl. Acad. Soc.*, 2005, **102**, 3284.
43. D. K. Lee, K. A. H. Wildman and A. Ramamoorthy, *J. Am. Chem. Soc.*, 2004, **126**, 2318.
44. K. J. Hallock, K. H. Wildman, D. K. Lee and A. Ramamoorthy, *Biophys. J.*, 2002, **82**, 2499.
45. C. R. Bowers and D. P. Weitekamp, *Phys. Rev. Lett.*, 1986, **57**, 2645.
46. E. Johansson, L. E. Olsson, S. Mansson, J. S. Petersson, K. Golman, F. Stahlberg and R. Wirestam, *Magn. Reson. Med.*, 2004, **52**, 1043.
47. S. B. Duckett, C. L. Newell and R. Eisenberg, *J. Am. Chem. Soc.*, 1993, **115**, 1156.
48. A. Pines, M. G. Gibby and J. S. Waugh, *J. Chem. Phys.*, 1973, **59**, 569.
49. J. Schaefer, E. O. Stejskal and R. Buchdahl, *Macromolecules*, 1975, **8**, 291.
50. S. Hediger, B. H. Meier, N. D. Kurur, G. Bodenhausen and R. R. Ernst, *Chem. Phys. Lett.*, 1994, **223**, 283.
51. M. H. Levitt, Symmetry-based pulse sequences in magic-angle spinning solid-state NMR, *Encyclopedia of Nuclear Magnetic Resonance*, D. M. Grant and R. K. Harris, eds., Vol. 9, Wiley, Chichester, 2002, p. 165.
52. A. Brinkmann, M. Eden and M. H. Levitt, *J. Chem. Phys.*, 2000, **112**, 8539.
53. T. Fujiwara, P. Khandelwal and H. Akutsu, *J. Magn. Reson.*, 2000, **145**, 73.
54. Y. Matsuki, H. Akutsu and T. Fujiwara, *J. Magn. Reson.*, 2003, **162**, 54.
55. M. F. Summers, L. G. Marzilli and A. Bax, *J. Am. Chem. Soc.*, 1986, **108**, 4285.

56. (a) M. Hong and S. Yamaguchi, *J. Magn. Reson.*, 2001, **150**, 43; (b) Y. Wei, D. K. Lee, K. J. Hallock and A. Ramamoorthy, *Chem. Phys. Lett.*, 2002, **351**, 42.
57. K. Saalwachter and A. Ramamoorthy, Sensitivity enhancement by inverse detection in solids, *NMR of Biological Solids*, A. Ramamoorthy, ed., Taylor and Frances, Oxfordshire, 2005, Chapter 6.
58. K. Takegoshi, S. Nakamura and T. Terao, *J. Chem. Phys.*, 2003, **118**, 2325.
59. K. Takegoshi and T. Terao, *J. Chem. Phys.*, 2002, **117**, 1700.
60. E. Katoh, K. Takegoshi and T. Terao, *J. Am. Chem. Soc.*, 2004, **126**, 3653.
61. C. M. Rienstra, M. Hohwy, M. Hong and R. G. Griffin, *J. Am. Chem. Soc.*, 2000, **122**, 10979.
62. R. A. Wind, M. J. Duijvestijn, C. van der Lugt, A. Manenschijn and J. Vriend, *Prog. Nucl. Magn. Reson. Spectrosc.*, 1985, **17**, 33.
63. R. A. Wind, in *Encyclopedia of Nuclear Magnetic Resonance*, vol. 3, D. M. Grant and K. H. Harris, eds., Wiely, Chichester, 1996, 1798.
64. A. W. Overhauser, *Phys. Rev.*, 1953, **92**, 411.
65. A. Henstra, P. Dirksen and W. Th. Wenckebach, *Phys. Lett. A*, 1988, **134**, 134.
66. M. Rosay, A.-C. Zeri, N. S. Astrof, S. J. Opella, J. Herzfeld and R. G. Griffin, *J. Am. Chem. Soc.*, 2001, **123**, 1010.
67. D. J. Lurie, M. A. Foster, D. Yeung and J. M. S. Hutchison, *Phys. Med. Biol.*, 1998, **43**, 1877.
68. J. H. Ardenkjaer-Larsen, B. Fridlung, A. Gram, G. Hansson, M. H. Lerche, R. Servin, M. Thaning and K. Golman, *Proc. Natl. Acad. Soc.*, 2003, **100**, 10158.
69. L. R. Becerra, G. J. Gerfen, B. F. Bellew, J. A. Bryant, D. A. Hall, S. J. Inati, R. T. Weber, S. Un, T. F. Prisner, A. E. McDermott, K. W. Fishbein, K. E. Kreischer, R. J. Temkin, D. J. Singel and R. G. Griffin, *J. Magn. Reson. A*, 1995, **117**, 28.
70. (a) T. Idehara, I. Ogawa, S. Mitsudo, M. Pereyaslavets, N. Nishida and K. Yoshida, *IEEE Trans. Plasma Sci.*, 1999, **27**, 340; (b) M. K. Hornstein, V. S. Bajaj, R. G. Griffin, K. E. Kreischer, I. Mastovsky, M. A. Shapiro, J. R. Sirigiri and R. J. Temkin, *IEEE Trans. Electr. Dev.*, 2005, **52**, 798.
71. K.-N. Hu, H. Yu, T. M. Swager and R. G. Griffin, *J. Am. Chem. Soc.*, 2004, **126**, 10844.
72. R. Tycko and J. A. Reimer, *J. Phys. Chem.*, 1996, **100**, 13240.
73. V. Callot, E. Canet, J. Brochot, M. Viallon, H. Humblot, A. Briguet, H. Tournier and Y. Crémillieux, *Magn. Reson. Med.*, 2001, **46**, 535.
74. J. Smith, K. Knagge, L. J. Smith, E. MacNamara and D. Raftery, *J. Magn. Reson.*, 2002, **159**, 111.
75. L. Dubois, P. D. Silva, C. Landon, J. G. Huber, M. Ponchet, F. Vovelle, P. Berthault and H. Desvaux, *J. Am. Chem. Soc.*, 2004, **126**, 15738.
76. H. W. Long, H. C. Gaede, J. Shore, L. Reven, C. R. Bowers, J. Kritzenberger, T. Pietrass, A. Pines, P. Tang and J. A. Reimer, *J. Am. Chem. Soc.*, 1993, **115**, 8491.
77. R. Tycko, *Solid State Nucl. Magn. Reson.*, 1998, **11**, 1.
78. A. Goto, K. Hashi, T. Shimizu, R. Miyabe, X. Wen, S. Ohki, S. Machida, T. Iijima and G. Kido, *Phys. Rev. B*, 2004, **69**, 075215-1.
79. H. W. van Kesteren, W. Th. Wenckebach and J. Schmidt, *Phys. Rev. Lett.*, 1985, **55**, 1642.
80. K. Takeda, K. Takegoshi and T. Terao, *J. Phys. Soc. Jpn.*, 2004, **73**, 2313.
81. R. Kaptein, in *Biological Magnetic Resonance*, Vol. 4, L. J. Berliner and J. Reuben, eds., Plenum press, New York, 1982, 145.
82. T. Polenova and A. E. McDermott, *J. Phys. Chem. B*, 1999, **103**, 535.
83. A. E. Roy, P. Gast, H. J. van Gorkom, H. J. M. de Groot, G. Jeschke and J. Matysik, *J. Am. Chem. Soc.*, 2004, **126**, 12819.
84. Y. Ishii, J. P. Yesinowski and R. Tycko, *J. Am. Chem. Soc.*, 2001, **123**, 2921.
85. Y. Ishii, N. P. Wickramasinghe and S. Chimon, *J. Am. Chem. Soc.*, 2003, **125**, 3438.
86. A. E. Bennett, C. M. Rienstra, M. Auger, K. V. Lakshmi and R. G. Griffin, *J. Chem. Phys.*, 1995, **103**, 6951.
87. A. K. Khitrin, T. Fujiwara and H. Akutsu, *J. Magn. Reson.*, 2003, **162**, 46.
88. M. Ernst, A. Samoson and B. H. Meier, *J. Magn. Reson.*, 2003, **163**, 332.
89. B. C. Gerstein, R. G. Pembleton, R. C. Wilson and L. M. Ryan, *J. Chem. Phys.*, 1977, **66**, 361.
90. D. Sakellariou, A. Lesage, P. Hodgkinson and L. Emsley, *Chem. Phys. Lett.*, 2000, **319**, 253.
91. A. T. Petkova and R. Tycko, *J. Magn. Reson.*, 2002, **155**, 293.

92. T. P. Peck, R. L. Magin and P. C. Lauterbur, *J. Magn. Reson. B*, 1995, **108**, 114.
93. K. Yamauchi, J. W. G. Janssen and A. P. M. Kentgens, *J. Magn. Reson.*, 2004, **167**, 87.
94. M. Ernst, A. Samoson and B. H. Meier, *Chem. Phys. Lett.*, 2001, **348**, 293.
95. J. J. Heckman, M. P. Ledbetter and M. V. Romalis, *Phys. Rev. Lett.*, 2003, **91**, 067601-1.
96. R. McDermott, S.-K. Lee, B. ten Haken, A. H. Trabesinger, A. Pines and J. Clarke, *Proc. Natl. Acad. Soc.*, 2004, **101**, 7857.
97. A. N. Matlachov, P. L. Volegov, M. A. Espy, J. S. George and R. H. Kraus Jr., *J. Magn. Reson.*, 2004, **170**, 1.
98. E. R. Davis, *Phys. Lett. A.*, 1974, **47**, 1.
99. B. Cagnac, J. Brossel and A. Katker, *C.R. Acad. Sci.*, 1958, **246**, 1827.
100. I. C. Bowater, J. M. Brown and A. Carrington, *Proc. Roy. Soc. Lond. A*, 1973, **333**, 265.
101. B. E. Kane, L. N. Pfeiffer and K. W. West, *Phys. Rev. B*, 1992, **46**, 7264.
102. G. Yusa, K. Muraki, K. Takeshina, K. Hashimoto and Y. Hirayama, 2005, *Nature*, 2005, **434**, 1001.
103. I. I. Rabi, J. R. Zacharias, S. Millman and P. Kusch, *Phys. Rev.*, 1938, **53**, 318.
104. A. Abragam, *Principles of Nuclear Magnetism*, Oxford University Press, Oxford, 1961, 1.
105. T. Takeda, S. Komura, H. Seto, M. Nagai, H. Kobayashi, E. Yokoi, T. Ebisawa, S. Tasaki, C. M. E. Zeyen, Y. Ito, S. Takahashi and H. Yoshizawa, *Phys. B*, 1995, **213,214**, 863.
106. O. Züger, S. T. Hoen, C. S. Yannoni and D. Rugar, *J. Appl. Phys.*, 1996, **79**, 1881.
107. A. Schaff and W. S. Veeman, *J. Magn. Reson.*, 1997, **126**, 200.
108. L. Krabben, B.-J. van Rossum, F. Castellani, E. Bocharov, A. A. Schulga, A. S. Arseniev, C. Weise, F. Hucho and H. Oschkinat, *FEBS Lett.*, 2004, **564**, 319.
109. R. Tycko, *Annu. Rev. Phys. Chem.*, 2001, **52**, 575.
110. S. Kim and T. Szyperski, *J. Am. Chem. Soc.*, 2003, **125**, 1385.
111. B. Shapira, E. Morris, K. A. Muszkat and L. Frydman, *J. Am. Chem. Soc.*, 2004, **126**, 11756.

This page is left intentionally blank

Applications of Low-Field NMR to Food Science

B.P. HILLS

Institute of Food Research, Norwich Research Park, Colney, Norwich NR4 7UA, UK

ANNUAL REPORTS ON NMR SPECTROSCOPY
VOLUME 58 ISSN 0066 4103
DOI 10.1016/S0066-4103(05)58004-9

1. INTRODUCTION

A cursory glance at the contents list to this chapter shows that novel aspects of Nuclear Magnetic Resonance (NMR) continue to appear more than 55 years after its discovery, and this testifies to the amazing richness of nuclear spin physics. New techniques, new hardware, novel pulse sequences and improved data processing methods continue to appear in the literature and are making NMR an ever more powerful probe of the intricacies of material structure and dynamics. Several general trends can be discerned. The appearance of ultrafast protocols for acquiring multidimensional high-resolution spectra in solution-state NMR[1] is a noteworthy development that is motivated by the need for faster methods for the determination of biopolymer structure. The need to resolve overlapping spectral lines in large biopolymer molecules is also driving the development of new self-shielding magnet systems with ever-higher-field strengths, some now exceeding proton frequencies of 800 MHz. A similar trend can be found in high-resolution solid state NMR spectroscopy where magic angle spinning (MAS) frequencies of 70 kHz or more are now possible and this, together with novel multidimensional decoupling and recoupling protocols, has greatly facilitated determination of biopolymer structure in the solid state.[2,3] Alongside these "high-resolution" trends, there is a parallel effort to try to liberate NMR from the requirement for highly homogeneous and strong magnetic fields. The development of *ex situ* devices such as the NMR-MOUSE typifies this effort that is motivated by the need to have "open-access", hand-held NMR sensors able to operate outside the confines of the NMR laboratory. This requires new ways of performing NMR in highly inhomogeneous magnetic fields without the constraints of enclosing the sample in numerous coils and shields. There is also continuing effort to develop low-cost, low-field NMR sensors suitable for location around fast-moving conveyors in the industrial sector, and these developments are especially relevant to automated internal quality assessment of food products.

Most real foods are (soft)-solids rather than liquids, so, in the following section we will largely ignore the high-resolution, high-field, solution state developments and instead focus on the more relevant low-field aspects. Section 5 dealing with nutation spectroscopy, shim pulses and z-rotation pulse methods is an exception to this statement because these novel techniques open the way to resolving spectral peaks even in the inhomogeneous magnetic fields used in low-cost bench-top NMR hardware. The reader interested in more conventional high-resolution, high-field developments in metabolomics and food authenticity will find refs. 4–11 a useful stepping stone into this extensive literature. Likewise, the reader interested in new NMR data analysis protocols will find refs. 12 and 13 on multiway chemometrics a useful entry into this intensive research area.

Real foods are also extremely complex multicomponent, multiphase systems that display heterogeneity over distance scales ranging from the molecular to the macroscopic. Understanding structure–function relations in food therefore presents one of the greatest challenges in materials science, especially when it is remembered that this structural and dynamic heterogeneity is usually time-dependent, exhibiting phase changes, matrix and water redistribution and compositional changes during processing

and storage. Probing food functionality with NMR in real time therefore presents an almost unique challenge where extremely complex soft-solid materials are being probed by a uniquely subtle and powerful technique. The focus of this chapter will therefore be on new low-field NMR techniques even where these only have a potential, rather than realised, application to food. This emphasis has had to be at the expense of reviewing the plethora of more routine applications of standard low-field methods to various classes of food each of which really merits a chapter of its own. The author has recently written reviews on the NMR of horticultural products[14] and cereals[15] and this exercise could be repeated for dairy, meat and fish products as well. Nevertheless the focus on new low-field methodologies in this chapter will, it is hoped, help identify future directions for research and serve to alert food scientists to the enormous potential of low-field NMR in their discipline. We begin with the extension of NMR relaxometry and diffusometry to higher dimensions.

2. MULTIDIMENSIONAL RELAXOMETRY AND DIFFUSOMETRY

To date, the majority of low-field relaxation and diffusion studies on foods could be classified as "one-dimensional" (1D), "fixed spectrometer frequency" and "single nucleus" measurements. Typically a CPMG or inversion recovery pulse sequence would be used at a fixed spectrometer frequency to report the dependence of the proton transverse or longitudinal relaxation on some quality factor, processing or storage variable. While this is a valid approach it fails to exploit the huge amount of information potentially available with low-resolution NMR and is reminiscent of the use of 1D proton spectra in the early days of high-resolution NMR before the widespread use of multidimensional, multinuclear techniques. The advent of multidimensional relaxation and diffusion methods that can be implemented on low-field spectrometers has therefore been a noteworthy development in recent years and one that opens the door to new research areas in the NMR of food.

2.1. Multidimensional relaxometry

The T_1–T_2 cross correlation method is central to this development.[16] An inversion recovery step with a variable recovery time, t_1, is followed by a CPMG sequence acquired in a time t_2. The resulting 2D-array of CPMG echo trains, $M(t_1,t_2)$, is given as:

$$M(t_1, t_2) = \int \int dT_1 dT_2 F(T_1, T_2) k_1(T_1, t_1) k(T_2, t_2) \tag{1}$$

where $F(T_1,T_2)$ is the desired 2D relaxation "spectrum", which, more precisely, is the probability density of protons having relaxation times T_1 and T_2. The kernels are, in this case, those for relaxation during the inversion recovery and CPMG steps, respectively

$$k_1(T_1, t_1) = 1 - 2\exp\left(-t_1/T_1\right) \tag{2}$$

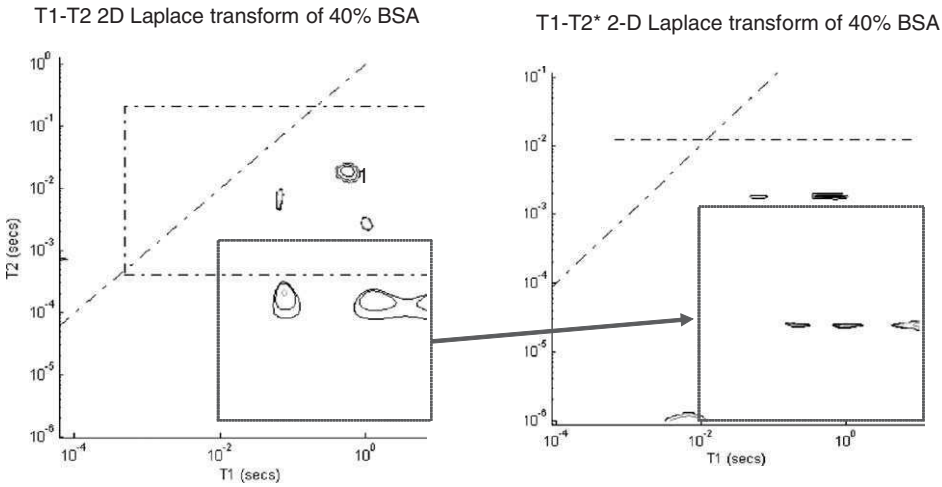

Fig. 1. (a) T_1–T_2 spectrum of a 40% BSA solution acquired at 100 MHz with a CPMG echo spacing of 200 μs. (b) The T_1–T_2* spectrum of the same sample showing the same peaks highlighted in the red box. The horizontal and vertical dashed lines show the limits of reliable measurement determined by the pulse spacings. The dashed diagonal line corresponds to $T_1 = T_2$. Courtesy of Dr. Nicola Woodward.

$$k(T_2, t_2) = \exp\left(-t_2/T_2\right) \tag{3}$$

The relaxation spectrum, $F(T_1,T_2)$ is obtained from $M(t_1,t_2)$ by a 2D inverse Laplace transformation. Hitherto this inversion step was an extremely lengthy computation that was rarely attempted, but the publication and dissemination of a fast 2D inverse Laplace algorithm[17] in 2002 transformed this situation and has opened the way to a revolution in multidimensional relaxometry and diffusometry. Fig. (1a) shows a representative T_1–T_2 spectrum of a 40% w/w solution of the globular protein bovine serum albumin (BSA), acquired in the authors laboratory. The main peak, labelled 1, corresponds to water protons, or, more precisely, to the pool of rapidly exchanging protons, which includes the pool of rapidly exchanging protons on the BSA, such as the hydroxyl and amino protons. The other peaks arise from the non-exchanging (and slowly exchanging) protein protons and these peaks appear even in quite dilute solution when they would not be observed in a simple CPMG sequence. The appearance of such peaks is to be expected because there will always be one value of the inversion recovery time, t_1, which nulls the longitudinal magnetisation of the water protons, leaving only the signal from the non-exchanging protein protons. In principle, therefore, this method permits an alternative way for studying the changing dynamics of biopolymers either in native form or in various states of aggregation and/or gelation. The shortest T_2 that can be meaningfully resolved in the T_1–T_2 sequence is, of course, limited by the shortest echo time in the CPMG part of the sequence, which is typically about 200 μs.

The horizontal and vertical dashed lines in the spectra show these measurement limits. Shorter transverse relaxation times can be observed with the T_1–T_2* sequence which replaces the CPMG part of the sequence with an FID. This sequence is, of course, appropriate to more solid-like systems with short intrinsic transverse relaxation times otherwise the FID is dominated by dephasing caused by magnet-field inhomogeneity. Fig. 1b shows the T_1–T_2* spectrum of the same sample and the correspondence in the protein proton peaks.

Because the data analysis is usually performed with MATLAB it is straightforward to integrate peak areas, ''zoom-in'' on interesting features and list peak positions in the usual way. However, great care is needed in implementing the 2D Laplace inversion to avoid the appearance of spurious peaks in the spectrum. In particular, the regularisation parameter in the algorithm should be adjusted according to the amount of signal/noise in the data even though this can be a time-consuming exercise. Indeed, the acquisition of a T_1–T_2 spectrum can take several hours so it is not to be considered a rapid analytical tool.

The acquisition of a single T_1–T_2 or T_1–T_2* spectrum at a fixed frequency is just the simplest weapon in the multidimensional armoury. Because of susceptibility effects, proton exchange and intercompartmental diffusion in biopolymer systems and cellular tissue, T_2 is, in general, a function of both the spectrometer frequency and of the CPMG pulse spacing, τ. In addition, T_1, usually has a dispersive dependence on spectrometer frequency, decreasing with decreasing frequency and this dispersion is usually studied with NMR field cycling relaxometry. In general, therefore, one should write $T_1(\omega_0)$–$T_2(\omega_0,\tau)$ and consider a 3D or 4D stacking of spectra in the additional ω_0 and τ dimensions. The ω_0 dimension is best explored by implementing the sequence on a field cycling spectrometer, but to date there appear to be no reports of this approach. A field-cycling $T_1(\omega_0)$–T_2 study would appear to have many advantages because peaks that overlap at high-spectrometer frequency in a T_1–T_2 spectrum may well be resolved at lower frequencies where the T_1 differences get amplified. This runs counter to the usual situation in the frequency domain where, of course, overlapping peaks are often resolved by moving to higher spectrometer frequencies. On the other hand, spectral resolution of peaks at higher spectrometer frequencies is also a possibility in multidimensional relaxometry. Instead of acquiring only a single point at the echo maximum in the CPMG dimension, whole echoes can be recorded in the third dimension and spectral peaks, such as those of lipid and water, resolved in the third dimension by Fourier transformation. A 2D-Laplace inversion of the 2D data set for each spectral peak then generates separate T_1–T_2 spectra. In this way multidimensional relaxation spectra can, in principle, be acquired for each chemically shifted proton species such as lipids, sugars and water, which can greatly assist in peak assignment.[18] At low frequencies, where water and lipid are not resolved in the frequency domain, it may be possible to obtain separate water and lipid spectra by exploiting the Dixon reconstruction method that separates the lipid and water signals by taking linear combinations of the CPMG spin echoes acquired at different echo times.[19,23]

A $T_{1\rho}$–T_2 or $T_{1\rho}$–T_2* spectrum could be acquired by replacing the initial inversion recovery sequence with a spin-locking sequence of a hard 90_x pulse followed

immediately by a phase shift for a variable time t_1 before the subsequent CPMG or FID in the t_2 dimension. The kernel k_1 then needs to be replaced by

$$k_1(T_1, t_1) = \exp\left(-t_1/T_1\rho\right) \tag{4}$$

Because $T_{1\rho}(\omega_0,\omega_1)$ is a function of both the spectrometer frequency, ω_0, and the radiofrequency (RF) field strength, ω_1, this could be useful in cases where there are exchange processes or slow molecular motions at frequencies in the range 10^5–$10^3 s^{-1}$. It is also possible to weight the T_1–T_2, T_1–T_2*, $T_{1\rho}$–T_2 and $T_{1\rho}$–T_2* sequences with various additional preparation sequences. For example, various degrees of water suppression could be introduced with an initial PGSE sequence with a pulsed gradient attenuation factor, $\exp(-q^2D\Delta)$, sufficient to suppress the more mobile water, allowing slower diffusing solutes such as sugars and biopolymers, as well as lipids, to be preferentially examined at higher receiver gain. Conversely, higher molecular weight species with shorter transverse relaxation times could be selectively suppressed with an initial Hahn echo with a suitably long echo time. It is surprising that such applications are yet to appear in the literature.

2.2. Multidimensional diffusometry

The PGSE sequence introduced for water suppression in the multidimensional relaxation sequences can, of course, be used to measure diffusivity by systematically varying the wavevector q and/or the diffusion time, Δ, and this idea is the basis for multidimensional diffusometry.[16] Perhaps the simplest such 2D sequence comprises a CPMG sequence with variable numbers of echoes in the first dimension followed by a PGSE sequence (either a Hahn echo or a stimulated echo) in the second dimension. The kernels are therefore,

$$k_1 = \exp(-q^2D\Delta) \text{ with variable } q^2\Delta \tag{5}$$

$$k_2 = \exp(-t_2/T_2) \text{ with variable } t_2 = 2n\tau \tag{6}$$

2D inverse Laplace transformation therefore yields the D–T_2 spectrum, examples of which can be seen in Figs. 6 and 8d. In systems containing both water and lipid, separate T_2–D spectra for the water and lipid can be obtained in an analogous way to the T_1–T_2 spectra, namely by working at high-spectrometer frequency and Fourier transforming the final stimulated echo and performing the 2D inverse Laplace transformation on either the water or oil signal. This was the protocol used by Hubbard and coworkers in their study of cheese,[18] discussed in greater detail in Section 2.4.3. It is worth bearing in mind that the kernel in Eq. (5) is formally valid only for unrestricted diffusion. In cases where diffusion is restricted it may be better to perform a higher dimensional analysis by varying both q and Δ independently. A 2D spectrum $D(q)$–T_2 could be obtained by first varying Δ at fixed q.

The q-dependence would then create a 3D stacked plot whose functional dependence on q would be a useful indicator of the nature of the restricted diffusion. This strategy was used in 1D measurements of $D(q,\Delta)$ of emulsions.[20]

2D diffusion correlation spectra of the type D_1-D_2 can also be acquired via double Laplace inversion of the echoes arising from independent double PGSE encoding in the q_1–q_2 dimension with the **q-**vectors in either collinear or orthogonal directions. If there is no mixing time between the q_1 and q_2 measurements, as in Fig. 2a, then the correlation spectrum, called the DDCOSY–PGSE sequence[16] reveals whether the microstructure creates local diffusive anisotropy in an otherwise macroscopically isotropic material. Indeed, any food matrix which locally restricts water diffusion in one or two dimensions within a small domain with a connection to another, differently oriented domain would be expected to show correlations in the D_1–D_2 spectra. Correlations between the diffusivities before and after a well-defined mixing time, t_m, can be detected with the sequence shown in Fig. 2b, and this has been called the DEXSY–PGSE sequence.[16] This is especially useful if the mixing time is long enough to permit water to diffuse between differently oriented microstructural domains in the matrix. Callaghan *et al.*[16] tested these sequences on the polydomain lamellar phase of the lyotropic liquid crystal, 25% aerosol OT/water.

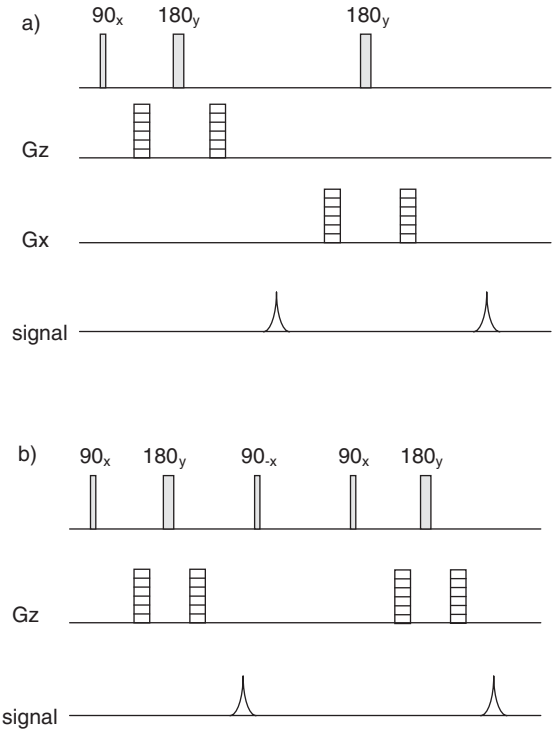

Fig. 2. Pulse sequences for 2D D_1–D_2 correlation spectroscopy. (a) DDCOSY (b) DEXSY.

Higher-dimensional relaxation–diffusion correlation spectra such as a 4D D_1–D_2–T_1–T_2 spectrum can, of course, be formulated but the author is unaware of any such combinations in the literature. The lengthy measurement times, which can run into many hours, place upper limits on practical combinations and it remains a future challenge to seek ways to reduce this acquisition time. Multinuclear applications are another aspect to be explored in multidimensional relaxometry. The deuterium resonance, especially in D_2O, would seem to be an obvious candidate for simplifying complex spectra by removing the non-exchanging CH resonances of biopolymers and solutes.

2.3. Cross-relaxation and diffusive exchange

Before turning to multidimensional applications it helps to consider the likely effects of cross-relaxation and diffusive exchange on T_1–T_2 spectra.[21] Consider 2 proton pools with intrinsic longitudinal or transverse relaxation rates T_a and T_b. In the absence of cross relaxation two peaks in the 2D T_1–T_2 spectrum would, of course, be observed at T_a and T_b but if there is cross-relaxation at rates k_b and k_a caused by proton exchange, or, in the case of longitudinal magnetisation, by secular dipolar interactions or spin diffusion, this is no longer necessarily the case. By solving the usual two-site chemical exchange equations for the case of equal populations it is straightforward to show that the relaxation rates emerge in the generalised form,

$$\begin{aligned} s^{\pm} = & -0.5(R_a + k_a + R_b + k_b) \pm 0.5\{(R_a + k_a + R_b + k_b)^2 \\ & - 4[(R_a + k_a)(R_b + k_b) - k_a k_b]\}^{1/2} \end{aligned} \tag{7}$$

where s^+ and s^- are exponential relaxation rates and $R_{a,b} = 1/T_{a,b}$. This shows that the relaxation rates, s^+ and s^-, are shifted by the exchange lifetime terms and can assume values that are much larger than the largest of the intrinsic rates R_a or R_b. For example, if the populations are equal and the intrinsic relaxation rates are $R_a = 2\,s^{-1}$ and $R_b = 10\,s^{-1}$ an intermediate exchange rate where $k_a = k_b = 10\,s^{-1}$ gives predicted rates$|s^+|$and$|s^-|$of 5.2 and 26.8 s^{-1} respectively. Note how a peak arises with a relaxation rate (26.8 s^{-1}) in excess of the fastest intrinsic relaxation rate (10 s^{-1}). Such peaks have been called "exchange peaks"[21] and, in the T_1 dimension, can give rise to peaks positioned to the left of the diagonal $T_1 = T_2$ line where T_1 is less than T_2, which for a non-exchanging single component proton pool would imply a unphysical spectral density that increases with increasing frequency. It is possible that the low intensity peaks with $T_1 < T_2$ in the spectra of sucrose solutions in Fig. 3 may arise in this way, but given their low relative intensity and the sensitivity of the 2D inverse Laplace transform to noise they could also be artefacts of the inversion process. Clearly more work is needed to clarify the role of exchange in these multidimensional spectra.

In cellular tissue such as fruit, vegetables and meat, there is not only proton exchange to consider but also diffusive exchange of water between subcellular organelles such as the vacuole, cytoplasm and the extracellular space. In general one cannot assume that the diffusion of water between subcellular compartments is

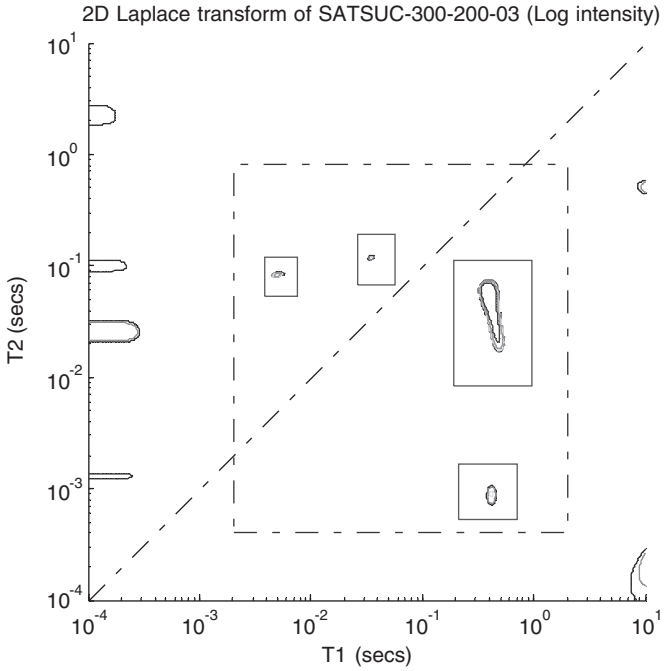

Fig. 3. The T_1–T_2 spectrum of a saturated sucrose solution acquired at 300.15 MHz with a CPMG echo spacing of 200 μs. The dominant peak arises from the exchangeable proton pool; the minor peak below it to non-exchanging CH protons. The two minor peaks above the diagonal dashed line (denoting $T_1 = T_2$) could be exchange peaks.

always slow on the NMR measurement timescale. In the limit of fast diffusive exchange only a single peak at the average relaxation time for all the compartments is observed and all morphological information is lost. But it is the intermediate exchange regime that is most difficult to analyse theoretically. The effect of coupled relaxation and diffusion in compartmentalised systems can, in principle, be predicted by 2D inverse Laplace transformation of the theoretical decay curves emerging from solution of the Bloch–Torrey equations, though this has yet to be attempted for cellular tissue. The data for cellular tissue to be discussed in the next section show that it is possible to distinguish water peaks from the vacuole, cytoplasm and cell wall, though the interpretation is complicated not only by possible diffusion effects but also by the biological variation in cell size and shape.

The effect of diffusion through internal gradients created by susceptibility discontinuities across interfaces has been studied in the context of water- or oil-saturated porous rocks[22] and this approach could be carried over into cellular tissue. Such internal gradients can be studied by dividing the CPMG sequence into two parts. The second part of the 2D sequence is acquired with a variable n echoes and a short pulse spacing, τ, so it measures pure transverse relaxation without the complications of diffusion through internal gradients. On the other hand the first part is

sensitised to diffusion through internal gradients by varying the 180°-pulse spacing, τ_1 by using different numbers of echoes in a fixed total acquisition time, t_1. The resulting echo attenuation is given as:

$$M(\tau_1, 2n\pi) = \int\int \mathrm{F}(\mathrm{DG}_{\mathrm{av}}^2, T_2)\ \exp[-(t_1 + 2n\tau)/T_2] \exp[-\gamma^2 \mathrm{DG}_{\mathrm{av}}^2 \tau_1^2/3)]\ \mathrm{d}T_2 \mathrm{d}(\mathrm{DG}_{\mathrm{av}}) \quad (8)$$

where 2D inverse Laplace inversion gives the distribution, $\mathrm{F}(\mathrm{DG}_{\mathrm{av}}^2, T_2)$, of the average internal gradient, G_{av}, (weighted by the diffusion coefficient, D) and the transverse relaxation time. In porous rocks the T_2 distribution is related to the pore size distribution so the spectrum, $F(DG_{\mathrm{av}}^2, T_2)$ shows the distribution of internal gradients for different pore sizes. A similar approach could be used for heterogeneous (porous) food materials but, as far as the author is aware, this has yet to be tried. If the gradient distribution arises not from the sample but from external B_0 inhomogeneities then a very similar approach can be used to acquire 2D relaxation spectra in inhomogeneous fields (see Section 3.3).

2.4. Applications

Multidimensional relaxation and diffusion protocols have been tested, for the most part, on phantoms and porous rock materials.[17] Food applications are beginning to appear in the literature but many are still of an exploratory nature.

2.4.1. *Horticultural products*

Because of the complex multi-compartment intracellular structure of cellular plant tissue, multidimensional methods are especially valuable for researching subtle quality defects in horticultural products, even though peak assignment cannot always be done with confidence.

2.4.1.1. Apple. Mealiness in apples is a quality problem that can arise during long-term storage and is associated with changes in cell wall adhesion. Intercellular adhesion is strong in a healthy apple so that chewing causes immediate cell rupture and liberation of the juice in the mouth. In contrast, the intercellular adhesion is weak in a mealy apple so that chewing merely causes intact cells to separate but not rupture, resulting in an unpleasant sensation akin to eating a dry powder rather than apple. Unfortunately this quality defect cannot be detected by external examination so fruit growers and sorters are keen to find a non-invasive method for its detection. Being sensitive to subcellular water compartmentation, NMR would seem to be a promising detection tool, and multidimensional methods are ideal for identifying which of the various NMR parameters such as T_1, T_2 and D are the best probes of mealiness. Fig. 4a shows the four main peaks characterising the T_1–T_2 correlation spectrum for parenchyma tissue of fresh red delicious apple measured at 23.4 MHz.[96] Peak 4 with T_1 and T_2 less than 100 ms has a relative area of only

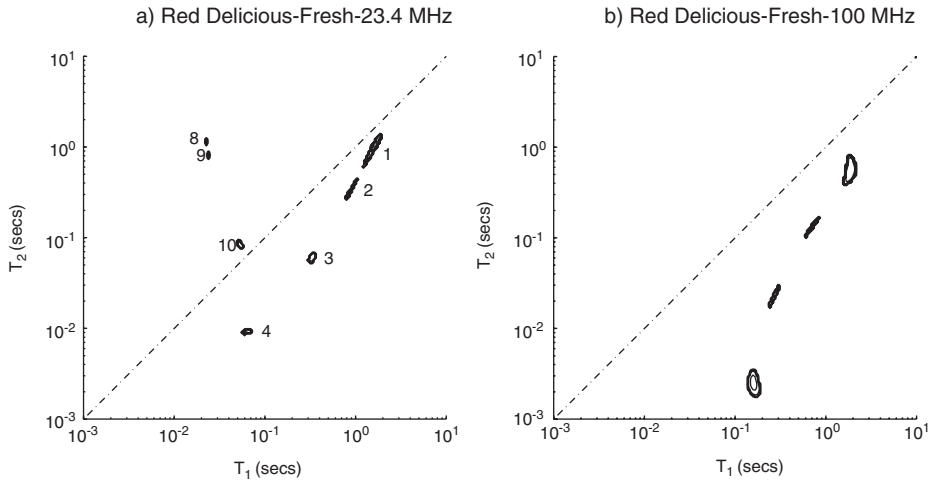

Fig. 4. Experimental T_1–T_2 spectrum of the parenchyma tissue of fresh red delicious apple measured with a CPMG echo spacing of 400 μs. (a) 23.4 MHz. (b) 300.15 MHz. Courtesy of Niusa Marigheto.

1% of the total, which, together with its short relaxation times suggests it arises from water closely associated with more rigid components of the cell wall. Earlier 1D CPMG studies have assigned the two dominant peaks 1 and 2 to water in the vacuole and water in the cytoplasm and extracellular water respectively. The elongated shape of these two peaks suggests that there may be an additional component that is not well resolved or it may simply be a consequence of cell size distribution. Fig. 4b shows the same sample measured at the higher frequency of 300.15 MHz, showing the shift to shorter T_2's expected when susceptibility-induced gradients dominate. The small peaks labelled 8–10 in the $T_1 < T_2$ domain in Fig. 4a may be an artefact of the Laplace inversion but it is tempting to argue that it is a consequence of proton exchange,[21] if it be so, it is strange that it does not appear in the higher frequency spectrum also.

Figs. 5a and 5b show the corresponding T_1–T_2 spectrum for the same sample of parenchyma tissue taken from a mealy red-delicious apple at spectrometer frequencies of 23.4 and 300 MHz respectively. A comparison with the fresh apple spectra (and of similar spectra for other apples) suggests that the mealy condition is associated with the transfer of water out of the vacuole into the cytoplasm and extracellular spaces resulting in a reduction in the vacuolar peak area from 83.7% (fresh) to 63.8% (mealy).[96] The radically different spectrum observed at 300 MHz is once again a result of diffusion through strong internal field gradients created by the magnetic susceptibility difference across the air–water interface in the air spaces in the tissue. This greatly increases the transverse dephasing rate and enhances the effects of polydispersity. The main result is the appearance of a large and distorted peak in Fig. 5b.

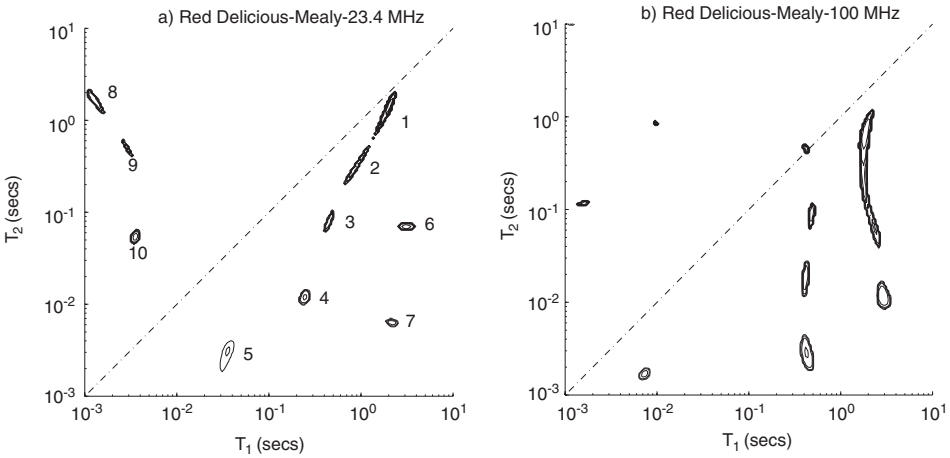

Fig. 5. Experimental T_1–T_2 spectrum of the parenchyma tissue of a mealy red delicious apple measured with a CPMG echo spacing of 400 μs. (a) 23.4 MHz. (b) 300.15 MHz. Courtesy of Niusa Marigheto.

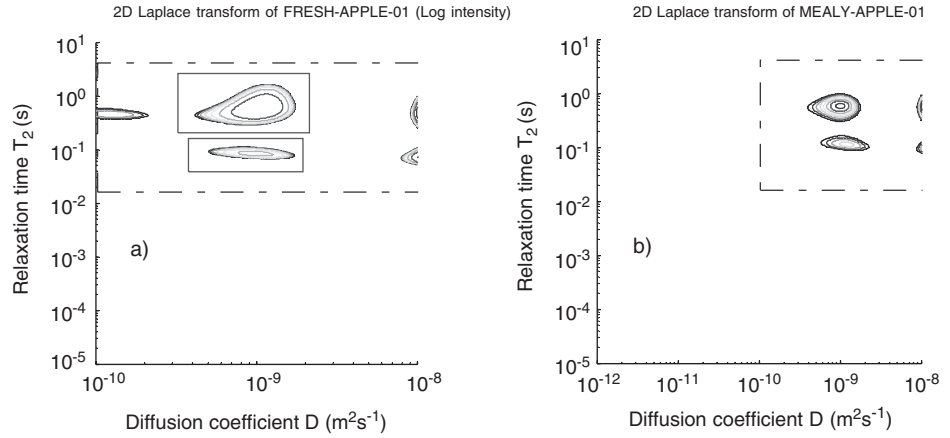

Fig. 6. T_2–D spectra of the parenchyma tissue of red delicious apple acquired at 23.4 MHz. (a) Fresh tissue (b) Mealy tissue. Courtesy of Niusa Marigheto.

The T_2–D spectra of both fresh and mealy apple in Fig. 6 consist of two peaks that can be provisionally assigned to water in the vacuole (upper peak) and to the cytoplasm (lower peak). In the relatively few samples studied, it was found that the effective diffusion coefficient of water in the cytoplasmic compartment was slightly increased relative to that of the vacuole in mealy apples, perhaps because of increased membrane permeability. Despite the tentative interpretation and the uncertainty in peak assignments, the apple data show the potential for correlation analysis of physiological conditions in many diverse kinds of cellular tissue.

2.4.1.2. Avocado. Multidimensional methods have also been used to study avocado where the appearance of hard lumps in the tissue and low oil content are important quality defects.[24] Indeed, finding fast, non-invasive methods for measurement of avocado oil content is an industrial priority because of legislation preventing the marketing of immature avocado.[28–32] For example, the South African Growers Association sets a lower limit of 9.8% oil (wet mass basis) for the harvesting of the Hass variety and similar regulations apply in both importing and exporting countries. The amount of avocado oil, which occurs as droplets in the parenchyma cells, increases with maturity from typical values of 5% w/w in the flesh of unripe fruit to maximum values of 34% in some varieties of ripe fruit.

The T_1–T_2 spectrum of oil extracted from fresh avocado acquired at a proton frequency of 23.4 MHz and short CPMG pulse spacing of 200 μs shows two overlapping peaks close to the diagonal ($T_1 = T_2$) (see Fig. 7a) and these separate in the higher frequency spectrum at 300.15 MHz (Fig. 7b). However it is unclear whether these two oil peaks arise from molecules of differing mobility, such as the oleic and palmitic constituents, or from non-equivalent proton pools of different mobility, such as those on methyl and olefinic groups. This could be decided from the frequency spectrum or by running T_1–T_2 spectra of the separated oil components, but these additional experiments were not undertaken.

Fig. 8a shows the T_1–T_2 correlation spectrum for fresh avocado tissue dissected from the middle part of the fruit and acquired at 23.4 MHz and a pulse spacing of 200 μs. In addition to the oil peaks there are now additional peaks from the water and exchangeable biopolymer protons. The longest T_2 peak presumably arises from vacuolar water; but assignment of the other water peaks to the extracellular, cytoplasm and cell wall compartments cannot be done with any confidence. Fig. 8b

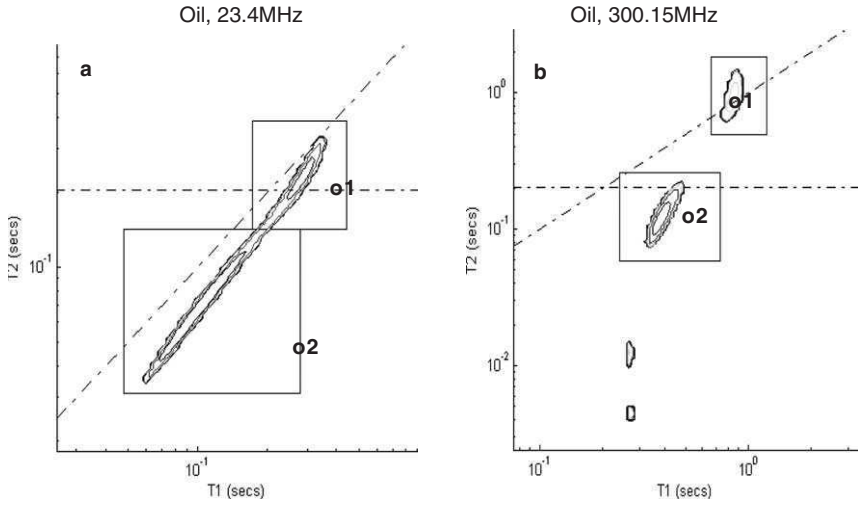

Fig. 7. T_1–T_2 spectra of avocado oil acquired with an echo spacing of 200 μs at. (a) 23.4 and. (b) 300.15 MHz.

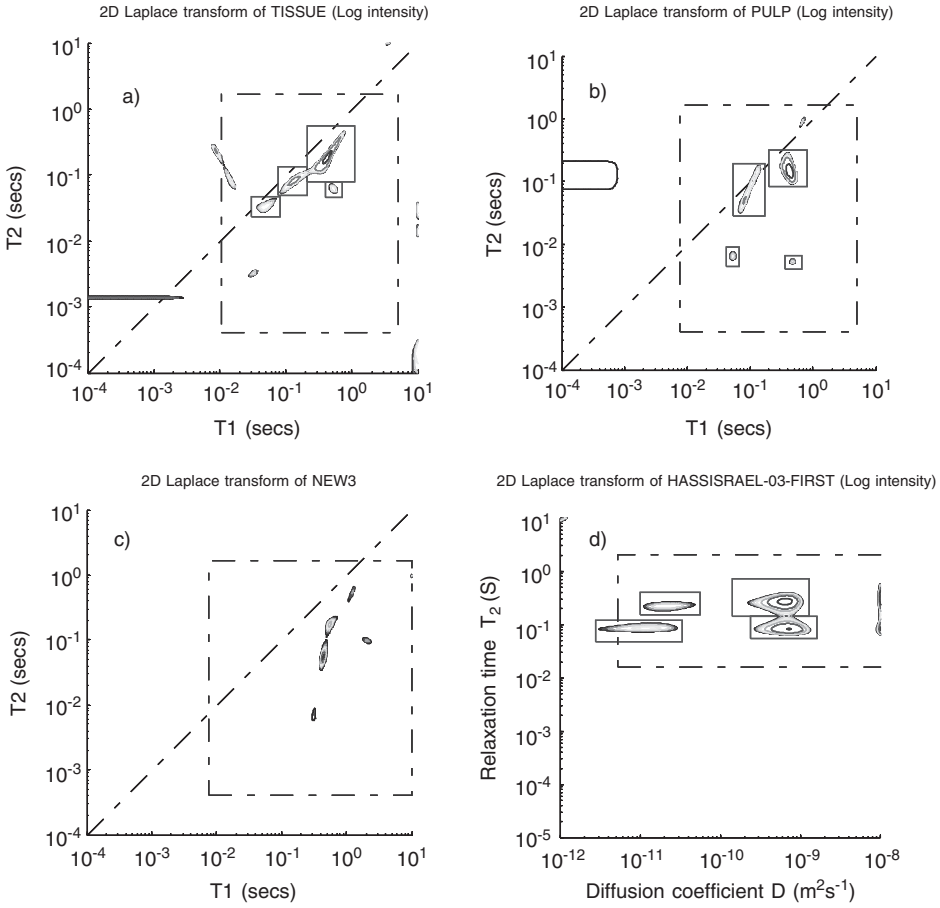

Fig. 8. Multidimensional spectra of avocado. (a) Parenchyma tissue at 23.4 MHz. (b) Pulped tissue at 23.4 MHz. (c) Parenchyma tissue at 300.15 MHz. (d) T_2–D spectrum of parenchyma tissue at 23.4 MHz.

shows the effect of destroying water compartmentation by pulping the tissue used to acquire spectrum 8a. Clearly, destruction of the cell walls and membranes causes microscopic redistribution of the water and this is reflected in changed peak positions and areas. What is more surprising is that the oil peaks also show significant changes, suggesting that pulping mixes the oil components and/or causes enzymic degradation of the oils. Fig. 8c shows the effect of increasing the spectrometer frequency to 300.15 MHz. Both the water and oil relaxation times are increased at the higher proton frequency, but the most puzzling feature of the data is the unreasonably large apparent increase in the total oil peak area at the higher frequency. It may be that the water signal is being attenuated by diffusion through strong internal field gradients created at the higher field by the susceptibility discontinuity across the oil–water droplet interface. The oil would not experience such severe

transverse dephasing because of its higher viscosity and restricted translational diffusion within small oil droplets. The susceptibility induced field gradients would also be much smaller inside the oil droplets. Regardless of the exact water peak assignments and whether one or two oil peaks are observed it is important to note that in all cases the oil peak(s) are sufficiently well defined to permit oil content to be determined from the peak areas. Fig. 8d shows a T_2–D cross-correlation spectrum of avocado tissue and shows two water peaks (high diffusivity) and two oil peaks (low diffusivity). This not only confirms that the effective water diffusion coefficient in avocado tissue is about 30 times greater than that of the oil it also provides the basis of a rapid, single-shot method of oil content determination in avocado to be discussed in Section 6.5.

Earlier imaging studies by Pathaveerat *et al.*[25] showed that the oil in avocado is not uniformly distributed throughout the tissue but increases in concentration from the outer layers towards the stone in the centre. This trend is also seen in the increasing relative intensity of the oil peaks in tissue dissected closer to the stone. There is also a systematic shift of the oil peak to shorter T_2's and longer T_1's towards the stone. This gradient in oil content implies that on-line determination of avocado oil content is best performed on the whole fruit and that surface detectors such as the MOUSE are unlikely to give reliable values.

The existence of harder 'lumps' in the avocado flesh is another troubling physiological disorder that can reduce its market value. The T_1–T_2 correlation spectrum of a 'lump' dissected from an overripe avocado shows that it is characterised by significantly shorter water proton relaxation times, which means that, given sufficient spatial resolution, it may be possible to detect the existence of hard lumps in T_2-weighted images in on-line applications.

2.4.1.3. Pears. Internal browning in pears (*Pyrus communis* L. cv. *Blanquilla*) has been studied by T_1–T_2 correlation spectroscopy at a proton frequency of 300.15 MHz (Fig. 9). Affected tissue has a shorter transverse relaxation rate compared to healthy tissue especially at higher magnetic field strength and long interpulse (tau) spacing when susceptibility effects dominate. Tissue disintegration as well as water evaporation appeared to be the main reason for this difference. Like apple (Fig. 6), the T_2–D spectra of fresh pears and pears with internal browning both showed two peaks corresponding to water in the vacuole and, tentatively, from the cytoplasm. Six repetitions showed that the vacuolar T_2 of the internally browned pear was in all cases shorter and its diffusion coefficient longer than in fresh pear (unpublished results).

2.4.1.4. Peas. Additional complexity arises with pea because the mature cells contain substantial quantities of starch granules and protein bodies. The effect of these on the spectra can be explored by comparing the spectra of (thawed) supermarket frozen peas that tend to be a young mutant variety with low starch and high sugar content, with canned mature marrow fat peas that have high starch granule content, thick cell walls and large numbers of protein (legumin) bodies. An additional complication arises because marrow fat peas have been heat treated before

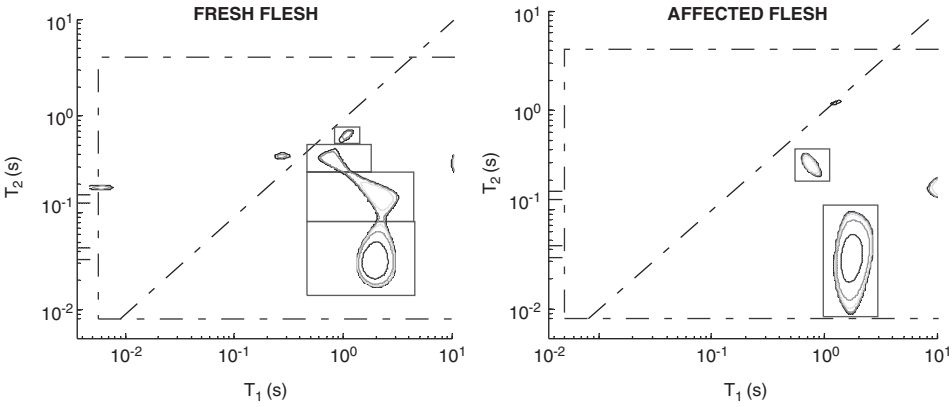

Fig. 9. T_1–T_2 spectra of pear acquired at 300.15 MHz and with an echo spacing of 8ms. (a) Healthy parenchyma tissue. (b) Brown parenchyma tissue.

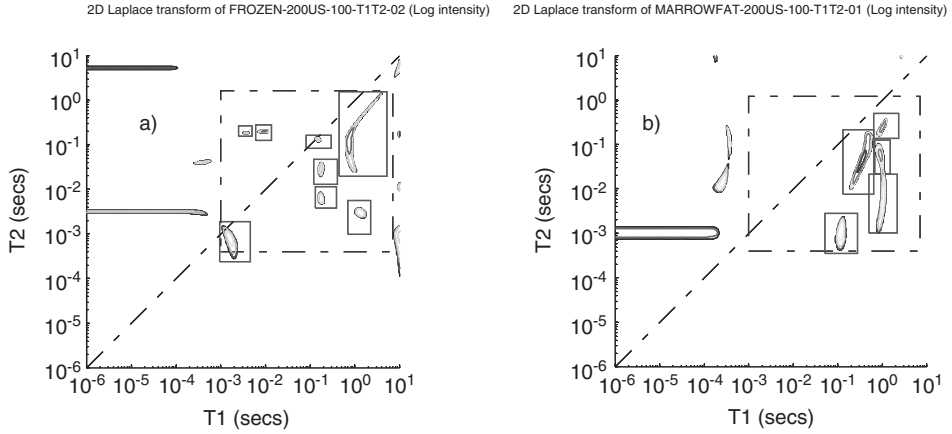

Fig. 10. T_1–T_2 spectra of pea acquired at 100 MHz with an echo spacing of 200 μs. (a) Young frozen-thawed pea. (b) Mature marrow fat pea.

canning so the starch granules have been partially gelatinised, whereas the frozen peas have been only lightly blanched. Fig. 10 shows representative spectra from these two types of processed pea and illustrates the high information content and also the difficulty in peak assignment. Indeed, these (unpublished) results are only preliminary and further work with water suppression weighting, optical microscopy and isolated pea starch granules will be needed before peaks can be assigned with confidence.

2.4.1.5. Potato and starch. 2D T_1–T_2 correlation spectroscopy has been used to monitor the effect of high pressure and microwave processing on the microscopic water distribution and starch chain dynamics in water-saturated packed beds of

native A- and B-type starches.[26] B-type starches were shown to be more resistant to pressure treatment than A-type starches. High pressure induced A-type starch gels were also shown to be radically different to the corresponding thermally induced gel. Similar high-pressure studies on raw potato tissue showed that although the cell walls of raw potato are resistant to high-pressure damage, the tonoplast and plasmalemma membranes were easily disrupted by quite low pressure.[26]

2.4.2. *Meat, egg and fish*

The tissue of marine cold-water species such as Atlantic salmon contains polyunsaturated fatty acids, which remain mobile even at low temperatures. It is therefore of interest to examine the multidimensional spectra of this species. A T_2–D spectrum of frozen-thawed white muscle excised from a farmed Atlantic salmon was reported by Veliyulin *et al.*[27] and revealed three peaks at 25 °C, which were assigned to extramyofibrillar water, intramyofibrillar water (major peak) and lipid. It was noteworthy that the peaks from extramyofibrillar water and lipid had the same T_2 overlapped in the 1D CPMG T_2 spectrum, which highlights the advantage of working in higher dimensions. This preliminary study clearly paves the way for more systematic studies on the effect of harvesting time and processing operations on the quality of the fish tissue.

T_1–T_2 spectra of egg albumin and yolk have been reported[21] and these will undoubtedly help in establishing fast on-line protocols for egg grading. Two peaks corresponding to the pools of exchangeable (upper peak) and non-exchanging protons (lower peak) are clearly distinguished in the 2D spectrum of raw hen-egg albumin on the basis of their T_2 differences (Fig. 11a). The exchangeable pool mainly comprises water together with a smaller fraction of exchangeable biopolymer protons. The fact that the non-exchanging biopolymer proton pool can be so clearly distinguished in the 2D spectrum is a consequence of the suppression of the exchangeable proton magnetisation near its null point in the t_1 dimension. The 2D spectrum for cooked egg white is dramatically different (Fig. 11b). The exchangeable and non-exchangeable peaks are still present, though with slightly reduced relaxation times and greatly reduced amplitude. However, a dominant new peak emerged with a short transverse relaxation time of 38.4 ± 0.3 ms. The simplest explanation for this is that some components of the protein mixture had denatured and cross-linked into a much more rigid gel network; while a significant fraction of the proteins and protein side chains remain in a mobile state and contribute to the peak with a T_2 of about 150 ms.

Three peaks are seen in the spectrum of raw egg yolk (Fig. 11c). The first two have almost the same T_2's as the exchangeable and non-exchangeable biopolymer proton pools of egg white; the new peak therefore presumably arises from the lipid CH proton pool and has a much shorter T_1 and T_2 of 399.3 $\pm$ 216 and 25.9 $\pm$ 0.3 ms, respectively. Cooking the yolk has the dramatic effect of removing the water (exchangeable proton) peak; reducing the protein CH proton peak from 150 to 105 ms and smearing out the lipid proton peak in the T_1 dimension while leaving the lipid T_2 unchanged (Fig. 11d). The interpretation of these changes is a matter of

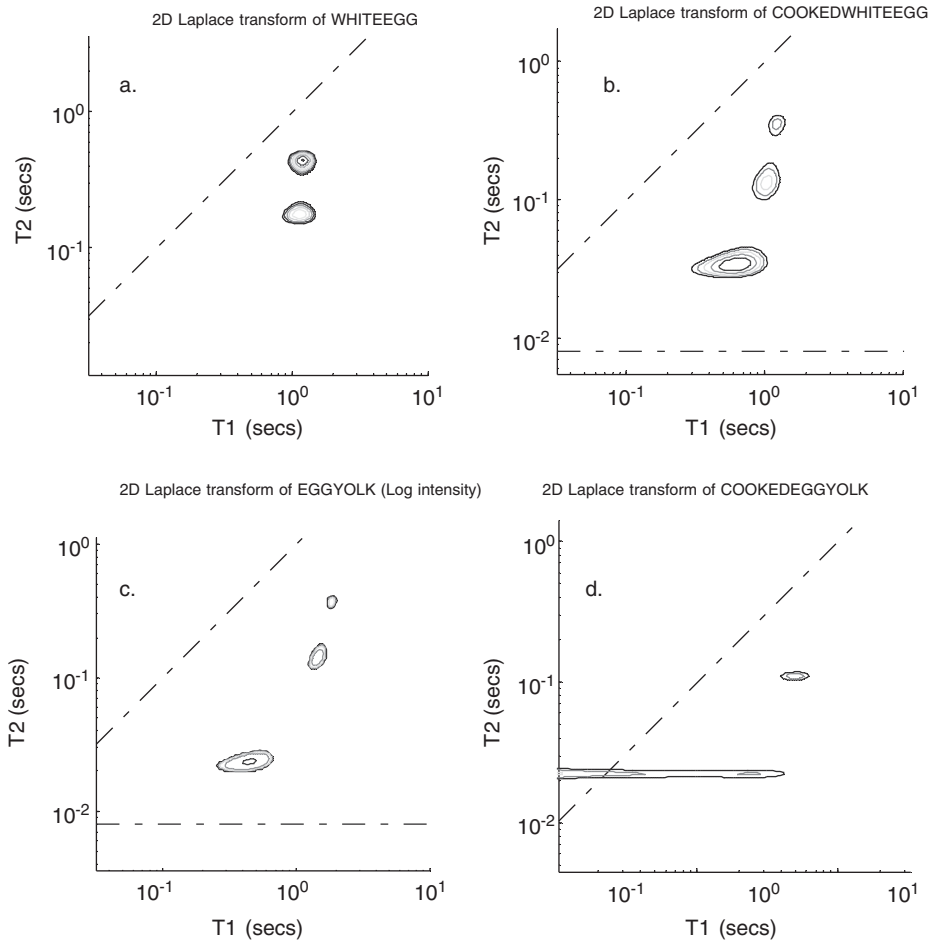

Fig. 11. T_1–T_2 spectra of hen egg albumin and yolk acquired at 23.4 MHz with an echo spacing of 400 μs. (a) Raw egg white. (b) Cooked egg white. (c) Raw egg yolk. (d) Cooked egg yolk.

speculation. It is probable that protein denaturation and aggregation exposes more hydrophilic side groups for hydrogen-bonding water. The "free water" in uncooked egg yolk is therefore converted to hydration water characterised by much longer correlation times. The exchangeable proton peak in raw egg therefore vanishes and the combined water–protein proton pool shifts to a shorter T_2 because of the more rigid protein network in the aggregated state. The smearing of the lipid peak is peculiar but can be understood if mobile lipid in the raw yolk is converted into a more rigid aggregated state. The dipole–dipole relaxation mechanism might then change to one involving spin diffusion of longitudinal magnetisation along rigid lipid chains to more mobile end-groups such as rapidly rotating methyl groups. There would then be a distribution of T_1's arising from different chain lengths and

end rotors. A 3D experiment on a field cycler where the frequency dependence of T_1 is resolved might help test this hypothesis.

As far as the author is aware, multidimensional relaxation and diffusion methods are yet to be applied to meat. This rather glaring omission is surprising given the importance of meat curing and processing operations. T_1–D (saturation recovery-PGSE sequence) and T_1–T_2 spectra have however been used to explore water compartmentation in rat heart tissue (myocardium). By selectively doping the intracellular compartment by infusion and wash-out with Mn (II) solution it was possible to distinguish intra- and extracellular water and estimate the exchange rate between these compartments.[84]

2.4.3. *Dairy products*

Both T_1–T_2 and T_2–D spectra have been acquired for mozzarella- and gouda-style cheese in an effort to establish markers for cheese quality as a function of storage time, temperature and salt concentration.[18] The T_1–T_2 spectra showed only a single water peak that shifted to shorter T_1's and longer T_2's with aging. Two oil peaks were detected, with a third higher-diffusivity peak appearing at longer storage times. The T_2–D spectra of the water component were more revealing and three distinct peaks were observed which were assigned to protein-associated water, larger transient pools of free bulk water and smaller pools tentatively assigned to water-in-oil emulsions. Having assigned the peaks, the 2D spectra were used to explore the effect of variable storage time and salt concentration on the uptake of the transient water pool by the protein matrix.[18]

2.4.4. *Hydrocolloids*

"Food hydrocolloids" is a label representing a plethora of complex multiphase, multicomponent processed foods of widely differing fat, water, biopolymer and sugar composition. Figs. 12 and 13 illustrate this class of food for a liquid emulsion (salad cream) and for lower water content (28.4% w/w) biopolymer foam (cake) respectively.

2.4.4.1. Salad cream. The three overlapping peaks in Fig. 12 can be tentatively assigned to the exchangeable proton pool (mainly water); a non-exchanging proton peak from biopolymer and sugar and a fat proton peak near the diagonal at about 100 ms.[21] Like the fat signal in yolk, the lipid peak is somewhat smeared out in the T_1 dimension suggesting spin diffusion and/or polydispersity in chain length associated with a more complex aggregated microstructure. A water-suppression presequence would help confirm these assignments, but this was not undertaken.

2.4.4.2. Cake. Cake exemplifies the whole class of complex solid foams of protein, polysaccharide and fat with low water content. The smeared out spectrum in Fig. 13 shows three overlapping peaks with short relaxation times but it is not easy to assign them to particular proton pools with any confidence without a systematically varying the amounts of biopolymer, fat, sugar and water, which may not always be

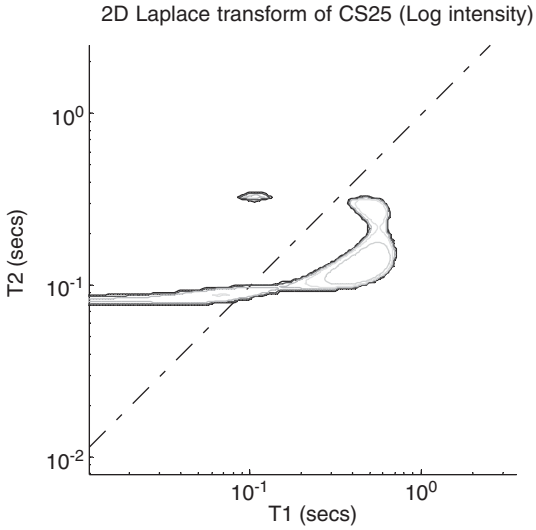

Fig. 12. T_1–T_2 of salad cream acquired at 23.4 MHz with an echo spacing of CPMG 400 μs.

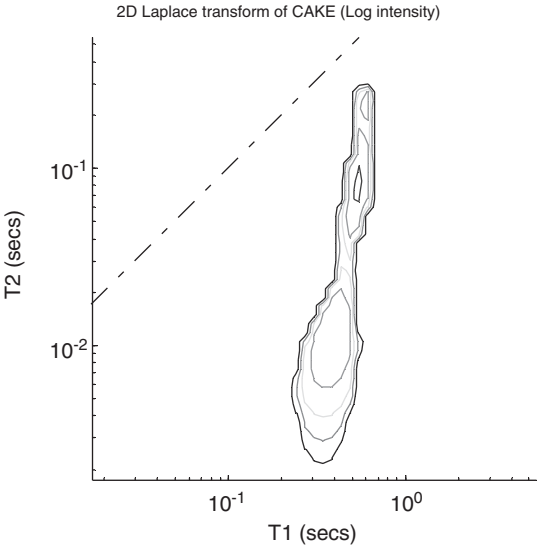

Fig. 13. The T_1–T_2 spectrum of cake acquired at 23.4 MHz with an echo spacing of 400 μs.

possible without dramatically changing the matrix structure. The dominant peak with the shortest T_2 and T_1 could well be the sugar proton CH signal, because a highly concentrated sugar solution would be expected to have short relaxation times and sugar is the dominant component in the recipe (29.8%). If so, the two remaining peaks at longer T_2 arise from water and biopolymer. One might have

expected a fourth peak from fat protons, but, in cake, the fat is in the solid state and would be expected to have a transverse relaxation time of less than a millisecond which is too short to measure with a CPMG sequence with an echo spacing of 400 ms. This preliminary spectrum shows the need to work in yet higher dimensions to try to resolve the components. It also points to the considerable potential of multidimensional correlation spectroscopy for studying baked products either during processing or of staling changes during storage.

3. RELAXOMETRY AND DIFFUSOMETRY IN INHOMOGENEOUS FIELDS

The multidimensional spectra discussed in the previous section have all been acquired with conventional spectrometers using hard, on-resonance RF pulses in a homogeneous external field. In this section we consider relaxometry and diffusometry undertaken with "*ex situ*" spectrometer devices such as the NMR-MOUSE,[36] "inside-out" NMR systems[37] or stray-field NMR probes. These systems operate in highly inhomogeneous magnetic fields where all pulses are slice selective and off-resonance effects must be taken into account. Indeed, when the field inhomogeneity approaches or exceeds the strength of the RF field, the relaxation and diffusive attenuation becomes non-exponential, even when the sample is characterised by single values of T_1, T_2 and D. Moreover, the echo shape depends on diffusion and relaxation and even the CPMG echo decay envelope depends on both T_1 and T_2. In this section we therefore review some of the major developments in relaxometry and diffusometry in inhomogeneous magnetic fields then consider their potential applications in food science.

3.1. Coherent pathway methods

In a seminal paper, Hurlimann[38] presented a general analysis for relaxation and diffusion in inhomogeneous fields that is valid for any multipulse sequence and for B_1 and B_0 fields of arbitrary homogeneity. Using this analysis he presented modified Inversion Recovery and CPMG sequences for determining T_1, T_2 and Diffusion coefficients in grossly inhomogeneous fields. A coherence pathway formalism was used whereby the magnetisation following a sequence of N arbitrary RF pulses was written as the sum over all possible coherence pathways and the rotation matrix elements for each pulse in every pathway were expressed as functions of the field inhomogeneity, or more precisely, the resonance offset, $\Delta\omega_0$, which is the difference between the local Larmor frequency, γB_0, and the RF frequency, ω_{RF}; as well as the RF amplitude, ω_1, and phase, ϕ. Formulating the problem in terms of coherent pathways has the major advantage that the attenuation caused by diffusion and relaxation is uniform across the spectrum of a given coherence pathway, but is, in general, different from one pathway to the next. Expressed differently, if a single coherence pathway is isolated then relaxation and diffusion do not affect the shape

of the echo, only its amplitude, so the relaxation parameters can be determined from the measured echo amplitude for that pathway. When there is no field inhomogeneity only the direct coherent pathway contributes to the desired echo, but field inhomogeneity adds in contributions from all other possible coherent pathways and greatly complicates the signal. The problem with NMR in inhomogeneous fields is that the number of possible coherent pathways increases almost exponentially with the number of RF pulses in the sequence and the observed magnetisation is obtained by summing over all such pathways. Fortunately because each pathway is associated with a characteristic and easily calculated phase, phase cycling can be used to reduce the number of pathways interfering with the desired signal. The method can be illustrated by reference to the modified inversion recovery sequence for T_1 measurement in an inhomogeneous field and to the modified CPMG sequence for T_2 and diffusion measurements in an inhomogeneous field.

3.1.1. *Inversion recovery in an inhomogeneous field*

An eight-step phase cycling scheme was used to reduce the number of coherent pathways contributing to the echo in the usual 3 pulse (180°-t_1-90°-180°-echo) inversion recovery sequence to just two, all other pathways cancelling. The resulting expression shows that the echo shape obtained by integrating over the resonance offset, $\Delta\omega_0$, depends on t_1/T_1 but that the total echo area obtained by a second integration over the echo acquisition time recovers according to the usual homogeneous field expression (1-2exp($-t_1/T_1$)), allowing the relaxation time to be extracted. Multiple exponential relaxation can, of course, be deconvoluted in the usual way.[38]

3.1.2. *CPMG sequences in an inhomogeneous field*

For an echo train of 15 echoes in the CPMG sequence there are over a million contributing coherent pathways so it is not possible to easily devise phase cycling schemes to select contributions from only a few coherent pathways at each echo. Nevertheless the analysis has been performed for the first 15 echoes for a simpler phase cycling scheme whereby, to remove any DC offset, the phase of the initial 90° pulse and of the acquisition is alternated between $+x$ and $-x$ without changing the phases of the 180° pulses, together with the standard CYCLOPS phase cycling. It was noteworthy that although the echo shapes for each contributing pathway were dramatically different (though symmetric about the echo centre) the observed echo shape obtained as the sum over pathways varied little, being roughly triangular. It was also found that, neglecting relaxation, the echo decay due to diffusion in a fringe field of constant gradient, G, was faster than predicted by the usual formula, $\exp(-\gamma^2 G^2 D t_e^3 N/12)$ for echoes $N>3$. This is ascribed to contributions from other faster decaying coherent pathways in the regions away from the centre of the excited slice. Nevertheless the overall decay still scaled with $\gamma^2 G^2 D t_e^3 N$ so that diffusion coefficients could be extracted from the dependence of integrated echo amplitude on the echo spacing, t_e. It is surprising that, despite their enormous potential, these sequences are yet to be used with *ex situ* NMR to study food materials.

3.2. Effective-rotation composite-pulse methods

In grossly inhomogeneous fields all RF pulses become slice selective and signal/noise is limited by the slice volume. By increasing the effective slice thickness, composite pulses can be used to improve signal/noise in relaxation time measurements with Carr–Purcell type sequences.[39] The ideal composite pulse should repeatedly refocus the magnetisation in grossly inhomogeneous fields and display improved bandwidth while preserving the intrinsic error compensation scheme of the CPMG sequence. The evolution of magnetisation caused by any composite pulse over a refocusing cycle can be described by a net rotation through an angle α about an axis, **n**. Using this fact it was shown[40] that the magnetisation at the time of the formation of the echo in a Carr–Purcell sequence rapidly approaches an asymptotic form, $M_{\text{asy}} = \mathbf{n}(\mathbf{n} \cdot R\{z\})$ where $R\{z\}$ is the net rotation caused by the excitation pulse. In grossly inhomogeneous fields this asymptotic form is rapidly approached even after the third echo. Because only transverse magnetisation is detected the effective rotation axis, **n**, for a composite pulse should be chosen to lie completely in the transverse plane over as large a range of resonance offset, $\Delta\omega_0$, and ω_1 as possible. In addition the excitation pulse should be such that it rotates the vector z onto **n** over the relevant range of inhomogeneities, i.e., the product $\mathbf{n} \cdot R(z)$ needs maximising. This strategy for the design of composite pulses is subtly different to previous approaches where composite pulses have been designed to give a particular overall rotation angle. In contrast, the present strategy shows that in inhomogeneous fields it is more important to ensure that the vector **n** lies in the transverse plane, regardless of the pulse rotation angle. In other words, in grossly inhomogeneous fields it is more important that the 180_y° composite refocusing pulse is a "y pulse" than a "180° pulse". Note that it is also not necessary that the direction of **n** is a constant within the transverse plane for all values of the offset frequency. It was further shown[40] that, neglecting diffusion effects, the asymptotic form of the echo amplitude decays exponentially with a weighted average of T_2 and T_1 such that

$$M_{\text{asy},\perp} = n_\perp(n.R\{z\}) \exp\left[-kt_e\left(n_\perp^2/T_2 + n_z^2/T_1\right)\right] \tag{9}$$

where kt_e is the effective echo time. Because both n and R depend on the offset frequency and RF field strength, the exact decay is also dependent on these variables. For large field inhomogeneities, the initial decay rate is of the form

$$1/T_{\text{eff}} = 1/T_2 - A\left(1/T_2 - 1/T_1\right) \tag{10}$$

where

$$A = [<n_z^2\, n_\perp(nR\{z\})>_{\Delta\omega 0,\, \omega 1} / <n_\perp(nR\{z\})>_{\Delta\omega 0,\, \omega 1}] \tag{11}$$

A is a positive constant, less than unity that needs determining for a given composite pulse, field inhomogeneity and acquisition bandwidth. This analysis establishes the important result that, with suitable calibration, it is possible to determine the relaxation times T_1 and T_2 as well as diffusion coefficients with Carr–Purcell type sequences even in grossly inhomogeneous fields. Once again these results are yet to be applied to *ex situ* studies of food materials.

3.3. Multidimensional relaxometry and diffusometry in inhomogeneous fields

The results of the last two sections can be used to formulate a strategy for analysing multidimensional relaxation and diffusion sequences in inhomogeneous fields when the kernels depend, in general, on the resonance offset and RF field strength.[41] Because the t_1 dimension comprises only a few RF pulses it is appropriate to use the coherent pathway technique of Section 3.1 with appropriate phase cycling to obtain the spectrum in the t_1 dimension. If the second t_2-dimension comprises a CPMG sequence then the number of coherent pathways increases astronomically so it is more appropriate to use the effective rotation method of Section 3.2 to calculate the asymptotic magnetisation decay in this dimension and to further simplify the analysis by using short echo spacings to remove the effects of diffusion.[41] The case of a stimulated echo in the t_1 dimension followed by a CPMG sequence in the t_2 dimension was analysed in detail.[41] By 16 step phase cycling of the 3 RF pulses in the stimulated echo it was possible to select only a single coherent pathway with a simple diffusive dependence, $\exp[-\gamma^2G^2\delta^2D(\Delta-\delta/3)]$, over the whole echo spectrum. When implementing this part of the sequence the time between the first and second 90° pulses, δ, was incremented at fixed diffusion time, Δ. The asymptotic magnetisation after the first few echoes in the CPMG sequence in the t_2 dimension then can be written, using the "effective rotation notation" of Section 3.2, as

$$M_{\text{asy}} = n(n.M_1)\ \exp\left[-t/T_{2\text{eff}}\right] \tag{12}$$

where M_1 is the magnetisation at the end of the stimulated echo sequence. For the whole 2D sequence the echo amplitudes can then be written as

$$M(t,\delta) = \int\int \mathrm{d}D\mathrm{d}T_{2\text{eff}}F(D,T_{2\text{eff}})\ \exp\left\{-q^2D(\Delta-\delta/3)\right\}\ \exp\left\{-t/T_{2\text{eff}}\right\} \tag{13}$$

The desired spectrum, $F(D,T_{2\text{eff}})$ is obtained in the usual way by 2D inverse Laplace transform. Eq. (13) corresponds closely to the conventional "on-resonance" kernels except that $T_{2\text{eff}}$ replaces T_2. Otherwise the effects of strong field inhomogeneities are only reflected in the echo shape and the transient effect on the first few echoes in the second dimension, which are removed before Laplace inversion.

The kernel, $\exp\{-q^2D(\Delta-\delta/3)\}$, in Eq. (13) is formally valid only for unrestricted diffusion. The case of restricted diffusion can be treated by considering the dependence of D on the diffusion time, Δ. This was done by performing a 3D experiment where the diffusion–relaxation distribution function was acquired for six different diffusion times and a 2D plot correlating the mean square diffusion length, $D(\Delta,T_{2\text{eff}})/D_0$ with $T_{2\text{eff}}$ was obtained for water in Indiana Limestone.[20] As expected, this mean squared displacement decreased with increasing diffusion time.

3.4. The NMR-MOUSE

Quite obviously, the various inhomogeneous field protocols presented in Sections 3.1–3.3 will find considerable application in the analysis of heterogeneous food

materials using the NMR-MOUSE (MObile Universal Surface Explorer),[42] as well as in the Halbach system to be discussed in the next section and other *ex situ* NMR devices,[92] but, so far, the methods have been mainly tested on phantoms and porous rock materials relevant to the oil industry. Nevertheless Pedersen *et al.*[43] have begun exploring the potential of the NMR-MOUSE in food science by comparing its performance with conventional low-field bench-top instruments for the determination of oil content in model oil-in-water emulsions using the conventional CPMG sequence. Although the optimum CPMG pulse parameters were determined by systematically varying the pulse width, pulse power and pulse lengths no attempt was made to use coherent pathway or effective rotation methods to simplify the analysis. Because of slice selection in the inhomogeneous field, the signal/noise ratio for the MOUSE was inferior to the bench-top spectrometer but this disadvantage is offset to some extent by the advantages of mobility and its ability to examine intact samples. The inhomogeneous field in the MOUSE also meant that attenuation of the water signal by molecular diffusion was the dominant effect, reducing its apparent transverse relaxation time to ca. 4 ms. The oil signal was less affected by diffusion because of the oils lower diffusivity and its confinement within small emulsion droplets. These effects meant that the CPMG-like decay with the MOUSE could be resolved into two exponential decays associated with the oil and water phases, permitting quantitative analysis of the oil content. Clearly future effort should focus on the exploitation of the coherent pathway and effective rotation-composite pulse methods in food applications with the MOUSE and other *ex situ* devices.

3.5. Open-access Halbach NMR

Although one-sided NMR systems such as the NMR-MOUSE are "open-access" in the sense that they do not enclose the sample in arrays of coils and magnets, they have the disadvantage of acquiring signal only from the surface layers. The recently proposed Halbach NMR spectrometer[44] can be considered as an intermediate case in that it is still "open-access" and can be hand-held, but, like conventional NMR systems, acquires signal from the interior of a sample, not just the surface layers. The Halbach system therefore has great potential for low-cost, easy-access analysis of intact food samples such as whole eggs and fruit. Moreover the open-access arrangement means that NMR measurements can be undertaken simultaneously with other spectroscopic techniques such as FTIR, microscopy and X-ray scattering in genuine sensor fusion. This possibility is particularly important for monitoring rapid and irreversible changes induced in a food material by, for example, processing operations.

Halbach dipole magnets, originally proposed by Klaus Halbach as focusing magnets for particle accelerators, are permanent magnets consisting of segments joined together in such a way as to create a dipole magnet with the dipole transverse to the long axis of the magnet. A number of Halbach dipoles can be combined in an array so as to create a homogeneous magnetic field transverse to the long axis of the array, an arrangement which is convenient for NMR because a solenoid coil (or even a multiple wound loop coil) can more easily be used for the RF rather than a

saddle or birdcage coil. Halbach arrays have previously been used in a number of NMR applications.[45–49] Most of these applications have tried to maximise the strength and homogeneity of the field by combining as many Halbach dipoles as possible in a polygonal or circular array. However this is achieved at the expense of enclosing the sample in magnets and RF solenoid coils. Recent work in the author's laboratory therefore considered the merits of reducing the number of dipoles, sacrificing strength and homogeneity in favour of a more open magnet design.[44] It was shown that a rectangular Halbach magnet array may be constructed with just four dipole magnets sufficiently far apart, relative to the NMR-sensitive region close to the field centre, that the arrangement may legitimately be described as *open-access* (or *easy-access*). This allows for larger samples or the introduction of other equipment for manipulating or observing the sample.

The disadvantages of such a design are obvious. By moving the magnets away from the sample and using permanent magnets, B_0 is reduced and more inhomogeneous so the sensitivity and signal/noise are also reduced. These disadvantages are offset, for certain applications, by three advantages: (1) the relative ease of construction and low cost of the magnet array, (2) the portability of the magnet, which does not require a heavy steel yoke to carry the flux lines, and, (3) most significantly, the open-access nature of the Halbach array allows for several lines of further development. These include:

(a) Multi-sensor technology – the combination of NMR/MRI with other spectroscopies (EPR, NIR, microwave reflectance etc.), scattering techniques (X-rays, neutrons, lasers), ultrasonics, and/or electrochemical measurements including impedance spectroscopy, voltammetry etc. Multi-spectral domains can be scanned independently or combined by means of multi-dimensional correlation spectroscopy techniques.[50]
(b) Easy access to the samples allows for mechanical micro-manipulation of samples during NMR or other spectroscopic investigation, facilitating a variety of NMR-rheology experiments.
(c) There is more available space (relative to a conventional design) to introduce the means to subject the sample to extremes of temperature and/or pressure. Samples might be physically moved through the magnet space by pipes, conveyors etc.
(d) In principle the size of the array can be scaled up or down. A sufficiently large array might allow NMR or even low-resolution MRI of large intact samples such as foodstuffs, human limbs etc.

Using a square array of four magnets a Halbach spectrometer operating at a proton frequency of 3.87 MHz has been built.[44] The probe dead time was $\lesssim 30\,\mu s$ and the best obtainable 90° RF pulse was 4.1 μs. CPMG echo decay envelopes were obtained for a variety of samples including an intact egg. The open-access nature of the design means that it is undesirable to block access to the RF coil by any kind of shielding. For this reason, external noise was suppressed using two counter-wound but otherwise identical RF coils, connected in series. The sample was placed in the primary coil while the secondary coil was placed well away from the sample but still

within the Halbach field. In this way external noise induces equal but opposite currents in the two coils which cancels at the receiver. A similar concept is used in SQUID gradiometers.[51] Another potential problem is the temperature-dependence of the B_0 field. In some applications it may be desirable to control the temperature of the permanent magnets independently of the sample. This should be possible without compromising the open-access facility too much, by enclosing each of the magnets in a cooling jacket.

Although the field in the 4-magnet Halbach array is more homogeneous than one-sided magnet systems, such as the MOUSE, the acquisition protocols for relaxation and diffusion will still benefit from the methods described in Sections 3.1–3.3.

4. FAST, ONE-DIMENSIONAL ANALYTICAL METHODS

The multidimensional methods discussed in Section 2 are high in information content but suffer from long acquisition times, which make them unsuitable as routine analytical tools for compositional analysis of food. In this section we examine a number of novel ultrafast 1D relaxation and diffusion methods suitable for rapid food analysis using conventional low-field spectrometers.

4.1. Continuous wave free precession

Continuous wave free precession (CWFP)[52] is a special case of steady-state free precession that arises when the pulse period is made small compared to T_2*. This means that the dephasing of isochromats taking place in the period between pulses, T_P, is small, leading to a continuous wave periodic signal. By recursive solution of the Bloch equations it can be shown[53] that the CWFP version of the CPMG sequence leads to a signal amplitude just preceding each 180° pulse equal to that just after the pulse and equal to $M_0T_2/(T_2+T_1)$, where M_0 is the equilibrium magnetisation in the external field. This observation is significant because it can be used for quantitative analysis with greatly enhanced signal/noise compared with conventional FID or CPMG protocols. This follows because the number of averaged signal samples in CWFP in a time ΔT is $\Delta T/t_w$ where t_w is the acquisition window. This compares with the number of accumulations in a standard FID or CPMG experiment, which, to avoid saturation effects, needs to be of the order $\Delta T/5T_1$. Since signal/noise is proportional to the square root of the number of accumulations, the net signal/noise gain using CWFP is of the order, $(5T_1/t_w)^{1/2}$ which can be substantial with many food samples with long T_1's. For a train of $\pi/2$ pulses it can also be shown that the signal decays in two transient regimes towards the stationary state. The first regime involves rapid alternation in signal amplitude between even and odd pulse numbers. This regime decays with a time constant related to T_2* to a quasi-stationary state where the alternations cease. The second regime then sets in with an exponential decay from the quasi-stationary state to the true stationary state with a time constant of $2T_1T_2/(T_1+T_2)$. Measurement of this time constant in the second regime, together with the steady-state magnitude, $M_0T_2/(T_2+T_1)$,

therefore allows rapid determination of both T_1 and T_2 in a single-shot experiment without the need for phase cycling.

The CWFP method does, of course, have its limitations. The effects of B_0 inhomogeneity and RF pulse imperfections rapidly accumulate but it was concluded[52,53] that, provided $T_P/T_2^* < 0.085$ the measured relaxation times would still be within 8% of their true value. The method does, however, become less reliable in the fast motion limit when the ratio T_1/T_2 approaches unity and the steady-state magnetisation approaches 0.5. In such cases the decay from the quasi steady state may involve too narrow a data range to be easily characterised. Not surprisingly the method also requires good RF homogeneity over the sample volume. In fact, 5% error in the pulse length causes an 8% error in the steady-state amplitude, which makes it an unlikely candidate for on-line determination of relaxation times where the sample moves through regions of differing B_1 (see Section 6).

Besides speed, the effectiveness of CWFP in discriminating each component in multicomponent systems is also a key consideration in food analysis. This aspect was tested by analysing the oil and water content of wet seeds of corn, wheat and sorghum where the water is compartmentalised between the endosperm and the germ, and each compartment differs in oil content. In this case the analysis used only variations in the amplitude of the stationary state and no attempt was made to exploit the different relaxation rates from the quasi-stationary state to the stationary state. The T_2's of the solid protein and polysaccharide matrix are vary short, typically a few tens of microseconds, and their T_1's are long so the ratio $T_2/(T_2 + T_1)$ is too small for these solid-like components to contribute to the amplitude of the steady-state magnetisation. The T_2 of the oil lies in the range 30–100 ms and T_1 is about 2–3 times longer, so the ratio $T_2/(T_2 + T_1)$ for the oil is expected to be ca. 0.3, independent of moisture content. On the other hand the relaxation times of the two water components depend on water content, becoming more solid-like ($T_2 \ll T_1$) at low water contents. Below moisture contents of ca. 5% the moisture can be considered part of the solid matrix and no longer contributes to the stationary state amplitude. The net result is that the experimental plot of stationary state amplitude versus moisture content shows an almost linear decrease with decreasing moisture content down to ca. 5% moisture when there is a transition to a constant plateau whose amplitude arises only from the oil. In this example, CWFP therefore succeeds in analysing oil and moisture content in a fraction of the acquisition time required by the more conventional FID or spin-echo methods. It does, however, require that the seeds are dried to ca. 5% moisture content for unambiguous oil content determination. It would be interesting to explore the potential of CWFP in other food systems, including situations giving rise to rapid compositional and/or phase changes.

4.2. Multiple modulation multiple echoes

Multiple modulation multiple echoes (MMME)[54] is a novel approach to the rapid determination of self-diffusion coefficients, transverse and longitudinal relaxation times in an ultrafast single-shot pulse sequence using either constant or pulsed field

gradients and without the need for repeated acquisition or phase cycling. It is based on the coherence pathway formalism discussed in Section 3.1 but instead uses on-resonance pulses in homogeneous B_0 and B_1 fields. The information content in each single-shot pulse sequence is then maximised by increasing the interpulse spacings so that all coherent pathways give echoes that are well separated in time. This is done by avoiding all phase cycling and setting the time periods between pulses to multiples of 3, such that the pth pulse is triggered at a time, $t_p = 3^{i-1}t_1$. For a sequence of N pulses there are then $(3^{(N-1)} - 1)/2 + 1$ coherent pathways generating observable signals, either as echoes or FID's. If linear external field gradients are applied each coherent pathway is associated with a unique attenuation factor due to diffusion and relaxation. Different permutations of the time periods between pulses results in different diffusion and relaxation effects for each coherence pathway, and this can be used to optimise the information content. This protocol was tested using a 4-pulse sequence labelled "MMME4" ($90°-90°-90°-180°$).[22] The coherent pathway formalism was used to calculate the shapes of all 14 echoes for each coherent pathway in the sequence and these agreed very well with the experimental data for bulk water. In principle all three parameters, D, T_1 and T_2 could be extracted from a single scan in MMME4 because there are 13 data points from the echo amplitudes and 13 unknowns (10 unknown amplitudes, D, T_1 and T_2). The fact that all this information is available from a single-shot pulse sequence is remarkable and, like CWFP, it is anticipated that MMME methods will find numerous applications in low-field bench-top studies of food, especially where ultrafast methods are needed to monitor the rapid and irreversible changes associated with food processing.

4.3. Single-shot water suppression

The observation that the water signal in the MOUSE studies on emulsions[43] is more strongly attenuated by molecular diffusion in the inhomogeneous field than oil suggests that oil content and soluble solid content (BRIX) can be measured in low-resolution instruments in a single-shot, rapid method by simply suppressing the water signal with appropriately applied pulsed gradients. Such methods might also find application in on-line NMR sensor measurements to be discussed in Section 6.

4.3.1. *Single-shot lipid determination by water suppression*

The single-shot water suppression method will be illustrated by returning to the problem of the oil content determination in avocado. As mentioned in Section 2.4.1.2 various methods have been developed for quantifying oil content in avocado[24] but none are free from difficulty. Chemical methods such as Soxhlet extraction are destructive and very labour intensive. Dry weight analysis gives accurate water contents but drying is slow and destructive and the method relies on calibrations between water and oil content that, unfortunately depend to some extent on the avocado variety.[29,30] Early work by Barry *et al.*[31] established a linear correlation between the NMR FID

signal amplitude and oil content for dried avocado tissue, but the method required sample drying and was therefore slow and destructive. Sometime later, Chen *et al.*[32,33] investigated the feasibility of using NMR imaging, spectroscopy and relaxometry as indices of maturity. Their measurements were, however, undertaken on a high field superconducting magnet system operating at 2 T (85.5 MHz) and while useful correlations were established between the signal intensities of the oil and water peaks in the frequency spectrum it is unlikely that these peaks could be resolved at the low-proton frequencies applicable to on-line situations. Useful correlations were also found between the water transverse and longitudinal relaxation times and percentage dry weight, but here also the relaxation times were measured only for the separated water peak in the spectrum and it is uncertain whether similar correlations can be established with CPMG relaxation time measurements made on the whole tissue. The conventional method of separating water and oil peaks in a CPMG transverse relaxation spectrum is also complicated by the observation[24] in the T_1–T_2 spectrum that one of the water T_2 components overlaps with the oil relaxation peak, suggesting that diffusion methods are preferable.

The observation in Fig. 8d that the effective water diffusion coefficient in avocado tissue is about 30 times greater than that of the oil, suggests that a single-shot pulse sequence consisting of a Hahn echo with a short echo time followed by a PGSE sequence shown in Fig. 19 should provide a suitable calibration. The first Hahn echo acquired with a short echo time (2 ms) is proportional to the total mobile proton signal (mainly water and oil); whereas the second echo acquired with a suitably long echo time of 40 ms arises only from oil because of diffusive attenuation of the water signal. A weak constant background gradient of $8.86. \times 10^{-3}$ T/m was imposed to help sharpen the echoes and improve signal/noise. The suppression gradient pulses were somewhat stronger (0.4 T/m). Fig. 14a shows the linear correlation between the ratio of the second and first echo amplitudes with oil content in avocado tissue

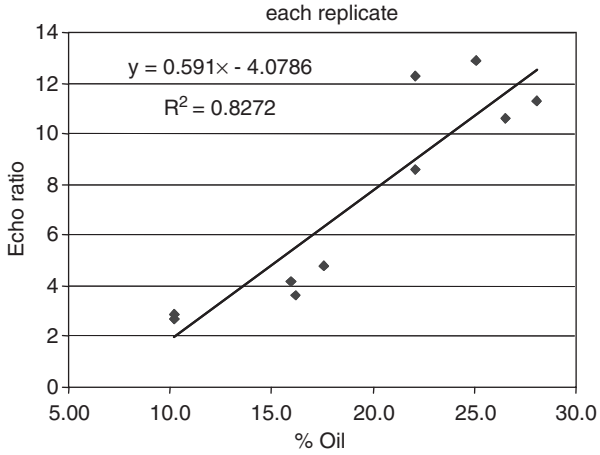

Fig. 14. Linear calibration between the echo amplitude ratio and oil content in avocado, acquired with the pulse sequence in Fig. 19.

determined by the dry weight method and converted to oil content. These measurements[24] were made on plugs of tissue bored towards the stone and therefore represent average oil content of the outer, middle and inner layers. Because the sequence is single-shot, fast and uses only hard RF pulses, it is also suitable for implementation with on-line NMR sensors (see Section 6).

4.3.2. *Single-shot BRIX determination by water suppression*

The same water suppression sequence of a Hahn echo with a short echo time followed by a PGSE in Fig. 19 has also been tested on 10 apples and gave a good linear correlation ($R^2 = 0.92$) between the echo height and Brix (soluble solid content) measured by refractometry. This is an important result because single-shot acquisitions were used in establishing the correlation, so it should be possible to use this method for on-line BRIX determination (see Section 6.4.5). The robustness of this correlation on other fruit is being tested in on-going work in our laboratory.

5. TOWARDS HIGH-RESOLUTION SPECTROSCOPY IN INHOMOGENEOUS FIELDS

As is well known, the main requirement for resolving the spectral lines of two non-equivalent, non-exchanging protons with chemical shifts, σ_1 and σ_2, is that the intrinsic spectral linewidth, roughly $1/T_2^*$, is less than their frequency separation, $\delta\omega$ which equals $\gamma B_0(\sigma_1-\sigma_2)$. Because T_2^* decreases with increasing B_0 field inhomogeneity, conventional wisdom states that it is necessary to incorporate expensive shim coil sets in high-resolution spectrometers to make the main B_0 field as homogeneous as possible over the sample volume. The same wisdom suggests that it is best to increase the frequency separation, $\delta\omega$, by working at the higher fields made possible with expensive superconducting magnet technology, and there is the added advantage of increased signal/noise at high fields. The result is, of course, the conventional, and expensive, high-resolution NMR spectrometer with all the bells and whistles. Recent years have, however, seen this conventional wisdom challenged in a number of ways. The next three subsections show that high field homogeneity is not a necessary requirement for spectral resolution, nor is it always necessary to use the high fields of expensive superconducting magnets to improve resolution and signal/noise. It is therefore anticipated that the next few years will see the emergence of a new generation of low-cost *ex situ* NMR Fspectrometers with (moderate) high-resolution capability. If so, the compositional analysis of the main lipid and sugar constituents of foods will be greatly facilitated.

5.1. Two-dimensional nutation spectroscopy

The principles of nutation spectroscopy have been developed in the context of rotating frame localisation[55] and of the spectroscopy of quadrupolar nuclei[56] and

can also be used to produce high-resolution spectra in inhomogeneous B_0 and B_1 fields.[57] The simplest pulse sequence comprises an RF pulse with a duration that is incremented as the t_1 evolution period in a 2D experiment, while the free induction decay following the pulse is recorded during the t_2 acquisition period. During t_1 the spins nutate in the rotating frame at a local frequency $\omega_1(\mathbf{r})$ ($= \gamma B_1(\mathbf{r})$) dictated by the RF field inhomogeneity; whereas during the free induction decay period they precess at a local frequency, $\omega_\sigma + \Delta\omega_0(\mathbf{r})$ where the resonance offset, $\Delta\omega_0(\mathbf{r})$ **(** $= \gamma B_0(\mathbf{r})$) is dictated by the main field inhomogeneity. However, the important point to note is that if $B_1(\mathbf{r})$ and $B_0(\mathbf{r})$ are spatially correlated such that in the sample volume each B_1 corresponds to a single B_0 then a hypercomplex Fourier transform of the 2D data yields a pure absorption spectrum where each chemical species gives rise to a "ridge" lineshape. The schematic in Fig. 15 for a 2-peak spectrum shows that, although the spectrum for the whole sample obtained by projection is broad and featureless a 1D high-resolution spectrum can be extracted by either taking a cross-section at a particular value of ω_1 (the dashed line in Fig. 15) or, preferably, by using a more sophisticated "banana" projection procedure that sums the intensity along the two curved ridges.[57] Note especially that the correlation between the B_1 and B_0 inhomogeneity need not be linear, though if it is, the ridges become straight diagonal lines rather than being curves as shown in Fig. 15.

So far this very simple protocol has only been tested with phantom samples in a 1D probe arrangement designed to give co-linear B_1 and B_0 field gradients at high field strengths corresponding to proton frequencies of ca. 200 MHz. Future work needs to generalise this method to the more realistic situation in *ex situ* devices where the B_1 and B_0 gradients are not necessarily collinear. It would also be interesting to try replacing the FID in the second dimension with multiecho sequences such as the CPMG. Echo addition would then improve signal/noise and the T_2- and diffusion-weighting might help discriminate overlapping spectral lines.

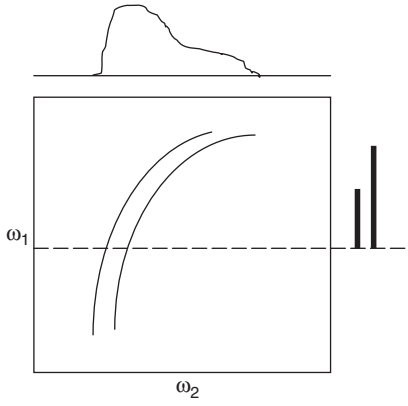

Fig. 15. Schematic of a nutation spectrum in a non-linear field. The dashed line gives the high-resolution projection spectrum. The top shows the broad inhomogeneous 1D spectrum.

5.2. Shim pulses

The second approach to high-resolution spectroscopy in inhomogeneous fields is more direct in that it seeks to correct local dephasing created by the inhomogeneity using modulated gradient pulses in so-called "shim-pulses".[58] The local nutation frequency induced by an inhomogeneous RF pulse can be written as

$$\omega_1(r,t) = -\gamma B_{1\max}(r) A_{\mathrm{rf}}(t) \tag{14}$$

where $B_{1\max}(\boldsymbol{r})$ is the maximum local RF field amplitude and the time-dependent coefficient, $A_{\mathrm{rf}}(t)$, modulates this amplitude. Likewise, the local resonance-frequency offset for a particular resonance can be written as

$$\Delta\omega_0(r,t) = -\gamma(1-\sigma)[B_0(r) + \Sigma_n B_{0,n}(r) A_n(t)] - \omega_{\mathrm{rf}} \tag{15}$$

where σ is the chemical shift, $B_0(\boldsymbol{r})$ is the local value of the main inhomogeneous magnetic field and $B_{0,\mathrm{n}}(\boldsymbol{r})$ is the maximum local field created by the nth gradient coil, while the coefficient $A_n(t)$ modulates the amplitude of the nth gradient. The objective with magnet and RF coil design is, of course, to create a pure rotation of the magnetisation around the z axis, lacking any dephasing by field inhomogeneities and the traditional approach to achieving this is to homogenise the $B_1(\boldsymbol{r})$, $B_0(\boldsymbol{r})$ and $B_{0,\mathrm{n}}(\boldsymbol{r})$ fields by clever RF and shim coil design. However Eqs. (13) and (14) show that, in principle, the same can be achieved by adjusting the time-dependent amplitudes $A_{\mathrm{rf}}(t)$ and $A_n(t)$ so as to give gradient pulses that modulate the phase $\phi(\boldsymbol{r})$ of the transverse magnetisation by an amount that cancels the dephasing induced by local field inhomogeneity. This is the alternative shim-pulse approach, details of which can be found in ref. 58. Like the earlier 2D-nutation approach, the feasibility of this approach has so far only been demonstrated with phantoms at high field strength but the same approach is applicable to lower field magnets so it is to be anticipated that shim pulse technology will find important applications in the NMR of food.

By modulating the gradient pulses the method does, in principle, obviate the need for the expensive shim coil stack altogether. Quite apart from the cost saving, this has several other advantages because gradient "shim pulses" can also be used to correct artefacts arising from imperfect magnet and gradient coil arrangements and thereby relax some of the design constraints on *ex situ* hardware. The *ex situ* devices such as the MOUSE (Section 3.4), the Halbach NMR system (Section 3.5) and on-line NMR sensors (Section 6) could therefore benefit greatly from shim pulse technology. It might also be possible for an inexpensive bench-top NMR system lacking shims and equipped only with a gradient set to produce sufficiently high-resolution spectra to distinguish the main food constituents such as lipids, sugars and water in quite large sample volumes, and this could find routine application in high-throughput food quality control.

5.3. *Z*-rotation pulse methods

z-rotation pulses[59] provide an alternative way of performing high-resolution NMR spectra in inhomogeneous magnetic fields. A train of *z*-rotation pulses interleaved with data sampling is used to directly refocus the position-dependent dephasing of the magnetisation caused by local field inhomogeneity. Like 2D-nutation spectroscopy the method relies on the existence of a correlation between the B_0 and B_1 inhomogeneities, so that a *z* rotation of the transverse magnetisation cancels out the local dephasing caused by precession in the inhomogeneity and results in the refocusing of the magnetisation as an echo between *z*-pulses. Unlike Hahn spin echoes, full chemical shift information is retained because no chemical shift evolution takes place during the *z*-pulse excitation only during the free induction period following the pulse. This means that if a single point is acquired at each echo maximum and this is immediately followed by another refocusing *z*-pulse the net result of an *N*-*z*-pulse train is an *N*-point FID free of dephasing by field inhomogeneity but which retains full chemical shift information. Fourier transformation therefore generates a high-resolution spectrum. Because it creates an FID, the same protocol can, of course, be used in multidimensional high-resolution pulse sequences; Pines *et al.*[60] have even generated COSY spectra in inhomogeneous fields. The technique has also been used in a portable single-sided NMR sensor comprising two concentric U-shaped NdFeB magnets.[37] This succeeded in reducing a preliminary linewidth of 2.5 kHz to just 65 Hz and produced a high-resolution fluorine spectrum of perfluorobenzene. Early applications relied on a linear correlation between the B_1 and B_0 inhomogeneities but more recently the method has been generalised to non-linear correlations. To achieve this a 2D-nutation spectrum (Section 5.1) was first used to produce a correlation map of the non-linear B_1 and B_0 field inhomogeneities then the pulse width, bandwidth and amplitude of adiabatic *z*-rotation pulses of the hyperbolic secant type[61,62] were adjusted to improve the refocusing.[63] This elegant procedure also has its limitations. Higher B_0 field inhomogeneity requires higher RF pulse power to keep refocusing the dephasing, so ultimately the method is limited by RF power. Also the chemical shift encoding is slower at lower B_0 fields, so the required echo train can become impractically long at low fields. Clearly the technique is still under development and it may be that some combination of *z*-rotation pulses with other line narrowing methods such as MAS or shim pulse methods will provide an even more powerful approach to overcome the limitations of field inhomogeneity.

6. TOWARDS ON-LINE NMR SENSORS

The last few years have seen increased effort to develop an on-line NMR sensor for examining food samples, such as fruit, moving continuously on industrial conveyors.[33–35,64] Table 1 lists a number of key studies in which fruit has been conveyed at constant speed through a horizontal bore MRI system in an effort to detect internal quality defects. Unfortunately most of these studies are only of academic interest either because the measurements were undertaken on expensive high-field superconducting

Table 1. On-line NMR studies of food quality

Fruit	Quality Factor	Conveyor Speed (m/s)	Proton Frequency (MHz)	Reference
Lemons, oranges	Seed detection	0.54	200	34
Oranges	Freeze injury	0.54	200	35
Apples	Internal Browning	0.25	5.55	87
Avocado	Maturity	0.25	85.5	88
Avocado	Maturity	0.3	25.9	89
Olives	Pit detection	0.15–0.25	85.5	90
Pear	Internal breakdown	0.5	200	91

magnet systems or at very low conveyor speeds, thereby preventing commercial implementation as a low-cost, rapid, on-line sensor in the food industry. The most recent study[87] is a possible exception to this statement since measurements were undertaken at the low field (5.55 MHz) created by permanent magnets at a moderate conveyor speed (0.25 m/s). Nevertheless most industrial conveyors move at speeds of 1 m/s or more so there is still some way to go before commercially viable NMR sensors are practical. Besides the problems associated with high conveyor speed and the requirement to avoid expensive superconducting magnet technology and costly gradient and RF amplifiers there are additional obstacles to overcome. These include the requirement for high magnetic field homogeneity over an extended distance and this is hard to implement in a factory environment. Moreover, there is the problem of sample polarisation. At high conveyor speeds there is insufficient time to fully polarise samples characterised by T_1's in excess of a second because samples need to travel a distance $5T_1v$ for complete polarisation. With a conveyor velocity, v, of 1 m/s and a typical T_1 of 1 s this amounts to 5 m, which is impractically long. Of course complete polarisation is not necessary, but then the price to be paid is decreased signal/noise.

Recent works[64,65] indicate that many of these problems can be overcome by exploiting the principle of ''motional relativity'', which uses the movement of the sample itself to modify, or even create, NMR signals. The motional relativity principle will be considered in the next few sections, but first it is worth examining the huge commercial potential for low-cost NMR sensors, which is the driving force behind these developments.

Food manufacturing is the largest industrial sector and many NMR papers have shown the existence of useful correlations between NMR parameters and food quality and these can, potentially, be developed into on-line quality control protocols. As we have seen in Section 2.4.1, NMR studies of quality defects in horticultural products (fruit, vegetables, bulbs) reveal numerous potential applications including the detection of bruising, infection and physiological defects induced by over-ripening or long-term storage.[14] Foreign body detection in processed food is another possibility. Bone fragments in processed meat and fish as well as metal, glass and plastic foreign bodies introduced during manufacture are a constant concern in the food industry as are a host of other quality concerns related to the

oil, fat and water content of processed meat, fish, dairy, egg and cereal products. Process control is another area where NMR sensors could make a significant impact. In process control the spatial aspect of imaging is not always needed and an on-line NMR sensor could continuously and non-invasively monitor the composition and/or viscosity and/or temperature of extruded or pumped semi-solid material. Such monitoring relies on the dependence of the NMR relaxation times and signal amplitudes on the processing variables.

6.1. Motional relativity and radiofrequency excitation

The principle of motional relativity has been discussed by the author in two recent publications.[64,65] In conventional NMR an on-resonance RF pulse of time-dependent amplitude, $B_1(t)$, tips the longitudinal magnetization vector in a polarised sample through an angle, θ, in the rotating frame, such that

$$\theta = \int \mathrm{d}t \gamma B_1(t) \tag{16}$$

An alternative way of achieving the same result is to set up a localised region of space containing a spatially characterised, time-invariant, continuous RF field, B_1, which is transverse to the main magnetic field, B_0. The excitation is then achieved by translation of the sample through this localised volume of RF radiation. With a simple variable transform the tip angle θ, in the on-resonance rotating frame for a spin moving in one dimension (along the z-axis) with a velocity u and acceleration, a, through an on-resonance RF field, $B_1(z)$, can be shown to be[65]

$$\theta = \int \mathrm{d}z \gamma B_1(z)/[u^2 + 2az]^{1/2} \tag{17}$$

Eq. (17) shows there are major advantages with this alternative excitation protocol in on-line situations. First, rapid translation of the sample through the RF field at velocities of several meters per second no longer requires extended regions of RF B_1 homogeneity along the direction of motion. Even quite inhomogeneous RF fields are effective because only the spatial integral of the RF field enters Eq. (17). Second, because the RF irradiation is continuous there is no need for expensive RF pulse programmers. Third, because the RF field is no longer pulsed there are no induced eddy currents or associated coil ring-down phenomena. Eq. (16) also shows that there is no reason to be restricted to samples moving at constant velocity. Accelerating samples, such as powders falling under gravity through the RF coil, can be excited in the same way. This excitation mode, which we call the "ST" mode (for Sample Translation), is especially suited to simple on-line applications requiring only one or two excitation pulses.

It is worth noting that, in principle, it may be possible to do away with RF excitation altogether by using sample translational motion through fixed orthogonally oriented external fields. In this scenario a sample is first polarised by translation through a magnetic field fixed in some direction, ϕ, perpendicular to its direction of

translational motion. The sample then moves rapidly into a magnetically shielded region of zero field and emerges into a second magnetic field also perpendicular to its direction of motion, but oriented at an angle, $\phi \pm 90^\circ$. Provided the transit time is less than the longitudinal relaxation time, an FID will be observed in a tuned receiver coil located in the second magnetic field. For this to succeed the field reorientation perceived by the sample must be non-adiabatic otherwise the magnetisation merely follows the changing direction of the external field. To ensure non-adiabatic rapid passage the resonance frequency must be much less than the apparent rate of field reorientation and the region of zero field ensures that this is the case. The major problem to overcome in this RF-free protocol appears to be the rapid dephasing caused by the field inhomogeneity as the sample emerges from the shielded region.

6.2. Motional relativity and signal acquisition

In the ST excitation mode, the FID of the spins emerging from a region of constant RF excitation will differ from the FID of a pulsed RF experiment on a stationary sample because spins at different locations in a finite-sized sample emerge from the RF field at different times and therefore end up with different phases owing to free precession in the main field, B_0. It can be shown[65] that the total signal is now given by the Fourier transform

$$S(t) = \exp(\mathrm{i}\omega_0 t) \int \mathrm{d}z\ \rho(z)\ \exp(\mathrm{i}k_0 z) \tag{18}$$

where $\rho(z)$ is the local slice transverse magnetisation density and the wavevector, k_0, is ω_0/v. Eq. (18) should be contrasted with the conventional FID on a stationary sample in a pulsed RF experiment, which is $S(k_0 = 0,t)$. A spin echo at a distance $2vT$ can be created by motion of the sample through a second region of continuous RF irradiation of an intensity and length sufficient to give an 180° pulse and located at a distance vT further down the track. This echo is attenuated not only by the samples' intrinsic transverse relaxation but also by a process called "translational relaxation",[61] which differs from conventional T_2, T_2* or diffusive processes because each spin experiences a unique path in time-frequency space as it moves down the track depending on its position within the sample and the z-dependence of the external field inhomogeneity at that position. In general the inhomogeneity will not be the same before and after the 180° excitation, so refocusing will be imperfect or non-existent. The best way to avoid such "translational dephasing" is to store the magnetisation as longitudinal magnetisation for passage between RF coils with a suitable flip-back pulse performed either in the ST- or pulsed RF mode.

The emergence of the Fourier transform in Eq. (18) suggests that image profiling is possible using a constant, time-invariant field gradient, G, oriented along the direction of sample motion. An analogous derivation shows that,

$$S(t) = \exp[\mathrm{i}\omega_0 t]\ \exp\left[\mathrm{i}\tfrac{1}{2}\gamma G v t^2\right] \int \mathrm{d}z\rho(z)\ \exp[\mathrm{i}(k_0 + k)z]\ \exp\left[\mathrm{i}\gamma(G/v)z^2\right] \tag{19}$$

Here the wavevector k is defined in the usual way as γGt. Providing $\gamma G/v$ is very small (the weak-gradient, high-velocity approximation) we can neglect the term in z^2, which prevents inverse Fourier transformation. The pre-exponential factor $\exp[i\omega_0 t]$ can also be set to unity if the experiment is performed "on-resonance", in which case

$$S(t) = \exp\left[i\tfrac{1}{2}\gamma G v t^2\right] . \int dz \rho(z)\ \exp[i(k_0 + k)z] \tag{20}$$

Eq. (20) shows that the image, $\rho(z)$, is obtained as the inverse Fourier transform of $S(t)\exp[-i1/2\gamma G v t^2]$ except that the k_0 wavevector introduces a constant offset in k space. Note especially that in this 1D ST-mode-imaging experiment all fields are time-invariant and only the sample moves so that expensive gradient amplifiers and controllers are no longer necessary and the RF is continuous, not pulsed. Because the gradient, G, is not pulsed there is, in fact, no need for a separate linear gradient coil. Instead the linear gradient, G, can be regarded as the first term in a Taylor expansion of the local B_0 field inhomogeneity over a region extending for a sample length from the RF coil. In other words, the main field, B_0, is deliberately made locally inhomogeneous to first order, so as to obtain an image. This runs counter to the conventional NMR wisdom based on stationary samples where B_0 homogeneity is paramount.

The motional relativity principle is trivially simple for gradients transverse to the direction of sample motion because the vector product $\mathbf{G} \cdot \mathbf{v}$ is then zero, and so the signal is not motionally modulated. Passage through a spatially localised time-invariant transverse gradient is therefore exactly equivalent to applying a pulsed transverse gradient to a stationary sample. This means that 2D back-projection imaging could, in principle, be done without any gradient pulsing by translating the sample through a set of permanent m transverse gradients equally spaced along the track and oriented at an angle ϕ to the vertical such that $\phi = 0, \pi/m, 2\pi/m \ldots \pi$ and acquiring a spin echo in each gradient. Because this requires multiple echoes it is probably best done with the pulsed RF excitation mode rather than the ST mode but this aspect is yet to be researched.

There are clearly a number of different ways for developing a low-cost, on-line NMR sensor based on motional relativity. Most conventional pulse sequences can be transposed, at least on paper, into the ST mode with arrays of constant gradients and RF sources arranged along the conveyor track, though in many cases the arrays would be impractical to construct and implement.

6.3. Motional relativity and coil design

To exploit motional relativity and maximise signal acquisition times with samples moving at several meters per second all RF, B_0, shim and gradient coils are best redesigned as cylindrical modules that can be wrapped around the conveyor and extended to arbitrary lengths along the direction of sample motion. At the same time it is essential to maintain commercial viability by keeping all costs to a minimum.

The prototype sensor[64,65] was based on an air-cooled double solenoid electromagnet. Air cooling rather than water-cooling was chosen because of its greater simplicity and lower cost. A double solenoid was used because the heat generated in a solenoid coil is proportional to the square of the current; whereas the magnetic field is proportional to the current itself, so the same field can be achieved with roughly $(1/n)$ of the current through each of the n coils and $(1/n)$ times less total heat output compared with a single coil of the same wire length. The increased surface area created by air gaps between the concentric coils also improves cooling efficiency. Despite their need for a power supply and efficient cooling, solenoid magnets have major advantages over permanent magnet arrangements because the field strength can be easily varied and stabilised using a constant current power supply, and the field homogeneity in a long solenoid is sufficiently high to permit NMR even without shim coils. Even so, the B_0 field was shimmed to order z^3 with concentric, cylindrical z and z^2 shim coils located inside the inner solenoid magnet and extending along its whole length, and these reduce the linewidth of a 10 cm long water phantom at the centre of the coil to about 150 Hz. As already mentioned, in any commercial version the constant current z- and z^2 coils could be incorporated into the main solenoid magnet by varying the solenoid winding density.

A novel design for the cylindrically symmetric, low-field, transverse RF coil was also necessary. A simple solenoid RF coil could not be used because B_1 needs to be transverse to B_0. Saddle and birdcage coils give the desired transverse field but are more expensive and have limited B_1 homogeneity and long pulse durations. These difficulties were overcome with a series-wound, eddy-compensated, tilted solenoid RF coil. This contains solenoid-like coils tilted at 45° and uses the induced currents in a set of concentric vertical inner "free-floating" coils to remove the undesired longitudinal B_1 field component. This design is similar to a parallel-wound tilted coil developed for extremity imaging,[66] but it was necessary to shorten the pulse durations and decrease the resonance frequency using series rather than parallel winding. This follows because N parallel connected loops reduce the inductance by a factor of N^2 compared to a series winding, so the resonance frequency of a parallel winding is a factor of N-times higher. Parallel winding also divides the current between the N loops, giving undesirably long pulse durations. The tilted solenoid design has the advantage of being extendable to arbitrary lengths limited only by the need to avoid destructive interference when the wire length approaches half the RF wavelength. The decreasing filling factor can also become a problem with extended coils. For this reason separate transmitter and receiver coils are desirable, and are essential for the ST excitation mode.

Signal/noise is of critical importance for on-line applications. Fortunately, in low frequency RF coils, signal/noise can be dramatically increased by simply reducing the probe ringdown time, τ_r, so that more of the early part of the signal is observable. In multipulse sequences a shorter ringdown time also permits shorter interpulse spacings and therefore more signal per unit time. The probe ringdown time is equal to $2Q/\omega_0$ (where Q is the quality factor of the probe) and this can amount to several hundred microseconds at low resonance frequencies, ω_0, of just a few megahertz. A simple Q-damper device for active probe recovery was presented,[81] which is inductively coupled

to the probe through a coupling transformer positioned away from the main RF coil, which makes it independent of the RF coil design. This simple device succeeded in reducing ringdown times by roughly an order of magnitude. There would appear to be no reason why this same approach could not also be used to increase signal/noise in the Halbach system and in other *ex situ* NMR probes.

6.4. Prepolarisation

The discussion in Sections 6.1 and 6.2 assume that the sample is fully polarised before entering the RF excitation coil. However a sample, such as an apple, with a T_1 of about 1 s travelling at 1.5 m/s would need to travel 7.5 m ($5T_1v$) before it is fully polarised, which requires an unreasonably long solenoid magnet. This difficulty can be overcome with a prepolarising module that contains low cost permanent magnets with a higher field strength positioned on either side of the conveyor track and oriented transverse to the sample motion. Samples first pass through the prepolarising module before entering the main solenoid sensor field. The adiabatic principle[67] ensures that the magnetisation in each isochomat will always follow the direction of the local magnetic field even when the sample emerges from the prepolariser polarised transverse to the direction of motion and the solenoid field is parallel to the motion. For the same reason the sample can be mechanically rotated as it travels through the prepolariser to ensure a more uniform polarisation.

Of course, the adiabatic principle merely determines the rate of reorientation of the longitudinal magnetisation not its magnitude, which is determined by longitudinal relaxation. It is therefore noteworthy that longitudinal relaxation as samples travel through the prepolariser, the gap and solenoid magnet can be exploited to give a new type of image contrast, namely the degree of polarisation, P. This depends not only on the field-dependent longitudinal relaxation time, T_1 at the frequency $\gamma B_0(z)$, which varies along the track, but also on the changing asymptotic longitudinal magnetisation, $\chi B_0(z)$. The stray field in the gap between the prepolariser and the solenoid corresponds to low resonance frequencies, $\gamma B_0(z)$, of just a few tens of kilohertz, so that $T_1\{\gamma B_0(z)\}$ in the gap differs significantly from its usual high-field value and needs to be measured with a field-cycling spectrometer. Because T_1 generally decreases with decreasing field strength in biological samples, polarisation contrast may offer greater sensitivity for distinguishing quality factors than high field T_1 measurements. However the relationship between polarisation contrast, $P(r)$, and sample quality factors is unknown for most applications and will need to be researched if commercial applications are to be optimised.

6.5. Single-shot on-line pulse Sequences

Because each sample travels through the sensor only once there is no possibility of using conventional pulse sequences based on repeated acquisition and/or phase

cycling. Instead maximum information must be extracted in a single passage through the sensor, which means it is necessary to develop novel single-shot on-line equivalents of the conventional pulse sequences for image profiling, T_2, T_1, self-diffusion (D) and solvent suppression. Whether the single-shot, ultrafast CWFP and MMME methods discussed in Section 3 can be adapted to the on-line situation where the sample moves through regions of RF, and B_0 inhomogeneity remains to be explored. The on-line determination of T_2 illustrates the problems.

6.5.1. *Single-shot on-line T_2 measurements*

There are potentially serious complications when implementing the CPMG sequence on-line because 180° pulses do not, in general refocus the dephasing caused by translational relaxation. So any attempt to convey transverse magnetisation down the magnet between two RF coils is likely to fail unless the B_0 field is homogeneous over the whole distance between RF coils. It is therefore best to perform the CPMG sequence in a multipulse RF mode within a single (extended) RF coil. But even within a single RF coil there are other difficulties because the B_0 and B_1 fields experienced in each region of the sample are effectively time dependent because of the sample motion through field inhomogeneities. The problem is compounded with gross B_0 inhomogeneity if the RF coil is positioned off-centre in the solenoid field. This is a realistic situation in any commercial sensor because multiple RF coils positioned along the solenoid magnet would permit increased sample throughput and/or multiple NMR measurements on each sample. There is also the problem that the position-dependent B_1 in the finite sized RF coil means that the same pulse duration gives different position-dependent tip angles. Clearly, all this means that the apparent on-line T_2 measured with the CPMG sequence in a single RF coil will depend on sample velocity, and at sufficiently high velocities, depending on the B_0 and B_1 field inhomogeneities, the measured "apparent T_2" will become less than the true sample T_2.

To calculate the magnitude of these effects a numerical simulation was undertaken,[61] which incorporated the effects of finite sample size, the B_0 and B_1 field inhomogeneities as well as RF coil position. The results are summarised in Fig. 16. The top part of Fig. 16 shows the field inhomogeneity maps used as input. The B_0 field map was calculated for a solenoid magnet, while a trapezoid B_1 profile mimics the measured B_1 field inhomogeneity of the tilted solenoid RF coil. Spherical sample geometry was assumed, which gives the semi-ellipsoid profile seen in Fig. 16 (top). The bottom part of Fig. 16 shows representative simulated CPMG echo decay envelopes, in this case for spherical samples, moving at the indicated speeds through the trapezoid RF field located one-third of the way along the solenoid magnet. The simulation shows that when the RF coil is well off-centre it is only possible to determine meaningful T_2's out to acquisition times of about 40 ms with samples moving at 1.25 m/s. Fig. 16 (bottom) also shows that if the sample velocity is reduced to 0.25 m/s it is possible to measure T_2's of several hundred milliseconds, but there are few industrial situations where such low conveyor speeds would be

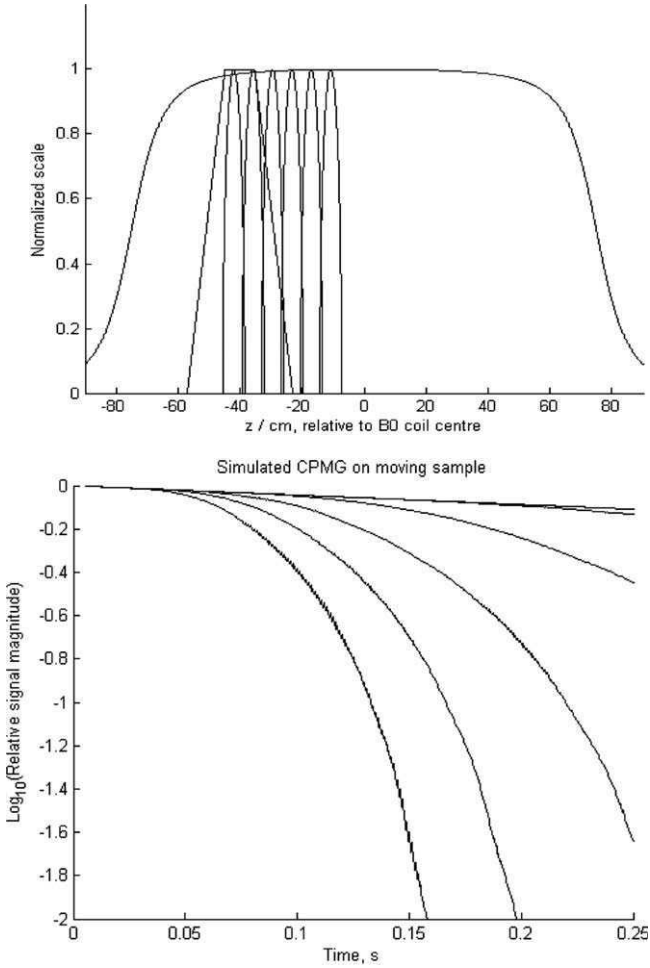

Fig. 16. (Top) This shows the trapezoid B_1 of an off-centre RF coil, the B_0 map of the solenoid magnet and the semi-ellipsoidal profile of a spherical sample used in the simulation. (Bottom) This shows the calculated CPMG echo decay envelopes for the indicated sample velocities.

economic. Fortunately there are NMR strategies for improving the situation. For example, the simulation assumes that the echoes are generated by a train of 180° pulses of equal duration, so that, as the sample moves through the RF coil, the tip angle varies. In principle it is possible to adjust the duration of each pulse to compensate for the B_1 variation and thereby extend the duration of the true 180°-pulse train. The experimental CPMG results[61] for a bottle of Cu (II)-doped water with the known static T_2's and moving at 1.25 m/s gave an upper limit of about 40–50 ms for reliable T_2 measurements. In this case all the refocusing pulses were of

equal duration fixed at that for a 180° pulse at the centre of the RF coil and the RF coil was located in the centre of the solenoid magnet.

6.5.2. *On-line image profiling for foreign body detection*

Eq. (23) shows that a 1D image profile can be obtained using a constant (non-switched) gradient oriented along the direction of motion provided the motionally modified spin echo is first multiplied by $\exp[-i1/2\gamma Gvt^2]$ before Fourier transformation. In this way a phantom foreign body was successfully detected in the prototype sensor.[61]

6.5.3. *Single-shot on-line T_1 measurements*

On-line, single-shot measurements of T_1 are also problematic because conventional sequences such as saturation or inversion recovery require repeated acquisition with step increases in the inversion or saturation recovery time. Fortunately the signal can be T_1-weighted either using polarisation contrast or by varying the degree of saturation with very rapid repeat acquisition on a timescale short compared to T_1 and the sample residence time in the RF coil. For more direct single-shot on-line measurement of T_1, a novel pulse sequence called FIRE (Fast Inversion REcovery) has been proposed.[65] This single-shot sequence shown in Fig. 17 actually measures both T_1 and T_2 and is similar to an inversion recovery sequence except that the signal is acquired not with an FID but with a truncated CPMG sequence of n-echoes. A 90_{-x} flip-back pulse on the $(n+1)$th echo of each truncated CPMG train then stores longitudinal magnetisation for a delay time t_1 before the next truncated CPMG sequence. The magnetisation eventually reaches a steady-state value that depends on both T_1 and T_2, so that fitting each CPMG echo train and the amplitude of the first echo of each truncated CPMG sequence gives both T_1 and T_2. Analytic expressions for extracting the relaxation times from the data have been derived.[61] Fig. 18 shows the magnitude data for the FIRE sequence on a stationary 15% sucrose solution. Fitting the data gave a T_1 of 1600 ms, which can be compared with the stationary sample, inversion recovery value of 1976 ms. The FIRE sequence naturally tends to emphasise the short-time relaxation components in multiple exponential relaxation because there is insufficient time to acquire accurate baselines. With a moving sample the number of inversion recovery steps (C1) and echoes (NECH) are limited by the sample residence time, though, as with the CPMG sequence, the sequence can be optimised by adjusting the RF pulse duration for each sample position in the RF coil and by using several RF coils positioned along the track. In the later case it is necessary to synchronise the pulse sequence so that only longitudinal magnetisation is transported between different RF coils during one of the C1 inversion recovery steps.

6.5.4. *Single-shot on-line diffusion measurements*

If the direction of sample motion is labelled z and the B_0 field is aligned along z then on-line diffusion measurements need to be done by translation of the sample

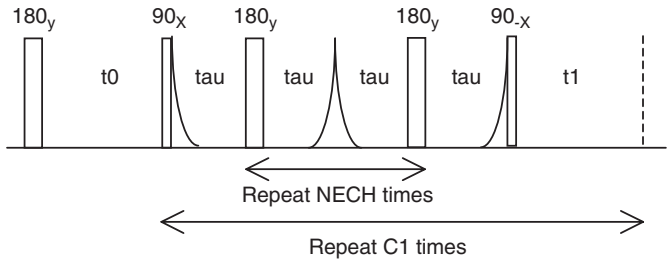

Fig. 17. The FIRE sequence for single-shot on-line measurement of T_1 (and T_2).

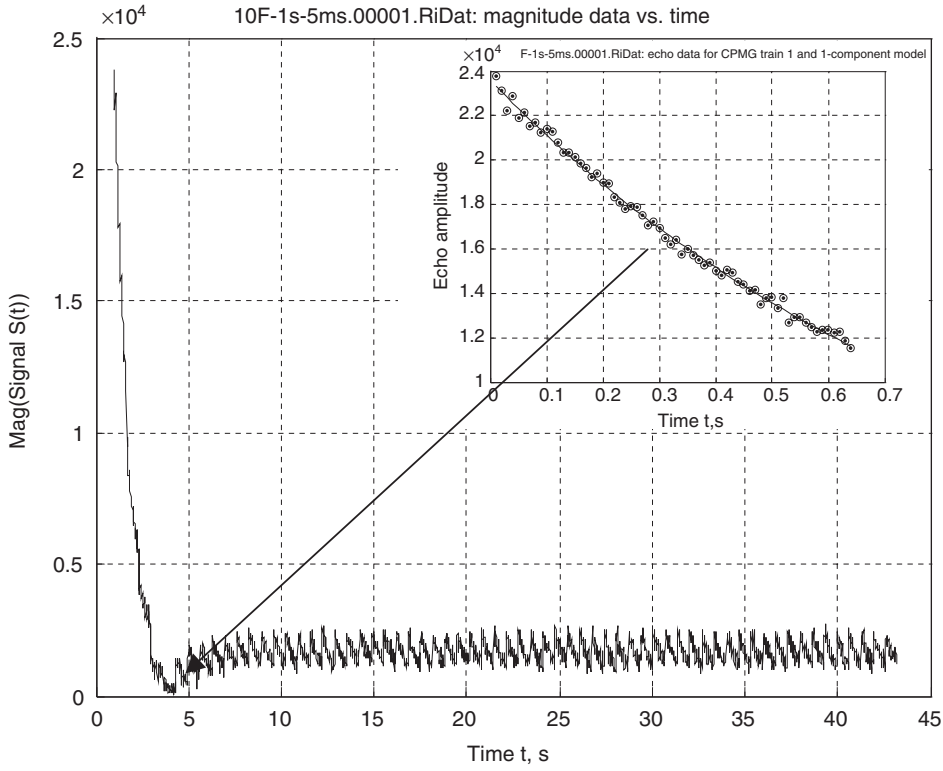

Fig. 18. Representative data for a 15% sucrose solution acquired with the FIRE sequence for single-shot, on-line T_1 and T_2 measurement. The saw-tooth structure arises from truncated CPMG echo trains, one of which is expanded and fitted in the inset.

through localised non-pulsed transverse gradients, G_x or G_y, which is motionally equivalent to applying pulsed gradients on a stationary sample. Passage through a localised gradient, G_z, will not cause diffusive dephasing because every spin in the sample will move through the whole of G_z and experience the same accumulated

phase change. Translational relaxation also means that longitudinal magnetisation and not transverse magnetisation must be conveyed between coils during the diffusion time. The simplest arrangement therefore mimics the pulsed gradient stimulated echo experiment and, in the pulsed RF mode, uses 2 RF coils and 2 constant-current transverse gradient coils, each gradient coil surrounding the RF coil. Passage through the first transverse gradient coil gives an accumulated phase twist characterised by the wavevector, q, where

$$q = \int \mathrm{d}z\gamma G_x(z)(z/v) \tag{21}$$

The second gradient coil reverses this dephasing twist and creates a motionally modified stimulated echo. Note especially that Eq. (21) implies that the gradient need not be a linear function of z, though it should be independent of (x,y) if meaningful diffusivities are to be measured. Unfortunately, in a single-shot sequence it is not possible to eliminate the effects of relaxation in the conventional way by taking the ratio of the stimulated echo amplitudes acquired with and without the gradient pulses. This on-line measurement will therefore only be of value for monitoring sample quality if diffusion is a more sensitive probe of sample quality than relaxation. The effect of variation in sample size on the stimulated echo amplitude needs to be taken into account when examining biological samples such as apples. This can be done by measuring the total magnetisation from the amplitude of the Hahn echo acquired in the first RF coil.

6.5.5. *Single-shot On-line Oil content and BRIX determination*

Although it has yet to be tested in an on-line situation, the pulse sequence shown in Fig. 19 could also be used for oil content determination by increasing the transverse gradient amplitudes to the point where the water signal is completely suppressed. The Hahn echo amplitude in the first RF coil then gives the total proton signal from both oil and water, whereas the stimulated echo amplitude arises only from oil. All that is then required is a linear calibration of the echo

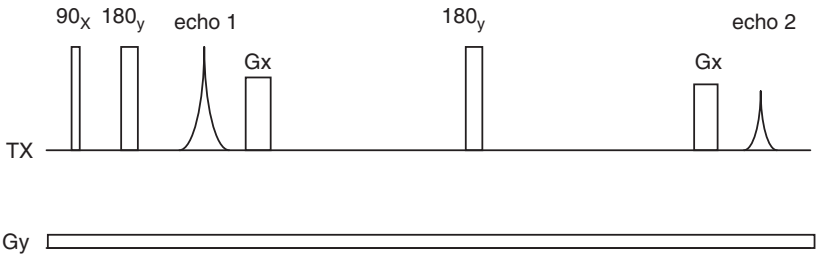

Fig. 19. The single-shot pulse sequence for on-line oil and Brix content determination.

amplitude ratio verses oil content. As already mentioned, a similar protocol could, in principle, also be used for the on-line determination of the soluble solid content (BRIX) value in fruit.

7. SOLID TECHNIQUES FOR *IN-VIVO* METABOLOMICS

7.1. PASS and PHORMAT

Intact cellular tissue does not normally yield a high-resolution spectrum of its small molecule metabolites even in high-field, high-resolution spectrometers. Instead the lines are broadened by local magnetic field gradients created by discontinuities in the magnetic susceptibility across intracellular and extracellular phase boundaries. Of course, magic angle spinning can narrow the lines by partially averaging out these local gradients, but spinning speeds of a few kilohertz or more are required to avoid the complication of spinning sidebands in the spectra. At rotor speeds of a few kilohertz most biological samples are destroyed by large centrifugal forces, which is one reason why most high-resolution metabolomic studies are performed on fluid extracts. Fortunately, the recent development of the PASS (Phase Adjusted Spinning Sidebands) and PHORMAT (PHase cORrected Magic Angle Turning) pulse sequences[68,69] for slow MAS has the potential for changing this situation. These sequences have been designed to eliminate spinning sidebands and permit the acquisition of high-resolution spectra even at spinning speeds as low as 1 Hz (with PHORMAT) or 30 Hz (with PASS).

PASS seeks to separate the desired centred band spectrum from the undesired spinning sideband spectra using a sequence of five π-refocusing pulses all fitted inside one rotor period. If there are n sideband spectra to be separated then n PASS experiments are made with n different time intervals between the π pulses while keeping the total duration to one rotor period. After 2D Fourier transformation a series of spectra is obtained that permits the separation of the desired centred band spectrum from the undesired sideband spectra.

PHORMAT is a continuous 2D variant of the Magic Angle Hopping (MAH) experiment. In MAH[70] the sample is hopped over angles of 120° about an axis at the magic angle. At each sample position the magnetisation is allowed to evolve for a variable time $t_1/3$ before being stored as longitudinal magnetisation with a flip-back pulse during consecutive hopping periods. In PHORMAT the sample is spun slowly and continuously and the effect of 120° hopping is achieved by synchronising the pulses to 1/3 of the rotor period. To avoid longitudinal relaxation between pulses the spinning speed in PHORMAT only needs to be large compared to $1/T_1$, which means that in many water-rich biological samples spinning speeds of just a few hertz are sufficient.

PASS and PHORMAT pave the way for metabolomic studies on the quality of fruit and meat and of metabolic changes induced by processing and storage.[71] PASS and PHORMAT metabolic spectra have been reported for sesame seed,[71] peanuts,[71] meat[72] and excised rat liver[85] and even for anaesthetised mouse.[86]

The spectra from a densely packed bacterial cell suspension (*Shewanella oneidensis*) was successfully recorded[71] and this opens the way to metabolic profiling of food-borne bacterial pathogens and spoilage organisms.

7.2. Field-MAS

An alternative to conventional slow MAS exploits the motional relativity principle by rotating the external magnetic field around a stationary sample. A spectrum of hyperpolarised solid ^{129}Xe was acquired in this way by magic angle rotation of the B_0 field by varying the current through three orthogonal pairs of Helmholtz coils.[82,83] However, rotating the field by modulating source currents in resistance coils is problematic for a number of reasons. To be widely applicable, the field needs to be strong enough to resolve proton resonances, but stronger fields require higher currents and therefore power requirements could become excessive. Moreover the receiver has to be gated to avoid saturation by the currents induced by the field modulation, which necessitates synchronising the pulse sequence with the rotation and/or the use of 2D acquisition schemes.[82,83] It occurs to this author that mechanical rotation of a Halbach magnet cylinder would seem to be one way of circumventing these difficulties, though this simple idea does not appear to have been tried yet. A Halbach cylinder creates a transverse magnetic field in the centre of the cylinder that is sufficiently homogeneous for NMR.[47,73] Slow MAS could then be achieved, at least in principle, with a stationary sample by rotating the cylinder continuously around its central axis and orienting the RF coil at the magic angle. If successful, this would permit high-resolution studies on intact biological samples. One problem would be creating a sufficiently strong field with permanent magnets such that metabolite resonances can be resolved. Fortunately, the field in a Halbach cylinder is not limited by the magnetisation of the materials but by the geometry. In fact the theoretical strength of the central field in a Halbach cylinder is given as

$$B_0 = B_r \ln(R_{out}/R_{in}) \tag{22}$$

where B_r is the residual magnetic field strength of the magnet material at zero magnetic intensity and $R_{out/in}$ is the outer and inner radius of the Halbach cylinder. This shows that, in principle, the central field can be increased by simply increasing the radius ratio, and the world record, so far, is a B_0 of 4 T in a Halbach cylinder constructed for use in a linear accelerator.[74] More modest radius ratios should be capable of producing field strengths and homogeneities sufficient to resolve the main lipid, water and sugar resonances. It might even be possible to further improve the resolution by combining the PHORMAT and Halbach MAS methods to remove the spinning sideband spectra. Of course, the use of a continuous Halbach cylinder means that the ''open-access'' advantage of the Halbach array referred to in Section 3.5 would need to be sacrificed for the sake of creating sufficiently high field strength.

8. MRI STUDIES OF FOOD PROCESSING

Recent years have seen an increased effort to use MRI in a quantitative way to monitor food-processing operations involving simultaneous heat and mass transfer as well as food structural changes. This is a great deal harder than merely producing qualitative images because it requires the determination of spatial maps of NMR parameters such as M_0, T_1, T_2 and/or D and establishing robust correlations between these parameters and the processing factors of interest such as temperature, water content or other food characteristics.[75] The following examples have been selected from the recent literature because they illustrate the intensive nature of the effort required to achieve this objective.

8.1. Cooking

As is well known, cooking a food such as potato or meat involves parallel changes in temperature, water content and matrix microstructure, which includes the denaturation, aggregation and/or gelatinisation of biopolymers and phase transitions such as the melting of fats and/or glass transitions. In principle MRI has the potential of monitoring all these changes in space and time but with so many variables this presents a considerable challenge. With a few notable exceptions, most of the research to date has focused on establishing that MRI can quantitatively image one or other of these food-processing variables in uniform model systems, such as gels. Indeed, 3D MRI has mapped microwave-induced changes in temperature in model gels[76] and, of course, many MRI studies have imaged moisture distribution from M_0 or T_2 maps.[75] MRI-relaxation time maps and magnetisation transfer maps have also been shown to be sensitive to food matrix structural changes such as gelatinisation and biopolymer denaturation.[77] The future challenge is to try to put these separate protocols together so that MRI simultaneously monitors changes in several variables, including temperature, moisture content and microstructure in a real food during a processing operation such as cooking. Two examples with this objective have been chosen from the work at the Herchel Smith Laboratory in Cambridge. The first concerns microwave heating of potato, the second oven cooking of chicken meat.

8.1.1. *Microwave heating of potato*

An attempt has been made to simultaneously map temperature changes (via phase mapping); moisture distribution (via M_0 mapping) and starch gelatinisation (via T_1 and T_2 mapping) during the microwave cooking of potato.[77] Temperature maps were acquired across a potato after just 1 min of heating in a domestic 800 W microwave oven at 100% power. Sample shrinkage and shape distortion hindered temperature mapping at longer heating periods. T_1 and T_2 maps as well as first echo images were also acquired at 1 min intervals up to 5 min after cooling back to 20 °C. These maps showed the loss of structural differentiation between the pith, parenchyma and

vascular internal structure during cooking, which was complete after 4 min. The MRI–M_0 maps obtained by extrapolation were however problematic because M_0 apparently increased with heating time despite the evaporative water loss. This was believed to be an artefact resulting from a single-exponential analysis with a TE of 12 ms, which is not truly representative of the intrinsically multiexponential T_2 spectra seen with bulk CPMG measurements. Indeed, bulk CPMG measurements of M_0 at short acquisition times showed the expected linear decrease with the weight loss arising from water evaporation during heating. Clearly, this study emphasises the power of the multi-parameter MRI approach to food processing but it remains to be seen whether it is practical to map the relaxation time in real time as the temperature also varies, rather than after the samples have cooled back to room temperature.

8.1.2. *Oven grilling of meat*

A quantitative study of the cooking of slabs of chicken meat at 200°C on the rotating "grill shelf" of a convection oven has also been reported by the team at the Herchel Smith.[78] The slabs were cooked for time periods between 3 and 21 min, cooled to room temperature then imaged at 2.35 T. Sets of T_1-weighted images were acquired with a saturation recovery sequence with 5 recovery times for 2D slices each 5 mm thick and converted to T_1 maps by assuming single exponential recovery. In a similar manner, a set of T_2-weighted images with 16 echo times were used to calculate a T_2 map. A spin-density map (M_0 map) was obtained by extrapolating the T_2-weighted images to zero echo time.

As was the case with potato cooking,[77] the interpretation of such MRI relaxation time, spin density (and diffusion) maps is far from straightforward because the use of a small number of echo or recovery times with single exponential fitting means the MRI-derived parameters are, at best, just weighted averages of the true relaxation behaviour. In this case a comparison with the triple exponential relaxation behaviour observed with a 1D CPMG sequence with 256 echoes on the bulk samples showed that the MRI-T_2 corresponded most closely with the intermediate relaxation time, conventionally labelled T_{22}, which characterises the water associated with the myofibrillar actin and myosin filaments. Because cooking denatures the proteins and causes water to be expelled, both T_2-MRI and T_{22} decrease with decreasing gravimetric moisture content and increased cooking time. The M_0–MRI value also correlated with gravimetric water loss but the correlation coefficient was only 0.71 because the water characterised with the shorter T_2 (labelled T_{23}) in the CPMG measurement and assigned to biopolymer hydration water and water with longer T_2 (labelled T_{21}) and assigned to intermyofibrillar water was MRI-invisible at the chosen echo spacings. As with the microwaving of potato, these calibrations were made at room temperature. Before quantitative MRI studies of the actual real-time cooking process can be undertaken it will be necessary to establish the temperature-dependence of these parameters, which is an even more daunting task. Nevertheless qualitative images of the real-time cooking process over a 36 min period at 102 °C were also undertaken using a purpose-built probe housed in a hot-air heated chamber.[78] These images suggested that the initial contrast changes are

associated with temperature; whereas in later cooking stages the contrast change is mainly moisture related.

8.2. Mixing

The mixing of two fluid streams is a basic operation in the food industry that is often performed with single-screw extruders. The efficiency of the mixing process can be placed on a quantitative basis by defining the "intensity of mixing", I, as a measure of divergence from the mean composition such that

$$I = S^2/[C_{\text{mean}}(1 - C_{\text{mean}})] \tag{23}$$

where S^2 is the variance in the concentrations of the mixture and C_{mean} is the mean concentration.[79] By producing quantitative concentration maps, MRI has shown itself capable of measuring the intensity of mixing. Two streams of 1% aqueous sodium carboxymethylcellulose (CMC) were mixed in a single screw extruder.[80] These steams were distinguished by doping them to different extents with manganese (II) ions, so that the relaxation times were sufficiently different to create image contrast. The mixing was performed in a specially designed single screw extruder made from non-ferromagnetic materials. This extruder was surrounded by an RF coil and placed inside an RF Faraday cage to shield it from external noise. The whole extruder and coil were then fitted inside a 31 cm horizontal bore imager. Images were gated so that each scan synchronised with the same screw position during each revolution. Prior to mixing the MRI signal intensity (SI) was calibrated against manganese concentration (C) and receiver gain (RG) as

$$\text{Log(SI)} = 5.38 - 0.05\text{RG} - 0.37C \tag{24}$$

This allowed the image signal intensity to be converted into a concentration map from which the intensity of mixing, I, was measured as a function of screw velocity and total fluid flow. Such MRI mixing studies will undoubtedly establish themselves as useful experimental checks on the validity of Computational Fluid Dynamics (CFD) calculations of mixing, especially for the highly non-Newtonian fluids and slurries usually used in the food industry.

8.3. Single-sided MRI

Relaxometry and diffusometry in the inhomogeneous fields associated with the NMR-MOUSE and other single-sided NMR probes have already been considered in Section 3 and the possibility of acquiring high-resolution spectra with such devices has been alluded to in Section 5. In this final section we complete our survey of MRI developments by briefly noting that Blumich's group at Aachen have been pioneering the development of 1D, 2D, and 3D imaging applications with single-sided magnets.[93–95] Most recently 1D profiling of a surface has been achieved with resolutions better than 5 μm over a depth of approximately 4 mm and also at a

lower resolution of 100 μm over a 10 mm depth.[95] Although this single-sided magnet probe is not yet commercially available it will undoubtedly find numerous applications in the food sector. One obvious use would be to monitor the changing structure and composition of surface coatings used as moisture barriers in food preservation. In food processing a single-sided MRI surface imager would be ideal for examining, in real time, surface phenomena such as case-hardening, which can affect mass and heat transport during drying and cooking.

9. CONCLUDING REMARKS

It is hoped that this brief review has given an exciting "snapshot" of the many fast-moving developments in low-field NMR. Of course, this "snapshot" is far from comprehensive but an attempt has been made to highlight those developments that have the potential of revolutionising quality control in the food sector. This includes new NMR devices such as *ex situ* NMR probes, on-line sensors, new ultrafast analytical methods and multidimensional approaches to relaxometry and diffusometry that dramatically increase the information content compared to traditional 1D relaxation or diffusion measurements. Nevertheless it is also clear that much research remains to be done to take these novel approaches to the point where they cease to be feasibility studies undertaken by NMR specialists and end up as user-friendly tools in the hands of food scientists and quality controllers. Besides food applications it is also obvious that many of the developments such as low-cost NMR sensors and Halbach NMR have the potential for spreading NMR and MRI technology throughout other industries, including those in the pharmaceutical, construction and energy sectors. If successful, these low-field developments could also have a major impact on the wider research community and even on the general public. If this happens it will herald a new and very exciting era for NMR.

ACKNOWLEDGMENTS

The author wishes to thank his colleagues Dr. Nicola Woodward for providing Fig. 1 and Niusa Marigheto for Figs. 3–6. Funding support from the BBSRC during the preparation of this chapter is gratefully acknowledged.

REFERENCES

1. A. Tal, B. Shapira and L. Frydman, *J. Magn. Reson.*, 2005, **176**, 107.
2. A. B. Siemer, C. Ritter, M. Ernst, R. Riek and B. H. Meier, *Angew. Chem. Int. Ed.*, 2005, **44**, 2441.
3. M. Ernst, A. Samoson and B. H. Meier, *J. Chem. Phys.*, 2005, **123**, 064102.
4. G. Le Gall and I. J. Colquhoun, NMR spectroscopy in food authentication, *Food Authenticity and Traceability*, Chap. 6, M. Lees, Ed., Woodhead, Cambridge, 2003, 131–155.
5. M. Defernez and I. J. Colquhoun, NMR approaches to detect unintended effects of genetic modification in plants, *Genomics for Biosafety in Plant Biotechnology*, J.-P. Nap, A. Atanassov and W. J. Stiekema, eds., IOS Press, Amsterdam, 2004, pp. 18–26.

6. M. Defernez, Y. M. Gunning, A. J. Parr, L. V. T. Shepherd, H. V. Davies and I. J. Colquhoun, *J. Agric. Food Chem.*, 2004, **52**, 6075.
7. M. Defernez and I. J. Colquhoun, *Phytochemistry*, 2003, **62**, 1009.
8. G. Le Gall, M. S. DuPont, F. A. Mellon, A. L. Davis, G. J. Collins, M. E. Verhoeyen and I. J. Colquhoun, *J. Agric. Food Chem.*, 2003, **51**, 2438.
9. G. Le Gall, I. J. Colquhoun, A. L. Davis, G. J. Collins and M. E. Verhoeyen, *J. Agric. Food Chem.*, 2003, **51**, 2447.
10. G. Le Gall, I. J. Colquhoun and M. Defernez, *J. of Agric. Food Chem.*, 2004, **52**, 692.
11. F. Cellini., A. Chesson., I. J. Colquhoun, A. Constable, H. V. Davies, K. H. Engel, A. M. R. Gatehouse, S. Karenlampi, E. J. Kok, J. J. Leguay, H. P. J. M. Noteborn, J. Pedersen and M. Smith, *Food Chem. Toxicol.*, 2004, **42**, 1089.
12. M. Dyrby, D. Baunsgaard, R. Bro and S. B. Engelsen, *Chemom Intell Lab Syst*, 2005, **76**, 79.
13. M. Dyrby, M. Petersen, A. K. Whittaker, L. Lambert, L. Nørgaard, R. Bro and S. B. Engelsen, *Anal. Chim. Acta.*, 2005, **531(2)**, 209.
14. B. P. Hills and C. J. Clark, *Annu. Rep. NMR Spectrosc.*, 2003, **50**, 75.
15. B. P. Hills, A. Grant and P. S. Belton, NMR characterization of cereal and cereal-based products, *Characterization of Cereals and Flours: Properties, Analysis and Applications*, G. Kaletunc and K. J. Breslauer, eds., Marcel Dekker, New York, 2003.
16. P. T. Callaghan, S. Godefroy and B. N. Ryland, *Magn. Reson. Imaging*, 2003, **21**, 243.
17. Y.-Q. Song, L. Venkataramanan, M. D. Hurlimann, M. Flaum, P. Frulla and C. Straley, *J. Magn. Reson.*, 2002, **154**, 261.
18. P. L. Hubbard, P. J. Wilkinson, L. K. Creamer, A Gottwald and P. T. Callaghan, *Magnetic Resonance in Food Science*, S. B. Englesen, P. S. Belton, H. J. Jakobsen, eds., Royal Society of Chemistry, Cambridge, 2005, 225.
19. W. T. Dixon, *Radiology*, 1984, **153**, 189.
20. B. P. Hills, P. Manoj and C. Destruel, *Magn. Reson. Imaging*, 2000, **18**, 319.
21. B. P. Hills, N. Marigheto, K. M. Wright and S. Benamira, *Appl. Magn. Reson.*, 2004, **26**, 543.
22. B. Sun and K.-J. Dunn, *Phys. Rev. E*, 2002, **65**, 51309.
23. G. H. Glover, *J. Magn. Reson. Imaging*, 1991, **1(5)**, 512.
24. N. Marigheto, S. Duarte and B. P. Hills, Appl. Magn. Reson. (in press).
25. S. Pathaveerat, M. J. McCarthy and P. Chen, *Abstracts of the Potsdam Symposium on Fruit Quality*, ATB, Potsdam, 2001.
26. B. P. Hills, A. Costa, N. Marigheto and K. M. Wright, *Appl. Magn. Reson.*, 2005, **28**, 13.
27. E. Veliyulin, I. G. Aursand and U. Erikson, *Magnetic Resonance in Food Science*, S. B. Englesen, P. S. Belton, H. J. Jakobsen, eds., Royal Society of Chemistry, Cambridge, 2005, 148.
28. C. E. Lewis, *J. Sci. Agric. Food*, 1978, **29**, 857.
29. F. J. Kruger, P. J. C. Stassen, and B. Snijder, Proceedings of the World Avocado Congress III, 1995, 285–288.
30. S. K. Lee, R. E. Young, P. M. Schiffman and Coggins Jr., *J. Am. Hort. Sci.*, 1983, **108(3)**, 390.
31. G. A. Barry, B. I. Brown and L. R. Barker, *J. Food Technol.*, 1983, **18**, 401.
32. P. Chen, M. J. McCarthy, R. Kauten and Y. Sarig, *J. Agr. Eng. Res.*, 1993, **55**, 177.
33. P. Chen, M. J. McCarthy, S.-M. Kim and B. Zion, *Am. Soc. Agric. Eng.*, 1996, **39**, 2205.
34. N. Hernández, P. Barreiro, M. Ruiz-Altisent and M. E. Fernández-Valle, *Concepts in magnetic resonance Part b: Magnetic Resonance Engineering*. 2005, Vol. 26B (in press).
35. N. Hernández-Sánchez, P. Barreiro, M. Ruiz-Altisent, J. Ruiz-Cabello and M. E. Fernández-Valle, *Appl. Magn. Reson.*, 2004, **26**, 431.
36. M. C. A. Brown, D. A. Verganelakis, M. J. D. Mallett, J. Mitchell and P. Blümler, *J. Magn. Reson.*, 2004, **169**, 308.
37. J. Perlo, V. Demas, F. Casanova, C. A. Meriles, J. Reimer, A. Pines and B. Blumich, *Science*, 2005, **308**, 1279.
38. M. D. Hurlimann, *J. Magn. Reson.*, 2001, **148**, 367.
39. M. D. Hurlimann, *J. Magn. Reson.*, 2001, **152**, 109.
40. M. D. Hurlimann and D. D. Griffin, *J. Magn. Reson.*, 2000, **143**, 120.

41. M. D. Hurlimann and L. Venkataramanan, *J. Magn. Reson.*, 2002, **157**, 31.
42. B. Blumich, P. Blumler, G. Eidmann, A. Guthausen, R. Haken, U. Schmitz and G. Zimmer, *Magn. Reson. Imaging*, 1998, **16**, 479.
43. H. T. Pedersen, S. Ablett, D. R. Martin, M. J. D. Mallett and S. B. Engelsen, *J. Magn. Reson.*, 2003, **165**, 49.
44. B. P. Hills, K. M. Wright and D. G. Gillies, *J. Magn. Reson.*, 2005, **175**, 336.
45. R. M. Pearson and C. Job, Instrumentation for the home builder *The Encyclopaedia of Nuclear Magnetic Resonance*, D. M. Grant and R. K. Harris, eds., Vol. 4, Wiley, 1996, 2569–2575.
46. G. Moresi and R. Magin, *Concepts in Magnetic Resonance Part B*, 2003, **19B(1)**, 35.
47. H. Raich and P. Blümler, *Concepts in Magnetic Resonance Part B*, 2004, **23B(1)**, 16.
48. S. Anferova, V. Anferov, D. G. Rata, B. Blümich, J. Arnold, C. Clauser, P. Blümler and H. Raich, *Concepts in Magnetic Resonance Part B*, 2004, **23B(1)**, 26.
49. Y. Maguire, E. Boyden and N. Gershenfeld, *IBM Systems J.*, 2000, **39(3&4)**, 823.
50. I. Noda and Y. Ozaki, *Two-Dimensional Correlation Spectroscopy – Applications in Vibrational and Optical Spectroscopy*, Wiley, 2004.
51. K. Yamazaki, K. Kato, K. Kobayashi, A. Igarashi, T. Sato, A. Haga and N. Kasai, *Neurol. Clini. Neurophysiol.*, 2004, **40**, 1.
52. T. Venancio, M. Engelsberg, R. B. V. Azeredo, N. E. R. Alem and L. A. Colnago, *J. Magn. Reson.*, 2005, **173**, 34.
53. R. B. V. Azeredo, L. A. Colnago, A. A Souza and M. Engelsberg, *Anal. Chim. Acta*, 2003, **478**, 313.
54. Y.-Q. Song and X. Tang, *J. Magn. Reson.*, 2004, **170**, 136.
55. P. Styles, Localization by rotating frame techniques, *The Encylcopedia of Nuclear Magnetic Resonance*, D. M. Grant and R. K. Harris, eds., Vol. 5, Wiley, New York, 1996, p. 2847.
56. B. C. Gerstein, Nutation spectroscopy of quadrupolar nuclei, *The Encylcopedia of Nuclear Magnetic Resonance*, D. M. Grant and R. K. Harris, eds., Vol. 5, Wiley, New York, 1996, p. 3360.
57. S. Antonijevic and S. Wimperis, *Chem. Phys. Lett.*, 2003, **381**, 634.
58. D. Topgaard, R. W. Martin, D. Sakellariou, C. A. Meriles and A. Pines, *PNAS*, 2004, **101**, 17576.
59. C. A. Meriles, D. Sakellariou, H. Heise, A. J. Moule and A. Pines, *Science*, 2001, **293**.
60. H. Heise, D. Sakellariou, C. A. Meriles, A. Moule and A. Pines, *J. Magn. Reson.*, 2002, **156**, 146.
61. C. A Meriles and D. Sakellariou, A Pines, *J. Magn. Reson.*, 2003, **164**, 177.
62. M. Garwood and L. DelaBarre, *J. Magn. Reson.*, 2001, **153**, 155.
63. D. Topgaard, D. Sakellariou and A. Pines, *J. Magn. Reson.*, 2005, **175**, 1.
64. B. P. Hills, in *Magnetic Resonance in Food Science: The multivariate challenge*, S. Engelsen, P. S. Belton, H. J. Jakobsen, eds., Royal Society of Chemistry, Cambridge, 2005, 175.
65. B. P. Hills and K. M. Wright, *J. Magn. Reson.*, (in press).
66. E.-K. Jeong, D.-H. Kim, M.-J. Kim, S.-H. Lee, J.-S. Suh and Y. K. Kwong, *J. Magn. Reson.*, 1997, **127**, 73.
67. C. P. Slichter, *Principles of Magnetic Resonance*, Berlin and Heidelberg GmbH & Co., Springer-Verlag, 1989 (chapter 2).
68. J. Z. Hu and R. A. Wind, *J. Magn. Reson.*, 2003, **163**, 149.
69. R. A. Wind, J. Z. Hu and D. N. Rommereim, *Magn. Reson. Med.*, 2003, **50**, 1113.
70. A. Bax, N. M. Szeverenyi and G. E. Maciel, *J. Magn. Reson.*, 1983, **52**, 147.
71. R. A. Wind, H. C. Bertram and J. Z. Hu, *Magnetic Resonance in Food Science*, S. B.Englesen, P. S. Belton and H. J. Jakobsen, eds., Royal Society of Chemistry, Cambridge, 2005, 156.
72. H. C. Bertram, J. Z. Hu, D. N. Rommereim, R. A. Wind and H. J. Andersen, *J. Agric. Food Chem.*, 2004, **52**, 2681.
73. S. L. Lee, I. A. Ames, D. Jiles, K. A. Gschneider and V. Pecharsky, Permanent magnet structure for generation of magnetic fields, (2004) US Patent no. 6,680,663.
74. M. Kumada, T. Fujisawa, Y. Hirao, M. Endo, M. Aoki, T. Kohda, Y. Iwashita, I Bolshakova and R. Holyaka, Proceedings of the second Asian Particle Accelerator Conference, China, 2001. (epaper.kek.jp/a01/PDF/FRAU04.pdf)
75. B. P. Hills, *Magnetic Resonance Imaging in Food Science*, Wiley, New York, 1998.

76. K. P. Nott, L. D. Hall, J. R. Bows, M. Hale and M. L. Patrick, *Int. J. Food Sci. Technol.*, 1999, **34**, 305.
77. K. P. Nott, S. M. Shaarani and L. D. Hall, The effect of microwave heating on potato texture studied with magnetic resonance imaging, *Magnetic Resonance in Food Science Latest Developments*, P. S. Belton, A. M. Gil, G. A. Webb, D. Rutledge, eds., Royal Society of Chemistry, Cambridge, 2003, 38.
78. S. M. Shaarani, K. P. Nott and L. D. Hall, Magnetic resonance measurements of structural changes during heating of chicken meat by hot air, *Magnetic Resonance in Food Science*, S. B. Englesen, P. S. Belton, H. J. Jakobsen, eds., Royal Society of Chemistry, Cambridge, 2005, 65.
79. C. K. Agemura, R. J. Kauten and K. L. McCarthy, *J. Food Eng.*, 1995, **25**, 55.
80. M. H. G. Amin, L. D. Hall, W. Wang and S. Ablett, Quantitative measurements by MRI of flow velocity and mixing index in a single-screw extruder, *Magnetic Resonance in Food Science*, S. B. Englesen, P. S. Belton, H. J. Jakobsen, eds., Royal Society of Chemistry, Cambridge, 2005, 96.
81. A. S. Peshkovsky, J. Forguez, L. Cerioni and D. J. Pusiol, *J. Magn. Reson.*, 2005, **177**, 69.
82. D. Sakellariou, C. A. Meriles, R. W. Martin and A. Pines, *Magn. Reson. Imaging*, 2005, **23**, 295.
83. C. A. Meriles, D. Sakellariou, A. Moule, M. Goldman, T. F. Budinger and A. Pines, *J. Magn. Reson.*, 2004, **169**, 13.
84. J. G. Seland, M. Bruvold, H. Anthonsen, H. Brurok, W. Nordhoy, P. Jynge and J. Krane, *Magn. Reson. Imaging*, 2005, **23**, 353.
85. J. Z. Hu, D. N. Rommerein and R. A. Wind, *Magn. Reson. Med.*, 2002, **47**, 829.
86. R. A. Wind, J. Z. Hu and D. N. Rommerein, *Magn. Reson. Med.*, 2003, **50**, 1113.
87. W. Chayaprasert and R. Stroshine, *Postharvest Biol. Technol.*, 2005, **36**, 291.
88. P. Chen, M. J. McCarthy, S. M. Kim and B. Zion, *Trans. ASAE*, 1996, **39(6)**, 2205.
89. S. Pathaveerat, P. Chen and M. J. McCarthy, Paper 01-3003, ASAE, St. Joseph, MI, 2001.
90. B. Zion, M. J. McCarthy and P. Chen, *Food Sci. Technol.*, 1994, **27**, 457.
91. N. Hernandez and P. Barreiro (personal communication).
92. J. Perlo, F. Casanova and B. Blumich, *J. Magn. Reson.*, 2005, **176**, 64.
93. F. Casanova and B. Blumich, *J. Magn. Reson.*, 2003, **163**, 38.
94. J. Perlo, F. Casanova and B. Blumich, *J. Magn. Reson.*, 2004, **166**, 328.
95. J. Perlo, F. Casanova and B. Blumich, *J. Magn. Reson.*, 2005, **176**, 64.
96. N. Marigheto and B. P. Hills, *Proceedings of the 7th Fruit, Nut and Vegetable Production Engineering Symposium*, Montpellier, France, September 2005.

Residual Dipolar Couplings: Measurements and Applications to Biomolecular Studies ☆

WEIDONG HU[1] AND LINCONG WANG[2,3]

[1]*Immunology Division, BRI, City of Hope, Duarte Rd. 1500, Duarte, CA 91010, USA*
[2]*Computer Science Department, Dartmouth College, Hanover, NH 03755, USA*
[3]*Chemistry Department, Dartmouth College, Hanover, NH 03755, USA*

☆ Both the authors contributed equally to the work.

ANNUAL REPORTS ON NMR SPECTROSCOPY
VOLUME 58 ISSN 0066 4103
DOI 10.1016/S0066-4103(05)58005-0

Since the first successful demonstration of the tunable alignment of ubiquitin in an anisotropic liquid crystal medium only eight years ago, much progress has been made in both nuclear magnetic resonance (NMR) pulse techniques for the measurements of various residual dipolar couplings (RDCs) in both proteins and nucleic acids, and applications of RDCs to many important problems in biochemistry and structural biology. In this annual report, we first review recent developments in NMR techniques for the measurements of many types of RDCs in both proteins and nucleic acids, especially a series of novel techniques for improving spectral resolution, signal-to-noise ratio and saving experimental time. We then describe the applications of RDCs to proteins including automated resonance assignment, structure determination, ligand–protein and protein–protein dockings as well as protein folding.

1. INTRODUCTION

Biological processes with the involvement of many different biomolecules are extremely complicated. Their characterization requires the use of very sophisticated experimental tools and computational techniques as well as comprehensive modelings. In this post-genomic era, biochemical research at the molecular level is focused on high-throughput determination of structures and screening of ligand–protein and protein–protein interactions. Work at the system level is focused on quantifying genetic regulatory networks and different pathways such as those involved in metabolism, signal transduction, as well as the integration of different pathways and regulatory networks. The quantitative information obtained from such researches is critical for understanding the function of a living cell and an organism as a coherent unit, and is the basis for developing therapeutic methods for many diseases. Solution nuclear magnetic resonance (NMR) spectroscopy, capable of exploring the electronic environments of individual nuclei, measuring a variety of geometric restraints and further monitoring the changes of these restraints with time, has become a very useful experimental tool for studying both individual biomolecules and their interactions. The electronic environments of individual nuclei can be investigated by the measurement of chemical shifts (CSs) and scalar couplings. The geometric restraints measurable by NMR include internuclear distance restraints from nuclear Overhauser effect (NOE), the local angular restraints from scalar couplings and more recently the global orientational restraints from residual dipolar couplings (RDCs). In the last decade, there are four major advances in biomolecular NMR spectroscopy that makes NMR indispensable for current biochemical research: perdeuteration[1,2] and TROSY techniques[3] for large sized-systems, RDCs[4,5] for measuring global orientational restraints and a series of new techniques[6] for reducing experimental time in multidimensional NMR. In this review, we focus on RDCs: the various techniques for the measurements of RDCs as well as the ever increasing applications of RDCs to many important biochemical problems such as structure determination, protein folding, ligand–protein and protein–protein interactions. Owing to the limitations of volume and our knowledge, we will not cover the application of RDCs to nucleic acids and carbohydrates. The interested readers can consult other excellent recent

reviews[7–10] for the application of RDCs to nucleic acids and carbohydrates.[11] The rest of the review is organized as follows. We begin with a description of the physical basis of RDCs where different forms of RDC equations are derived. The various alignment media currently available are then described very briefly, followed by a presentation of the basic NMR techniques for RDC measurement. Next, we review the recent developments in NMR pulse-sequence techniques for measuring RDCs in both proteins and nucleic acids. Finally, we describe the applications of RDCs to study a series of problems in biochemistry and structural biology. Compared with several recent reviews[12–16] on RDCs, the unique features of our review are (a) extensive coverage of pulse-sequence techniques for RDC measurement of both proteins and nucleic acids and (b) the coverage of new RDC applications such as automated CS resonance assignment and protein folding.

1.1. The physical basis of RDC

The physical basis of RDCs is the dipole–dipole (DD) interaction between two nuclear spins. The RDC equation can be derived as follows. From classical electrodynamics (ref. 17, p. 101), the magnetic field B_L produced by a spin $\mathbf{I}_k$ at the location r_{kl}, far away compared with its own dimension, is

$$\mathbf{B}_L = \frac{3(\mathbf{I}_k\mathbf{r}_{kl})\mathbf{r}_{kl} - r_{kl}^2\mathbf{I}_k}{r_{kl}^5} \tag{1}$$

where we have ignored the physical constants. The DD interaction Hamiltonian, $\mathscr{H}_D$, between two spins $\mathbf{I}_k$ and $\mathbf{I}_l$ is

$$\mathscr{H}_D = -\mathbf{B}_L\mathbf{I}_l = r_{kl}^{-3}(\mathbf{I}_k\mathbf{I}_l - 3\frac{1}{r_{kl}^2}(\mathbf{I}_k\mathbf{r}_{kl})(\mathbf{I}_l\mathbf{r}_{kl})) \tag{2}$$

Eq. (2) can be represented in tensor form in order to separate the spin and space terms,

$$\mathscr{H}_{\mathrm{D}} = r_{kl}^{-3}\sum_{q=-2}^{2} F_{kl}^{(q)}A_{kl}^{(q)} \tag{3}$$

where both F_{kl} and A_{kl} are second rank tensors:

$$\begin{aligned}
A_{kl}^{(0)} &= I_{kz}I_{lz} - \tfrac{1}{4}(I_k^+I_l^- + I_k^-I_l^+), & F_{kl}^{(0)} &= 1 - 3\cos^2\theta_{kl},\\
A_{kl}^{(1)} &= -\tfrac{3}{2}(I_{kz}I_l^+ - I_k^+I_{lz}), & F_{kl}^{(1)} &= \sin\theta_{kl}\cos\theta_{kl}e^{-i\phi_{kl}},\\
A_{kl}^{(-1)} &= -\tfrac{3}{2}(I_{kz}I_l^- + I_k^-I_{lz}), & F_{kl}^{(-1)} &= \sin\theta_{kl}\cos\theta_{kl}e^{+i\phi_{kl}},\\
A_{kl}^{(2)} &= -\tfrac{3}{4}I_k^+I_l^+, & F_{kl}^{(2)} &= \sin^2\theta_{kl}e^{-2i\phi_{kl}},\\
A_{kl}^{(-2)} &= -\tfrac{3}{4}I_k^-I_l^-, & F_{kl}^{(-2)} &= \sin^2\theta_{kl}e^{+2i\phi_{kl}},
\end{aligned}$$

where θ_{kl} and ϕ_{kl} are polar angles specifying the orientation of the internuclear vector $\mathbf{r}_{kl}$ in a frame with the external magnetic field $\mathbf{B}_0$ in the $+z$ axis (laboratory

frame). In the high field approximation, only the $q = 0$ term of A_{kl} contributes (all other terms account for $< 2\%$ at 500 MHz) so we have

$$\mathscr{H}_{\mathrm{D}}^{\mathrm{trunc}} = \frac{1}{2r_{kl}^3}(1 - 3\cos^2\theta_{kl})[3\boldsymbol{I}_{kz}\boldsymbol{I}_{lz} - \mathbf{I}_k\mathbf{I}_l] \tag{4}$$

In heteronuclear spin systems (e.g. $I_k =$ proton and $S_l =$ nitrogen) we can further approximate the Hamiltonian as

$$\mathscr{H}_{\mathrm{D}}^{IS} = \frac{3}{2r_{kl}^3}(1 - 3\cos^2\theta_{kl})I_{kz}I_{lz} \tag{5}$$

This approximation is good for both solid- and solution-state NMR. If the tensor F_{kl} is also represented in Cartesian coordinates, its expressions will be identical to those for A_{kl}. From a mathematical viewpoint, we can draw a similarity between spins in spin space and points in real space. The basis for such a similarity (Eq. (3)) can be directly traced to group representation of angular moments and spins. The two tensors form the basis for the representation of rotation groups in their respective spaces (spin space and real three-dimensional (coordinate space). Eq. (5) is also the basis for the fact that the same experiments can be used to measure both scalar couplings and RDCs since the RDC Hamiltonian have the same spin terms as those for scalar couplings.

In order to describe DD interactions in solution NMR experiments, we must resort to statistical mechanics since the signals observed in an NMR experiment are averages over an ensemble of molecules such as proteins. In solution, the solute (target) molecules tumble very fast, so that the average DD interaction becomes zero. However, it is a mistake to assume that DD interactions do not exist in an isotropic solution. In fact, only the first-order term, which is proportional to $1/\mathrm{r}^3$ of an expansion for the evolution of an NMR observable such as an I_z spin operator under the DD interaction Hamiltonian $\mathscr{H}_{\mathrm{D}}$, becomes zero. The second-order term of the same expansion is non-zero and proportional to $1/\mathrm{r}^6$, which can be observed in an NOE experiment.[18,19] When solute molecules such as proteins are weakly aligned with an external magnetic field either by the intrinsic anisotropic magnetic susceptibility of the solute or by putting the solute in a medium such as a dilute liquid crystal (LC) medium, the first-order term is no longer zero. What remains is called RDC. Thus, the equation for RDC Hamiltonian, Eq. (5), becomes [20]

$$\mathscr{H}_{\mathrm{D}}^{IS} = \frac{3}{2r_{kl}^3}\langle 1 - 3\cos^2\theta_{kl}\rangle I_{kz}I_{lz} \tag{6}$$

where the brackets denote the ensemble average. If we choose a molecular frame in which the direction of $\mathbf{B}_0$ is specified by three angles $\theta_{x'}$,$\theta_{y'}$ and $\theta_{z'}$, and the direction of $\mathbf{r}_{kl}$ by three angles $\phi_{x'}$, $\phi_{y'}$ and $\phi_{z'}$, then Eq. (6) becomes

$$\mathscr{H}_{\mathrm{D}}^{IS} = \frac{3}{2r_{kl}^3}\langle\sum_{i,j}\cos\phi_i S_{i,j}\cos\phi_j\rangle I_{kz}I_{lz} \tag{7}$$

where $S_{i,j} = 3\cos\theta_i\cos\theta_j - \delta_{i,j}/2$, $i,j = x'$, y', z' and $\delta_{i,j}$ is the Kronecker delta. The matrix $\mathbf{S}$ is a 3×3 traceless and symmetric matrix called the Saupe order

matrix, or alignment tensor, or order tensor. The matrix **S** specifies the ensemble-averaged anisotropic orientation of a molecule in the laboratory frame. Assuming that the overall rotation of the entire molecule can be decoupled from the internal motions of its individual internuclear vectors, Eq. (7) becomes

$$\mathscr{H}_{\mathrm{D}}^{IS} = \frac{3}{2r_{kl}^3} \sum_{i,j} S_{i,j} \langle \cos\ \phi_i \cos\ \phi_j \rangle I_{kz} I_{lz} \tag{8}$$

The ensemble average over the internal motions, $\langle \cos \phi_i \cos \phi_j \rangle$, can be described in different levels of detail. Similar to the Saupe matrix used to describe the overall anisotropic motion of the entire molecule, the most detailed representation of the anisotropic internal motion for an internuclear vector relevant to RDCs is a 3×3 symmetric matrix with five independent elements. Such a representation gives of the basis for extracting, simultaneously, the structural and dynamic information from RDCs measured in multiple media[21–23].

In the simplest case, the internal motion can be described by a single variable, order parameter S^2, then Eq. (8) becomes

$$\mathscr{H}_{\mathrm{D}}^{IS} = \frac{3}{2r_{kl}^3} S^2 \sum_{i,j} \cos\ \phi_i S_{i,j} \cos\ \phi_j I_{kz} I_{lz} \tag{9}$$

The matrix **S** can be diagonalized, and in that frame S, Eq. (9) becomes

$$\mathscr{H}_{\mathrm{D}}^{IS} = \frac{3S^2}{2r_{kl}^3} (S_{xx}x^2 + S_{yy}y^2 + S_{zz}z^2) I_{kz} I_{lz} \tag{10}$$

where S_{xx}, S_{yy} and S_{zz} are the three diagonal elements of a diagonalized Saupe matrix **S**. $x = \cos \phi_x$, $y = \cos \phi_y$ and $z = \cos \phi_z$ are, respectively, the x, y and z components of an internuclear unit vector $\mathbf{v} = (x,y,z)$ in the principal-order frame (POF) which diagonalizes **S**. Since diagonalizing a 3×3 matrix is equivalent to a rotation in the 3D space, three Euler angles can be used to specify the relative rotation between a POF and any molecular-fixed frame. Finally, since RDCs are usually measured in NMR experiments by following the changes in either scalar couplings or the modulation of peak intensities by scalar couplings, the equation for a RDC r is generally written with only the space terms while the spin term ($I_{kz}I_{lz}$) is ignored. The RDC equation can be written as

$$r = D_{\max} S^2 (S_{xx}x^2 + S_{yy}y^2 + S_{zz}z^2), \quad D_{\max} = \frac{\mu_0 \hbar \gamma_N \gamma_H}{4\pi r_{kl}^3} \tag{11}$$

where we have introduced the physical constants back into the equation. Note that $x^2 + y^2 + z^2 = 1$ and $S_{xx} + S_{yy} + S_{zz} = 0$. Thus, given S, Eq. (11) represents an ellipse on a 2-sphere, and the RDC data constrains onto the ellipse the orientation of the unit vector **v** with respect to a POF *common* to all the RDCs measured on the same

aligned biomolecule. In other words, extracting global orientation restraints on internuclear vectors from scalar RDC data requires the Saupe matrix S to be known *a priori*. Another RDC equation, which is equivalent to Eq. (11) but use polar angles θ and ϕ to specify the direction of $\mathbf{v}$ is

$$r = D_{\max} S^2 D_a \left((3\cos^2 \theta - 1) + R \frac{3 \sin^2 \theta \cos 2\phi}{2} \right) \tag{12}$$

where $D_a = S_{zz}/3$ and $R = (S_{xx} - S_{yy})/S_{zz}$ are called, respectively, axial and rhombicity alignment parameters. Another variable called D_r defined as $D_r = RD_a$, also appears frequently in the literature. In most applications, the order parameter S^2 in Eqs. (9)–(12) is assumed to be 1.

1.2. Alignment media

Since the first successful demonstration of the alignment of ubiquitin in lipid bicelles,[4] many types of alignment media have been developed for the following reasons:

1. Some alignment media may not be suitable for the target solute (biomolecule) due to unwanted interactions, such as electrostatic interactions between the solute and alignment media, which can increase the total correlation time for the target molecules;
2. Some alignment media may be incompatible with certain sample conditions such as pH, ionic strength and temperature etc.;
3. More than one alignment media is needed to compute more precise structures[24,25] and quantify dynamics.[21,22]

The following is a list of recently discovered alignment media: cetylpyridinium-based media,[26,27] filamentous phage,[28,29] purple membrane fragments,[30] cellulose crystallites,[31] compressed polyacrylamide gel,[32] alkyl poly(ethylene glycol) based media,[33] strained acrylamide/acrylate copolymers[34] and embedded filamentous Pf1 phage in polyacrylamide matrix.[35] Nice summaries of the properties of alignment media and how to prepare oriented samples with different alignment media can be found in several recent reviews.[11,36,37]

2. THE BASIC TECHNIQUES FOR MEASURING RESIDUAL DIPOLAR COUPLINGS

The experiments for measuring RDCs are based on two basic techniques: *frequency-displacement* techniques, where RDCs are measured directly by following changes in J couplings (for example, the difference in $^1J_{\mathrm{NH}}$ coupling as measured on a partially oriented sample and the same $^1J_{\mathrm{NH}}$ coupling as measured on an isotropic

sample), and *quantitative J-modulation* techniques, where the couplings are obtained from variations in peak intensities induced by both the J couplings and RDCs. The frequency-displacement techniques can be further classified into three distinct categories:

1. Direct measurement of the resolved J couplings from heteronuclear edited spectra for small or medium-sized proteins;
2. Spin-state-separation techniques such as the IPAP experiment,[38] S^3E[39,40] and S^3CT scheme[41] to resolve crowded spectra;
3. E.COSY-type[42] experiments to resolve small couplings between a pair of spins through a larger coupling between another pair of spins.

In addition, the TROSY scheme[3] has been widely used in RDC measurement for large-sized biomolecules. In the following, we will first discuss the principles and *pros* and *cons* of these commonly used techniques.

2.1. *J*-resolved experiment

The *J*-resolved experiment is the most straightforward approach to coupling measurement. It is particularly useful for measuring large one-bond heteronuclear couplings such as $^{13}C_\alpha$–$^1H_\alpha$ and ^1H–^{15}N couplings in proteins. In two-dimensional (2D) heteronuclear correlation experiments, the couplings can evolve in either t_1 or t_2 dimension, and the cross peaks are split into doublets for isolated spin pairs such as $^{13}C_\alpha$–$^1H_\alpha$ or ^1H–^{15}N. The couplings can be extracted from the split separation. Since it is a frequency-based approach, measurement accuracy is less likely to be affected by factors that affect the peak intensity. The peak separation should be large compared to the linewidth in order to avoid potential measurement errors. The approach works well for small-sized biomolecules. For medium- and large-sized proteins, the coupled spectrum becomes crowded, and consequently makes it very difficult to measure a complete or near-complete set of couplings. To overcome this problem, spin-state-selection (see Section 2.2) can be used to separate doublets into two sub-spectra. Alternatively, the 2D experiment can be extended to 3D to enhance the resolution, such as the measurement of C_α–H_α coupling with 3D $^1J_{C_\alpha H_\alpha}$-resolved (HA)CACONH[43]and 3D HA(CA)CONH[44] experiments.

2.2. Spin-state-selection technique

Spin-state-selection is a technique developed to reduce the overlap of coupled spectra obtained from *J*-resolved experiments. It separates the two components of a doublet in a *J*-resolved experiment into two different spectra, where one spectrum corresponds to the α spin state of the coupled spin and the other spectrum the β state. The spectral resolution is thus enhanced significantly. More importantly, small couplings not accessible directly via the *J*-resolved method become measurable because the individual peaks of doublets are now separated into two different

spectra. There are several approaches to achieving this goal.[38–41,45] In the following, we focus on IPAP, S^3E and S^3CT schemes because they are most frequently used in current experiments.

IPAP-HSQC experiment: The experiment is carried out by acquiring two data sets in an interleaved manner.[38] The first experiment is a regular heteronuclear single quantum correlation (HSQC) with ^1H coupled to ^{15}N during t_1 evolution. The ^{15}N chemical shifts are modulated by cos ($J_{HN}t_1$), and the doublets have the same sign. The spectrum is called in-phase (IP). In the second experiment, an extra insensitive nuclear enhancement by polarization transfer (INEPT) step (the block within the rectangular box in Fig. 1a) is used to transfer the ^{15}N anti-phase term to an in-phase term prior to the ^{15}N evolution. After the ^{15}N evolution period, only the term modulated by sin ($J_{HN}t_1$) is detected, and the doublets have the opposite sign. The spectrum is called anti-phase (AP). The 90°purge pulse on ^1H prior to the t_1 period is used to transfer the remaining residual cos ($\pi J_{HN}\,\Delta$)H_zN_x to unobservable multiple quantum terms. A more detailed description in product operator formalism, such as how to obtain the IP and AP spectra, can be found in the original paper.[38] The addition and subtraction of the IP and AP spectra give two simplified spectra just like regular HSQCs with the ^{15}N chemical shifts displaced by either $+J_{NH}/2$ or $-J_{NH}/2$ as schematically shown in Fig. 2. The couplings can be readily measured from the frequency difference of the corresponding peaks in the two spectra.

S^3E element: Fig. 1b shows the basic pulse scheme for spin-state-selective excitation (S^3E).[39,40] The S^3E can be easily understood using product operator formalism. Just

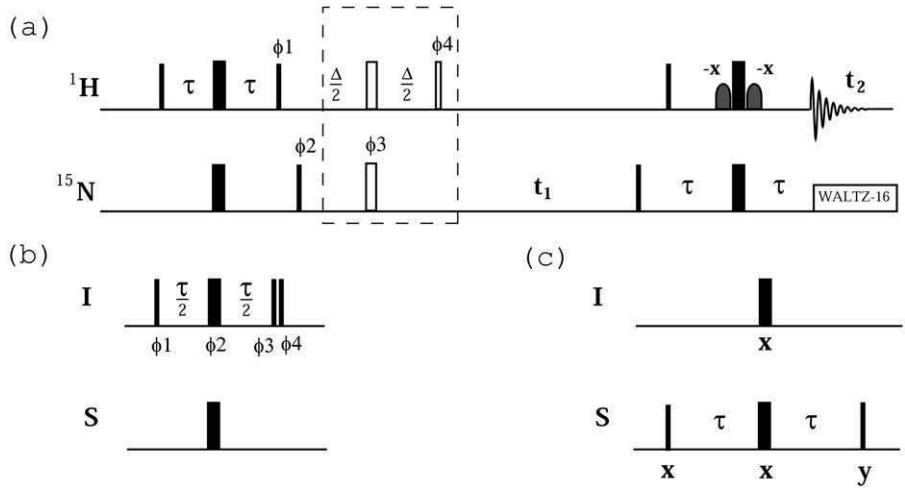

Fig. 1. Basic spin-state-selection elements used in experiments for coupling measurements: (a) IPAP-HSQC, (b) S^3E and (c) S^3CT. The phases of all the pulses are on x unless indicated otherwise. The narrow and wide bars stand for 90° and 180° pulses, respectively. τ is set to $1/4J_{NH}$ in (a), $1/4J_{IS}$ in (b) and (c). Δ is set to $1/2J_{NH}$ in (a). More technical details can be found in the original papers 38 for (a), 39, 40 for (b), and 41 for (c).

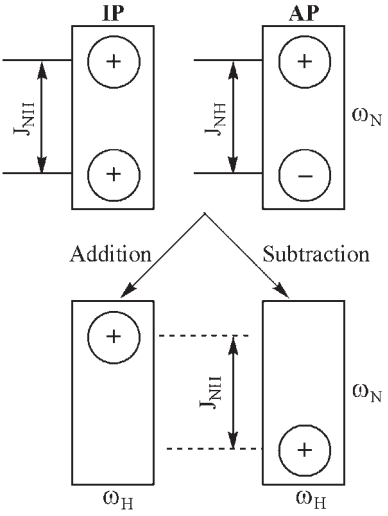

Fig. 2. Schematic illustration of a procedure for extracting ^{1}H–^{15}N couplings from an IPAP-HSQC experiment.

before the second 90° pulse on spin I, two terms evolve from magnetization I due to J_{IS} evolution: $I_y \cos(\pi J_{IS}\tau) + 2I_x S_z \sin(\pi J_{IS}\tau)$. The terms have equal intensities if τ is set to $1/4J_{IS}$. The selective observation of either one of the two terms can be achieved by phase cycling of ϕ_3 and ϕ_4 of the last two 90° pulses on spin I. The two data sets are stored separately, and then the addition and subtraction separate the upfield and downfield components of doublets I–$\{S\}$ into two sub-spectra. An S^3E element is usually applied in the preparation period of the pulse sequence.

S^3CT element: Spin-state-selective coherence transfer (S^3CT)[41] combines coherence transfer with spin-state-selection. The basic function of this unit is to transfer double-quantum (DQ) or zero-quantum (ZQ) terms of a coupled I–S spin pair to a desired single-quantum (SQ) term. The collective effect of the pulses shown in Fig. 1c is equivalent to a $\pi I^{\alpha} S_y$. Thus the α and β states of the S nucleus exchange only if they are coupled to I^{α}, but not I^{β}. These can be expressed using product operator formalism as follows:

$$
\begin{aligned}
I^- S^- &\xrightarrow{\pi I^{\alpha} S_y} I^- S^{\beta}, \\
I^- S^+ &\xrightarrow{\pi I^{\alpha} S_y} -I^- S^{\alpha}, \\
I^+ S^- &\xrightarrow{\pi I^{\alpha} S_y} -I^+ S^{\alpha}, \\
I^+ S^+ &\xrightarrow{\pi I^{\alpha} S_y} I^+ S^{\beta}.
\end{aligned}
$$

Through phase cycling, the coherence transfer from DQ to $I^- S^{\beta}$ and $I^+ S^{\beta}$ can be separated from the coherence transfer from ZQ to $I^- S^{\alpha}$ and $I^+ S^{\alpha}$, and the coherence of I spin coupled to either α or β state of S spin can be selected.

The efficiency of spin-state-selection can be affected by (a) differential relaxation rates of the consisting components due to the cross-correlation of chemical shift anisotropy (CSA) and DD, (b) pulse imperfections in the spin-state-filter elements and (c) J mismatch. A J mismatch happens when the value of a measured RDC + J is different from the value used in the spin-state-selection element. J mismatch results in phase distortion for the observed peaks, although this can be removed by purge pulses.[38] In addition, J mismatch causes the intensities of the in- and anti-phase terms to become unequal, and thus makes unwanted components appear in the spectrum of selected components, the so-called J crosstalk. Among the three spin-state-selection elements, IPAP and S^3CT have better tolerance than S^3E for J mismatch. To remove or suppress the J-crosstalk, a scaling factor has been used when the IP and AP data sets are combined linearly.[38,46] A more recently proposed scheme claims to better suppress the J mismatch.[47]

2.3. E.COSY method

Exclusive correlation spectroscopy (E.COSY) was originally developed to enhance the resolution of experiments measuring ^1H–^1H couplings.[42] It requires an A–M–X three coupled spin system to work, making use of the larger J_{MX} coupling to resolve the smaller J_{AX} coupling in an [A, M] correlated experiment. The spin X is called a passive spin, whose α and β states are not mixed between the detection of A and M spins. E.COSY's application to heteronuclear coupling measurement was first demonstrated in a 2D HNCA-J experiment,[48] which made use of large ^1H–$^{13}C_\alpha$ couplings to resolve the small $^3J_{HN-H_\alpha}$ couplings. For ease of exposition, a 2D [^{15}N, ^1H]-HSQC is used as an example. If the experiment is carried out without perturbing the spin-state of C′ on a small peptide, then the regular cross peaks become doublets due to the coupling to C′ in both ^{15}N and ^1H dimensions. One component of the doublet is coupled to $C'(\alpha)$ and can be described as $[\cos(\omega_N + \pi\ ^1J_{NC'})t_1]\exp[i(\omega_{HN} + \pi\ ^2J_{HN-C'})t_2]$ while the other component is coupled to $C'(\beta)$ and can be represented as $[\cos(\omega_N - \pi^1J_{NC'})t_1]\exp[i(\omega_{HN} - \pi\ ^2J_{HN-C'})t_2]$. An E.COSY pattern with two cross peaks is shown schematically in Fig. 3. Although the small coupling of $^2J_{HN-C'}$ is not resolved along the ^1H dimension, it can now be measured from the two cross peaks because they are well resolved along the ^{15}N dimension. One advantage of the E.COSY method is that the slope of two cross peaks reflects the relative sign of two measured couplings as shown in the two trigonometry terms given above. Basically, if the two couplings have the same sign, then the direction of the line connecting two cross peaks goes from the lower left to the upper right; otherwise, the direction of the line goes from the lower right to the upper left. Please note that the sign of slope can be reversed if there is a 180° pulse issued on the passive spin between two coupling evolution periods.

To form an E.COSY pattern, the α and β states of passive nucleus should not be mixed. T_1 relaxation of passive spin between the two coupling evolution periods and during the data acquisition may mix the two spin states, reducing the separation of E.COSY doublets. Thus, E.COSY methods may underestimate coupling

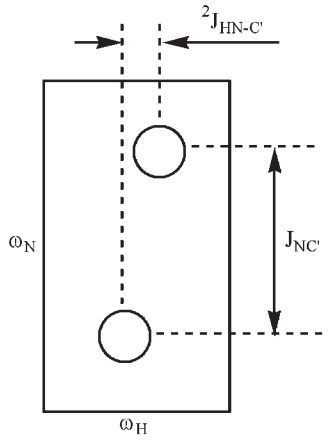

Fig. 3. E.COSY pattern. Schematic illustration of doublet obtained from an [^{15}N, ^{1}H]-HSQC experiment without C′ decoupling for both ^{15}N and ^{1}H dimensions. Doublet are well resolved along the ^{15}N dimension due to $J_{NC'}$ coupling, thus the small coupling $^2J_{HN-C'}$ can be measured from doublet along the ^{1}H dimension.

values. This is not a big problem if the passive spin is a ^{13}C or ^{15}N because their T_1 values are usually long compared to experimental time scales. However, caution should be taken if the passive spin is a proton.

2.4. Quantitative *J*-correlation experiment

The experiment is based on the observation that NMR signal intensities can be modulated by coupling evolution. There are several different ways to implement this idea.[49] The first approach is to acquire two data sets where the signal is modulated with a cosine function in one experiment, but not modulated in the other so-called reference experiment. The coupling can then be derived from the intensity ratio of the two experiments. A second approach is to run a series of experiments where the signal is modulated by an array of time delays with active coupling interactions. The coupling constants can then be extracted from a curve fitting of the observed peak intensities versus the coupling evolution time.[50] This approach usually offers higher precision than the first one. A third approach is to determine the couplings from a single spectrum where the intensity ratio of cross and diagonal peaks is a well defined function of the magnitude of targeted couplings.[51,52]

2.5. TROSY experiment

Transverse relaxation optimized spectroscopy (TROSY) is a powerful experiment for studying large-sized biomolecules.[3] It makes use of cross-correlation interference between CSA and DD interactions and selects only the narrowest component

out of four coupled multiplets. For an isolated coupled spin-1/2 system, I–S, in a protein, the T_2 relaxation rates of both spins are dominated by the DD interaction between I and S as well as the CSA of each spin. To explain how TROSY works, we can take a look at the T_2 relaxation of I spin. The CSA of I spin contributes equally to T_2 relaxation of I^-S^α and I^-S^β transitions (SQ transitions), while the DD contributions to T_2 relaxation of I^-S^α and I^-S^β transitions have opposite sign. Thus, the contributions of CSA and DD add up for I^-S^α transition, and counteract for the I^-S^β transition. The same phenomenon also holds true for the relaxation rates of S spin SQ transitions. When two interactions are collinear and their magnitudes are comparable, the T_2 relaxation rates of I^-S^β and S^-I^β can be significantly reduced. In particular, since CSA is proportional to the field strength, the CSA and DD interactions are almost canceled for an amide spin pair, ^{1}H–^{15}N, when the magnetic field strength corresponding to a ^{1}H frequency is at 1.1 GHz.[3] Experimentally, the [^{1}H, ^{15}N]-TROSY sequence chooses only the transition $N^{\pm}H^{\beta} \rightarrow H^{\mp}N^{\beta}$ through a combination of proper phase cycling and echo/anti-echo quadrature detection.[53] A schematic illustration of the TROSY effect of a coupled ^{15}N–^{1}H spin pair is shown in Fig. 4.

The TROSY method makes it much easier to use NMR spectroscopy to study large-sized proteins (up to 100 kDa)[54] by providing optimal sensitivity and resolution. Specifically, the TROSY scheme can be easily implemented in all kinds of pulse sequences for coupling measurement (see Section 3).

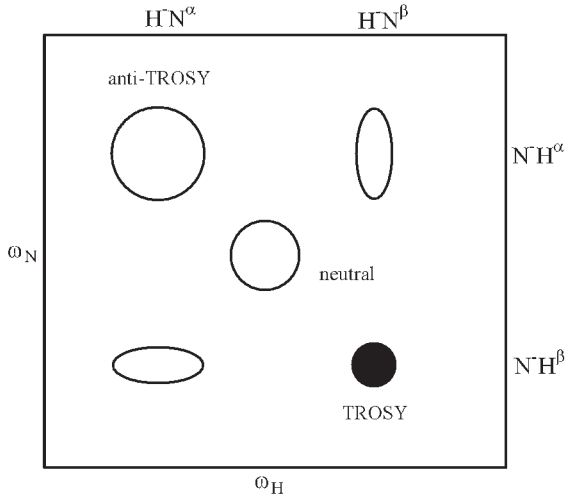

Fig. 4. Schematic multiplets of a coupled ^{15}N–^{1}H spin pair with TROSY effect. The diameters of circles, and the major and minor axes of ellipses reflect the linewidth of each component. The components coupled with partner's β states have narrower linewidth. TROSY experiment only observes the narrowest component (black circle). The broadest one is called anti-TROSY peak.[55] The middle neutral component represents a peak from a regular decoupled HSQC.

However, before going into a detailed discussion of the applications of these basic methods to RDC measurement, we will first consider the measurement precision and sensitivity.

2.6. General considerations for measurement precision and sensitivity

Before the RDCs of partially ordered protein samples prepared using a variety of alignment media (Section 1.2) can be measured successfully, they can only be obtained from the magnetic field-dependent alignment.[36,56,57] Such RDCs are rather small, ranging from a few Hertz for a system with large magnetic susceptibility anisotropy,[57] to as small as a few tenths of a Hertz for diamagnetic protein samples.[50] In order to measure such small RDCs accurately, several different versions of [^{15}N, ^{1}H]-HSQC experiments have been designed based on either frequency displacement or *J*-quantitative modulation approaches.[50,51,58] The precisions of these experiments range from 0.5 to 0.02 Hz.

In practice, the relatively large uncertainty in RDC values (measurement error versus measurement value) obtained from field aligned samples severely limit the application of RDCs to structural and dynamic studies of biomolecules in solution. The relative error was reduced by more than an order of a magnitude by Bax and Tjandra,[4,59] who adopted the LC medium, used in LC NMR to align small organic molecules,[20] to align proteins to an extent that balances the line broadening with the increase in RDC values. The LC medium (bicelles) can be easily made from a mixture of dihexanoyl phosphatidylcholine (DHPC) and dimyristoyl phosphatidylcholine (DMPC) in water, and the concentration of bicelles can range from 3 to 10% w/v. The method provides a tunable ordering of the solutes (proteins), and the dipolar contribution to the ^{1}H–^{15}N splitting is proportional to the bicelle concentration. The RDC magnitude obtained on ubiquitin in such bicelle media is about two orders larger than that obtained in field-dependent alignment.[50]

As is well known in LC NMR for small molecules, increasing the ordering enlarges not only the RDCs for the specific pairs of interest, but all the RDCs, including those between two protons. The latter will significantly broaden the linewidths of NMR signals and lead to a reduction in both the resolution and sensitivity of the signals. As the size of the molecules being studied increases, the resolution and sensitivity deteriorate quickly, and this is a major force for the invention of many new pulse schemes for measuring RDCs.

Generally, quantitative *J*-modulation experiments can deliver higher measurement precision than frequency-displacement ones. However, in the *J*-modulation method systematic errors[60] may occur, caused by differential relaxation properties of the two components (due to DD–CSA cross correlation, DD–DD cross correlation), coupling to a third spin, or pulse imperfection etc. Details of the errors' effect on the accuracy of coupling measurement and how to overcome them can be found in original works.[51,60,61] In addition, a good S/N ratio is critical for obtaining accurate couplings because the *J*-modulation method is based on intensity analysis. In frequency-displacement experiments, measurement accuracy is proportional to

both the S/N ratio and spectral resolution, and is inversely related to peak linewidth.[61] For large macromolecules, differential relaxation can significantly broaden one of the two components, thus making accurate determination of peak position difficult. In addition, peak overlaps and imperfect pulse phase can also introduce errors in the measurement of peak positions.

As discussed above, a good S/N ratio is critical to coupling measurement accuracy in both approaches. The S/N ratio of oriented samples is usually lower than that of corresponding isotropic samples due to the lower concentration of oriented samples compared to isotropic samples,[36] the broader linewidth caused by RDCs and a possible reduction in the tumbling rate of aligned biomolecules. The following techniques are generally used for increasing the S/N ratio:

1. Sensitivity enhancement using multiple-quantum (MQ) coherence transfer for an isolated heteronuclear spin pair,[62] TROSY technique[3] for large-sized proteins with or without perdeuteration, and RANCE-KAY scheme.[63,64]
2. Removal of the unwanted proton homo-coupling interactions (J and RDC) either using shaped pulse in the indirect dimension [65,66] or using band-selective adiabatic decoupling during the acquisition.[67]
3. Removal of the unresolved couplings between ^{15}N and remote protons in TROSY-type experiments *via* use of the G-BIRD (gradient bilinear rotation decoupling) module in the t_1 dimension. The ^{15}N linewidth of ubiquitin can be reduced by as much as 25% using this technique.[68]
4. More recently, a numerically optimized coherence transfer scheme has been developed, which allows for selective observation of individual ^{1}H-transitions in ^{13}C-labeled methyl groups with optimal sensitivity. The applications of this technique to the measurement of ^{1}H–^{1}H and ^{1}H–^{13}C couplings in magnetically equivalent CH_3 groups have been demonstrated.[69,70]

3. MEASUREMENT OF RESIDUAL DIPOLAR COUPLINGS IN PROTEINS

RDC measurement is a prerequisite for the application of RDCs to studying the structure, dynamics and biochemical properties of biomolecules. The RDC measurement experiments published prior to 2001 have been recently reviewed.[36] In this review, we will concentrate on newly developed pulse sequences whose applications have been demonstrated on both isotropic and anisotropic protein samples. We have tried our best to cover the literature as comprehensively as possible. However, since RDC measurement is still an active research area in biomolecular NMR and new results are being published daily, we may still have missed some important recent results. In the following sections, we will first describe experiments for measuring individual types of RDC, then present experiments for simultaneous measurement of several types of RDCs. To facilitate the discussion, shown in Fig. 5 are the magnitudes of some measurable RDCs on proteins.

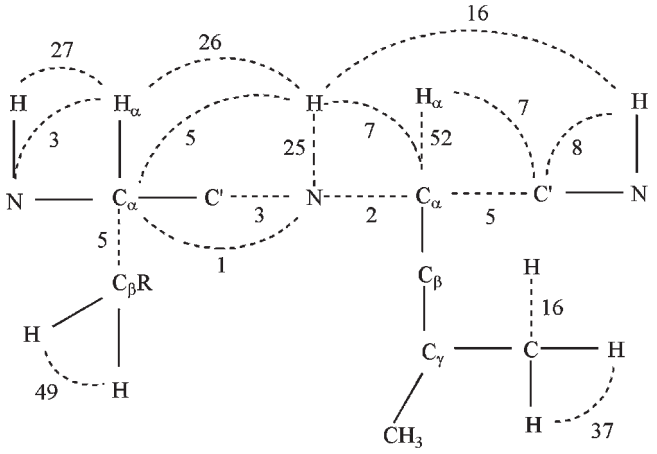

Fig. 5. The calculated maximal RDCs (relative to 25 Hz of a ^{1}H–^{15}N spin pair) on proteins. All these RDCs can be experimentally measured (see this review). Some of these numbers are taken directly from Permi and Annila's work [71] or calculated based on relative scales given in Table 1 in ref. 36. Bond lengths and angles used to calculate RDCs are taken from ref. 72. The bond lengths of H–N and C–H are 1.04 and 1.09 Å, respectively. For spin pairs separated by three or more bonds, only the shortest possible distance is used. The shortest distance for the intra $^{1}H_{\alpha}$–H_N is 2.17 Å, taken from ubiquitin X-ray structure .[73] The distances between $H_N(i)$ and $H_{\alpha}(i\text{-}1)/H_N(i\text{-}1)$ are 2.2/2.6 Å, respectively .[74] The value of ^{1}H–^{1}H RDC (D_{HH}) in a methyl group was calculated using $D_{HH} = 2.3\ D_{CH}$,[75] where the D_{CH} is the RDC of C–H vector in a methyl group.

3.1. ^{1}H–^{15}N dipolar coupling

Both NH (^{1}H–^{15}N) and CH ($^{13}C_{\alpha}$–$^{1}H_{\alpha}$) RDCs can be measured more accurately than other backbone one-bond RDCs because their dipolar couplings are large (Fig. 5) due to the large ^{1}H gyromagnetic ratio and short bond lengths (Eq. (11)). These RDCs have been used most frequently in various biochemical applications. Compared to CH RDCs, NH RDCs can be measured more easily since the interference from other nuclei can be readily removed, and [^{1}H, ^{15}N] correlated spectra are generally well resolved. Previously, NH RDCs were usually measured using [^{1}H, ^{15}N]-HSQC experiments with either *J*-resolved or *J*-quantitative modulation approaches.[50,51,58] To reduce the overlap of coupled spectra, an IPAP-HSQC experiment[38] was introduced. More recent developments have focused on enhancing resolution and improving the sensitivity, especially for large molecules.

The DSSE–HSQC (doublet separation and sensitivity enhancement) experiment[76] combines features of both IPAP[38] techniques and sensitivity enhancement schemes.[64] The sequence is similar to the TROSY experiment, with ^{15}N decoupled during data acquisition. In each t_1-increment, four FIDs are recorded in order to perform simultaneous quadrature detection and spin-state editing. The precision on ubiquitin is 0.05 Hz. The precision on hepatitis C protease complex is estimated to

be 0.13 Hz; this protein has an isotropic rotational correlation time of 10.1 ns at 37°C.

A suite of 2D [^{1}H, ^{15}N] correlation experiments have been proposed for different size proteins by choosing different components of multiplets caused by a ^{1}H–^{15}N coupling.[55] Fig. 6 illustrates schematically how to use spin-state-selective coherence transfer (S^3CT) and a modified TROSY sequence to determine $^1J_{NH}$ by selectively observing only one out of four possible components. In Fig. 6a, the overlay of two sub-spectra through a linear combination of two data sets from a modified TROSY sequence is shown. The two peaks used to extract the couplings are called anti-TROSY/TROSY and TROSY/anti-TROSY (see Fig. 4), respectively. This approach is applicable to medium-sized molecules. Shown in Fig. 6b is the overlay of two sub-spectra from the S^3CT sequence, where ^{15}N is decoupled from ^{1}H. The doublet of an ^{1}H spin is separated into two different spectra depending on whether it is coupled to the α or β spin state of the ^{15}N nucleus. This approach is applicable to small-sized molecules because one component is neutral/anti-TROSY peak. For large-sized molecules, a combination of regular TROSY and ^{15}N-decoupled TROSY experiments can be used. The overlay of the spectra from these two experiments is shown in Fig. 6c. The methods have been demonstrated on ^{15}N-labeled protein chymotrypsin inhibitor 2 in a lipid bicelle mixture.

TROSY-based HNCO experiments can be used to measure five different dipolar couplings on deuterated large-sized proteins.[77] Here we will only discuss the strategy used to measure $^1J_{NH}$ and $^1D_{NH}$; applications to the measurement of other RDCs will be discussed later. $^1J_{NH}$ couplings are measured in two separate experiments with three resonances at $(\omega_{C'} - \pi^2 J_{HC'}, \omega_N - (k+1)\pi^1 J_{NH}, \omega_{HN} + \pi^1 J_{NH})$, where k is a J-enhancement factor with values of 0 and 2. The CSs for a given particular cross peak in two experiments are separated by $^1J_{NH}$ along the ^{15}N dimension. Since both experiments only observe the narrowest component (the TROSY peak), TROSY–HNCO is a highly sensitive and resolution-optimized experiment for large-sized proteins with or without perdeuteration. It has been tested on an ^{15}N, ^{13}C, ^{2}H-labeled human carbonic anhydrase II (259 residues), and on a complex of Val, Leu, Ile

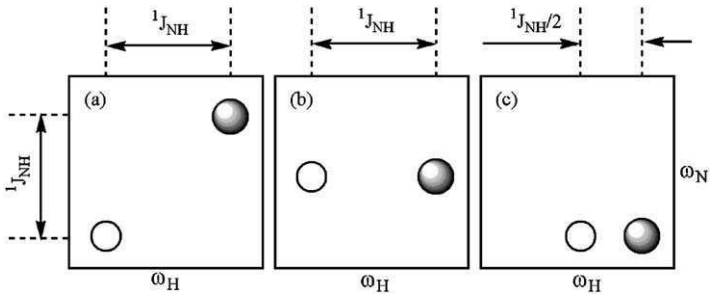

Fig. 6. Overlays of two different 2D [^{15}N, ^{1}H]-correlated spectra (gray and blank circles). These different experiments are designed to measure couplings on different sized-protein samples. The overlays in (a) and (c) are from modified TROSY sequences; (b) is from S^3CT sequences.

(δ_1 only) methyl protonated $^{15}N/^{13}C/^{2}H$-labeled maltose-binding protein (MBP, 370 residues) and β-cyclodextrin. The average value for $^{1}J_{NH}$ measured in the unori-ented 1 mM MBP sample is -93.7 ± 1.1 Hz.

(δ, J)-E.COSY HSQC[78] is an experiment where the doublet in an E.COSY pattern is separated by $2\omega_N$ along the ^{15}N dimension. The experiment differs from the regular water gate-HSQC in two aspects. Firstly, there is an extra 90° pulse on ^{15}N before the acquisition recovers both orthogonal transverse magnetization components in a way that is similar to the sensitivity enhancement scheme,[63] but there is no extra INEPT unit. Secondly, it leaves ^{15}N coupling on during the acquisition period. The spectral width in the ^{15}N-dimension is set to twice the ^{15}N chemical shift range. The final spectrum is composed of two distinct regular HSQC spectra with cross peak resonances at (ω_N, $\omega_H + \pi J_{NH}$) and ($-\omega_N$, $\omega_H - \pi\ J_{NH}$), respectively. Thus, the E.COSY pattern is composed of frequency displacement of $2\omega_N$ along the ^{15}N dimension and $^{1}J_{NH}$ along the ^{1}H dimension. The accuracy of the coupling measurement is controlled by the digital resolution along the ^{1}H dimension. The pulse scheme has been demonstrated on a 1.0 mM ^{15}N, ^{13}C-labeled protein GB1 with 56 residues. One attractive feature of this approach is that there is no interference of unwanted components due to the J mismatch as seen in the spin-state-selective approaches such as the IPAP-HSQC or S^3E. Another advantage is convenience: it is easier to extract couplings from a single spectrum than from two sub-spectra.

Sensitivity-enhanced IPAP, TROSY-anti-TROSY and E.COSY HSQC experiments provide choices for measuring $^{1}D_{NH}$* on proteins of different sizes.[79] The principles for sensitivity improvement and the appearances of spectra acquired from the three experiments are similar to that of the (δ, J)-E.COSY HSQC experiment discussed above. The key difference is that the couplings are encoded in the ^{15}N dimension, rather than the ^{1}H dimension. All three experiments have been tested on GB1 protein (56 residues); Ding and Grouenbom[79] suggested that sensitivity-enhanced IPAP-HSQC can be used for large-sized protein samples. Interestingly, the authors found that the RDCs measured from the ^{1}H dimension are always smaller than those from the ^{15}N dimension. Further analysis revealed that systematic deviations arise from the influence of un-resolved three-bond $^{1}H_N$–$^{1}H_\alpha$ couplings and cross-correlated relaxation between ^{1}H–^{15}N and $^{1}H_N$–$^{1}H_\alpha$ dipolar couplings.

Quantitative J-modulated HSQC[80] is an experiment similar to works previously published by Tjandra and coworkers[50] and Tolman and coworkers.[51] In Tjandra's approach, the peak intensity is not only modulated by couplings but also the T_2 relaxation rate of ^{15}N nuclei, while in Tolman and Prestegard's approach, the J coupling is extracted from the intensity ratios of both in-phase and anti-phase peaks

*As shown in Section 1.1, any experiment for measuring scalar couplings can also be used to measure the corresponding RDCs. Hence, we use the following convention for notations: if the scalar coupling is to denoted by J, then the corresponding RDC will be denoted by D. For example, $^{1}J_{NH}$ is used to represent the one-bond scalar coupling between an amide nitrogen and the attached amide proton, the corresponding NH RDC is represented by $^{1}D_{NH}$.

from the same constant time period. The quantitative *J*-modulated HSQC proposed by McFeetsers and coworkers uses constant time HSQC so that the peak intensity is not a function of the transverse relaxation of ^{15}N nuclei. The *J* modulation is realized by moving the refocused 180° ^{15}N pulse within the constant time period ($2T_N = 33.4$ ms) according to a series of positions (Δ). The coupling values are determined by fitting peak intensities to a function of $I_0 \cos(2\pi J_{HN}(T_N - \Delta))$. The sequence has been tested on three proteins: ubiquitin in both isotropic and oriented condition, interleukin-4 (IL-4, 16 kDa) and NusB (18 kDa) in isotropic condition. The precision on ubiquitin is 0.07 Hz without data mirroring and 0.04 Hz with data mirroring. The precision obtained under the same experimental condition using IPAP-HSQC is 0.06 Hz.

It is worth mentioning that an experiment has been developed to measure couplings from individual vectors of $^1H^{N1}$–^{15}N and $^1H^{N2}$–^{15}N in Asn and Gln side chains. It is an NH_2-edited and spin-state-selected HSQC experiment. The couplings of individual vectors can be extracted from the frequency displacement along the ^1H dimension in two-subspectra.[81]

3.2. $^{13}C_\alpha$–$^1H_\alpha$ dipolar coupling

The CH RDC of a $^{13}C_\alpha$–$^1H_\alpha$ bond is about two times larger than the NH RDC of a ^1H–^{15}N bond (Fig. 5), and can be as large as 50 Hz under the conditions routinely used for anisotropic samples.[36] Even with low precision, CH RDCs are very useful in structure determination and refinement since the orientational information extracted from CH RDCs is non-redundant to that provided by NH RDCs.[82] Previously, CH RDCs were measured from constant-time [^1H, ^{13}C] correlated HSQC experiments by a peak intensity modulation method.[83] The method is applicable to small-sized proteins, but not practical for medium- or large-sized proteins due to poor dispersion in $^1H_\alpha/^{13}C_\alpha$ regions. Two approaches have been developed to alleviate the overlap problem. The first is to make use of the good dispersion of [^1H, ^{15}N] correlation by encoding $^1J_{C_\alpha H_\alpha}$ couplings into [^1H, ^{15}N] correlation. The second is to use an extra dimension to enhance the resolution.

The regular 3D (HA)CA(CO)NH experiment has been modified to measure $^1J_{C\alpha H\alpha}$ and $^1D_{C\alpha H\alpha}$ by encoding CH RDCs into a ^{13}C-dimension.[36,43] The coherence is transferred as follows:

$$^1H_\alpha(i-1) \rightarrow {}^{13}C_\alpha(i-1)(CT, t_1) \rightarrow {}^{13}C'(i-1) \rightarrow {}^{15}N(i)(t_2) \rightarrow {}^1H_N(i)(t_3).$$

A constant time, $CT = 1/J_{C_\alpha C_\beta} \approx 28$ ms, is used in the ^{13}C evolution dimension to suppress the coupling interaction between C_α and C_β. The doublets of $^{13}C_\alpha$–$\{^1H_\alpha\}$ are in anti-phase mode because the $\sin \pi {}^1J_{C\alpha H\alpha}$ term is detected. Unfortunately, the long delay ($1/J_{C\alpha C\beta}$) reduces the sensitivity significantly for medium or large-sized proteins due to fast T_2 relaxation of C_α. Another concern is that the cross correlation of C_α–CSA and $^{13}C_\alpha$–$^1H_\alpha$ DD interaction is not canceled during the t_1 period, leading to different intensities for the two components of a doublet, even though the TROSY effect of a $^{13}C_\alpha$–$^1H_\alpha$ spin pair is rather small.[3]

A 3D HNCO(CA) experiment has been proposed[84] to measure CH RDCs by modifying the out-and-back HN(CO)CA.[85] Firstly, a spin-state-filter ($\alpha/\beta-{}^1J_{C\alpha H\alpha}$), in a fashion of IPAP,[38] is inserted right after the magnetization has been transferred from C′ to C_α. Post-acquisition addition and subtraction of the IP and AP spectra separates $^{13}C_\alpha$–$\{^1H_\alpha\}$ doublets into two sub-spectra. Secondly, the $^{13}C_\alpha$–$\{^1H_\alpha\}$ doublet are concatenated with C′ chemical shift evolution to take advantage of the better CS dispersion in C′. The experiment has been tested on 1.0 mM $^{13}C/^{15}N$-labeled ubiquitin. The pair-wise RMSD is 1.35 Hz for 63 residues, according to two independent measurements. The drawback of this approach is that the coupling of C_α–C_β is also active during the $^{13}C_\alpha$–$^1H_\alpha$ coupling evolution period, limiting the maximum acquisition time for $^{13}C_\alpha$–$^1H_\alpha$ coupling evolution, and may potentially reduce measurement precision due to line broadening from C_α–C_β couplings.

2D (HACACO)NH is a quantitative ${}^1J_{C_\alpha H_\alpha}$-modulated triple resonance experiment[86] with a coherence transfer pathway similar to that of (HA)CA(CO)NH.[36,43] After the magnetization of $^1H_\alpha$ is converted into $C_\alpha^y H_\alpha^z$, the antiphase term is refocused by a variable delay over a constant time period (CT = 28 ms). Signal magnitudes are thus modulated by sin (π ${}^1J_{C_\alpha H_\alpha}$ Δ). The magnetization is finally transferred to ^{15}N through C', and a 2D [^1H, ^{15}N]-HSQC spectrum is acquired. Thus, the resolution is much higher than that in [^1H, ^{13}C]-HSQC experiments.[83] Another advantage of this approach is that no $^1H_\alpha/^{13}C_\alpha$ assignment is needed in order to obtain CH RDCs. The experiment has been demonstrated on a 15 kDa RNA-binding domain of *Eicherchia coli* Rho factor. The average error in the measured coupling constants was $<0.8\%$. The authors anticipated that the experiment should be applicable to fully protonated medium-sized proteins (20–25 kDa), although the C_α transverse relaxation is active for about 28 ms during the constant time period. Later on, a modified version was published[80] where the duration of constant time is shortened in order to limit the sensitivity loss due to fast T_2 relaxation of C_α.

3D HA(CA)CONH experiment uses the same coherence transfer pathway as in (HA)CA(CO)NH,[43] with critical improvement in sensitivity.[44] The key features of HA(CA)CONH are as follows:

1. In order to avoid a long T_2 relaxation of C_α during constant-time period, the ${}^1J_{C_\alpha H_\alpha}$ coupling evolution is moved to the $^1H_\alpha$ dimension at the beginning of the sequence (point a to b as shown in Fig. 7), and combined with the magnetization transfer from $^1H_\alpha$ to $^{13}C_\alpha$.
2. Simultaneous 180° pulses are applied to both ^1H and ^{13}C to remove effects of CSA and DD cross-correlation resulting more uniform peak intensities for anti-phase doublets.
3. From the point c to d, the magnetization is further relayed to C′ and the duration is set to 7.6 ms, which is an optimized value to suppress coherence dephase due to C_α – C_β couplings, and to maintain the transfer efficiency from C_α to C′. The duration of the same period is set to 28 ms as in the (HA)CA(CO)NH sequence.
4. The ${}^1J_{C_\alpha H_\alpha}$ coupling evolution is concatenated with the C′ chemical shift labeling period to take advantage of the favorable resonance dispersion of C′ nucleus.

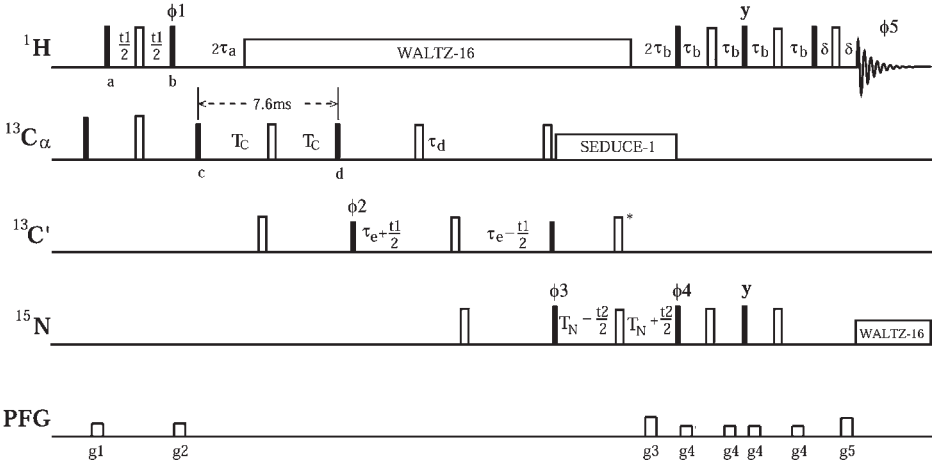

Fig. 7. The pulse sequence HA(CA)CONH. Narrow filled and wide blank bars stand for 90° and 180° pulses. Phases of pulses are on x axis unless indicated otherwise. Note that the 180° pulse on $^{13}C'$ marked with "*" was mistakenly missed in the original paper. Technical details can be found in the original work. The figure was adapted from ref. 44, with permission from Elsevier.

Since the constant time duration is reduced from 28 to 7.6 ms, the intensity loss due to T_2 relaxation of C_α is reduced significantly. The sequence has been tested on a C-terminal domain of the human Ku-80 protein (152 residues) at a concentration of 1.2/0.6 mM for isotropic/anisotropic samples. The results showed that sensitivity enhancement is profound for structured regions, with an average of 50–60% enhancement being observed when compared with the (HA)CA(CO)NH sequence. It should be applicable to a protein with a molecular weight of 20 kDa.

HCACO (α/β-J-$^1H_\alpha$-C_α) is an experiment designed to extract $^1J_{C_\alpha H_\alpha}$ from samples not suitable for ^{1}H–^{15}N correlation detection.[87] These include samples that may require high pH or temperature, where the amide protons exchange so fast with water that the sensitivity of [^{1}H, ^{15}N] correlation experiment is greatly reduced, and the proline-rich proteins that lack many amide protons. This experiment is an out-and-back experiment and can be carried out in D_2O. The coherence is transferred as follows:

$$^1H_\alpha \rightarrow {}^{13}C_\alpha \rightarrow {}^{13}C'(t_1) \rightarrow {}^{13}C_\alpha(CT - t_2) \rightarrow {}^1H_\alpha(t_3).$$

A spin-state filter, S^3 90° pulse on C_α before the acquisition period was used to separate $^1H_\alpha$–{$^{13}C_\alpha$} doublets into two sub-spectra.[88] The frequency displacement along the $^1H_\alpha$ dimension from the two spectra is the ^{1}H–^{13}C couplings. Although the experiment uses an approach similar to an earlier version of HCACO-α/β,[45] the sensitivity is improved by a factor of $\sqrt{2}$ because both orthogonal magnetization components are recovered after the C_α evolution period. The pulse scheme has been demonstrated on a 1.5 mM ubiquitin sample with a precision of a fraction of Hertz.

Like all other spin-state-editing techniques, the J crosstalk due to J mismatch could affect the accuracy of measurement. The effect may not be significant since $^{1}J_{C\alpha H\alpha}$ doublets are usually well resolved.

3.3. C_α–C′ dipolar coupling

The intrinsic RDC values of a C_α–C′ bond are about one-fifth of that of NH RDCs, but larger than both C′–N and N–C_α RDCs (Fig. 5). C_α–C′ RDCs can be measured easily with experiments such as 3D HNCO experiments without ^{13}C decoupling during the C′ chemical shift evolution.[36,89] Since HNCO is the most sensitive and well-resolved triple resonance experiment, the approach is applicable for most medium-sized proteins. More recently, methods have been developed to extract the C_α–C′ couplings from either 2D ^{1}H–^{15}N HSQC experiments to save spectrometer time, or TROSY approaches for large-sized molecules. Pulse sequences have also been developed for specifically labeled proteins, such as [^{13}C, ^{13}C′, ^{15}N, ^{2}H], where the interference from C_β can be removed. The C_α–C′ couplings can be directly observed from either HNCA or HNCO experiments with high precision on these labeled proteins. Alternatively, they can also be determined from J-modulated HNCA experiments where a constant time period is used in the C_α chemical evolution period.[90]

HN(α/β-COCA-J) is a modified 2D version of HNCO[91] for measuring C_α–C′ RDCs. The flow of coherence is:

$$^{1}H_N \rightarrow {}^{15}N \rightarrow {}^{13}C' \rightarrow {}^{15}N(t_1) \rightarrow {}^{1}H_N(t_2).$$

The active C_α–C′ coupling and ^{15}N evolution period (t_1) are concatenated. To simplify the spectra, a spin-state-filter element (using $J_{C_\alpha C'}$) similar to IPAP[38] is used prior to t_1 evolution to enhance the resolution. The doublet are separated into two-subspectra. The spin-state-filtration is very efficient. Assuming a deviation of up to ± 10 Hz from the tuned 55 Hz of a C_α–C′ coupling, the intensity of the minor component is 30 times smaller than that of the major peak. The pulse sequence was tested on 1.0 mM regulatory domain of human cardiac tropnin (cTnC, 10 kDa). Similarly, a 2D HN(CO-α/β-C′C_α-J)-TROSY[71] experiment, modified from a TROSY-HNCO experiment,[92] has been proposed for large-sized proteins and can be easily extended to 3D. The sequence has been tested on 18 kDa U-(^{15}N, ^{13}C) cNTnC protein in both a dilute LC medium (0.5 mM) and isotropic solution (2.0 mM).

2D HN(J-COCA) is a quantitative J-modulated HNCO experiment.[80] The coherence is transferred as follows:

$$^{1}H_N \rightarrow {}^{15}N \rightarrow {}^{13}C' \cos(2\pi J_{C_\alpha C'}\Delta) \rightarrow {}^{15}N(t_1) \rightarrow {}^{1}H_N(t_2).$$

After the magnetization transfer to ^{13}C′, a constant time period (≈ 56 ms) is used, during which a series of delays allow the evolution of C_α–C′ couplings, which can then be extracted from a curve fitting of peak intensities versus the coupling evolution time. The average error is less than ± 0.05 Hz on ubiquitin. For large-sized molecules, the sensitivity can be potentially improved by adapting TROSY schemes. Another J-modulated 2D HN(J-CACO) experiment to measure the couplings of C_α–C′ is also

proposed in the same paper. The experiment starts from $^{1}H_{\alpha}$ and ends at H_N with a coherence transfer similar to that in an (HA)CACONH experiment. The constant time for the C_{α}–C′ evolution is 28 ms, during which the C_{α} magnetization sits on the X–Y plane. Since the T_2 relaxation of C_{α} is faster than C′, and the choice of constant time duration is restrained by $J_{C_{\alpha}C_{\beta}}$, neither the intensity nor the precision of this scheme is as good as those of out-and-back experiments such as the HN(*J*-COCA) experiment.

3D HCACO(α/β-*J*-C′C_{α}) is an out-and-back experiment with the following coherence transfer pathway:[87]

$$^{1}H_{\alpha} \rightarrow {}^{13}C_{\alpha} \rightarrow {}^{13}C'(t_1) \rightarrow {}^{13}C_{\alpha}(CT, t_2) \rightarrow {}^{1}H_{\alpha}(t_3).$$

The evolution of C_{α}–C′ couplings is embedded in the C′ chemical shift evolution period. To simplify the spectra, a spin-state filter (using large $^{1}J_{C_{\alpha}H_{\alpha}}$) is inserted prior to the t_1 period. Addition and subtraction of IPAP spectra result in two subspectra with cross peaks at $\{\omega_{C'} + \pi^{1}J_{C'C_{\alpha}}, \omega_{C_{\alpha}}, \omega_{H\alpha}\}$ and $\{\omega_{C'} - \pi^{1}J_{C'C_{\alpha}}, \omega_{H\alpha}\}$, respectively. The couplings are extracted by a frequency-displacement method. The sequence has been demonstrated on human ubiquitin. The experiment is a useful alternative if the [^{1}H, ^{15}N] correlation experiment is not sensitive due to unfavorable pH or temperature conditions.

3.4. C_{α}–C_{β} dipolar coupling

Similar to $^{1}J_{C_{\alpha}H_{\alpha}}$, the RDCs of C_{α}–C_{β} bonds provide non-redundant orientational constraints with respect to the RDCs of bond vectors located in a peptide plane. This information can be critical for the accurate determination of alignment tensors.[93,94] In addition, C_{α}–C_{β} RDCs provide information on side chain orientation and backbone dihedral angles.[95,96] Unfortunately, poor separation of the CS ranges between C_{α} and C_{β} groups, fast T_2 relaxation of C_{α}, and medium-sized $J_{C_{\alpha}C_{\beta}}$ couplings make the measurement of C_{α}–C_{β} RDCs a big challenge. There are not many experiments published to date for the measurement of C_{α}–C_{β} RDCs.

HNCO(C_{α}–C_{β}-*J*)-TROSY is a modification of HNCO-TROSY,[92] and the C_{α}–C_{β} couplings are embedded in the C′ chemical shift evolution period.[97] The coherence is transferred as follows:

$$^{1}H_N \rightarrow {}^{15}N \rightarrow {}^{13}C' \rightarrow C_{\alpha}\cos(\pi J_{C_{\alpha}C_{\beta}}\lambda t_1) \rightarrow C'(t_1) \rightarrow {}^{15}N(t_2) \rightarrow {}^{1}H_N(t_3).$$

Both the C_{α}–C_{β} coupling and C′ chemical evolution are concatenated in the t_1 period, while the C′ chemical shift evolution is modulated by $\cos(\pi^{1} J_{C_{\alpha}C_{\beta}}\lambda t_1)$, where λ is used to amplify the couplings in order to resolve the two components of the doublet. The split along the C′ dimension yields the C_{α}–C_{β} couplings. The sequence has been demonstrated on a ubiquitin sample with λ set to 2.

2D HN(*J*-CACB) is a quantitative *J*-modulated experiment which monitors the intensity of [^{1}H, ^{15}N] correlated peaks versus the evolution time of $J_{C_\alpha C_\beta}$.[80] The magnetization transfer scheme is as follows:

$$^1H_\alpha \rightarrow {}^{13}C_\alpha \cos(2\pi J_{C_\alpha C_\beta}(CT - \Delta)) \rightarrow C' \rightarrow {}^{15}N(t_1) \rightarrow {}^1H_N(t_2).$$

A key feature of the experiment is that the signal intensity is modulated by $J_{C\alpha C\beta}$ during a constant time period (2CT = 28.4 ms), achieved by a very selective inversion pulse on C_β at different time intervals. The total coupling evolution time is 2(CT-Δ). Special attention should be given to the selective 180° inversion pulse on C_β, since the imperfection of this pulse can generate significant errors in the measured couplings. The experiment is not suitable for serine and threonine residues since their C_β chemical shifts are not well separated from C_α chemical shifts. The total duration of the constant time is $1/J_{C_\alpha C_\beta} \approx 28$ ms, and thus the precision of the *J* measurement is compromised by the limited array points, although the precision can be improved by data-mirroring. When tested on ubiquitin, 81% of the possible C_α–C_β RDCs can be extracted.

3.5. N–C′ and H_N–C′ dipolar coupling

The intrinsic RDC values between one-bond N–C′ and two-bond H_N–C′ nuclei are, respectively, about eight and three times smaller than that of $^1D_{NH}$ (See Fig. 5). In principle, N–C′ couplings can be measured from regular [^{1}H, ^{15}N]-HSQC or TROSY experiments without the decoupling of C′ during an ^{15}N evolution time. Furthermore, if the spin states of C′ are not perturbed after the ^{15}N evolution and no decoupling is applied on C′ during the ^{1}H acquisition period, an E.COSY pattern appears in the [^{1}H, ^{15}N] correlation spectrum. Thus, both N–C′ and H_N–C′ couplings can be measured from a single [^{1}H, ^{15}N] correlation experiment,[36] as schematically illustrated in Fig. 3. N–C′ splittings can also be measured along the ^{15}N dimension in 3D HNCO-TROSY by omitting the ^{13}C′ 180° pulse during the ^{15}N evolution period.[61] In practice, the spectrum is crowded since there is twice the number of cross peaks compared to a regular HSQC experiment. It is quite difficult to obtain high-precision data from the direct measurement of peak splitting since the N–C′ scalar couplings are rather small. More sophisticated experiments have been designed to enhance both the resolution and precision.

2D IPAP-H(N)CO is designed to measure H_N–C′ couplings in a 2D H_N–C′ correlated experiment.[38] The coherence transfer is similar to that in HNCO except that C′ and H_N are detected. To resolve the doublets, a spin-state-filter (use J_{HN}) is inserted in the INEPT step for magnetization transfer from C′ to ^{15}N. Thus, two interleaved AP/IP experiments detect, respectively, the $2N_zC'_y$ and $4H_zN_zC'_y$ terms. Through addition and subtraction of IP and AP spectra, doublets of C′–{^1H_N} are separated into two sub-spectra. The frequency displacement of the corresponding

cross peaks in two sub-spectra along the C′ dimension yields the C′–H_N couplings, although the values are small. The experiment has been demonstrated on a 0.7 mM ubiquitin sample. When compared with the C′ coupled-E.COSY-[^{1}H,^{15}N]-HSQC experiment, the pairwise RMSD is 0.38 Hz for $^2D_{HN-C'}$ with an error of less than 0.3 Hz in individual measurements. A very similar scheme called H(α/β-NC′-*J*)CO experiment has also been proposed where the spin-state-filter part is inserted after the INEPT magnetization transfer step from N to C′ and prior to the t_1 period.[98]

3D HNCO(α/β-NC′-*J*) and 3D HNCO(α/β-NC′-*J*)-TROSY,[97] based respectively on HNCO and HNCO-TROSY schemes with the insertion of a spin-state filter to increase the resolution, have been developed to measure N–C′ couplings. HNCO (α/β-NC′-*J*) is suitable for small-and medium-sized proteins, while HNCO(α/β-NC′-*J*)-TROSY has been tailored for medium and large-sized proteins. The magnetization transfer pathways of both experiments are very similar and can be described as follows:

$$^1H_N \rightarrow {}^{15}N \rightarrow C'(t_1) \rightarrow {}^{15}N(t_2) \rightarrow {}^1H_N(t_3).$$

After the magnetization is transferred to C′ from ^{15}N, a spin-state filter using large $^1J_{NH}$ couplings turns the density operator into either $4H_z^N N_z C'_y$ or $2H_z^N C'_y$ prior to the t_1 period. Both the C′ chemical shifts and C′–N couplings evolve during the t_1 period. The term $4H_z^N N_z C'_y$ yields an in-phase spectrum while $2H_z^N C'_y$ gives an anti-phase spectrum. Addition and subtraction of the in- and anti-phase spectra generate two 3D sub-spectra. The relevant coordinates for extracting couplings along the C′ dimension in the two sub-spectra are $\{\omega_{C'} + (1+\lambda)\pi\ {}^1J_{NC'}\}$ and $\{\omega_{C'} - (1+\lambda)\pi\ {}^1J_{NC'}\}$, respectively. The parameter λ is used to amplify C′–N couplings in order to enhance the precision of measurement. The application of these experiments at high field spectrometers is limited by the fast T_2 relaxation of C′. The authors suggested carrying out these experiments at a field strength of 600 MHz proton frequency or lower. Analysis showed that the *J* crosstalk does not significantly affect the precision of peak positions. The precision of the experiments was about 0.1 Hz when tested on 1.4 mM ^{15}N/^{13}C-labeled human cardiac Troponin C (cTnC, 18 kDa).

A 3D TROSY-HNCO quantitative $J_{C'-N}$ experiment has been developed by Chou and coworkers.[99] Compared to a regular TROSY-HNCO experiment,[92] a long delay of $2T = 66.7$ ms is used in its INEPT step to transfer magnetization from ^{15}N to C′. Two experiments are carried out in an interleaved manner with the positions of the 180° pulse on C′ located at two different places. The signal intensities of the two experiments are modulated by C′–N couplings with different durations. Thus, C′–N couplings can be extracted from the intensity ratio of the two experiments. Details for data analysis can be found in the original work. The sequence has been demonstrated on a 1.0 mM ^{13}C/^{15}N-labeled Ca^{2+}-mammalian calmodulin (CaM, 17 kDa) sample. The RMSD between the measured and predicted dipolar couplings is 0.21 Hz. The precision of the measured couplings is proportional to the *S*/*N* ratios.

3.6. $^{1}H–^{1}H$ dipolar coupling

RDCs between $^{1}H–^{1}H$ can be observed and applied as long-range conformational constraints[4] for structure determination. Compared to traditional NOE distance constraints, $^{1}H–^{1}H$ RDCs can potentially provide distance constraints longer than 5 Å since $^{1}H–^{1}H$ RDCs are proportional to r^{-3} while NOEs are proportional to r^{-6}. Nevertheless, the overwhelming $^{1}H–^{1}H$ dipolar coupling network, especially those neighboring protons reduce greatly the values of $^{1}H–^{1}H$ RDCs. It is also difficult to assign the sign of remote $^{1}H–^{1}H$ RDCs if there is no scalar couplings between them, or the magnitude of their scalar couplings are smaller than that of RDCs. Although the absolute values of $^{1}H–^{1}H$ RDCs can be used in structural study, RDCs with known sign can speed up the convergence in structure calculation.[100] Two approaches have been proposed to determine the sign of $^{1}H–^{1}H$ RDCs for the spin system of $X–^{1}H \leftrightarrow {}^{1}H^{r}$, where X can be either ^{13}C or ^{15}N, *r* stands for a remote proton.[101,102] Another experiment, called soft HNCA-E.COSY (see section 3.7), can determine both the magnitude and sign of $^{3}D_{HN–HA}$ and $^{4}D_{HN–HA}$.[103]

Dipolar couplings in methyls (DiM) is a 2D [^{1}H, ^{13}C]-correlated experiment for measuring $^{1}H–^{1}H$ couplings in methyl groups.[75] Theoretical analysis shows that for an isolated methyl group, dipolar couplings result in a triplet with relative line intensities of 1:2:1. The experiment was designed to detect the two outermost lines of the triplet, and suppress the middle one by creating a $^{1}H–^{1}H$ anti-phase term right before the data acquisition. The final cross peaks are proportional to $\sin(\pi D_{HH} t_2) \cos(\pi D_{HH} t_2)$. Thus, the two outermost lines of the triplet along the ^{1}H dimension yield $2D_{HH}$, while the sign of the D_{HH} is also shown in $\sin(\pi D_{HH} t_2)$. The experiment has been demonstrated on 10 mM BPTI at natural isotopic abundance. The pulse scheme should also be useful for perdeuterated proteins with protonated methyl groups,[1,75] because such labeling pattern would suppress the scalar and dipolar interaction between methyl and non-methyl protons.

An ^{15}N-resolved CT-COSY experiment[104] with enhanced spectrum resolution has been extended from an earlier 2D CT-COSY experiment[105] for the measurement of $^{1}H–^{1}H_N$ couplings. ^{15}N evolution is added in the constant time period, which is also used for $^{1}H_N$ chemical shift labeling and the magnetization transfer from $^{1}H_N$ to other proximate protons. The $^{1}H–^{1}H$ couplings can be extracted from the ratios of the cross-peaks to auto-peaks in an ^{15}N-resolved 2D [^{1}H, ^{1}H] plane. The pulse sequence has been tested on rubredoxin (5.9 kDa) and *E. coli* acyl carrier protein (ACP, 8.8 kDa). The quality of the measured $^{3}J_{HN–H\alpha}$ values on rubredoxin has been evaluated by a comparison with the data measured from an HNHA experiment,[100] the RMSD between these two data sets is 0.6 Hz.

A 3D SS-HMQC2 (two semi-selective HMQC) experiment has been developed by Wu and coworkers[106] for measuring long-range $^{1}H_N–^{1}H_N$ couplings. For ease of exposition, let P and Q denote two pairs of $^{1}H–^{15}N$ spin vectors. The experiment is composed of two constant-time (CT) periods. In the first CT period, the $^{15}N^{P}$ chemical shifts evolve and the magnetization of $^{1}H_N^{P}$ is transferred partially and selectively to other nearby $^{1}H_N$ protons, say $^{1}H_N^{Q}$. The selective transfer is achieved by a 180° selective pulse on $^{1}H_N$. Then, the magnetization is relayed to $^{15}N^{Q}$

through $^{1}H_{N}^{Q}$. During the second CT period, the ^{15}N chemical shifts evolve and anti-phase terms of the two $^{1}H_{N}$ protons are rephased. The experiment is basically a ^{15}N–^{15}N COSY experiment correlated by $^{1}H_{N}$–$^{1}H_{N}$ RDC interaction. Finally, the magnetization is transferred back to the attached $^{1}H_{N}$ and detected. Thus, in a 2D [^{15}N, ^{15}N] plane, the intensities of both cross and diagonal peaks contain RDC information between their attached two $^{1}H_{N}$ protons. The $^{1}H_{N}$–$^{1}H_{N}$ RDCs can be extracted readily (see the original paper). The sequence has been demonstrated on 1.0 mM $^{13}C/^{15}N/^{2}H$-labeled Ca^{2+}-calmodulin, and cross peaks can be observed between two $^{1}H_{N}$ protons up to 6 Å apart. When tested on a ubiquitin sample, the RDC interaction between two $^{1}H_{N}$ protons can be observed with distance up to 7 Å. Although only demonstrated on the $^{1}H_{N}$–$^{1}H_{N}$ RDC measurement, the strategy used in the sequence should be applicable to other groups of protons. The method cannot determine the sign of D_{HN-HN}.

2D D_{HH}-CT-HSQC and 3D D_{HH}-CT-HSQC experiments measure ^{1}H–^{1}Hdipolar couplings in CH_2D methyl groups of highly deuterated $^{13}C/^{15}N$-labeled proteins.[107] D_{HH} in methyl group provides useful information for defining χ_1 torsion angles and stereo-specific assignment of methyl groups in valine side chains.[107] Such restraints are particularly useful for perdeuterated proteins where no sufficient NOE distance restraints are available for defining methyl groups. In order to selectively observe the signals from CH_2D groups, the signals from CHD_2 and CH_3 groups are suppressed through isotopomer selection filters. In addition, an α/β spin-state-selection step (using J_{CH}) is used before the final INEPT to enhance the resolution. Through addition and subtraction of IPAP spectra, two subspectra (α/β) are generated with the frequencies along the ^{1}H dimension at $\omega_\beta = \omega_H + D_{HH}/2$ and $\omega_\alpha = \omega_H - D_{HH}/2$, respectively. Since there is no scalar coupling between two protons in methyl groups, no reference spectrum is needed to extract the RDCs. For large-sized proteins, the 2D experiment can be extended to 3D by labeling the ^{13}C next to the methyl ^{13}C using an out-and-back method. Both 2D and 3D pulse schemes have been demonstrated on $^{13}C/^{15}N$, and 77% ^{2}H-labeled SiR-FP18 protein.

3.7. Experiments for the simultaneous measurement of more than one types of RDCs

In above sections, we have discussed experiments for measuring one type of RDCs at a time. There are several advantages for the simultaneous measurement of different types of RDCs using a single experiment:[108–110]

1. In high-throughput biological structure determination, it is preferred to obtain as many types of RDCs as possible in a timely fashion.[109,111]
2. In practice, the conditions of alignment samples may change in the course of measuring different types of RDCs in a sequential manner. The changes can be caused by (a) different alignments since it may take a long time for reaching the equilibrium alignment state,[110] (b) the instability of alignment samples and (c) different NMR experimental conditions such as pulse imperfection and heating associated with different pulse sequences. Consequently, the different

types of sequentially measured RDCs may not share a common alignment tensor, which introduces additional errors in RDC applications.

However, compared with the spectra of only one type of RDCs, the spectra of several types of RDCs are more crowded and their S/N ratios are lower. In general, E.COSY schemes[42] have been used for enhancing resolution and TROSY techniques for increasing S/N ratios. For examples, the couplings of ^1H_N–$^{13}C'$, ^{15}N–$^{13}C'$ and ^1H–^{15}N can be measured using [^1H, ^{15}N]-HSQC or -TROSY type experiments in combination with E.COSY schemes:

1. 2D E.COSY-IPAP-HSQC for simultaneous measurement of RDCs of ^1H_N–$^{13}C'$, ^{15}N –$^{13}C'$ and ^1H–^{15}N for large-sized perdeuterated proteins.[112]
2. 2D HN(α/β-NC′-J)-HSQC and HN(α/β-NC′-J)-TROSY for measuring ^1H_N–$^{13}C'$ and ^{15}N–$^{13}C'$ couplings,[98] as well as the couplings of ^{15}N–$^{13}C'$ and ^1H_N–$^{13}C'$ in Asn and Gln side chains with an NH_2 selection filter.[81]
3. 2D (δ, J)-E.COSY HSQC for measuring ^1H-^{15}N, ^{15}N–$^{13}C'$ and ^1H_N–$^{13}C'$ couplings.[78,113]
4. 3D E.COSY-HNCO-TROSY experiment for measuring ^1H_N–$^{13}C'$ and ^{15}N–$^{13}C'$ couplings on large-sized proteins.[77]

In addition to the experiments listed above, many different experiments have been proposed. It is difficult to group them based on the types of RDCs since each experiment measures a different combination of RDCs. We will discuss the experiments in the order of publication date. For easy of reference, in the following the measured RDCs are listed right after the name of the experiment.

[^1H–^{13}C]-CT-HSQC measures J_{CH} couplings of methane, methylene and methyl groups.[114] It is an extension of CT-HSQC with the third dimension modulated with active J_{CH} couplings. The constant-time duration is set to be $1/J_{CC} \approx 28$ ms. The dwell time for J_{CH} modulation (t_2 dimension) is about 2 ms, thus less than 15 increments are needed for the J modulation. The individual 2D [^1H, ^{13}C] planes appear like a regular decoupled CT-HSQC. The intensity depends on the t_2 duration with cosine functions for methane, methylene and methyl groups. The coupling interactions between carbon and remote protons are accounted for the decay of the signal in the t_2 dimension. Although only the sum of the two J_{CH} splittings can be determined for methylene sites, RDCs of the sum can still be used for structure calculation. For methyl groups, the dipolar couplings are measured from the outer ^{13}C quartet components. These outer quartet components are modulated by 3π ($^1J_{CH} + {}^1D_{CH}$), and thus the RDC can be measured accurately although it is scaled down by a factor of -0.31 due to the rapid rotation about a three-fold symmetry axis.[115] The RMSD of measured RDCs from ^{13}C inner and outer quatet components of methyl group is <0.3 Hz. The pairwise RMSD is less than 0.4 Hz for methylene sites. The sequence has been tested on 0.7 mM $^{13}C/^{15}N$-labeled ubiquitin, and should be applicable to small and medium-sized proteins.

3D E.COSY-HNCO-TROSY measures RDCs of $H_N(i)$–$C_\alpha(i-1)$ and $C'(i-1)$–$C_\alpha(i-1)$ internuclear vectors.[116] To establish an E.COSY pattern, both $C'(i-1)$–$C_\alpha(i-1)$ and $H_N(i)$–$C_\alpha(i-1)$ couplings are active during the $^{13}C'$ evolution (t_1) and ^1H acquisition (t_3)

periods. The α and β spin states of C_α are not mixed from the t_1 to t_3 periods. Thus, E.COSY patterns of doublets appear in the plane of [$^{13}C'$, ^1H_N] with relevant coordinates at $\{\omega_{C'} + \pi^1 J_{C'C\alpha}, \omega_{HN} - \pi^3 J_{HN-C\alpha}\}$ and $\{\omega_{C'} - \pi^1 J_{C'C\alpha}, \omega_{HN} + \pi^3 J_{HN-C\alpha}\}$, and from them the couplings of H_N (i)–C_α(i–1) and C'(i–1)–C_α(i–1) can be extracted readily. The reproducibility of coupling measurement has been evaluated on a 1 mM isotropic MBP sample with repeated experiments. The average values for $^1J_{C'-C\alpha}$ and $^3J_{HN-C\alpha}$ are, respectively, 52.5 ± 1.0 and 0.3 ± 0.4 Hz based on the values from 275 well-resolved cross peaks in the spectra. This approach can be further improved in resolution by inserting a spin-state filter to separate the doublets of C'-$\{C_\alpha\}$ into two sub-spectra as demonstrated in 3D HNCO(α/β-$C'C_\alpha$-J) and 3D HNCO(α/β-$C'C_\alpha$-J)-TROSY experiments.[97]

Soft HNCA-E.COSY measures RDCs of $H_\alpha(i)$–$C_\alpha(i)$, $H_N(i)$–$H_\alpha(i)$ and $H_N(i)$–$H_\alpha(i-1)$ internuclear vectors.[103] The experiment is modified from an earlier version of HNCA-E.COSY sequence.[117] The coherence is transferred as follows:

$$^1H_N(i) \rightarrow {}^{15}N(i)(CT, t_2) \rightarrow {}^{13}C_\alpha(i)(t_1)/C_\alpha(i-1)(t_1) \rightarrow {}^{15}N(i) \rightarrow {}^1H_N(i)(t_3).$$

The duration of CT for the magnetization transfer from ^{15}N to C_α is 27.2 ms. This CT period is also used for the ^{15}N chemical shift evolution. Both the CSs of $C_\alpha(i)$ and $C_\alpha(i-1)$, and their couplings to the $^1H_\alpha(i)$ evolve during the t_1 period. When the magnetization is transferred back to ^1H_N from ^{15}N, a net 360° rotation of $^1H_\alpha$ keeps its spin state the same as that during the C_α evolution time. The couplings between H_N and $H_\alpha(i)/H_\alpha(i-1)$ are active during the data acquisition. The cross peaks in [^{13}C, ^1H_N] planes form E.COSY patterns, and the large $^1J_{C_\alpha H_\alpha}$ coupling makes the small couplings of $^1H_\alpha - {}^1H_N$ resolved. Consequently, the couplings of $H_\alpha(i)$–$C_\alpha(i)$, $H_N(i)$–$H_\alpha(i)$ and $H_N(i)$–$H_\alpha(i-1)$ can be measured readily. When tested on a FK506-binding protein complexed to FK506, 90% of the possible $H_N(i)$–$H_\alpha(i)$ RDCs and 52% of the possible $H_N(i)$–$H_\alpha(i-1)$ RDCs could be obtained.

The $^1D_{N-C\alpha}$, $^2D_{N-C\alpha}$, $^2D_{HN-C\alpha}$ and $^3D_{HN-C\alpha}$ RDCs can be measured by either 2DHN(CO-α/β-NC_α-J)-TROSY or 3D-HNCO(α/β-NC_α-J)-TROSY.[71,97] It is challenging to measure $^1D_{N-C\alpha}$ and $^2D_{N-C\alpha}$ since they are small and difficult to be resolved from one another. The proposed experiments make use of large $^1J_{C'-C\alpha}$ coupling to distinguish the inter/intra-residue couplings of N–C_α. The coherence is transferred in 2D HN(CO-α/β-NC_α-J)-TROSY as follows:

$$^1H_N \rightarrow {}^{15}N \rightarrow {}^{13}C' \rightarrow {}^{15}N(t_1) \rightarrow {}^1H_N(t_2).$$

A spin-state-filter (using large $^1J_{C'-C\alpha}$ couplings) is inserted right after the magnetization has been transferred from ^{15}N to C'. Before the ^{15}N evolution period, the filter generates a $4H_zN_y(i)C'_Z(i-1)$ term for in-phase experiment and a $8H_zN_y(i)C'_z(i-1)C^\alpha_z(i-1)$ term for anti-phase experiment. During the t_1 evolution, these two terms yield in-phase and anti-phase spectra for the doublets of $^{15}N(i)$-$\{C_\alpha(i-1)\}$, respectively. These doublets are further split by the couplings to $C_\alpha(i)$. Finally, the couplings between C_α and ^1H_N are active during the data (^1H_N) acquisition. Since the C_α spin states are preserved and coupled to both ^{15}N and ^1H_N dimensions, an E.COSY pattern forms. The linear combination of the in-phase and anti-phase spectra generates two sub-spectra, where the $^1J_{N-C\alpha}$ and $^2J_{HN-C\alpha}$

couplings can be measured directly from the E.COSY pattern within each sub-spectra. The $^{2}J_{N-C\alpha}$ and $^{3}J_{HN-C\alpha}$ couplings can be extracted from the frequency difference of corresponding peaks in these two spectra. Shown in Fig. 8 are the cross peaks of two sub-spectra illustrating the strategies for extracting the couplings. All the four couplings can be determined twice, and thus provide an internal check for the quality of measurement. The sequence has been demonstrated on 1.0 mM $^{13}C/^{15}N$-labeled ubiquitin. For large-sized protein samples, a third dimension ($^{13}C'$) can be added to enhance the resolution.[97] Later on, a similar 2D [^{15}N, ^{1}H] correlation experiment has been proposed for measuring the same four couplings, $^{1}J_{N-C\alpha}$, $^{2}J_{N-C\alpha}$, $^{2}J_{HN-C\alpha}$ and $^{3}J_{HN-C\alpha}$.[118] The experiment is based on a sensitivity-enhanced HNCO rather than a TROSY scheme, this approach is more suitable for small-sized proteins (<10 kDa, or the ^{15}N linewidth is <8.5 Hz). The sequence had been tested on protein GB1 (6.2 kDa).

SPITZE-HSQC (SPIn sTate selective Zero overlap HSQC) measures $^{2}J_{H-H}$ and two individual couplings of C–H bonds in a methylene group.[119] SPITZE-HSQC is a fully coupled HSQC experiment in both ^{13}C and ^{1}H dimensions. Along the ^{13}C dimension, only two outer components are observable, while the middle component is canceled. Each of these two outer components is further split into four components along the ^{1}H dimension by the one-bond C–H and two-bond H–H couplings. Using an $S^{3}E$ scheme,[39,40] four out of the eight components containing information of the three couplings can be selectively observed from four individual experiments. Thus, all the three RDCs of CH^{1}, CH^{2} and H–H for moiety of methylene can be determined. The combination of these three RDCs can be used to define the orientation of methylene groups.[119] The experiment is quite sensitive since the coherence is transferred selectively for each observed component. The sequence works well on Gly residue. The applications to other residues are compromised because the carbon–carbon couplings are

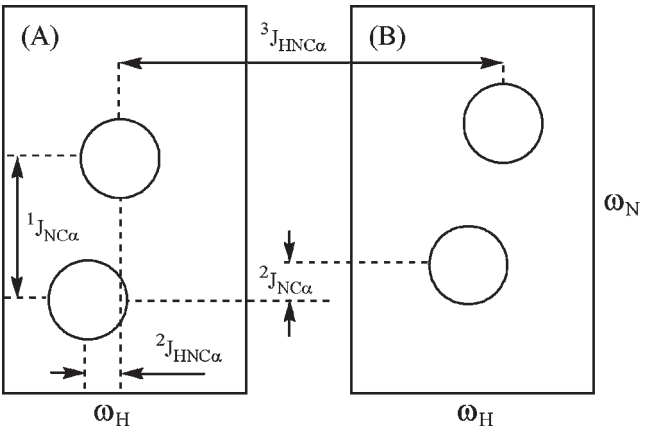

Fig. 8. Two sub-spectra obtained from the sequence of 2D HN(CO-α/β-NC_{α}-*J*)-TROSY. $^{1}J_{N-C\alpha}$ and $^{1}J_{HN-C'}$ a couplings can be measured twice from E.COSY patterns within the panels of (A) and (B), while $^{2}J_{N-C\alpha}$ and $^{3}J_{HN-C\alpha}$ couplings can be measured twice from the corresponding components in two sub-spectra.

active during the t_1 evolution. The pulse scheme has been demonstrated on a 1.5 mM $^{13}C/^{15}N$-labeled ubiquitin sample.

3D CBCA(CO)NH measures the couplings of $^{13}C_\alpha$–$^1H_\alpha$ and $^{13}C_\beta$–$^1H_\beta$ bonds.[120] The experiment is modified from an original CBCA(CO)NH pulse sequence.[121] The magnetization transfer pathway is as follows:

$$^1H_{\alpha/\beta} \rightarrow {}^{13}C_{\alpha/\beta}(CT, t_1) \rightarrow {}^{13}C' \rightarrow {}^{15}N(t_2) \rightarrow {}^1H_N(t_3).$$

In order to measure couplings of both $^{13}C_\alpha$–$^1H_\alpha$ and $^{13}C_\beta$–$^1H_\beta$, a quantitative J modulation is introduced in the constant time period (t_1 evolution). Three data sets are acquired in an interleaved manner where the signal intensities are modulated by J_{CH} with three different time periods $2\Delta_1$. Without considering cross-correlated relaxation effect, the signal intensities, $S(\Delta_1)$, associated with C_α and C_β can be described by

$$S(\Delta_1) = A \sin\left[\pi \sum J_{CH}(2\Delta_1 + D_{eff})\right] \tag{13}$$

where A is a constant, D_{eff} accounts for J_{CH} dephasing due to various necessary delays and pulses, $\sum J_{CH}$ is the sum of the scalar couplings. The $\sum J_{CH}$ couplings can be derived from Eq. (13) by a SIMPLEX minimization routine using the three $2\Delta_1$ values. Although only the sum of the two $^{13}C_\beta$–$^1H_\beta$ RDCs is available from the experiment, they are still useful for defining the χ_1 dihedral angles of side-chain conformations. The first experiment is called reference experiment with $2\Delta_1 + D_{eff} = 1.93$ ms, which is basically the same as a regular CBCA(CO)NH experiment. The S/N ratio of the reference experiment determines the error in the coupling measurement. The sequence has been tested on 0.4 mM Ca^{2+}-calmodulin.

A 3D HNCO-based experiment has been developed to simultaneously measure ^1H–^{15}N and C'–C_α couplings[108] by letting $J_{C'C\alpha}$ to be active during the $^{13}C'$ evolution and J_{HN} to be active during the ^{15}N evolution periods. An IPAP scheme[38] is inserted after the ^{15}N evolution to enhance the resolution. Addition and subtraction of the IP and AP spectra result in two 3D spectra with cross peaks at $\{\omega_{C'} \pm \pi^1 J_{C'C\alpha}, \omega_N + \pi^1 J_{HN}, \omega_{HN}\}$ and $\{\omega_{C'} \pm \pi^1 J_{C'C\alpha}, \omega_N - \pi^1 J_{HN}, \omega_{HN}\}$. $J_{C'C\alpha}$ couplings can be measured twice from the two spectra. ^1H–^{15}N couplings can be extracted from the frequency displacement of the corresponding peaks along the ^{15}N dimension in the two spectra. The experiment has been tested on an exclusive α-helical protein, apoptotic inducing protein Bax (22 kDa). A regular 3D (HA)CA(CO)NH experiment has also been modified in a similar manner to measure, simultaneously, ^1H–^{15}N and $^{13}C_\alpha$–$^1H_\alpha$ couplings.[108] The interested readers can refer to the original paper for the details.

A quantitative HCN-HSQC experiment has been developed to measure long range (span more than three bonds) ^1H_N–^{13}C couplings in perdeuterated proteins.[122] It is challenging to measure and assign such long range RDCs. The proposed experiment

takes advantage of perdeuterated protein samples. The magnetization transfer pathway is as follows:

$$^1H_N \rightarrow ^{13}C(t_1) \rightarrow ^1H_N \rightarrow ^{15}N(t_2) \rightarrow ^1H_N(t_3).$$

The duration (2T) for the transfer from ^1H_N to ^{13}C and back was set to be 20 ms. The ^{13}C can be either aliphatic or carbonyl ^{13}C nuclei in proximity of ^1H_N spins. The intensity of the 3D spectrum is proportional to $\sin^2(2\pi J_{HN-C}T)$. To extract J_{HN-C} couplings, a second (reference) spectrum is acquired where only the in-phase term $^1H_z^N$ after the first 2T INEPT transfer period is selected, and a 2D [^{15}N, ^1H] correlated spectrum is collected. The intensity of the signals is proportional to $\cos^2(2\pi J_{HN-C}T)$. With a suitable scaling factor to normalize the difference between the 2D and 3D acquisition schemes, the J_{HN-C} can be extracted from the intensity ratios of the cross and reference peaks. When tested on a 2.2 mM $^{13}C/^{15}N/^2H$-labeled protein G, many correlations between ^1H_N and C_α, C_β and $^{13}C'$ of both the intra or inter residues can be observed. In some cases, the correlation across a hydrogen bond ($^1H_N \leftrightarrow ^{13}C'$) can be observed. In addition to the correlation of ^1H_N and ^{13}C, many correlations between ^1H_N and ^1H_N can also be observed using a regular ^1H–^1H COSY-HMQC,[123] the distance of this correlation can span up to 7.2 Å. The precision of the measurement has been evaluated, and the statistical error is smaller than 0.14 Hz for the measurement of D_{HN-C} RDCs.

A quantitative *J*-correlated [^{15}N, ^1H]-TROSY-HNC has been designed to measure $^1J_{N-C'}$, $^1J_{N-C\alpha}$ and $^2J_{N-C\alpha}$ couplings.[110] The experiment is similar to an earlier TROSY-HNCO or TROSY-HNCA experiment.[92] The coherence transfer pathway is as follows:

$$^1H_N \rightarrow ^{15}N \rightarrow (C'(i-1)(t_1), C_\alpha(i-1)(t_1), C_\alpha(i)(t_1), N(\omega_C = 0)) \rightarrow ^{15}N(t_2) \rightarrow ^1H_N(t_3).$$

The magnetization is first transferred, simultaneoussly, to $C'(i-1)$, $C_\alpha(i-1)$ and $C_\alpha(i)$ using an HMQC scheme, then these three carbon nuclei evolve during the t_1 period and appear as cross peaks. In the meantime, the partial magnetization not transferred to ^{13}C from ^{15}N is also sampled during the t_1 period through phase cyclings. These peaks appear as axial peaks since there exist no modulations from ^{13}C chemical shifts. Thus, both cross and axial peaks are in the same spectrum. The volume ratios of cross peaks versus axial peaks can be used to determine $^1J_{N-C'}$, $^1J_{N-C\alpha}$ and $^2J_{N-C\alpha}$ couplings. Since the couplings between C'/C_α and C_α/C_β are active during the t_1 period, the linewidths of cross peaks are broader than those of axial peaks. To avoid systematic errors, it is also critical to use peak volumes not peak intensities to compute these couplings. The experiments have been tested on three different proteins: $^{13}C/^{15}N$-labeled flavodoxin (16 kDa), $^{13}C/^{15}N$-labeled xylanase (23 kDa) and $^{13}C/^{15}N/^2H$-labeled DFPase (35 kDa). RDC values have been extracted on flavodoxin. The reproducibility of the experiments have been evaluated by acquiring two data sets on three isotropic and one aligned samples. The RMSD is <0.4 Hz for all the three couplings measured from the four different samples, while the uncertainties increase from $^1J_{N-C'}$ to $^1J_{N-C\alpha}$ and to $^2J_{N-C\alpha}$

couplings. The precision is proportional to the S/N ratio of cross peaks. It is interesting that authors compared the RMSDs measured from this experiment with those measured from two other experiments: a 2D HN(α/β-NC′-J)-TROSY (measures N–C′ couplings) and HN(CO-α/β-NC$_\alpha$-J)-TROSY (measures N–C$_\alpha$ couplings) experiments. Under the same conditions, the spin-state-selection approaches appear to be more precise. It is also noted that when the $^1J_{N-C\alpha}$ couplings are small, their values measured from the HN(CO-α/β-NC$_\alpha$-J)-TROSY experiment tend to be systematically smaller than those measured from a quantitative J-correlated [^{15}N, ^{1}H]-TROSY-HNC experiment. A possible explanation is that the covariance effects of in-phase doublets from the HN(CO-α/β-NC$_\alpha$-J)-TROSY experiment cause an underestimation of the $^1J_{N-C\alpha}$ couplings, but no such effect exists for $^2J_{N-C\alpha}$ because they are measured from two separated spectra. The correlation coefficients for $^1J_{N-C'}$, $^1D_{N-C\alpha}$ and $^2D_{N-C\alpha}$ couplings measured from the two different approaches are, respectively, 0.976, 0.922 and 0.293. The low measurement precision in both approaches is thought to be responsible for the poor correlation of $^2D_{N-C\alpha}$ couplings. Thus, caution must be taken when $^2D_{N-C\alpha}$ RDCs are used in either structural or dynamical study if the uncertainty of measurement is comparable with the magnitude of the $^2D_{N-C\alpha}$ RDCs.

A 3D HNCA(α/β-J-CAHAN)-TROSY experiment has been designed to measure $^1J_{C_\alpha H_\alpha}$, $^2J_{N-H\alpha}$ and $^3J_{N-H\alpha}$ couplings.[124] The coherence transfer scheme is similar to an earlier HNCA-TROSY experiment:[92]

$$^1H_N \rightarrow {}^{15}N \rightarrow {}^{13}C_\alpha(t_1) \rightarrow {}^{15}N(t_2) \rightarrow {}^1H_N(t_3).$$

After the magnetization is transferred to C$_\alpha$ from ^{15}N, a spin-state filter is used so that either an $8H_N^z N^z H_\alpha^z C_\alpha^y$ or $4H_N^z N^z C_\alpha^y$ term evolves during the t_1 period, yielding, respectively, the anti-phase and in-phase doublets of $^{13}C_\alpha$–$\{^1H_\alpha\}$ couplings. The $^1H_\alpha$ is coupled, respectively, to ^{13}C (during the t_1 period) and ^{15}N (during the t_2 period). The cross peaks in a plane [^{13}C, ^{15}N] appear as an E.COSY pattern since the spin states of $^1H_\alpha$ are not mixed. Two sub-spectra are generated after the addition and subtraction of the in-phase and anti-phase experiments. The resonances associated with the intra C$_\alpha$ peaks appeared in [^{13}C, ^{15}N] planes at, respectively, $\{\omega_{C\alpha(i)} + \pi^1 J_{C\alpha H\alpha}, \omega_{N(i)} - \pi^2 J_{NH\alpha}\}$ and $\{\omega_{C\alpha(i)} - \pi^1 J_{C\alpha H\alpha}, \omega_{N(i)} + \pi^2 J_{NH\alpha}\}$. However, the shifts due to the TROSY scheme are not shown since they are irrelevant for coupling determination. The resonances associated with the inter-C$_\alpha$ peaks can also be obtained and the couplings of $^1J_{C\alpha H\alpha}$, $^2J_{N-H\alpha}$ and $^3J_{N-H\alpha}$ can be deduced readily. Two other experiments to measure the same couplings have also been proposed in the same paper.[124] The experiments have been tested on 1.9 mM ^{13}C/^{15}N-labeled ubiquitin (76 residues). A detailed discussion was given as to how the accuracy for the measurement of C$_\alpha$–H$_\alpha$ couplings is affected by the DD–DD cross-correlation between C$_\alpha$–H$_\alpha$ dipolar and ^{1}H$_\alpha$–H$_r$ dipolar interactions (H$_r$ is a remote proton coupled to ^{1}H$_\alpha$), and by the homonuclear $J_{C\alpha C\beta}$ coupling during the t_1 period. The authors also discussed the errors in the measurement of $^2J_{N-H\alpha}$ and $^3J_{N-H\alpha}$ couplings caused by the partial collapse of E.COSY patterns, which in turn, is caused by the ^{1}H spin flip between the t_1 and t_2 evolution periods.

A 2D-[^{13}C,^{13}C]-TOCSY experiment has been developed to measure side-chain ^{13}C–^{13}C RDCs.[125,126] Side-chain ^{13}C–^{13}C RDCs may prove to be indispensable for high-quality structure determinations of perdeuterated proteins, since for such protein samples there are, in general, not enough NOE restraints to define side-chain conformations. The proposed experiment starts from ^{13}C, after the CS labeling of ^{13}C, the magnetization is transferred to other ^{13}C nuclei using a FLOPSY-16 scheme. The couplings between aliphatic ^{13}C nuclei are active during the direct ^{13}C observation period. Thus, the cross peaks along the direct ^{13}C dimension split into doublets, quadruplets, and octets dependent upon the numbers of ^{13}C nuclei directly attached to the observed ^{13}C. The couplings can be readily available from the doublets. Theoretically, the sum of two RDC values from the outer components in the quadruplet can also be decomposed into individual contributions by starting from the outermost ^{13}C nuclei. The sum can also be used directly as structural constraints.[114] When applied on ^{13}C/^{15}N/^{2}H-labeled ubiquitin, ^{13}C–^{13}C RDCs can be extracted from the doublets, and 10 RDCs can be obtained from the outer components of quadruplets. The deviation between the RDCs measured independently from different cross peaks is <0.3 Hz.

A 3D HCACO(α/βC′HA) experiment has been designed to measure $^{2}J_{C'-H\alpha}$ and $^{1}J_{C\alpha-H\alpha}$ couplings.[87] The experiment is suitable for proline-rich proteins or for proteins which must be studied at high pH or temperature conditions. The magnetization transfer pathway is as follows:

$$^{1}H_{\alpha} \rightarrow {}^{13}C_{\alpha} \rightarrow {}^{13}C'(t_1) \rightarrow {}^{13}C_{\alpha}(CT, t_2) \rightarrow {}^{1}H_{\alpha}(t_3).$$

A spin-state-filter (using $J_{H\alpha-C\alpha}$) is inserted in the INEPT magnetization transfer step (from $^{13}C_{\alpha}$ to C′) to generate either a $2C_{\alpha}^{z}C'^{y}$ or $4H_{\alpha}^{z}C_{\alpha}^{z}C'^{y}$ term which evolves into observable terms after the t_1 period. Both the C′ chemical shifts and the couplings between C′ and $^{1}H_{\alpha}$ evolve during the t_1 period, while the ^{13}C chemical shifts and the couplings between C_{α}–$^{1}H_{\alpha}$ evolve during the t_2 period. Since the spin states of $^{1}H_{\alpha}$ are not mixed between the t_1 and t_2 periods, cross peaks with E.COSY patterns appear in the [C′, C_{α}]correlation planes. After the addition and subtraction of the in-phase and anti-phase spectra, the two cross peaks in an E.COSY pattern are further separated into two sub-spectra according to the upfield or downfield component of a C′ spin. Thus, the small splitting of $^{2}J_{C'-H\alpha}$ becomes well resolved indirectly, and can be measured accurately. To increase the measurement accuracy, a large number of time points are required for both the t_1 and t_2 dimensions. The pulse scheme has been demonstrated on ^{13}C/^{15}N-labeled ubiquitin samples under both the isotropic and anisotropic conditions.

A 3D TROSY-HNCO based-experiment has been developed to measure the N–C′ and N–H couplings[109] using a total of three experiments with one of them to be a common reference experiment. For the measurement of N–C′ couplings, it uses the same pulse sequence scheme as in a 3D TROSY-HNCO quantitative $J_{N-C'}$ experiment[99] (Section 3.5). Two experiments are used in that approach with the peak intensity being modulated by $J_{N-C'}$ during the C′ evolution period. The experiment with the optimal intensity is called a reference experiment. In order to use the reference experiment for measuring the H–N couplings, Vijayan and Zweckstetter

added a third TROSY-based HNCO experiment, where an amplified H–N coupling evolution period is inserted right after the constant-time ^{15}N evolution period. The cross peaks appear at $\omega_N - (\kappa + 1)\pi^1 J_{NH}$ along the ^{15}N dimension in the third experiment, while in the reference spectrum they appear at $\omega_N - \pi^1 J_{NH}$. The H–N couplings can be extracted readily from these two experiments. By sharing the same reference experiment and acquiring the three experiments in an interleaved manner, the experiment can save up to 25% instrumental time. The experiment has been demonstrated on both ^{13}C/^{15}N-labeled 0.8 mM ubiquitin and 0.8 mM DcuS (17 kDa). The experiment is applicable for proteins which can yield a TROSY-HNCO spectrum with $S/N > 20{:}1$ in a reasonable amount of time.

A 3D CBCA(CO)NH experiment has been developed to measure the one-bond couplings of $^{13}C_\alpha$–$^1H_\alpha$, $^{13}C_\beta$–$^1H_\beta$ and ^{13}C–^{13}C′[109] where four spectra are acquired in an interleaved manner. The $^{13}C_\alpha$–$^1H_\alpha$ and $^{13}C_\beta$–$^1H_\beta$ couplings are measured in a same manner as discussed earlier in this section.[120] The fourth experiment is the same as a regular CBCA(CO)NH (reference) experiment used to measure the couplings of $^{13}C_\alpha$–$^1H_\alpha$ and $^{13}C_\beta$–$^1H_\beta$, except that $J_{C'-C\alpha}$ is active in the step of $C' \rightarrow {}^{15}$N transfer for about 18.7 ms, not 9 ms as in the reference experiment. The C_α–C′ couplings can be extracted from the intensity ratio of the fourth and the reference experiments. Compared to the measurement of C_α–C′ couplings using an HNCO-based quantitative J modulation experiment,[80] the resolution of CBCA(CO)NH is usually lower. However, the low resolution is offset somewhat by the possibility that the C_α–C′ couplings can be extracted from both C_α and C_β resonances. Analysis showed that for an S/N ratio of 50:1 in the reference spectrum, a random error of 0.35 Hz is observed in $J_{C\alpha-C'}$ coupling measurement. The experiments have been demonstrated on both ^{13}C/^{15}N-labeled 0.8 mM ubiquitin and 0.8 mM DcuS (17 kDa).

A 3D CH_2-S^{3}CT HBCBCA experiment has been designed to measure eight couplings for CH_2–CH moiety in proteins and nucleic acids.[127] The pulse scheme is an extension of a 2D CH_2-TROSY experiment.[128] It is an out-and-back-type experiment where the magnetization starts from and ends at two $^1H_\beta$ protons. For simplicity, only one $^1H_\beta$ is shown in the following magnetization transfer pathway:

$$^1H_{\beta 2} \rightarrow {}^{13}C_\beta \rightarrow {}^{13}C_\alpha(t_1) \rightarrow {}^{13}C_\beta(CT, t_2) \rightarrow {}^1H_{\beta 2}(t_3).$$

During the C_α chemical shift evolution period (t_1), the couplings between C_α and the three protons ($^1H_\alpha$ and two $^1H_\beta$) are active, while the couplings between C_α and C_β, C′ and ^{15}N are refocused to increase the sensitivity. Similarly, during the C_β chemical shift evolution (t_2) period, the couplings between C_β and the three protons ($^1H_\alpha$ and two $^1H_\beta$) are active. There are no ^{1}H pulses between t_1 and t_2 periods, and thus the spin states of $^1H_\alpha$, $H_{\beta 2}$ and $H_{\beta 3}$ are preserved and each observable term has specific transition pathway. In the final stage, a CH_2 spin-state-selective scheme is used to transfer the magnetization from C_β to its attached two $^1H_\beta$ protons. The $^1H_\alpha$ spin experiences a net 360° rotation in the last steps since no pulses are applied on C_α in the last transition step. Finally, four components are observed for each cross peak as in a regular 3D HBCBCA experiment. Conceptually, eight couplings of $^1J_{C\alpha H\alpha}$, $^2J_{C\alpha H\beta 2} + {}^2J_{C\alpha H\beta 3}$, $^2J_{C\beta H\alpha}$, $^1J_{C\beta H\beta 2} + {}^1J_{C\beta H\beta 3}$, $^1J_{C\beta H\beta 2} - {}^2J_{H\beta 2H\beta 3}$, $^1J_{C\beta H\beta 3} - {}^2J_{H\beta 2H\beta 3}$, $^3J_{H\alpha H\beta 2}$ and $^3J_{H\alpha H\beta 3}$ can be extracted from the frequency displacement of the

corresponding two components in the 3D spectra. Interested readers can refer to the original work for the details on how to extract eight couplings from four components. Although both the precision of measurement and sensitivity are a concern since so many active couplings are allowed in the experiment, several nice features make the experiment a rather sensitive one. These features include (a) all the four observed components are relaxation favorable components; (b) significant linewidth broadening from small couplings such as $^2J_{C\alpha H\beta 2}$, $^2J_{C\beta H\alpha}$, $^3J_{H\alpha H\beta 2}$ and $^3J_{H\alpha H\beta 3}$ is removed; (c) finally, each coupling can be measured independently two to four times, improving the measurement precision. When tested on a 1.5 mM $^{13}C/^{15}N$-labeled third IgG-binding domain from Streptococcal Protein G (GB3), it was found the error was well below 0.5 Hz for the majority of the couplings. The application of the experiment is limited to certain residues with relatively isolated CH_2–CH moiety such as C, F, Y, W, D, N and H. Other residues do not interfere with the extraction of couplings from these residues since either the signals from the former are suppressed by a factor of 10 or larger, or the $^1H_\beta$ chemical shifts of the former are in regions different from the residues with relatively isolated CH_2–CH moiety.

4. MEASUREMENT OF RESIDUAL DIPOLAR COUPLINGS IN NUCLEIC ACIDS

Traditional NMR methods[74] for structure determination of nucleic acids rely mainly on distance restraints from NOE and dihedral angle restraints from scalar coupling. However, due to the low proton density, the amount of restraints measurable by the traditional NMR methods is not sufficient for computing precise and accurate structures. In addition, the elongated shape of nucleic acids makes it challenging to compute precise structures. The newly introduced RDC constraints provide much needed additional global restraints, since with RDCs the orientations of all the internuclear vectors in a nucleic acid can be evaluated with respect to a unique global frame. Most current experiments for measuring RDCs in nucleic acid bases use TROSY and MQ coherence schemes to minimize the loss of coherence by relaxation. Furthermore, E.COSY scheme is often employed to overcome peak overlap problems, especially for measuring RDCs in ribose. Compared to amino acids, the structural networks in nucleic bases are more complicated and the chemical shift ranges of both ^{13}C and ^{15}N are much wider. Therefore, shaped pulses are often used in the experiments. Shown in Fig. 9 are some measurable RDCs in nucleic acid bases.[129]

4.1. RDC measurement in nucleic acid bases

A suite of spin-state-selective excitation (S^3E)-IS(T) experiments have been developed to measure many one and two-bond couplings in purine and pyrimidine bases.[129] Showed in Fig. 10 is a basic experiment typical for measuring coupling in

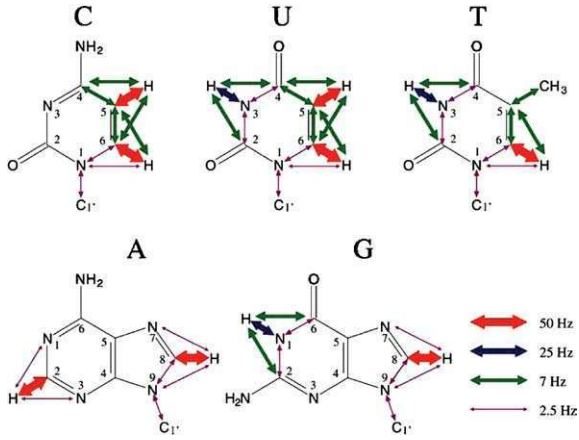

Fig. 9. Measurable Residual Dipolar Couplings in nucleic acid bases. The line thickness represents the upper limit of RDC magnitudes. The scale on right is calibrated to a maximal $^{1}D_{NH}$ coupling of 25 Hz. Reprinted from ref. 129, with permission from Springer Science and Business Media.

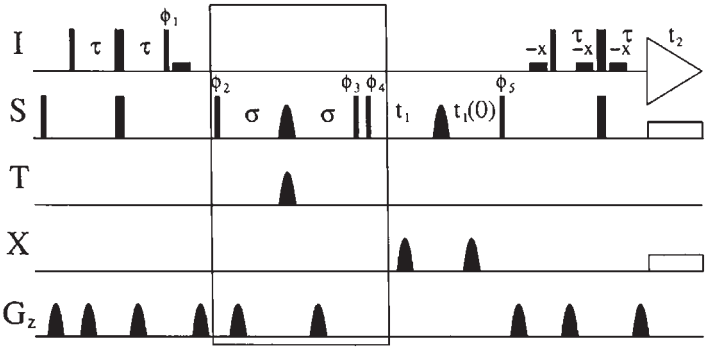

Fig. 10. A schematic representation of a basic S^3E IS[T] experiment. Narrow and wide bars indicate hard 90° and 180° pulses, respectively. Shown in the box is the S^3E element. The experiment can be used to measure the couplings of both S–T and I–T. More technical details can be found in the original paper. Reprinted from ref. 129, with permission from Springer Science and Business Media.

nucleic acids. The I spin represents ^{1}H, S represents either ^{13}C or ^{15}N dependent on which couplings are being measured. T is coupled to S, and X is decoupled from S during the chemical shift evolution of S spin. The unit in the rectangular box is an S^3E scheme,[39,40] which can separate S_xT^{α} and S_xT^{β} states into two sub-spectra. Furthermore, if nucleus T is coupled during both t_1 evolution and acquisition periods, the components of doublet in two sub-spectra shift in both S and I dimensions away from their respective resonance frequencies by the values of $\pm J_{S-T}/2$

and $\pm J_{I-T}/2$. When these two spectra are added, the doublet appear as typical E.COSY pattern. Different pulse sequences can be derived from this basic scheme by tuning the shaped pulses to measure many different one and two-bond RDCs as shown in Fig. 9. For example, HC[N] experiment yields the values of ^{1}D(N1C1′), ^{1}D(N1C6) and ^{2}D(N1H6) in pyrimidines, and ^{1}D(N9C1′), ^{1}D(N9C8) and ^{2}D(N9H8) in purines. HN[C] experiment measures ^{1}D(NC) and ^{2}D(C-H_N) couplings in H–N–C moieties of thymines, uracils and guanines. HC[C] experiment determines ^{1}D(CC) and ^{2}D(CH) couplings at positions 5 and 6 in pyrimidines. HN[H] experiment yields the couplings of ^{2}D(N1H2), ^{2}D(N3H2), ^{2}D(N7H8) and ^{2}D(N9H8) in purines. In the last experiment, the magnetization of the proton in moiety of H–C–N is transferred directly to the ^{15}N through two-bond scalar couplings because the one-bond $^1J_{NC}$ is too small. These experiments have been tested on a ^{13}C/^{15}N-labeled DNA hairpin and a 12-mer DNA duplex sample. The accuracy and precision of the RDC measurement have been discussed in great details in the original paper.[129]

MQ-HCN experiment plays a key role in correlating the ribose and base through the N_1 or N_9 nucleus.[130] HCN experiments have been reported from several groups. Here we only review the more recent ones.[62,131–133] The experiments use an out-and-back scheme and either correlate the three nuclei of moiety $H_{1'/6/8}$-$C_{1'/6/8}$-$N_{1/9}$, or directly correlate $H_{1'}$ with base $H_{6/8}$ using an $H_sC_sN_bC_bH_b$ scheme through the detection of three frequencies from five different nuclei, where *s* and *b* indicate, respectively, a ribose and base. Another interesting experiment is the bi-directional 3D MQ-HCNCH, which dictates all the five frequencies in the moiety of $H_sC_sN_bC_bH_b$, and is a powerful tool for correlating bases and riboses.[134] MQ-HCN experiment offers excellent resolutions and is very useful for the measurement of many different types of RDCs in nucleic acids. The RDCs of $C_{1'}$–$H_{1'}$, $C_{6/8}$–$H_{6/8}$ can be measured with a 3D MQ-HCN if the ^{13}C is not decoupled during the data acquisition. The 3D HCN experiment[130] with intrinsic high resolution is also a favorable choice for measuring large C–H couplings since there is no significant difference in relaxation rates between the different components of ^{1}H doublets. To measure the one-bond couplings of $C_{1'}$–$N_{1/9}$, and $C_{6/8}$–$N_{1/9}$ using the MQ-HCN experiment, a J_{CN} enhance factor (about five-fold amplification) is used in the ^{13}C chemical shift evolution. Since the spin states of ^{15}N are not perturbed after the t_2 period and no ^{15}N decoupling is applied during the data acquisition, the couplings of ^{15}N to both ^{13}C and proton make a doublet appear as an E.COSY pattern, and thus $^2J_{HN}$ can be readily extracted. This E.COSY-based MQ-HCN sequence can be used to determine the couplings of $C_{1'}$–$N_{1/9}$, C_6–N_1, C_8–N_9, $H_{1'}$–$N_{1/9}$, H_6–N_1 and H_8–N_9. Similarly, if the one-bond ^{13}C–^{13}C coupling is active during either the $C_{1'}$ or C_6 evolution period, the MQ-HCN experiment can measure the couplings of $C_{1'}$–$C_{2'}$ and C_6–C_5. If only $C_{1'}$ and C_6 are selectively decoupled, the two bond couplings of $H_{1'}$–$C_{2'}$ and H_6–C_5 can also be detected in an E.COSY pattern. All the experiments have been demonstrated on a 0.4 mM ^{13}C/^{15}N-labeled 18 bp DNA duplex in a 47 kDa ternary complexed with two proteins, CBF_β and CBF_α. The accuracy of measurement has been discussed and the RMSD from two independent measurements have been listed for RDCs of different spin pairs.

HC(C) hd-TROSY-E.COSY experiment measures $^{1}D_{CC}$ and $^{2}D_{CH}$ couplings in pyrimidines (U and C),[135] where "hd" stands for proton homo-decoupling. It is a pseudo-3D experiment where the ^{1}H and ^{13}C chemical shifts are labeled by using either a $C_5(t_1)$–$H_5(t_2)$–$H_5(t_3)$ or $C_6(t_1)$–$H_6(t_2)$–$H_6(t_3)$ scheme. During the $C_5(t_1)$ evolution, either the $^{1}J_{CC}$ coupling between C_5 and C_4 or that between C_5 and C_6 evolves selectively. During the $H_5(t_2)$ evolution, a proton homo-decoupling is used to suppress unwanted couplings. A very narrow spectral window is used in the t_2 dimension and the resulting aliasing is unfolded with the t_3 dimension to get a 2D [^{1}H, ^{13}C] correlated spectrum with a proton-decoupled ^{1}H dimension.[66] During the direct detection, no ^{13}C decoupling is applied. Since the α and β states of C_4 or C_6 are not mixed during the experiment, an E.COSY pattern appears which allows the couplings H_5–C_4 or H_5–C_6 be measured readily from the peak displacement along the ^{1}H dimension. The experiments can determine the couplings of $^{2}D_{C5-H6}$, $^{2}D_{C6-H5}$, $^{2}D_{C4-H5}$, $^{1}D_{C5-C6}$ and $^{1}D_{C4-C5}$. One bond couplings (C_5–H_5 and C_6–H_6) can also be measured with the sequence hd-TROSY. To measure the couplings of C_4–C_5 or C_5–C_6 in purines, an experiment called HCC(C)-TOCSY has been proposed. HCC(C) stands for H8C8C4(C5) or H8C8C6(C5) for guanine. Thus, the 3D experiment uses an out-and-back scheme with magnetization starting from H_8, and then being selectively transferred to either C_4 or C_6 through C_8. During the evolution of C_4 or C_6, one-bond coupling of C_4–C_5 or C_5–C_6 evolves. Thus, the couplings of C_4–C_5 or C_5–C_6 can be measured readily from the t_1 dimension (C_4 or C_6) in a well-resolved 3D spectrum. For adenine, the HCC(C) stands for H2C2C5(C4) or H2C2C5(C6), and the couplings of C_4–C_5 or C_5–C_6 can be measured in a similar fashion as discussed above. In addition, the couplings of C_8–H_8 and C_2–H_2 can be measured using an IPAP[38] version of [^{1}H, ^{13}C]-HSQC. The sequences have been demonstrated on both isotropic and anisotropic ^{13}C-labeled RNA oligomer (24 nt) with a concentration of 1.9 mM. Details of the measurement precision and shaped pulses can be found in the original work.[135]

MQ-HCN-QJ and TROSY-HCN-QJ experiments measure one-bond $^{15}N_{1/9}$–^{13}C RDCs.[136] These quantitative *J*-correlated MQ HCN experiments focus on the moiety of $H_{1'}$–$C_{1'}$–$N_{1/9}$ in nucleic acids. It combines the features of quantitative *J* correlation[49] with relaxation favored MQ coherence for the measurement of the couplings in an $H_{1'}$–$C_{1'}$ moiety.[132] The 3D MQ HCN uses an out-and-back scheme, after the magnetization is transferred to $N_{1/9}$. A constant-time period (2 T) is used for the evolution of ^{15}N chemical shifts. In the reference experiment, no couplings between $^{15}N_{1/9}$ and the three attached ^{13}C are evolved. In the *J*-modulated experiment, only a single coupling between $^{15}N_{1/9}$ and one of the three attached ^{13}C is active. Thus, the individual one-bond $^{15}N_{1/9}$–^{13}C couplings can be determined from the ratio of peak intensities of the two experiments. Similarly, a TROSY-HCN experiment[132] has been modified to measure the couplings of $^{15}N_{1}$– $C_{1'/2/6}$ and $^{15}N_{9}$– $_{1'/4/8}$. The sequences have been tested on a 1.5 mM $^{13}C/^{15}N$-labeled 24-nRNA oligomer. There is a detail discussion about the source of measurement errors in the original paper. The one-bond ^{13}C–^{15}N couplings can be measured accurately with uncertainties of ± 0.5 Hz provided that the S/N ratio is larger than 20:1 in the reference spectra.

4.2. RDC measurements in ribose and backbone of nucleic acids

In nucleic acids, the NOE constraints on backbone atoms is sparse. Consequently, the dihedral angles from three-bond *J* couplings play important roles in defining the backbone conformation. Recently, quantitative *J*-modulated [^{1}H, ^{13}C] CT-HMQC experiments have been proposed to measure $^{3}J(H_{3'}, P)$.[137,138] Here, a quantitative *J*-modulated CT-NOESY ^{31}P difference experiment is used to measure $^{1}H_{3'}$–^{31}P RDCs.[139] The scheme is composed of a reference and a *J*-modulated experiment. During the constant time period, the CSs of protons evolve, the couplings between $^{1}H_{3'}$ and other protons are removed by two selective 180° pulses on $^{1}H_{3'}$, while the couplings between $^{1}H_{3'}$ and ^{31}P are either coupled or decoupled in two separate experiments. Following the t_1 period, a long NOE mixing time (300 ms) is used so that the magnetization of $^{1}H_{3'}$ can be transferred to well-dispersed $^{1}H_{1'}$ or base protons. This results in a rather complete set of ^{1}H–^{31}P couplings. The sequence has been tested on a 12-mer DNA sample. The uncertainties of measured RDCs are <0.15 Hz.

3D HCcH-COSY and 3D Relay HCcH-COSY measure the couplings of $H_{2'}$–$C_{2'}$ and $H_{3'}$–$C_{3'}$ in RNA molecules.[140] The experiments are similar to a constant-time HCcH-COSY experiment proposed before.[141] The magnetization transfer scheme is as follows:

$$^{1}H_{1'}(t_1) \rightarrow {}^{13}C_{1'}(t_2) \rightarrow {}^{13}C_{2'} \rightarrow {}^{1}H_{2'}(t_3).$$

The experiment makes use of the good dispersion of $^{1}H_{1'}$–$^{13}C_{1'}$ to enhance the resolution of $^{1}H_{2'}$ region. To further reduce the overlap problem, an IPAP filter is used during the last reverse INEPT step so that the components of of $^{1}H_{2'}$ doublet can be separated into two sub-spectra. In the 3D relay HCcH-COSY experiment, the magnetization is further relayed to $^{13}C_{3'}$ from $^{13}C_{2'}$ and the signals of $^{1}H_{3'}$ are detected. One advantage of this approach is that no assignment for $^{13}C_{2'}$–$^{1}H_{2'}$ or $^{13}C_{3'}$–$^{1}H_{3'}$ are required in extracting RDCs for these two vectors as long as the $^{13}C_{1'}$–$^{1}H_{1'}$ can be assigned. The sequence has been tested on a 1.6 mM ^{13}C/^{15}N 42-nt RNA sample. The RMS errors are within 2.7 Hz for RDC values ranging from 32 to -32 Hz.

CH_2-S^{3}E HSQC is a 2D experiment tailored to measure the couplings of germinal $^{1}H_A$–$^{1}H_B$, and the sum of ^{13}C–$^{1}H_A$ and ^{13}C–$^{1}H_B$ couplings for the CH_2 groups in RNAs.[142] There are two novel features in the experiment. Firstly, an S^{3}E element is used to separate the upfield and downfield components of a ^{13}C triplet into two sub-spectra. Secondly, when the magnetization is transferred back from ^{13}C to ^{1}H, it is selectively transferred from the downfield component of a CH_2 triplet into the upfield components of the $^{1}H_A$–{$^{1}H_B$} and $^{1}H_B$–{$^{1}H_A$} doublets in a way similar to that used in SPITZE-HSQC experiment.[119] Thus, when two spectra are overlaid, E.COSY patterns appear. The displacements along the ^{13}C dimension are the sum of ^{13}C–$^{1}H_A$ and ^{13}C–$^{1}H_B$ couplings, while the displacements along the ^{1}H dimension are the $^{3}J_{HA-HB}$. The sequence has been applied to a 1.9 mM 24-nt ^{13}C-labeled RNA oligomer to extract the couplings of $^{1}H_{5'}$–$^{1}H_{5''}$ and the sum of $^{13}C_{5'}$–$^{1}H_{5'}$ and $^{13}C_{5'}$–$^{1}H_{5''}$ couplings.

3D H1C1C2 experiment measures five dipolar couplings from an $H_{1'}$–$C_{1'}$–$C_{2'}$–$H_{2'}$ moiety of RNA ribose sugars.[143] It is an E.COSY type experiment with out-and-back style. Starting from $H_{1'}$, the magnetization is transferred to $C_{2'}$ through $C_{1'}$ two constant-time periods are used for CS evolution of $C_{2'}(t_1)$ and $C_{1'}(t_2)$. Protons are not decoupled during both t_1 and t_2 periods when the ^{1}H spin-states are also retained. E.COSY patterns appear in the [$C_{1'}$, $C_{2'}$]-planes, from which the couplings of $C_{1'}$–$H_{1'}$, $C_{2'}$–$H_{2'}$, $C_{1'}$–$H_{2'}$, and $C_{2'}$–$H_{1'}$ can be extracted. Finally, when magnetization is transferred to $H_{1'}$ from $C_{1'}$, the $H_{2'}$ spin states are not perturbed. $H_{1'}$–$H_{2'}$ couplings can be measured from the frequency differences in $C_{2'}$–$\{H_{2'}\}$ doublets along the $H_{1'}$ dimension. The pulse sequence has been tested on a 1.9 mM ^{13}C-labeled RNA 24-nt oligomer. The random errors have been given for five different measured RDCs.

3D CH_2–S^3CT HBCBCA experiment measures eight couplings for the $C_{5'}$–$C_{4'}$ group innucleic acids.[127] Conceptually, the experiment is a modification of the approach used to measure eight couplings for CH_2–CH moiety in proteins. The eight couplings extracted from two 3D experiments are $^1J_{C4'-H4'}$, $^2J_{C4'-H5'} + {}^2J_{C4'-H5''}$, $^2J_{C5'-H4'}$, $^1J_{C5'-H5'} + {}^1J_{C5'-H5''}$, $^1J_{C5'-H5'}$-$^2J_{H5'-H5''}$, $^1J_{C5'-H5''}$−$^2J_{H5'-H5''}$, $^3J_{H4'-H5'}$ and $^3J_{H4'-H5''}$. The data analysis is similar to what have been discussed for the CH_2–CH groups in proteins. The sequence has been demonstrated on a 1.9 mM 24-nt ^{13}C-labeled RNA oligomer, out of 552 possible splitting, 508 can be obtained from an isotropic sample.

5. APPLICATIONS OF RDCs TO PROTEINS

With the advent of tunable alignment media about eight years ago, RDCs have been applied to study an increasing number of problems in biochemistry and structural biology ranging from automated backbone resonance assignment, structure determination, protein folding to ligand–protein and protein–protein interactions. In the following we will focus on the application of RDCs to study proteins. However, we will not discuss the application of RDCs to study protein dynamics in solution since that topic was reviewed extensively just a few years ago.[11]

5.1. Automated backbone resonance assignment

Chemical shift resonance assignment is a prerequisite for applying NMR spectroscopy to study proteins and nucleic acids in solution such as structure determination, the characterization of dynamics and ligand–protein, protein–protein interactions, and the elaboration of the mechanism of enzyme catalysis. The automation of resonance assignment is highly desirable since manual assignments can be very time consuming. The traditional approaches for automated assignment focus on either the through-bond triple-resonance or through-space NOE experiments. Recently, several algorithms have been developed to assign the resonances of backbone nuclei

using either RDCs alone or RDCs in combination with the NMR data used for the traditional approaches. These RDC-based automated assignment algorithms all require that either there exists an a priori structure[144–146] or intermediate structures can be determined on-the-fly.[147–150]

5.1.1. *Assignment requiring an a priori structure*

A bipartite-matching[†]-based protocol developed by Bruschweiler and coworkers[145] for backbone resonance assignment uses both NH RDCs and C_α, C_β chemical shifts but does not rely on any sequential NMR connectivity information. The algorithm requires ^{15}N and ^{13}C doubly labeled samples and triple-resonance experiments for C_α and C_β chemical shifts. The assignment problem is formulated in terms of a weighted bipartite-matching problem that can be solved in $O(n^3)$ time, where n is the number of residues. The weight for bipartite match is set to be

$$\chi^2 = \sum_i^n C(i, \pi(i)), \qquad C(i,j) = C_r(i,j) + KC_s(i,j) \tag{14}$$

where $\pi(i)$ is a permutation of 1,2 … n, $C_r(i, j)$ and $C_s(i, j)$ are, respectively, the differences between the experimental RDCs and the RDCs back-computed from the *a prior* structure using Eq. (11), and the experimental CSs and the average values for the corresponding amino acids in the BioMagResBank (BMRB) database. The K is the relative weight. The matrix C or C_r or C_s in Eq. (14) with elements $C(i, j)$ or $C_r(i, j)$ or $C_s(i, j)$ is called a cost matrix. The key steps of the algorithm are shown in Fig. 11. Though the bipartite-matching can be solved in $O(n^3)$ time, the complexity of the entire algorithm is actually more complicated since bipartite-matching is performed for each grid-point for three Euler angles α, β, γ, and it is not guaranteed that D_a and R values can be estimated accurately. Thus, the minimum weight computed by the algorithm is not guaranteed to be the real global minimum. In addition, since the assignment problem is formulated as a bipartite-matching problem, adding any sequential-connectivity information will make the problem NP-hard[‡], which means that it is difficult to extend the protocol to incorporate such information. The protocol has been applied to human ubiquitin using two or three RDCs per residue measured in a single medium (Pfl phage medium) together with C_α and C_β chemical shifts. The algorithm yields the correct assignment for more than 90% of the protein backbone resonances.

The NP-hardness of bipartite matching with (sequential connectivity) restraints was solved statistically in the program nuclear vector replacement (NVR)[144] using

[†]A bipartite graph is a graph $G = (V, E)$ with a set of nodes L and a set of nodes R such that $L \cap R = \varnothing$, $L \cup R = V$, and for all edges $(u, v) \in E, u \in L$ and $v \in R$. A bipartite-matching is a subset of edges of $M \subseteq E$ such that for all vertices $v \in V$, at most one edge of M is incident on v. A maximum bipartite matching is a matching of maximum cardinality.[151]

[‡]NP-hard means that the running time of the algorithm increases exponentially with the size of the input.

1. Convert experimental C_α and C_β chemical shifts into cost matrix C_s
2. Estimate from RDCs the initial values for axial and rhombic components of the alignment tensor, D_a and R.
3. WHILE convergence has not been reached,
   (a) Choose new Euler angles α, β, γ.
   (b) Compute the cost matrix C based on the a prior structure and chemical-shift difference.
   (c) Solve the weighted matching problem.
   (d) Define the subset of peptide planes that show good agreement between experimental RDCs and the RDCs predicted from the a prior structure.
   (e) Refine Euler angles α, β, γ and the alignment tensor D_a and R values on this subset with the assignment obtained in step c.
   (f) Compute a new cost matrix C.
   (g) Solve weighted matching problem.
4. END WHILE

Fig. 11. A bipartite-matching algorithm for backbone resonance assignment. Grid-search is used for choosing Euler angles α, β, γ in steps 3(a) and 3(e).

expectation/maximization (E/M) method[§]. NVR is built upon CS prediction algorithms (ShiftS and ShiftX) and bipartite-matching algorithm to perform assignment using RDCs measured in two aligning media in combination with unambiguous backbone H_N–H_N NOE restraints (d_{NN}) and amide-proton exchange (HD) data. HD data is used to identify surface residues. NVR is divided into two phases: tensor determination and resonance assignment phases. In the first phase, chemical shift predictions from the BMRB database, ShiftS and ShiftX, d_{NN} restraints, and HD data are used to make a small number of assignments using an E/M method. Specifically, this phase attempts to assign at least five peaks for the purpose of determining the two alignment tensors directly by *singular-value decomposition* (SVD).[153] The estimated tensors are then used to convert RDCs into probabilistic constraints in the resonance assignment phase. Seven bipartite graphs were built in the second phase: B_{HD}, B_{BMRB}, B_{NOE}, B_{SHIFTS}, B_{SHIFTX}, B_{RDC1} and B_{RDC2}. The six graphs B_{HD}, B_{BMRB}, B_{SHIFTS}, B_{SHIFTX}, B_{RDC1} and B_{RDC2} were then synchronized and used in an E/M step for updating the assignment by the maximum-bipartite-matching. However, B_{NOE} was used after the E/M step to make more assignment using d_{NN} restraints since the maximum-bipartite-matching algorithm cannot handle d_{NN} restraints. This step is called Apply-NOE step. Each cycle of the E/M step followed by the Apply-NOE step made at least one assignment. The algorithm stops when all the residues have been assigned. The alignment tensors were also updated in each cycle of the E/M step followed by the Apply-NOE step. The a priori structure required by NVR can be either an X-ray structure with the identical protein sequence or homologous structure. The algorithm requires only uniform ^{15}N-labeled sample and ^{1}H–^{15}N HSQC spectrum, ^{1}H–^{15}N RDCs, and sparse backbone d_{NN} restraints from a 3D ^{15}N-edited NOESY spectrum. NVR runs in minutes and can efficiently assign the ^{1}H–^{15}N backbone resonances as well as the

[§]E/M is an algorithm for computing maximum likelihood estimates from incomplete data.[152] The maximum returned from an E/M is not guaranteed to be the global maximum.

sparse NOE restraints d_{NN} from the 3D ^{15}N-NOESY spectrum, in $O(n^3)$ time. Though the best solution obtained from NVR is not guaranteed to be the real global minimum since E/M can only achieve local maximum, NVR performed rather well in practice. NVR has been tested on several proteins: human ubiquitin (76 residues), hen lysozyme (129 residues) and streptococcal protein G (56 residues) where for ubiquitin, RDCs were matched to four different structures, including one mutant (homolog). NVR achieved an average assignment accuracy of over 99% when the CS errors for amide proton $^{1}H_N$ and amide nitrogen ^{15}N were set to be, respectively, ± 0.01 and ± 0.1 ppm.

Jung and Zweckstetter have developed an *ad-hoc* algorithm, MARS,[146,154] for sequential assignment of backbone resonances based on (a) the chemical shift predication obtained via a secondary structure prediction method and (b) the identification of amino acid types from the chemical shifts for C_α, C_β and C'. MARS requires an ^{15}N and ^{13}C doubly labeled sample and triple-resonance experiments. The original MARS algorithm[154] was extended to incorporate RDCs where RDCs are used essentially for filtering out the false positives in connectivity obtained from the original MARS using chemical shift information alone. In case of small proteins and with three RDCs per residue, MARS[146] can assign more than 90% of backbone resonances with an assignment reliability of 56% without the need for sequential connectivity information. For bigger proteins, the combination of sequential connectivity information with RDC-matching enables more residues to be assigned. In MARS, RDC-enhanced assignment is particularly useful when chemical shifts and sequential connectivity only provide a few reliable assignments. Since there are many manual steps and the performance of the algorithm depends critically on a set of parameters such as the error ranges set for C_α, C_β chemical shifts, the worst-time complexity[¶] of MARS is most likely to be exponential. For examples, in practice, the running time for malate synthase G (723 residues) vary from 2 h using C_α, C_β, C' connectivity with the thresholds of 0.2, 0.4 and 0.15 ppm for C_α, C_β, C', respectively, to 13 h using only C_α, C_β connectivity with thresholds of 0.2 and 0.4 ppm, respectively, and up to 150 h when only C_α, C_β connectivity information is available with a resolution of 0.5 and 0.5 ppm, respectively. Since RDCs is used only for enhancing the reliability, the extension of MARS to RDCs is also expected to be exponential in the worst-case. MARS with RDCs requires an *a prior* structure for matching the experimental RDCs with the RDCs back-computed from the *a prior* structure.

5.1.2. *Simultaneous assignment and structure determination*

Prestegard and coworkers[148] have developed a protocol for simultaneous backbone resonance assignment and structure determination with the intermediate structures computed on-the-fly. The protocol requires chemical shifts of protons, nitrogen and carbons from triple-resonance experiments. Six RDCs per residue in two media (12

[¶]The worst-time complexity means the longest possible running time of the algorithm with particular inputs.

RDCs per residue) were used to compute the structures and filter the false connections obtained from the CSs of C_α and C_β alone. The (ϕ, ψ) angles connecting a pair of peptide planes were systematically varied and the best (ϕ, ψ) values were selected by comparing the back-computed RDCs with the 12 RDCs (six in each medium) in each peptide plane (nine unique for a pair of planes). Additional peptides were then added along with other RDCs (3–6 RDCs) to extend the fragments to lengths of 6–16 residues. In the case of a small protein rubredoxin (54 residues), geometries for six fragments, each separated by a single proline, were identified. These fragments were then combined using the fact that fragments must be oriented so that the principal order frames as viewed from each fragment must coincide. In most cases, bonding restrictions imposed by the single connecting proline provided unique translational positioning. RDC data from a second medium helped to resolve any remaining 4-fold orientational degeneracy of the individual order frames. This brute-force algorithm is exponential with the number of residues since it varies (ϕ, ψ) angles of each residue systematically by grid-search. The algorithm was tested on a 4.5 mM ^{15}N-labeled rubredoxin while ^{13}C experiments were performed on natural abundance. For the collection of the six types of RDC data, a phase-modulated HSQC experiment[51] (Section 3.1), a soft HNCA-E.COSY experiment[117] (Section 3.7) and a 2D IP-HSQC experiment[112] (Section 3.7) were selected. Both the original HNCA-E.COSY pulse sequence and the IP-HSQC pulse sequence were modified for acquiring dipolar couplings from natural abundance ^{13}C protein samples.

Meiler and Baker have also developed an automated simultaneous resonance assignment and structure determination approach[149,150] using RDCs in combination with NOEs and CSs. The original version[149] relies on a *de novo* protein structure prediction algorithm, ROSETTA and a Monte-Carlo (MC) procedure that searches for the assignment of resonances to atoms that produces the best fit to the experimental NMR data to candidate 3D structures from ROSETTA. A large ensemble of models is generated from sequence information alone by ROSETTA, an optimal assignment is identified for each model, and the models are then ranked based on their fit with the NMR data using the previously identified assignments. The original method was tested on nine protein sequences between 56 and 140 amino acids and *published* CS, NOE and RDC data. The procedure yielded models with backbone RMSD between 3 and 6 Å, and, in four of the nine cases, the partial assignments obtained by the method could be used to refine the structures to high resolution (0.6–1.8 Å) by repeated cycles of structure generation guided by the partial assignments, followed by reassignment using the newly generated models. With the *published* NOEs, the distances given in the NOE lists were replaced with intensities computed from Cr^{-6} where C and r are, respectively, a constant and the internuclear distance. However, it is not clear from the paper how the NOE intensity is generated if only a range of distances, rather than a single distance is reported. When the protocol is applied to *real* NMR data acquired on a 140 amino acids fumarate sensor, DcuS, the original approach can only generate a fold with a 6.0 Å backbone RMSD with respect to the structure determined by either a traditional NMR method or X-ray diffraction. The real NMR data consists of 1,100 CS signals, 3,000 NOESY cross

peak intensities, and 209 RDCs extracted directly from the original spectra. After both the X-ray and NMR structures become available, the approach was modified by weighting the assignment against a wide range of models generated from various structure prediction techniques,[150] in addition to those models generated from ROSETTA. The new procedure improves both the accuracy and assignment. With the new protocol, the backbone fold was refined to an accuracy of 3.7 Å RMSD from a previous 6.0 Å RMSD obtained from the original protocol.

An approach called CAP has also been developed for simultaneous assignment and tertiary structure determination of RNAs.[147] The approach has been demonstrated on a uniformly ^{15}N–^{13}C doubly labeled 27 nt variant of the trans-activation response element (TAR) RNA from HIV-I. The approach involves examination of all the allowed sequence-specific resonance assignment permutations for best-fit agreement between measured RDCs and RDCs back-computed from the coordinates for sub-structures in a target RNA. Using idealized A-form geometries to model Watson–Crick helices and coordinates from a previous X-ray structure to model a hairpin loop in TAR, the best-fit RDC assignment solutions are determined very rapidly (<5 min of computational time) and are in agreement with the corresponding NOE-based assignments. Orientational constraints derived from RDCs are used to assemble sub-structures into an RNA tertiary conformation. The approach can assign the resonance in minutes for the 27 nt RNA though the algorithm is exponential in the worst-case. More specifically, the exhaustive search performed by CAP over all permutations makes it difficult to scale up to larger RNAs.

5.2. Structure Determination using RDCs

Three dimensional structures are critical for understanding biochemical functions of proteins at atomic level, structure-based drug design and genomic annotation. The application of RDCs to structure determination can be classified into three categories based on the roles RDCs played in the computation:

1. Refinement by RDCs of structures computed mainly from NOE and other NMR restraints.
2. *De novo* structure determination using RDCs in combination with other NMR restraints.
3. *De novo* structure determination using RDCs alone.

These algorithms also differ in how all the conformations consistent with the experimental data are searched. The main search methods are the following:

1. Simulated annealing (SA) in combination with molecular-dynamics (MD) simulation.
2. MC method for assembling the structural fragments[‖] obtained from the Protein data bank (PDB) by best matching the experimental RDCs with all the fragments in the PDB.

[‖]A structural fragment consists of m consecutive residues ($m \geqslant 7$ in general).

3. Systematical search over all the possible conformations determined by backbone dihedral angles computed directly from RDCs.

For the structure determination of native proteins, the goal of the search is to find a conformation which has the minimum pseudoenergy. The terms for the pseudoenergy also differ greatly in different algorithms with MD/SA has the most elaborate energy terms including all the molecular mechanics energy terms and pseudoenergy terms for various NMR restraints. The pseudoenergy terms in the last two approaches are much simpler. The results of the applications of various algorithms to experimental NMR data were summarized in Table 2. Those algorithms for simultaneous resonance assignment and structure determination have been described above and will not be repeated here.

5.2.1. *Refinement*

RDCs were first applied to refine NMR structures computed using mainly NOE distance restraints and scalar couplings by restrained MD in combination with SA approach for searching the conformational space. In these approaches, RDCs are incorporated as an additional pseudoenergy term[155,156] while the relative orientation between the alignment tensor and the molecular frame is kept in flow during the structure computation. The Saupe elements (alignment tensor) are either estimated by grid search[93] or from RDC powder pattern[94] obtained from multiple RDCs measured in a single aligning medium. The quality of structures was improved greatly by the addition of several RDC restraints per residue.[156] Up to now, refinement remains to be the most frequent application of RDCs to protein structure determination.

5.2.2. *RDC in combination with other NMR restraints*

Several research groups[157–159] have developed different approaches to compute structures using *mainly* backbone RDCs in combination with a relatively small amount of NOE distance restraints and scalar couplings. In the input, the amount of NMR restraints other than RDCs were, typically, <7 per residue. Brown and coworkers[157] has applied MD/SA to compute the fold of human ubiquitin using more than three RDCs per residue in two media in combination with backbone H_N–H_N NOEs. Using the MD/SA approach implemented in Xplor/CNS to search the conformational space, the computed structures have 1.40 Å backbone RMSD with respect to the X-ray structure[73] (Table 2). Using both RDCs and sparse NOEs (about seven NOEs per residue), Kay and coworkers[158] computed the global fold of maltose-binding protein (MBP, 370 residues) in complex with the substrate beta-cyclodextrin. Initial structures were calculated using Xplor/CNS with default parameters on the basis of 1943 NOE distance restraints of H_N–H_N, H_N–CH_3 and CH_3–CH_3, 48 hydrogen bond and 555 dihedral angle restraints. The computed structures have large numbers of violations of RDC restraints, with distortion of peptide plane geometry. Next, the structure was refined using one-bond HN, C_α–C′, N–C′, two-bond H_N–C′ and three-bond H_N–C′ RDCs to compute the

discrete orientations of each peptide plane. These RDCs were measured using the methyl-protonated, ^{15}N, ^{13}C, ^{2}H-labeled MBP sample with TROSY-based HNCO pulse sequences as described in ref. 77 (Section 3.1). The orientation which best matches that in the initial NMR structures calculated from NOE and dihedral angle restraints exclusively is used to refine further the structures using a new module written for the program Xplor/CNS. When applied to experimental data recorded on MBP, the precision of the family of structures generated improves from 5.5 to 2.2 Å, while the backbone RMSD with respect to the X-ray structure is reduced from 5.1 to 3.3 Å. The protocol was further improved[159] by direct refinement of structures against measured dipolar couplings and the changes in anisotropic carbonyl CSs upon alignment using MD/SA in torsion-angle space (torsion angle dynamics protocol in Xplor/CNS).

5.2.3. *RDC Alone*

Recently, approaches have been developed to determine backbone structures or folds using RDC data alone or in combination with very sparse NOEs. The approaches include RDC-restrained MD [157,160], molecular fragment replacement (MFR) methods[24,161–163], and positioning of ideal α-helices oriented by RDCs.[164]

Bruschweiler and coworkers[160] employed a least-square fitting procedure followed by MD/SA to compute a backbone structure using five RDCs per residue in two media. All the backbone (ϕ, ψ) angles, together with the seven independent Saupe elements required to convert the RDC data into orientational restraints, were estimated by a least-square fitting procedure with many variables (more than 100 variables even for the small protein human ubiquitin). It is not guaranteed that the least-square fitting procedure can find the real global minimum and thus the Saupe matrices and (ϕ, ψ) angles may have large errors. However, the next MD/SA step may greatly reduce these errors. Baker and Rohl[162] have developed a database-based approach Rosetta-NMR where they incorporated RDCs into their *ab initio* structure prediction method Rosetta. In Rosetta-NMR, RDCs were first employed to select structural fragments from the PDB. The whole structures constructed from the chosen fragments were further refined by Rosetta using a MC method. In principle, their method can work with any number of RDCs per residue but the accuracy with fewer than two RDCs per residue was relatively poor (Table 2). All these algorithms use heuristic methods such as simulated annealing[157,160] or MC simulation[162] to find a solution. The fragment replacement method was pioneered by Bax and coworkers;[24] their method used five RDCs per residue in two media plus CSs to select seven-residue fragments from the PDB. Following the same idea, Levy and coworkers[161] have developed an approach to compute the fold of ubiquitin using five RDCs per residue measured in a single medium. The key feature of their approach is that they employed a filter that requires overlapping fragments to select the same structural form. The approach was tested with ubiquitin. Compared with the fold for ubiquitin computed from five RDCs per residue in two media, the fold by their approach was less accurate. A different approach was demonstrated by Prestegard and coworkers,[164] where RDCs were used only to orient ideal α helices.

However, in their study the helices were not refined any further using the experimental RDCs, and no β sheet structure was computed.

Wang and Donald have developed *ab-initio* algorithms[25,82,165,166] for computing backbone structures using a few NOEs and 2 RDCs per residue in one or two different aligning media. Specifically, the algorithms (Fig. 12) compute the conformation and global orientations of individual secondary structure elements, independently, by an exact solution, systematic search-based minimization method using only two RDCs per residue. The systematic search (Fig. 13) is built upon quartic equations for computing, *exactly* and *in constant time,* the directions of an internuclear vector from RDCs, and linear or quadratic equations for computing the sines and cosines of backbone dihedral (ϕ, ψ) angles from two vectors in consecutive peptide planes. In contrast to heuristic search such as SA or MC used by other NMR structure determination algorithms, the minimization algorithm can be analyzed rigorously in terms of expected algorithmic complexity and the coordinate precision of the protein structure as a function of error in the input (experimental) data. The algorithm has been successfully applied to compute the backbone structures of three proteins (Table 1) using experimental NMR data. Compared with MD/SA-based or database-based methods, the results demonstrated that the exact solution and systematic search based algorithms can achieve similar or better accuracy (Table 2).

5.2.4. *Fold recognition by RDCs*

Xu and coworkers[167] have developed a computer program, RDC-PROSPECT, for the identification of a structural homolog or analog of a target protein in the PDB, which best matches the ^{1}H–^{15}N RDC data of the protein recorded in a single ordering medium. The identified structural homolog/analog can then be used as a starting model for RDC-based structure calculation. Since RDC-PROSPECT uses only RDC data and secondary structure information predicted from protein sequence by the program PSIPRED, its performance is virtually independent of sequence similarity between a target protein and its structural homolog/analog, making it applicable to protein targets out of the scope of current protein threading techniques. RDC-PROSPECT identifies a structural fold through finding a template fold in the PDB, which best aligns with NH RDC data, secondary structure prediction and gap penalty. The best alignment here means to minimize the following scoring function:

$$\Sigma\left[\omega_1 \frac{\left|r_i - r'_{\mathrm{A}(i)}\right|}{\sigma} + \omega_2 M\left(S_i, S'_{\mathrm{A}(i)}\right)\right] + \Sigma pG_j \tag{15}$$

where r_i and $r'_{A(i)}$ are, respectively, the experimental RDC and the RDC back-computed from the aligned template structure $A(i)$ for residue i; S_i and $S'_{A(i)}$ are, respectively, the predicted secondary structure type of position i of the target protein and the assigned secondary structure of position $A(i)$ of the template structure and $M(S_i, S'_{A(i)})$ is a function of secondary structures; pG_j is the gap penalty for the

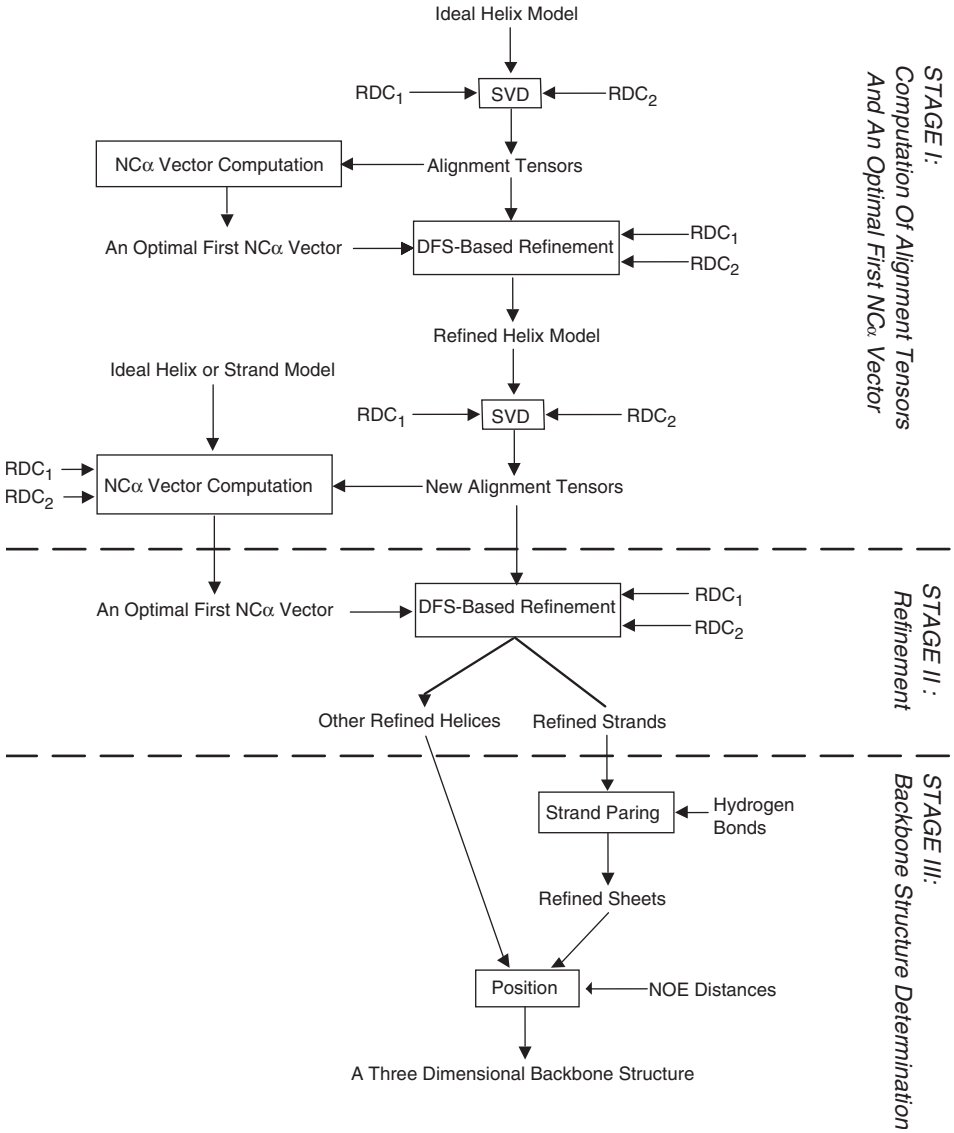

Fig. 12. A flow chart illustrating the algorithm. A chart illustrating the three major stages (delimited by two dashed lines) of the algorithm beginning with the input RDC data and ideal helix and strand models to a final 3D backbone structure. RDCs refer to RDCs measured in two media. As stated in the main text, stage I is an iterative process for refining the helix and computing alignment tensors. DFS refers to depth-first search and SVD refers to singular value decomposition. Reprinted from ref. 25, with permission from Springer Science and Business Media.

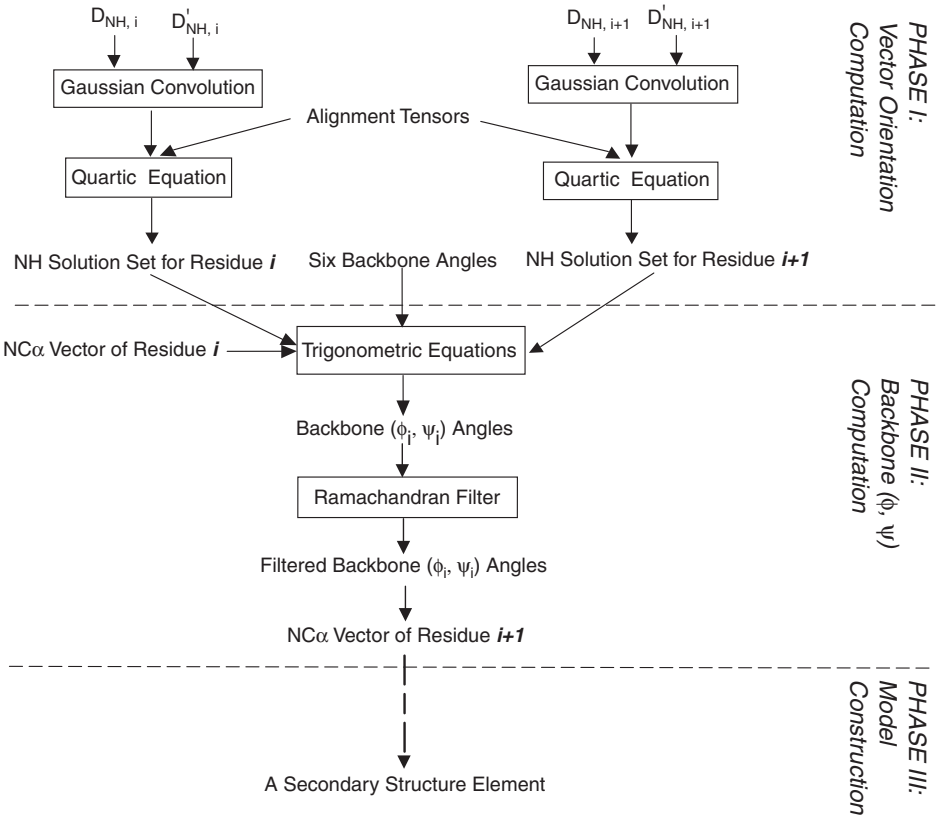

Fig. 13. A flow chart of a single step of the DFS-based refinement stage. The three major phases are delimited by two dashed lines. Refer to the original paper[25] for the definitions of the six angles, the quartic and trigonometric equations. The Ramachandran filter represents filtering through the favorable Ramachandran regions and the Gaussian convolution corresponds to the simulation of the experimental error by a Gaussian distribution with the experimental RDC values in two different media ($D_{NH,i}$ or $D'_{NH,i}$) as its mean and the error as its variance. Many such steps are required for refining a secondary structure element as shown by a dashed arrow. Reprinted from ref. 25, with permission from Springer Science and Business Media.

*j*th gap in the alignment; ω_1 and ω_2 are weights. The minimization is achieved by a dynamic programming (DP)**. The RDC-PROSPECT program has been tested on all ^1H–^{15}N RDC data (representing 33 proteins) available in the BMRB database and the literature (by October 2003). The program correctly identified the structural

**Dynamic programming[151] is a computational technique for finding a global extreme (minimum or maximum) for those optimization problems where the problem can be solved, recursively, through the solutions to the subproblems of the same form and the original problem can be solved by using the solutions to the subproblems many times. In dynamic programming, the solutions to the subproblems are saved in a table.

Table 1. Results of our algorithm on 3 proteins; experimental RDC data for Ubiquitin, Dini and Protein G was taken from the BMRB. The second column indicates how many residues were in either α helicesor β sheets. The given RMSD values were computed by comparing the oriented and translated secondary structure elements computed by our algorithm to existing structures. Ubiquitin to a high-resolution X-ray structure; Dini to one NMR structure; and Protein G to on NMR structure (with no β-strands)

Protein	α/β residues	RDCs	Type of RDCs	Hydrogen bonds	NOEs	RMSD(Å)
Ubiquitin	39/75	78	NH, NH in two media	12	4	1.23
Ubiquitin	41/75	76	NH, CH in one medium	12	4	0.97
Dini	41/81	75	NH, CH in two media	6	9	1.55
Dini	41/81	80	NH, $C_\alpha C'$ in one medium	6	9	1.35
Protein G	29/56	53	NH, NH in two media	9	4	0.98
Protein G	33/56	61	NH, $C_\alpha C'$ in one medium	9	4	1.30

Table 2. Comparison of the ubiquitin backbone structure computed by our algorithm with the best structures computed by existing heuristic approaches

Programs	Techniques	Number of restraints per Residue	Accuracy(Å)	Reference
Xplor/CNS	MD/SA	6 RDCs	1.40	157
SCULPTOR	MD/SA	11 RDCs,	1.00	160
MFR	Database	10 RDCs, 5 Chemical shifts	1.21	24
Rosetta-NMR	Database/MC	3 RDCS, 5 Chemical shifts	1.65	162
Rosetta-NMR	Database/MC	1RDCS	2.75	162
	Exact solution/ systematic search	2 RDCs	1.45	25

folds for approximately 80% of the target proteins, significantly better than previously reported results, and achieved an average alignment accuracy of 97.9% residues within 4-residue shift. The authors claimed that RDC-PROSPECT is at least one order of magnitude faster than previously reported algorithms for principal order frame search, making the algorithm fast enough for large-scale applications.

Griesinger and coworkers[168] have developed a program, DipoCoup, for structural homology search using RDCs in combination with secondary structure prediction based on NMR CSs. Annila and coworkers[169] are the first to use assigned RDC to search for structural homologs, while Levy and coworkers have also developed an approach to recognize the structural motif using RDCs[170]. More recently, Langmead

and Donald have developed an approach for identifying protein folds from sequences using *unassignedRDCs*.[171] The interested readers can refer to their original papers for the details.

5.3. Protein folding

A very interesting recent application of RDCs is to study the structures of denatured proteins and the protein-folding process. Understanding how a protein can fold, in less than a second, from the denatured state to the native state, is a fundamental problem in structural biology. Such knowledge also has biochemical applications ranging from structure prediction to protein design. Moreover, it may provide clues to the causes of certain diseases such as Alzheimer's, which appears to involve misfolding of the amyloid protein. Though much progress has been made in understanding the folding process in recent years, some fundamental questions remain. One of them is the distribution of structures in the denatured state.[172–174] In contrast to the *native state* where a single conformation dominates, the denatured state appears to be an ensemble of heterogeneous random coils,[172,175] a conclusion reached through the measurement of radius of gyration by small-angle X-ray scattering.[176] The quantification of such structure distribution will be critical for answering two key questions in protein-folding: (a) are the denatured structures random-coils? and (b) are the denatured structures native-like? If stable nativelike topologies persist on unfold states as claimed by some studies using RDC data measured in the denatured state,[177–179] it may be straightforward to explain the rapid refolding kinetics displayed by many proteins. However, if no such native-like topology exists in the denatured state,[180–182] some unknown mechanisms must be responsible for the observed fast rates of refolding. RDCs measured in the denatured state may provide quantitative answers to these perplexing questions.

5.3.1. *Alignment media for denatured proteins*

The possibility of measuring RDCs on denatured proteins was first demonstrated by Shortle and coworkers.[177,183] They reported the measurement of RDCs in the denatured forms of the protein staphylococcal nuclease, a small $\alpha + \beta$ protein of 149 amino acids, oriented in either strained polyacrylamide gels,[32,184] a bicelle medium, and a liquid crystalline phase formed by a cationic lipid: cetylpyridinium bromide. All the three types of media can be used at high urea concentrations. While polyacrylamide gels and bicelles produce similar alignment tensors through steric interactions, a liquid crystalline phase of cetylpyridinium bromide aligns denatured nucleases along a different set of axes, presumably through electrostatic effects.

5.3.2. *Native-like topology persistent in the denatured state*

Shortle and Ackerman[177] observed a highly significant correlation among NH RDCs for individual residues between the denatured and native states of a 131-residues

(residues 10–140) fragment system of staphylococcal nuclease. Their result suggested that a native-like spatial positioning and orientation of chain segments (topology) persist to concentrations of at least 8.0 M urea. The RDC data demonstrated that long-range ordering can occur well before a folding protein attains a compact conformation, a conclusion not anticipated by any of the standard models of protein folding. In another study, Shortle and coworkers[178] measured both NH and CH RDCs at a low pH, urea denatured state and the native state in order to characterize the long-range structure that persists in the unfolded form of a 70-residue protein eglin C. When the data sets for the two different structural states were compared, a statistically significant correlation was found between the RDCs measured in the denatured and native states with a correlation coefficient of $r = 0.47$ for CH RDCs and $r = 0.51$ for NH RDCs. The authors claimed that the finding directly demonstrated that the denatured state of eglin C had a native-like global structure. They further developed a simple simulation procedure to show that the degree variation in (ϕ, ψ) angles that yields a RDC correlation of $r = 0.5$ was inversely dependent on the statistical segment length, ranging from $\pm 6^\circ$ to $\pm 30^\circ$ at the upper limit.

The persistence of native topology was also used by Poulsen and coworkers[179] to explain the RDCs measured in the denatured state of bovine acyl-coenzyme A-binding protein (ACBP) oriented in strained polyacrylamide gels. ACBP is an 86-residue protein consisting of four helices, A1, A2, A3 and A4. The data includes RDCs measured under denaturing conditions (pH 2.3 and 2.5 M GuHCl), no-denaturing conditions (pH 2.5 and 2.8) and the native state. The data were analyzed using the MFR program[24] (Section 5.2.3), which demonstrated alpha-helix propensity in four isolated stretches along the protein backbone of ACBP, and these four stretches coincide with the location of the four native helices. This is in agreement with the findings based on secondary CS values. The authors further showed that replacement of the hydrophobic side-chain of residue Ile27 with alanine in helix A2 leads to large decreases of RDCs in residues that form helix A4 in the native state. The results suggest that the Ile to Ala mutation changes the probability for the formation of long-range interactions, which are present in the acid-denatured state of the wild-type ACBP. These long-range interactions are similar to those proposed to form in the transition state of folding of ACBP. The application of RDCs in combination with a comparative mutation study thus demonstrated the presence of precursors to the folding transition state under acid-unfolding conditions. The NH RDCs were measured from spin-state-selective (S^3CT) filtered ^1H-^{15}N-HSQC experiments[41,55] (Sections 2.2 and 3.1), while C_α–C', C'–^{15}N, and C_α–$^1H_\alpha$ dipolar couplings were measured from 3D HNCO-based experiments[84,97] (Sections 3.2 and 3.7). The RDCs were extracted by frequency-displacement method.

5.3.3. *No native-like topology in the denatured state*

Annila and coworkers[180] try to explain, theoretically, the characteristics of the RDCs on the denatured state using random-walk on 2D plane with reflection walls. The reflection here models the effects of aligning medium on the motion of the

dissolved proteins. A 2D random-walk model is used since exact expressions for various probabilities are readily available in 2D, while a 3D random-walk is much more complicated.[185] The denatured structure was modeled as a random-flight chain.[175] They applied the probability distributions for a 2D random-walk with reflection walls[186] to calculate RDCs and residual CSAs measured on the denatured proteins. Their calculations yield chain length and residue position-dependent values of RDCs which is in good agreement with simulations. Thus, it is not necessary to use native-like topology to explain the RDCs measured on the denatured state. However, the proposed model is rather crude since it may introduce errors to describe the alignment in 3D solution with a 2D random-walk with reflecting walls. Errors may also be introduced in their model by using a homopolymer to represent a heteropolymer such as a protein in solution.

Gronenborn and coworkers[181] as well as Wright and coworkers,[182] also questioned, experimentally, the hypothesis that the RDCs in the denatured state must be interpreted using similarity to the native state. Gronenborn and coworkers[181] studied a destabilized mutant of the B1 domain of protein G (GB1), a 56-residue small protein consisting of four α helices and the β sheet. They systematically investigated the equilibrium unfolding by recording backbone NH RDCs, the tryptophan N_{ε}–H resonance and the amide nitrogen transverse relaxation rates (*R2s*) for varying pH values and different temperatures. The NH RDCs were recorded with a sensitivity-enhanced E.COSY method[79] (Section 3.1) and extracted by frequency displacement. The backbone NH RDCs indicated that prior to complete unfolding, two melting hot spots were formed at the turn around T11, L12 and K13 and the N terminus of the helix at A24 and T25. The RDCs for the low pH, thermally unfolded state of GB1 were very small and did not indicate the presence of any native-like structure. Amide nitrogen transverse relaxation rates for GB1 in the folded state at different temperatures exhibited large contributions from exchange processes and the associated dynamics displayed considerable heterogeneity. After a careful analysis of the RDC and NMR relaxation data they believed that the data provided clear evidence for intermediate conformations and multi-state equilibrium unfolding and folding for this GB1 variant.

Wright and coworkers studied the conformational propensities of the unfolded states of apomyoglobin by measurement of NH RDCs. Weak alignment of apomyoglobin in acid and urea-unfolded states was induced with both stretched and compressed polyacrylamide gels. For the acid-unfolded states, NH RDCs were measured in ^{15}N,^{13}C-labeled protein using a 3D HNCO IPAP pulse program because of poor ^{1}H resonance dispersion. The RDCs were extracted by frequency displacement. In 8 M urea solution at pH 2.3, conditions under which apomyoglobin contains no detectable secondary or tertiary structure, significant RDCs of uniform sign were observed for all residues. At pH 2.3 in the absence of urea, a change in the magnitude and/or sign of the RDCs occurs in local regions of the polypeptide where there is a high propensity for helical secondary structure. These results are interpreted on the basis of the statistical properties of the unfolded polypeptide chain, viewed as a polymer of statistical segments. For a folded protein, the magnitude and sign of the RDCs depend on the orientation of each bond vector

relative to the alignment tensor of the entire molecule, which reorients as a single entity. For unfolded proteins, there is no global alignment tensor; instead, RDCs are attributed to alignment of the statistical segments or of transient elements of secondary structure. For apomyoglobin in 8 M urea, the backbone is highly extended, with ϕ and ψ dihedral angles favoring the β or P(II) regions. Each statistical segment has a highly anisotropic shape, with the N–H bond vectors approximately perpendicular to the long axis, and becomes weakly aligned in the anisotropic environment of the strained acrylamide gels. Local regions of enhanced flexibility or chain compaction are characterized by a decrease in the magnitude of the RDCs. The formation of a small population of helical structure in the acid-denatured state of apomyoglobin leads to a change in sign of the RDCs in local regions of the polypeptide; the population of helix estimated from the RDCs is in excellent agreement with that determined from CSs. They further claimed that the above alignment model for the denatured apomyoglobin can also explain the patterns of RDCs reported previously for the denatured states of staphylococcal nuclease and all other denatured proteins.

Sosnick and coworkers[174] generated an unfolded state ensemble using a self-avoiding random-walk based-statistical coil model using the frequencies for the backbone (ϕ, ψ) angles in a coil library, a subset of the PDB. The model reproduces two apparently contradicting behaviors observed in the chemically denatured state for a variety of proteins, random coil scaling of the radius of gyration and the presence of significant amounts of local backbone structure as indicated by the existence of RDCs in the denatured state. The most stretched members of their unfolded ensemble dominate the RDC signal, whereas the uniformity of the sign of the couplings follows from the preponderance of polyproline II and β conformers in the coil library. Agreement with the NMR data substantially improved when the backbone conformational preferences included correlations arising from the chemical and conformational identity of neighboring residues. Although the unfolded ensembles match the experimental observables, they do not display evidence of native like topology. One concern about their model is that the ensemble for the *denatured* state was generated using, *exclusively,* the (ϕ, ψ) angles appeared in the PDB where only the structures of *native* states are present.

5.4. Protein–ligand interaction

Ligand–protein interaction plays key roles in many biological processes and has been the focus of structure-based drug design. Solution NMR spectroscopy can be used to investigate such interactions. Furthermore, even when a crystal structure of the ligand–protein complex is available, NMR is still very useful for providing complementary dynamical information in solution. It is well documented that both the bound ligand and the binding site on the protein are rather dynamical in solution, at least for most ligand–protein systems.[187,188] Previously, CS perturbation, intermolecular NOEs, transfer NOEs in particular, and possibly relaxation measurement are

the main techniques for quantifying ligand–protein interactions by NMR. More recently, RDCs measured on the bound ligand have been applied to characterize the ligand–protein interactions. In combination with other methods such as SAR by NMR, RDCs can potentially become a tool for high-throughput screening for ligands that bind the target proteins.

Prestegard and coworkers[189] have used RDCs to investigate the conformation of trimannoside and the differential motion at the glycosidic linkages. Each of the three pyranose rings that make up trimannoside was considered a separate rigid molecular fragment. In the structure of trimannoside, ring III is situated between rings I and II. Using the RDCs to derive the generalized degree of order, which in turn is used to assess the extent of motion experienced by a rigid fragment, it was shown that internal motion between rings III and I is restricted but that inter-ring motion between rings III and II is more significant. As a result, the relative orientation of rings III and I can be determined by superimposing their alignment tensors. Doing the same for rings III and II is not possible, as it would result in a motionally averaged orientation because the alignment tensors are not equivalent. Thus, they concluded that there exist differential motions among the three rings.

Bax and coworkers[190] measured both NH and CH RDCs (including both backbone and sidechain CH RDCs) of a ligand (an undecapeptide analog) that is in fast exchange between a free state and a state where it is bound to a macroscopically ordered membrane protein (MII intermediate photoreceptor rhodopsin). RDCs were used to determine the peptide orientation with respect to the membrane by Xplor/CNS. Furthermore, RDCs in combination with NOE distance restraints obtained from transfer NOE experiments were input into the Xplor/CNS program to determine the structure of the bound peptide. The approximate distance restraints of the bound conformation were derived from transferred NOEs, as measured from the difference of NOES Y spectra recorded prior to and after photoactivation. However, it is rather tricky to interpret the RDCs measured on a ligand that is in fast exchange between a free state and a bound state. Several dynamic processes occurred simultaneously: the tumbling of membrane with respect to the external magnetic field, the motion of ligand in the bound state, and the ligand-exchange between the free and bound forms. The authors showed that with a simplifying assumption it is possible to use a uniform scaling factor to interpret all the RDCs, and use the interpreted RDCs in combination with NOEs to compute the structures of the bound ligand.

Prestegard and coworkers[191] have used RDCs to determine the average orientation of α-methyl mannose bound to mannose–binding protein, and Prestegard and coworkers[192] have examined the lectin protein Galectin-3 in the absence and presence of the disaccharide LacNAc by measuring NH RDCs of both the free and complexed forms of Galectin-3. A comparison of the RMSD values for RDCs measured on Galectin-3 in solution and for RDCs calculated from a crystal structure suggests that there may be small conformational differences between the unliganded and liganded solution structures of Galectin-3. Interested reader can refer to the original papers for the details.

5.5. Protein–protein interaction

Protein–protein interaction is fundamental for understanding the working of a cell as a coherent unit since it plays key roles in many biological processes such as signal transduction pathways, metabolic pathways and genetic regulatory networks. At heart of these biochemical activities is the problem of molecular recognition, the physical basis for the specificity in individual pathways and in communication between different pathways and the regulatory networks. In particular, the details of protein–protein interaction are the basis for understanding why receptors interact with particular targets, and how the proteins of one pathway can be insulated from related signaling components of the other pathways, and for the development of drugs specifically targeting the interfaces of protein–protein interactions. Current experimental techniques for studying protein-protein interaction at atomic detail are mainly X-ray diffraction and NMR spectroscopy. However, it is rather difficult to crystallize a protein–protein complex due to the transient nature of many protein–protein interactions. Furthermore, crystal packing may have larger effects on the interface between two proteins than on the core of the individual proteins. Studying protein–protein interaction using NMR also is challenging. First, the complex may be too large to be characterized in detail by NMR. Second, the intermolecular NOEs are in general weak, again due to the low S/N ratio caused by the size of the system and the inherent dynamical nature of the protein–protein interaction. However, helped by TROSY techniques, RDC alone or in combination with other NMR parameters such as CS perturbation and intermolecular NOEs have been increasingly used to characterize the interaction. The details of the interactions obtained from NMR depend on the amount of experimental data: ranging from the relative orientation between two proteins by RDC alone, to the atomic detail of the interface by RDCs in combination with either CS perturbation, or intermolecular NOEs or molecular force fields with terms such as the electrostatic and VDW interactions between the two proteins. In the following, we focus on the application of RDCs to studying protein–protein interactions. Readers who are interested in other NMR techniques for mapping protein–protein interactions should refer to an excellent recent review by Zuiderweg[193].

5.5.1. *Protein–protein orientation by RDCs*

Given the structures of two proteins or domains, Prestegard and coworkers[194] have developed an approach to orient them using RDCs measured on the complex by SVD. Given a structure of a protein and the experimental RDCs, an alignment tensor $\mathbf{S}$ can be computed by using SVD to minimize the RDC RMSD, E_r, with $E_r = \sqrt{\Sigma_{i=1}^{n}(r'_i - r_i)^2/n - 1}$ where n is the total number of RDCs, r_i and r'_i are, respectively, the experimental RDC for residue i of the protein and the RDC back-computed from the structure using the tensor $\mathbf{S}$ by Eq. (11). As shown in Eq. (11), given a structure, r'_i is a function of $\mathbf{S}$ so by minimizing E_r, $\mathbf{S}$ can be computed by SVD.[153] After the diagnolization of the alignment tensor $\mathbf{S}$ computed by SVD, the relative orientation of the two domains in a common POF can be obtained. However,

there exists four-fold degeneracy in the relative orientation obtained from RDCs measured in a single aligning medium. The authors also compared the alignment tensor computed from SVD with that computed by SA as implemented in Xplor/CNS[93,195] where additional restraints can be added. They applied the approach to orient the domains B (residues 59–81) and C (residues 100–126) of Barley lectin (BL), a 126-residue protein. Comparison of principal order frames (POFs) as separately determined for each domain indicates that the two domains are not oriented as in the crystal structure of wheat germ agglutinin, a highly homologous protein (approximately 95% sequence identity to protein BL). Furthermore, differences in the alignment tensors suggest that the two domains are not statically positioned but are experiencing different reorientational dynamics.

In a study reported by Bax and coworkers,[196] the relative orientations of monomers in the tetrameric human normal adult carbonmonoxy-hemoglobin have been determined in solution at near-physiological conditions of pH, ionic strength, and temperature using ^{1}H–^{15}N RDCs measured in both bicelles and Pf1 phages by TROSY-based sequences[3,61] (Section 3.5). The input individual structures are derived from X-ray diffraction. The relative orientations obtained by fitting the X-ray structures to individual types of RDCs using either an SVD[153] method or a nonlinear least-squares method, were found to be a dynamic intermediate between two previously solved crystal structures, known as the R and R2 states. In combination with exchange broadening at the subunit interface, the authors concluded that a rapid equilibrium exists between different structures that presumably include the crystallographically observed states.

In an interesting paper by Zhang and Zuiderweg,[197] the relative orientation of two lobes of a 44-kDa nucleotide-binding domain (NBD) of the 70-kDa heat shock cognate (Hsc70) chaperone has been determined by an SVD method using RDCs in a single aligning medium measured by TROSY techniques[77] (Section 3.1). The pulse sequence was optimized for NBD by selecting a best value for the parameter *k*. NBD allosterically regulates, by binding either ADP or ATP in a cleft between the two main lobes, the chaperoning affinity of the attached substrate-binding domain of Hsc70 and is also a center of interaction with cochaperones that couple into the allostery. The orientation of two lobes computed from RDCs in solution deviates up to 10° from their positions in 14 superimposing X-ray structures. Additional orientational differences of subdomains within the lobes, also from the analysis of the RDC data, unveil that the Hsc70 NBD in solution exists as a flexible molecular machine that can adjust the relative positions of all of its four subdomains.

Blackledge and coworkers[198] have developed an approach for computing the diagonalized Saupe matrix elements S_{yy} and S_{zz} (what they really computed is D_α and R but they are equivalent to S_{yy} and S_{zz}, see Eqs. (11) and (12)) and the orientation of a POF in a molecular frame as specified by three Euler angles (α, β, γ). These five parameters are computed by a least-square minimization of the following target function over all n couplings associated with a given domain:

$$\chi^2 = \sum_n \frac{r_i - r_i'(D_a, D_r, \alpha, \beta, \gamma, v_i)}{\sigma_i} \tag{16}$$

where r_i and $r'_i(D_a, D_r, \alpha, \beta, \gamma, \mathbf{v}_i)$ are, respectively, the experimental RDC for internuclear vector i and the RDCs back-computed from the structure, $\mathbf{v}_i$ is the orientation of the vector i in a molecular-fixed frame, α, β, γ define the orientation of POF relative to the molecular-fixed frame; σ_i is the uncertainty in the experimentally measured coupling. The minimization algorithm searches the D_a, D_r, α, β, γ parametric space by random variation of these parameters, using a combination of simulated annealing, temperature regulation using fuzzy logic and Levenberg–Marquardt minimization. However, this approach is less accurate and slow compared with the method based on SVD followed by diagnolization to compute the same five parameters.

5.5.2. *Protein–protein interface by RDCs in combination with other NMR restraints*

Since RDCs can only provide the information on relative orientation of two proteins, translational restraints such as distance restraints must be supplied in order to obtain the interaction interface between two proteins. Such distance information can be in different forms: intermolecular NOEs, transfer NOEs, paramagnetic relaxation enhancements (PREs), vdW and electrostatic interactions as well as those NMR parameters such as CS perturbation, which are complicated functions of the internuclear distances.

The details of protein–protein interaction can be obtained through the structure determination of the entire complex using RDCs in combination with other NMR restraints. For example, Clore and coworkers[199] have determined the solution structure of the first protein–protein complex of the bacterial phosphoenolpyruvate: sugar phosphotransferase system between the N-terminal domain of enzyme I (EIN) and the histidine-containing phosphocarrier protein (HPr) using RDCs in combination with other NMR restraints. More often, RDCs in combination with other geometric restraints have been used to determine the interface between two proteins with known individual structures. Clore and coworkers[200] have developed an approach based on conjoined rigid body/torsion angle dynamics and simulated annealing for determining the relative orientations of covalently linked protein domains using RDCs. In this approach, each domain is treated as a rigid body and the relevant degrees of conformational freedom are restricted to the backbone torsion (ϕ, ψ) angles of the linker between the two domains. The translational restraints were provided by the requirement that the standard geometric configuration must be kept for the linker. The target function for the minimization included both the RDC and energy terms for keeping standard configuration for the linkers. This approach was first applied to compute the relative orientation of the two-halves of a domain-swapped dimer of the HIV-inactivating protein cyanovirin-N,[200] and later to determine the structure of the complex between the cytoplasmic A domain (IIA(Mtl)) of the mannitol transporter II(Mannitol) and the HPr of the *E. coli* phosphotransferase system.[201].

In a more recent application, Prestegard and coworkers[202] have used RDCs to characterize the relative orientation of a 95 kDa homotrimeric complex of the acyltransferase protein, LpxA (UDP-*N*-acetylglucosamine acyltransferase) and acyl carrier protein (ACP). NH RDCs for perdeuterated ACP were measured by a

TROSY-based method. The bound state RDCs for ACP were calculated from the following equation since the experimentally measured RDCs for ACP bound to LpxA correspond to an average between the free state and bound state of ACP.

$$r_b = \frac{r_o - x_f r_f}{x_b} \tag{17}$$

where r_b is the RDC in the bound state, r_o the observed RDC, x_f the fraction of ACP in the free state, r_f the RDC measured in the free state and x_b the fraction of ACP in the bound state. x_f and x_b were estimated from the known value ($2.0\,\mu M^{-1}$) for the K_m of ACP to LpxA. The transverse relaxation in the bound state is ignored. The calculated bound RDCs were first used to compute the alignment tensor for ACP by SVD. With the computed alignment tensors by SVD, the program HADDOCK1.1[203] was used to dock ACP onto LpxA using RDCs, ambiguous interaction restraints (AIRs) derived from mutagenesis data and CS perturbation data.

McCoy and coworkers have developed a method for docking two proteins with known structures using RDCs in combination with CSs[204] with the goal to replace the distance derived usually from intermolecular NOEs with restraints derived from CS perturbations. The authors showed the structure built from the crystal structures of EIN and HPr in their uncomplexed form and docked with both RDCs and CS perturbations, places HPr within 2.5 Å of the position determined from the mean NMR structure of the EIN–Hpr complex. The relative position of the two proteins was obtained indirectly by minimizing the difference between the observed CS perturbations with the theoretical perturbations predicated by SHIFTS 3.0 (David Case, Scripps).

Gronenborn and coworkers[205] have used RDCs in combination with CS mapping, biochemical knowledge about point-to-point interactions, and contact potentials to select and filter structural models of the complex generated by docking of known substructures such as individual proteins or domains. The program FTDOCK[206] is used for docking the substructures. The empirical contact potentials are between a pair of residues from the two docking substructures, the point-to-point interaction is set to be between two Cα–Cα atoms obtained from biochemical data. The models from the FTDOCK are ranked by RDCs using a Q factor, Q, defined as $Q = \sum_{i=1}^{n}(r'_i - r_i)^2 / \sum_{i=1}^{n}(r'_i - r_a)^2$ where n is the total number of RDCs, r_i and r'_i are, respectively,the experimental RDC for residue i of the protein and the RDC back-computed from the structure using the tensor S computed by SVD, r_a is the average RDC value. If $Q<0.5$ the structures from FTDOCK is then selected. The CS perturbation data were used for ranking as follows. The perturbation data are first clustered into several patches on each protein surface. Next the number of contacts between the patches from the two docking proteins are counted and the docked structures from FTDOCK are then ranked based on the number of contacts. The power of RDCs for selection was demonstrated by the determination of protein–protein complexes using the EIN/HPr complex as an example and for establishing the domain–domain orientation in a chimeric protein, the recently determined hybrid human-*E . coli* thioredoxin.

Nakamura and coworkers[207] has combined the distance restraints extracted from saturation transfer (SAT) experiment with RDCs to compute the protein–protein

complex. To detect the region of the complex molecule responsible for the interaction between two proteins by cross saturation measurements, both ^{2}H, ^{15}N-labeled and non-labeled molecules were prepared. Saturation was applied with a WURST-20 adiabatic pulse. The reduction ratios of the peak intensities in the two ^{1}H–^{15}N HSQC spectra with and without cross saturation were simulated by a relaxation matrix using the proton coordinates of the protein–protein complex. The simulated ratios were then applied to the calculation of the pseudo potential energy, $E_s = \sum(\eta_s - \eta_e)^2/2$ where η_s and η_e are respectively the simulated and experimental reduction ratios. RDCs were measured by the pulse sequences as described in ref. 50 (Sections 2.4 and 3.1). A MD/SA program was developed to compute the complex structure by combining the pseudoenergy term for SAT, E_s, as computed above, and a term for RDCs with Amber96 force field. The method was successfully applied to determine the complex between the CAD domain of mouse caspase-activated deoxyribonuclease (CAD-CD: residues 1–87) and the CAD domain of its inhibitor (ICAD-CD: residues 1–100).

A computational approach HADDOCK (high ambiguity driven protein–protein docking) based on restrained MD/SA (Xplor/CNS) has been developed by Bonvin and coworkers[203] to incorporate, systematically, RDCs and other distance restraints. HADDOCK makes use of biochemical and/or biophysical interaction data such as CS perturbation data resulting from NMR titration experiments or mutagenesis data. This information is introduced as AIRs to drive the docking process. An AIR is defined as an ambiguous distance between two residues shown to be involved in the interaction. The accuracy of the approach is demonstrated with three molecular complexes. For two of these complexes, for which both the complex and free protein structures have been solved, NMR titration data were available. Mutagenesis data were used in the last example. In all cases, the best structures generated by HADDOCK, that is, the structures with the lowest intermolecular energies, were the closest to the published structure of the respective complexes (within 2.0 Å backbone RMSD).

6. CONCLUSIONS AND FUTURE PERSPECTIVES

Since the first successful demonstration of the tunable alignment of ubiquitin in an anisotropic LC medium only eight years ago, we have witnessed a flurry of new developments in NMR pulse techniques for the measurement of an increasing number of RDCs on both backbone and sidechain internuclear vectors. The development focuses on (a) reducing spectral overlap through various spin-state selection techniques, (b) increasing the signal-to-noise ratio through the minimization of magnetization loss by relaxation and (c) saving spectrometer time and improving data quality by simultaneous measurement of several kinds of RDCs in a single experiment. During the same short eight years, the applications of RDCs have expanded from the original goal of improving the quality of biomolecular structures computed using mainly NOE distance restraints, to dynamics of biomolecules, automated CS resonance assignment, protein folding, ligand–protein and protein–protein interactions. However, some hurdles remain before RDC

measurement and applications become a routine NMR technique accessible to non-NMR-specialized biochemists and structural biologists. It is not always easy to find the right alignment medium or conditions for some biomolecules, and thus a better understanding of the alignment mechanism will be useful. New measurement techniques for improving both the S/N ratio and spectral resolution are always desirable, especially for large-sized proteins and protein–protein complexes. Compared to the internuclear vectors in the protein backbone region, there are not many experiments available for the RDC measurements of internuclear vectors in the sidechains. The sidechain RDCs, especially carbon–carbon RDCs, can provide indispensable information for both the structural and dynamic study of large and perdeuterated proteins. It is still tricky to interpret and apply the measured RDC values quantitatively. As shown in Eqs. (6)–(12), the interpretation of the measured RDCs can be complicated, especially the separation of dynamics from structural information. This is because it is not easy to obtain the necessary dynamical information by either experimental or theoretical approaches to deconvolve structural information from dynamic one. As for the application of RDCs to structure determination, it has been rather subjective as far as the quality of the computed structures is concerned. In fact, the following problem exists for NMR structural determination in general: if heuristic methods such as SA or MC are used to search the conformational space, the computed structures are not guaranteed to be the real global minimum; that is, these search methods may themselves introduce additional errors. Furthermore, these heuristic methods make it very tricky to correlate the precision of the computed structures with the experimental errors. Structure determination algorithms using RDCs which can overcome the above problems are highly desirable. When RDCs are applied to determine the ligand–protein or protein–protein interactions, care must be taken that the relative orientation between two biomolecules is not perturbed by the alignment. When RDCs are used to study the conformations of denatured proteins, it is critical that the alignment does not favor certain conformations over the others. A systematic investigation of the effects of alignment on the biochemical properties of the aligned biomolecules is needed for assuring the minimum perturbation in these RDC applications. In summary, we expect continuing development of better pulse techniques for RDC measurement, especially for the sidechain RDCs. With these improved techniques, we believe that RDCs will be applied to more biological systems to answer complicated questions in biochemistry and structural biology by providing quantitative structural and dynamical information, which can not be easily obtained from other current biophysical techniques.

ABBREVIATIONS

2D	two dimensional
3D	three dimensional
AP	anti-phase

BMRB	BioMagResBank
CH	the vector between C_α and H_α
CSA	chemical-shift anisotropy
CT	constant time
DD	dipole–dipole
DFS	depth-first search
$^1D_{NH}$	residual dipolar coupling of internuclear vector between amide nitrogen and amide proton
E.COSY	exclusive correlation spectroscopy
FID	free-induction decay
H-bond	hydrogen bond
H–D	exchange experiment, hydrogen–deuterium exchange experiment
HMQC	heteronuclear multiple quantum coherence
HSQC	heteronuclear single quantum coherence
INEPT	insensitive nuclei enhanced by polarization transfer
IP	in-phase
LC	liquid crystal
MC	Monte Carlo
MD	molecular dynamics
MQ	multiple quantum
NH	the internuclear vector between amide nitrogen (N) and amide proton (H)
NMR	nuclear magnetic resonance
NOE	nuclear Overhauser effect
NOESY	nuclear Overhauser effect spectroscopy
PDB	protein databank
POF	principal order frame
RDC	residual dipolar coupling
RMSD	root mean square deviation
SA	simulated annealing
S^3CT	spin-state-selective coherence transfer
S^3E	spin-state-selective excitation
SQ	single quantum
SVD	singular variable decomposition
TROSY	transverse relaxation optimized spectroscopy
ZQ	zero-quantum.

ACKNOWLEDGMENTS

We would like to thank Prof. G. A. Webb for asking us to write the review, and for his encouragement, support and patience. We would like to thank Prof. Erik Zuiderweg for teaching us biomolecular NMR. Lincong Wang would like to thank

Prof. Bruce Donald for his support. Lincong's work is supported by National Institutes of Health (R01 GM 65982) to Prof. Bruce Donald of Computer Science Department, Dartmouth College. We would like to thank Quincy Teng for numerous discussions, Candace Seu and Mark Dizik for their reviewing the manuscript, and Yuan Chen for her encouragement.

REFERENCES

1. M. K. Rosen, K. H. Gardner, R. C. Willis, W. E. Parris, T. Pawson and L. E. Kay, Selective methyl group protonation of perdeuterated proteins, *J. Mol. Biol.*, 1996, **263(5)**, 627–636.
2. K. H. Gardner and L. E. Kay, The use of $^{2}H^{13}C$, ^{15}N multidimensional NMR to study the structure and dynamics of proteins, *Annu. Rev. Biophys. Biomol. Struct.*, 1998, **27**, 357–406.
3. K. Pervushin, R. Riek, G. Wider and K. Wuthrich, Attenuated t2 relaxation by mutual cancellation of dipole–dipole coupling and chemical shift anisotropy indicates an avenue to NMR structures of very large biological macromolecules in solution, *Proc. Natl. Acad. Sci. USA*, 1997, **94**, 12366–12371.
4. N. Tjandra and A. Bax, Direct measurement of distances and angles in biomolecules by NMR in a dilute liquid crystalline medium, *Science*, 1997, **278**, 1111–1114.
5. J. R. Tolman, J. M. Flanagan, M. A. Kennedy and J. H. Prestegard, Nuclear magnetic dipole interactions in field-oriented proteins: information for structure determination in solution, *Proc. Natl. Acad. Sci. USA*, 1995, **92**, 9279–9283.
6. R. Freeman and E. Kupce, New methods for fast multidimensional NMR, *J. Biomol. NMR*, 2003, **27(2)**, 101–113.
7. H. M. Al-Hashimi and D. J. Patel, Residual dipolar couplings: synergy between NMR and structural genomics, *J. Biomol. NMR*, 2002, **22(1)**, 1–8.
8. P. J. Lukavsky and J. D. Puglisi, Structure determination of large biological RNAs, *Methods Enzymol.*, 2005, **394**, 399–416.
9. D. MacDonald and P. Lu, Residual dipolar couplings in nucleic acid structure determination, *Curr. Opin. Struct. Biol.*, 2002, **12(3)**, 337–343.
10. L. Zidek, R. Stefl and V. Sklenar, NMR methodology for the study of nucleic acids, *Curr. Opin. Struct. Biol.*, 2001, **11(3)**, 275–281.
11. J. R. Tolman and H. M. Al-Hashimi, NMR studies of biomolecular dynamics and structural plasticity using residual dipolar couplings, *Annu. Rep. NMR Spectrosc.*, 2003, **51**, 105–166.
12. A. Bax, Weak alignment offers new NMR opportunities to study protein structure and dynamics, *Protein Sci.*, 2003, **12(1)**, 1–16.
13. R. S. Lipsitz and N. Tjandra, Residual dipolar couplings in NMR structure analysis, *Annu. Rev. Biophys. Biomol. Struct.*, 2004, **33**, 387–413.
14. J. H. Prestegard, C. M. Bougault and A. I. Kishore, Residual dipolar couplings in structure determination of biomolecules, *Chem. Rev.*, 2004, **104**, 3519–3540.
15. J. H. Prestegard, K. L. Mayer, H. Valafar and G. C. Benison, Determination of protein backbone structures from residual dipolar couplings, *Methods Enzymol.*, 2005, **394**, 175–209.
16. H. Valafar, K. L. Mayer, C. M. Bougault, P. D. LeBlond, F. E. Jenney Jr., P. S. Brereton, M. W. Adams and J. H. Prestegard, Backbone solution structures of proteins using residual dipolar couplings: application to a novel structural genomics target, *J. Struct. Funct. Genomics*, 2004, **5(4)**, 241–254.
17. L. D. Landau and E. M. Lifshitz, *The Classical Theory of Fields*, Pergamon Press, Oxford, 1980.
18. A. Abragam, *The Principles of Nuclear Magnetism*, Clarendon Press, Oxford, 1961.
19. L. Wang, A. V. Kurochkin and E. R. P. Zuiderweg, An iterative fitting procedure for the determination of longitudinal NMR cross—correlation rates, *J. Magn. Reson.*, 2000, **144**, 175–185.
20. A. Saupe, Recent results in the field of liquid crystals, *Angew. Chem.*, 1968, **7**, 97–112.

21. J. Meiler, J. J. Prompers, W. Peti, C. Griesinger and R. Bruschweiler, Model-free approach to the dynamic interpretation of residual dipolar couplings in globular proteins, *J. Am. Chem. Soc.*, 2001, **123**, 6098–6107.
22. J. R. Tolman, A novel approach to the retrieval of structural and dynamic information from residual dipolar couplings using several oriented media in biomolecular nmr spectroscopy, *J. Am. Chem. Soc.*, 2002, **124**, 12020–12030.
23. W. Peti, J. Meiler, R. Bruschweiler and C. Griesinger, Model-free analysis of protein backbone motion from residual dipolar couplings, *J. Am. Chem. Soc.*, 2002, **124**, 5822–5833.
24. F. Delaglio, G. Kontaxis and A. Bax, Protein structure determination using molecular fragment replacement and NMR dipolar couplings, *J. Am. Chem. Soc.*, 2000, **122(9)**, 2142–2143.
25. L. Wang and B. R. Donald, Exact solutions for internuclear vectors and backbone dihedral angles from NH residual dipolar couplings in two media, and their application in a systematic search algorithm for determining protein backbone structure, *J. Biomol. NMR*, 2004, **29**, 223–242.
26. L. G. Barrientos, C. Dolan and A. M. Gronenborn, Characterization of surfactant liquid crystal phases suitable for molecular alignment and measurement of dipolar couplings, *J. Biomol. NMR*, 2000, **16**, 329–337.
27. R. S. Prosser, J. A. Losonczi and I. V. Shiyanovskaya, Use of a novel aqueous liquid crystalline medium for high-resolution nmr of macromolecules in solution, *J. Am. Chem. Soc.*, 1998, **120(42)**, 110010–110011.
28. G. M. Clore, M. R. Starich and A. M. Gronenborn, Measurement of residual dipolar couplings of macromolecules aligned in the nematic phase of a colloidal suspension of rod-shaped viruses, *J. Am. Chem. Soc.*, 1998, **120**, 10571–10572.
29. M. R. Hansen, L. Mueller and A. Pardi, Tunable alignment of macromolecules by filamentous phage yields dipolar coupling interactions, *Nat. Struct. Biol.*, 1998, **5(12)**, 1065–1074.
30. B. W. Koenig, J. S. Hu, M. Ottiger, S. Bose, R. W. Hendler and A. Bax, NMR measurement of dipolar couplings in proteins aligned by transient binding to purple membrane fragments, *J. Am. Chem. Soc.*, 1999, **121**, 1385–1386.
31. K. Fleming, D. G. Gray, S. Prasannan and S. Matthews, Cellulose crystallites: a new and robust liquid crystalline medium for the measurement of residual dipolar couplings, *J. Am. Chem. Soc.*, 2000, **122**, 5224–5225.
32. R. Tycko, F. J. Blanco and Y. Ishii, Alignment of biopolymers in strained gels: a new way to create detectable dipole–dipole couplings in high-resolution biomolecular NMR, *J. Am. Chem. Soc.*, 2000, **122**, 9340–9341.
33. M. Ruckert and G. Otting, Alignment of biological macromolecules in novel nonionic liquid crystalline media for NMR experiments, *J. Am. Chem. Soc.*, 2000, **122**, 7793–7797.
34. S. Meier, D. Haussinger and S. Grzesiek, Charged acrylamide copolymer gels as media for weak alignment, *J. Biomol. NMR*, 2002, **24(4)**, 351–356.
35. J. F. Trempe, F. G. Morin, Z. Xia, R. H. Marchessault and K. Gehring, Characterization of polyacrylamide-stabilized Pfl phage liquid crystals for protein NMR spectroscopy, *J. Biomol. NMR*, 2002, **22(1)**, 83–87.
36. A. Bax, G. Kontaxis and N. Tjandra, Dipolar couplings in macromolecular structure determination, *Meth. Enzymol.*, 2001, **339**, 127–174.
37. K. Fleming and S. Matthews, Media for studies of partially aligned states, *Meth. Mol. Biol.*, 2004, **278**, 79–88.
38. M. Ottiger, F. Delaglio and A. Bax, Measurement of J and dipolar couplings from simplified two-dimensional NMR spectra, *J. Magn. Reson.*, 1998, **131(2)**, 373–378.
39. A. Meissner, J. O. Duus and O. W. Sorensen, Integration of spin-state-selective excitation into 2D NMR correlation experiments with the heteronuclear ZQ/2Q π rotations for $^{1}J_{XH}$-resolved E.COSY-type measurements of heteronuclear coupling constants in proteins, *J. Biomol. NMR*, 1997, **10(1)**, 89–94.
40. A. Meissner, J. O. Duus and O. W. Sorensen, Spin-state-selective excitation, Application for E.COSY-type measurement of j_{hh} coupling constants, *J. Magn. Reson.*, 1997, **128(1)**, 92–97.

41. M. D. Sorensen, A. Meissner and O. W. Sorensen, Spin-state-selective coherence transfer via intermediate states of two-spin coherence in IS spin systems: application to E.COSY-type measurement of J coupling constants, *J. Biomol. NMR*, 1997, **10**, 181–186.
42. C. Griesinger, O. W. Sorensen and R. R. Ernst, Two-dimensional correlation of connected NMR transitions, *J. Am. Chem. Soc.*, 1985, **107**, 6394–6396.
43. N. Tjandra and A. Bax, Large variations in 13C chemical shift anisotropy in proteins correlate with secondary structure, *J. Am. Chem. Soc.*, 1997, **119(40)**, 9576–9577.
44. W. Hu, Z. Zhang and Y. Chen, A high sensitivity 3D experiment for measuring $^{13}C_{\alpha} - {}^{1}H_{\alpha}$ residual dipolar coupling constants, *J. Magn. Reson.*, 2003, **165(2)**, 248–252.
45. P. Andersson, J. Weigelt and G. Otting, Spin-state selection filters for the measurement of heteronuclear one-bond coupling constants, *J. Biomol. NMR*, 1998, **12**, 435–441.
46. M. D. Sorensen, A. Meissner and O. W. Sorensen, ^{13}C natural abundance S3E and S3CT experiments for measurement of J coupling constants between $^{13}C_{\alpha}$ or $^{1}H_{\alpha}$ and other protons in a protein, *J. Magn. Reson.*, 1999, **137(1)**, 237–242.
47. B. Brutscher, Accurate measurement of small spin-spin couplings in partially aligned molecules using a novel J-mismatch compensated spin-state-selection filter, *J. Magn. Reson.*, 2001, **151**, 332–338.
48. G. T. Montelione and G. Wagner, Accurate measurements of homonuclear HN-H_{α} coupling constants in polypeptides using heteronuclear 2D NMR experiments, *J. Am. Chem. Soc.*, 1989, **111(14)**, 5474–5475.
49. A. Bax, G. W. Vuister, S. Grzesiek, F. Delaglio, A. C. Wang, R. Tschudin and G. Zhu, Measurement of homo-heteronuclear J couplings from quantitative J correlation, *Methods Enzymol.*, 1994, **239**, 79–105.
50. N. Tjandra, S. Grzesiek and A. Bax, Magnetic field dependence of nitrogen-proton j splittings in ^{15}N-enriched human ubiquitin resulting from relaxation interference and residual dipolar coupling, *J. Am. Chem. Soc.*, 1997, **118**, 6264–6272.
51. J. R. Tolman and J. H. Prestegard, A quantitative J-correlation experiment for the accurate measurement of one-bond amide 15N-1H couplings in proteins, *J. Magn. Reson.*, 1996, **112**, 245–252.
52. G. W. Vuister and A. Bax, Quantitative J correlation: a new approach for measuring homonuclear three-bond j(hnh.alpha.) coupling constants in ^{15}N-enriched proteins, *J. Am. Chem. Soc.*, 1993, **115(17)**, 7772–7777.
53. K. Pervushin, G. Wider and K. Wuthrich, Single transition-to-single transition polarization transfer (st2-pt) in [^{15}N,^{1}H]-TROSY, *J. Biomol. NMR*, 1998, **12**, 345–348.
54. K. Pervushin, Impact of transverse relaxation optimized spectroscopy (TROSY) on NMR as a technique in structural biology, *Q. Rev. Biophys.*, 2000, **33(2)**, 161–197.
55. M. H. Lerche, A. Meissner, F. M. Poulsen and O. W. Sorensen, Pulse sequences for measurement of one-bond ^{15}N–^{1}H coupling constants in the protein backbone, *J. Magn. Reson.*, 1999, **140**, 259–263.
56. J. H. Prestegard, H. M. al Hashimi and J. R. Tolman, NMR structures of biomolecules using field oriented media and residual dipolar couplings, *Q. Rev. Biophys.*, 2000, **33(4)**, 371–424.
57. J. H. Prestegard, J. R. Tolman, H. M. al Hashimi and M. Andrec, Protein structured dynamics from field-induced residual dipolar couplings, *Biol. Magn. Reson.*, 1999, **17**, 311–355.
58. J. R. Tolman and J. H. Prestegard, Measurement of amide ^{15}N–^{1}H one-bond couplings in proteins using accordion heteronuclear-shift-correlation experiments, *J. Magn. Reson. B*, 1996, **112(3)**, 269–274.
59. A. Bax and N. Tjandra, High-resolution heteronuclear NMR of human ubiquitin in an aqueous liquid crystalline medium, *J. Biomol. NMR*, 1997, **10**, 289–292.
60. B. Cutting, J. R. Tolman, S. Nanchen and G. Bodenhausen, Accurate measurement of residual dipolar couplings in anisotropic phase, *J. Biomol. NMR*, 2002, **23**, 195–200.
61. G. Kontaxis, G. M. Clore and A. Bax, Evaluation of cross-correlation effects and measurement of one-bond couplings in proteins with short transverse relaxation times, *J. Magn. Reson.*, 2000, **143**, 184–196.

62. J. P. Marino, J. L. Diener, P. B. Moore and C. Griesinger, Multiple-quantum coherence dramatically enhances the sensitivity of CH and CH2 correlations in uniformly ^{13}C-labeled rna, *J. Am. Chem. Soc.*, 1995, **119**, 7361–7366.
63. A. G. Cavanagh, J. Palmer III, P. E. Wright and M. Rance, Sensitivity improvement in proton-detected two-dimensional heteronuclear relay spectroscopy, *J. Magn. Reson.*, 1991, **91**, 429–436.
64. L. E. Kay, P. Keifer and T. Saarinen, Pure absorption gradient enhanced heteronuclear single quantum correlation spectroscopy with improved sensitivity, *J. Am. Chem. Soc.*, 1992, **114**, 10663–10665.
65. B. Luy and J. P. Marino, JE-TROSY: combined J- and TROSY-spectroscopy for the measurement of one-bond couplings in macromolecules, *J. Magn. Reson.*, 2003, **163(1)**, 92–98.
66. J. Boisbouvier, F. Delaglio and A. Bax, Direct observation of dipolar couplings between distant protons in weakly aligned nucleic acids, *Proc. Natl. Acad. Sci. USA*, 2003, **100**, 11333–11338.
67. C. W. Vander Kooi, E. Kupce, E. R. Zuiderweg and M. Pellecchia, Line narrowing in spectra of proteins dissolved in a dilute liquid crystalline phase by band-selective adiabatic decoupling: application to 1HN-15N residual dipolar coupling measurements, *J. Biomol. NMR*, 1999, **15(4)**, 335–338.
68. K. E. Kover and G. Batta, More line narrowing in TROSY by decoupling of long-range couplings: shift correlation and 1JNC′ coupling constant measurements, *J. Magn. Reson.*, 2004, **170(2)**, 184–190.
69. K. Pervushin and B. Vogeli, Observation of individual transitions in magnetically equivalent spin systems, *J. Am. Chem. Soc.*, 2003, **125(32)**, 9566–9567.
70. K. Pervushin, B. Vogeli, T. N. Heinz and P. H. Hunenberger, Measuring ^{1}H–^{1}H and ^{1}H–^{13}C RDCs in methyl groups: example of pulse sequences with numerically optimized coherence transfer schemes, *J. Magn. Reson.*, 2005, **172(1)**, 36–47.
71. P. Permi and A. Annila, Transverse relaxation optimised spin-state selective NMR experiments for measurement of residual dipolar couplings, *J. Biomol. NMR*, 2000, **16(3)**, 221–227.
72. R. A. Engh and R. Huber, Accurate bond and angle parameters for X-ray protein structure refinement, *Acta Cryst.*, 1991, **A47**, 392–400.
73. S. Vijay-Kumar, C. E. Bugg and W. J. Cook, Structure of ubiquitin refined at 1.8 Å resolution, *J. Mol. Biol.*, 1987, **194**, 531–544.
74. K. Wuthrich, *NMR of Proteins and Nucleic Acids*, Wiley, 1986.
75. A. Kaikkonen and G. Otting, Residual dipolar ^{1}H–^{1}H couplings of methyl groups in weakly aligned proteins, *J. Am. Chem. Soc.*, 2001, **123(8)**, 1770–1771.
76. F. Cordier, A. J. Dingley and S. Grzesiek, A doublet-separated sensitivity-enhanced HSQC for the determination of scalar and dipolar one-bond J-couplings, *J. Biomol. NMR*, 1999, **13**, 175–180.
77. D. Yang, R. A. Venters, G. A. Mueller, W. Y. Choy and L. E. Kay, TROSY-based HNCO pulse sequences for the measurement of 1HN-15N, 15N-13CO, 1HN-13CO, 13CO-13C$_\alpha$ and 1HN-13C$_\alpha$ dipolar couplings in 15N, 13C, 2H-labeled proteins, *J. Biomol. NMR*, 1999, **14**, 333–343.
78. K. Ding and A. M. Gronenborn, Sensitivity-enhanced E.COSY-type HSQC experiments for accurate measurements of one-bond ^{15}N – ^{1}H$_N$ and ^{15}N – ^{13}C and two-bond ^{13}C′ – ^{1}H$_N$ residual dipolar couplings in proteins, *J. Magn. Reson*, 2002, **158(1-2)**, 173–177.
79. K. Ding and A. M. Gronenborn, Sensitivity-enhanced 2D IPAP, TROSY-anti-TROSY, and E.COSY experiments: alternatives for measuring dipolar ^{15}N–^{1}H$_N$ couplings, *J. Magn. Reson*, 2003, **163**, 208–214.
80. R. L. McFeeters, C. A. Fowler, V. V. Gaponenko and R. A. Byrd, Efficient and precise measurement of ^{1}H$_\alpha$ – ^{13}C$_\alpha$, C$_\alpha$–C′, C_α–C_β and H(N)–N residual dipolar couplings from 2D H(N)–N correlation spectra, *J. Biomol. NMR*, 2005, **31(1)**, 35–47.
81. P. Permi, Two simple nmr experiments for measuring dipolar couplings in asparagine and glutamine side chains, *J. Magn. Reson.*, 2001, **153(2)**, 267–272.
82. L. Wang and B. R. Donald, Analysis of a systematic search-based algorithm for determining protein backbone structure from a minimal number of residual dipolar couplings, *IEEE Computer Society Bioinformatics Conference,* Stanford University, Stanford CA, 2004, 319–330.

83. N. Tjandra and A. Bax, Measurement of dipolar contributions to $^{1}J_{C\alpha H\alpha}$ splittings from magnetic-field dependence of J modulation in two-dimensional NMR spectra, *J. Magn. Reson.*, 1997, **124(2)**, 512–515.
84. D. Yang, J. R. Tolman, N. K. Goto and L. E. Kay, An HNCO-based pulse scheme for the measurement of, $13C_{\alpha}$–$1H_{\alpha}$ one-bond dipolar couplings in ^{15}N, ^{13}C labeled proteins, *J. Biomol. NMR*, 1998, **12**, 325–332.
85. A. Bax and M. Ikura, An efficient 3D NMR technique for correlating the proton and ^{15}N backbone amide resonances with the alpha-carbon of the preceding residue in uniformly $^{15}N/^{13}C$ enriched proteins, *J. Biomol. NMR*, 1991, **1**, 99–104.
86. T. K. Hitchens, S. A. McCallum and G. S. Rule, A J^{CH}-modulated 2D (HACACO)NH pulse scheme for quantitative measurement of $^{13}C_{\alpha}$–$^{1}H_{\alpha}$ couplings in ^{15}N, ^{13}C-labeled proteins, *J. Magn. Reson.*, 1999, **140(l)**, 281–284.
87. P. Wurtz, K. Fredriksson and P. Permi, A set of HA-detected experiments for measuring scalar and residual dipolar couplings, *J. Biomol. NMR*, 2005, **31(4)**, 321–330.
88. T. Parella and J. Belloc, Spin-state-selective excitation in selective 1D inverse NMR experiments, *J. Magn. Reson.*, 2001, **148(1)**, 78–87.
89. M. Ottiger and A. Bax, Determination of relative N–HN, N–C′, C–C′, and C–H effective bond lengths in a protein by NMR in a dilute liquid crystalline phase, *J. Am. Chem. Soc.*, 1998, **120(2)**, 12334–12341.
90. A. W. Giesen, L. C. Bae, C. L. Barrett, J. A. Chyba, M. M. Chaykovsky, M. C. Cheng, J. H. Murray, E. J. Oliver, S. M. Sullivan, J. M. Brown and S. W. Homans, ^{1}H-filtered correlation experiments for assignment and determination of coupling constants in backbone labelled proteins, *J. Biomol. NMR*, 2002, **22(1)**, 21–26.
91. P. Permi, T. Sorsa, I. I. Kilpelainen and A. Annila, H^{N}(α/β-COCA-J) experiment for measurement of $^{1}J_{C'\,C\alpha}$ couplings from two-dimensional [^{15}N, ^{1}H] correlation spectrum, *J. Magn. Reson.*, 1999, **141(1)**, 44–51.
92. M. Salzmann, K. Pervushin, G. Wider, H. Senn and K. Wuthrich, Trosy in triple-resonance experiments: new perspectives for sequential NMR assignment of large proteins, *Proc. Natl. Acad. Sci. USA*, 1998, **95(23)**, 13585–13590.
93. G. M. Clore, A. M. Gronenborn and N. Tjandra, Direct structure refinement against residual dipolar couplings in the presence of rhombicity of unknown magnitude, *J. Magn. Reson.*, 1998, **131**, 159–162.
94. G. M. Clore, A. M. Gronenborn and A. Bax, A robust method for determining the magnitude of the fully asymmetric alignment tensor of oriented macromolecules in the absence of structural information, *J. Magn. Reson.*, 1998, **133**, 216–221.
95. J. Evenas, A. Mittermaier, D. Yang and L. E. Kay, Measurement of $^{13}C_{\alpha} - {}^{13}C_{\beta}$ dipolar couplings in ^{15}N,^{13}C,^{2}H-labeled proteins: application to domain orientation in maltose binding protein, *J. Am. Chem. Soc.*, 2001, **123(12)**, 2858–2864.
96. A. Mittermaier and L. E. Kay, χ_1 torsion angle dynamics in proteins from dipolar couplings, *J. Am. Chem. Soc.*, 2001, **123(28)**, 6892–6903.
97. P. Permi, P. R. Rosevear and A. Annila, A set of HNCO-based experiments for measurement of residual dipolar couplings in 15N, 13C,(2H)-labeled proteins, *J. Biomol. NMR*, 2000, **17**, 43–54.
98. P. Permi, S. Heikkinen, I. Kilpelainen and A. Annila, Measurement of $^{1}J_{NC'}$ and $^{2}J_{HN-C'}$ couplings from spin-state-selective two-dimensional correlation spectrum, *J. Magn. Reson.*, 1999, **140(l)**, 32–40.
99. J. J. Chou, F. Delaglio and A. Bax, Measurement of one-bond ^{15}N–$^{13}C'$ dipolar couplings in medium sized proteins, *J. Biomol. NMR*, 2000, **18**, 101–105.
100. N. Tjandra, J. Marquardt and G. M. Clore, Direct refinement against proton–proton dipolar couplings in NMR structure determination of macromolecules, *J. Magn. Reson*, 2000, **142(2)**, 393–396.
101. G. Otting, M. Ruckert, M. H. Levitt and A. Moshref, NMR experiments for the sign determination of homonuclear scalar and residual dipolar couplings, *J. Biomol. NMR*, 2000, **16(4)**, 343–346.

102. W. Peti and C. Griesinger, Measurement of magnitude and sign of H, H-dipolar couplings in proteins, *J. Am. Chem. Soc.*, 2000, **122(16)**, 3975–3976.
103. M. Cai, H. Wang, E. T. Olejniczak, R. P. Meadows, A. H. Gunasekera, N. Xu and S. W. Fesik, Accurate measurement of H^N–H^α residual dipolar couplings in proteins, *J. Magn. Reson.*, 1999, **139**, 451–453.
104. F. Tian, C. A. Fowler, E. R. Zartler, F. A. Jenney Jr., M. W. Adams and I. H. Prestegard, Direct measurement of ^1H–^1H dipolar couplings in proteins: a complement to traditional NOE measurements, *J. Biomol. NMR*, 2000, **18(1)**, 23–31.
105. F. Tian, P. J. Bolon and J. H. Prestegard, Intensity-based measurement of homonuclear residual dipolar couplings from CT-COSY, *J. Am. Chem. Soc.*, 1999, **121(33)**, 7712–7713.
106. Z. Wu and A. Bax, Measurement of long-range ^1H–^1H dipolar couplings in weakly aligned proteins, *J. Am. Chem. Soc.*, 2002, **124(33)**, 9672–9673.
107. N. Sibille, B. Bersch, J. Coves, M. Blackledge and B. Brutscher, Side chain orientation from methyl ^1H–^1H residual dipolar couplings measured in highly deuterated proteins, *J. Am. Chem. Soc.*, 2002, **124(49)**, 14616–14625.
108. E. de Alba, M. Suzuki and N. Tjandra, Simple multidimensional NMR experiments to obtain different types of one-bond dipolar couplings simultaneously, *J. Biomol. NMR*, 2001, **19**, 63–67.
109. V. Vijayan and M. Zweckstetter, Simultaneous measurement of protein one-bond residual dipolar couplings without increased resonance overlap, *J. Magn. Reson.*, 2005, **174(2)**, 245–253.
110. H. L. Wienk, M. M. Martinez, G. N. Yalloway, J. M. Schmidt, C. Perez, H. Ruterjans and F. Lohr, Simultaneous measurement of protein one-bond and two-bond nitrogen-carbon coupling constants using an internally referenced quantitative J-correlated [^{15}N,^1H]-TROSY-HNC experiment, *J. Biomol. NMR*, 2003, **25(2)**, 133–145.
111. J. H. Prestegard, H. Valafar, J. Glushka and F. Tian, Nuclear magnetic resonance in the era of structural genomics, *Biochemistry*, 2001, **40(30)**, 8677–8685.
112. Y. X. Wang, J. L. Marquardt, P. Wingfield, S. J. Stahl, S. Lee-Huang, D. Torchia and A. Bax, Simultaneous measurement of ^1H–^{15}N, ^1H–$^{13}C'$, and ^{15}N–$^{13}C'$ dipolar couplings in a perdeuterated 30 kDa protein dissolved in a dilute liquid crystalline phase, *J. Am. Chem. Soc.*, 1998, **120(29)**, 7385–7386.
113. K. Ding and A. M. Gronenborn, Simultaneous and accurate determination of one-bond $^{15}N - {}^{13}C'$ and two-bond $^1H_N - {}^{13}C$ dipolar couplings, *J. Am. Chem. Soc.*, 2003, **125(38)**, 11504–11505.
114. M. Ottiger, F. Delaglio, J. L. Marquardt, N. Tjandra and A. Bax, Measurement of dipolar couplings for methylene and methyl sites in weakly oriented macromolecules and their use in structure determination, *J. Magn. Reson.*, 1998, **134(2)**, 365–369.
115. M. Ottiger and A. Bax, How tetrahedral are methyl groups in proteins? a liquid crystal NMR study, *J. Am. Chem. Soc.*, 1999, **121(19)**, 4690–4695.
116. D. Yang and L. E. Kay, Improved 1HN-detected triple resonance TROSY-based experiments, *J. Biomol. NMR*, 1999, **13**, 3–9.
117. R. Weisemann, H. Ruterjans, H. Schwalbe, J. Schueler, W. Bermel and C. Griesinger, Determination of HN, H_α and HN, C′ coupling constants in ^{13}C, ^{15}N-labeled proteins, *J. Biomol. NMR*, 1994, **4**, 231–240.
118. K. Ding and A. M. Gronenborn, Protein backbone ^1H_N–$^{13}C_\alpha$ and ^{15}N–$^{13}C_\alpha$ residual dipolar and J couplings: new constraints for NMR structure determination, *J. Am. Chem. Soc.*, 2004, **126(20)**, 6232–6233.
119. T. Carlomagno, W. Peti and C. Griesinger, A new method for the simultaneous measurement of magnitude and sign of $^1D_{CH}$ and $^1D_{HH}$ dipolar couplings in methylene groups, *J. Biomol. NMR*, 2000, **17**, 99–109.
120. J. J. Chou and A. Bax, Protein side-chain rotamers from dipolar couplings in a liquid crystalline phase, *J. Am. Chem. Soc.*, 2001, **123**, 3844–3845.
121. S. Grzesiek and A. Bax, Correlating backbone amide and side chain resonances in larger proteins by multiple relayed triple resonance NMR, *J. Am. Chem. Soc.*, 1992, **114**, 6291–6293.
122. S. Meier, D. Haussinger, P. Jensen, M. Rogowski and S. Grzesiek, High-accuracy residual ^1H_N–^{13}C and ^1H_N–^1H_N dipolar couplings in perdeuterated proteins, *J. Am. Chem. Soc.*, 2003, **125(1)**, 44–45.

123. H. Kuboniwa, S. Grzesiek, F. Delaglio and A. Bax, Measurement of H^N–H^α J couplings in calcium-free calmodulin using new 2D and 3D water-flip-back methods, *J. Biomol. NMR*, 1994, **4(6)**, 871–878.
124. P. Permi, Measurement of residual dipolar couplings from $^1H_\alpha$ to $^{13}C_\alpha$ and ^{15}N using a simple HNCA-based experiment, *J. Biomol. NMR*, 2003, **27(4)**, 341–349.
125. A. Eletsky, O. Moreira, H. Kovacs and K. Pervushin, A novel strategy for the assignment of side-chain resonances in completely deuterated large proteins using ^{13}C spectroscopy, *J. Biomol. NMR*, 2003, **26(2)**, 167–179.
126. B. Vogeli, H. Kovacs and K. Pervushin, Measurements of side-chain ^{13}C–^{13}C residual dipolar couplings in uniformly deuterated proteins, *J. Am. Chem. Soc.*, 2004, **126(8)**, 2414–2420.
127. E. Miclet, J. Boisbouvier and A. Bax, Measurement of eight scalar and dipolar couplings for methine–methylene pairs in proteins and nucleic acids, *J. Biomol. NMR*, 2005, **31(3)**, 201–216.
128. E. Miclet, D. C. Williams Jr., G. M. Clore, D. L. Bryce, J. Boisbouvier and A. Bax, Relaxation-optimized NMR spectroscopy of methylene groups in proteins and nucleic acids, *J. Am. Chem. Soc.*, 2004, **126(34)**, 10560–10570.
129. L. Zidek, H. Wu, J. Feigon and V. Sklenar, Measurement of small scalar and dipolar couplings in purine and pyrimidine bases, *J. Biomol. NMR*, 2001, **21(2)**, 153–160.
130. J. Yan, T. Corpora, P. Pradhan and J. H. Bushweller, MQ-hCN-based pulse sequences for the measurement of $^{13}C1'$–$^1H1'$, $^{13}C1'$–^{15}N, $^1H1'$–^{15}N, $^{13}C1'$–$^{13}C2'$, $^1Hl'$–$^{13}C2'$, $^{13}C6/8$–$^1H6/8$, $^{13}C6/8$–^{15}N, $^1H6/8$–^{15}N, $^{13}C6$–$^{13}C5$, $^1H6$–$^{13}C5$ dipolar couplings in ^{13}C, ^{15}N-labeled DNA (and RNA), *J. Biomol. NMR*, 2002, **22(1)**, 9–20.
131. R. Fiala, F. Jiang and V. Sklenar, Sensitivity optimized HCN and HCNCH experiments for $^{13}C/^{15}N$ labeled oligonucleotides, *J. Biomol. NMR*, 1998, **12(3)**, 373–383.
132. R. Fiala, J. Czernek and V. Sklenar, Transverse relaxation optimized triple-resonance NMR experiments for nucleic acids, *J. Biomol. NMR*, 2000, **16(4)**, 291–302.
133. V. Sklenar, T. Dieckmann, S. E. Butcher and J. Feigon, Optimization of triple-resonance HCN experiments for application to larger RNA oligonucleotides, *J. Magn. Reson.*, 1998, **130(1)**, 119–124.
134. W. Hu, Y. Q. Gosser, W. Xu and D. J. Patel, Novel 2D and 3D multiple-quantum bi-directional HCNCH experiments for the correlation of ribose and base protons/carbons in $^{13}C/^{15}N$ labeled RNA, *J. Biomol. NMR*, 2001, **20(2)**, 167–172.
135. J. Boisbouvier, D. L. Bryce, E. O'Neil-Cabello, E. P. Nikonowicz and A. Bax, Resolution-optimized NMR measurement of $^1D_{CH}$, $^1D_{CC}$ and $^2D_{CH}$ residual dipolar couplings in nucleic acid bases, *J. Biomol. NMR*, 2004, **30**, 287–301.
136. C. P. Jaroniec, J. Boisbouvier, I. Tworowska, E. P. Nikonowicz and A. Bax, Accurate measurement of ^{15}N–^{13}C residual dipolar couplings in nucleic acids, *J. Biomol. NMR*, 2005, **31(3)**, 231–241.
137. W. Hu, S. Bouaziz, E. Skripkin and A. Kettani, Determination of $^3J(H3'_i, P_{i+1})$ and $^3J(H5'_i/5''_i, P_i)$ coupling constants in ^{13}C-labeled nucleic acids using constant-time HMQC, *J. Magn. Reson.*, 1999, **139(1)**, 181–185.
138. T. Szyperski, C. Fernandez, A. Ono, K. Wuthrich and M. Kainosho, The 2D {31P} spin-echo-difference constant-time [^{13}C, ^1H]-HMQC experiment for simultaneous determination of $^3J_{H3'P}$ and $^3J_{C4'P}$ in ^{13}C-labeled nucleic acids and their protein complexes, *J. Magn. Reson.*, 1999, **140(2)**, 491–494.
139. Z. Wu, N. Tjandra and A. Bax, Measurement of 1H3'–31P dipolar couplings in a DNA oligonucleotide by constant-time NOESY difference spectroscopy, *J. Biomol. NMR*, 2001, **19(4)**, 367–370.
140. P. Vallurupalli and P. B. Moor, Measurement of H2′–C2′ and H3′–C3′ dipolar couplings in RNA molecules, *J. Biomol. NMR*, 2002, **24(1)**, 63–66.
141. C. G. Hoogstraten and A. Pardi, Measurement of carbon-phosphorus J coupling constants in RNA using spin-echo difference constant-time HCCH-COSY, *J. Magn. Reson.*, 1998, **133(l)**, 236–240.
142. E. Miclet, E. O'Neil-Cabello, E. P. Nikonowicz, D. Live and A. Bax, ^1H–^1H dipolar couplings provide a unique probe of RNA backbone structure, *J. Am. Chem. Soc.*, 2003, **125(51)**, 15740–15741.

143. E. O'Neil-Cabello, D. L. Bryce, E. P. Nikonowicz and A. Bax, Measurement of five dipolar couplings from a single 3D NMR multiplet applied to the study of RNA dynamics, *J. Am. Chem. Soc.*, 2004, **126(1)**, 66–67.
144. C. J. Langmead and B. R. Donald, An Expectation/Maximization nuclear vector replacement algorithm for automated NMR resonance assignments, *J. Biomol. NMR*, 2004, **29(2)**, 111–138.
145. J. C. Hus, J. J. Prompers and R. Bruschweiler, Assignment strategy for proteins with known structure, *J. Magn. Reson.*, 2002, **157**, 119–123.
146. Y. S. Jung and M. Zweckstetter, Backbone assignment of proteins with known structure using residual dipolar couplings, *J. Biomol. NMR*, 2004, **30**, 25–35.
147. H. M. Al-Hashimi, A. Gorin, A. Majumdar, Y. Gosser and D. J. Patel, Towards structural genomics of RNA: rapid NMR resonance assignment and simultaneous RNA tertiary structure determination using residual dipolar couplings, *J. Mol. Biol.*, 2002, **318(3)**, 637–649.
148. F. Tian, H. Valafar and J. H. Prestegard, A dipolar coupling based strategy for simultaneous resonance assignment and structure determination of protein backbones, *J. Am. Chem. Soc.*, 2001, **123(47)**, 11791–11796.
149. J. Meiler and D. Baker, Rapid protein fold determination using unassigned NMR data, *Proc. Natl. Acad. Sci. USA*, 2003, **100**, 15404–15409.
150. J. Meiler and D. Baker, The fumarate sensor DcuS: progress in rapid protein fold elucidation by combining protein structure prediction methods with NMR spectroscopy, *J. Magn. Reson.*, 2005, **173**, 310–316.
151. T. H. Cormen, C. E. Leiserson, R. L. Rivest and C. Stein, *Introduction to Algorithms*, The MIT Press, Cambridge, MA, 2001.
152. A. P. Dempster, N. M. Larid and D. B. Rubin, Maximum likelihood from incomplete data via the EM-algorithm, *J. R. Statist. Sco. B*, 1977, **39**, 1–38.
153. J. A. Losonczi, M. Andrec, M. W. Fischer and J. H. Prestegard, Order matrix analysis of residual dipolar couplings using singular value decomposition, *J. Magn. Reson.*, 1999, **138(2)**, 334–342.
154. Y. S. Jung and M. Zweckstetter, MARS-robust automatic backbone assignment of proteins, *J. Biomol. NMR*, 2004, **30**, 11–23.
155. N. Tjandra, J. G. Omichinski, A. M. Gronenborn, G. M. Clore and A. Bax, Use of dipolar ^{1}H–^{15}N and ^{1}H–^{13}C couplings in the structure determination of magnetically oriented macromolecules in solution, *Nat. Struct. Biol.*, 1997, **4**, 732–738.
156. G. M. Clore, M. R. Starich, C. A. Bewley, M. Cai and J. Kuszewski, Impact of residual dipolar couplings on the accuracy of NMR structures determined from a minimal number of noe restraints, *J. Am. Chem. Soc.*, 1999, **121**, 6513–6514.
157. A. W. Giesen, S. W. Homans and J. M. Brown, Determination of protein global folds using backbone residual dipolar coupling and long-range NOE restraints, *J. Biomol. NMR*, 2003, **25**, 63–71.
158. G. A. Mueller, W. Y. Choy, D. Yang, J. D. Forman-Kay, R. A. Venters and L. E. Kay, Global folds of proteins with low densities of NOEs using residual dipolar couplings: application to the 370-residue maltodextrin-binding protein, *J. Mol. Biol.*, 2000, **300**, 197–212.
159. W. Y Choy, M. Tollinger, G. A. Mueller and L. E. Kay, Direct structure refinement of high molecular weight proteins against residual dipolar couplings and carbonyl chemical shift changes upon alignment: an application to maltose binding protein, *J. Biomol. NMR*, 2001, **21**, 31–40.
160. J. C. Hus, D. Marion and M. Blackledge, Determination of protein backbone using only residual dipolar couplings, *J. Am. Chem. Soc.*, 2001, **123**, 1541–1542.
161. M. Andrec, P. Du and R. M. Levy, Protein backbone structure determination using only residual dipolar couplings from one ordering medium, *J. Biomol. NMR*, 2001, **21(4)**, 335–347.
162. C. A. Rohl and D. Baker, De Novo determination of protein backbone structure from residual dipolar couplings using ROSETTA, *J. Am. Chem. Soc.*, 2002, **124(11)**, 2723–2729.
163. W. J. Wedemeyer, C. A. Rohl and H. A. Scheraga, Exact solutions for chemical bond orientations from residual dipolar couplings, *J. Biomol. NMR*, 2002, **22**, 137–151.
164. A. C. Fowler, F. Tian, H. M. Al-Hashimi and J. H. Prestegard, Rapid determination of protein folds using residual dipolar couplings, *J. Mol. Biol.*, 2000, **304(3)**, 447–460.

165. L. Wang and B. R. Donald, An efficient and accurate algorithm for assigning nuclear overhauser effect restraints using a rotamer library ensemble and residual dipolar couplings, *IEEE Computer Society Bioinformatics Conference,* Stanford University, Stanford CA, 2005, 189–202.
166. L. Wang and B. R. Donald, An algebraic geometry approach to backbone structure determination from NMR data, *IEEE Computer Society Bioinformatics Conference,* Stanford University, Stanford CA, 2005, 235–246.
167. Y. Qu, J. T. Guo, V. Olman and Y. Xu, Protein fold recognition using residual dipolar coupling data, *Nucleic Acids Research*, 2004, **32**, 551–561.
168. J. Meiler, W. Peti and C. Griesinger, Dipocoup: a versatile program for 3d-structure homology comparison based on residual dipolar couplings and pseudocontact shifts, *J. Biomol. NMR*, 2000, **17**, 283–294.
169. A. Annila, H. Aitio, E. Thulin and T. Drakenberg, Recognition of protein folds via dipolar couplings, *J. Biomol. NMR*, 1999, **14**, 223–230.
170. M. Andrec, P. Du and R. M. Levy, Protein structural motif recognition via NMR residual dipolar couplings, *J. Am. Chem. Soc.*, 2001, **123**, 1222–1229.
171. C. Langmead and B. R. Donald. High-throughput 3D structural homology detection via NMR resonance assignment, *IEEE Computer Society Bioinformatics Conference,* Stanford University, Stanford CA, 2004, 278–289.
172. C. Tanford, Protein denaturation. part C. theoretical models for the mechanism of denaturation, *Adv. Protein Chem.*, 1970, **24**, 1–95.
173. N. C. Fitzkee and G. D. Rose, Reassessing random-coil statistics in unfolded proteins, *Proc. Natl. Acad. Sci. USA*, 2004, **101**, 12497–12502.
174. A. K. Jha, A. Colubri, K. F. Freed and T. R. Sosnick, Statistical coil model of the unfolded state: resolving the reconciliation problem, *Proc. Natl. Acad. Sci. USA*, 2005, **102**, 13099–13104.
175. P. J. Plory, *Statistical Mechanics of Chain Molecules*, Oxford University Press, New York, 1988.
176. I. S. Millett, S. Doniach and K. W. Plaxco, Toward a taxonomy of the denatured state: small angle scattering studies of unfolded proteins, *Adv. Protein Chem.*, 2002, **62**, 241–262.
177. D. Shortle and M. S. Ackerman, Persistence of native-like topology in a denatured protein in 8 M urea, *Science*, 2001, **293**, 487–489.
178. S. Ohnishi, A. L. Lee, M. H. Edgell and D. Shortle, Direct demonstration of structural similarity between native and denatured eglin c, *Biochemistry*, 2004, **43**, 4064–4070.
179. S. Fieber, W. Kristjansdottir and F. M. Poulsen, Short-range, long-range and transition state interactions in the denatured state of acbp from residual dipolar couplings, *J. Mol. Biol.*, 2004, **339**, 1191–1199.
180. M. Louhivuori, K. Paakkonen, K. Fredriksson, P. Permi, J. Lounila and A. Annila, On the origin of residual dipolar couplings from denatured proteins, *J. Am. Chem. Soc.*, 2003, **125**, 15647–15650.
181. J. M. Ding, K. Louis and A. M. Gronenborn, Insights into conformation and dynamics of protein GB1 during folding and unfolding by NMR, *J. Mol. Biol.*, 2004, **335**, 1299–1307.
182. R. Mohana-Borges, N. K. Goto, G. J. Kroon, H. J. Dyson and P. E. Wright, Structural characterization of unfolded states of apomyoglobin using residual dipolar couplings, *J. Mol. Biol.*, 2004, **340**, 1131–1142.
183. M. S. Ackerman and D. Shortle, Molecular alignment of denatured states of staphylococcal nuclease with strained polyacry-lamide gels and surfactant liquid crystalline phases, *Biochemistry*, 2002, **41**, 3089–3095.
184. H. J. Sass, G. Musco, S. J. Stahl, P. T. Wingfield and S. Grzesiek, Solution NMR of proteins within polyacrylamide gels: diffusional properties and residual alignment by mechanical stress or embedding of oriented purple membranes, *J. Biomol. NMR*, 2000, **18**, 303–309.
185. W. Feller, *An Introduction to Probability Theory and Its Applications*, Wiley, New York, 1970.
186. S. Chandrasekhar, Stochastic problems in physics and astronomy, *Rev. Mod. Phys.*, 1943, **15**, 1–89.
187. L. Wang and H. Yan, NMR studies of type II human cellular retinoic acid binding protein, *Biochimica et Biophysica Acta*, 1999, **1433**, 240–252.

188. L. Wang, Y. Pang, T. Holder, J. Brender, A. V. Kurochkin and E. R. P. Zuiderweg, Functional dynamics in the active site of the ribonuclease binase, *Proc. Natl. Acad. Sci. USA*, 2001, **98**, 7684–7689.
189. F. Tian, J. L. Al-Hashimi, H. M. Craighead and J. H. Prestegard, Conformational analysis of a flexible oligosaccharide using residual dipolar couplings, *J. Am. Chem. Soc.*, 2001, **123**, 485–492.
190. B. W. Koenig, G. Kontaxis, D. C. Mitchell, J. M. Louis, B. J. Litman and A. Bax, Structure and orientation of a g protein fragment in the receptor bound state from residual dipolar couplings, *J. Mol. Biol.*, 2002, 441–161
191. H. M. Bolon, P. J. Al-Hashimi and J. H. Prestegard, Residual dipolar coupling derived orientational constraints on ligand geometry in a 53 kDa protein–ligand complex, *J. Mol. Biol.*, 1999, **293**, 107–115.
192. K. Umemoto, H. Leffler, A. Venot, H. Valafar and J. H. Prestegard, Conformational differences in liganded and unliganded states of Galectin-3, *Biochemistry*, 2003, **423**, 3688–3695.
193. E. R. Zuiderweg, Mapping protein–protein interactions in solution by NMR spectroscopy, *Biochemistry*, 2002, **41**, 1–7.
194. M. W. Fischer, J. A. Losonczi, J. L. Weaver and J. H. Prestegard, Domain orientation and dynamics in multidomain proteins from residual dipolar couplings, *Biochemistry*, 1999, **38**, 9013–9022.
195. A. T. Brunger, *XPLOR: A System for X-ray Crystallography and NMR*, Yale University Press, New Haven, 1993.
196. J. A. Lukin, G. Kontaxis, V. Simplaceanu, Y. Yuan, A. Bax and C. Ho, Quaternary structure of hemoglobin in solution, *Proc. Natl. Acad. Sci. USA*, 2003, **100**, 517–520.
197. Y. Zhang and E. R. Zuiderweg, The 70-kDa heat shock protein chaperone nucleotide-binding domain in solution unveiled as a molecular machine that can reorient its functional subdomains, *Proc. Natl. Acad. Sci. USA*, 2004, **101**, 10272–10277.
198. P. Dosset, J. C. Hus, D. Marion and M. Blackledge, A novel interactive tool for rigid-body modeling of multi-domain macro-molecules using residual dipolar couplings, *J. Biomol. NMR*, 2001, **20**, 223–231.
199. D. S. Garrett, Y. J. Seok, A. Peterkofsky, A. M. Gronenborn and G. M. Clore, Solution structure of the 40,000 Mr phosphoryl transfer complex between the N-terminal domain of enzyme I and HPr, *Nat. Struct. Biol.*, 1999, **6**, 166–173.
200. G. M. Clore and C. A. Bewley, Using conjoined rigid body/torsion angle simulated annealing to determine the relative orientation of covalently linked protein domains from dipolar couplings, *J. Magn. Reson.*, 2002, **154**, 329–335.
201. G. Cornilescu, B. R. Lee, C. C. Cornilescu, G. Wang, A. Peterkofsky and G. M. Clore, Solution structure of the phosphoryl transfer complex between the cytoplasmic a domain of the mannitol transporter II mannitol and HPr of the *Escherichia coli* phosphotransferase system, *J. Biol. Chem.*, 2002, **277**, 42289–42298.
202. N. U. Jain, T. J. Wyckoff, C. R. Raetz and J. H. Prestegard, Rapid analysis of large protein–protein complexes using NMR-derived orientational constraints: the 95 kDa complex of lpxa with acyl carrier protein, *J. Mol. Biol.*, 2004, **343**, 1379–1389.
203. C. Dominguez, R. Boelens and A. M. J. J. Bonvin, HADDOCK: a protein–protein docking approach based on biochemical or biophysical information, *J. Am. Chem. Soc.*, 2003, **125**, 1731–1737.
204. M. A. McCoy and D. F. Wyss, Structures of protein–protein complexes are docked using only NMR restraints from residual dipolar coupling, chemical shift perturbations, *J. Am. Chem. Soc.*, 2002, **124**, 2104–2105.
205. A. Dobrodumov and A. M. Gronenbornm, Filtering and selection of structural models: combining docking and NMR, *Proteins*, 2003, **53**, 18–32.
206. H. A. Gabb, R. M. Jackson and M. J. E. Sternberg, Modelling, protein docking using shape complimentarity, electrostatics, and biochemical information, *J. Mol. Biol.*, 1997, **272**, 106–112.
207. T. Matsuda, T. Ikegami, N. Nakajima, T. Yamazaki and H. Nakamura, Model building of a protein–protein complexed structure using saturation transfer and residual dipolar coupling without paired intermolecular noe, *J. Biomol. NMR*, 2004, **29**, 325–328.

This page is left intentionally blank

Index

This page is left intentionally blank